

**INTERNATIONAL CONFERENCE ON MATERIALS
heat treatment, corrosion, testing and tribology, 2023**



MTECH 2023

OCTOBER, 2 - 5, 2023, Cavtat, CROATIA

Conference Proceedings

ORGANISED BY:

Croatian Society for Heat Treatment and Surface Engineering – HDTOIP

Croatian Society for Materials Protection – HDZaMa

Croatian Society for Materials and Tribology – HDMT

Center for Non-destructive Testing – CENI

ISSN: 2584-4334



INTERNATIONAL CONFERENCE ON MATERIALS heat treatment, corrosion, testing and tribology, 2023

MTECH 2023

October 02-05, 2023, Cavtat, Croatia

ORGANISED BY

Croatian Society for Heat Treatment and Surface Engineering – HDTÖIP
Croatian Society for Materials Protection – HDZaMa
Croatian Society for Materials and Tribology – HDMT
Center for Non-destructive Testing – CENI



WITH THE SUPPORT OF

PARTNERS



SPONSORED BY



REPUBLIC OF CROATIA
Ministry of Science and Education



mtech-conf.hr



INTERNATIONAL CONFERENCE ON MATERIALS
heat treatment, corrosion, testing and tribology, 2023

IZDAVAČ/PUBLISHER:

Hrvatsko društvo za toplinsku obradu i inženjerstvo površina
Croatian Society for Heat Treatment and Surface Engineering
c/o FSB, Ivana Lučića 1, 10000 Zagreb
tel.: +385 1 616836

**GLAVNI UREDNIK
/CHIEF EDITOR:**

Dr. sc. Željko Alar, dipl. ing., redoviti profesor

**UREDNICI
/EDITORS:**

Jurica Jačan, mag. ing. mech.
Filip Žanetić, mag. ing. mech.

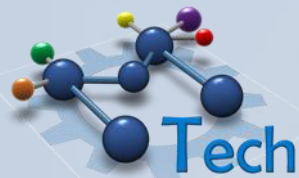
**NASLOVNICA/
COVER:**

Jurica Jačan, mag. ing. mech.

**EFC Event No. 503
ISSN: 2584-4334**

Zagreb, listopad 2023.

mtech-conf.hr



INTERNATIONAL CONFERENCE ON MATERIALS

heat treatment, corrosion, testing and tribology, 2023

SCIENTIFIC AND PROGRAM COMMITTEE

Božidar Matijević (President), Ivan Stojanović, Željko Alar, Vesna Alar, Imre Felde University of Obuda, Budapest, HU, Lauralice de Campos Franceschini Canale, University of São Paulo, Faculty of Mechanical Engineering, São Carlos, Brasil, M.T. Mathew, Ph.D., University of Illinois College, Chicago, USA, Nikolai Kobasko, USA, Damir Markučić, Duško Pavletić (RITEH), Angela Topić (FSR Mostar), Danko Ćorić, Zdravko Schauperl, Suzana Jakovljević, Mateja Šnajdar Musa (UniRi), Ivan Juraga, Helena Otmačić Ćurković (FKIT), Marko Katić, Morana Mihaljević, Johgann Wilhelm Erning (BAM), Marijana Serdar, Ivica Kladarić (UNISB), Ivan Samardžić (UNISB), Claus Qvist Jessen (Damstahl).

ORGANIZING COMMITTEE

Dario Iljkić, Suzana Jakovljević, Jurica Jančić, Tomislav Kezele, Ivica Kladarić, Marin Kurtela, Darko Landek, Johgann Wilhelm Erning (BAM), Srećko Godež (SLO), Nikola Knezović (FSR Mostar), Izabela Martinez, Morana Mihaljević, Jurica Jačan, Daniel Pustički, Filip Žanetić

TECHNICAL COMMITTEE

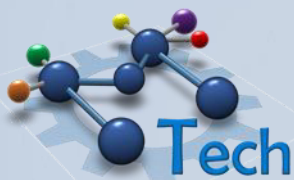
Ante Dizdar (OPT d.o.o.), Marko Rakvin (TUV Croatia), Mladen Franjković (STSI), Karla Rončević (Helios), Ivana Radić Boršić (Cortec Corporation Europe), Robert Iveković (IVEKOVIĆ-TZM), Martin Miculinić (ZIT), Branko Šeparović (Altmont), Krešimir Kekez (PA-EL)

TOPICS

Materials and processes, Materials characterization, Nanomaterials and nanotechnology, Friction, wear and lubrication, Metallurgy, Quenchants and quenching technology, Coatings, Advanced surface modification and coating technologies, Vacuum heat treatment, Heat treatment equipment, Mathematical modeling and process simulation of heat treatment, Corrosion and corrosion protection methods, Corrosion resistant materials, Non-destructive and destructive testing methods, In-service inspection, Certification and accreditation, Measurement and quality assurance

Conference Chairman

Prof. dr. sc. Božidar Matijević



INTERNATIONAL CONFERENCE ON MATERIALS

heat treatment, corrosion, testing and tribology, 2023

VENUE AND DATE

MTECH International Conference will be held at Croatia hotel, Cavtat, from **2-5 October 2023**.

Rising above a pine forested peninsula overlooking unspoiled Cavtat Bay, Hotel Croatia Cavtat is the leading five-star resort and conference center in the South Adriatic. Just 5km from Dubrovnik airport, Hotel Croatia Cavtat combines a stunning waterfront location with easy access to the halcyon treasures of the Adriatic coast. Medieval Dubrovnik across the bay is a must and less than half an hour by car, or a relaxed 45-minute boat ride away. Closer to home, we offer access to two quiet beaches – one facing Cavtat Bay, the other the crystal-clear Adriatic – an outdoor pool shaded by pine trees, a spa and excellent restaurants. It is an idyllic, design award-winning base from which to explore the region's historic charm.



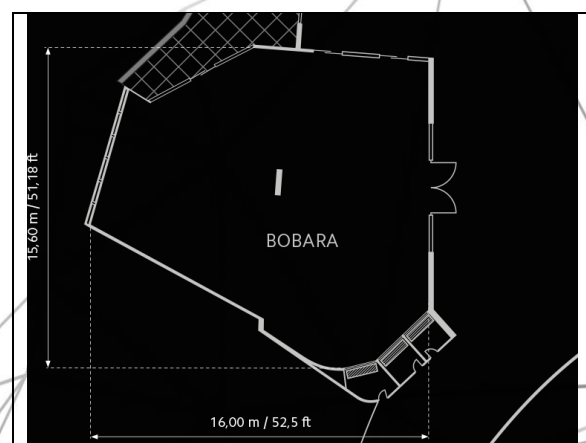
To book preferential accommodation the conference participants are kindly asked to follow the link on mtech-conf.hr under "Venue & Accommodation" using promo code MTECH2023 (deadline till 15th Sept 2023.)

EFC-Event No. 503

CONFERENCE VENUE ADDRESS:

Adress: Hotel Croatia
Frankopanska 9
20210, Cavtat
Croatia
Telephone: [+385 20 475 555](tel:+38520475555)

mail: reservations@alh.hr
Airport distance: Dubrovnik Airport 5,8 km





INTERNATIONAL CONFERENCE ON MATERIALS

heat treatment, corrosion, testing and tribology, 2023

CONFERENCE HALLS:

Halls and lobbys in Hotel Croatia used for the purpose of the conference are:

- **Ragusa conference hall** - Opening ceremony, Invited and commercial lectures, Workshops, Lectures
- **Bobara conference hall** - Lectures, Workshops, more than 500m² of exhibition space



- **Cavtat Buffet Restaurant** - Lunch
- **Gala dinner** - Spinaker Restaurant of Hotel Croatia



PROGRAMME OVERVIEW

mtech-conf.hr



INTERNATIONAL CONFERENCE ON MATERIALS

heat treatment, corrosion, testing and tribology, 2023

DAY 1 – MONDAY 02. 10. 2023.

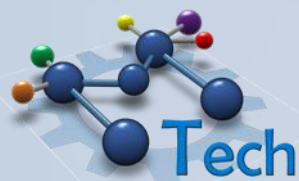
14.00 h	Workshops mtech-conf.hr	Bobara Conference Hall
18.00 h	REGISTRATION	REGISTRATION DESK
20.00 h	WELCOME RECEPTION for Conference participants	Piano bar

DAY 2 – TUESDAY 03. 10. 2023.

8.00-9.00 h	REGISTRATION DESK	Hotel Croatia Conference Reception desk
9.00-9.15 h	OPENING CEREMONY	BOBARA HALL
9.15-10.45 h	INVITED & COMMERCIAL LECTURES	BOBARA HALL
10.45-11.15 h	COFFEE BREAK	Piano bar, Lobby (Level 1)
11.15-12.30 h	LECTURES	BOBARA HALL
12.30-13.45 h	LUNCH BREAK	Restoran CAVTAT
13.45-14.45 h	POSTER SESSION	Lobby (Level 1)
9.00 – 14.45 h	EXHIBITION	Lobby (Level 1)
15.00 h	Social Event Visit to Dubrovnik	Departure from Hotel Croatia by the Bus Return to Cavtat by Galleon Tirena

DAY 3 – WEDNESDAY 04. 10. 2023.

9.00-10.30 h	INVITED & COMMERCIAL LECTURES	BOBARA HALL
10.30-11.00 h	COFFEE BREAK	Piano bar, Lobby (Level 1)
11.00-12.45 h	LECTURES	BOBARA HALL
12.45-14.00 h	LUNCH BREAK	Restoran Cavtat
14.00-15.30 h	LECTURES <i>In memoriam izv. prof. dr. sc. Vinko Šimunović</i>	BOBARA HALL
15.30-16.00 h	COFFEE BREAK	Piano bar, Lobby (Level 1)
16.00-17.30 h	LECTURES	BOBARA HALL
9.00-17.30 h	EXHIBITION	Lobby (Level 1)
20.00 h	GALA DINNER	Spinaker Restaurant of Hotel Croatia



INTERNATIONAL CONFERENCE ON MATERIALS

heat treatment, corrosion, testing and tribology, 2023

DAY 4 – THURSDAY 05. 10. 2023.

9.00-10.30 h	INVITED & COMMERCIAL LECTURES	BOBARA HALL
10.30-11.00 h	COFFEE BREAK	Piano bar, Lobby (Level 1)
9.00 – 11.00 h	EXHIBITION	Lobby (Level 1)
11.00-11.30 h	The Commemoration for prof. dr. sc. Božidar Liščić	BOBARA HALL
11.30-12.00 h	THE CONFERENCE CLOSING CEREMONY	BOBARA HALL

PROGRAMME

DAY 2 – TUESDAY 03. 10. 2023.

TIME / EVENT / LOCATION		
8.30-9.00 h	REGISTRATION DESK	Hotel Croatia Conference Reception desk
9.00-9.15 h	OPENING CEREMONY	BOBARA HALL
9.15-10.45 h	INVITED & COMMERCIAL LECTURES	BOBARA HALL
CHAIRMEN: dr. sc. Božidar Matijević , dr. sc. Ivan Stojanović		
INVITED LECTURE: Wilhelm Erning : "GRABENKORROSION": HOW SCIENTIFIC DEBATE LEADS TO AN SOLUTION. AND MODERN FAILURES DUE TO NEGLECTION OF WELL DESCRIBED FACTS		
INVITED LECTURE: Imre Felde : APPLICATION OF MACHINE LEARNING FOR CHARACTERIZATION OF TRANSIENT HEAT TRANSFER		
COMMERCIAL LECTURES: Trokut Test Group		
10.45-11.15 h	COFFEE BREAK	Piano bar, Lobby (Level 1)
11.15-12.30 h	LECTURES	BOBARA HALL
CHAIRMEN: dr. sc. Željko Alar , dr. sc. Damir Markučić		
DEPOSITION OF PACVD TiN COATING ON ADDITIVELY MANUFACTURED TITANIUM ALLOY Jurica Jačan, Darko Landek, Miho Klaić		
BORIDE LAYER GROWTH KINETICS ON 42CRMO4 STEEL Filip Žanetić, Božidar Matijević, Darko Landek, Igor Vukić		
VpCI FOR MULTIMETAL PROTECTION IN HEATING SYSTEMS Ivana Radić Boršić, Ivan Stojanović, Marin Kurtela, Vesna Alar, Boris. A. Mikšić		
KONZERVACIJA VATRENOG ORUŽJA PRIMJENOM ISPARAVAJUĆIH INHIBITORA KOROZIJE Katarina Sabelja, Ivan Leutar, Mirko Jakopčić		



INTERNATIONAL CONFERENCE ON MATERIALS

heat treatment, corrosion, testing and tribology, 2023

12.30-13.45 h

LUNCH BREAK

13.45-14.45 h

POSTER SESSION

Lobby (Level 1)

THE EFFECT OF SHOT-PEENING ON BENDING FATIGUE FAILURE IN CARBURIZED SPUR GEARS

Ivan Čular, Krešimir Vučković, Željko Alar, Srećko Glodež

THE INFLUENCE OF APPLYING PVD COATINGS ON ADHESION WEAR RESISTANCE OF HARDENING AND TEMPERING STEEL C45E

Ivica Kladarić, Stjepan Golubić, Slavica Kladarić, Andrijana Milinović

FAILURE ANALYSIS OF THE HAY TEDDER

Tomislav Vukes, Suzana Jakovljević

PROPERTIES OF WATER-BASED COATINGS FOR WOOD BURNING STOVE PROTECTION

Borna Škrlec, Ivan Stojanović, Vesna Alar, Marin Kurtela

EXPERIMENTAL DETERMINATION OF RESIDUAL STRESSES ON BUTT WELDS OF AL-MG ALLOYS OBTAINED WITH MIG WELDING

Mislav Štefok, Ivica Garašić, Maja Jurica, Vedran Jurlina

DEPENDENCE OF SPOT-WELDED JOINT GEOMETRY ON ANTI-CORROSIVE PROPERTIES OF CONVERSION COATING AND EPOXY-POLYESTER POWDER COATING

ANNA POROPAT, IVAN STOJANOVIĆ

MATHEMATICAL MODELLING OF TEMPERED HARDNESS OF QUENCHED STEEL

Dario Iljkić, Sunčana Smokvina Hanza, Božo Smoljan, Dario Kvrđić

VERIFICATION OF PAUT SYSTEM FOR AT RAIL WELD TESTING

Morana Mihaljević, Tomislav Kezele, Jure Burnać

EFFECT OF AL AND AG NANOPARTICLES ON THE ANTICORROSION AND ANTIBACTERIAL PROPERTIES OF EPOXY COATING

Marina Samardžija, Vesna Alar, Vedrana Špada, Suzana Jakovljević, Biserka Runje

PROJECT "SMART PLANT FOR DRYING LIQUID COATINGS"

Mirta Logar, Ivan Stojanović, Ivan Juraga, Zdenka Keran

COMPARISON OF DIFFERENT TESTING MACHINE CONTROL IN STATIC TENSILE TESTING DURING COLD DEFORMATION

Tin Brlić, Stoja Rešković, Ivan Jandrić, Željko Alar, Branko Grizelj, Lorena Mrkobrada

EXPLORING ORGANIZATIONAL COMPETENCE IN LABORATORY ENVIRONMENT: A HOLISTIC APPROACH

Branimir Buntak, Željko Alar

15.00 h

Visit to Dubrovnik



INTERNATIONAL CONFERENCE ON MATERIALS

heat treatment, corrosion, testing and tribology, 2023

DAY 3 – WEDNESDAY 04. 10. 2023.

TIME / EVENT / LOCATION		
9.00-10.30 h	INVITED & COMMERCIAL LECTURES	BOBARA HALL
CHAIRMEN: dr. sc. Alar Željko , dr. sc. Damir Markučić		
INVITED LECTURE Mathew T. Mathew: TRIBOCORROSION ASPECTS OF BIOMEDICAL IMPLANTS: CURRENT STATUS AND NEW DIRECTIONS		
GUEST LECTURE: Pascal Collet: THE EFC, A FEDERATION FOR ALL CORROSION SPECIALISTS AND EXPERTS IN MATERIAL SUSTAINABILITY		
COMMERCIAL LECTURE: Cortec Corporation		
10.30-11.00 h	COFFEE BREAK	Piano bar, Lobby (Level 1)
11.00-12.45 h	LECTURES	BOBARA HALL
CHAIRMEN: dr. sc. Darko Landek , dr. sc. Morana Mihaljević		
COMPARISON OF VARIOUS MINERAL AND VEGETABLE OILS AS QUENCHING MEDIA IN THE HARDENING PROCESS Izabela Martinez, Božidar Matijević, Tonča Čaleta Prolić		
EFFECT OF HEAT TREATMENT ON MECHANICAL AND CORROSION PROPERTIES OF ALSI1MGMN ALUMINUM ALLOY Darko Landek, Marin Kurtela, Domagoj Fekonja, Jurica Jačan		
COMMENTS ON ULTRASONIC THICKNESS MEASUREMENT DEVIATIONS Damir Markučić		
PA ULTRASONIC TESTING OF AT WELD JOINTS IN RAILS Aleksandar Dragojević, Ivica Garašić, Tomislav Kezele		
ULTRASONIC CHARACTERIZATION OF ADDITIVELY MANUFACTURED SAMPLE Maria Grozdanić, Morana Mihaljević		
RISK ASSESSMENT OF PRESSURE VESSELS BY USING FRACTURE MECHANICS AND ADVANCED ULTRASONIC TESTING Mirjana Opačić, Aleksanda Sedmak, Gordana Bakić, Nenad Milošević, Nikola Milovanović		
12.45-14.00 h	LUNCH BREAK	



INTERNATIONAL CONFERENCE ON MATERIALS

heat treatment, corrosion, testing and tribology, 2023

DAY 3 – WEDNESDAY 04. 10. 2023.

14.00-15.30 h

LECTURES

BOBARA HALL

CHAIRMEN: dr. sc. **Ivan Stojanović**, dr. sc. **Vesna Alar**

In memoriam izv. prof. dr. sc Vinko Šimunović

ANALYSIS OF ELECTRICAL RESISTANCE OF ELASTOMER COMPONENTS OF THE FASTENING SYSTEMS IN URBAN RAILWAY TRACKS

Katarina Vranešić, Stjepan Lakušić, Marijana Serdar, Vesna Alar

TESTING OF GALVANIC CORROSION IN A SALT ATMOSPHERE

Ivan Stojanović, Vesna Alar, Marin Kurtela

ALUMINIUM NANOCOMPOSITES EPOXY COATING FOR ANTICORROSION AND ANTIBACTERIAL PROTECTION

Marina Samardžija, Vesna Alar, Ivan Stojanović, Vedrana Špada, Marin Kurtela

DRYING PARAMETERS OF WATER-BORNE COATINGS

Ivan Stojanović, Vesna Alar, Marin Kurtela, Ivan Juraga, Mirta Logar, Ivan Fatović

CORROSION PROPERTIES OF AA5083 IN MARINE ENVIRONMENT UNDER STAGNANT AND FLOW CONDITIONS

Lea Lokas, Vesna Alar

15.30-16.00 h

COFFEE BREAK

Piano bar, Lobby (Level 1)

16.00-17.30 h

LECTURES

BOBARA HALL

CHAIRMEN: dr. sc. **Ivica Kladarić**, dr. sc. **Danko Ćorić**

SURFACE HARDNESS UNIFORMITY OF THE HARDNESS REFERENCE BLOCKS PRODUCED BY SLM TECHNOLOGY AND HEAT TREATMENT

Daniel Pustički, Željko Alar

ANNEALING OF THICK-SOLID WELDED SHEETS TO REDUCE RESIDUAL STRESSES

Darko Landek, Ivica Garašić, Mislav Štefok, Jurica Jačan

THE INFLUENCE OF DIFFERENT FOAMING AGENTS ON ALUMINIUM FOAM PORE SIZE

Tomislav Rodinger, Danko Ćorić

ANALYSIS OF WELDED LAYER WEAR ON HELICOPTER SLIDE LINER

Darko Landek, Anita Peran, Mirko Jakopčić

MATERIAL CHARACTERIZATION OF THE FREE-FORGED MACHETE

Andrija Cestar, Vera Rede, Helena Lukšić

9.00 – 17.30 h

EXHIBITION

20.00 h

GALA DINNER

Spinaker Restaurant of Hotel Croatia



INTERNATIONAL CONFERENCE ON MATERIALS

heat treatment, corrosion, testing and tribology, 2023

DAY 4 – THURSDAY 05. 10. 2023.

TIME / EVENT / LOCATION		
9.00-10.30 h	INVITED & COMMERCIAL LECTURES	BOBARA HALL
CHAIRMEN: dr. sc. Alar Željko , dr. sc. Damir Markučić		
INVITED LECTURE Stefan Valkov: ELECTRON-BEAM PROCESSING OF METALS AND ALLOYS – TECHNIQUES AND TRENDS		
Zoltan Koloszvary		
COMMERCIAL LECTURE: MESA Electronic GmbH		
APPLICATION OF VISCOELASTIC COATINGS BASED ON POLYISOBUTENE Sven Radimiri		
QUALITY EVALUATION OF CORROSION PROTECTIVE SYSTEMS IN EXPLOITATION CONDITIONS IN INDUSTRY Zoran Čeralinac, Tomislav Karažija, Dijana Vrsaljko		
OVERVIEW OF MODIFICATION AND COATING OF SURFACE Božidar Matijević, Izabela Martinez		
10.30-11.00 h	COFFEE BREAK	Piano bar, Lobby (Level 1)
11.00-11.30 h	The Commemoration for Prof. dr. sc. Božidar Liščić	BOBARA HALL
11.30-12.00 h	THE CONFERENCE CLOSING CEREMONY	BOBARA HALL

Participants are invited to visit the

EXHIBITION

Trokut Test Group

IDEF d.o.o.

Cortec Corporation & EcoCortec

CorteCros d.o.o.

Ina maziva d.o.o.

EDC d.o.o.

MESA Electronic GmbH

Gracotech Grupa d.o.o.

Instrumentacija ELI-MP d.o.o.

IRT3000 ADRIA

mtech-conf.hr



INVITED LECTURERS



Dr. rer. Nat. Johann Wilhelm Erning

Works at Bundesanstalt für Materialforschung und -prüfung (BAM), Berlin, Germany. Studied Chemistry in Cologne and Bonn. Worked for the research centre Jülich from 1993 – 1996. Worked as post-doc at South Westphalia University of Applied Sciences from 1996-1998. Currently working at Bundesanstalt für Materialforschung und -prüfung (BAM) since 1998. Topics: electrochemistry, metals in contact with drinking water, failure analysis. Participation in various committees at EFC, CEN, DIN, DVGW...



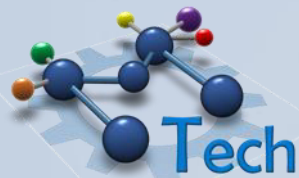
Dr. Imre Felde

Dr. Imre Felde was born 19.07.1973. in Hungary. He achieved his PhD in Materials Science and Technology from Miskolc University (Hungary) in 2007. From 1995. to 2008. he was head of department and from 2008 to 2012. CEO of Bay Zoltán Foundation for Applied Research, Budapest, Hungary. From 2012. he is Vice Dean of Faculty of Informatics, Obuda University in Budapest, Hungary. He has published more than 100 scientific and technical papers in field of engineering, computer science, mathematics and process modeling. He is member of editorial board of Strojnicki Vestnik-Journal of Mechanical Engineering, International Journal of Microstructure and Mechanical Properties, Surface Engineering and Hindawi Advanced Materials Science and Technology.



Dr. Mathew Mathew

Mathew is a faculty at Department of Biomedical Science, UIC School of Medicine at Rockford and leading Disability Research lab. He holding adjunct position at Department of Bionengineering at UIC, Chicago and Department of Orthopedic Surgery, Rush University Medical Center, Chicago. His research is supported by the federal agencies (NIH and NSF) and research foundations. He is also Editor-in-chief of Journal of Bio and Tribo-corrosion by Springer. He was an instrumental for initiating an international research institute called "Institute of Biomaterials, Tribocorrosion, and Nanomedicine" (IBTN), which is a joint venture of University of Illinois (UIC) and UNESP, Brazil. Currently, he actively involved in the IBTN and the director of tribocorrosion division.



Dr. Stefan Valkov



Dr. Stefan Valkov is Associate Professor at the Technical University of Gabrovo and Institute of Electronics of the Bulgarian Academy of Sciences. Currently, he is a team leader of the laboratory "Physical technologies" located at the Institute of Electronics, Bulgarian Academy of Sciences. His scientific interests are related to the modern materials science: thin films and coatings deposition, electron-beam surface treatment and modification of metals and alloys, materials characterization, X-ray diffraction, crystallography.

GUEST SPEAKER

Mr. Pascal Collet



Mr. Pascal Collet received a degree in chemical engineering at Hautes Etudes Industrielles in Lille, France. He has over 30 year-experience in technical services, sales, business development and marketing in the chemicals and protective coatings industries for markets which have included the oil & gas, water sectors, the nuclear industry, the automotive sector and building. His main current employment is the European Federation of Corrosion (EFC) as Chief Operating Officer from April, 2023. He is also involved with the French Corrosion Society Cefracor.



WORKSHOPS

Monday 02.10.2023.

14.00 – 19.00

WORKSHOP 1

PRIMJENA HLAPIVIH INHIBITORA KOROZIJE U INDUSTRIJI

Organizator: Hrvatsko društvo za zaštitu materijala i Cortec Corporation

Predavač: **Ivana Radić Boršić**

Kontakt i slanje prijave: dubravka.ulaga@fsb.hr

WORKSHOP 2

OCJENE ULTRAZVUČNIH INDIKACIJA NEPRAVILNOSTI U ZAVARIMA PREMA ISO 17640

Organizator: Hrvatski centar za nerazorna ispitivanja – CeNI

Kontakt i slanje prijave: info@ceni.hr

WORKSHOP 3

TRIBOCORROSION BASICS

Organizator: Hrvatsko društvo za toplinsku obradu – HDTOIP

Predavač: M.T. Mathew, Ph.D., Professor, Department of Biomedical Engineering, UIC, Chicago

Kontakt i slanje prijave: bozidar.matijevic@fsb.hr

WORKSHOP 4

ISPITIVANJA MEHANIČKIH SVOJSTAVA MATERIJALA I UMJERAVANJA OPREME

Organizator: Hrvatsko društvo za materijale i tribologiju – HDMT

Prijava za seminar putem e-mail adrese: zeljko.alar@fsb.hr



INTERNATIONAL CONFERENCE ON MATERIALS

heat treatment, corrosion, testing and tribology, 2023

OFFICIAL LANGUAGES:

Official languages of the Conference are Croatian and English.

CONFERENCE BADGE:

Everyone is kindly requested to wear her/his name badge during the Conference as it provides access to the scientific sessions, poster session, coffee breaks and gala dinner.

COFFEE BREAKS:

Coffee breaks will be served at the Lobby (Level 1) according to the program timetable.

DURATION OF PRESENTATION:

Due to the tight presentation schedule each participant selected for presentation is kindly asked to present his work in max. 12 min. Additional 3 min is left for the discussion of each presentation. All speakers are kindly asked to prepare the presentation in English in a Power Point format and to bring it on a USB memory device.

POSTER PRESENTATION:

Posters will be exhibited in the Cuiet Salon in front of the Bobara Hall.

All authors participating at MTECH 2023 with posters must print posters and bring them to the conference. The Conference Secretariat will provide tapes to fix posters. Poster size should be 70 cm x 100 cm (that is width x height; portrait format). Organizing Committee is unfortunately not able to offer a Poster Printing Service.

REGISTRATION:

All participants at MTECH 2023 must register via https://mtech-conf.hr/?page_id=513&lang=en.

ENDORSED BY:

European Federation of Corrosion, EFC-Event No. 503

CONFERENCE WELCOME DRINK:

Date and time: Monday, 2th October, 20:00

Venue: Piano bar Lobby, Hotel Croatia

The Organizers invite all guests to enjoy a breathtaking panorama, together with the appropriate welcome drink and snack in the terrace of the Hotel.

Dress code: Casual

CONFERENCE SOCIAL EVENT:

Date and time: Thursday, 3th October, 15:00

Venue: Vistit old town of Dubrovnik

Departure: from Hotel Croatia with bus

CONFERENCE GALA DINNER:

Date and time: Wednesday, 4th October, 19:00

Venue: Spinaker Restaurant of Hotel Croatia

Consistently oted one of the best restaurants at Hotel Croatia Cavtat.

Dress code: Formal / **Accompanying person fee:** price on request



"GRABENKORROSION": HOW SCIENTIFIC DEBATE LEADS TO AN SOLUTION. AND MODERN FAILURES DUE TO NEGLIGENCE OF WELL DESCRIBED FACTS

Johgann Wilhelm Erning

FEDERAL INSTITUTE FOR MATERIAL RESEARCH AND TESTING, BERLIN, GERMANY

Abstract

In the late 1980s, a new type of corrosion appeared in drinking water installations where galvanized steel pipes failed forming a deep groove with no corrosion at the other surfaces. The reason was discussed quite fiercely between failure analysts and material suppliers. In the end the discussion lead to the solution: inductive welded pipes of a certain sulphur content were prone to selective corrosion. The history of the arguments is discussed using old communications between Wilhelm Schwenk and Wolfgang Stichel, who later published the results in a paper unfortunately only I german.

Thus the knowledge got lost and new cases based on the same material problems are observed in application of so-called C-Steel piping systems. Failure cases are shown.

Keywords: *Grooving Corrosion, Circle of neglecton*

1. GROOVING CORROSION IN 1994 IN GERMANY

After the German reunification, a lot of buildings were reconstructed due to former neglect of maintenance. In certain areas drinking water installations were refurbished using galvanised steel pipes, a material still often used in this time. In certain cases after 1-2 Years of operation, leakages, predominantly in hot water (PWH) were observed, this obviously caused by higher corrosion velocity.

The Pipes used had official certificates from DVGW stating they fulfilled all the standardised requirements but still showed major corrosion problems after short time.

1.1. Details of the failures

The pipes showed a localised corrosion in the area of the weld leading to a high material loss and thus a fast leakage. Fig. 1 shows a typical cross-section.

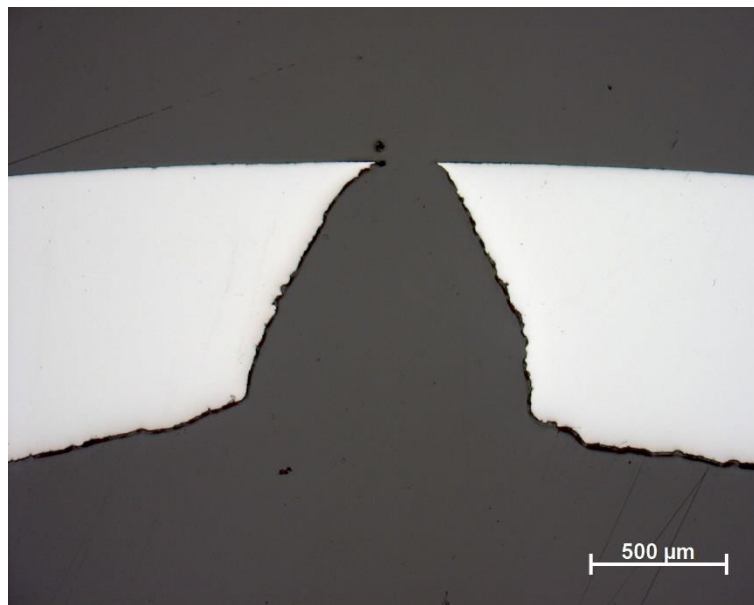


Fig. 1: Typical appearance of the corrosion damage

Many of these failures were analysed by Wolfgang Stichel from BAM. He noticed the common failures and decided to notify the certification body at DVGW and the most important corrosion committee in Germany, DVGW "Fachausschuss Innenkorrosion". There, people from industry, research and authorities met and discussed issues concerning corrosion issues in drinking water.

2. THE DISCUSSION

After Stichel had presented his results, the manufacturers of galvanised steel pipes were not exactly happy. The most important person at that time was Wilhelm Schwenk, working for Mannesmann. He was a man of a sometimes effervescent temper, which was not so rare at those times in such committees in Germany. And he wrote a letter to Stichel which gave some information on grooving corrosion and trying to give alternative failure causes.

The discussion by Schwenk came to an important conclusion concerning the question of implementing additional information into the European standard. And he gave additional information on corrosion failures predominantly occurring at certain welds.

Unfortunately, the files do not include minutes of the DVGW- Meetings, where the topic was discussed in detail.

The pipes affected were all made via ERW (electrical resistive welding). They were made by smaller and previously unknown companies.

3. INFORMATION FROM LITERATURE

The literature about grooving corrosion goes back until at least 1978, when Kato et al. [1] described the effect of grooving corrosion in sea water. Here ERW-made pipes were investigated and showed a sensitivity for grooving corrosion if the sulfur content of the sheets used to make the pipes exceeded a certain level. The heat treatment due to the ERW-process resulted in sulphide formation that “activated” the grooving corrosion. While this is not the same exact electrolyte, the complete story of the cause for the localised corrosion at the weld is given. Herbsleb did publish additional results [2-4], unfortunately mostly in German language.

In the end the picture was very clear from the 1970ies: If you produce steel pipes from sulphur-containing sheets by ERW and there is no heat treatment after the welding process, those pipes are sensitive to local corrosion at the weld.

The result of the discussions was another publication by Stichel [5] that came to the conclusion: ERW pipes without thermal treatment of the weld and a sulphur content $> 0,008\%$ are affected by grooving corrosion.

So far, so good. Unfortunately ref. 3-5 (and some others) were published in German language...

4. PROCESS OF NEGLECTION

In the years 2010ff new failure cases appeared. Due to the change in use of galvanised pipes, this time not in drinking water installations (where galvanised pipes are no longer used in Germany) but in cooling or heating systems.



Fig. 2: Corrosion in a cooling circuit, grooving corrosion at bottom pipe half shell.



Fig. 3: Corrosion of heating pipes, damage from outside.



Fig. 4: Corrosion of heating pipes, damage from inside.

All these independently occurring failures (and more!) were caused by a wrong use of the pipes. Grooving corrosion was an indicator for the wrong operation but would not have happened if the pipe systems had been operated properly. Inside corrosion always was caused by oxygen that should not have been present in the circulating water, outside corrosion by the presence of humidity outside the pipes.

All the corroded pipes showed a similar appearance in the cross sections, a typical example is shown in fig. 5:

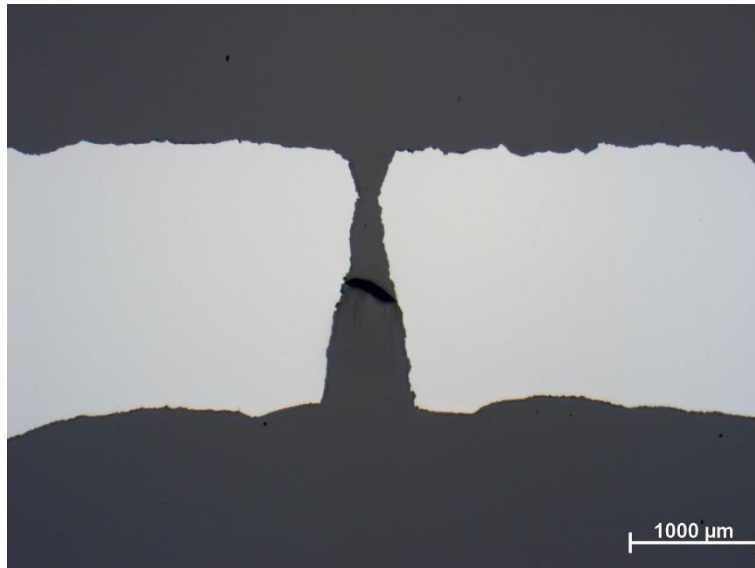


Fig. 5: Cross section of pipe showing grooving corrosion.

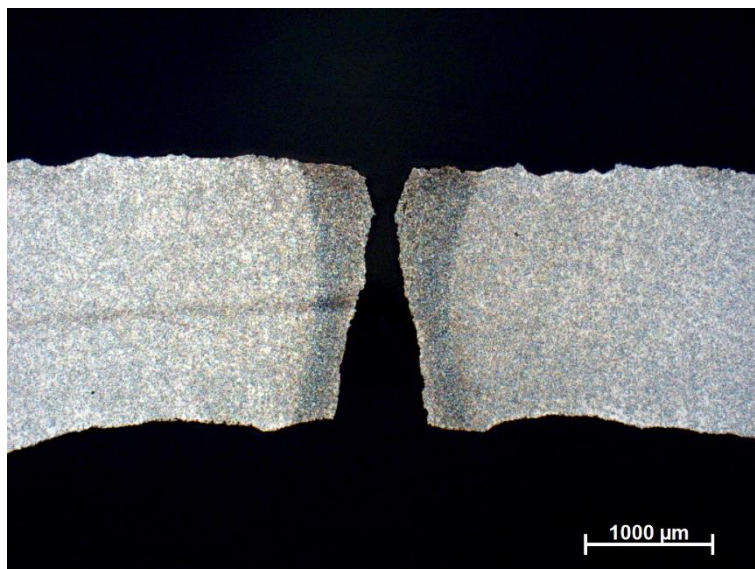
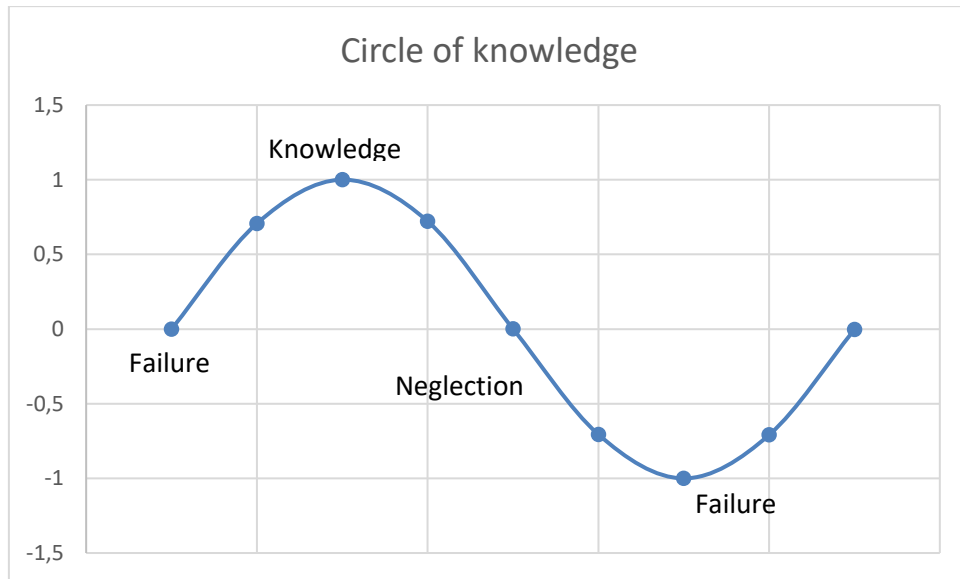


Fig. 5: Cross section of pipe showing grooving corrosion, sulphides in the HAZ visible by etching.

All the pipes were produced using ERW, all had a sulphur content higher than 0,008 %. This was described in detail decades ago.

5. CONCLUSION

Obviously, the development of knowledge and the use of it follow a circular process.



Where you start with a problem, here a failure, leading to research and a solution of the problem. Afterwards you will lose the knowledge again and return to the problems. Grooving corrosion has at least two cycles from the 1970ies to now.

Important for the knowledge to persist is information in an accessible format (i.e. NOT in german language only). And it would have been quite a good idea to write the facts down in the European standard.

REFERENCES

- [1] C. Kato, Y Otoguro, S. Kado, Y Hisamatsu, Corrosion Science, 1978, **18**, 61.
- [2] C. Düren, E. Treiss, G. Herbsleb, Materials performance 1986, **25**, 41
- [3] G. Herbsleb, Schweißtechnik, 2 und 3 /85, 21-24 and 40-44.
- [4] P. Drodten, G. Herbsleb, W. Schwenk, steel research, 1989, 471.
- [5] W. Stichel; Materials and corrosion, 1996, **47**, 452



APPLICATION OF MACHINE LEARNING FOR CHARACTERIZATION OF TRANSIENT HEAT TRANSFER

Akos Szabo-Gali¹, Zoltan Biczó², Robert Kohleb³, Gabor Kertesz¹, Okumiva Masahiro⁴, Levente Kovacs¹, Imre Felde¹

¹ Department of Biomatics and Applied Artificial Intelligence Institute, John von Neumann Faculty of Informatics, Obuda University, Budapest, Hungary

² Doctoral School of Applied Informatics and Applied Mathematics, Obuda University, Budapest

³ Doctoral School of Safety Science Doctoral School, Obuda University, Budapest, Hungary

⁴ Toyota Technological Institute, Nagoya, Japan

Abstract

The knowledge of the heat transfer coefficient plays a crucial role in evaluating coolants utilized for immersion quenching of steels. This coefficient effectively characterizes the heat exchange occurring between the immersed workpiece and the liquid coolant. The calculation of the heat transfer coefficient involves solving an inverse heat transfer problem, typically addressed using stochastic optimization algorithms. These algorithms rely on iterative processes and are computationally intensive, often requiring hundreds or even thousands of iterations to obtain a solution. To alleviate the computational burden, this paper introduces an initialization technique based on a non-iterative approach for solving the inverse heat transfer problem. The proposed method utilizes an artificial neural network to solve the problem. Specifically, a multi-layer feedforward neural network is utilized, trained using the backpropagation algorithm. In order to train the network, a synthetic database containing 150,000 records of heat transfer coefficients is created. The coefficient is determined as a function of temperature, with an unconventional utilization of the Fourier transform of the cooling curve as input for the inference system. Furthermore, the performance of the neural network is compared with other conventional learning algorithms. It is observed that when combined with stochastic algorithms, the network achieves comparable solutions in a shorter timeframe.

Keywords: *inverse heat conduction, immersion quenching, heat transfer coefficient, mlp, afwa*

1. INTRODUCTION

In the industrial sector, the post-production process of steel and alloys involves subjecting them to a heat treatment regimen. This entails heating the workpiece to a specified temperature and maintaining it at that temperature until the desired structural transformation occurs within the material. Subsequently, controlled cooling is applied to the workpiece. The primary objective of this process [1] is to enhance the mechanical, physical, and chemical properties of the product by inducing structural changes. In heat treatment programs, precise control of the cooling rate is crucial, as it directly influences the resulting structures. The heat transfer coefficient governs the rate at which the coolant effectively dissipates heat from the workpiece. The complexity of fluid dynamics and mechanical flow during the cooling process affects the magnitude of this coefficient. Consequently, determining the coefficient necessitates a combination of technical examinations, experimental measurements, and theoretical calculations. Previous studies [2-3] have demonstrated the feasibility of approximating the heat transfer coefficient by employing inverse methods and utilizing measurements. However, bio-inspired heuristic algorithms utilized for this purpose exhibit a high level of predictability, these algorithms are computationally intensive, often requiring over 10 hours to complete. Additionally, prior to initiating these calculations, the user must specify the locations at which the nominal functions, derived from measurements, are to be compared with the functions obtained from the inverse algorithm. Failure to set these points correctly may result in incomprehensible outcomes that are only evident after several hours of simulation. To mitigate unnecessary and erroneous simulations, it is desirable to develop a rapid estimation method that can provide users with nearly instantaneous feedback on the results. Moreover, this method can be executed even before using bio-inspired heuristic algorithms, allowing successful heuristics to be initiated based on the initial estimation. The aim of this research is to develop a method that is suitable for approximating the heat transfer coefficient function in an environment where accuracy is not that important, but the speed is in focus. Application of the method is, for example, incorporation into a hybrid algorithm. In previous research, the application of deep neural networks has already been demonstrated to be efficient in solving complex problems, such as assessment and disease diagnosis [5-6]. This precedent underscores the suitability of employing a neural network to address the present heat transfer coefficient approximation problem.

2. METHODOLOGY

2.1. Heat transfer model

As part of the numerical method a heat transfer model was applied, which is described by the following differential equation, assuming central-symmetric heat transfer conditions for a cylinder with finite length of L :

$$\nabla \cdot (\lambda(\mathbf{r}, T) \cdot \nabla T) + Q(T, \mathbf{r}, t) = C_p(\mathbf{r}, T) \rho(\mathbf{r}, T) \cdot \frac{\partial T}{\partial t} \quad (1)$$

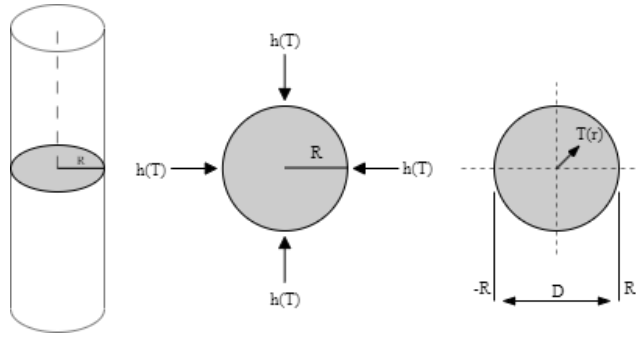
where r is the coordinate along the radius, t is time, T is temperature, λ is thermal conductivity, C_p is heat capacity, ρ is density, Q is latent heat (its value is zero during the entire heat transfer process). The initial condition is described by the following equation:

$$T(\mathbf{r}, t = 0) = T_a(\mathbf{r}) \quad (2)$$

where T_a is the initial temperature of the domain. The boundary conditions are described by the following equations:

$$\begin{aligned} -\lambda \frac{\partial T}{\partial r} &= h_1(T)(T(\mathbf{r}, t) - T_{am}) \\ &\dots \\ -\lambda \frac{\partial T}{\partial r} &= h_p(T)(T(\mathbf{r}, t) - T_{am}) \end{aligned} \quad (3)$$

where T_{am} is the coolant temperature, h_i is i. heat transfer coefficient for the rim.



1. Figure - Axisymmetric cylindrical geometry

The edges of the cylinder are marked as Γ , and the conditions $\Gamma_1 \cup \Gamma_2 \cup \dots \cup \Gamma_p = \Gamma$ and $\Gamma_1 \cap \Gamma_2 \cap \dots \cap \Gamma_p = \emptyset$ hold true for these edges. Each edge Γ possesses a temperature-dependent heat transfer coefficient $h_i(T)$. The heat transfer coefficient function is implemented using (T, h) data pairs, with the coefficient value determined through linear interpolation between the points. In the case of an axisymmetric cylinder, three edges are considered: the curved surface and the two bases, as depicted in Figure 1. However, if the heat transfer calculations are limited to the inner circle of an infinitely long cylinder, only the curved surface edge remains. Consequently, in this study, one-dimensional heat transfer analysis is performed, with a single edge defined at the coordinate $r=R$. The temperature distribution along the radius is calculated at $N \times$ points. To solve the differential equation, the Smith's [7] explicit finite difference method is employed.

2.2. Inverse Heat Conduction Problem

The specimen's temperature was measured at p points within the boundary. Following the thermal field calculation, T_i^C is obtained and utilized to compute the difference between T_i^C and T_i^M as defined in 4. equation. The solution to the inverse heat conduction problem [7] can be achieved by minimizing this objective function.

$$S = \sum_{i=1}^p (T_i^C - T_i^M)^2 \quad (4)$$

2.3. Inverse Heat Conduction Problem

A robust optimization method is recommended to solve the inverse problem, ensuring avoidance of local extreme values. Bio-inspired heuristic algorithms [3-4] are well-suited for this purpose. By exploring global extreme values at multiple calculation points instead of a single point, these algorithms prevent getting trapped in local optima. In a previous study, the author [8] used the Adaptive Fireworks Algorithm (AFWA), a variant of the Fireworks Algorithm, to address this specific problem. Computational efficiency

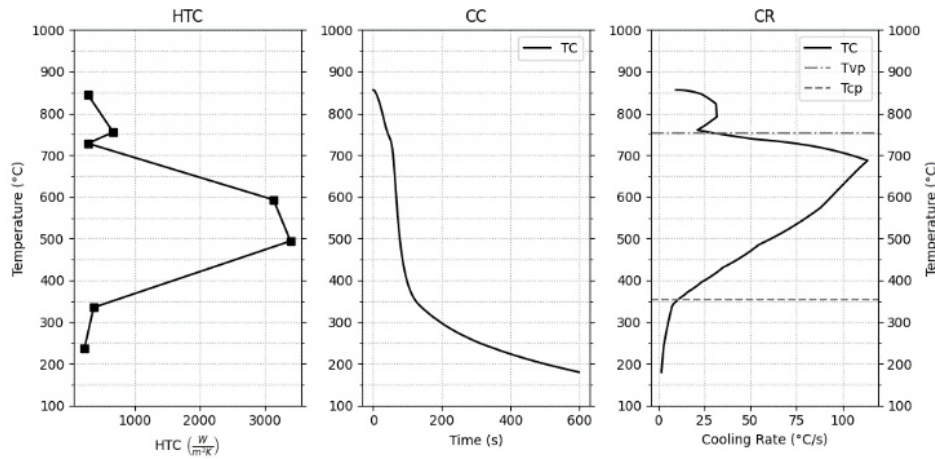
comparisons were made between AFWA and the Genetic Algorithm. Numerical tests demonstrated that AFWA can estimate heat transfer coefficients; however, it exhibits significant computational intensity. When dealing with a higher number of dimensions, obtaining results from AFWA can take several hours. To mitigate this weakness, learning algorithms offer a viable solution as they do not operate iteratively. For instance, artificial neural networks, which fall under the category of learning algorithms, require considerable training time (the iterative phase); however, once the model is trained, heat transfer coefficient estimations can be quickly obtained. Although the accuracy may not be on par with swarm-based algorithms, leveraging these initial results can significantly reduce the overall running time. This approach is referred to as an initialization strategy, and it allows for the creation of hybrid methods by combining learning algorithms with swarm-based optimization algorithms.

2.4. Artificial Neural Network

The Universal Approximation Theorem [9] states that any function can be approximated with an artificial neural network with the appropriate number of neurons. An artificial neural network is a learning-based model that (partially) mimics the biological processes of the human brain. It has already been demonstrated in previous research [10] that the artificial neural network can be used to solve the inverse heat transfer problem. The utilized model is a feed-forward artificial neural network. Each neuron in a layer is connected to all neurons in the adjacent layers. The input layer of the model consists of 15 neurons, corresponding to the number of Fourier coefficients, while the output layer comprises 14 neurons, representing the control points of the heat transfer coefficient. A total of 14 (T, HTC) data pairs are used, resulting in the derivation of 7 control points. The network incorporates a single hidden layer, consisting of 100 neurons. Sigmoid activation functions are applied to the neurons in the hidden layer, while the input and output layers use linear activation functions.

2.5. Dataset

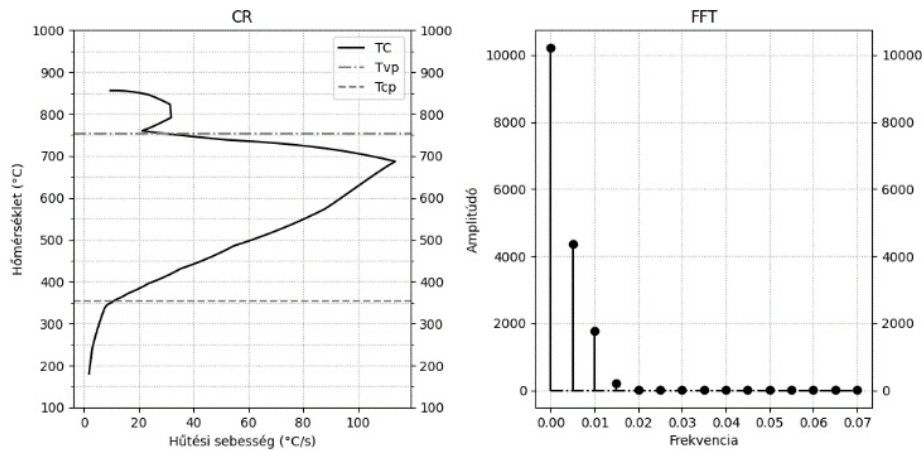
The dataset was generated by recording the cooling curve of a 12.5 mm diameter cylinder composed of Inconel 600 alloy at a specific location along the axis during immersion hardening. For the purpose of heat transfer analysis, a one-dimensional heat transfer assumption is made, considering the cylinder to have infinite length, which will be simulated later. Subsequently, the heat transfer coefficient functions were reconstructed using a well-established Inverse Heat Conduction Problem (IHCP) algorithm. The heat transfer coefficient functions were encoded with 7 control points, representing the (temperature - HTC) pairs. By averaging the heat transfer coefficient functions, a single average heat transfer coefficient function was obtained. To introduce variability, 150,000 heat transfer coefficient functions were randomly generated around the control points of the mean function, with a standard deviation.



2. Figure - Generated heat transfer coefficient and the associated drop curve and its derivative

2.6. Preprocessing

The data preprocessing steps were carried out during the dataset creation process. The first step involved numerically deriving the cooling curve, resulting in the CR cooling rate. To determine the Tvp and Tcp points that define the source section, the cooling curve was analyzed. By identifying the maximum point and subsequently moving left and right until reaching the inflection points, the Tvp and Tcp points were determined. In the second preprocessing step, the Tvp - Tcp range of the cooling curve was isolated for further analysis, and this range was saved as CR_TvpTcp in a file.



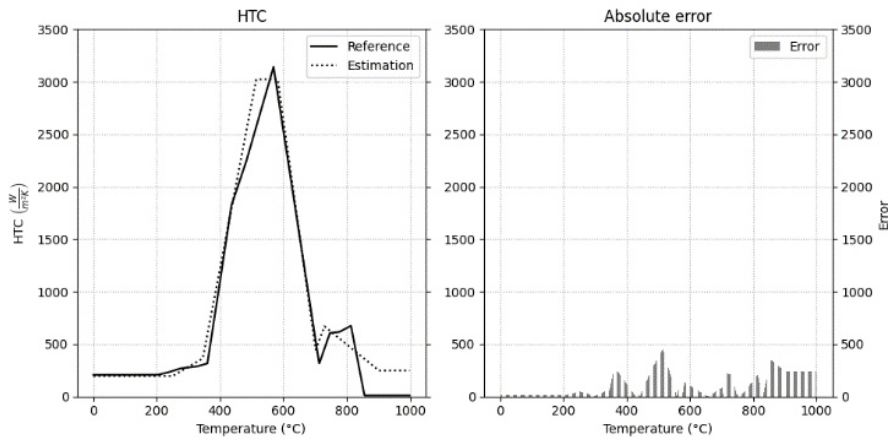
3. Figure - Fourier transformed applied on Cooling Rate

The final preprocessing step aimed to remove the time dependency of the cooling curve. This was achieved by transforming the cooling curve into the frequency domain using the Fourier transformation. By encoding the curve with its Fourier coefficients, the cooling curve could be represented with significantly fewer numbers. This process was applied to the CR_TvpTcp curve, as depicted in Figure 3. where the negative range was omitted due to symmetry. The one-dimensional discrete Fast Fourier Transformation algorithm was utilized to perform the Fourier transform on the CR_TvpTcp curve.

2.7. Evaluation

2.7.1. Result

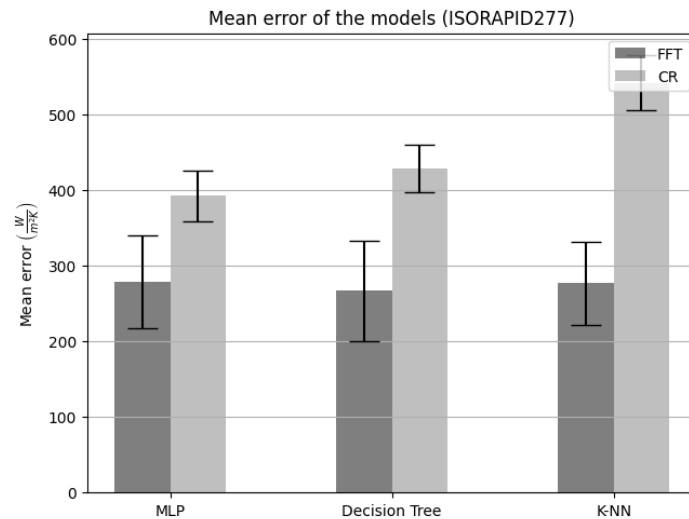
Upon completion of pre-processing, the heat transfer coefficient was estimated using a trained feed-forward artificial neural network (MLP). It should be noted that the expected output heat transfer coefficient of the test dataset is encoded with 32 control points, whereas the MLP can estimate only 7 control points. Hence, a direct comparison between the two is not feasible. To enable comparison, the heat transfer values in the temperature range of 0-1000 °C were calculated via linear interpolation between the control points of both HTC functions. Subsequently, the two functions were compared at 1000 temperature points, with the absolute error between them computed and presented in the right side of Figure 4. On the left side of the figure, the two HTC curves are depicted. It can be observed that the maximum error does not exceed 500. While it is challenging for a function encoded with 7 points to precisely approximate the original function encoded with 32 points, the MLP model provides a suitable approximation from which another optimization algorithm can be initiated. Furthermore, by increasing the number of search dimensions, additional control points can be interpolated between the existing ones, facilitating a closer approximation to the original function. Additionally, it is worth noting that the MLP achieved a satisfactory estimate of the function within 1 second, whereas an iterative optimization algorithm would have required thousands of iterations to achieve a comparable result.



4. Figure - Estimation

2.7.2. Comparison with conventional learning algorithms

The performance evaluation of the algorithms was conducted using average error and standard deviation metrics. The average error and standard deviation were calculated for all the curves in the test dataset. The results, including the average error and error standard deviation, are presented in Figure 5. The artificial neural network is denoted as MLP, the decision tree as Decision Tree [11] and the K-nearest neighbors algorithm [12] as K-NN. The heat transfer coefficient was estimated using each model with the preprocessed data as described earlier. Additionally, to demonstrate the importance of preprocessing, the heat transfer coefficient was estimated based solely on the cooling rate and without any preprocessing. The average error of the estimates made on preprocessed inputs is indicated with the label FFT, while the error of the estimate based on the unprocessed cooling rate is indicated with the label CR.

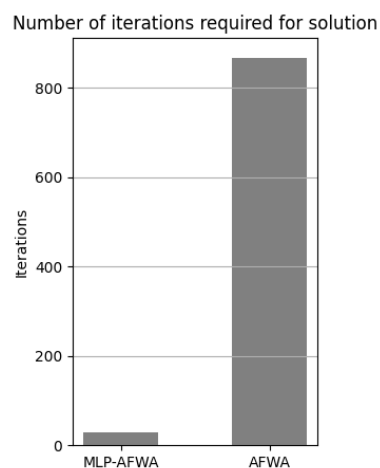


5. Figure - Comparison of learning algorithms

From the figure, it is evident that the learning algorithms achieve significantly improved performance with Fourier transformed data, with the average error of the FFT models being nearly half compared to the CR models. Furthermore, the diagram reveals that MLP, Decision Tree, and K-NN yield similar estimation results, exhibiting almost identical error levels. Consequently, it can be inferred that all three learning algorithms can be utilized interchangeably for heat transfer coefficient estimation.

2.7.3. Hybrid solution

In the first scenario, the presented initialization strategy was employed, where the heat transfer coefficient function was approximated using an artificial neural network. Subsequently, the Adaptive Fireworks Algorithm (AFWA) was initialized based on the obtained approximation. The search was initiated from these points, considering the swarm-based nature of AFWA. To prevent the algorithm from converging to a single point, the points were initialized around the approximation.



6. Figure - Number of total iterations

In the second scenario, AFWA was executed independently without the neural network initialization. The results of both optimizations are displayed in Figure 6. Both methods were terminated based on the same stopping condition. It is noteworthy that the AFWA initialized with MLP required only 28 iterations to reach the solution, whereas the standalone AFWA necessitated over 900 iterations to achieve the same outcome. Consequently, employing this hybrid approach significantly reduces the optimization runtime, as demonstrated by the results.

3. CONCLUSION

The aim of this research was to develop a robust method for estimating the heat transfer coefficient using an artificial neural network, specifically designed for time-independent analysis in a one-dimensional heat transfer domain. To train the neural network, a dataset comprising 150,000 records was generated based on filtered measurements using predefined rules. Prior to training, the dataset was Fourier transformed to transition the data from the time domain to the frequency domain. This preprocessing step ensured that the trained network was not reliant on the duration of the entire cooling process. The network was then trained on this preprocessed dataset and validated using a separate test dataset. The Fourier transform of the trained artificial neural network enabled the estimation of the heat transfer coefficient function from the cooling curve. Additionally, estimations were performed on unprocessed cooling curves and with alternative learning algorithms such as Decision Trees and K-nearest neighbors. Results indicated that superior estimations could be achieved using Fourier transformed inputs, and all the considered learning algorithms could perform the estimation. Thus, each model can be utilized within the initialization strategy. Subsequently, a heat transfer coefficient function was reconstructed using the Adaptive Fireworks Algorithm. The initial points of the algorithm were initialized based on the results obtained from the artificial neural network. The algorithm was then executed independently. Notably, the network-initialized optimization required significantly fewer iterations to converge to the same solution. It is important to note that the network estimation is applicable exclusively to one-dimensional heat transfer models but has the potential for extension to two-dimensional models.

Acknowledgement(s):

This research was funded by the 2020-1.1.2-PIACI-KFI-2020-00129 project. The authors acknowledge the financial support of this work by Hungarian-Japanese bilateral project (2019-2.1.11-TÉT-2020-00204)

REFERENCES

- [1] Rosa L. Simencio Otero, Lauralice C.F. Canale, and George E. Totten. "Use of vegetable oils and animal oils as steel quenchant: A historical review-1850-2010". In: *Journal of ASTM International* 9 (1 Jan. 2012). ISSN: 1546962X. DOI: 10.1520/JAI103534
- [2] Imre Felde. "Estimation of thermal boundary conditions by gradient based and genetic algorithms". In: vol. 729. Trans Tech Publications Ltd, 2013, pp. 144–149. ISBN: 9783037854914. DOI: 10.4028/www.scientific.net/MSF.729.144.
- [3] Rosa L. Simencio Otero et al. "Parallelized particle swarm optimization to estimate the heat transfer coefficients of a series of vegetable oils in comparison with typical fast petroleum quench oil quenchant". In: vol. 2. ASM International, 2019, pp. 260–271. ISBN: 9781713802730. DOI: 10.31399/asm.cp.ht2019p0260

- [4] Zoltan Fried, Sandor Szenasi, and Imre Felde. "Prediction of objective function value for heat transfer coefficient function reconstruction by FWA". In: Institute of Electrical and Electronics Engineers Inc., May 2019, pp. 304–307. ISBN: 9781728106854. DOI: 10.1109/SACI46893.2019.9111623.
- [5] Aleksandar Pejić and Piroška Stanic Molcer. "Predictive Machine Learning Approach for Complex Problem Solving Process Data Mining". In: Acta Polytechnica Hungarica 18 (Jan. 2021), pp. 45–63. DOI: 10.12700/APH.18.1.2021.1.4.
- [6] Suganthe Ravi Chandaran et al. "Deep Learning-based Transfer Learning Model in Diagnosis of Diseases with Brain Magnetic Resonance Imaging". In: Acta Polytechnica Hungarica 19 (Jan. 2022), pp. 2022–127. DOI: 10.12700/APH.19.5.2022.5.7.
- [7] M.N. Ozisik. Inverse Heat Transfer: Fundamentals and Applications. Taylor & Francis, 2000. ISBN: 9781560328384.
- [8] Akos Szabo-Gali, Imre Felde, and Sandor Szenasi. "Adaptive Fireworks Algorithm to solve 2D Inverse Heat Conduction Problem". In: 2021 IEEE 15th International Symposium on Applied Computational Intelligence and Informatics (SACI). 2021, pp. 443–448. DOI:10.1109/SACI51354.2021.9465543.
- [9] Kurt Hornik, Maxwell Stinchcombe, and Halbert White. "Multilayer feedforward networks are universal approximators". In: Neural Networks 2.5 (1989), pp. 359–366. ISSN: 0893-6080. DOI: [https://doi.org/10.1016/08936080\(89\)90020-8](https://doi.org/10.1016/08936080(89)90020-8).
- [10] Sandor Szenasi et al. "Estimating the Heat Transfer Coefficient Using Universal Function Approximator Neural Network". In: 2018 IEEE 12th International Symposium on Applied Computational Intelligence and Informatics (SACI). 2018, pp. 000401–000404. DOI: 10.1109/SACI.2018.8440928.
- [11] J. R. Quinlan. "Induction of decision trees". In: Machine Learning 1.1 (Mar. 1986), pp. 81–106. ISSN: 1573-0565. DOI: 10.1007/BF00116251. DOI: 10.1007/BF00116251.
- [12] T. Cover and P. Hart. "Nearest neighbor pattern classification". In: IEEE Transactions on Information Theory 13.1 (1967), pp. 21–27. DOI: 10.1109/TIT.1967.1053964.



THE EFC, A FEDERATION FOR ALL CORROSION SPECIALISTS AND EXPERTS IN MATERIAL SUSTAINABILITY

COLLET Pascal

European Federation of Corrosion
Avenue des Arts 56, 1000 Brussels – Belgium

Abstract

The EFC is a federation of organisations with interests in corrosion, active in Europe and beyond. Its aim is to advance the science of corrosion and protection of materials by promoting cooperation in Europe and collaboration internationally through the management of working parties, publications and the organization of the well-recognised EUROCORN scientific congress. The federation also supports events, courses and webinars to disseminate knowledge, encourage networking and help develop the next generation of corrosion professionals.

Keywords: *EFC, federation, Corrosion science, Corrosion prevention*

1 INTRODUCTION AND MISSION

The federation was founded in 1955 by three Corrosion Societies, based in France, Germany and in the UK as a non-profit organization. Today, it's the largest corrosion organisation in Europe and one of the largest in the world (it's estimated that ca. 26,000 corrosionists are members of the federation through Corrosion societies, research institutes, universities and companies (see section §4)

The EFC is a founding member of the World Corrosion Organisation (WCO), a non governmental organisation recognized by the United Nations.

The missions of the federation are to

- strengthen output of corrosion science and protection of materials by promoting cooperation in Europe and collaboration internationally.
- Disseminate scientific excellence and technical knowledge.
- Foster the connection all actors in the corrosion and durability value chain.

2 ORGANIZATION

2.1 General Assembly

The General Assembly is the decision making body of the federation. It is composed of all Member Societies (see §4). Honorary Fellows and Affiliate Members (see §4) may take part in the meetings of the General Assembly and shall have an advisory vote but shall not have the right to vote on any matters relating to the affairs of the federation.

The following matters (but not only) are within the exclusive competence of the General Assembly:

- the admission and exclusion of Member Societies and Affiliate Members;
- the granting of the status of Honorary Fellow;
- the election, dismissal or replacement of administrators;
- the adoption of the budget,
- the approval of the accounts;
- the modifications to the structure of the General Secretariat;
- the adoption of Bye-laws;
- the modification of the Statutes;
- the dissolution of the Association;
- the election of a President, a Vice-President and a Treasurer;
- the discharge to be granted to the Directors, the Secretariat General and/or the Auditor.

The General Assembly is chaired by the President or an alternate from either the immediate Past President or Vice-President.

2.2 Administrative Body

The federation shall be administered and managed by a Board of Administrators (BoA), composed of a President and Vice-President, the Immediate Past President and twelve administrators. They are assisted by a Treasurer and a Scientific Secretary who shall be ex officio members of the BoA. The twelve administrators are chosen from among the

Member Societies of the Association. All elected administrators shall serve on the BoA for a period of three years in the first instance.

The General Assembly shall endeavour to maintain a balance between representatives of industry and academic representatives.

The BoA has, among other responsibilities, the duty to institute, or approve the creation of study groups/task forces and working parties.

The President, the Vice-President and the Treasurer are elected by the General Assembly on the proposal by the Board of Administrators. The functions of the President and the Vice-President begin on the first of January following the General Assembly that elected them.

The STAC (Scientific and Technical Advisory Committee) Chair will be nominated by the BoA and elected from among its voting members. The Science and Technology Advisory Committee shall advise the EFC on scientific, technological and educational matters and the implementation of decisions concerning these.

The Scientific Secretary is appointed by the BoA in consultation with the Chairman of the Science and Technology Advisory Committee (STAC). He/She is in charge of the development and coordination of the activities of STAC in cooperation with the STAC Chair, Member Societies, the BoA and the General Secretariat. He / She is also in charge of the preparation of papers and reports for the dissemination of corrosion information across the boundaries, through publication in an EFC series of reports, guidelines, ... and also through partner journals. He/She is also in charge of maintaining an awareness of and collaboration with Standardisation bodies.

The meetings of the BoA shall be chaired by the President.

The Chief Operating Officer is selected and appointed by the Board of Administrators.

The work of the Association is carried out by a General Secretariat and is shared between the three offices of the following members at the origin of the federation:

- DECHEMA e.V., Frankfurt
- CEFRACOR, Paris
- The Institute of Materials, Minerals and Mining, London

The General Secretariat administers the following affairs of the Association, such as Affiliations, Finances, Publications, Awards, EUROCORR Congress,

3 ACTIVITIES

The numerous activities of the federation can be described as follows:

- . Knowledge exchange through Congresses, workshops, Business Meetings, Green Books,...).
- . Identification of challenges, trends and industrial needs.
- . Peer review of novel techniques, mechanisms, standards, monitoring and inspection.
- . Release of guidelines, good practices and standard tests.
- . Training and practical work exchange of young researchers (e.g. summer schools/grants).

. Network for international collaboration.

These activities are structured with working parties, congress, events , courses, ...

3.1 Working Parties

The EFC accomplishes its most important activities through 23 Working Parties (WPs) devoted to various aspects of corrosion and its prevention. One of the main tasks of the WPs is to organise, singly or jointly with other WPs, strong technical sessions at EUROCORR (see §3.2). Other valuable activities include participation in collaborative research and testing programmes, the organisation of courses and workshops, and the preparation of reports, guidelines, and proceedings for publication in the highly regarded EFC Series of 'Green Books', (see §3.6). The WPs are overseen by the Science and Technology Advisory Committee (STAC), composed of all of the WP Chairs.

A Working Party may be formed on the proposal of the General Assembly, the BoA, the STAC, a Member Society or industry with the support of at least four Member Societies. A WP should be proposed only where the topic has significance in a European context. It is received by the Scientific Secretary who will bring the proposal to the attention of the STAC, for its approval and finally by the General Assembly.

Anyone can participate in the activities of the WPs, either as a member of an EFC Member Society or as a 'friend' without being a member of an EFC Member Society. If you are interested in any of the topics covered by the EFC WPs, simply inform a Chair personally or using a contact form on the EFC website, <https://efcweb.org/Scientific+Groups.html>. The Chair will then keep you up to date about the WP activities.

During the EUROCORR congress (see §3.2), each WP holds a short 'business meeting', where activities are presented and discussed. Anyone is welcome to join any of the meetings. All WP Chairs and Vice-Chairs are now elected at these meetings for the next three-year term. Every EUROCORR participant physically present at a business meeting automatically has a voting right.

Currently, there are 23 WP operating in various domains, i.e.

- WP1: Corrosion & Scale Inhibition
- WP3: Corrosion by Hot Gases and Combustion Products
- WP4: Nuclear Corrosion
- WP5: Environment Sensitive Fracture
- WP6: Surface Science and Mechanisms of Corrosion and Protection
- WP7: Corrosion Education
- WP8: Physico-chemical Methods of Corrosion Testing
- WP9: Marine Corrosion
- WP10: Microbial Corrosion
- WP11: Corrosion of Steel in Concrete
- WP13: Corrosion in Oil and Gas Production
- WP14: Coatings

- WP15: Corrosion in the refinery and Petrochemistry Industry
- WP16: Cathodic Protection
- WP17: Automotive Corrosion
- WP18: Tribo-Corrosion
- WP19: Corrosion of Polymer Materials,
- WP20: Corrosion and Corrosion Control of Drinking Water Systems
- WP21: Corrosion of Archeological and Historical Artefacts
- WP22: Corrosion Control in Aerospace
- WP23: Corrosion Reliability of Electronics
- WP24: CO₂-Corrosion in Industrial Applications
- WP25: Atmospheric Corrosion

Beside these WP, Task Forces (TF) may be established to carry out specific tasks that are not normally the responsibility of existing Working Parties. They may be set up by the BoA, STAC or Working Parties. There are actually two TF running,

. TF1: Corrosion in Green & Low Carbon Energy Technologies, which is being transformed into a new Working Party (decision made during the last STAC meeting in August, 2023)

. TF2: Corrosion of medical implants & devices

One of the duties of the Working parties is to offer technical sessions as well as joint sessions with other Working Parties at EUROCORR and arrange their programme.

3.2 EUROCORR congress

EUROCORR is the title of the annual EFC corrosion conference and it's the flagship event of the federation. It's held in an European country and organised by an EFC Member Society or Societies.

All Working Party Chairs shall be invited to join the International Scientific Committee of EUROCORR. The outlines of the technical programme are discussed in the STAC to make appropriate recommendations to the local organiser. They decide together about the themes of the joint sessions, aside the "normal" sessions, associated to the WP.

The location of EUROCORR congress is decided by the BoA, based on bid submission.

Last August, EUROCORR2023 took place in Brussels and the thematic proposed by the local organizer was " Driving corrosion prediction and protection towards a circular economy" – it gathered more than 1,000 delegates from over 50 countries during 4 days. Plenary sessions with highly recognized experts in the field of corrosion took place along with 11 joint sessions and more than 30 sessions and additional workshops were part of the scientific programme of the conference, allowing the presentations of ca. 650 papers. For information, there was a strong joint session named "Hydrogen and metallic materials " during the 4 days.

Regarding the process to submit abstracts, the call for abstracts starts mid of October, the year preceeding the EUROCORR congress, to end usually in January/February. The authors are invited to choose the most relevant session or joint session when they submit

their abstracts. The abstracts selection is made and announced by April generally speaking

Beside the submission of abstracts for lectures, authors can propose alternatively for the poster session. The timing of submission and approval is slightly different.

A third option, named “flash presentation” will be proposed for this first time for EUROCORR 2024. It will be based on a few-minutes presentation, taking place during one session.

In parallel to the conference, an exhibition takes place during the same period at the same place, allowing societies / companies to promote their products and services, to reinforce the link between academics and the industry during EUROCORR.

The EUROCORR series is scheduled as follows for the next 3 years:

- Paris, France from 1 to 5 September, 2024 with the theme “A step forward in societal awareness of material degradation issues”
- Stavanger, Norway from 7 to 11 September 2025 with the general theme “Joining forces for smart and sustainable solutions for fighting corrosion in society”.
- Dublin, Ireland from 20 to 24 September, 2026 with a special emphasis on “Corrosion Challenges for Net-Zero Technologies “

3.3 Awards, prizes & grants

EUROCORR Congress is the right moment and the right place to celebrate and recognize the contribution of experts in the field of corrosion, in particular with the

. European Corrosion medal (recognising achievements by a scientist in the application of corrosion science)

. EFC Honorary Fellow award (given for outstanding accomplishment in corrosion science)

In parallel, the Cavallero medal (instituted by the University of Ferrara, Italy) awards under the auspices of the EFC to honour the memory of and the work accomplished by this Professor. It awards every two years, a scientist who is particularly distinguished by his/her activity and publications in the field of corrosion research.

Every three years, on the initiative of the Hungarian Corrosion Society HUNKOR and supported by the “Kurt Schwabe Foundation”, this prize is awarded to a young scientist in recognition of his/her scientific and technical contribution to the field of corrosion on the basis of publication.

Other awards dedicated to young researchers and engineers are also organised, such as the best oral presentation and the 3M Plenary Lecture competition associated to EUROCORR.

To encourage the scientists to present posters during EUROCORR, a dedicated prize is awarded to the best poster – ca. 150 posters were presented during the last EUROCORR in Brussels.

Grants are also offered to young corrosionists, such as EUROCORN travel grant to support them to attend EUROCORN. In 2023, two ladies from Turkey and Colombia got grants for that purpose.

Another grant, named “Young Scientist grant” helps to stimulate interaction and collaboration within the international corrosion community, by providing financial support to junior corrosionists to enable them to visit and interact with other corrosionists at their home institute abroad and to discuss research issues of mutual concern relevant to the field.

3.4 EFC events

The EFC label helps the Members to communicate wider about their events – the federation informs the EFC community via different channels: EFC Newsletters, website, emailing, social media to give more visibility with special promotion.

The event must be concerned with a topic or topics that fall within the interests of the EFC. The event must be organised by a Member Society, Working Party of the EFC, or an affiliate member.

EFC summer schools are organised, focusing on the young community, with one of them backed to EUROCORN, to attract people for both events.

Here after the link to the dedicated page on the EFC website

<https://efcweb.org/Events/Calendar+of+events.html>

3.5 EFC labelled courses

As education is one of the main missions of the federation by disseminating the highest level of scientific knowledge by organising globally recognised events and by allowing the knowledge exchange in Europe and beyond, the EFC supports initiatives of the Members when organizing courses related to corrosion education, by granting the EFC Approved label courses with high professional standards.

It's an opportunity for all the Members to include their EFC labelled courses in the EFC calendar and rely on the federation for special promotion through the EFC channels (Newsletters, website, emailing, social media).

Here after the link to the dedicated page on the EFC website
[https://efcweb.org/Events/EFC+Approved+Course+Label/EFC+Approved+Courses.htm](https://efcweb.org/Events/EFC+Approved+Course+Label/EFC+Approved+Courses.html)

l

3.6 EFC Newsletter, Publication & Journals

EFC Newsletters are distributed to the EFC community, allowing members and the federation to communicate about the activities of the WP, events, courses, workshops, seminars and giving a chance to the members to share experience in the field of corrosion with case studies and projects reports.

The dissemination of the knowledge is also monitored by the publication of so-called EFC Green series. As many as 70 books are available in e-format or print, covering many aspects of the corrosion industry and the work of the Working Parties. This ranges from general corrosion education (EFC 52 Progress in corrosion – the first 50 years of the EFC)

to specific investigations (EFC 66 – Understanding Biocorrosion / EFC 69 – Nuclear Corrosion: Research, Progress and Challenges), as well as providing guidelines (EFC 53 – Standardisation of thermal cycling exposure testing / EFC 55 – Corrosion Under Insulation guidelines). The entire Green Book series is available on the EFC website in partnership with Elsevier to market them.

The EFC can rely on Journals in Czech republic, France, Germany, Poland, Switzerland and UK, to regularly publish information about the EFC and its activities.

3.7 Young EFC

Young EFC is an initiative created in 2016 by the EFC that aims to support early career researchers and engineers in the field of corrosion and protection of materials. The work of Young EFC is based on collaboration between early career researchers and engineers, senior advisors, and the support of the board of the EFC. The membership of Young EFC is open to all scientists and professionals linked to corrosion science and engineering topics, with a focus on early career researchers and professionals from all over the world.

Young EFC is organised by a Board constituted by members affiliated to one of the Member Societies that collaborates with the EFC.

In terms of initiatives, Young EFC is active by organising webinars (related to careers, science communication), collecting and sharing events related to the World Corrosion Awareness Day (April 24th), highlighting and celebrating Women working in Corrosion by sharing videos via the EFC social media.

4 MEMBERSHIP

The EFC is composed of the following categories of members:

- . Member Societies (European), ie. European scientific and technical societies and organisations that act to enhance progress, best practice and education in the science and technology of corrosion and its prevention for the socio-economic benefits of mankind and the good condition of the environment.

- . Member Societies (International), also scientific and technical societies and organisations acting for the same purpose as the European Member Societies, and located in a country which is not a member state of the Council of Europe. They become members on the recommendation of three European Member Societies.

- . Affiliate Members are Organisations that support the aims and objects of the Association. Two classes of Affiliate Member exist; one for Companies and one for Universities and Research Organisations.

4.1 Member Societies

Member Societies are entitled to be represented in the General Assembly (with voting rights), propose candidates to the BoA and appoint delegates to EFC Working Parties. They have the benefits of participation of their individual members in EFC Working Parties as a matter of right, volunteer to host a EUROCORR event (held only in a European country), propose the formation of an EFC Working Party, register meetings as EFC events, subject to approval of the EFC, apply for an EFC Approved Course Label, subject to approval of the EFC Course Endorsement Committee, receive current information via the

EFC Newsletter, propose nominees for awards presented by, or in conjunction with the EFC.

4.2 Affiliate Members

Affiliate Members are entitled very similarly as the Member Societies, except the voting right at the General Assembly, the representation at the BoA, the possibility to form an EFC Working Party, the organization of EUROCORN. However, they receive discount on fees for EUROCORN booths. They also have discount on advertisement in the EFC Newsletters and ability for free publication of case studies, activities in the EFC Newsletters.

4.3 Branches

Beside these two types of members, Branches are structures, which may bring together individuals and/or institutions, which act to strengthen the progress, best practices and education of the science and technology of corrosion and its prevention for the socio-economic benefit of mankind and the good condition of the environment. Branches must be non-profit. Branches are admitted by invitation subjected and are subject to the recommendation of the Board of Administrators and the approval of the General Assembly

4.4 Honorary Fellows and members

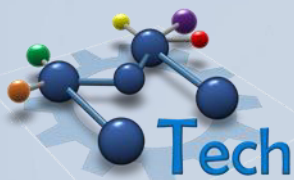
Honorary Fellows status is conferred by the General Assembly on any natural person who, in the opinion of the BoA, has made a special contribution to the achievement of the aims of the federation.

De facto, natural persons belonging to Member Societies (European and International) and Branches are considered as Members of the Association.

Members and Honorary Fellows are entitled to have the benefit of reduced registration fees for EUROCORN, have the benefit of participation in EFC Working Parties as a matter of right.

5 CONCLUSION

The EFC is a federation of organisations with interests in corrosion, active in Europe and beyond. Its aim is to advance the science of corrosion and protection of materials by promoting cooperation in Europe and collaboration internationally through the management of working parties, publications and the organization of the well-recognised EUROCORN scientific congress. The federation also supports events, courses and webinars to disseminate knowledge, encourage networking and help develop the next generation of corrosion professionals.



PREVLAČENJE ADITIVNO PROIZVEDENE TITANIJEVE LEGURE PREVLAKOM PACVD TiN

DEPOSITION OF PACVD TiN COATING ON ADDITIVELY MANUFACTURED TITANIUM ALLOY

Jurica Jačan¹, Darko Landek¹, Miho Klaić¹

¹ University of Zagreb, Faculty of Mechanical Engineering and Naval Architecture, Zagreb, Croatia

Sažetak

Titanijeve legure posjeduju iznimno povoljnu kombinaciju mehaničkih i fizikalnih svojstava uz dobru korozijsku postojanost te biokompatibilnost zbog čega imaju široko područje primjene u različitim industrijama. Aditivna proizvodnja titanijevih legura otklanja nedostatke tradicionalne proizvodnje u izradi proizvoda složene geometrije, koji se manifestiraju u visokim troškovima polaznog i otpadnog materijala i teškoj obradljivosti odvajanjem čestica. Primjenom postupka plazmom potpomognutog kemijskog prevlačenja iz parne faze (PACVD) moguće je povećati tvrdoću i otpornost na trošenje titanijeve legure nanošenjem tvrdih prevlaka. U radu je istražen utjecaj obrade odvajanjem čestica na kvalitetu površine titanijeve legure proizvedene postupkom taljenja snopom elektrona (EBM) i njenu prikladnost za PACVD prevlake. Nakon prevlačenja uzoraka aditivno i konvencionalno proizvedene legure Ti6Al4V PACVD TiN prevlakom, ispitana je adhezivnost prevlake prema VDI 3198 metodi, debljina prevlake kalotestom i nanotvrdoća prema normi EN ISO 14577-2:2002.

Ključne riječi: aditivna proizvodnja, Ti6Al4V, EBM, PACVD, TiN

Abstract

Titanium alloys have an extremely favorable combination of mechanical and physical properties, as well as good corrosion resistance and biocompatibility, making them widely applicable in a variety of industries. Additive manufacturing of titanium alloys eliminates the drawbacks of traditional manufacturing methods in producing complex geometric products, characterized by high costs of raw and waste materials and difficult machinability. By using the Plasma Assisted Chemical Vapour Deposition (PACVD) process it is possible to enhance the hardness and wear resistance of titanium alloys through the application of hard coatings. The influence of machining operations on the surface quality of Electron Beam Melted (EBM) titanium alloy, and its suitability for PACVD coatings has been investigated in this work. After coating samples of additively and conventionally produced Ti6Al4V alloy with PACVD TiN coating, the adhesion of the coating was tested according to VDI 3198 method, the coating thickness was measured by calotest, and the nanohardness was evaluated according to EN ISO 14577-2:2002 standard.

Keywords: additive manufacturing, Ti6Al4V, EBM, PACVD, TiN

1. INTRODUCTION

Titanium alloys are widely recognized for their remarkable mechanical and physical properties, encompassing a high strength-to-weight ratio, exceptional corrosion resistance, and biocompatibility. These alloys find extensive applications in various industries, such as aerospace, biomedical, chemical, and automotive, where high-performance materials are required. However, traditional manufacturing methods for titanium alloys suffer from drawbacks, such as the high costs associated with starting and waste materials, as well as limitations in producing complex geometries. Additive manufacturing (AM), commonly referred to as 3D printing, has emerged as a promising technology that can overcome these limitations and offer numerous advantages in the production of titanium alloy components [1,2].

According to the ISO/ASTM 52900:2015 standard, AM technologies are divided into seven basic groups, of which the following four are suitable for the production of metal products: powder bed fusion (PBF), binder jetting (BJ), sheet lamination (SL) and direct energy deposition (DED). Among the named additive manufacturing techniques for metal products, the most commonly used methods for titanium alloys are Selective Laser Melting (SLM), Electron Beam Melting (EBM) from the group of PBF technologies, and Directed Energy Deposition (DED) [3–5]. In SLM and EBM processes, the selective melting of a pre-set layer of metal powder is carried out to create the desired three-dimensional object. On the other hand, in DED processes, metal powder is continuously fed through a nozzle and melted during the process [2].

While titanium alloys have numerous advantages, they also have some limitations. Prolonged exposure to the human body can result in the release of metal ions, leading to tissue inflammation and other adverse reactions [6,7]. Additionally, the surface quality, porosity, residual stresses, and compositional and property homogeneity of additively manufactured titanium alloys can be a concern [2]. To mitigate these challenges, post-processing techniques such as heat treatment and surface finishing are employed to improve the properties of the final product, including reducing surface roughness and residual stresses [8].

To enhance the wear resistance and achieve a favorable combination of tribological properties, physical vapor deposition (PVD) and plasma-assisted chemical vapor deposition (PACVD) techniques are employed to deposit coatings onto titanium alloys. Hard coatings produced by PVD process, such as TiN, TiCN, and TiAlN coatings, have been commonly applied to conventional titanium alloys to improve wear resistance. Furthermore, studies have explored the potential of PACVD coatings, such as TiN, for medical applications and the importance of multi-layered coatings for improved adhesion, bioactivity, and implant wear resistance [9–11]. The combination of additive manufacturing processes and vapor deposition coating techniques has shown promise in enhancing the surface quality and wear resistance of titanium alloy components [12].

By comprehensively exploring the effects of machining operations and the application of PACVD coatings on EBM titanium alloy, this research aims to enhance the surface properties and overall performance of additively manufactured components. The findings of this study will contribute to the knowledge base of additive manufacturing in the field of titanium alloys and facilitate advancements in surface engineering techniques for improved applicability in various industries.

2. MATERIALS AND METHODS

For the purpose of this study, the titanium alloy Ti6Al4V was utilized, and its chemical composition is presented in Table 1.

Tab. 1: Elementary composition of the Ti6Al4V alloy

Elements	wt. %
Ti	90
Al	6
V	4
Fe	max. 0,25
O	max. 0,2

The investigation was conducted on three test specimens produced using the Electron Beam Melting (EBM) additive manufacturing process in the AIDIMME Institute at the ARCAM A2 machine, and one test specimen produced using the conventional metallurgy process followed by hot forming. The initial samples were cylindrical with a diameter of 18 mm and required fine turning and grinding procedures to reduce the surface roughness, which was unsuitable for subsequent coating.

The fine turning process was performed with common parameters, including a cutting depth of 0.1 mm and a cutting speed of $V_c = 0.042$ m/s on the turning center SBL 500 Trens Trenčín. The turning parameters that varied depending on the sample are shown in Table 2. Samples produced additively are designated with the letter "AM," while the conventionally produced sample is designated with the letter "K."

Tab. 2: Tool offset during sample processing

Sample	f [mm/okr]	f' [mm/s]
AM1	0,05	0,0375
AM2	0,15	0,1125
AM3	0,26	0,195
K1	0,05	0,0375

After the turning process, the diameter of the samples was reduced from 18 mm to 16 mm, and the surface roughness was measured using an electromechanical device with a stylus, the Surface Roughness Tester TR200/210/220. Following the roughness testing, the cylindrical samples were cut into 10 mm disks. The surface roughness test was repeated after the deposition of a TiN coating using the PACVD process.

Prior to the PACVD TiN coating, the cut disks underwent grinding using a waterproof range of sandpapers with grit sizes P600, P800, P1200, and P2000 to further reduce surface roughness and enhance coating adhesion.

The PACVD coating process for both additively and conventionally produced titanium alloys was carried out in a Rübige GmbH type PC 70/90 commercial vacuum furnace, as shown in Figure 1, with parameters presented in Table 3.



Fig. 1: Rübig PC 70/90

Tab. 3: PACVD process parameters

Process	T [°C]	t [h]	p [mbar]	N ₂ [l/h]	H ₂ [l/h]	Ar [l/h]	TiCl ₄ [l/h]	P [W]
Heating	510	3	2	/	/	/	/	/
Sputtering	520	1	2	20	200	10	/	/
Coating process	520	6	2	45	200	10	7	3000
Cooling	20	4	2	/	/	/	/	/

Following the completion of the PACVD process, surface roughness measurements were conducted, and coating evaluation included coating thickness determination using the calotest method, coating adhesion according to the VDI 3198 method, and nanohardness testing based on EN ISO 14577-2:2002 standard.

The calotest method involves rotating a ball pressed onto the coated test sample while introducing an abrasive mixture between the ball and the sample. After a fixed number of rotations, the size of the formed crater can be used to calculate the wear and the thickness of the deposited layer. The equipment used for calotest thickness evaluation is shown in Figure 2.



Fig. 2: Calotest thickness testing machine

A hard metal ball with a diameter of 15 mm was used in the process, rotating at a frequency of 300 rev/min for 20 seconds. The coating thickness is calculated using the formula 1. Variables D and d are represented in Figure 3.

$$e = \frac{D^2 - d^2}{8 \cdot R} \quad (1)$$

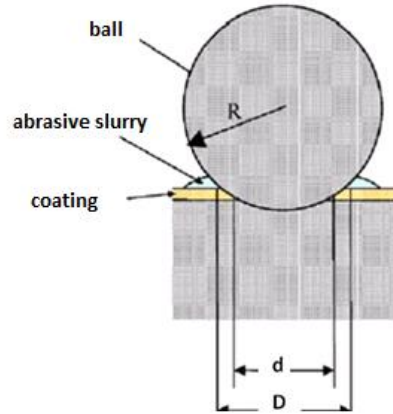


Fig. 3: Coating thickness determination using calotest

The Rockwell test prescribed by the VDI 3198:1991 standard is a destructive test of the quality of coated components. This method involves using a diamond cone with a 120° angle to penetrate the coating's surface, causing plastic deformation of the substrate and fracture of the coating. The appearance of the coating around the indentation site is shown in Figure 4a for coatings with good adhesion and in Figure 4b for coatings with poor adhesion.

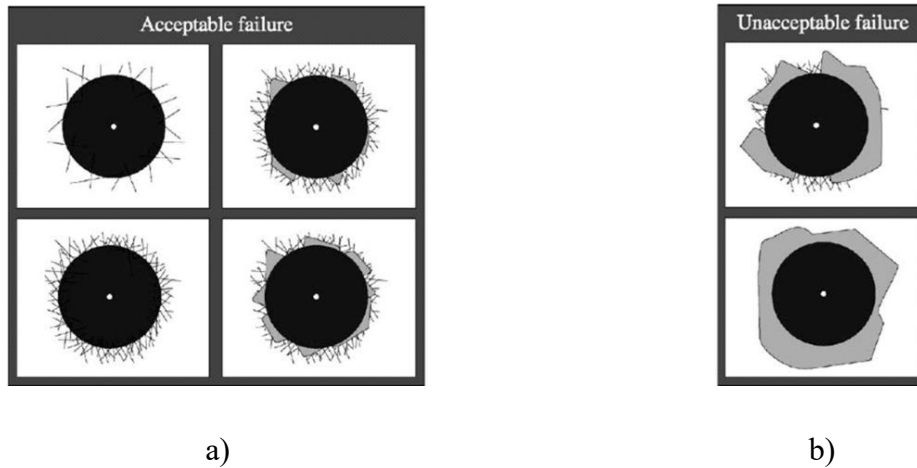


Fig. 4: a) Coatings with Acceptable failure, b) Coatings with Unacceptable failure

Nanohardness testing of the samples was performed using a DUH-211/211S device (Figure 5) manufactured by Shimadzu Corporation, serial number I62304700117, in accordance with EN ISO 14577-2:2002.



Fig. 5: DUH-211/211S nanohardness testing device

The nanohardness testing process, shown in Figure 6, consists of two phases. In the first phase, the coating layer is penetrated by an indenter, while in the second phase, the indenter is removed, and relaxation of the coating layer and the substrate occurs. During the testing, the depth of penetration did not exceed 0.2 μm .

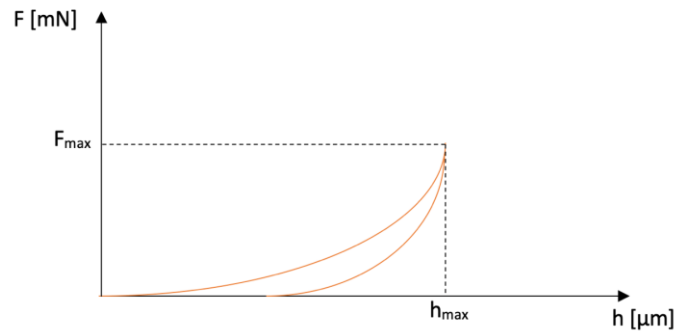


Fig. 6: Dependence of Indentation Force on Penetration Depth

3. RESULTS

3.1. Surface machinability of samples by fine turning

Results obtained from the application of turning parameters shown in Table 2, along with constant geometry, cutting speed, and cutting depth, are presented in Figure 7a-c for additively manufactured samples and Figure 8 for conventionally produced titanium samples.

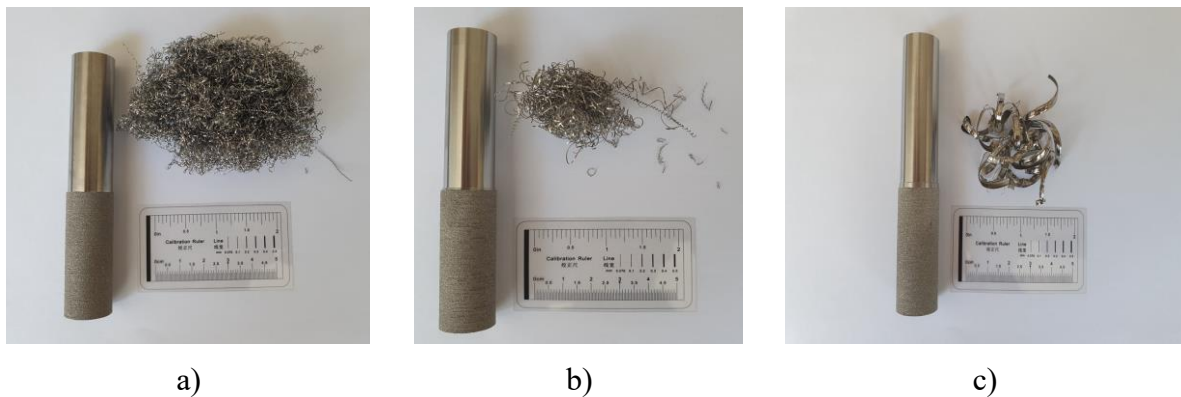


Fig. 7: a) Fine turned sample AM1, b) Fine turned sample AM2, c) Fine turned sample AM3



Fig. 8: Fine turned sample K1

The results indicate that additively manufactured samples exhibit better machinability compared to conventionally produced ones, as the K1 sample shows an excessively long separated chip that wraps around the tool, necessitating process interruption and chip removal. In AM samples, there is an increase in the width of the separated chip with the increase in feed rate; however, these chips are not as long as those in the K1 sample. Lower feed rates ensure reduced surface roughness, but samples processed using this method face issues with separated chips that are highly likely to wrap around the tool, further slowing down the process due to the need for chip removal.

3.2. Surface roughness

Surface roughness was first examined on AM samples after turning. The graphical representation of the arithmetic mean of the deviation of the profile from the mean line (R_a), the ISO 10-point height parameter (R_z), and the maximum peak-to-valley height of the profile within a sampling length (R_{max}) of additively manufactured samples is shown in Figure 9.

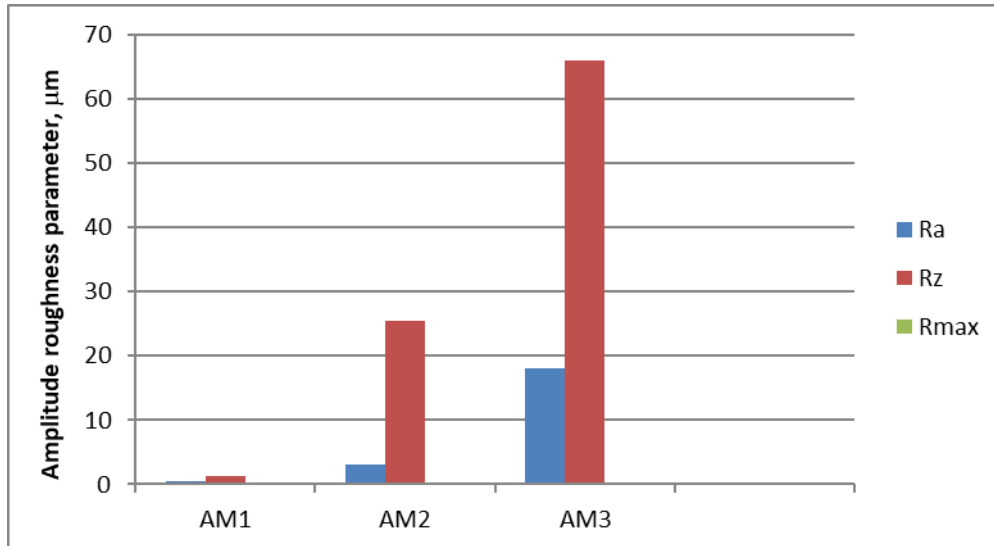


Fig. 9: Graphical representation of surface roughness parameters of AM samples after fine turning

Figure 9 illustrates that increasing the feed rate during turning results in higher surface roughness due to inadequate material removal, leaving numerous surface irregularities.

Surface roughness test results after PACVD coating of TiN on the samples are presented in Table 4 and Figure 10. The reported roughness parameters include the arithmetic

mean of the deviation of the profile from the mean line (R_a), the ISO 10-point height parameter (R_z), and the maximum height of the profile above the mean line within the sampling length (R_p).

Tab. 4: Results of surface roughness examination for coated samples

Sample	$R_a, \mu\text{m}$	$R_z, \mu\text{m}$	$R_p, \mu\text{m}$
K1 untreated	$0,070 \pm 0,022$	$0,678 \pm 0,180$	$0,462 \pm 0,134$
K1 with PACVD TiN	$0,097 \pm 0,028$	$0,926 \pm 0,416$	$0,848 \pm 0,514$
AM1 with PACVD TiN	$0,061 \pm 0,008$	$0,569 \pm 0,191$	$0,461 \pm 0,121$

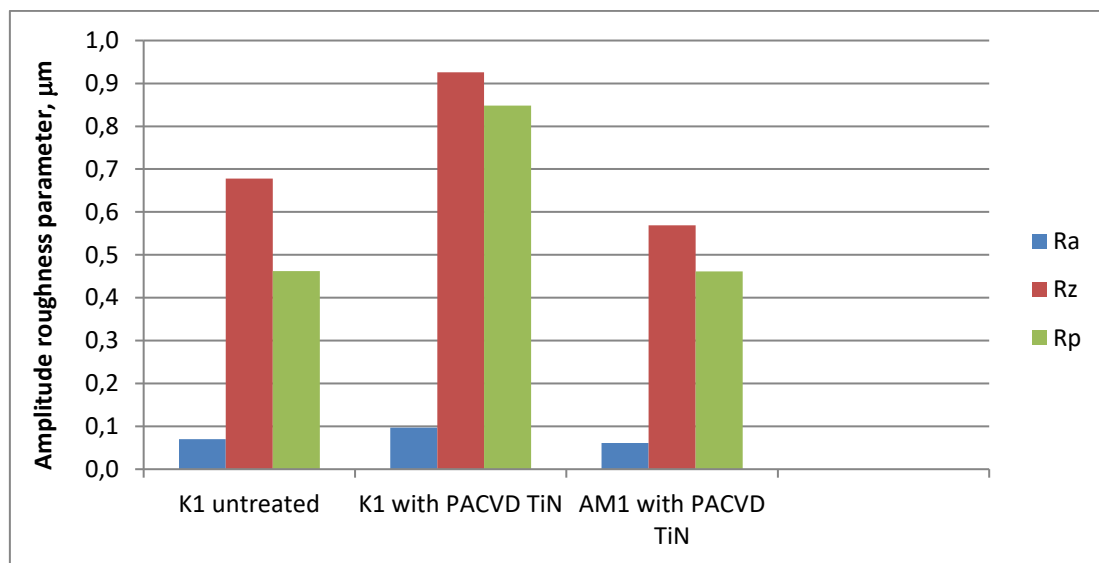
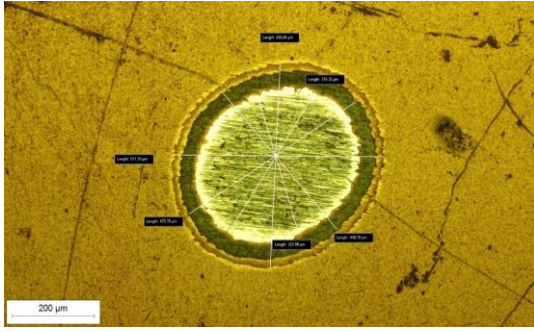


Fig. 10: Graphical representation of surface roughness parameters of coated samples

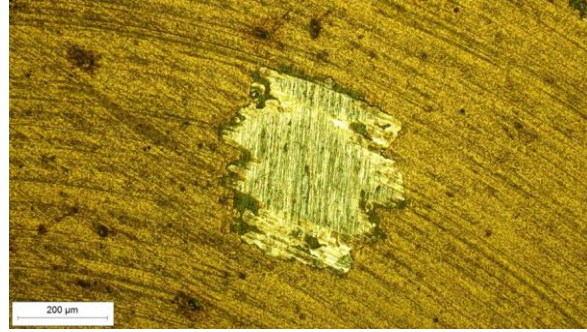
From Table 4 and Figure 10, it is evident that the AM1 sample with PACVD TiN has the lowest values of roughness parameters R_a , R_z , and R_p . This can be attributed to its smoother machinability, resulting in better surface quality before and after coating.

3.3. Coating tickness

Figures 11a and 11b illustrate wear marks obtained from calotest method for measuring coating thickness on K1 sample coated with TiN (Figure 11a) and AM1 sample coated with TiN (Figure 11b).



a)



b)

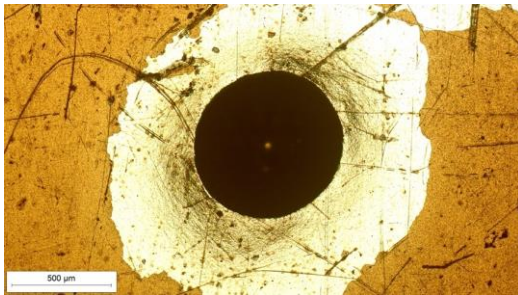
Fig. 11: a) Coating thickness examination for K1 sample coated with TiN, b) Coating thickness examination for AM1 sample coated with TiN

The measured coating thickness for the K1 sample coated with TiN is determined by incorporating the measured values of the inner and outer diameter of the impression and the radius of the ball into Equation 1. The average coating thickness is $e = 1.58 \mu\text{m}$.

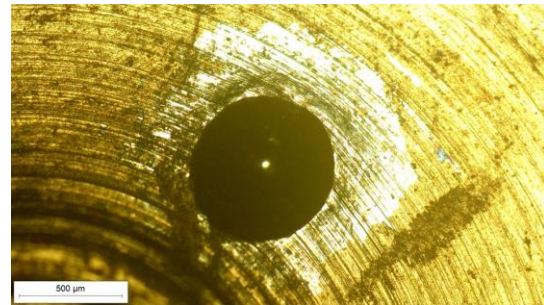
The coating layer on the AM1 sample with TiN is not sufficiently thick to determine its thickness using Equation 1. To achieve better adhesion and coating thickness, surface roughness needs to be reduced. Additionally, reducing the amount of titanium oxide on the surface of the base material is recommended, as it decreases the mechanical properties of the coating.

3.4. Coating adhesion

Results of coating adhesion testing using the VDI 3198:1991 method for the K1 sample coated with TiN (Figure 12a) and the AM1 sample coated with TiN (Figure 12b) are presented.



a)



b)

Fig. 12: a)) Coating adhesion testing for K1 sample coated with TiN, b)) Coating adhesion testing for AM1 sample coated with TiN

Both types of samples exhibited complete delamination of the coating. The conventionally produced sample appeared to have a slightly better coating, while the additively manufactured sample's coating was extremely thin and prone to fracture.

3.5. Coating nano-hardness

Results of coating nano-hardness testing according to EN ISO 14577-2:2002, consisting of mean values and standard deviations, are provided in Table 5.

Tab. 5: Results of mean nano-hardness values

Sample	HV 0,01
K1 with PACVD TiN	2440,3 ± 644,4
AM1 with PACVD TiN	2183,2 ± 418,7

The testing showed that the conventionally produced K1 sample coated with a PACVD TiN layer exhibited 12% higher hardness compared to the additively manufactured sample coated with the same method and coating. This discrepancy is attributed to the porous structure of the additively produced sample, resulting in reduced hardness of the base material, and consequently, weaker support for the coating, leading to decreased hardness.

4. CONCLUSION

The examination results demonstrated that additively manufactured TiAl6V4 alloy samples have superior machinability compared to conventionally produced samples. However, to improve the adhesion and thickness of the coating, it is necessary to reduce surface roughness. The average coating thickness achieved on the conventionally produced sample was $e = 1.58 \mu\text{m}$, whereas for the additively manufactured sample, the high degree of delamination and its brittleness made it impossible to determine the average coating thickness using Equation 1.

To enhance the quality of the coating layer, it is recommended to reduce the presence of titanium oxide on the surface, as this negatively impacts the adhesion and mechanical properties of the coating. During the PACVD process, adjusting parameters should be considered to optimize the process for desired workpiece dimensions, as the coating process depends on the component's geometry.

Furthermore, nano-hardness testing revealed that the conventionally produced sample coated with a PACVD TiN layer exhibited 12% higher hardness compared to the additively manufactured sample coated with the same method and coating. This is due to the porous structure of the additively produced sample, resulting in reduced hardness of the base material and, consequently, a weaker support for the coating, leading to decreased hardness.

In conclusion, additively manufactured TiAl6V4 samples show better machinability, but efforts are needed to improve coating adhesion and thickness. Addressing surface roughness and titanium oxide content on the surface can positively impact the coating quality. Further optimization of the PACVD process and consideration of workpiece geometry are essential for enhancing coating performance.

REFERENCES

- [1] S. Gorsse, C. Hutchinson, M. Gouné, and R. Banerjee, "Additive manufacturing of metals: a brief review of the characteristic microstructures and properties of steels, Ti-6Al-4V and high-entropy alloys," *Science and Technology of Advanced Materials*, vol. 18, no. 1. Taylor and Francis Ltd., pp. 584–610, Dec. 31, 2017. doi: 10.1080/14686996.2017.1361305.
- [2] S. Liu and Y. C. Shin, "Additive manufacturing of Ti6Al4V alloy: A review," *Mater Des*, vol. 164, Feb. 2019, doi: 10.1016/j.matdes.2018.107552.

- [3] D. Herzog, V. Seyda, E. Wycisk, and C. Emmelmann, "Additive manufacturing of metals," *Acta Mater*, vol. 117, pp. 371–392, Sep. 2016, doi: 10.1016/j.actamat.2016.07.019.
- [4] W. E. Frazier, "Metal Additive Manufacturing: A Review," *J Mater Eng Perform*, vol. 23, no. 6, pp. 1917–1928, Jun. 2014, doi: 10.1007/s11665-014-0958-z.
- [5] G. B. Kannan and D. K. Rajendran, "A Review on Status of Research in Metal Additive Manufacturing," in *Advances in 3D Printing & Additive Manufacturing Technologies*, Singapore: Springer Singapore, 2017, pp. 95–100. doi: 10.1007/978-981-10-0812-2_8.
- [6] M. Kazemi, S. Ahangarani, M. Esmailian, and A. Shanaghi, "Investigation on the corrosion behavior and biocompatibility of Ti-6Al-4V implant coated with HA/TiN dual layer for medical applications," *Surf Coat Technol*, vol. 397, p. 126044, Sep. 2020, doi: 10.1016/j.surfcoat.2020.126044.
- [7] D. de Castro Girão et al., "An assessment of biomedical CoCrMo alloy fabricated by direct metal laser sintering technique for implant applications," *Materials Science and Engineering: C*, vol. 107, p. 110305, Feb. 2020, doi: 10.1016/j.msec.2019.110305.
- [8] B. Blakey-Milner et al., "Metal additive manufacturing in aerospace: A review," *Mater Des*, vol. 209, p. 110008, Nov. 2021, doi: 10.1016/j.matdes.2021.110008.
- [9] T. Zlamal, I. Mrkvica, T. Szotkowski, and S. Malotova, "The Influence of Surface Treatment of PVD Coating on Its Quality and Wear Resistant," *Coatings*, vol. 9, no. 7, p. 439, Jul. 2019, doi: 10.3390/coatings9070439.
- [10] M. Niinomi, "Mechanical properties of biomedical titanium alloys," *Materials Science and Engineering: A*, vol. 243, no. 1–2, pp. 231–236, Mar. 1998, doi: 10.1016/S0921-5093(97)00806-X.
- [11] S. S. Eskildsen, C. Mathiasen, and M. Foss, "Plasma CVD: process capabilities and economic aspects," *Surf Coat Technol*, vol. 116–119, pp. 18–24, Sep. 1999, doi: 10.1016/S0257-8972(99)00142-5.
- [12] A. Moll et al., "Coupling powder bed additive manufacturing and vapor phase deposition methods for elaboration of coated 3D Ti-6Al-4V architectures with enhanced surface properties," *Surf Coat Technol*, vol. 415, p. 127130, Jun. 2021, doi: 10.1016/j.surfcoat.2021.127130.



KINETIKA RASTA BORIDNOG SLOJA NA ČELIKU 42CRM04

BORIDE LAYER GROWTH KINETICS ON 42CRM04 STEEL

Filip Žanetić¹, Božidar Matijević¹, Darko Landek¹, Igor Vukić

¹Fakultet strojarstva i brodogradnje, Sveučilište u Zagrebu, Ivana Lučića 5, Zagreb, Hrvatska

¹ University of Zagreb, Faculty of mechanical engineering and naval architecture, Ivana Lučića 5, Zagreb, Croatia

Sažetak

Boriranje je vrsta toplinsko difuzijske obrade s primarnim ciljem povećanja površinske tvrdoće, otpornosti na trošenje i korozije. Otpornost na trošenje boriranih dijelova ovisi o vrsti borida koji nastaju na površini čelika i njihovoj debljini. U ovom radu ispitana je kinetika rasta boridnih slojeva na čeliku za poboljšavanje 42CrMo4. Boriranje je provedeno u granulatu na temperaturama od 800 do 900°C, u trajanju od 1, 3 i 5 sati. Nakon boriranja ispitane su razlike u nastalim boridnim slojevima za različite temperature i vremena boriranja. Izmjerena je debljina boridnog sloja i tvrdoća po poprečnom presjeku uzoraka. Vrijednosti frekvencijskog faktora (d) i aktivacijske energije za nastali borirani sloj određene su pomoću Arrheniusove jednadžbe. Iz faktora frekvencije i aktivacijske energije modelirana je jednačba za predviđanje rasta boridnog sloja. Rezultati pokazuju razliku u debljini boridnog sloja i volumnom udjelu boridnih faza u ovisnosti o temperaturi i vremenu boridiranja.

Ključne riječi: boriranje, 42CrMo4, boridna faza

Abstract

Boronizing is a type of thermal diffusion process with primary goal of increasing the surface hardness, wear, and corrosion resistance. Wear resistance of boronized parts depends on the type of borides that form on steel surface and their thickness. This paper focuses on evaluation of borides layers that form on 42CrMo4 steel. Pack boronizing was carried out at temperature range of 800-900°C in duration of 1, 3 and 5 hours. After boronizing differences in surface boride layers were observed for different temperatures and time of boriding. Boriding compound depth and cross section hardness was measured. From boriding compound depth values of frequency factor (d) and activation energy were determined by means of Arrhenius equation. From frequency factor and activation energy equation predicting growth of boride layer was determined. Results indicate difference in boride layer thickness and volume share of boride phases depending on temperature and time of boriding.

Keywords: Boronizing, 42CrMo4, boride phase

1. INTRODUCTION

Boronizing is a type of thermal diffusion process with the primary goal of increasing the surface hardness, wear, and corrosion resistance of different types of steel [1]. Pack boronizing, the most used method of boronizing today can be carried out at different temperatures ranging from 800 to 1050°C and duration of 1 to 8 hours [2]. Depending on temperature, time and type of steel, different boride layer forms on the steel surface. Besides the type of boride layer, thickness of achieved layer is also very important. Understanding growth of boride layer is important for predicting part wear and scheduling maintenance. For some types of steel like C45, the boride layer growth rate is already calculated using the Arrhenius equation [3,4,5]. In this study using Arrhenius equation frequency factor and activation energy were determined for 42CrMo4 borided steel. Frequency factor and activation energy were used for construction of equation that predicts boride layer thickness depending on time and temperature of boronizing process.

2. EXPERIMENTAL PART

42CrMo4 is a commonly used steel known for quenching and tempering heat treatment, offering a favorable balance of strength and toughness. In the presented study, 42CrMo4 steel underwent boronization using Durborid 3 solid agent at temperatures ranging from 850 to 950°C for durations of 1, 3, and 5 hours. The boronizing process was conducted in a chamber furnace without the use of an inert atmosphere. To ensure uniform temperature distribution among all samples, the specimens were gradually heated from room temperature within the furnace. An additional hour was added to the boronizing duration to attain the desired temperature of the samples due to the heat-insulating properties of the boronizing agent. Following boronizing, the samples were transferred to a separate furnace held at 300°C to achieve a ferrite-perlite microstructure. After boronizing all samples were longitudinal cross-sectional cut and prepared for metallographic examinations. This preparation involved grinding with emery paper up to 2000 grit, alumina polishing, and etching with a 3% nital solution. After the metallographic procedures, the thickness of the boride layers was measured using light microscopy. Cross-sectional hardness assessments were performed using Vickers hardness testing to confirm the presence of borides in the surface layer.

3. RESULTS

The boride layers formed on 42CrMo4 steel are compact and consist of a mono Fe₂B boride layer. The boride layer exhibits a saw-tooth morphology characteristic of boronizing low alloy steels. Although the thickness of the boride layer increases with higher boronizing duration and temperature, the growth rate slows down with an increase in duration, consistent with earlier studies [6,7,8]. To measure the thickness of the boride layers and perform other experimental measurements, 27 samples were boronized at temperatures of 850°C, 900°C, and 950°C for durations of 1, 3, and 5 hours.

Table 2: Boride layer thickness for 42CrMo4 steel [μm]

Temperature	t=1h	σ_{1h} [μm]	t=3h	σ_{3h} [μm]	t=5h	σ_{5h} [μm]
850°C	23,30	1,61	38,12	1,31	48,44	2,04
900°C	42,47	0,165	59,37	1,38	81,47	1,77
950°C	58,64	0,860	93,44	3,42	102,69	1,78

Table 1 represents the different boride layer thicknesses [μm] achieved at various durations and temperatures of boronizing. Standard deviation [σ] is also included in Table 1 to indicate the degree to which boride layer thickness varies among different temperature and duration. Since the formation of boron layers does not involve carbon, a carbon-rich region is present beneath the boride layer, referred to as the 'carbon barrier,' within the steel diffusion zone. This carbon barrier effectively slows down the growth of the boride.

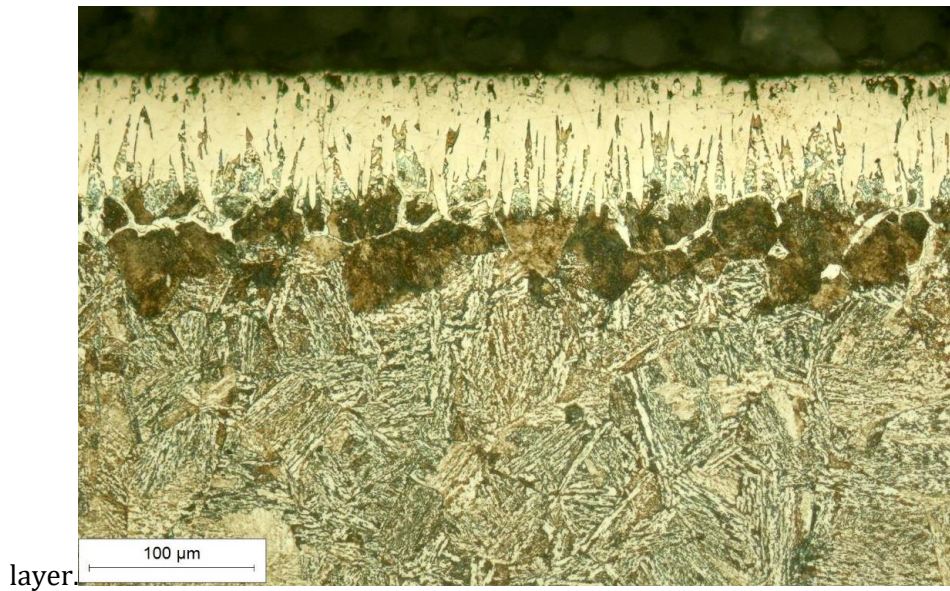


Figure 1: Microstructure of boride layers formed by boronizing for 5 h at temperature of 900°C, magnification 200:1

Figure 1 displays the morphology of the boride layer achieved after 5 hours of boronizing at a temperature of 900°C. The boride layer measures 81.47 μm in thickness and comprises of mono Fe_2B layer along with other alloying elements and boron compounds. Following the metallographic examination, cross-sectional microhardness was assessed at every 20 μm using the Vickers method (HV0.1), starting from the surface and extending to the sample's core. The Boronizing Hardness Depth (BHD) was calculated as the distance from the sample's surface to the average depth of peaks and troughs of the Fe_2B compound. All samples exhibit a robust outer layer with hardness exceeding 1000 HV0.1, and the core that remains unchanged after boronizing. Notably, the hardness of the base material within the diffusion zone, between the teeth and boron layer exhibits higher hardness. This phenomenon arises due to elevated carbon content, a result of its suppression beneath the border layer. Microhardness is illustrated in Figure 2.

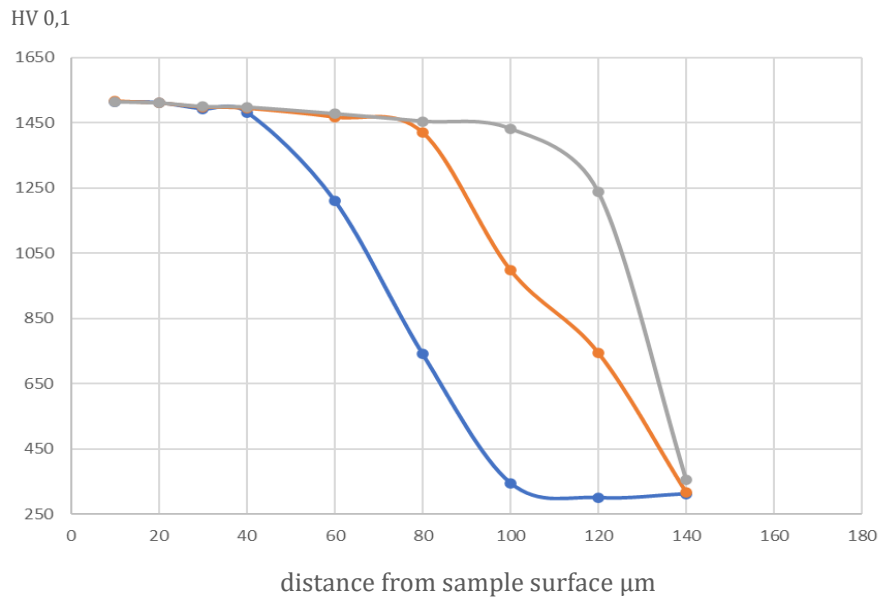


Figure 2: Hardness distribution for samples borided at 950°C for 1, 3 and 5 hours

Figure 2 shows hardness distribution across borided samples, blue curve represents hardness of sample borided for 1h at 950°C, orange curve sample borided for 3h at 950°C and gray curve sample borided for 5h at 950°C.

Growth kinetics of boride layer is analysed by using classic kinetic method based on Arrhenius equation. Diffusion process obeys parabolic law:

$$d^2 = D t, \quad (1)$$

where d is diffusion layer thickness [m], D is growth rate constant [m²/s], t is diffusion duration [s]. Dependence between boride layer thickness and square root of boronizing duration is shown in Figure 3.

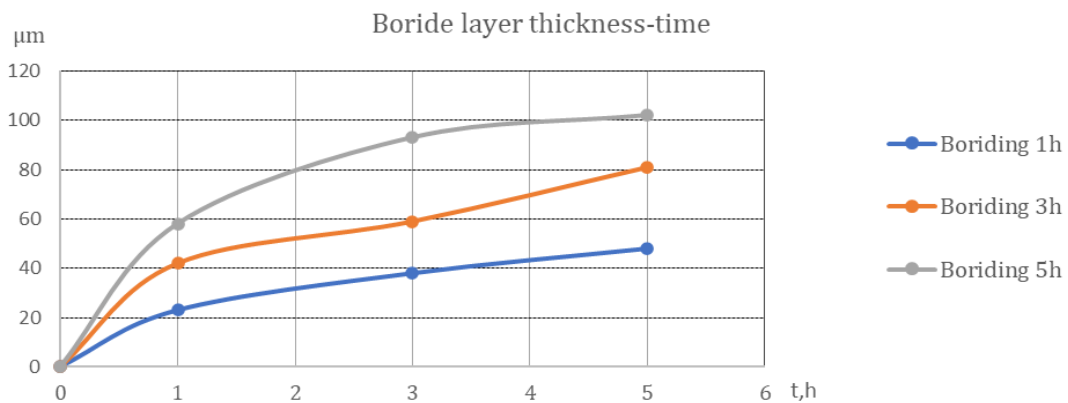


Figure 3: Boride layer thickness as a function of boronizing time

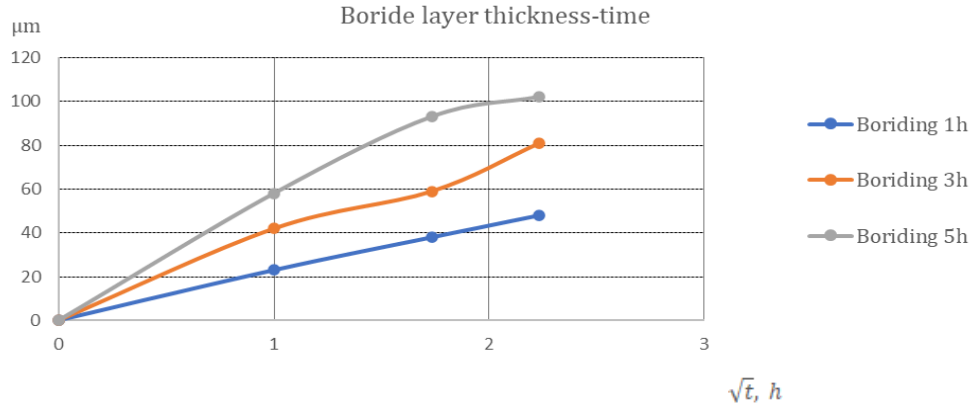


Figure 4: Boride layer thickness as a function of square root of boronizing duration

Figure 3 and Figure 4 confirm diffusion nature of boronizing described with parabolic rule. The graf in Figure 4 reveals that thickness of diffusion layer linearly increases with square root of duration.

The growth rate constants are estimated from data. The growth rate constants are $1,27 \cdot 10^{-13}$, $3,37 \cdot 10^{-13}$ and $4,97 \cdot 10^{-13}$ m²/s at temperatures 850, 900 and 950 °C, respectively.. Activation energy and frequency factor are estimated from the slope and y-intercept of the straight of log K-time diagram. The frequency factor is $2,736 \cdot 10^{-6}$ m²·s⁻¹ and the activation energy is 156 178 J·mol⁻¹. If considering used equations and determined data, expression for boronizing 42CrMo4 steel in observed temperature range and duration is derived as follows:

$$d = \sqrt{2,736 * 10^{-6} t * e^{-\frac{156178}{RT}}} \quad (1)$$

The thickness of the borided layer (m) can be calculated using expression (1) for a given time and temperature. This expression can be verified by comparing it to values measured on real samples. The results show errors in the expression ranging from 0.26% to 5.13% for different temperatures and times.

4. CONCLUSION

This paper examines boride layers formed on 42CrMo4 steel, displaying a characteristic saw-tooth morphology common for boronizing low-alloy steels. To analyze boride layer thickness growth, 27 samples were boronized at temperatures between 850 and 950°C for durations of 1, 3, and 5 hours. Micro hardness measurements show presence of a hard outer layer and unchanged core after boronizing, with hardness decreasing with distance from the surface. The growth kinetics of the boride layer follow the Arrhenius equation, with diffusion obeying a parabolic law. Growth rate constants are determined for different temperatures, and an expression for boronizing 42CrMo4 steel is derived. The growth rate constants are estimated from data. The growth rate constants are $1,27 \cdot 10^{-13}$, $3,37 \cdot 10^{-13}$ and $4,97 \cdot 10^{-13}$ m²/s at temperatures 850, 900 and 950 °C, respectively. Figure 4 shows dependence between natural logarithm of growth rate constants and reciprocal values of boronizing temperatures. Activation energy and frequency factor are estimated from the slope and y-intercept of the straight of log K-time diagram. The frequency factor is $2,736 \cdot 10^{-6}$ m²·s⁻¹ and the activation energy is 156 178 J·mol⁻¹. This expression is validated through measurements, revealing errors ranging from 0.26% to 5.13% for various temperatures and durations.

REFERENCES

- [1] Milinović A., Marušić V., Samardžić I., Research into boride layers growth kinetics on C45 carbon steel, *Metalurgija*, 55.4: 671-674, (2016).
- [2] Gunes, Ibrahim. (2016). Rate of growth of boride layers on stainless steels. Oxidation Communications. In Press.Cai, Wei & Meng, Fanna & Gao, Xinyan & Hu, Jing. (2012).
- [3] Campos-Silva I, Ortiz-Dominguez M, Tapia-Quintero C, Rodríguez-Castro G, Jimenez-Reyes M Y and Chávez-Gutiérrez E (2012), 'Kinetics and boron diffusion in the FeB/Fe₂B layers formed at the surface of borided high-alloy steel', J. Mater. Eng. Perform., 21, 1714–1723.Wang, X. & Wu, C. & Sun, M. & Xie, C.. (2014).
- [4] Bican, O., Bayca, S. U., Ocak-Araz, S., Yamanel, B. and Tanis, N. (2019): Effects of the boriding process and of quenching and tempering after boriding on the microstructure, hardness and wear of aisi 5140 steel', surface review and letters. world scientific pub co pte lt, 27(06), p. 1950157. doi: 10.1142/s0218625x19501579.
- [5] Lee, Y. C., et al. (2017). "Effects of Boronizing Temperature on Microstructure and Wear Behavior of Boride Layers on 42CrMo4 Steel." Journal of Materials Engineering and Performance, 26(7), 3343-3352.
- [6] Sathiya, P., et al. (2015). "Influence of Boronizing Process Parameters on the Formation of Boride Layers on 42CrMo4 Steel." Surface and Coatings Technology, 269, 201-210.
- [7] Sundararajan, G., et al. (2018). "Boronizing of 42CrMo4 Steel: Microstructure, Hardness, and Wear Behavior." Journal of Thermal Spray Technology, 27(8), 1327-1339.
- [8] Cui, X., et al. (2019). "Effect of Boronizing Process Parameters on the Microstructure and Hardness of Boride Layers on 42CrMo4 Steel." Journal of Materials Science & Technology, 35(9), 1775-1784.



VpCI FOR MULTIMETAL PROTECTION IN HEATING SYSTEMS

VpCI ZA MULTIMETALNU ZAŠTITU OD KOROZIJE U SUSTAVIMA ZA GRIJANJE

Ivana Radić Boršić¹, Ivan Stojanović², Marin Kurtela³, Vesna Alar⁴, Boris. A. Mikšić⁵

¹Cortec Corporation Europe, Gramača 5F, Zagreb, Croatia

²Faculty of Mechanical Engineering and Naval Architecture, Ivana Lučića 5, Zagreb, Croatia

³Faculty of Mechanical Engineering and Naval Architecture, Ivana Lučića 5, Zagreb, Croatia

⁴Faculty of Mechanical Engineering and Naval Architecture, Ivana Lučića 5, Zagreb, Croatia

⁵Cortec Corporation, FNACE, 4119 White Bear Parkway, St. Paul, MN, USA

Abstract

Carbon steel is a material often used in heating systems in civil buildings. It is generally susceptible to uniform corrosion in water but localized corrosion like pitting and crevice corrosion can also occur due to media contamination or local deposits on the pipeline walls. Stagnant water in the system, especially during the period when the heating system is not working, can be very detrimental for materials and can further accelerate corrosion. One method of corrosion protection of heating systems is to add vapor phase corrosion inhibitors (VpCI) to the media, considering that the system often consists of fittings and valves made of more noble metals like copper and copper alloys. This paper investigates the protective performance of vapor phase corrosion inhibitors for the reduction of corrosion in heating systems. In order to evaluate corrosion inhibiting performance and to determine the optimal product concentration at room and elevated temperatures, electrochemical polarization techniques including open circuit potential, polarization resistance and Tafel extrapolation were utilized. The optimal concentration of corrosion inhibitor was determined for efficient corrosion protection of all tested materials including carbon steel, aluminium, and copper parts, which are the main metal components in the tested heating system.

Keywords: heating system; multimetal components; media; vapor phase corrosion inhibitor

Sažetak

Ugljični čelik je materijal koji se često koristi u sustavima grijanja u civilnim zgradama. Općenito je osjetljiv na opću koroziju u vodi, ali lokalizirana korozija poput rupičaste i korozije u procijepu također se može pojaviti zbog kontaminacije medija ili lokalnih naslaga na stijenkama cjevovoda. Stagnacija vode u sustavu, posebno u razdoblju kada sustav grijanja ne radi, može biti vrlo štetna za materijale i može dodatno ubrzati koroziju. Jedan od načina zaštite od korozije sustava grijanja je dodavanje hlapivih inhibitora korozije (VpCI) u medij, s obzirom da se sustav često sastoji od armatura i ventila izrađenih od plemenitijih metala poput bakra i bakrenih legura. Ovaj rad istražuje zaštitnu učinkovitost inhibitora korozije za smanjenje korozije u sustavima grijanja. Kako bi se procijenila učinkovitost inhibicije korozije i odredila optimalna koncentracija proizvoda pri sobnoj i povišenoj temperaturi, korištene su tehnike elektrokemijske polarizacije uključujući potencijal otvorenog strujnog kruga, polarizacijski otpor i Tafelovu ekstrapolaciju. Određena je optimalna koncentracija inhibitora korozije za učinkovitu zaštitu od korozije svih ispitivanih materijala uključujući ugljični čelik, aluminij i bakrene dijelove koji su glavne metalne komponente u ispitivanom sustavu grijanja.

Ključne riječi: sustavi grijanja; multimetalne komponente; medij; hlapivi inhibitori korozije

1. INTRODUCTION

A hot water heating system in civil buildings usually consists of a boiler and a system of pipes connected to radiators. Common radiator materials are mild steel, stainless steel, aluminium and cast iron. Mild steel tends to be the most popular material used to make radiators due to its relatively low price, different design options and colours. However, mild steel radiators can be prone to rusting, so they come with shorter guarantees/durability. Mild steel is a material which corrodes uniformly on the surface when exposed to open atmosphere, soils, and waters [1]. It is generally not susceptible to localized corrosion in water, but pitting corrosion and crevice corrosion may occur due to media contamination or deposits on the walls [2].

Figure 1 shows the damage and leakage of mild steel panel radiators in an office building. Panel radiators were produced from cold rolled steel plate Fe P 01 according to EN 10130. The wall thickness was 1.25 mm. Paint blistering, traces of water leaks and corrosion products are visible at the damaged location. The first leakage was observed after 3 years in service.



Fig. 1: Delivered radiators and location of wall perforation and leakage. Paint blistering at the site of the leak.

Visual inspection of the cut sample at the leakage location revealed general corrosion damage with pitting corrosion sites on the inner wall of the delivered radiators. Observed corrosion products and oxides on the radiator walls indicate the corrosivity of water in the heating system.

Damage and leaking were predominantly observed at the edges of or below the black non-metallic layers/deposits on the inner walls of the radiator, which are likely the remnants of an organic component (glue, melt or similar) from radiator production. Such localities are the sites of crevice corrosion. Stereomicroscopic examination of the inner surface of the cut radiator sample confirmed that damage occurred at the edge of the black deposits on the inner wall of the radiator, which is shown in Figure 2.

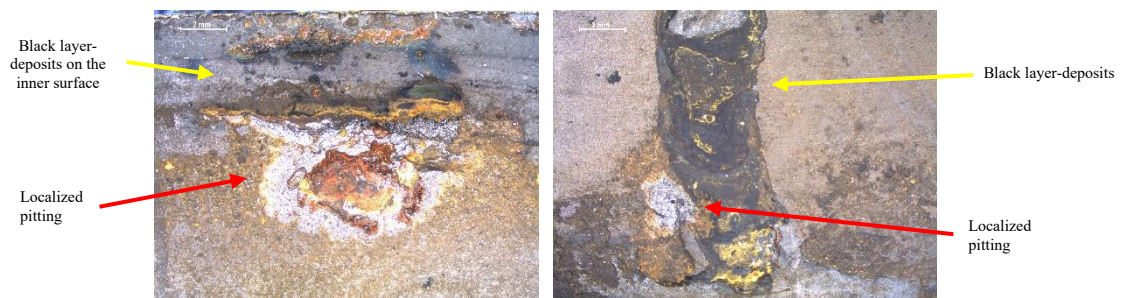


Fig. 2: Stereomicroscopic view of the observed intense localized corrosion and perforation on the inside wall of the cut-out specimen. The corrosion damage is localized on the edge of the black non-metallic layers.

After the stereomicroscopic analysis, the sample was cleaned with hydrochloric acid (HCl) solution to remove corrosion products for better insight into the condition of the base material, which is shown in Figure 3. Gray deposits dissolved into the HCl solution. However, a black layer was observed that did not dissolve, which indicates that it is an organic component most likely from the production of radiators.

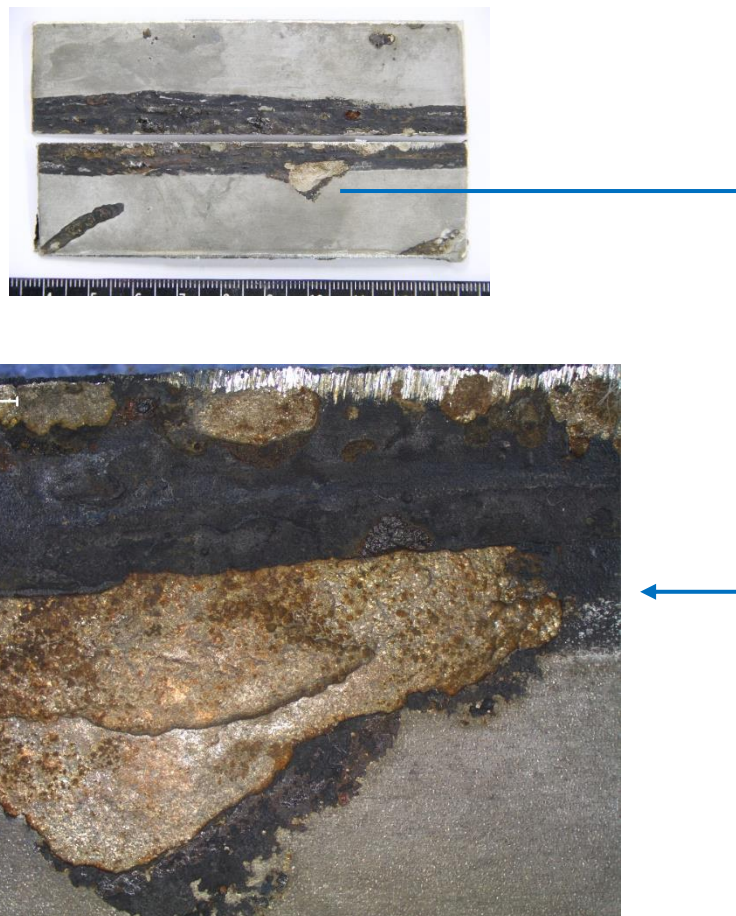


Fig. 3: Inner surface of the cut sample after cleaning in HCl solution. Intensive corrosion wear is located at the edges of the black layer.

The Langelier saturation index ($LSI = -0.46$) and the Ryznar stability index ($RSI = 8.5$) were calculated from physicochemical parameters of the analysed soft water. These results indicate that the water in the radiator is aggressive at 20 °C, which is the water temperature during the summer period when the water rests in the heating system. Also, turbidity and black sediment were observed in the water samples taken from the radiator. Chemical analysis showed that the black precipitate in the water is most likely to be magnetite (Fe_3O_4), which is a product of general corrosion of mild steel radiators.

There are 3 possible solutions to mitigate the localized corrosion seen in the analysis of the radiator internals:

- 1) change the material of the radiators,
- 2) discharge the water from the system during the summer period of dormancy and drying,
- 3) reduce the aggressiveness of water by adding corrosion inhibitors.

Considering the need to maintain the same working conditions, elements, and the material of the heating system parts, it was decided to use corrosion inhibitors. Mild steels in general are susceptible to corrosion and the use of corrosion inhibitors is important for their extended, safe, and cost-effective operation [3].

Corrosion inhibitors are chemical substances which, when added to a corrosive environment, reduce the corrosion rate of metal. A special class of inhibitors are Vapor phase Corrosion Inhibitors (VpCIs). VpCI products contain organic substances that have moderately high vapor pressures which allow them to prevent corrosion in the vapor space where the VpCI is not in direct contact with the metal surface. The volatile components of VpCI form a thin monomolecular film which, through ion activity, protects the metal from corrosion. The resulting barrier prevents the corrosion reaction from occurring on the metal surface [4].

2. EXPERIMENTAL STUDY

Based on the chosen solution, it was decided to add a multimetal corrosion inhibitor, VpCI-649, to the soft water (SW) in the heating system to minimize corrosion. VpCI-649 is a concentrated liquid formulation that protects ferrous and non-ferrous metals from corrosive solutions designed for open and closed looped systems. It combines contact and volatile corrosion inhibitors along with antiscalants in a formulation that does not contain nitrites, phosphates, or chromates [5, 6]. In 1 lit of soft water, 2.5 ml of inhibitor was added.

To evaluate corrosion inhibiting performance and to determine its optimal concentration at room (22 ± 2) °C and elevated temperature (70 ± 2) °C, electrochemical polarization techniques including open circuit potential measurement, polarization resistance and Tafel extrapolation in the heating water were employed. The testing was conducted in a

standard three electrode test cell in relation to the reference saturated calomel electrode (SCE), using a Potentiostat/Galvanostat device, Model VersaSTAT 3 (Princeton applied research AMETEK). Metals tested were carbon steel, aluminium, and copper, which are the main metal components in the tested heating system.



Polarization curves were registered after 1000 seconds of exposure to the testing solution (water from the ion exchanger) in order to allow corrosion potential (E_{corr}) stabilization. Polarization resistance (R_p) was determined in a ± 20 mV potential range around the corrosion potential. During the potentiodynamic measurements, the working electrode was polarized to the potential of ± 250 mV relative to the corrosion potential and the current (I_{corr}) response was measured. For interpretation of the obtained data, the ZSimpWin Version 3.2 software was used. Assessment of rusting after corrosion testing was conducted using stereomicroscope Leica MZ6.



3. RESULTS

Based on measured data of unprotected and protected samples, the corrosion rate (v_{corr}) and corrosion inhibitor efficiency (η) were calculated [7]. Photomicrographs of the mild steel samples after testing in uninhibited water showed traces of pitting and crevice corrosion at room and elevated temperatures. Copper samples retained their general appearance, while aluminium samples showed slight uniform corrosion at 70 °C.



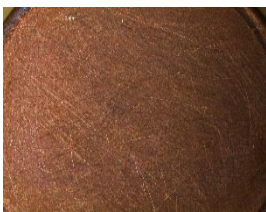
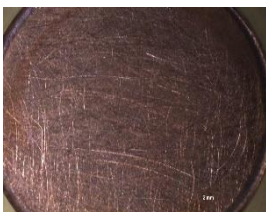
The results are given in Tables 1, 2, and 3.

Tab. 1: Test results for mild steel

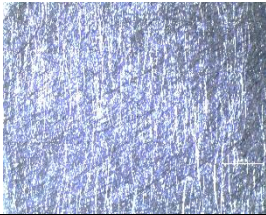
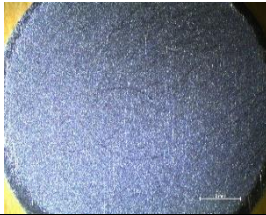
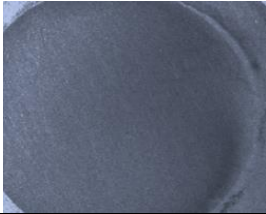

Electrolyte	Soft water	2.5 ml inh. + 1 lit soft water
Temperature	22±2 °C	22±2 °C
E_{corr} vs. SCE	-697.45 mV	-271.13 mV
R_p	2.627 kΩ	8.016 kΩ
I_{corr}	39.197 μA	4.714 μA
v_{corr}	0.455 mm/year	0.0547 mm/year
η	-	87.98 %
		
Temperature	70±2 °C	70±2 °C
E_{corr} vs. SCE	-694.997 mV	-270.822 mV

R_p	1.457 k Ω	6.192 k Ω
I_{corr}	53.285 μ A	6.443 μ A
V_{corr}	0.6187 mm/year	0.0748 mm/year
η	-	87.91 %
		

Tab. 2: Test results for copper

Electrolyte	Soft water	2.5 ml inh. + 1 lit soft water
Temperature	22 \pm 2 $^{\circ}$ C	22 \pm 2 $^{\circ}$ C
E_{corr} vs. SCE	-75.76 mV	-440.22 mV
R_p	16.648 k Ω	440.218 k Ω
I_{corr}	2.612 μ A	186.974 nA
V_{corr}	0.0606 mm/year	0.00433 mm/year
H	-	92.85 %
		
Temperature	70 \pm 2 $^{\circ}$ C	70 \pm 2 $^{\circ}$ C
E_{corr} vs. SCE	-98.15 mV	-137.40 mV
R_p	50.393 k Ω	88.059 k Ω
I_{corr}	1.121 μ A	525.032 nA
V_{corr}	0.0259 mm/year	0.0122 mm/year
η	-	52.86 %
		

Tab. 3: Test results for aluminium

Electrolyte	Soft water	2.5 ml inh. + 1 lit soft water
Temperature	22±2 °C	22±2 °C
$E_{\text{corr vs. SCE}}$	-590.41 mV	-604.21 mV
R_p	11.389 kΩ	184.22 kΩ
I_{corr}	2.533 μA	793.697 nA
v_{corr}	0.0281 mm/year	0.0088 mm/year
η	-	68.68 %
		
Temperature	70±2 °C	70±2 °C
$E_{\text{corr vs. SCE}}$	-731.49 mV	-848.35 mV
R_p	4.2038 kΩ	3.891 kΩ
I_{corr}	4.839 μA	4.404 μA
v_{corr}	0.0537 mm/year	0.0489 mm/year
η	-	8.94 %
		

4. DISCUSSION

Soft water does not act aggressively on copper and aluminium, with the corrosion rate of copper being the lowest of all tested materials.

The corrosion rate of aluminium in the uninhibited water is approximately equal to the corrosion rate of mild steel in the inhibited water, which indicates that aluminium can be used in the heating system instead of mild steel radiators.

5. CONCLUSION

Based on the conducted tests of the effectiveness of corrosion protection VpCI-649 proved to be an effective inhibitor for steel, copper, and aluminium at room temperature and for steel and copper at elevated temperature. The tested inhibitor showed lower efficiency

protection for aluminium at 70 °C, although the corrosion rate was lower than in uninhibited water. The recommended concentration of VpCI-649 inhibitor, for all tested materials, in soft water was 0.25 vol%.

REFERENCES

- [1] Zehra S., Mobin M., Aslam J., An overview of the corrosion chemistry, *Environmentally Sustainable Corrosion Inhibitors Fundamentals and Industrial Applications*, Ed. C. M. Hussain, C. Verma, J. Aslam, Elsevier, pp. 3-23, (2022).
- [2] Jelinek J., Neufeld P., Pickup G. A., Plastic deformation and Pitting Corrosion in Mild Steel in Neutral Media, *Br. Corros. J.*, 13, pp. 112-117, (1978).
- [3] Dwivedi D., Lepkova K., Becker T., Carbon steel corrosion: a review of key surface properties and characterization methods, *RSC Adv.*, 7, pp. 4580–4610, (2017).
- [4] Mikšić Boris A., *FNACE: VpCI Technology Handbook*, vol. 1, Ed. S. Garrow, Cortec Corporation, USA, (2014).
- [5] VpCI-649 Series Corrosion Inhibitors – Cortec Corp., *Engineered Systems Magazine*, BNP Media, USA, 38 12, (2021).
- [6] Corrosion inhibitor for heating and cooling applications, *Plant Engineering*, CFE Media, (2015).
- [7] Kurtela M., Šimunović V., Stojanović I., Alar V., Effect of the cerium (III) chloride heptahydrate on the corrosion inhibition of aluminum alloy, *Materials and Corrosion*, 71, pp. 1–23, (2020).

KONZERVACIJA VATRENOG ORUŽJA PRIMJENOM ISPARAVAJUĆIH INHIBITORA KOROZIJE

Katarina Sabelja¹, Ivan Leutar¹, Mirko Jakopčić²

¹ Remontni zavod, Josipa Lončara 2A, Zagreb, Republika Hrvatska

² Hrvatsko vojno učilište „Dr. Franjo Tuđman“, Ilica 256b, Zagreb, Republika Hrvatska

Sažetak

U radu su prikazane metode i postupci konzervacije vatrenog oružja primjenom isparavajućih inhibitora korozije. Težište rada usmjereno je na prikaz tehnoloških faza pripreme materijala i vatrenog oružja za konzervaciju te neposrednog izvođenja kratkoročne i dugoročne konzervacije oružja i pripadajućeg pričuvnog alata i pribora. Prikazani su postupci i kriteriji međufazne i završne kontrole izvedenih radova konzervacije, kontrole stanja konzerviranog vatrenog oružja tijekom skladištenja te slučajevi u kojima se provodi dekonzervacija i rekonzervacija. U zaključku rada dati su prijedlozi za racionalizaciju troškova konzervacije vatrenog oružja, uz zadržavanje zahtijevane učinkovitosti primijenjenog tehnološkog postupka.

Ključne riječi: vatreno oružje, konzervacija, isparavajući inhibitori korozije, kontrola kvalitete

Abstract:

This paper presents methods and procedures for the conservation of firearms using volatile corrosion inhibitor. The focus of the paper is to show the technological stages of the preparation of materials and firearms for conservation and also the direct implementation of short-term and long-term conservation of weapons and spare parts, tools and accessories. Procedures and criteria for intermediate and final control of the performed conservation works, control of the condition of preserved firearms condition during storage, and cases in which deconservation and reconservation are carried out are presented. In the conclusion of the paper, proposals are given for the firearms conservation costs rationalization, while maintaining the required efficiency of the applied technological procedure.

Keywords: firearms, conservation, vapor corrosion inhibitors, quality control

1. UVOD

Vatreno oružje je prijenosno cijevno oružje koje kroz cijev ispaljuje sačmu, zrna ili projekte, koristeći tlak plinova nastalih izgaranjem barutnog punjenja. Prema namjeni vatreno oružje se može podijeliti na vojno (borbeno), civilno, lovačko i sportsko. Najširu primjenu ima vojno vatreno oružje, koje se, ovisno o konstrukciji, dijeli na: pištolje, revolvere, puške, puškostrojnice, kratke strojnice, strojnice i ručne bacače. Bez obzira na široku primjenu i masovnu proizvodnju, najveća količina vojnog vatrenog oružja se u mirnodopskim uvjetima malo koristi. Zbog toga se ono čuva i skladišti u tehnički ispravnom stanju, u uvjetima koji u predviđenom vremenskom periodu moraju osigurati visoki stupanj ispravnosti, pouzdanosti i raspoloživosti. Uvjeti i način skladištenja i čuvanja vatrenog oružja moraju osigurati njegovu privremenu zaštitu od korozije, koja u protivnom može uzrokovati neželjeno razaranje materijala pod utjecajem kemijskog ili elektrokemijskog djelovanja okoline. Korozija uvijek počinje na površini, a zatim se sporije ili brže razvija i prodiire u materijal, izazivajući pri tome promjene vanjskog izgleda i mehaničkih svojstava materijala, koji se djelomično ili potpuno razara, pri čemu se na njemu formiraju produkti korozije u obliku taloga (hrđe). Kako bi se tehnički ispravno vatreno oružje, koje se privremeno nalazi izvan uporabe, zaštitilo od korozije te bi se na taj način osigurala ili produžila njegova uporabna vrijednost, potrebno je poduzeti propisane mjere i postupke njegove zaštite. Postoji više metoda i sredstava zaštite od korozije, čiji izbor može ovisiti o nizu čimbenika (zahtjevi u pogledu mobilnosti, vremena i uvjeta skladištenja, materijala, oblika, konstrukcije, ekonomskih čimbenika), a jedna od metoda je primjena inhibitora korozije.

2. INHIBITORI KOROZIJE

Zaštita od korozije najčešće se postiže odabirom korozijski postojanih konstrukcijskih materijala, konstrukcijsko – tehnološkim mjerama u fazi projektiranja, nanošenjem zaštitnih prevlaka, elektrokemijskom zaštitom i zaštitom inhibitorima korozije [1].

Inhibitori korozije su tvari anorganskog ili organskog podrijetla u čijem prisustvu agresivnost neke sredine postaje manja, što za posljedicu ima smanjenje brzine korozije do tehnički prihvatljivih granica.

Prema načinu djelovanja, inhibitori korozije se mogu podijeliti na anodne, katodne i mješovite (anodno-katodne) [1].

2.1. Anodni inhibitori korozije

Anodni inhibitori su kemijske tvari koje tvore zaštitni sloj oksidnog filma na anodnim dijelovima metala, uslijed čega se smanjuje brzina korozije formiranog sprega. U ovu grupu inhibitora se ubrajaju pasivatori (kromati, nitriti, molibdati, volframati i vanadati), koji u otopinama s pH 5-9 prevode Fe, Ni, Co i njihove legure u pasivno stanje. Među anodne inhibitore ubrajaju se i tzv. taložni inhibitori (npr. vođeno staklo), koji s ionima konstrukcijskog metala daju slojeve netopljivih korozijskih produkata [2].

2.2. Katodni inhibitori korozije

Katodni inhibitori izravno koče katodnu reakciju djelovanjem ili na reakciju izdvajanja vodika ili na reakciju izdvajanja kisika, a mogu djelovati i kao taložni inhibitori koji na lokalnim katodama tvore netopljive produkte. Najvažniji katodni inhibitori su spojevi s

arsenom, antimonom, kositrom, bizmutom, itd. (izravno koče katodnu reakciju) te cinkove i kalcijeve soli, koje djeluju kao taložni inhibitori.

2.3. Mješoviti inhibitori korozije

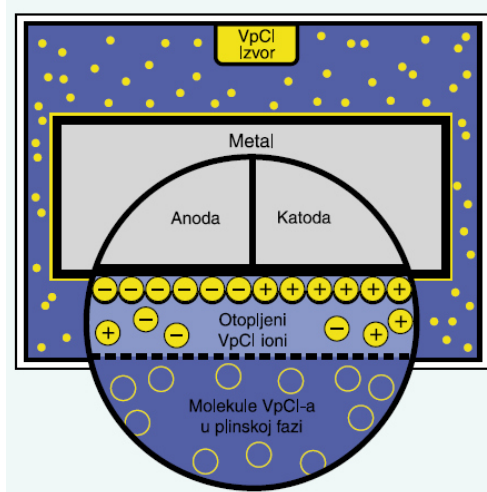
Mješoviti inhibitori imaju dvostruko djelovanje, i anodno i katodno. To su najčešće organski spojevi koji se adsorbiraju na metalnu površinu, stvarajući zaštitne monomolekulske filmove, pa se često nazivaju i adsorpcijski inhibitori (želatina, agar-agar, škrob, tanin, K-glukonat). U ovu skupinu inhibitora spadaju i derivati acetilena, soli organskih kiselina, amini, nitrati, spojevi sa sumporom, tioalkoholi i sulfidi [2].

2.3.1. Isparavajući inhibitori korozije

Isparavajući inhibitori korozije (VCI – Volatile Corrosion Inhibitors) čine posebnu skupinu inhibitora koji štite metal od atmosferske korozije.

Ovi inhibitori štite površinu metala na način da kondicioniraju atmosferu zatvorenog (hermetičnog) prostora zaštitnom parom koja sadrži inhibitore (Slika 1.). Širenjem nastale pare unutar zatvorenog prostora, migriraju prema svim površinama metala koje mogu biti izložene korozivnim procesima. Pri dodiru s površinom metala dolazi do kondenzacije pare i stvaranja tankog monomolekularnog zaštitnog filma, koji putem ionskog djelovanja štiti površinu metala od korozije.

Specifičnost ovog zaštitnog filma je da se kontinuirano održava i obnavlja daljnjom kondenzacijom pare. Ove inhibitore također karakteriziraju još dva važna svojstva, a to su: visoka otpornost apsorbiranog zaštitnog filma na koroziju i dobra toplinska stabilnost na visokim temperaturama [3].



Slika 1: Mehanizam djelovanja isparavajućih inhibitora korozije [4]

Kada je riječ o preventivnom održavanju naoružanja i vojne opreme, najšira praktična primjena zaštite metala od utjecaja atmosferske korozije isparavajućim inhibitorima korozije je pri izvođenju postupaka konzervacije vatrenog oružja.

Sukladno potrebama, novim spoznajama i razvoju novih tehnologija i materijala za zaštitu, ovu primjenu je moguće proširiti i na ostala, složenija sredstva, koja su sastavljena od više različitih sustava i podsustava, te proizvedena uporabom različitih konstrukcijskih materijala.

3. KONZERVACIJA VATRENOG ORUŽJA

Konzervacija vatrenog oružja predstavlja skup mjera i postupaka preventivnog održavanja koje se izvode radi privremene zaštite vatrenog oružja od korozije, odnosno radi produženja njegove uporabne vrijednosti i osiguranja ispravnosti u određenom vremenskom periodu.

Konzervaciji podliježu sva vatrena oružja koje se:

- privremeno stavljaju izvan uporabe,
- čuvaju u skladištima,
- planiraju za remont ili popravak, a neće biti remontirana u doglednom vremenu,
- isporučuju iz proizvodnje ili sa remonta, a neće odmah ići na uporabu.

Konzervirano vatreno oružje nužno je prije ponovne uporabe dekonzervirati (odstraniti zaštitna sredstva), a tijekom kontrole konzervacije i po isteku predviđenog roka konzervacije, izvodi se rekonzervacija. Rekonzervacija se sastoji od dekonzervacije, utvrđivanja tehničkog stanja vatrenog oružja, otklanjanja eventualno utvrđenih neispravnosti i ponovne konzervacije.

U sklopu konzervacije vatrenog oružja izvode se pripremni radovi (čišćenje i sušenje), tehnički pregledi, postupci nanošenja zaštitnog premaza na metalne površine koje je potrebno zaštititi od korozije, hermetizacija i pakiranje u za to predviđenu ambalažu.

Priprema vatrenog oružja za konzervaciju sastoji se od:

- odstranjivanja nečistoća, starih ulja i masti,
- mehaničkog ili kemijskog uklanjanja produkata korozije,
- čišćenja cijevi oružja od produkata izgaranja,
- uklanjanja starih zaštitnih premaza i naslaga bakra (debakarizacija) i
- sušenja.

Tehnički pregledi se izvode kako bi se utvrdilo stvarno stanje ispravnosti vatrenog oružja i njegova pouzdanost, otklonile utvrđene neispravnosti te vatreno oružje pripremio za sljedeći propisani period eksploatacije, odnosno kako bi se uputilo na viši stupanj održavanja, reviziju ili remont, ukoliko za to postoji potreba.

Nanošenje zaštitnog premaza predstavlja temeljnu fazu konzervacije, s tim da primijenjeni zaštitni premazi moraju zadovoljavati zahtijevane tehničke uvjete ili utvrđene standarde propisane odobrenim tehnološkim postupkom konzervacije. Osim tehničkih uvjeta i standarda koji se odnose na zaštitne premaze, tehnološkim postupkom konzervacije propisuju su i ostala sredstva koja se koriste za pripremu i zaštitu od korozije vatrenog oružja, a podijeljena su na: sredstva za čišćenje, sredstva za zaštitu te sredstva za hermetizaciju i pakiranje.

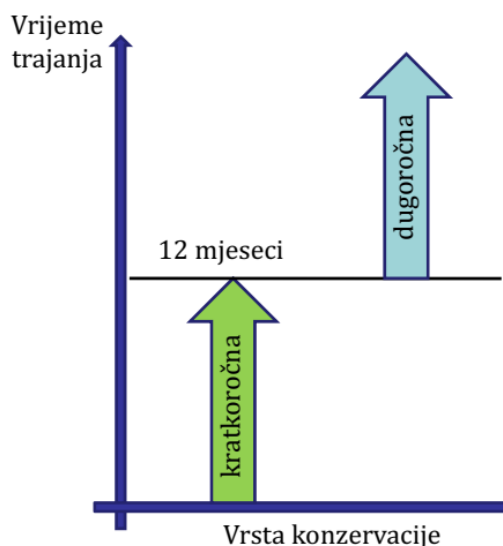
Hermetizacija vatrenog oružja tijekom konzervacije izvodi se u cilju zaštite vatrenog oružja od vanjskih utjecaja (izolacija od vlage i drugih kemijskih agenasa, zaštita od mikroorganizama i dr.).

Pakiranjem vatrenog oružja u propisanu ambalažu osigurava se njegova zaštita od mehaničkih ili drugih neželjenih djelovanja i oštećenja, koja mogu nastati tijekom transporta, prenošenja ili skladištenja.

Vrijeme trajanja konzervacije ovisi o:

- kvaliteti izvedene konzervacije,
- primijenjenim materijalima za konzervaciju,
- klimatskim uvjetima i mjestu čuvanja,
- kvaliteti primijenjenih konstrukcijskih materijala u izradi vatrenog oružja,
- kvaliteti temeljne zaštite,
- primijenjenoj metodi konzervacije.

Ovisno o vremenu trajanja zaštite, konzervacija može biti kratkoročna i dugoročna (Slika 2.) [5].



Slika 2: Vrsta i vrijeme trajanja konzervacije [6]

Kratkoročna konzervacija izvodi se na tehnički ispravnom vatrenom oružju koje će biti izvan uporabe do 12 mjeseci, a koje se isporučuje korisniku iz proizvodnje ili sa remonta te neispravnom vatrenom oružju koje je kod korisnika, a planirano je i čeka na popravak ili remont. Pri kratkoročnoj konzervaciji primjenjuju se zaštitni premazi koji se koriste za podmazivanje i zaštitu naoružanja tijekom redovne eksploatacije. Raspoloživost ovako konzerviranog oružja je gotovo trenutna, jer je dekonzervacija i priprema za uporabu brza i jednostavna, a izvode je neposredni korisnici.

Dugoročna konzervacija izvodi se na tehnički ispravnom vatrenom oružju koje će biti izvan uporabe duže od jedne godine, na vatrenom oružju koje je planirano za prekomorski transport ili koje će se skladištiti i čuvati kraći vremenski period, ali pod izuzetno nepovoljnim uvjetima. Za dugoročnu konzervaciju primjenjuju se posebna zaštitna sredstva koja su propisana tehnološkim postupkom dugoročne konzervacije vatrenog oružja, a izvodi je stručno osoblje koje je osposobljeno za preventivne i korektivne radove održavanja.

3.1. Uvjeti rada i mjere zaštite tijekom konzervacije isparavajućim inhibitorima korozijske

Vatreno oružje konzervira se primjenom kontaktne metode nanošenja zaštitnog premaza na metalne dijelove oružja, premazivanjem ili uranjanjem, zaštitom kožnih i gumenih dijelova mašću te stavljanjem oružja u prozirne polietilenske vrećice, uz hermetizaciju i pakiranje u pripadajuću ambalažu.

Tijekom konzervacije posebnu pozornost treba posvetiti uređajima, alatu i priboru, kao i uvjetima rada i mjerama zaštite (zaštita osoblja koje izvodi konzervaciju, protupožarna zaštita i zaštita okoliša).

Uređaji, alat i pribor koji se koriste moraju biti tehnički ispravni te zadovoljavati uvjete koji su neophodni za kvalitetnu i sigurnu provedbu konzervacije.

Osnovni uređaji, oprema, alati i pribori koji se primjenjuju tijekom konzervacije vatrenog oružja su:

- komplet standardnog alata za održavanje vatrenog oružja,
- komplet specijalnog alata za tehnički pregled konkretnih vrsta i modela vatrenog oružja (kontrolnici kalibra i ravnosti cijevi, kontrolnici čeonog zračnosti, kontrolnici izlaza vrha darne igle i dr.),
- četke za pranje i odmašćivanje,
- mesingane četkice za čišćenje cijevi vatrenog oružja,
- posude za smještaj odmašćivača, konvertera korozije i zaštitnog premaza,
- aparat za zavarivanje plastičnih polietilenskih vrećica,
- pamučne i platnene krpe,
- vješalice i rešetke za cijeđenje i sušenje oružja,
- uređaji za mjerenje temperature i vlažnosti zraka u prostoru namijenjenom za konzervaciju,
- radna i zaštitna oprema (platnene rukavice, gumene rukavice otporne na naftu i naftne derivate, zaštitne naočale, pregače, respiratori i dr.).

Radi što bolje kvalitete konzervacije, istu se izvodi po suhom i toplom vremenu (relativna vlažnost manja od 60 %, temperatura zraka iznad 15 °C). Prostori u kojima se izvodi konzervacija moraju biti čisti, bez prašine, ne smiju biti izloženi djelovanju agresivnih korozivnih agenasa. Konzervacija se izvodi u zatvorenom, dobro ventiliranom prostoru, u pravilu u tehničkim radionicama, ali se u iznimnim okolnostima može izvoditi i na mjestima čuvanja i skladištenja.

Iako su isparljivi inhibitori korozije tvari čije su osobine slične eksploatacijskim tekućinama koje se koriste u naoružanju i vojnoj opremi, sa donekle sličnim stupnjem opasnosti po zdravlje ljudi i okoliš, mjere zaštite tijekom konzervacije se posebno reguliraju ovisno o:

- dnevnoj količini vatrenog oružja koje se konzervira,
- količini i raznolikosti sredstava za konzervaciju koja se nalaze na mjestu izvođenja radova,
- brojnosti i osposobljenosti osoblja koje izvodi konzervaciju,
- mjestu i vremenu konzervacije.

Zbog navedenih razloga, potrebno je dobro poznavati karakteristike svih materijala koji se koriste tijekom pripreme vatrenog oružja za konzervaciju i neposrednu konzervaciju, a prije svega one koje se odnose na opasnost po zdravlje ljudi, zapaljivost i reaktivnost.

3.2. Priprema materijala i priprema vatrenog oružja za konzervaciju

Na mjestu gdje se izvodi konzervacija vatrenog oružja doprema se samo dnevna količina materijala za konzervaciju koja će se planirano utrošiti. Priprema materijala podrazumijeva odabir odgovarajućih dimenzija antikorozivnih polietilenskih vrećica temeljem vrste i dimenzija vatrenog oružja koje će se konzervirati, vizualni pregled vrećica kako bi se utvrdilo ima li na istima mehaničkih oštećenja i jesu li svi spojevi vrećica nepropusni. Također, potrebno je pregledati i zaštitni premaz koji će se primjenjivati, dobro ga promiješati te se uvjeriti da istome nije istekao rok uporabe. Oštećene i neispravne vrećice, kao i premaz kojem je istekao rok uporabe, se ne upotrebljavaju za provedbu konzervacije.

Priprema vatrenog oružja za konzervaciju provodi se kroz sljedećih pet faza:

- čišćenje oružja od produkata izgaranja,
- vizualni pregled i uklanjanje produkata korozije,
- tehnički pregled oružja,
- odmašćivanje i
- pregled i priprema ambalaže za pakiranje.

3.2.1. Čišćenje oružja od produkata izgaranja

Postupku čišćenja oružja od produkata izgaranja podliježu svi dijelovi i površine oružja koje tijekom opaljenja dolaze u kontakt sa produktima izgaranja baruta i inicijalnih kapsula (cijev, klip, cilindar, plinska komora, zatvarač, dijelovi mehanizma za okidanje i opaljenje, tromblonski nastavak, pojačivač trzaja i dr.) [3].

Čišćenje dijelova oružja izvodi se sredstvima za čišćenje i rastvaranje gareži, kao što su INA ASOL-S, VpCI-340 CLP, Bull Frog Rust Hunter i dr. Čišćenje se izvodi na način da se oružje rastavi na sastavne dijelove te se odvoje metalni dijelovi od drvenih i plastičnih dijelova. Pamučna se krpa ili četka za čišćenje natopi u sredstvo za čišćenje oružja te se provuče nekoliko puta kroz cijev kako bi se uklonio ostatak produkata izgaranja. Ukoliko su onečišćenja izražena, kanal cijevi oružja potrebno je ostaviti premazan da odstoji do 15 minuta, nakon čega je unutrašnjost cijevi nužno dobro obrisati čistim i suhim krpama. Mehanizam za opaljenje i okidanje, zatvarač, plinski cilindar, klip, pojačivač trzaja i drugi metalni dijelovi izloženi djelovanju produkata izgaranja također se čiste četkama ili brisanjem krpama natopljenim u sredstvo za čišćenje.

Slika 3. prikazuje primjere nastanka korozije uslijed nepravovremenog ili neadekvatnog čišćenja vatrenog oružja na korisničkoj razini.



Slika 3: Pojava korozije na klipu plinskog cilindra uslijed neadekvatnog čišćenja oružja

Poput cijevi oružja, i drugi dijelovi se mogu ostaviti premazani (natopljeni) sredstvom za čišćenje u trajanju do 15 minuta, kako bi se nakon toga sa njih lakše odstranili svi produkti izgaranja. Ako se poslije brisanja i dalje primijete tragovi produkata izgaranja u kanalu cijevi ili na drugim dijelovima i sklopovima oružja, postupak čišćenja je potrebno ponoviti.

Pri radu sa sredstvima za čišćenje, u posude za rad se ulijevaju minimalne količine koje su neophodne za nesmetano čišćenje jedne serije oružja (2 do 3 litre), iz razloga brzog onečišćenja i isparavanja sredstva. Nakon utroška sredstva za čišćenje, unutrašnjost posude je potrebno obrisati krpom, a tek nakon toga uliti svježe količine sredstva za čišćenje [3].

3.2.2. Vizualni pregled i uklanjanje produkata korozije

Nakon čišćenja od produkata izgaranja, na vatrenom oružju se izvodi vizualni pregled, kako bi se utvrdilo je li na metalnim dijelovima oružja došlo do pojave korozije. Ako se uoči pojava korozije, ona se uklanja mehaničkim ili kemijskim putem. Slika 4. prikazuje primjere korozije cijevi vatrenog oružja kalibra 9 mm.



Slika 4: Korozijska cijevi vatrenog oružja kalibra 9 mm

Mehaničko uklanjanje korozijskih produkata izvodi se mesinganim četkama, brusnim platnom, papirom i sličnim abrazivnim materijalima.

Kemijsko uklanjanje korozijskih produkata izvodi se na površinama koje imaju visoke tolerancije izrade, pri čemu se koriste različite tekućine za transformaciju produkata korozijske. U ovu svrhu primjenjuju se biokemijske formulacije bez kiselina i helata, kao što su VpCI-422, VpCI-423 i dr. Ove tekućine omogućuju uklanjanje produkata korozijske sa metala bez stvaranja štetnih naslaga. Na površinu oružja nanose se prskanjem, premazivanjem ili uranjanjem metalnih dijelova. Ovisno o stupnju razvoja korozijske, ovako tretirane površine dijelova oružja potrebno je ostaviti da odstoje 15 minuta, a po potrebi i duže (i do 5 sati), nakon čega se dijelovi oružja ispiru vodom [7].

3.2.3. Tehnički pregled vatrenog oružja

Tehnički pregledi vatrenog oružja izvode se prema tehničkim uputama koje su propisane za svaku vrstu i model sredstava posebno. Ovi pregledi spadaju u preventivno održavanje, jer predstavljaju planski i unaprijed određen skup aktivnosti koji se provode s ciljem utvrđivanja ispravnosti i uporabljivosti oružja, pravilnosti uporabe i korisničkog održavanja oružja te kompletnosti oružja.

U okviru tehničkog pregleda izvode se vizualni pregledi, provjere i podešavanja svih značajki oružja propisanih tehničkim uputama za održavanje, pri čemu se primjenjuju sljedeće osnovne metode i sredstva [5]:

- provjera kalibra (Slika 5.) i savijenosti cijevi,
- određivanje stupnja nagriženosti cijevi,
- provjera čeonog zračnog (Slika 6.),
- provjera veličine izlaza vrha udarne igle.



Slika 5: Provjera kalibra cijevi



Slika 6: Provjera čeonog zračnog

Neispravno vatreno oružje, pričuvni alat i pribor se dugoročno ne konzervira, nego se popravlja ili se neispravni dijelovi oružja, alata i pribora zamjenjuju ispravnim, nakon čega se izvodi dugoročna konzervacija.

3.2.4. Odmašćivanje, pregled i priprema ambalaže

Metalne površine vatrenog oružja odmašćuju se premazivanjem ili uranjanjem dijelova i sklopova oružja u posudu sa sredstvom za odmašćivanje (Slika 7.). Sa ovako uronjenog oružja se pomoću četki za čišćenje i pranje uklanjaju zaostali talozi konzervansa, stare zaštitne masti i druge nečistoće koje su prisutne. Tijekom odmašćivanja, posebnu pažnju nužno je posvetiti teško pristupačnim mjestima na oružju, kako u istima nebi ostalo zaostalih onečišćenja koja naknadno mogu izazvati pojavu korozije. Nakon odmašćivanja, metalne površine se ne smiju dodirivati golim rukama, nego isključivo uz primjenu zaštitnih platnenih rukavica.

Kao sredstva za odmašćivanje koriste se biorazgradiva sredstva na bazi vode, poput VpCI-414, 415, 416 ili 419, koja imaju sposobnost uklanjanja naslaga teških ugljikovodika, masti i drugih spojeva koji stvaraju slojevite naslage, a ujedno pružaju i privremenu zaštitu od korozije u vremenu između odmašćivanja i provedbe postupka konzervacije [8].



Slika 7: Odmašćivanje uranjanjem u posudu

Paralelno sa odmašćivanjem oružja izvodi se pregled i priprema ambalaže za smještaj vatrenog oružja nakon konzervacije. Ovisno o vrstama i modelima oružja, ono se pakira u drvene sanduke pojedinačno (teške strojnice) ili u većim količinama, najčešće 5 ili 10 komada u jednom sanduku (jurišne puške, poluautomatske puške, kratke strojnice). U sklopu pripreme ambalaže, sanduci se čiste brisanjem suhim krpama ili četkama natopljenim u sredstvo za odmašćivanje te se na taj način odstranjuju zaostali konzervansi, staro ulje, prašina i druge nečistoće. Provodi se vizualni pregled sanduka i unutarnjih pregrada, na kojima se nalaze ležišta za smještaj oružja (obložena filcom ili gumom), da bi se utvrdilo ima li na istima oštećenja koja bi mogla narušiti hermetičnost oružja nakon njegovog pakiranja u sanduke.

3.2.5. Nanošenje zaštitnog premaza, hermetizacija i pakiranje

Odmašćeni i očišćeni dijelovi vatrenog oružja, koji nisu zaštićeni postupcima bruniranja, kromiranja i bojenja, premazuju se zaštitnim premazom pomoću četke (Slika 8.) ili krpe

natopljene u zaštitno sredstvo. U izuzetnim slučajevima, kod vatrenog oružja većih gabarita i složene konstrukcije, gdje se sve površine ne mogu premazati pomoću četki ili krpom, primjenjuje se postupak uranjanja oružja u posude sa zaštitnim premazom (Slika 9.) [3].



Slika 8: Nanošenje zaštitnog premaza četkom



Slika 9: Nanošenje zaštitnog premaza uranjanjem u posudu

Ukoliko se primjenjuje postupak uranjanja oružja u zaštitno sredstvo, nakon uranjanja oružje je potrebno ocijediti stavljanjem na za to pripremljene vješalice (Slika 10.) u trajanju 10 do 15 minuta, kako bi se uklonio višak zaštitnog premaza sa metalnih površina.



Slika 10: Cijeđenje i sušenje oružja

Kao zaštitni premazi za konzervaciju primjenjuju se tekućine na bazi biljnih biološko razgradivih ulja (VpCI-325 ili VpCI-369D) koje djeluju na dva načina. Prvo, ulje stvara tanki zaštitni sloj koji čvrsto prijanja uz metalne površine i sprječava pristup vlazi. Drugo, pored ove uljne barijere, isparavajući inhibitori korozije ulaze u prostor iznad ulja, te se formira monomolekularni film na površini metala, stvarajući zaštitnu prepreku za ostale agresivne komponente prisutne u zraku [9].

Nakon premazivanja zaštitnim premazom, cijeđenja i sušenja, oružje se stavlja u polietilenske vrećice, koje se zatvaraju pomoću aparata za zavarivanje plastičnih vrećica (Slika 11.). Isti postupak se provodi na pričuvnom alatu i priboru, dok se dijelovi od gume i kože premazuju odgovarajućim zaštitnim mastima. Ovako hermetizirano oružje i

pripadajući pričuvni alat i pribor se pakira u za to pripremljenu ambalažu za čuvanje i skladištenje (Slika 12.).



Slika 11: Umetanje oružja u polietilenske vrećice i hermetizacija

Podaci o izvedenim radovima konzervacije upisuju se u tehničku dokumentaciju (tehnički knjižicu) oružja, a na sanduke, odnosno pakiranja, postavljaju se liste pakiranja, kontrolni kartoni konzervacije i naputci za dekonzervaciju. U tehničku dokumentaciju se upisuju podaci o metodi izvedene konzervacije, nadnevku izvođenja radova, roku valjanosti zaštite te osoblju i ustanovi koja je izvršila konzervaciju. Navedeni podaci se upisuju i u kontrolni karton konzervacije, koji se postavlja na vidnom mjestu sa vanjske strane pakiranja. Na kontrolnom kartonu konzervacije se nalaze i dodatni podaci koji govore o sadržaju pakiranja, bez potrebe za njegovim otvaranjem (naziv i vrsta oružja, broj komada u pakiranju, tvornički brojevi oružja, kalibar, nagriženost cijevi).



Slika 12: Pakiranje oružja u sanduk

Ovako konzervirano vatreno oružje skladišti se u zatvorenim objektima, sa rokom trajanja konzervacije do 6 godina.

Stanje konzerviranog vatrenog oružja tijekom čuvanja i skladištenja kontrolira se redovnim (dnevnom, tjednim, tehničkim i zapovjednim), izvanrednim (komisijski, tehnička kontrola) i specijalnim pregledima (revizija). Za svaki pregled propisuje se opseg radova, nadležnost, postupak i periodičnost. Pregledi se izvode na propisanom broju slučajno odabranih uzoraka, ovisno o vrsti i cilju pregleda.

Po isteku roka valjanosti konzervacije ili uslijed narušavanja konzervacije, provodi se rekonzervacija. Rekonzervacija obuhvaća postupke dekonzervacije, ponovnog tehničkog

pregleda, eventualnog popravka ukoliko se utvrde neispravnosti te (ponovne) konzervacije.

Dekonzervacija je postupak kojim se vatreno oružje priprema za upotrebu odstranjivanjem zaštitnih sredstava, a izvodi se u slučajevima isteka roka konzervacije, pri izvođenju tehničkog pregleda, pri kontroli stanja i pri izvanrednoj upotrebi [5].

4. ZAKLJUČAK

Konzervacija kao sastavni dio strategije preventivnog održavanja ima izuzetan značaj za osiguranje zahtijevanog stupnja pouzdanosti i raspoloživosti vatrenog oružja koje se privremeno nalazi izvan uporabe. Primjenom različitih metoda i postupaka konzervacije, osigurava se tehnička ispravnost vatrenog oružja u propisanom periodu trajanja zaštite, uz niže troškove održavanja nego da se ono nalazi nekonzervirano kod korisnika ili na skladištu. Bez obzira koja se metoda konzervacije primijeni, izuzetnu važnost za njenu učinkovitost ima pravilna priprema materijala i oružja za konzervaciju te provedba svih faza konzervacije, sukladno propisanim tehnologijama. Postupci konzervacije i dekonzervacije isparavajućim inhibitorima korozije su jednostavni i zahtijevaju znatno kraće vrijeme za njihovu provedbu, u odnosu na ranije primjenjivane metode i postupke. Ovako propisani postupci smanjuju troškove održavanja sa aspekta uporabe radne snage i racionalizacije kapaciteta za njihovu realizaciju, ali i osiguravaju gotovo trenutnu spremnost vatrenog oružja za uporabu. Osim zadržavanja zahtijevanog stupnja ispravnosti i pouzdanosti vatrenog oružja u propisanom roku trajanja konzervacije, primjena isparavajućih inhibitora korozije na odgovarajući način dovodi do smanjenja opasnosti od zagađenja okoliša i ukupnog smanjenja opasnog otpada, iz čega se može zaključiti da ona predstavlja znatan tehnološki i ekonomski napredak i održivost. Daljnje smanjenje troškova konzervacije moguće je postići praćenjem stanja konzerviranog vatrenog oružja na odabranom uzorku i nakon isteka roka valjanosti konzervacije te eventualnim revidiranjem postojećih tehnoloških postupaka u segmentu koji se odnosi na kontrolu i produljenje vijeka trajanja zaštite.

LITERATURA:

- [1] Juraga I., Alar V., Stojanović I., Korozija i zaštita premazima, Fakultet strojarstva i brodogradnje, Zagreb, str. 36, 48 [2019.]
- [2] Juraga I., Šimunović V., Stojanović I., Alar V., Mehanizmi zaštite od korozije (skripta), Fakultet strojarstva i brodogradnje, Zagreb, str. 68-69 [2012.]
- [3] Madžar T., Učinkovitost primjene hlapljivih inhibitora korozije u zaštiti pješačkog naoružanja, Magistarski rad, fakultet strojarstva i brodogradnje, Zagreb, str. 24 [2005.]
- [4] <https://cortecros.com/wp-content/uploads/2017/05/Opcabrosura.pdf>, 11.05.2023.
- [5] Jakopčić M., Održavanje naoružanja, Zapovjedništvo HKoV, Karlovac, str. 88, 189-190, [2006.]
- [6] Leutar I., Organizacija i tehnologija održavanja vojne tehnike, HVU „Dr. Franjo Tuđman“, Zagreb, 16.05.2023. (Predavanje)
- [7] https://www.korozija.hr/upload_data/site_files/vpci-422-423.pdf, 15.05.2023.
- [8] <https://cortecros.com/wp-content/uploads/2019/05/VpCI-415.pdf>, 15.05.2023.
- [9] <https://cortecros.com/hr/product/vpci-325-ulje-za-zastitu-u-zatvorenim-prostorima>, 15.05.2023.



THE EFFECT OF SHOT-PEENING ON BENDING FATIGUE FAILURE IN CARBURIZED SPUR GEARS

Ivan Čular¹, Krešimir Vučković¹, Željko Alar¹, Srečko Glodež²

¹ University of Zagreb, Faculty of Mechanical Engineering and Naval Architecture, Ivana Lučića 5, 10 000 Zagreb, Croatia

² University of Maribor, Faculty of Mechanical Engineering, Smetanova ulica 17, 2000 Maribor, Slovenia

Abstract

Spur gears are often shot peened in addition to carburizing to increase the surface's hardness and improve their bending fatigue properties. However, even though shot peening increases bending fatigue lives, it may have an undesirable effect regarding the fatigue crack initiation location. In this paper, an experimentally validated computational model based on the finite element and fatigue analyses is employed to compare bending fatigue lives and crack initiation locations between carburized and carburized and shot peened spur gears. The multilayer method is utilized to find the most critical surface and subsurface layers at the gear's tooth root. Their respective bending fatigue lives are calculated based on the hardness and strain-life method, and the layer with the lowest fatigue life is denoted as critical, obtaining the crack initiation location. The results demonstrate that, even though shot peening increases the fatigue life of a spur gear, the crack initiation location shifts below the surface, making it harder to detect. Hence, some guidelines are provided to lower the probability of subsurface fatigue crack initiation.

Keywords: *Finite element method, spur gears, shot peening, carburizing, bending fatigue*

1. INTRODUCTION

Shot peening is one of the most commonly used surface-hardening methods for metal components. In addition to carburizing, components such as metal gears are often shot peened to increase the surface hardness while inducing compressive residual stresses, prolonging the fatigue life in the gear's tooth root, i.e., bending fatigue life [1-4]. However, even though the induced compressive residual stresses benefit the fatigue life of a surface layer, the fatigue crack may initiate below the surface, as demonstrated in [5-7], lowering the probability of its timely detection.

In this paper, an already established and experimentally validated computational model [8] is employed to demonstrate the effect of shot peening and differentiate between the location (surface vs. subsurface initiation) of bending fatigue failure in surface-hardened spur gears. Two cases of surface-hardened spur gears are considered: only carburized and carburized with the addition of shot peening. Their hardness, residual stress profiles, and crack initiation locations are compared. Lastly, some guidelines are provided for lowering the probability of subsurface fatigue crack initiation.

2. MATERIALS AND METHODS

2.1. Geometric and material parameters

A computational model of a single-tooth bending fatigue (STBF) test is employed in this paper to demonstrate the effect of shot peening on bending fatigue in surface-hardened spur gears. A schematic representation of an STBF test with the corresponding numerical model of 18CrNiMo7-6 spur gear established via the finite element method (FEM) is shown in Fig. 1. The numerical model of an STBF test is modelled based on [1], where the pulsating load F_p is applied in a sinusoidal manner to induce bending fatigue. It should be noted that a detailed description of the computational model can be found in [6]. Only the most important aspects of the computational model are shown here due to simplicity.

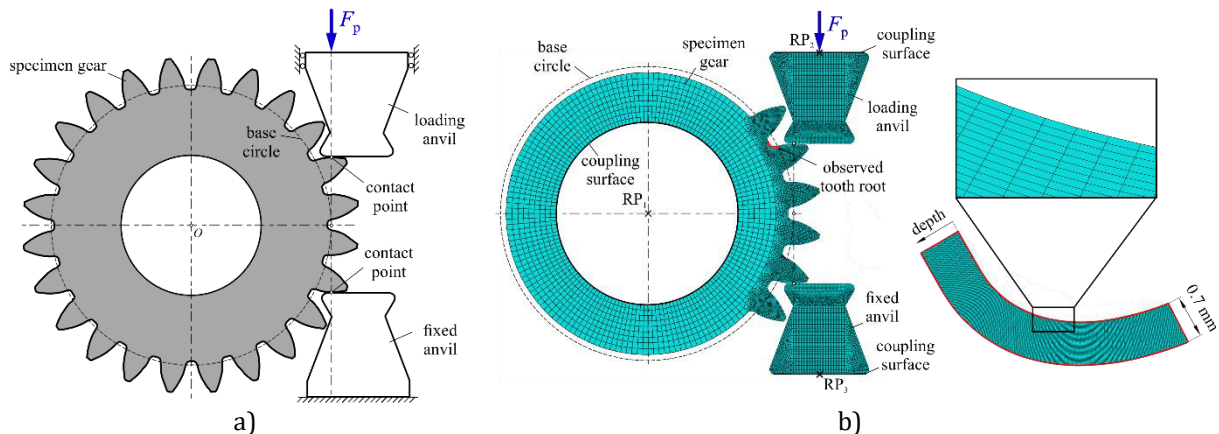


Fig. 1: STBF test: a) schematic representation, and b) the numerical model with a close-up of the observed tooth root region [6]

The finite element software Abaqus [10] was employed for the simulation. According to Pehan et al. [11], plane stress can be assumed if the gear's width is equal to or lower than six times its module, which is the case in this paper according to Tab. 1. Hence, a 2D numerical analysis was carried out to reduce computational costs. Plane stress quadrilateral elements (CPS4 in Abaqus) are applied to the entire model.

Material and geometric parameters of the specimen gear are taken from [2] and [3], respectively, and shown in Table 1.

Tab. 1: Parameters of the specimen gear [2, 3]

Parameter	Value
Number of teeth	24
Module	5 mm
Profile shift coefficient	0.11
Face width	30 mm
Normal pressure angle	20°
Tip diameter	134 mm
Base material	18CrNiMo7-6
Modulus of elasticity	210 GPa
Poisson's ratio	0.3

Lastly, hardness and residual stress profiles for only carburized and carburized and shot peened gears are taken from [9], where the effect of shot peening was investigated on steel discs made of the same material as the gear used for an STBF test, i.e., 18CrNiMo7-6. Hardness and residual stress profiles are shown in Fig. 2.

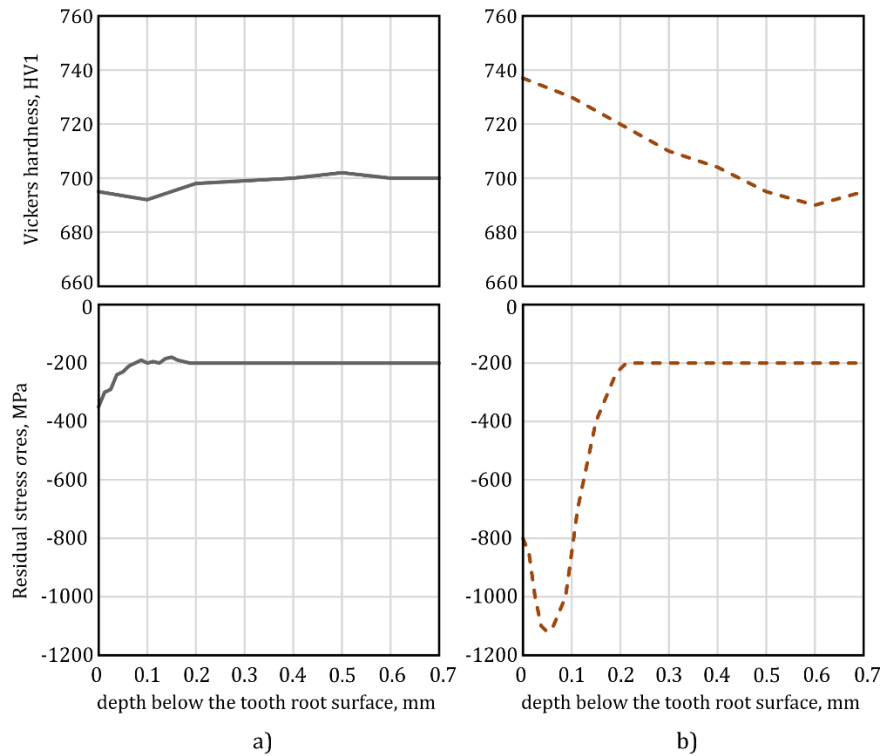


Fig. 2: Hardness and residual stress profiles applied to the tooth root of the specimen gear for: a) carburized gear, and b) carburized and shot peened gear [9]

The depth of the tooth root region is taken as 0.7 mm (Fig. 1) to ensure that the regions where hardness and residual stresses change the most are covered (Fig. 2). The observed tooth root region is meshed with equally sized rectangular elements to facilitate the employment of the multilayer method (Section 2.2.), as shown in Fig. 3. A total of 56 elements are assigned to the observed tooth root region in the depth direction. Hence, the width of each element is $0.7 \text{ mm}/56 = 0.0125 \text{ mm}$. To increase the accuracy of the results, each of the three layers shown in Fig. 3 is equally partitioned two more times, obtaining

12 layers. Hence, for 12 layers, the first four layers are each two elements wide, the second four are four elements wide, and the last four layers are eight elements wide.

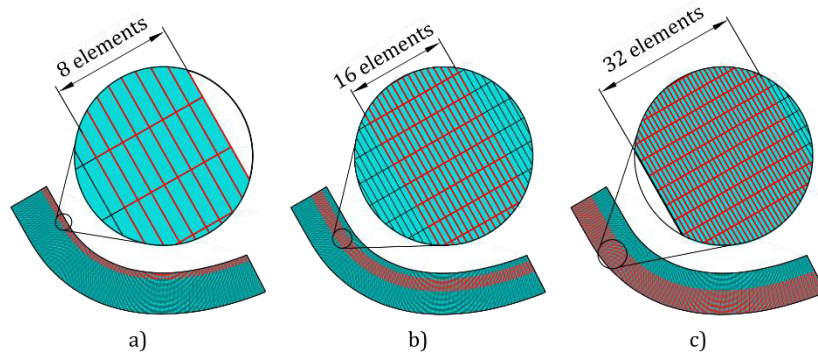


Fig. 3: Assigning layers to the observed tooth root region: a) surface layer, b) first subsurface layer, and c) second subsurface layer

Lastly, previous investigations [6, 7] have already demonstrated that the critical location for subsurface failure is near the region where compressive residual stresses are the lowest. However, the load-induced stress is still relatively high, i.e., the region closest to the surface with the lowest compressive residual stresses (or, absolutely speaking, highest residual stresses). According to Fig. 2, these regions are located at 0.1 mm (for carburized gears) and 0.2 mm (for carburized and shot-peened gears) from the surface.

Therefore, only the first surface layer represented by the first two rows of elements (almost always the critical region for fatigue failure) is modelled for simplicity. In addition to the first surface layer, two subsurface layers located at the aforementioned critical regions are modelled for each case. Specifically, for a carburized gear, layers 4 and 5 are chosen, representing depths between 0.075-0.1 mm and 0.1-0.125 mm, respectively. For a carburized and shot peened gear, layers 6 and 7 are chosen, which represent depths between 0.15-0.2 mm and 0.2-0.25 mm.

2.2. Methods

A detailed explanation of the employed method can be found in [6]. Here, only a brief description is provided.

Firstly, constant hardness and residual stress values are assigned to each of the 12 layers (or in this case, only layers 1, 4, 5, 6, and 7, as previously mentioned) by averaging the values from Fig. 2 based on the multilayer method [12], which assumes homogenous material behaviour within each layer. It should be mentioned that, for the carburized gear (without shot peening), it is assumed that all investigated layers (1, 4, and 5) have the same hardness of 700 HV due to the negligible change in hardness shown in Fig. 2. For the carburized and shot peened gear, the hardness values are averaged for each layer due to an obvious change in hardness shown in Fig. 2.

The hardness method [13] is then employed to obtain strain-life fatigue properties for each layer according to the following equations:

$$\sigma'_f = 4.25 \cdot HB + 225 \quad (1)$$

$$\varepsilon'_f = \frac{0.32 \cdot HB^2 - 487 \cdot HB + 191\,000}{E} \quad (2)$$

$$b = -0.09 \quad (3)$$

$$c = -0.56 \quad (4)$$

where σ'_f is the fatigue strength coefficient, HB is the averaged Brinell hardness for each layer (Vickers hardness is converted to Brinell hardness according to the hardness conversion tables in [14]), b is the fatigue strength exponent, ε'_f is the fatigue ductility coefficient, c is the fatigue ductility exponent, and E is the modulus of elasticity.

The bending fatigue life of each layer is calculated according to the strain-life (ε - N) method. Specifically, for the surface layer, the Basquin-Coffin-Manson relation with Morrow's mean stress correction is employed via Eq. (5), while Smith-Watson-Topper's mean stress correction is employed for subsurface layers via Eq. (6):

$$\frac{\Delta\varepsilon_1^a}{2} = \frac{(\sigma'_f - \sigma_m^a - \sigma_{res})^2}{E} (2N_f)^b + \varepsilon'_f (2N_f)^c \quad (5)$$

$$\frac{\Delta\varepsilon_1^a}{2} (\sigma_a + \sigma_m^a + \sigma_{res}) = \frac{(\sigma'_f)^2}{E} (2N_f) + \sigma'_f \varepsilon'_f (2N_f)^{b+c} \quad (6)$$

where $\frac{\Delta\varepsilon_1^a}{2}$ is the actual strain amplitude corrected for elastoplastic behaviour via Neuber's rule, σ_m^a is the actual load-induced mean stress also corrected via Neuber's rule, σ_{res} is the averaged residual stress for each layer, and $2N_f$ is the number of reversals until fatigue failure.

Finally, the number of cycles required for bending fatigue crack initiation, i.e., bending fatigue life, is obtained for each of the three layers in a carburized spur gear (layers 1, 4, and 5), as well as layers 1, 6, and 7 in carburized and shot peened spur gear. Due to the relative complexity of the analysis, the fatigue calculation software FE-Safe [15] is employed. Lastly, according to [9], the steel discs had a surface finish of $Ra = 0.8 \mu\text{m}$ after carburizing. Hence, a predefined range of $0.6 \mu\text{m} < Ra < 1.6 \mu\text{m}$ is chosen in FE-Safe and applied only to the surface layer (layer 1) in both cases.

3. RESULTS AND DISCUSSION

Predicted bending fatigue lives with corresponding failure locations for a carburized gear and carburized and shot peened gear are shown in Fig. 4. Layers 1, 4, and 5 are shown in Fig. 4a), while layers 1, 6, and 7 are shown in Fig. 4b).

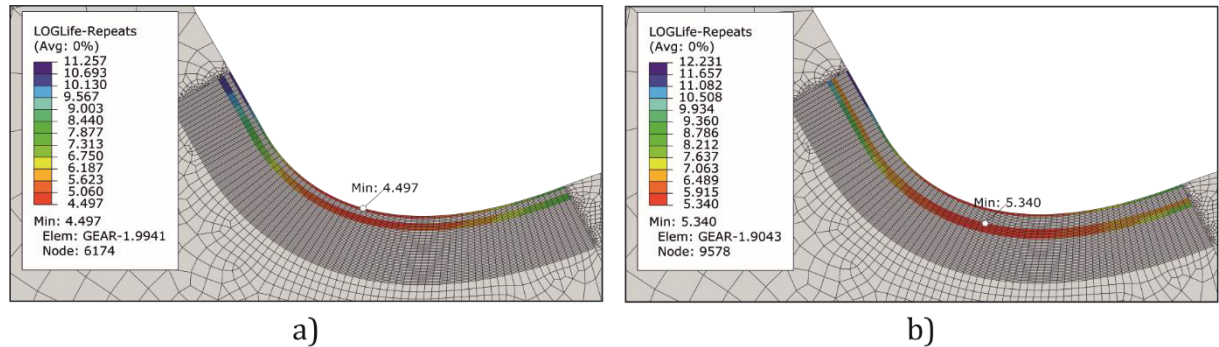


Fig. 4: Predicted bending fatigue lives and locations for a pulsating load of 90 kN: a) carburized gear, and b) carburized and shot peened gear

The predicted fatigue lives are shown in logarithmic measurement. In other words, the estimated bending fatigue life for a carburized gear (Fig. 4a) is $10^{4.497} = 31\,405$ cycles, with the critical location being the surface layer (layer 1). The estimated bending fatigue life for a carburized and shot peened gear is $10^{5.340} = 218\,776$ cycles (Fig. 4b), with a critical location being layer 6 (0.15-0.2 mm below the surface).

The results in Fig. 4 demonstrate that bending fatigue lives of gears can be significantly increased by shot peening (an increase in the number of cycles by almost 10 times)—however, the location of bending fatigue crack initiation shifts from the surface to the subsurface region. Consequently, detecting the fatigue crack is more difficult, especially since non-visible subsurface fatigue crack may rapidly propagate through the brittle, carburized layer and reach the critical length required for sudden fracture.

A possible solution to the abovementioned problem may be a longer carburization time or decreasing the gear's module [8]. Longer carburization time will increase the presence of compressive residual stresses at the critical subsurface location (0.2 mm in this paper according to Fig. 2b). As a result, the critical subsurface location will be additionally “protected” with beneficial compressive residual stresses. However, one should be careful not to exceed the recommended carburizing depth according to ISO 6336-5 [16].

On the other hand, decreasing the gear's module increases the gradient at which load-induced stresses decrease from the surface in a depth direction [17, 18]. Consequently, the critical subsurface location will be subjected to lower load-induced stresses, increasing the fatigue life.

The abovementioned two possible solutions are schematically depicted in Fig. 5.

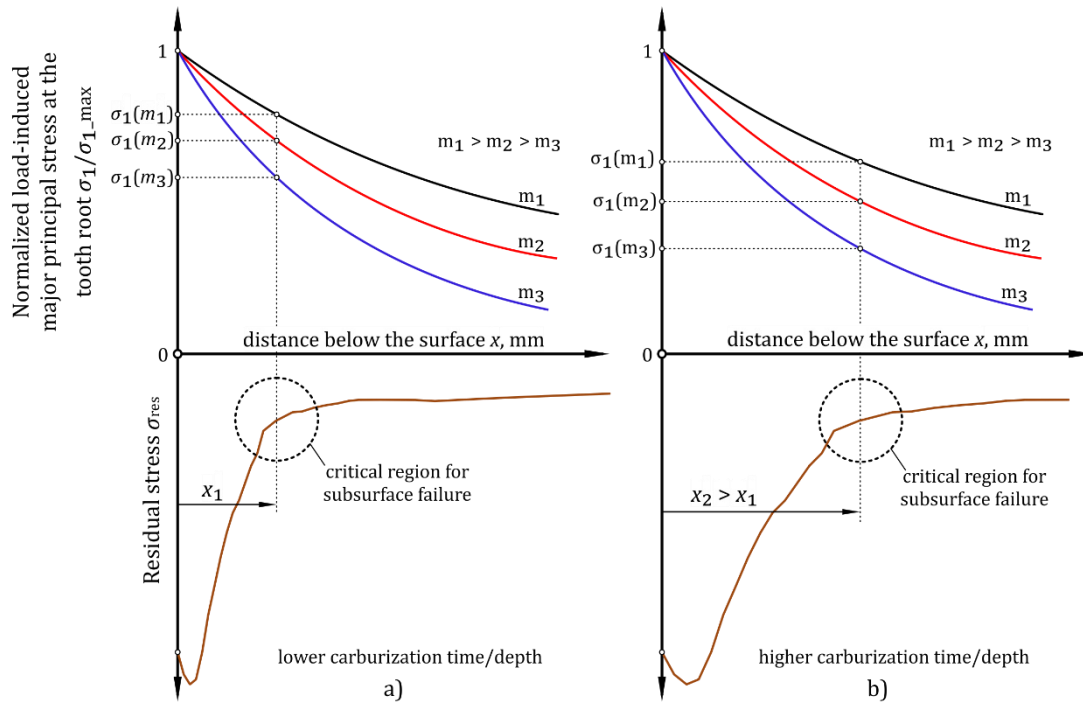


Fig. 5: Schematic representation of the critical region for subsurface bending fatigue failure in carburized and shot peened gears for two identical sets of load-induced stress curves: a) lower carburization time/depth, and b) higher carburization time/depth

4. CONCLUSION

In this paper, an experimentally validated computational model was employed to investigate the bending fatigue behaviour of only carburized and carburized and shot-peened spur gears. The computational model comprises a finite element model used to obtain stresses and strains of the observed gear's tooth root. Then, the multilayer method was employed to separate the observed tooth root region into 12 layers (starting from the surface in the depth direction) and assign constant hardness and residual stress values to each layer. The hardness method was employed to obtain the fatigue parameters of each layer, and the strain-life method with Morrow's and Smith-Watson-Topper's mean stress correction was used to estimate the bending fatigue lives of each layer. The layer with the lowest fatigue life was denoted as critical. The following conclusions can be drawn:

- 1) Additional shot peening of carburized spur gears increases their bending fatigue lives. For a pulsating load of 90 kN on a single tooth bending fatigue (STBF) device simulated in this paper, an increase in bending fatigue lives of nearly 10 times was observed.
- 2) Even though shot peening increases the bending fatigue lives, the failure location shifts from surface to below the surface, making it harder to detect timely. This may result in misdiagnosing a faulty gear as healthy since the subsurface crack is not visible. As a result, through further exploitation, the crack may rapidly propagate through the brittle carbonized layer, causing tooth fracture and gear failure. Hence, special care should be taken during service intervals of carburized and shot-peened gears to account for possible subsurface fatigue crack initiations.
- 3) Longer carburization time or lower gear's module may alleviate the problem of subsurface bending fatigue crack initiation. Longer carburization time will increase the presence of beneficial compressive stresses while lowering the gear's module will decrease load-induced stresses at the critical subsurface region.

In future work, longer carburization times and lower gear modules will be investigated in more detail via computational models to explore their effect on decreasing the probability of subsurface bending fatigue cracks.

REFERENCES

- [1] Fuchs D., Schurer S., Tobie T., Stahl K., On the determination of the bending fatigue strength in and above the very high cycle fatigue regime of shot-peened gears, *Forschung im Ingenieurwesen (Engineering Research)*, 86, pp. 81-92, (2021).
- [2] Winkler KJ., Schurer S., Tobie T., Stahl K., Investigations on the tooth root bending strength and the fatigue fracture characteristics of case-carburized and shot-peened gears of different sizes, *Journal of Mechanical Engineering Science* 0(0), pp. 1-12, (2019).
- [3] Fuchs D., Schurer S., Tobie T., Stahl K., Investigations into non-metallic inclusion crack area characteristics relevant for tooth root fracture damages of case carburised and shot-peened high strength gears of different sizes made of high-quality steels, *Forschung im Ingenieurwesen (Engineering Research)*, 83, pp. 579-587, (2019).
- [4] Guntner C., Tobie T., Stahl K., Influences of the Residual Stress Condition on the Load-Carrying Capacity of Case-Hardened Gears, *GearTechnology*, August 2018, pp. 60-69, (2018).

- [5] Čular I., Vučković k., Žeželj D., Glodež S., Analytical approach for low and high cycle bending fatigue life prediction of carburized gear steel specimens, *Engineering failure analysis*, 108, (2020).
- [6] Čular I., Vučković K., Glodež S., Tonković Z., Computational Model for Bending Fatigue Prediction of Surface Hardened Spur Gears Based on The Multilayer Method, *International Journal of Fatigue*, 161, (2022).
- [7] Čular I., Vučković K., Galić I., Žeželj D., Computational model for bending fatigue life and failure location prediction of surface-hardened running gears, *International Journal of Fatigue*, 166 (2023).
- [8] Čular I., "Fatigue modelling in tooth root of surface-hardened gears" Doctoral dissertation, Zagreb, Croatia, (2022).
- [9] Wu J., Liu H., Wei P., Zhu C., Lin Q., Effect of shot peening coverage on hardness, residual stress and surface morphology of carburized rollers, *Surface & Coatings Technology*, 384, (2020).
- [10] SIMULIA, "Abaqus 6.13", Analysis User's Guide, Dassault Systems, (2013).
- [11] Pehan S., Hellen TK., Flašker J., Glodež S., Numerical methods for determining stress intensity factors vs crack depth in gear tooth roots, *International Journal of Fatigue*, 19 (10), pp. 677-685, (1997).
- [12] Baumel AJ., Seeger T., The influence of residual stresses and surface strengthening on components fatigue life, *Fatigue*, 90, (1990).
- [13] Roessle ML., Fatemi A., Strain-controlled fatigue properties of steels and some simple approximations, *International Journal of Fatigue*, 22(6), pp. 495-511, (2000).
- [14] ASTM, "E140-07 Standard hardness conversion tables for metals relationship among brinell hardness, vickers hardness, rockwell hardness, superficial hardness, knoop hardness, and scleroscope hardness," ASTM, pp. 1-21, (2007).
- [15] "FE Safe version 6.5." Dassault Systemes, (2014).
- [16] ISO 6336, Calculation of Load Capacity of Spur and Helical Gears, (2006).
- [17] Bretl N., Schurer S., Tobie T., Stahl K., Hohn B., Investigations on Tooth Root Bending Strength of Case Hardened Gears in the Range of High Cycle Fatigue, *Thermal Processing for Gear Solutions*, pp. 52-59, (2014).
- [18] Fuchs D., Schurer S., Tobie T., Stahl K., A model approach for considering nonmetallic inclusions in the calculation of the local tooth root load-carrying capacity of high-strength gears made of high-quality steels, *Proceedings of the Institution of Mechanical Engineers, Part C: Journal of Mechanical Engineering Science*, vol. 233, no. 21-22, pp. 7309-7317, (2019).



UTJECAJ NANOŠENJA PVD PREVLAKA NA OTPORNOST ADHEZIJSKOM TROŠENJU ČELIKA ZA POBOLJŠAVANJE C45E

THE INFLUENCE OF APPLYING PVD COATINGS ON ADHESION WEAR RESISTANCE OF HARDENING AND TEMPERING STEEL C45E

Ivica Kladarić¹, Stjepan Golubić¹, Slavica Kladarić², Andrijana Milinović¹

¹ University of Slavonski Brod, Mechanical Engineering Faculty in Slavonski Brod, Trg Ivane Brlić-Mažuranić 2, 35000 Slavonski Brod, Croatia

² University of Slavonski Brod, Technical Department, Ul. 108. brigade ZNG 28, 35000 Slavonski Brod, Croatia.

Sažetak

PVD prevlake tvrdih spojeva smanjuju adhezijsko i abrazijsko trošenje, a pojedine vrste prevlaka također smanjuju faktor trenja. Temperatura PVD postupka je niža od temperature popuštanja čelika za poboljšavanje, nema deformacija dijelova i unošenja novih naprezanja. Tijekom toplinske obrade PVD postupak se izvodi na kraju. U radu je ispitan utjecaj nanošenja PVD prevlaka (cVlC i nACVlC) na otpornost adhezijskom trošenju čelika za poboljšavanje C45E. Uzorci su prije postupka prevlačenja toplinski obrađeni normalizacijom, poboljšavanjem i kaljenjem. Rezultati mjerenja su obrađeni statistički. Na temelju provedenih eksperimentalnih ispitivanja utvrđeno je da otpornost adhezijskom trošenju PVD prevlaka ovisi o vrsti prevlake, a manje o prethodnoj toplinskoj obradi čelika.

Ključne riječi: *PVD (Physical Vapour Deposition) prevlake, adhezijsko trošenje*

Abstract

PVD coatings of hard compounds reduce adhesion and abrasion wear, and some types of coatings also reduce the friction factor. The temperature of the PVD process is lower than the tempering temperature of hardening and tempering steels, there is no deformation of the parts and no additional stresses. In the case of heat treatment, the PVD process is carried out at the end. In this work, the influence of PVD coatings (cVlC and nACVlC) on the adhesive wear resistance of hardening and tempering steel C45E was studied. Before coating, the specimens were heat treated by normalizing, hardening and tempering and hardening. The measurement results were statistically evaluated. Based on the experimental tests performed, it was found that the adhesive wear resistance of PVD coatings depends on the type of coating and less on the previous heat treatment of the steel.

Keywords: *PVD (Physical Vapour Deposition) coatings, Adhesion Wear*

1. INTRODUCTION

The desired properties of machine parts and tools are achieved by selecting the appropriate material and applying various methods of classical heat treatment and heat treatment of surface layers.

One of the methods of heat treatment of surface layers is physical vapor deposition or PVD (Physical Vapor Deposition). In vapor deposition, a surface layer is created that has a different composition than the substrate material, and there is no diffusion into the surface layers of the substrate. The coatings are created by transporting particles, i.e. atoms, molecules and ions, in a vacuum. In PVD processes, the metal component of the coating is physically converted from a solid to a vapor phase. PVD processes can be used to produce very thin hard or protective coatings of various chemical compounds. PVD coatings made of hard compounds reduce abrasive wear, and the reduction of the friction factor leads to a reduction in adhesive wear [1, 2]. The coatings produced by PVD process generally adhere well to the base material and reduce its surface roughness. The PVD process is carried out as a final treatment, since the PVD coating does not require any subsequent heat treatment. This process is carried out at temperatures below 500 °C, which is why steels tempered at high temperatures (high-speed steels, tool steels for hot work, hardening and tempering steels) are also suitable for it [3].

PVD processes are used in the manufacture of parts in numerous industries: Automotive, military, textile, food, wood, chemical and paper industries, as protective and decorative coatings for medical devices and various products made of metal, glass, ceramics, etc. For environmental protection reasons, PVD process is also introduced as a substitute for electroplating with cadmium, zinc, hard chrome, nickel, etc. [4].

2. EXPERIMENTAL WORK

As part of research into the applicability of PVD coatings to structural steels, the effect of applying PVD coatings on the resistance to adhesive wear of C45E structural steel was investigated experimentally. The test was performed on 18 test specimens fabricated according to the drawing shown in Figure 1.

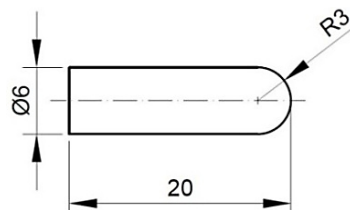


Fig. 1: Test specimen for wear resistance measurement

Before the coating process, three groups of six specimens each were heat treated by normalizing, hardening and tempering, and hardening. After heat treatment of each group, two specimens were coated with cVlc type coating, two specimens were coated with nACVlc type coating, and two specimens were left without coating.

C45E steel is an unalloyed carbon structural steel for hardening and tempering. Due to its low through-hardening ability, it is used up to a diameter of 40 mm, and in exceptional cases

up to 100 mm for less heavily loaded parts. It is often used in the normalized condition. It is used for the production of medium strength machine parts, such as screws, shafts, spindles, larger gears in pairs, connecting rods, etc. [5].

The selected parameters of heat treatments normalizing, hardening and tempering and hardening for the above three groups of test specimens are listed in Table 1.

Tab. 1: Heat treatment parameters for C45 steel [6]

Normalizing	Hardening and tempering		Hardening
$\vartheta_N = 840\text{ }^{\circ}\text{C}$	$\vartheta_a = 840\text{ }^{\circ}\text{C}$	$\vartheta_T = 560\text{ }^{\circ}\text{C}$	$\vartheta_a = 840\text{ }^{\circ}\text{C}$
$t_N = 1\text{ h}$	$t_a = 1\text{ h}$	$t_T = 2\text{ h}$	$t_a = 1\text{ h}$
Cooling in air	Water quenching	Cooling in air	Water quenching

The coatings of type cVlc and nACVlc were selected due to the requirements for high hardness of the surface layer and low friction factor, which are important in the selection of steel for the production of machine parts. The application temperature is in the temperature range in which hardened and tempered structural steels are used.

The cVlc type coating is a double coating with a nanostructure formed by the combination of TiCN + CBC coating. TiCN coating is a conventional coating and CBC (Carbon Based Coating) is a basic carbon coating. The CBC component is used as a dry lubricant to reduce the friction factor.

The nACVlc type coating is a double coating with a nanostructure formed by the combination of nACRo + CBC coating. nACRo (nc AlCrN/a-Si₃N₄) is a nanocomposite coating and the CBC component is used as a dry lubricant to reduce the friction factor. For the nACVlc coating, a titanium layer is applied to improve the bond with the base material.

The basic properties of the selected coatings are listed in Table 2.

Tab. 2: Properties of the selected PVD coatings [7]

Coating	Color	Nanohardness, GPa	Coating thickness, μm	Friction factor (on steel)	Service temperature $^{\circ}\text{C}$
cVlc	grey	25	1 - 2	0.15	400
nACVlc	blue-grey	40-25	1 - 10	0.15	450

2.1. Coating of the specimens

Coating of the specimens with PVD coatings was carried out in the Gazela-Platit company (Krško, Slovenia). The coating parameters were chosen according to the type of individual coatings. For the cVlc type coating, the process temperature was 450 $^{\circ}\text{C}$, and for the nACVlc type coating, the process temperature was 460 $^{\circ}\text{C}$. The duration of the two processes was the same. In the first phase of the process, the object is heated to the coating

temperature for 1 hour. In the second phase, electronic cleaning was performed for 15 minutes. The third phase of the process is a coating for 3 hours. The transformation of the metal (metal component of the coating) from a solid to a gaseous state was carried out using an electric arc. Before removal, the specimens were cooled in the oven to a temperature of 100 °C for 1 hour.

2.2. Testing of adhesive wear resistance

Tribological tests were performed using the pin-on-disk method on the Taber-Abraser device (model 503) in the Materials Testing Laboratory of the Mechanical Engineering Faculty in Slavonski Brod.

The test specimen was in a friction coupling with a plate of ductile cast iron EN-GJS-400-12S. Ductile cast iron was chosen because it has been shown to be an optimal tribological mating material for the manufacture of parts exposed to adhesive wear [8]. The test was performed with two test specimens for each heat treatment condition. A digital optical microscope was used to measure the diameter of the wear surface on the test specimens, after which the volume losses and wear indices were calculated.

Before each test, the plate was sanded with 320 grit sandpaper, which corresponds to roughness class N4, i.e. Ra is between 0.1 µm and 0.2 µm, and cleaned with alcohol to remove the influence of the previous test. The examination of the specimens and the measurement of the diameter of the wear surface were carried out after 10, 20, 30, 40, 50, 60, 70, 80, 90, 100, 200, 300, 400, 500, 600, 700, 800, 900 and 1000 revolutions. At each revolution, the specimen travels a distance of 257.6 mm, and after 1000 revolutions, the distance traveled was 257.6 m.

In accordance with ASTM G99 standard, the specimen was loaded with a force of 9.81 N [8]. The volume loss was calculated based on the average of two measurements of the diameter of the wear surface of a single specimen according to equation (1):

$$\Delta V = \frac{\pi \cdot d^4}{64 \cdot R} \quad (1)$$

where: ΔV – volume loss, mm³

d - diameter of the wear surface, mm

R - radius of the calotte of the specimen, mm ($R = 3$ mm) [9].

Examples of the measurement of the diameter of the wear surface and the appearance of the specimens after 1000 revolutions of the plate are shown in Figures 2 to 10.

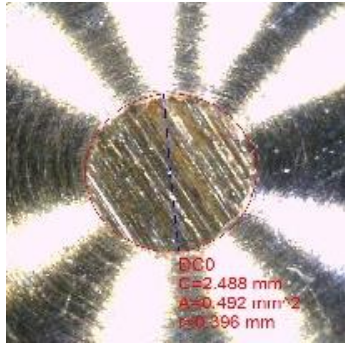


Fig. 2: Wear marks on normalized C45E steel after 1000 revolutions

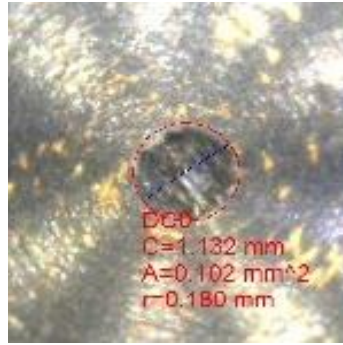


Fig. 3: Wear marks on normalized C45E steel with cVlc coating after 1000 revolutions

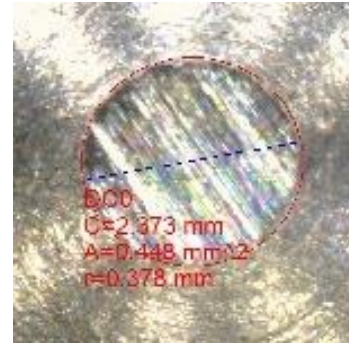


Fig. 4: Wear marks on normalized C45E steel with nACVlc coating after 1000 revolutions

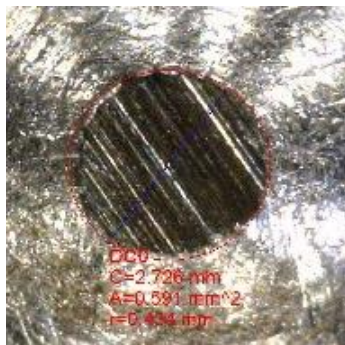


Fig. 5: Wear marks on hardened and tempered C45E steel after 1000 revolutions

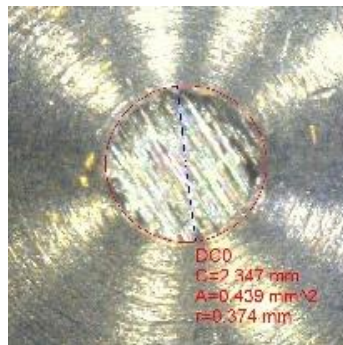


Fig. 6: Wear marks on hardened and tempered C45E steel with cVlc coating after 1000 revolutions

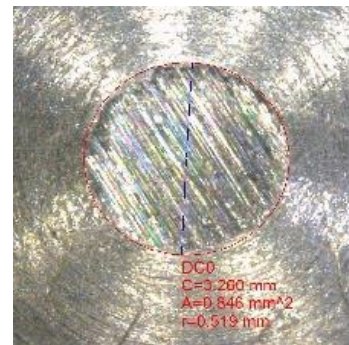


Fig. 7: Wear marks on hardened and tempered C45E steel with nACVlc coating after 1000 revolutions

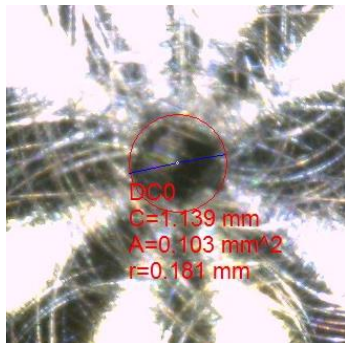


Fig. 8: Wear marks on hardened C45E steel after 1000 revolutions

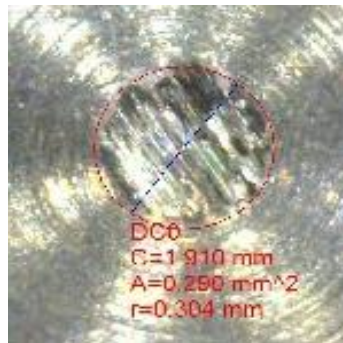


Fig. 9: Wear marks on hardened C45E steel with cVlc coating after 1000 revolutions



Fig. 10: Wear marks on hardened C45E steel with nACVlc coating after 1000 revolutions

A diagrammatic representation of the calculated volume loss values of C45E steel for the normalized, hardened and tempered and hardened condition, without coating, with cVlc type coating and with nACVlc type coating can be found in Figures 11, 12 and 13.

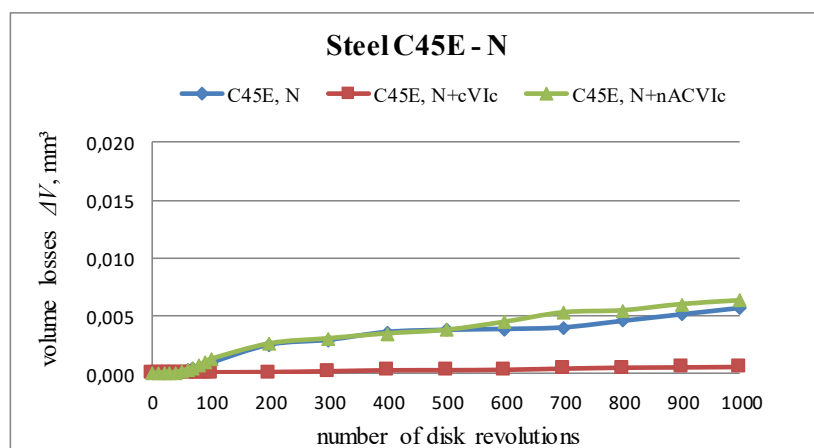


Fig. 11: Diagrammatic representation of the calculated volume losses on normalized C 45E steel without coating, with cVIc coating and with nACVIc coating

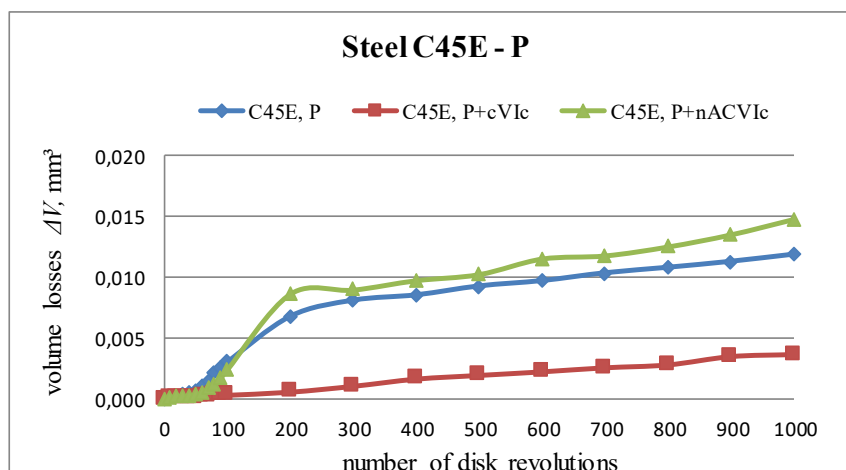


Fig. 12: Diagrammatic representation of the calculated volume losses on hardened and tempered C 45E steel without coating, with cVIc coating and with nACVIc coating

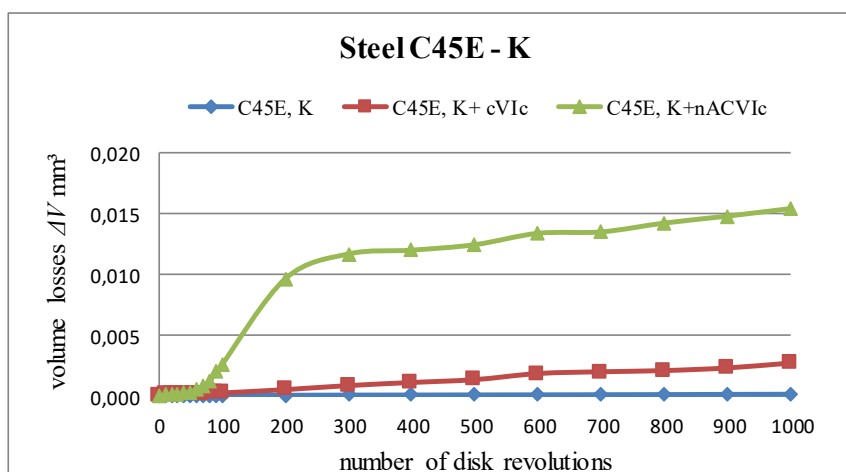


Fig. 13: Diagrammatic representation of the calculated volume losses on hardened C 45E steel without coating, with cVIc coating and with nACVIc coating

2.3. Wear index

The effect of PVD coating application on the wear resistance of normalized, hardened and tempered and hardened C45E structural steel was investigated by comparing the wear index. Wear indices are used to quantify the wear resistance of different materials. Materials with a lower wear index have better wear resistance. Wear indices are calculated using the volume loss method after 1000 revolutions of the disc. The volume loss wear indices are calculated according to equation (2):

$$i_{\Delta V} = \frac{\Delta V \cdot 1000}{n} \quad (2)$$

where: $i_{\Delta V}$ = wear index of volume loss
 ΔV = volume loss, mm³
 n = number of disk revolutions [10].

Table 3 shows the calculated wear indices of volume loss of the test specimens after 1000 revolutions of the disk.

Tab. 3: Wear indices of volume loss of test specimens after 1000 revolutions of the disc

Steel	Heat treatment	Coating type	Specimen mark	Wear index of volume loss
C45E	Normalized	Without coating	1.1.1	0.004907
			1.1.2	0.006438
		cVIc	1.2.1	0.001064
			1.2.2	0.000275
		nACVIc	1.3.1	0.005317
			1.3.2	0.007398
	Hardened and tempered	Without coating	2.1.1	0.009288
			2.1.2	0.014605
		cVIc	2.2.1	0.002529
			2.2.2	0.005095
		nACVIc	2.3.1	0.018995
			2.3.2	0.011122
	Hardened	Without coating	3.1.1	0.000099
			3.1.2	0.000109
		cVIc	3.2.1	0.002236
			3.2.2	0.003086
		nACVIc	3.3.1	0.009160
			3.3.2	0.023956

2.4. Analysis of the results

In order to determine the influence of the heat treatment and the type of coating on the adhesive wear of the structural steel C45E, a statistical analysis of the wear index of the volume loss after 1000 revolutions of the disk was performed, according to the data shown in Table 3.

Table 4 shows the results of statistical data processing of the wear index of volume loss of test specimens for structural steel C45E which were heat treated by normalizing, hardening and tempering and hardening before coating with cVlc and nACVlc PVD coatings.

Tab. 4: Analysis of variance of the wear index of the volume loss of the test specimens for the probability of the first defect of type 5%

Source of variation	Sum of squares, SS	Degrees of freedom, df	Mean square, MS	F-ratio, F	P-value	F critical value for a significance level of 0.05	Comentar
A – Heat treatment	0,0001121	2	$5,6025 \cdot 10^{-5}$	3,1146	0,093765	4,256495	No significant factor
B – Coating type	0,00032725	2	0,0001636	9,0965	0,006903	4,256495	A significant factor
Interaction AB	0,00015981	4	$3,9952 \cdot 10^{-5}$	2,2210	0,1472	3,633089	No significant interaction
Error	0,0001619	9	$1,7988 \cdot 10^{-5}$				
Total	0,000761	17					

By analyzing the data variance of the wear index of volume loss of specimens of structural steel C45E, which is shown in Table 4, it can be claimed with a confidence level of 95% that:

- the heat treatment of the steel has no significant effect on the resistance to adhesive wear ($F < F$ critical value for a significance level of 0.05)
- the type of coating has a significant influence on the resistance to adhesive wear ($F > F$ critical value for a significance level of 0.05)
- there is no significant interaction between the heat treatment of the steel and the type of coating ($F < F$ critical value for a significance level of 0.05).

3. CONCLUSION

Increasing wear resistance is one of the reasons for using PVD coatings. When analyzing the results of the adhesive wear resistance test, a significant difference in wear depending on the type of coating was found for structural steel C45E.

For C45E steel in normalized and hardened and tempered condition, the lowest wear was observed after coating with cVlc coating. Although both coatings have the same friction factor, the adhesive wear resistance of C45E steel with the cVlc coating is higher than with the nACVlc coating. The reason for this is probably to be due to the adhesive properties of cVlc and nACVlc coatings.

C45E steel in the hardened condition had the lowest wear without a coating and the highest with nACVlc type coating. The reason for the lowest wear achieved in the hardened condition of C45E steel without coating is that the hard PVD coating can peel off during adhesive wear, which would then also lead to abrasive wear as individual particles act as abrasives.

The resistance of PVD coatings to adhesive wear depends primarily on the type of coating and less on the steel grade and prior heat treatment.

REFERENCES

- [1] Filetin T., Grilec K., Postupci modificiranja i prevlačenja površina, HDMT, 2004, Zagreb.
- [2] Burakowski T., Wierzchoń T., Surface Engineering of Metals Principles, Equipment, Technologies, CRC Press, 1999, London (New York).
- [3] Krumes D., Površinske toplinske obrade i inženjerstvo površina, Strojarski fakultet u Slavanskom Brodu, 2004, Slavonski Brod.
- [4] Gojić M., Površinska obradba materijala, Sveučilište u Zagrebu, 2010, Sisak.
- [5] Filetin T., Kovačiček F., Indof J., Svojstva i primjena materijala, Sveučilište u Zagrebu, Fakultet strojarstva i brodogradnje, 2007, Zagreb.
- [6] Novosel M., Krumes D., Kladarić I., Željezni materijali Konstrukcijski čelici, Strojarski fakultet u Slavanskom Brodu, 2013, Slavonski Brod.
- [7] Gazela-Platit, Katalog tvrdih prevlaka, Interni katalog tvrtke Gazela d.o.o., Krško.
- [8] Golubić S., Primjena triboloških prevlaka na dijelovima vijčanih pumpi, magistarski rad, Fakultet strojarstva i brodogradnje, 2004, Zagreb.
- [9] ASTM G99-17, Standard Test Method for Wear Testing with a Pin-on-Disk Apparatus, 2017, ASTM International.
- [10] Golubić S., Utjecaj nanošenja PVD prevlaka na svojstva konstrukcijskih čelika za poboljšavanje, doktorska disertacija, Strojarski fakultet u Slavanskom Brodu, 2018, Slavonski Brod.



ANALIZA UZROKA KVARA OKRETAČA SIJENA

FAILURE ANALYSIS OF THE HAY TEDDER

Tomislav Vukes¹, Suzana Jakovljević²

¹ Centar toplinske obrade d.o.o., Slavonska avenija 22D, 10000 Zagreb, Hrvatska

Centar toplinske obrade d.o.o., Slavonska avenija 22D, 10000 Zagreb, Croatia

² Sveučilište u Zagrebu, Fakultet strojarstva i brodogradnje, Ivana Lučića 5, 1000 Zagreb, Hrvatska

University of Zagreb, Faculty of Mechanical Engineering and Naval Architecture, Ivana Lučića Street, No.5, Zagreb, Croatia

Abstract

The appearance of modern agromechanization drastically simplifies and makes the job of processing and storage of hay easier, but the use of machinery entails certain maintenance conditions of machine parts and equipment. If machine parts, which are necessary to transmit power from the drive unit to the working machine, are improperly designed or maintained, difficult working conditions and failure may occur. This paper describes failure analysis of a bevel gear from a hay tedder. The tests carried out on the sample involved studying the microstructure on the border and in the core of the bevel gear, chemical composition analysis and hardness measuring.

Keywords: hay tedder, gear, bevel gear, failure analysis

Sažetak

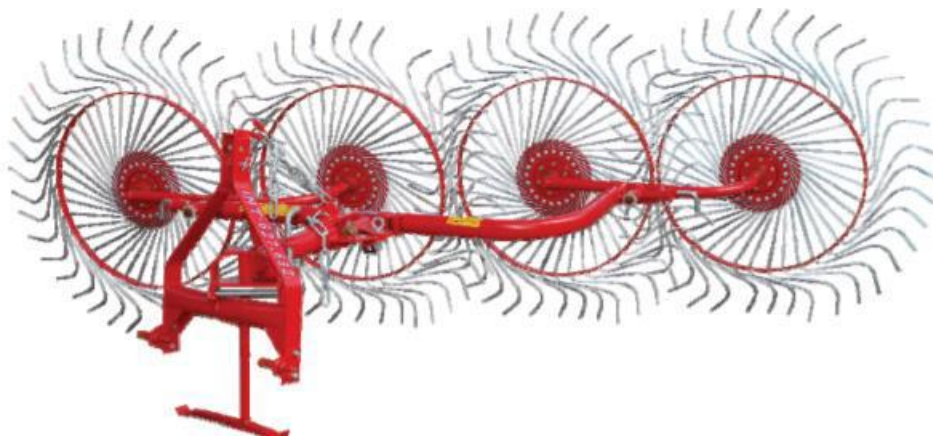
Pojavom moderne agromehanizacije znatno je olakšan i pojednostavljen posao obrade i skladištenja sijena, ali je prilikom korištenja mehanizacije nužno redovito održavanje korištenih strojnih dijelova i opreme. Ukoliko strojni dijelovi koji sudjeluju u prijenosu snage sadrže konstrukcijske greške ili su nepravilno održavani, nastupaju otežani uvjeti rada i dolazi do pojave kvara. U radu je provedena analiza uzroka kvara pogonskog stožnika okretača sijena. Proučavana je mikrostruktura jezgre stožnika i ruba zuba, analiziran je kemijski sastav materijala stožnika, te je izmjerena tvrdoća.

Ključne riječi: okretač sijena, zupčanik, stožnik, analiza uzroka kvara

1. UVOD

Košnjom trave i sušenjem na suncu se dobiva sijeno koje ima veliku ulogu u prehrani životinja. Do kvalitetne hrane za stoku i ostale preživače u zimskom dobu dolazi se pravovremenim provođenjem postupaka košnje trave, ispravnim sušenjem i manipulacijom pokošene trave, te odgovarajućim postupcima kompaktiranja i skladištenja suhog sijena. Razvojem tehnologije i agrotehničke mehanizacije prijedeno je s manualnog rada na rad s mehanizacijom. Takav način rada znatno olakšava manipulaciju sijena i omogućuje kvalitetnu nutritivnu prehranu životinja u ruralnim dijelovima, čak i u zimskim razdobljima uz pravilno izveden proces baliranja sijena. Kod procesa košnje trave razlikuju se oscilirajuće kose koje mogu biti s „prstima“ ili u izvedbi s dva noža, te rotacijske kose koje mogu biti s bubnjevima ili tanjurima. Mehanizaciju koja omogućuje prešanje sijena nakon njegovog pravilnog sušenja čine preše za sijeno kojima se smanjuje volumen rasutog sijena i olakšava njegova manipulacija. Razlikuju se preše za male kockaste bale, koje na većim gospodarstvima postaju preše za velike kockaste bale, te preše za valjkaste bale koje mogu biti preše s elastičnom tlačnom komorom, te preše s tlačnom komorom stalnog oblika.[1]

U ovom radu opisana je mehanizacija za preokretanje i skupljanje sijena. Cilj korištenja navedenog tipa mehanizacije je brže prosušivanje pokošene krme koja se tako može uskladištiti prije pojave kiše, s minimalnim gubicima hranjivih tvari. Strojevi koji se koriste za rastresanje, natresanje i okretanje sijena zovu se natresači i okretači sijena. Stariji okretači sijena nisu bili pogonjeni pogonskim vratilom nego su se pokretali samim kretanjem agregata (traktora). Primjer takvog stroja su nošene zvjezdaste grablje prikazane na slici 1.[1]



Slika 1. Nošene zvjezdaste grablje [2]

Stroj koji služi za manipulaciju sijena je rotacijski okretač-rastresač sastavljen od konstrukcije s pričvršćenim rotorima i pripadajućim vilama koje u paru rotiraju u suprotnim smjerovima. Najčešći kvarovi na ovakvom tipu stroja su lom zubaca na vilama, te oštećenja unutarnjih dijelova prijenosa uslijed ulaska nečistoća između dvaju zupčanika u zahvatu ili zbog nedostatka maziva. Primjer rotacijskog okretača-rastresača prikazan je na slici 2.[1]



Slika 2. Rotacijski okretač-rastresač proizvođača SIP [1]

Rotacijski okretač-prigrtač (slika 3) sličan je rotacijskom okretaču-rastresaču, te uz sve operacije koje obavlja rotacijski okretač-rastresač, može obavljati i operaciju prikupljanja krme u zbojeve (redove). [1]



Slika 3. Rotacijski okretač-prigrtač proizvođača Deutz [1]

Primjeri strojeva koji služe za manipulaciju sijena su rotacijske grablje i okretač sijena s beskrajnom trakom i elastičnim zupcima. Rotacijske grablje obavljaju samo operaciju prikupljanja osušenog sijena u redove (slika 4). Okretač sijena s beskrajnom trakom i elastičnim zupcima priključuje se, kao i ostali okretači sijena, na stražnji dio traktora, na trozglobnu hidrauličnu poteznicu, povezivanjem u tri točke (slika 5). Rad stroja ostvaruje se povezivanjem traktora i radnog stroja priključnim kardanskim vratilom. [1]



Slika 4. Rotacijske grablje [3]



Slika 5. Okretač sijena s beskrajnom trakom i elastičnim zupcima

2. MATERIJALI I METODE

U radu je analiziran uzrok kvara stožnika rotacijskog okretača-rastresača sijena, tj. oštećeni pogonski stožnik jednog od četiri rotora okretača sijena koji se pogoni priključivanjem na kardansko vratilo radnog stroja (traktora). Spomenuti okretač sijena KRONE KW 5.50 / 4 x 7 T prikazan je na slici 6.



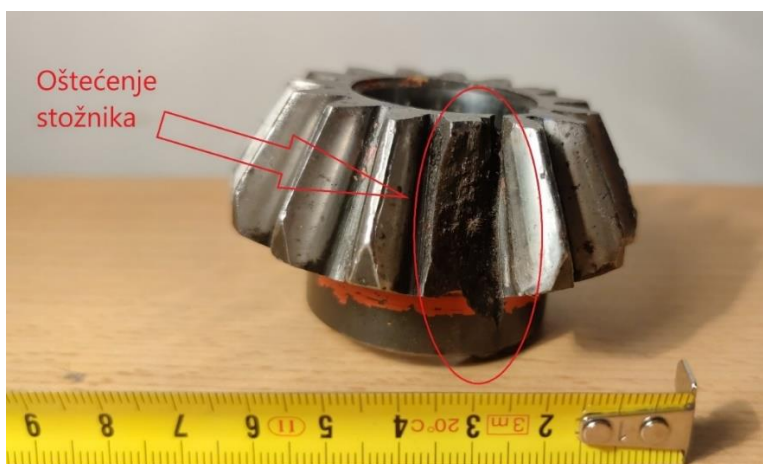
Slika 6. Okretač sijena KRONE KW 5.50 / 4 x 7 T [4]

2.1. Vizualni pregled uzroka

Vizualnim pregledom uzorka utvrđeno je da je došlo do djelomičnog odvajanja zuba stožnika. Po cijelom obodu stožnika vidljivi su tragovi trošenja (*pitting*). Također je uočena i pukotina s unutrašnje strane utora za pero koja je uslijed trošenja propagirala duž cijele visine stožnika. Opisana oštećenja stožnika i pukotina prikazani su na slikama 7 i 8.

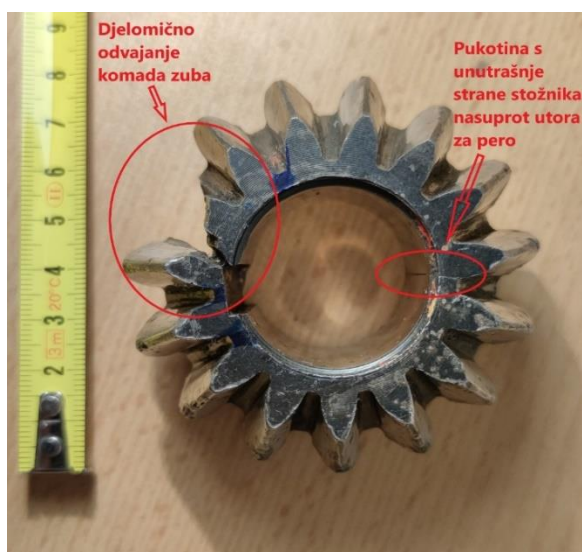


Slika 7. Tragovi trošenja po cijelom obodu stožnika

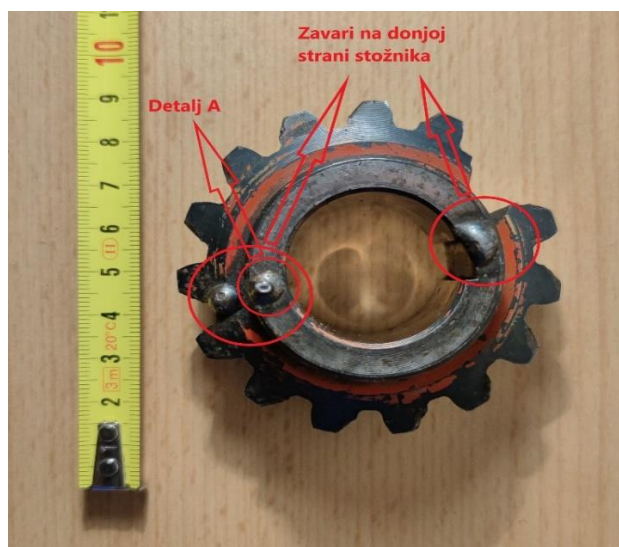


Slika 8. Oštećeni stožnik

Daljnim vizualnim pregledom stožnika uočena je i pukotina nasuprot utora za pero koja je također propagirala cijelom visinom stožnika. Također je uočeno kako je vlasnik pokušao popraviti pukotine koje su izbile na površinu stožnika postupkom zavarivanja. Pukotina nasuprot utora za pero i zavari na donjoj strani stožnika prikazani su na slikama 9 i 10.



Slika 9. Oštećeni stožnik – odozgo



Slika 10. Zavari na donjoj strani stožnika

Nakon što je zabilježeno početno stanje stožnika, primjenjene su razorne metode kako bi se stožnik prerezao na tri dijela i potom izvadio dio u kojem je bilo oštećenje. Rezanje stožnika provedeno je uz vodeno hlađenje i podmazivanje u Laboratoriju za metalografiju na Fakultetu strojarstva i brodogradnje. Za daljnje izdvajanje uzoraka za ispitivanje korišten je dio s pukotinom i utorom za pero. Na slici 11 prikazani su dijelovi stožnika dobiveni rezanjem stožnika, a na slici 12 preostali dijelovi stožnika na svojim originalnim pozicijama.

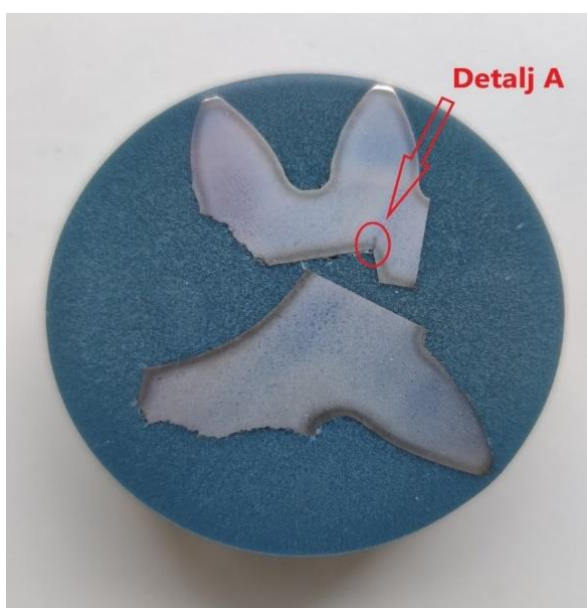


Slika 11. Izrezani dijelovi oštećenog stožnika



Slika 12. Preostali dijelovi stožnika na originalnim pozicijama

Iz izdvojenog komada stožnika s utorom za pero izrezani su reprezentantni dijelovi za daljnju analizu. Nakon izdvajanja reprezentativnih dijelova uzorak je stavljen u kalup i zaliven polimernom masom (slika 13). Uzorak je potom brušen papirima različite granulacije (P120, P32, P600, P1200, P2400 i P4000), te poliran dijamantnim pastama granulacije 3 μm i 0,03 μm . Nakon brušenja i poliranja uzorak je nagrižen u 3% otopini nitala.

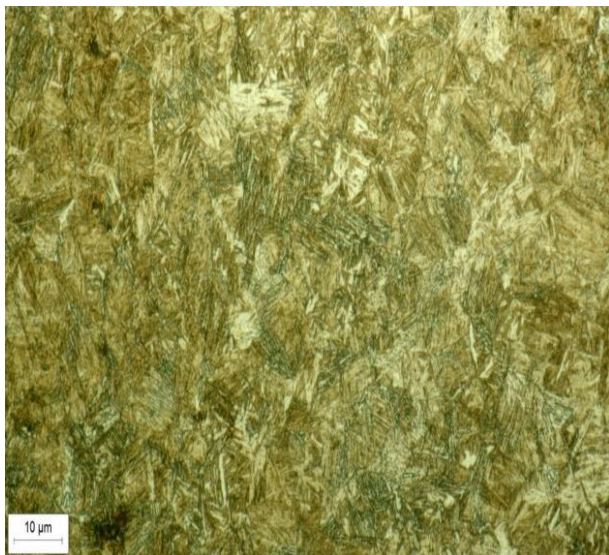


Slika 13. Ispitni uzorci

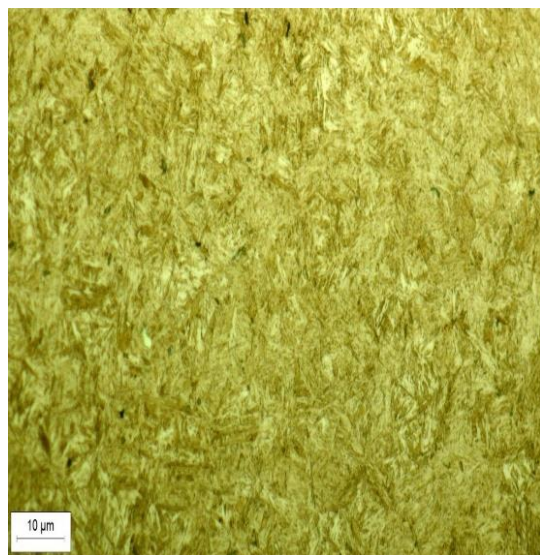
3. REZULTATI ISPITIVANJA

3.1. Analiza mikrostrukture svjetlosnim mikroskopom

Mikrostruktura jezgre i ruba zuba uzorka analizirana je svjetlosnim mikroskopom Olympus GX51. Na slici 13 detalj A predstavlja pukotinu na suprotnoj strani utora za pero. Na slikama 14 i 15 prikazane su mikrostrukture jezgre i ruba zuba uzorka koristeći povećanje 500x, te je vidljivo kako je i u jezgri i na rubu zuba prisutna martenzitna mikrostruktura.

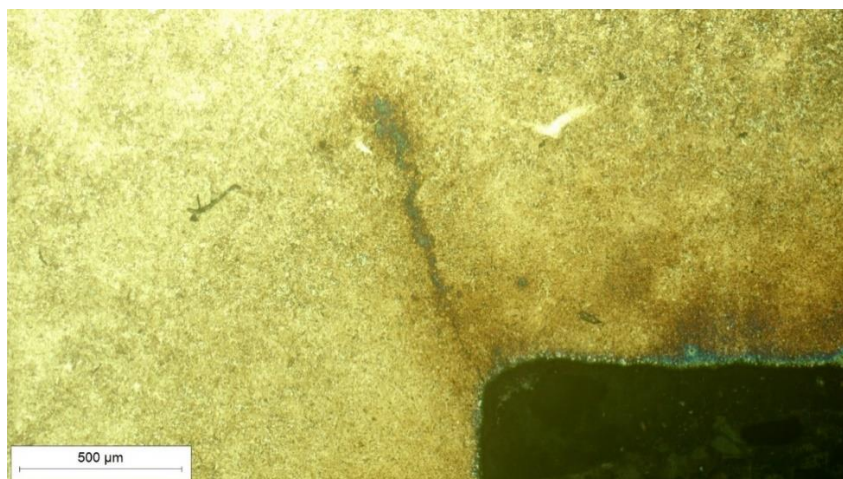


Slika 14. Mikrostruktura u jezgri stožnika



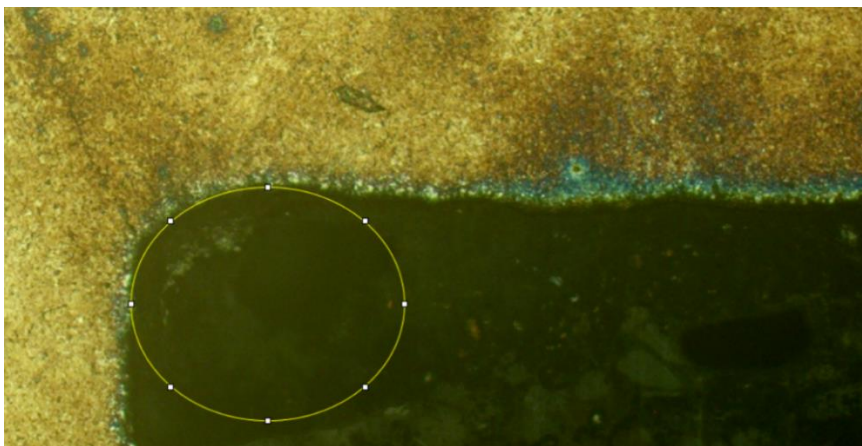
Slika 15. Mikrostruktura na rubu zuba

Pukotina, označena kao detalj A na slici 13, prodire u unutrašnjost materijala ali ne propagira po cijelom poprečnom presjeku već se zaustavlja na određenoj dubinu unutar stožnika (slika 16).



Slika 16. Pukotina na uzorku

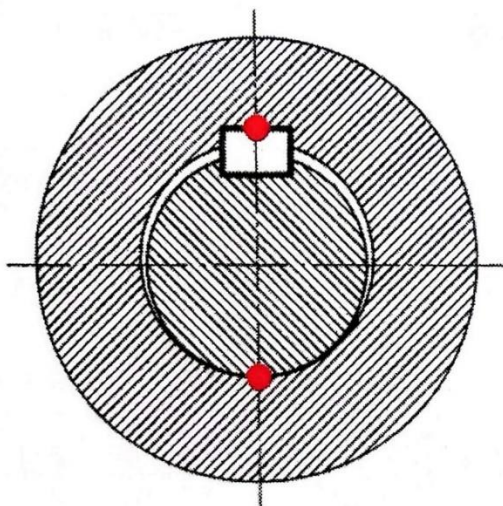
Pretpostavlja se da je uzrok pojave pukotine premali radijus u korijenu utora za pero. Radijus u korijenu utora za pero izmjeren je koristeći programski paket *ImageJ* upisivajući kružnicu u zaobljeni rub utora (slika 17). Mjerenjem je dobivena vrijednost radijusa zaobljenja 0,185 mm.



Slika 17. Mjerenje radijusa pomoću programskog paketa *ImageJ*

Prema normi BS 42135-1:1972 (ISO/R773) izmjereni bi radijus trebao biti minimalno 0,25 mm. Vrijednost izmjerenog radijusa u ovom radu (na slici 17) je premala i kao takva predstavlja konzentator naprezanja. Prema [5] potrebno je zaobliti rubove korijena utora za pero u glavini i u vratilu kako bi se smanjilo zarezno djelovanje, što u ovom slučaju nije napravljeno.

Pukotina nasuprot utora za pero nastala je zbog nastanka dodira u dvije točke spajanjem vratila i glavine. Na jednoj strani dolazi do dodira preko pera, dok na drugoj strani dolazi do neposrednog dodira. Slika 18 prikazuje dodir u dvije točke vratila i glavine.



Slika 18. Dodir u dvije točke vratila i glavine [5]

3.2. Analiza kemijskog sastava

Analizom kemijskog sastava u Laboratoriju za analizu metala Fakulteta strojarstva i brodogradnje postupkom optičke emisijske spektrometrije utvrđeno je da je stožnik izrađen od čelika za cementiranje EN 20MnCr5. U tablici 1 prikazani su rezultati kvantitativne kemijske analize.

Tablica 1. Kemijski sastav uzorka

Uzorak	%									
	C	Si	Mn	P	S	Cr	Mo	Ni	Cu	Fe
Stožnik	0,25	0,26	1,13	0,015	0,025	1,06	0,06	0,17	0,19	ostatak

3.3. Mjerenje tvrdoće

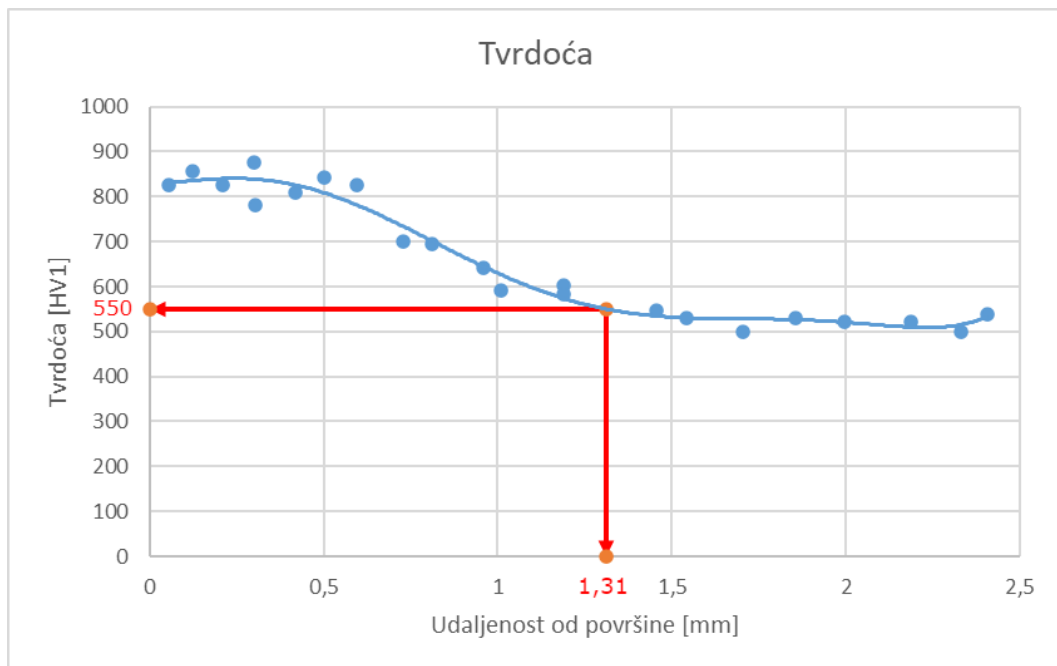
U radu je provedena metoda ispitivanja tvrdoće prema Vickersu. Tvrdoća je mjerena u dva niza od ruba prema sredini zuba stožnika koristeći opterećenje od 9,8 N (HV1). U prvom nizu je bilo 12 mjerenja, a u drugom nizu 10. U tablicama 2 i 3 prikazani su rezultati mjerenja tvrdoće, dok je na slici 19 prikazan graf koji prikazuje iznose tvrdoće na različitim dubinama od površine gdje je vidljivo da efektivna dubina cementiranja (definirana prema DIN EN ISO 2639) iznosi 1,31 mm.

Tablica 2. Rezultati prvog niza mjerenja tvrdoće

Udaljenost od površine [mm]	Tvrdoća [HV1]
0,055	826
0,210	826
0,302	781
0,420	810
0,595	826
0,810	694
1,010	592
1,190	602
1,455	547
1,705	500
1,995	523
2,330	500

Tablica 3. Rezultati drugog niza mjerenja tvrdoće

Udaljenost od površine [mm]	Tvrdoća [HV1]
0,125	858
0,300	875
0,500	842
0,730	701
0,960	643
1,190	583
1,540	531
1,855	531
2,185	523
2,405	539



Slika 19. Dijagram titra tvrdoće po presjeku stožnika i označena efektivna dubina cementiranja

4. ZAKLJUČAK

Na temelju provedenih analiza promatranog oštećenog dijela, analize mikrostrukture svjetlosnim mikroskopom, analize kemijskog sastava uzorka i ispitivanja tvrdoće uzorka dolazi se do sljedećih zaključaka:

- materijal uzorka stožnika po kemijskom sastavu i mikrostrukтури odgovara čeliku za cementiranje EN 20MnCr5,
- izmjerena tvrdoća stožnika je 875 HV1 u rubnom sloju, te 500 HV1 u jezgri uzorka,
- efektivna dubina cementiranja iznosi 1,31 mm,
- vizualnim pregledom je utvrđena prisutnost pukotine koja se pružala cijelom visinom stožnika i pritom izazvala djelomično odvajanje komada zuba istog,
- vidljivi su i tragovi trošenja (pittinga) po cijelom obodu stožnika koji su najvjerojatnije nastali zbog manjka podmazivanja, te se mogao izbjeći nastanak istih češćom primjenom maziva,
- uzrok djelomičnog loma zuba je nastanak pukotine u korijenu utora za pero i njena propagacija kroz cijeli stožnik zbog premalog radijusa korijena utora za pero,
- nastanak pukotine koja prodire duž cijele visine stožnika uzrokujući odvajanje dijela zuba je bilo moguće spriječiti kvalitetnijom obradom unutarnjeg ruba utora za pero izbjegavajući premale radijuse kao moguće uzroke koncentracije naprezanja.

5. LITERATURA

- [1] Zimmer R, Košutić S, Zimmer D. Poljoprivredna tehnika u ratarstvu. Osijek: Poljoprivredni fakultet u Osijeku; 2009.
- [2] Zvezdaste grablje sunce Agromehanika Boljevac [Internet]. (pristupljeno: 06/26/2022). Dostupno na: http://www.agrocoop.ba/images/proizvodi/mehanizacija/sijeno_sjenaza/zvezdaste_grablje_sunce_agro_mehanika.pdf
- [3] Dundović D. Tehnika spremanja sjenaže na farmi tovne junadi Simental-commerce d.o.o. Osijek: Poljoprivredni fakultet, Sveučilište Josipa Jurja Strossmayera u Osijeku; 2015.
- [4] KRONE KW 5.50 / 4 x 7 T [Internet]. (pristupljeno: 06/15/2022). Dostupno na: T <https://www.manualslib.com/manual/1791305/Krone-Kw-5-50-4-X-7-T.html#manual>
- [5] Decker KH. Elementi strojeva. Zagreb: Golden marketing-Tehnička knjiga; 2006.

STVOJSTVA VODORAZRJEDIVIH PREMAZA ZA ZAŠTITU PEĆI NA DRVA

PROPERTIES OF WATER-BASED COATINGS FOR WOOD BURNING STOVE PROTECTION

Ivan Stojanović¹, Borna Škrlec¹, Vesna Alar¹, Marin Kurtela¹

¹ Sveučilište u Zagrebu, Fakultet strojarstva i brodogradnje, Ivana Lučića 5, Zagreb, Hrvatska

Sažetak

Kamini na drva naširoko se koriste za grijanje u stambenim i poslovnim okruženjima, ali njihove su vanjske površine izložene visokim temperaturama i korozivnim tvarima, poput čađe, pepela i vlage. Premazi mogu zaštititi peć od ovih teških uvjeta, ali tradicionalni premazi na bazi otapala imaju značajne ekološke i zdravstvene nedostatke. Vodorazrjeđivi premazi obećavajuća su alternativa, ali njihova svojstva za zaštitu štednjaka još nisu u potpunosti definirana. Ovaj rad predstavlja jasan pregled nekih od ključnih svojstava premaza na bazi vode za zaštitu kamina i peći na drva kao što su prionjivost i otpornost na toplinski zamor i uspoređuje ih s premazima na bazi otapala. Na temelju provedenih ispitivanja dani su rezultati koji ističu neke od prednosti i nedostataka premaza na bazi vode i pružaju uvid proizvođačima peći, dobavljačima premaza i regulatorima kako bi mogli donositi kvalitetnije odluke o odabiru i regulaciji premaza za peći na drva.

Ključne riječi: Vodorazrjeđivi premazi, prionjivost, otpornost na toplinu, premazi na bazi otapala.

Abstract

Wood burning stoves are widely used for heating in residential and commercial settings, but their exterior surfaces are exposed to high temperatures and corrosive substances, such as soot, ash, and moisture. Coatings can protect the stove from these harsh conditions, but traditional solvent-based coatings have significant environmental and health drawbacks. Water-based coatings are a promising alternative, but their properties for stove protection are not yet fully understood. This article presents a comprehensive review of some of the key properties of water-based coatings for wood burning stove protection and compares them with solvent-based coatings, such as adhesion and cyclic heat resistance based on conducted tests. The review highlights some of the advantages and disadvantages of water-based coatings and provides insights for stove manufacturers, coating suppliers, and regulators to make informed decisions on the selection and regulation of coatings for wood burning stoves.

Keywords: Water-based coatings, adhesion, heat resistance, solvent-based coatings.

1. UVOD

Zaštita od korozije višestruko utječe na funkcionalnost konstrukcije, njenu trajnost i sigurnost u radu, a samim time čini i veliki udio u gradnji i održavanju. Zaštita premazima je najraširenija metoda zaštite od korozije različitih čeličnih konstrukcija. Kod tehnologije zaštite premazima vrlo je važno korektno izvođenje svih tehnoloških operacija i pripreme površine i nanošenja premaza. Uz kvalitetu, postupci zaštite sve više moraju udovoljiti i zahtjevu ne-štetnosti na okoliš i čovjeka.

Visoka temperatura vrlo je bitan faktor koji utječe na pojavu i razvoj korozije te uvelike smanjuje vijek trajanja proizvoda ili dijelova stroja. Visokotemperaturna korozija je tip korozije koji se pojavljuje tamo gdje su temperature daleko iznad 100 °C kao na primjer u dimovodima, ispušnim sustavima automobila, dizelskim motorima, termoelektranama, plinskim turbinama te ostalim strojevima koji dolaze u kontakt s vrućim plinom koji sadrži određena onečišćenja [1, 2].

Među metodama zaštite od korozije ističe se metoda zaštite prevlakama zbog svoje učinkovitosti koja ovisi o brojnim čimbenicima kao što su korozivnost okoliša, vrsta površine koja se zaštićuje, trajnost sustava premaza, priprema površine te sama tehnologija nanošenja prevlake. Granica toplinske stabilnosti uobičajeno dostupnih sustava premaza je unutar 60 °C [3], a na temperaturama u rasponu između 200 °C do 300 °C većina premaza na organskoj bazi postaje karbonizirana, a nekim slučajevima ta karbonizacija je popraćena razvojem agresivnih plinova kao što je klorovodik iz PVC-a [4] pa se za zaštitu od visokotemperaturne korozije koriste posebne vrste premaza. Svrha tih visokotemperaturnih zaštitnih premaza je održanje vanjskog izgleda i otpornosti na toplinu tijekom duljeg razdoblja pri visokim temperaturama [5]. Visokotemperaturnim prevlakama stvara se oksidni zaštitni sloj između okoline i samog materijala. Kako bi taj oksidni sloj ispunio svoju zadaću zaštite materijala potrebno je da bude postojan na visokim temperaturama, da dobro prijanja uz podlogu materijala, da ima određenu gustoću te da je otporan na temperaturni šok koji se javlja zbog naglih promjena temperature. Najčešće se koriste aluminijev oksid, kromov (III) oksid koji se koristi na temperaturama do 900 °C, te silicijev dioksid koji može podnijeti i temperature do 1800 °C, ali je zbog velike potrebne količine silicija uporaba ovakvih vrsta premaza ograničena [6]. Dakle, materijali koji se koriste u visokotemperaturnoj okolini moraju ispunjavati određene kriterije kao što su čvrstoća i otpornost na mehanički ili termodinamički zamor, a premaz kao takav mora pružiti odgovarajuću otpornost na okoliš, biti kemijski i mehanički kompatibilan s podlogom, odnosno biti primjenjiv [7]. Premazi na bazi silikonskih smola široko se primjenjuju kao materijali za nanošenje zbog svojih jedinstvenih svojstava, posebno onih vezanih uz vrlo dobru otpornost na visoke temperature [6].

S druge strane, tu su vodorazrjedivi, također poznati kao premazi na bazi vode. Radi se o premazima u kojima se voda koristi kao glavno otapalo ili nosač umjesto tradicionalnih organskih otapala. Ti premazi se sastoje od mješavine vode, smola, pigmenata, dodataka i drugih sastojaka.

Vodeni premazi pružaju nekoliko prednosti u odnosu na premaze na bazi otapala. Ekološki su prihvatljivi jer imaju niže razine hlapljivih organskih spojeva, koji su štetni za okoliš i ljudsko zdravlje. Također imaju smanjenu zapaljivost i manji miris. Vodeni premazi se često koriste u različitim industrijama, uključujući automobilsku, građevinsku, namještajnu i općenito industrijske primjene [8].

Ovi premazi se mogu nanositi na različite podloge kao što su drvo, metal, beton i plastika. U načelu, pružaju izvrsnu adheziju, trajnost i otpornost na abraziju, zahvaljujući aditivima koji su važne komponente vodorazrjedivih premaza. Međutim, prisustvo tih aditiva dovodi do faktora koji utječu na odgovarajuću adhezivnu snagu vodenih polimernih premaza, tako da postaje složenija nego adhezivna snaga premaza na bazi otapala [9].

Vodorazrjedivi premazi su dostupni u različitim formulacijama, uključujući akrilne, epoksidne, poliuretanske i alkidne premaze, pri čemu svaki ima specifična svojstva i primjene, a važno je napomenuti kako ti premazi nisu bez mana. Voda, naizgled obećavajuća zamjena za otapala u nekim situacijama, također je i ključna komponenta korozije. Ako voda dođe u dodir s podlogom prije nanošenja premaza, može se početi pojavljivati točkasta hrđa. Kako bi se osiguralo da se to ne dogodi, vodorazrjedivi premazi moraju biti formulirani tako da se sva voda izvlači kroz površinski sloj prije nego što može doći do korozije, što nije slučaj kod premaza na bazi otapala [8, 9].

U ovom radu ispituju se svojstva četiriju premaza: Solvalitt Black (SO), Senotherm UHT 2K-Hydro 3590 (SE), Thermodur 600 Aqua (TH) i Resist 78 (RE).

2. MATERIJALI I METODE

Provedeno je ispitivanje na četiri vrste visokotemperaturnih premaza spomenutih u uvodu, od kojih su dva na bazi otapala (plavo obojani u Tab. 1), a druga dva premaza su nove formulacije visokotemperaturnih premaza na bazi vode. Uzorci su nanoseni na pločice od ugljičnog čelika koji se koristi za proizvodnju peći. Površina uzoraka je pripremljena na dva načina, dio uzoraka je pjeskaren, a drugi dio sačmaren u toj kompaniji. Korišteno je ukupno 24 uzorka, po šest od svakog navedenog premaza, uz uvjet da su tri uzorka istog premaza prethodno obrađena pjeskarenjem (slovo P u oznaci uzorka), a tehnika obrade površine korištena kod druga tri uzorka bila je sačmarenje (slovo S u oznaci uzorka). Dakle, ispitano je 12 pjeskarenih i 12 sačmarenih uzoraka.

Tab. 1: Svojstva ispitanih premaza

Premaz	Komp.	Baza	Otpornost na temperaturu, °C	Gustoća kg/l	Deblji-na mokrog filma, µm	Deblji-na suhog filma, µm	Volumni sadržaj suhe tvari, %	Teoretska izdašnost
Solvalitt Black	1	Silikonski akrilni premaz	600	1,3	50 - 70	20 - 30	-	21 - 14 m ² /l
Thermodur 600 Aqua	1	Modificirana silikonska smola na bazi vode	600	-	-	15 - 30	44	11 m ² /kg
Senotherm UHT 2K-Hydro 3590	2	Na bazi vode	600	-	-	Od 25	53	9 m ² /kg
Resist 78	2	Anorgan-ski cink etil silikat koji otvrdnja-va vlagom	540	2,5	70 - 125	50 - 90	-	14,4 - 8 m ² /l

Nakon premazivanja čeličnih pločica, izmjerena je i određena debljina premaza. Od tri seta uzoraka, jedan je ispitan u slanoj, drugi u vlažnoj komori, a treći set bio je podvrgnut visokotemperaturnom cikličkom ispitivanju, tj. ta je grupa uzoraka ispitana na postojanost na cikličku promjenu temperature, s maksimalnom postignutom temperaturom od 450 °C. Potom je na uzorcima ispitana prionjivost „Cross-cut“ metodom nakon izlaganja u komorama, odnosno u visokotemperaturnoj peći.



Fig. 1: Uzorci spremni za ispitivanje (redom: slana komora, vlažna komora, peć)

3. REZULTATI I RASPRAVA

3.1. Ispitivanje debljine uzoraka

Nakon premazivanja čeličnih pločica, mjerena je debljina premaza. Debljina je izmjerena na deset različitih mjesta na svakom uzorku i zabilježena je srednja vrijednost te minimalna i maksimalna vrijednost također.

Tab. 2: Debljina pjeskarenih uzoraka

Pjeskareni uzorci				
Uzorak	Lo (μm)	Hi (μm)	\bar{x} (μm)	Ispitivanje
SO-P1	68,9	89,8	76,02	slana
SO-P2	16,4	22	18,6	vlažna
SO-P3	10	15,9	12,74	peć
SE-P1	65,1	126	90,54	slana
SE-P2	10,1	15,3	11,86	vlažna
SE-P3	12,4	17,1	14,92	peć
TH-P1	41,8	53,2	46,32	slana
TH-P2	7,3	11,1	10,44	vlažna
TH-P3	7,3	11	8,92	peć
RE-P1	32,7	38,7	35,92	slana
RE-P2	29,2	33,3	31,48	vlažna
RE-P3	29	35,3	31,24	peć

Tab. 3: Debljina sačmarenih uzoraka

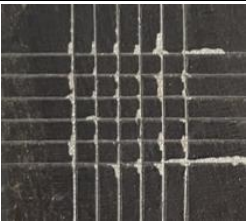







Sačmareni uzorci				
Uzorak	Lo (μm)	Hi (μm)	\bar{x} (μm)	Ispitivanje
SO-S1	60,8	69,6	65,05	slana
SO-S2	19,4	24	22,28	vlažna
SO-S3	16,2	20,3	17,54	peč
SE-S1	34,3	45,4	40,05	slana
SE-S2	9,3	12	10,68	vlažna
SE-S3	9,8	13,3	11,68	peč
TH-S1	42,5	52,3	46,86	slana
TH-S2	4,5	9,2	5,98	vlažna
TH-S3	4,7	7,3	5,92	peč
RE-S1	26,5	28,5	27,64	slana
RE-S2	32,3	36,3	33,86	vlažna
RE-S3	25,8	30,1	27,86	peč

3.2. Ispitivanje prionjivosti premaza – slana i vlažna komora

U narednim tablicama prikazani su rezultati ispitivanja prionjivosti premaza zarezivanjem mrežice, tj. „Cross-cut“ metodom prema normi HRN EN ISO 2409. Na uzorcima je skalpelom povučeno i urezano šest linija na udaljenosti 1 mm (iznimke su navedene kasnije) u vodoravnom i okomitom smjeru tvoreći tako mrežicu. Prema klasifikaciji rezultata testa po normi HRN EN ISO 2409, uzorci su ocijenjeni ocjenom od 0 do 5, gdje ocjena 0 označava najbolju prionjivost.

U Tab. 4 i Tab. 5 prikazani su rezultati ispitivanja prionjivosti premaza nakon izlaganja ubrzanim ispitivanjima u slanoj te vlažnoj komori. Vezano uz slanu komoru, uzorci su ispitivani u slanoj komori Ascott S450 prema normi HRN EN ISO 9227, a trajanje ispitivanja trajalo je 48 sati, odnosno dva dana.

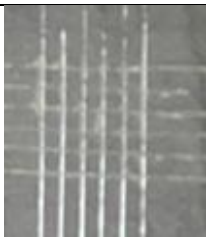
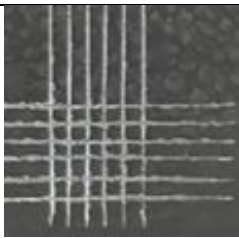

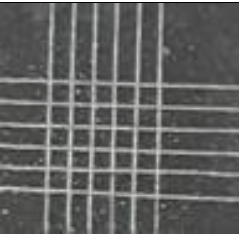


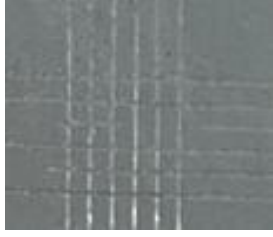
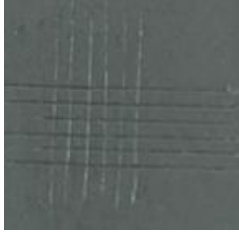
Tab. 4: Rezultati prionjivosti na premazima nakon 48 sati ispitivanja u slanoj komori

Priprema površine	Sačmareno		Pjeskareno	
Premaz	Izgled uzorka/ vl.kom.	Ocjena	Izgled uzorka/ vl.kom.	Ocjena
Solvalit ATM (SO-S1, SO-P1)		2		1
Senoterm UHT 2K Hydro ATM (SE-S1, SE-P1)		5		3
Thermodor 600 Aqua ATM (TH-S1, TH-P1)		5		3
Resist 78 (RE-S1, RE-P1)		2		0

Valja napomenuti kako je za uzorak SO-S1 kod „Cross-cut” testa korišten razmak između linija mrežice od 2 mm (budući da se radi o debljini iznad 60 μm), a za uzorke SE-S1 i TH-S1 korišten je razmak od 1 mm (debljina ispod 60 μm). Analogno tome, za uzorke SO-P1 i SE-P1 korišten je razmak 2 mm, a za uzorak TH-P1 korišten je razmak od 1 mm.

Što se tiče vlažne komore, ona oponaša uvjete tople i vlažne atmosfere uz vodeni kondenzat. Ispitivanja u vlažnoj komori provedena su u uređaju Humidity Cabinet Model AB6, proizvođača C&W, sukladno normi HRN EN ISO 6270-2:2018, a trajanje ispitivanja je bilo 96 sati, tj. četiri dana. Temperatura u komori bila je 40 °C, a relativna vlažnost zraka je oko 100 %, s orošavanjem uzoraka.

Tab. 5: Rezultati prionjivosti na premazima nakon 96 sati ispitivanja u vlažnoj komori

Priprema površine	Sačmareno		Pjeskareno	
Premaz	Izgled uzorka/ vl.kom.	Ocjena	Izgled uzorka/ vl.kom.	Ocjena
Solvalit ATM (SO-S2, SO-P2)		1		1
Senoterm UHT 2K Hydro ATM (SE-S2, SE-P2)		5		0
Thermodor 600 Aqua ATM (TH-S2, TH-P2)		2		0
Resist 78 (RE-S2, RE-P2)		1		1

Kad se sagledaju rezultati jasno je kako su pjeskareni uzorci pokazali znatno bolju prionjivost premaza nakon ispitivanja u komorama nego uzorci koji su bili sačmareni. Ispitivanjima je dokazan utjecaj pripreme površine i profila hrapavosti na prionjivost premaza. Uzevši u obzir ispitivanja obje komore i obje vrste pripreme površine, najbolju prionjivost je pokazao premaz Resist 78. Također se vrlo lako da primjetiti kako je Senoterm UHT 2K Hydro pokazao najlošiju prionjivost nakon ispitivanja u vlažnoj komori i u slanoj komori na sačmarenim uzorcima. Generalno, uzorci koji su ispitani u slanoj komori polučili su gore rezultate od onih ispitanih u vlažnoj ne samo po pitanju prionjivosti nego i u estetskom smislu budući da je na uzorcima bila prisutna hrđa u značajnoj količini, vidljivo na Fig. 2.

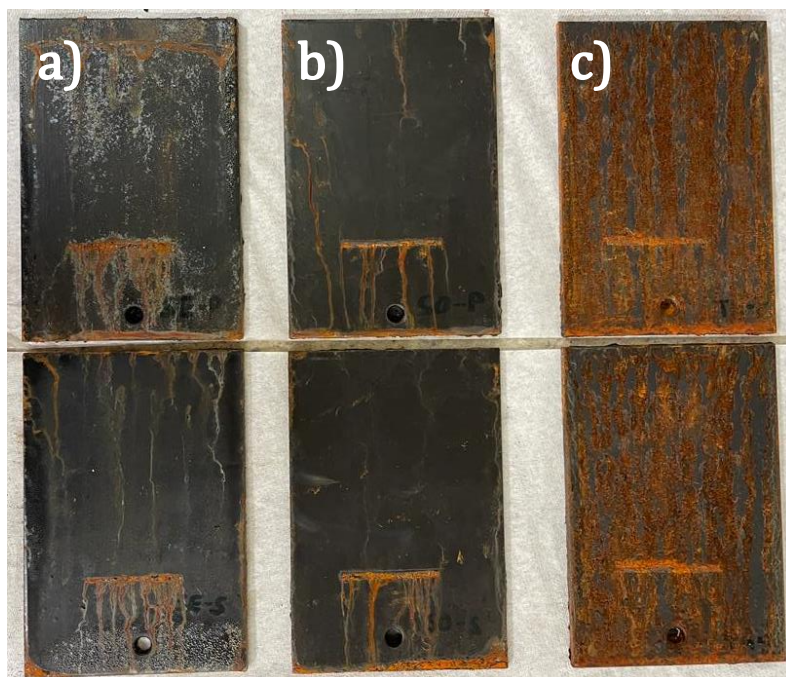
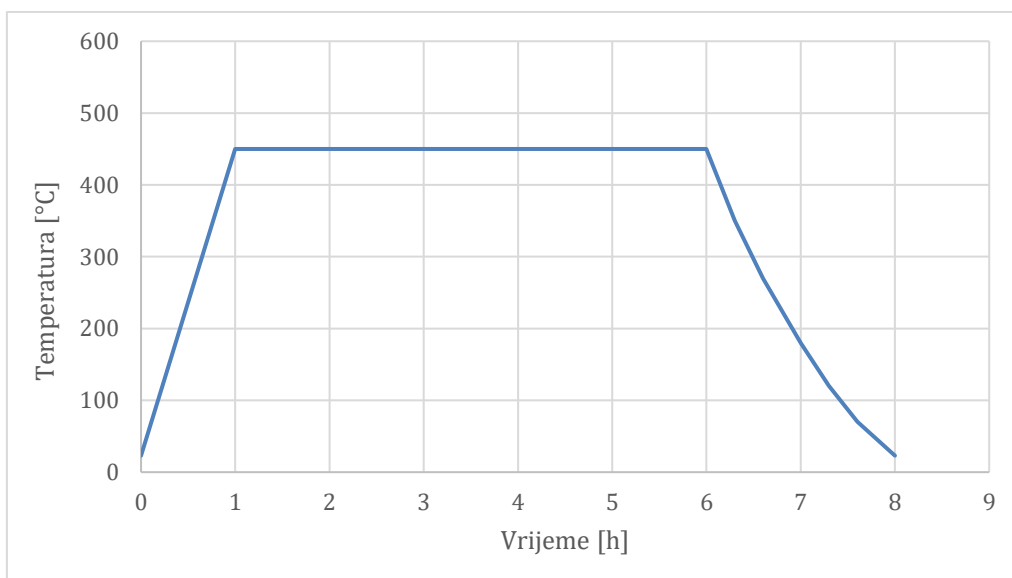


Fig. 2: Hrđa na uzorcima Senotherma (a), Solvalitta (b) i Thermodura (c) nakon ispitivanja u slanoj komori (gore – pjeskareno, dolje – sačmareno)

3.3. Ispitivanje prionjivosti premaza – povišena temperatura

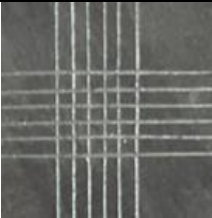
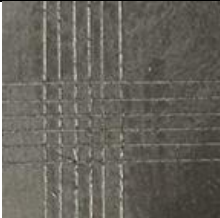
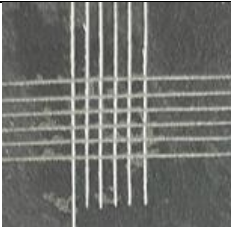
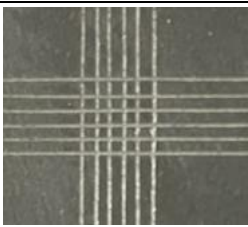
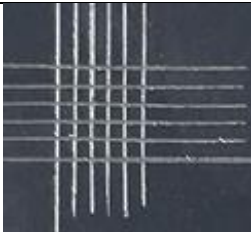
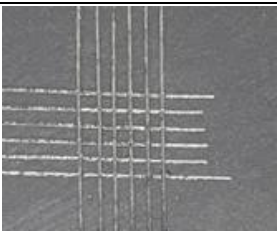
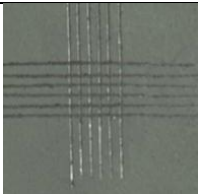
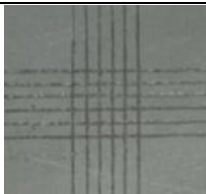
Kako bi se što bolje simuliralo okruženje kamina ili peći na drva, treći set uzoraka bio je podvrgnut temperaturnom ispitivanju na način da su uzorci prvo zagrijavani na temperaturu od 450 °C u trajanju od sat vremena, zatim su držani na toj temperaturi u trajanju od 5 h, a nakon toga su hlađeni na sobnu temperaturu u trajanju od 2 h. Za potrebe tog ispitivanja korištena je posebna peć, prikazana sasvim desno na Fig. 1. Dijagram opisanog visokotemperaturnog ciklusa kojem su uzorci bili podvrgnuti ukupno pet puta u pet dana zaredom prikazan je na Fig. 3.

Fig. 3: Kretanje temperature u jednom ciklusu visokotemperaturnog ispitivanja



Nakon odrađenog ispitivanja i simulacije visokotemperaturnih ciklusa, testirana je prionjivost premaza prethodno opisanom „Cross-cut“ metodom, a dobiveni rezultati prikazani su u Tab. 6.

Tab. 11: Rezultati prionjivosti na premazima nakon visokotemperaturnog testiranja

Priprema površine	Sačmareno		Pjeskareno	
	Izgled uzorka	Ocjena	Izgled uzorka	Ocjena
Solvalit ATM (SO-S3, SO-P3)		0		0
Senoterm UHT 2K Hydro ATM (SE-S3, SE-P3)		2		0
Thermodor 600 Aqua ATM (TH-S3, TH-P3)		0		0
Resist 78 (RE-S3, RE-P3)		1		0

Kao što je i vidljivo, praktički svi uzorci su pokazali odličnu prionjivost nakon izlaganja visokim temperaturama što je iznimno važno jer je okruženje ovog ispitivanja bilo najbliže realnoj situaciji u kaminu ili peći na drva, a pjeskarenje se opet pokazalo kao superiornija metoda pripreme površine od sačmarenja u aspektu prionjivosti. To je zbog toga što površina čelične pločice na koju se nanosio premaz, iako ima veću vrijednost srednje hrapavosti, ima i ujednačeniju visinu neravnina što omogućava premazima da se bolje prime za površinu. Vezano uz spomenutu hrapavost, srednja vrijednost hrapavosti na pjeskarenim uzorcima iznosila je 23,58 μm , a na sačmarenim 18,65 μm .

4. ZAKLJUČAK

Zaštita od korozije izuzetno je važna u održavanju i produženju trajnosti konstrukcija, a proizvodnja kamina i peći tu nije iznimka. Metode zaštite premazima, posebice visokotemperaturnim premazima, pokazuju se kao učinkovite na tom području. Visokotemperaturni premazi široko se koriste za premazivanje metalnih predmeta koji su redovito izloženi visokim temperaturama (350 do 600°C) kao što su ložišta, peći, roštilji, automobilski ispušni sustavi itd. Takvi premazi u slučaju primjene kod kamina na drva, uz to što moraju imati dobra korozijska svojstva, moraju imati i dekorativno dobar izgled površine koji će teško biti održan ako će premazi biti izloženi slanoj atmosferi što je istraživanje jasno pokazalo. Također, priprema površine i profil hrapavosti imaju velik utjecaj na prionjivost premaza, a na temelju provedenih ispitivanja preporuka je da se površina priprema pjeskarenjem.

Ispitivanja prionjivosti premaza nakon izlaganja u slanoj i vlažnoj komori pokazala su bolje rezultate za pjeskarene uzorke u usporedbi sa sačmarenom površinom, a Resist 78, premaz na bazi otapala, pokazao je najbolja svojstva. Uzorci ispitani u slanoj komori imali su lošije rezultate u pogledu prionjivosti i prisutnosti hrđe u usporedbi s uzorcima ispitanim u vlažnoj komori.

Ispitivanje na cikličku promjenu temperature pokazalo je da su i premazi na bazi otapala, ali i vodorazrjedivi premazi zadržali odličnu prionjivost čak i nakon izlaganja visokim temperaturama. U konačnici, iako su premazi na bazi otapala u provedenim ispitivanjima generalno pokazali bolje rezultate, u okruženju visoke temperature koje najbolje simulira stvarnu situaciju kamina ili peći i vodorazrjedivi premazi su polučili zadovoljavajuće rezultate.

U svakom slučaju, zaštita premazima i odgovarajuća priprema površine ključni su faktori za uspješnu zaštitu od korozije i održavanje trajnosti konstrukcija u različitim okruženjima i uvjetima, a daljnja istraživanja trebala bi se usredotočiti na utjecaj debljine premaza na postojanost i prionjivost pri sobnoj i povišenoj temperaturi te eksperimentiranju s formulacijom vodorazrjedivih premaza kako bi se unaprijedila učinkovitost postojećih.

Zahvala:

Istraživanje je provedeno u sklopu projekta „Razvoj energetske visokoučinkovitog sustava za zagrijavanje na kruta goriva iz obnovljivih izvora energije korištenjem inovativnih tehnoloških postupaka“ (Referentna oznaka: KK.01.2.1.02.0226.) kojeg je sufinancirala Europska unija iz Europskog fonda za regionalni razvoj. Sadržaj ove publikacije isključiva je odgovornost Fakulteta strojarstva i brodogradnje Sveučilišta u Zagrebu.

LITERATURA

- [1] Bose S., High Temperature Coatings. Butterworth-Heinemann, (2017).
- [2] Lai, G. Y., High-Temperature Corrosion and Materials Applications, ASM International, (2007).
- [3] Mathivanan L., Selvaraj M., Azim S. S., Balakrishnan, K., Evaluation of heat resistant properties of silicone-based coatings by SEM and a.c. Impedance techniques. Progress in Organic Coatings, pp. 113–116, (1996).
- [4] Mathivanan L., Arof A. K., The degradation of silicone coatings in high temperature atmospheres. Anti-Corrosion Methods and Materials, pp. 403–412, (1998).
- [5] Chew K. W., Yahaya A. H., Arof, A. K., Studies on the properties of silicone resin films on mild steel. Pigment & Resin Technology, pp. 364–368, (2000).

- [6] Zielecka M., Rabajczyk A., Cygańczuk K., Pastuszka Ł., Jurecki L., Silicone Resin-Based Intumescent Paints. *Materials*, (2020).
- [7] Mévrel R., State of the art on high-temperature corrosion-resistant coatings. *Materials Science and Engineering: A*, pp. 120–121, 13–24, (1989).
- [8] <https://www.uscoatings.com/blog/water-based-coating-vs-solvent-based-coating/>, consulted on 26 June 2023.
- [9] Al-Janabi A., Malayeri M. R., Environmentally Friendly Solvent- and Water-Based Coatings for Mitigation of Crystallization Fouling. *Chemical Engineering & Technology*, pp. 147–154, (2015).

EKSPERIMENTALNO ODREĐIVANJE ZAOSTALIH NAPREZANJA SUČELJENOG SPOJA AL-MG LEGURA DOBIVENOG MIG ZAVARIVANJEM

EXPERIMENTAL DETERMINATION OF RESIDUAL STRESSES ON BUTT WELDS OF AL-MG ALLOYS OBTAINED WITH MIG WELDING

Mislav Štefok¹, Ivica Garašić¹, Maja Jurica¹, Vedran Jurlina

¹University of Zagreb, Faculty of Mechanical Engineering and Naval Architecture, Ivana Lučića 5, Zagreb

Sažetak

Zaostala naprezanja značajno utječu na stabilnost i trajnost zavarenih konstrukcija, te je vrlo važno pažljivo kontrolirati parametre zavarivanja kao i brzinu hlađenja kako bi se reducirala pojava zaostalih naprezanja. U ovom eksperimentalnom radu zavarena su dva para ploča od aluminijske legure 5083 u obliku sučeljenog spoja, primjenom AC i DC MIG postupka zavarivanja. Zaostala naprezanja mjerena su metodom rendgenske difrakcije temeljene na $\cos\alpha$ metodi. Prije provođenja postupka mjerenja rendgenskom difrakcijom, mjerne točke su elektropolirane kako bi se uklonio površinski sloj metala. Raspodjela zaostalih naprezanja postignuta je na način da se vlačna zaostala naprezanja javljaju u blizini zavara u zoni utjecaja topline, dok tlačna naprezanja prevladavaju u zoni osnovnog materijala na većim udaljenosti od zavara. Analiza rezultata pokazuje da se kod izmjenične struje postižu povoljniji rezultati zaostalih naprezanja nego kod DC struje, s obzirom da su postignuta manja vlačna naprezanja u zoni utjecaja topline, koja su u kontekstu zavarivanja puno problematičnija od tlačnih naprezanja u osnovnom metalu.

Ključne riječi: AC MIG, sučeljeni spoj, rendgenska difrakcija, zaostala naprezanja, $\cos\alpha$ metoda.

Abstract

Residual stresses have a significant effect on the durability and fracture behavior of welded structures, as well as on their dimensional stability and durability, and it is very important to carefully control the welding parameters and cooling rate to reduce the generation of residual stresses during welding. In this paper, two pairs of aluminum alloy 5083 plates were butt welded using the AC and DC MIG welding process. Residual stresses were measured using the non-destructive X-ray diffraction method based on the $\cos\alpha$ method. The measurement points were electropolished before measurement to remove the surface layer of the metal. The stress distribution was achieved in such a way that tensile residual stresses occur near the weld in the heat-affected zone, while compressive stresses prevail in the zone of the base material at some distance from the weld. Analysis of the results shows that more favorable residual stress results are obtained with alternating current because it achieves lower tensile stresses values than direct current in the heat-affected zone, which are much more problematic in the context of welding than compressive stresses in the base material.

Keywords: AC MIG, Butt joint, X-ray diffraction, XRD, Residual stresses, $\cos\alpha$ method

1. INTRODUCTION

Residual stress is a type of stress that remains in a material after the load that caused it has been removed. During the welding, residual stresses can occur due to thermal expansion and contraction of the welded material. Over time, these residual stresses can cause deformation, cracking, and even failure of the welded structure [1]. Residual stresses in welding are an important factor to consider in the design and welding of structures because they significantly affect the fatigue life and fracture behavior of machines and welded structures, as well as their dimensional stability and durability [2]. Therefore, it is important to carefully control welding parameters and cooling rates to minimize the generation of residual stresses during welding [3]. The measurement of heat transfer helps predict the thermal stresses (TS) that will affect the amount of residual stresses formed in the weld [4].

Several methods are available to measure and quantify residual stresses in welded structures. These include destructive and non-destructive testing methods, such as X-ray diffraction, neutron diffraction, and hole-drilling methods [5]. By accurately measuring and analyzing residual stress distributions, engineers can better understand the behavior of welded structures and develop strategies to reduce the negative effects of residual stress on its performance [6].

X-ray stress measurement is a commonly used non-destructive method for measuring residual stresses in polycrystalline solids. The advantage of the method is that the required equipment is relatively cheap compared to other diffraction techniques, the lateral resolution is relatively high and radiation protection can be achieved very easily due to the low energy level (usually 30 - 40 keV) [7]. The $\sin^2\psi$ method is the conventional approach for determining stress values in X-ray stress measurement. However, in recent years, the $\cos\alpha$ method has attracted the attention of engineers as a new approach to stress measurement. In this method, two-dimensional detectors, such as imaging plates, are used to obtain stress measurements [8].

The fundamental principle of X-ray stress measurement is based on the diffraction of X-rays by crystals. When X-rays interact with a crystalline structure, they diffract in a specific pattern that depends on the crystal lattice spacing. Residual stresses in the material cause deformation of the crystal lattice, resulting in a change in the X-ray diffraction pattern. The lattice strain caused by the residual stress can then be measured using X-ray diffraction techniques and the stress can be determined using the theory of elasticity [9].

There are many factors that affect residual stress distribution in welded components, such as the presence of residual stresses prior to welding that were created during the manufacturing process, material properties (weld and base metal), geometry of the joined parts, applied stress, restraint, welding procedure, post-weld operation, etc. Residual stresses can be beneficial or detrimental to some components, depending on their nature. In general, tensile residual stresses can be detrimental to components, while compressive residual stresses can improve component quality [10]. In addition, tensile residual stresses significantly accelerate crack propagation, while compressive residual stresses retard crack propagation [11], [2].

The distribution of residual stresses in a butt joint can be affected by several factors, including the welding procedure, welding parameters, and material properties of the joint. During welding, the material in the weld bead is heated and then rapidly cooled, which can result in significant thermal stresses that lead to residual stresses [12]. These

residual stresses are usually highest near the center of the weld bead and decrease toward the edges of the bead. Another area where residual stresses can occur in a butt weld is the heat-affected zone (HAZ) adjacent to the weld. The HAZ is an area of the material that is exposed to elevated temperatures during welding, but the temperatures are not as high as in the weld bead. Thermal cycling in the HAZ can cause metallurgical changes and the development of residual stresses that extend beyond the weld bead into the base metal. During welding, the material in the weld bead is heated and then rapidly cooled, which can result in significant thermal stresses that lead to residual stresses. These residual stresses are usually highest near the center of the weld bead and decrease toward the edges of the bead. The curve of the distribution of longitudinal residual stress in the butt weld resembles a Gaussian distribution, the tensile stress is high in the center of the weld and gradually decreases toward the outside, the tensile stress decreases rapidly and changes to a compressive stress toward the base material [13].

2. MATERIALS AND METHOD

Two pairs of plates with a thickness of 8 mm were butt welded using MIG welding technology with different set of parameters. The dimensions of the plates were 300x100 mm. Aluminum alloy 5083 (Group 22.4 according to HRI CEN ISO / TR 15608:2018) was used as the base material. A 1.2 mm thick wire of aluminum alloy 5356 (group 22.4 according to HRI CEN ISO / TR 15608:2018) was used as filler metal, and argon 5.0 (group I1 according to EN ISO 14175:2008) was used as shielding gas. The mechanical and chemical properties of the base and filler materials are shown in Table 1. The plates were welded in one pass without any joint preparation before welding. The first sample was welded using the DC pulse MIG welding method, and the second sample was welded using the AC MIG WAVE PULSE welding method. The welding power source used in the experiment was Daihen Varstroj WB -W400. The welding parameters of sample 1 and 2 are shown in Table 2.

Table 1. Chemical and mehanical properties of filler and base material [14]

Chemical composition	%Si	%Fe	%Cu	%Mn	%Mg	%Cr	%Zn	%Ti
Aluminum alloy 5356	0.05	0.09	0.03	0.12	4.9	0.08	< 0.01	0.15
Aluminum alloy 5083	0.40	0.40	0.10	0.4 – 1.0	4.0 – 4.9	0.05 – 0.25	< 0.25	0.15
Mechanical properties	$R_{p0.2}$, MPa		R_m, MPa					
Aluminum alloy 5356	110		240					
Aluminum alloy 5083	115		270 - 345					

Table 2. Welding parametars of sample 1 and 2

Sample	Tehnology	Welding current, A	Welding voltage, V	Frequency of wave pulse, Hz	Welding speed, cm/min	wire feed speed cm/min	Gas flow, l/min	Heat input, kJ/cm
1	DC pulse	230	24.9	/	60	15	22.5	4.58
2	AC wavepulse	246	24.5	3	46	16.1	22.5	6.29

Residual stresses were measured using the non-destructive X-ray diffraction method based on the $\cos\alpha$ method. For this purpose, a portable Pulstec μ -X360 instrument (from Pulstec Industrial Co. Ltd., Fig. 1) was used. Before starting the measurement, the measurement locations were electropolished for 60 seconds. The measurement was performed after removing the surface layer of the metal at a depth of 30 μm below the surface. Electropolishing was performed to remove aluminum oxides that could affect the residual stress measurement results. The device EP -3 (from Pulstec Industrial Co. Ltd.) was used to perform electropolishing. Residual stresses were measured on the top of the plates, on three transverse lines for plate 2, and on one transverse line for plate 1. On each transverse line, 8 locations (4 on each side) were measured at distances of 5, 15, 30 and 45 mm from the weld (Fig. 2). No measurements were made on the weld itself because the surface of the weld is too rough. On plate 1, residual stresses were measured at the same location as in line 1 of plate 2 to compare the effects of the current AC on the residual stress values. The residual stresses were measured in the longitudinal direction, and results were obtained for normal and tangential residual stress values.

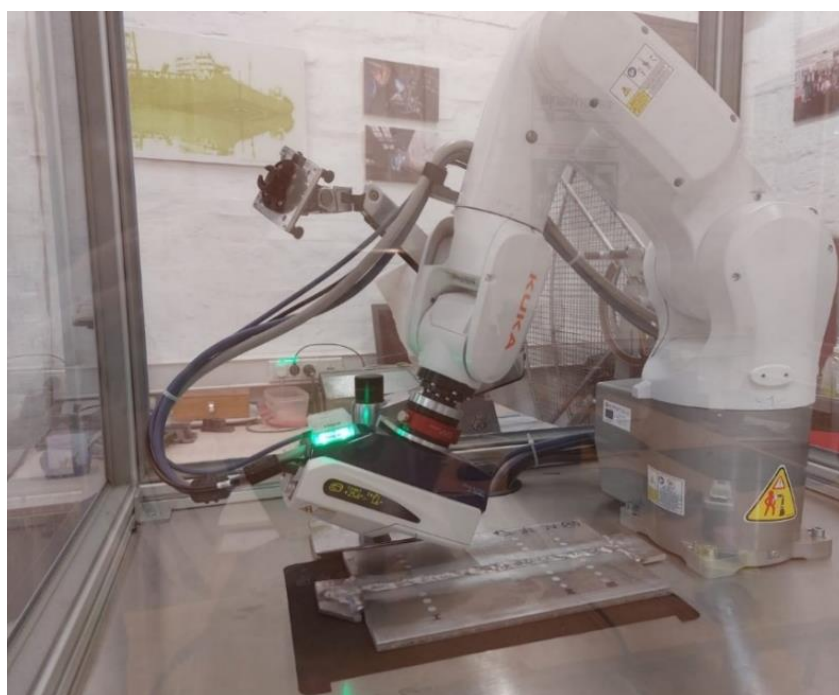
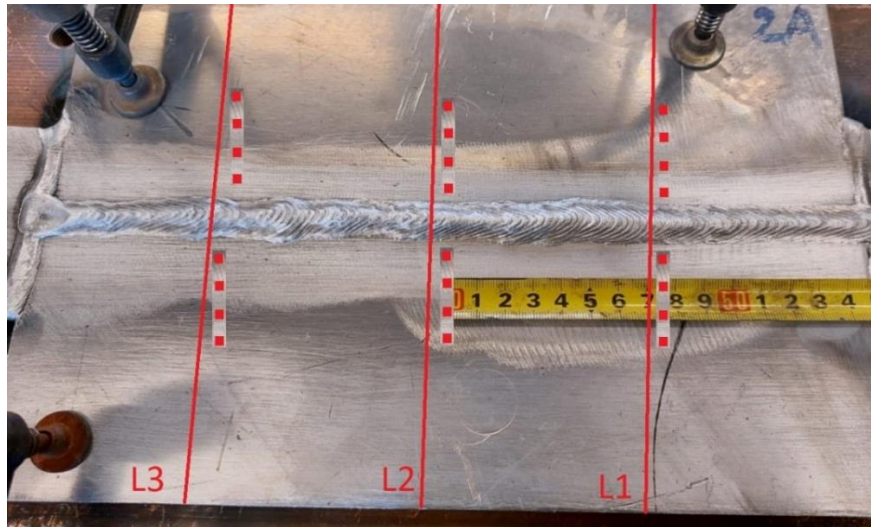
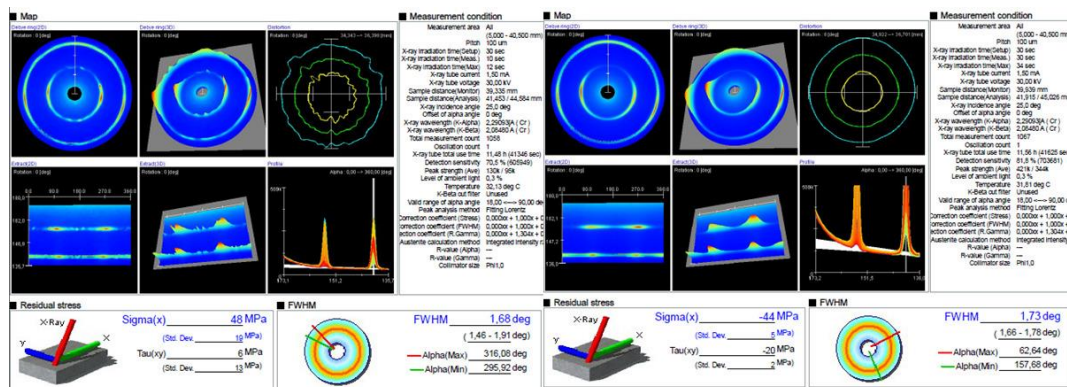


Figure 1. X-ray measurement of residual stress with the portable Pulstec μ -X360 device on sample 2



3. RESULTS

In the reports on the measurement results, the amounts of normal and tangential residual stresses for the measurement locations and their standard deviations are given. Figure 3 shows the measurement report of the XRD measurement; the left image shows an inaccurate measurement, while the right image shows a good measurement. The most important factor for the quality of the measurement is the indication of the Debye-Scherrer ring, and even inaccurate measurements can be confirmed by the value of the standard deviation. Negative stress values indicate that they are compressive stresses, positive values that they are tensile stresses. The results compared and studied in this experiment are normal and tangential residual stresses and their independence from the measurement location, and the effect of the alternating current on them.



As can be seen from the diagram in Figure 4., a uniform distribution of residual stresses was obtained for each of the transverse measurement lines. It can also be observed that the normal longitudinal stresses have the expected “bell shape”. The stress distribution was achieved in such a way that tensile residual stresses occur near the weld in the heat-

affected zone, while compressive stresses prevail in the zone of the base material at some distance of weld. The absolute value of residual stresses does not exceed 150 MPa, which is the expected value for an aluminium-magnesium alloy. The tangential stresses have significantly lower values compared to the normal stresses and their values do not exceed 40 MPa. They are mainly tensile stresses (Fig. 5.)

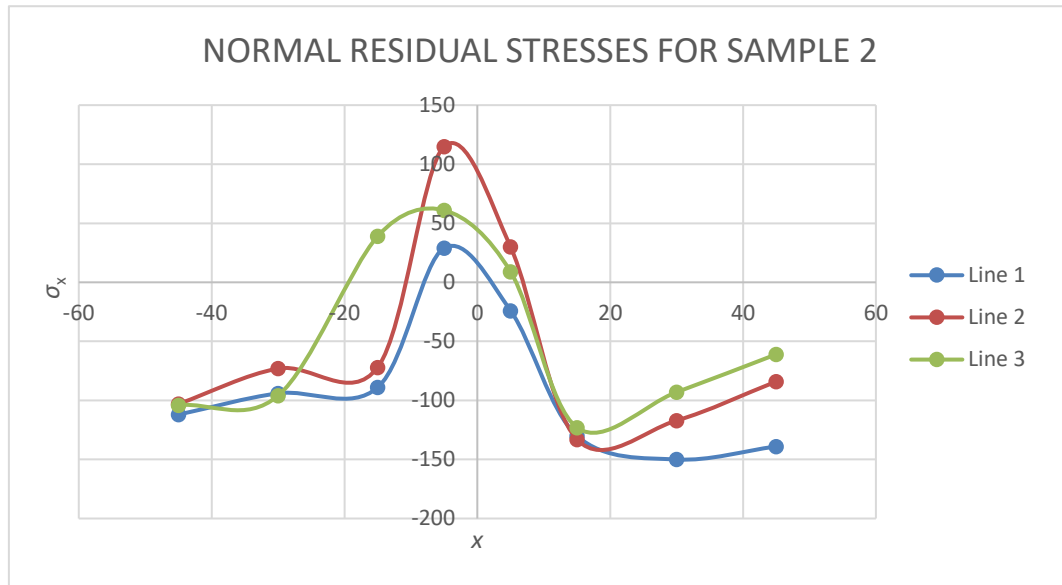


Figure 4. Distribution of normal residual stresses for sample 2

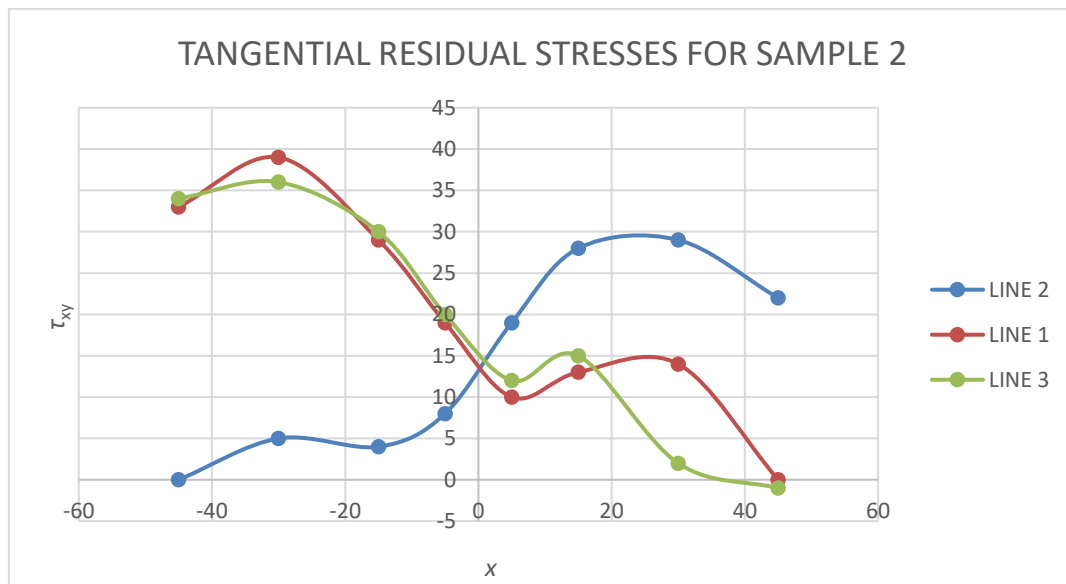


Figure 5. Distribution of tangential residual stresses for sample 2

Figure 6. shows a comparison of residual stresses for AC and DC MIG welding. The measurements for DC MIG weld sample were taken at the transverse line at the same location as line 1 of the sample obtained AC MIG welding. From the comparison of the results, it can be concluded that the tensile stresses near the weld are significantly higher for DC MIG weld sample, while the compressive stresses in the base material are slightly

lower for the DC MIG weld sample. When analyzing the tangential stresses, a different trend of the tangential stresses can be observed, and it can be found that the magnitudes of the tangential stresses are slightly higher for the sample fabricated with DC MIG welding (Fig. 7). The analysis of the results shows that more favorable residual stress results are achieved with alternating current because it achieves lower tensile stresses in the heat-affected zone, which are much more problematic in the context of welding than compressive stresses in the base metal.

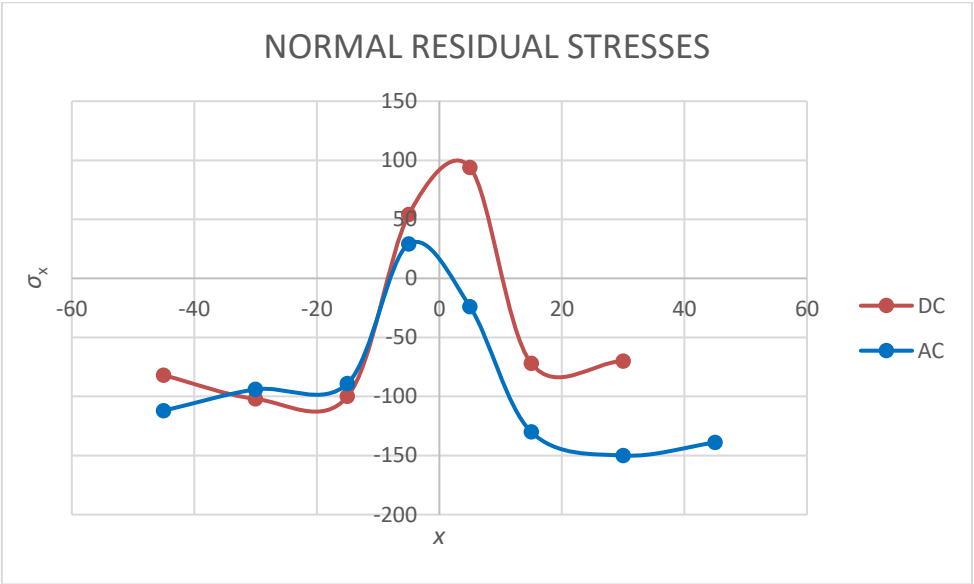


Figure 6. Comparison of normal residual stresses for sample 1 and 2

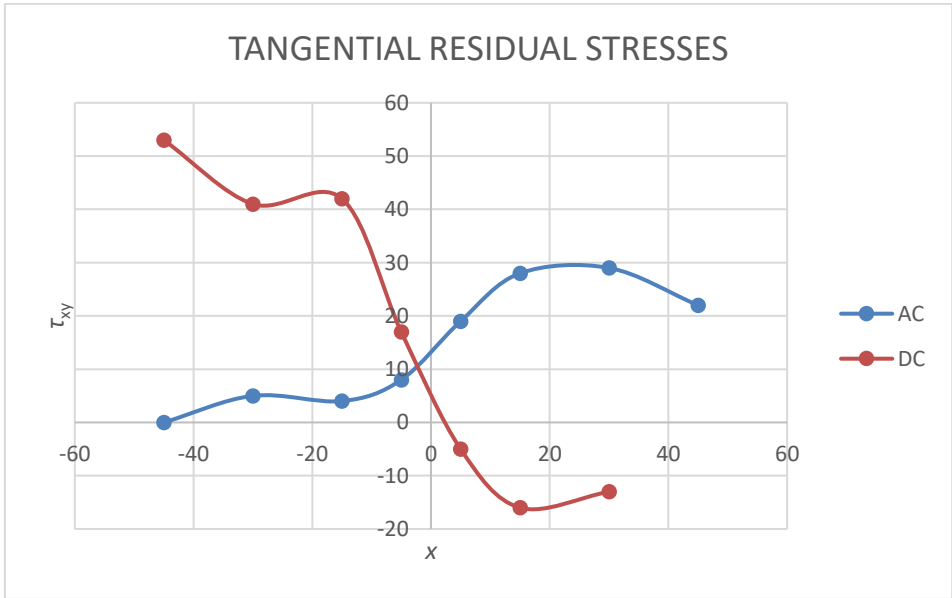


Figure 7. Comparison of normal residual stresses for sample 1 and 2

4. CONCLUSION

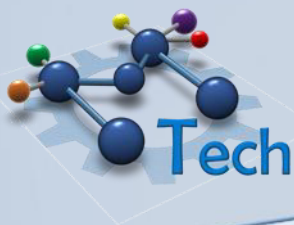
Two plates were butt welded using the welding methods AC and DC MIG with their own sets of parameters, and the residual stresses were determined by X-ray diffraction. From the obtained results it can be concluded:

- XRD is a non-destructive method suitable for examining residual stresses in welds.
- Tensile residual stresses occur in the area in the immediate near of the weld in the heat-affected zone, while away from the weld they transform into compressive stresses.
- Longitudinal normal residual stresses on three different cross-sections show the same tendency of distribution of residual stresses for sample made with AC MIG.
- From the comparison of the results, it can be concluded that the tensile stresses near the weld are significantly higher for the sample with DC MIG, while the compressive stresses in the base metal are slightly lower for the sample with DC MIG.
- The analysis of the results shows that more favorable residual stress results are achieved with alternating current because it achieves lower tensile stresses in the heat-affected zone, which are much more problematic in the context of welding than compressive stresses in the base metal.

REFERENCES

- [1] Zhuang, J. Ni, X., Abdel Wahab, M., 'Review on the prediction of residual stress in welded steel components', *CMC - COMPUTERS MATERIALS & CONTINUA*, vol. 62, no. 2, Art. no. 2, 2020, doi: 10.32604/cmc.2020.08448.
- [2] Shahani, A. R., Shakeri, I., Rans, C. D., 'Effect of residual stress redistribution and weld reinforcement geometry on fatigue crack growth of butt welded joints', *International Journal of Fatigue*, vol. 139, p. 105780, Oct. 2020, doi: 10.1016/j.ijfatigue.2020.105780.
- [3] Costa S., *et al.*, 'Experimental and numerical study to minimize the residual stresses in welding of 6082-T6 aluminum alloy', *AIMSMATES*, vol. 8, no. 2, Art. no. matersci-08-02-018, 2021, doi: 10.3934/matensci.2021018.
- [4] Rodrigues L. A. S., *et al.*, 'Welding Residual Stresses to the Electric Arc', in *Welding - Modern Topics*, IntechOpen, 2020. doi: 10.5772/intechopen.93533.
- [5] Ueda, Y., Murakawa, H., Ma, N., 'Chapter 2 - Introduction to Measurement and Prediction of Residual Stresses with the Help of Inherent Strains', in *Welding Deformation and Residual Stress Prevention*, Y. Ueda, H. Murakawa, and N. Ma, Eds., Boston: Butterworth-Heinemann, 2012, pp. 35–53. doi: 10.1016/B978-0-12-394804-5.00002-5.
- [6] Leggatt, R. H., 'Residual stresses in welded structures', *International Journal of Pressure Vessels and Piping*, vol. 85, no. 3, pp. 144–151, Mar. 2008, doi: 10.1016/j.ijpvp.2007.10.004.
- [7] Nitschke-Pagel, T., 'Recommendations for the measurement of residual stresses in welded joints by means of X-ray diffraction—results of the WG6-RR test', *Weld World*, vol. 65, no. 4, pp. 589–600, Apr. 2021, doi: 10.1007/s40194-020-01029-4.
- [8] Tanaka, K., 'The cosa method for X-ray residual stress measurement using two-dimensional detector', *Mechanical Engineering Reviews*, vol. 6, Oct. 2018, doi: 10.1299/mer.18-00378.
- [9] Sakaida, Y., Suzuki, K., Tanaka, K., 'STANDARD OF THE COSa METHOD FOR X-RAY STRESS MEASUREMENT USING TWO-DIMENSIONAL DETECTOR', presented at the ICRS 11 - The 11th International Conference of Residual Stresses, Mar. 2022. Accessed: May 21, 2023. [Online]. Available: <https://hal.science/hal-04015069>

- [10] Nasir, N., Abdul Razab, M. K. A., Mamat, S., Ahmad, I., 'Review on Welding Residual Stress', vol. 11, pp. 6166–6175, May 2016.
- [11] Kusano, R., Hiyoshi, T., Yonezu, A., 'Estimation method of residual stress and plastic strain in austenitic stainless steel by single indentation test', in *Recent Advances in Structural Integrity Analysis - Proceedings of the International Congress (APCF/SIF-2014)*, L. Ye, Ed., Oxford: Woodhead Publishing, 2014, pp. 555–559. doi: 10.1533/9780081002254.555.
- [12] Chang, P. H., Teng, T., 'Numerical and experimental investigations on the residual stresses of the butt-welded joints', *Computational Materials Science*, vol. 29, pp. 511–522, Apr. 2004, doi: 10.1016/j.commatsci.2003.12.005.
- [13] Lai, H. H., Wu, W., 'Practical examination of the welding residual stress in view of low-carbon steel welds', *Journal of Materials Research and Technology*, vol. 9, no. 3, pp. 2717–2726, May 2020, doi: 10.1016/j.jmrt.2020.01.004.
- [14] 'BS EN 485-2: Aluminium and aluminium alloys - Sheet, strip and plate Part 2: Mechanical properties.



**OVISNOST GEOMETRIJE TOČKASTO ZAVARENOG SPOJA O
ANTI-KOROZIVNIM SVOJSTVIMA KONVERZIJSKE PREVLAKE I
PREVLAKE NA BAZI EPOKSID-POLIESTERA**

***DEPENDENCE OF SPOT-WELDED JOINT GEOMETRY ON ANTI-CORROSIVE
PROPERTIES OF CONVERSION COATING AND EPOXY-POLYESTER
POWDER COATING***

Anna Poropat¹, Ivan Stojanović¹

¹ Sveučilište u Zagrebu, Fakultet stojarstva i brodogradnje, Ul. Ivana Lučića 5, 10000, Zagreb

Sažetak

Korozija metalnih površina je neizbježna pa ju je potrebno spriječiti odgovarajućim načinom zaštite. Antikorozivna zaštita uglavnom uključuje nanošenje praškastih prevlaka elektrostatskim načinom nanošenja u kombinaciji s prethodnom konverzijom kao kemijskom predtretmanom. Posebnu pozornost treba posvetiti točkasto zavarenim žičanim elementima. Zbog različite geometrije zavora i deformacija, točkasto zavareni spojevi mogu negativno utjecati na trajnost premaza, čineći ih kritičnim područjem za pojavu korozije. Manja je vjerojatnost da će praškasti premaz osigurati potpunu pokrivenost, što su deformacije zavarenih spojeva izraženije. Cilj ovog rada bio je ispitati otpornost na koroziju nekoliko vrsta elektrootpornih zavora premazanih s dvije vrste praškaste prevlake. Svi su uzorci obrađeni pod istim parametrima s razlikom u kemijskoj predobradi (fosfat i cirkonij) i geometriji (deformacija) zavora. Naime, u ispitivanju su sudjelovala tri tipa zavora: 1. zavori s minimalnom ili bez deformacije, 2. zavori s malim stupnjem izbacivanja materijala, a zavori tipa 3 su imali značajne i vrlo značajne (igle, izbočine i pjenaste deformacije). Rezultati ovog rada pokazali su da fosfatna konverzija prevlaka u kombinaciji s epoksid-poliesterskom prevlakom osigurava dužu antikorozivnu postojanost proizvoda od zavarene žice sa značajnim deformacijama zavora.

Ključne riječi: *Korozija, elektrootporni zavori, geometrija zavora, praškaste prevlake, konverzija*

Abstract

Corrosion of metal surfaces is inevitable, so it is necessary to prevent it with an appropriate protection method. Anti-corrosion protection mainly involves applying powder coatings by the electrostatic method combined with previously formed conversion coating as chemical pretreatment. Special attention should be given to spot-welded wire elements. Due to different weld geometry and deformations, spot welded joints can negatively impact the coating's durability,

making them a critical area for corrosion occurrence. The powder coating is less likely to provide complete coverage, the more the deformations of the welded joints are pronounced. The aim of this work was to investigate the corrosion resistance of several types of electric resistance welds coated with two types of powder coating. All samples were treated under the same parameters with the difference in chemical pretreatment (phosphate and zirconium) and geometry (deformation) of the weld. Namely, three types of welds participated in the investigation: 1. welds with minimal or no deformation, 2. welds with a slight degree of ejection material, and type 3 welds had significant and very significant (pins, protrusions, and foamy deformations). The results of this work showed that the phosphate conversion coating combined with an epoxy-polyester coating provides longer anti-corrosive durability of the welded wire product with significant weld deformations.

Keywords: *Corrosion, electric resistance welds, weld geometry, powder coatings, conversion*

MATHEMATICAL MODELLING OF TEMPERED HARDNESS OF QUENCHED STEEL

Dario Iljkić¹, Sunčana Smokvina Hanza¹, Božo Smoljan², Dario Kvrđić¹

¹ University of Rijeka, Faculty of Engineering, Vukovarska 58, Rijeka, Croatia, EU

² University North, University Center Koprivnica, Trg dr. Žarka Dolinara 1, 48000 Koprivnica, Croatia, EU

Sažetak

Tvrdoća čelika obično je osnova za predviđanje ostalih mehaničkih svojstava poboljšanog čelika. Matematički model tvrdoće čelika nakon popuštanja može se temeljiti na tvrdoći nakon kaljenja. Jedan posebno koristan izraz tvrdoće poboljšanog čelika daje njemačka norma DIN 17021. Osim toga, postoji stariji odnos koji je dao E. Just. Predviđanje tvrdoće poboljšanog čelika moglo bi biti preciznije ako se uzmu u obzir svojstva prokaljivosti čelika. U skladu s njim, specifična Jominyjeva udaljenost (E_d) i ekvivalent ugljika (CE) čelika uključeni su u izraz kako bi se postiglo preciznije predviđanje tvrdoće poboljšanog čelika. Implementacijom svojstava prokaljivosti čelika u odnos za predviđanje tvrdoće poboljšanog čelika, uzet će se u obzir utjecaj difuzije ugljika i drugih elemenata na kinetiku procesa popuštanja čelika. Utvrđeni matematički izraz primijenjen je u računalnoj simulaciji popuštanja kaljenog čeličnog obratka. Predviđanje kaljene tvrdoće čeličnog obratka temelji se na odnosu između kaljene tvrdoće i karakterističnog vremena hlađenja od 800 do 500 °C.

Ključne riječi: Matematičko modeliranje, popuštena tvrdoća, čelici za poboljšavanje

Abstract

Steel hardness is usually the basis for prediction of other mechanical properties of quenched and tempered steel. The mathematical model of the steel's hardness after tempering can be based on the as-quenched hardness. One particularly useful expression of hardness of quenched and tempered steel is provided by German standard DIN 17021. In addition, there is an older relationship given by E. Just. The prediction of quenched and tempered steel's hardness could be more precise if, hardenability properties of steels will be taken into account. In accordance with it, the specific Jominy distance (E_d) and carbon equivalent (CE) of steel are included in the expression to achieve a more precise prediction of quenched and tempered steel hardness. By implementation of the hardenability properties of steel in relation for prediction of tempered steel's hardness, the influence of diffusivity of carbon and other elements on the kinetics of the tempering processes of steel will be taken into account. Established mathematical expression were applied in computer simulation of tempering of as-quenched steel workpiece. Prediction of the as-quenched hardness of steel workpiece is based on the relationship between as-quenched hardness and the characteristic cooling time from 800 to 500 °C.

Keywords: Mathematical modelling, tempered hardness, quenched and tempered steels

1. INTRODUCTION

Steel hardness is usually the basis for prediction of other mechanical properties of quenched and tempered steel. Mathematical modeling of the hardness of quenched and tempered steel usually begins with mathematical modeling of the as-quenched hardness [1].

The mathematical model of the as-quenched hardness of steel can be based on the cooling time from 800 to 500 °C ($t_{8/5}$) during quenching [2,3]. The cooling time from 800 to 500 °C at different specimen points during quenching of steel can be predicted by numerical simulation of cooling using the finite volume method [4]. The hardness at different specimen points can be predicted by converting the cooling time $t_{8/5}$ to hardness using both, the relationship between the cooling time and the distance from the quenched end of the Jominy specimen and the Jominy hardenability curve [5].

The mathematical model of the steel's hardness after quenching and tempering can be based on the as-quenched hardness. For this purpose, numerous mathematical models have been developed for the relationship between the as-quenched hardness of steel and the hardness of steel after quenching and tempering [1,6]. Very useful expressions for the hardness of steel after quenching and tempering are the relations according to the German standard DIN 17021 and the relation established by E. Just [7]. These expressions assume a tempering time of one hour. These expressions do not take into account the rate of diffusion processes during tempering.

The distribution of other mechanical properties of quenched and tempered steel can be predicted based on the hardness distribution. All mechanical properties of the quenched steel are directly dependent on the degree of quenched steel hardening [8].

The aim of this research is to contribute to the methods of prediction of quenched and tempered hardness based on the as-quenched hardness. For this purpose, experimental work has been carried out on numerous carbon and low-alloy steels. It is supposed that the prediction of quenched and tempered steel hardness could be more accurate if the hardenability properties of steels are taken into account. The hardenability properties of steels for quenching and tempering were considered by the specific Jominy distance (E_d) and the carbon equivalent (CE).

2. PREDICTION OF QUENCHED AND TEMPERED HARDNESS

The relationship between the as-quenched hardness, HRC_q , and the hardness after quenching and tempering, HRC_t can be defined by standard DIN 17021 [6]. According to DIN 17021, the hardness HRC_t of the quenched steel after one-hour tempering is taken as a reference. According to DIN 17021, the hardness after quenching and tempering can be expressed by:

$$HRC_t = \frac{HRC_q + 17}{\left(\frac{T_t}{T_{ref}} - 2.8\right)}; \quad T_{ref} = 167 \text{ K} \quad (1)$$

where:

T_t - tempering temperature (K)

T_{ref} - referent temperature (K)

According to E. Just hardness of steel decreases during tempering when the as-quenched hardness is higher. It was shown that the hardness prediction of quenched and tempered steel is more accurate if the degree of hardening, S , is taken into account. According to E. Just, the relationship between the as-quenched hardness, HRC_q and the hardness after quenching and tempering, HRC_t is equal to [7]:

$$\text{HRC}_t = 8 + (\text{HRC}_q - 8) \exp[-S(T_t/917)^6] \quad (2)$$

where:

T_t - tempering temperature (K)

S - degree of hardening

The degree of hardening is equal to:

$$S = \frac{\text{HRC}_q}{\text{HRC}_{\text{max}}} \quad (3)$$

where:

HRC_q - as-quenched hardness

HRC_{max} - the maximum hardness that can be achieved by quenching

In purpose to investigate the possibilities of contributing to the methods of prediction of quenched and tempered hardness based on the as-quenched hardness, experimental work has been carried out on numerous carbon and low-alloy steels. In addition to tempering temperature and degree of hardening, hardness after tempering could depend on other steel properties. It is known that the kinetics of the tempering process depends on the diffusivity of carbon and other elements in the steel. At the same time, steels with lower diffusivity of carbon and other elements have higher hardenability. It can be assumed that the prediction of quenched and tempered steel hardness could be more accurate if the hardenability properties of steels are considered in the mathematical modeling of the kinetics of tempering processes. In this way, the influence of diffusivity on tempering kinetics is indirectly taken into account by including hardenability properties.

To establish a relationship between the as-quenched hardness and the quenched and tempered hardness of steel, an experimental work was carried out. This relationship includes the hardenability properties for mathematical modeling of the tempered hardness of steel. The chemical composition of the studied steels is given in Table 1. The relevant data and experimental results of quenching and tempering of the studied steel are listed in Table 2. In order to improve the accuracy of prediction of hardness of steel after quenching and tempering, the hardness HRC_{min} , a material constant corresponding to the hardness of steel after annealing, is included in the mathematical expressions of hardness [7]. For this reason, the factor K can be defined and included in the regression analysis of the hardness of quenched and tempered steel:

$$K = \frac{HRC_q - HRC_{min}}{HRC_t - HRC_{min}} \quad (4)$$

Tab. 1: Chemical composition of the studied steels

Steel EN	Chemical composition (wt%)											
	C	Si	Mn	P	S	Cr	Cu	Mo	Ni	V	Al	Ti
Ck45	0.44	0.22	0.66	0.022	0.029	0.15	-	-	-	0.02	-	
42MnV7	0.43	0.28	1.67	0.021	0.008	0.32	0.06	0.03	0.11	0.10	-	
41Cr4	0.44	0.22	0.80	0.030	0.023	1.04	0.17	0.04	0.26	<0.01	-	
25CrMo4	0.22	0.25	0.64	0.010	0.011	0.97	0.16	0.23	0.33	<0.01	-	
16MnCr5	0.16	0.22	1.12	0.030	0.008	0.99	-	0.02	0.12	0.01	0.015	
71Si7	0.73	1.62	0.73	0.019	0.012	0.10	0.19	-	0.12	0.01		
15CrNi6	0.13	0.31	0.51	0.023	0.009	1.50	-	0.06	1.55	<0.01	0.010	
28NiCrMo74	0.30	0.32	0.51	0.011	0.007	0.07	-	-	3.03	-	0.032	<0.01
34Cr4	0.35	0.23	0.65	0.026	0.013	1.11	0.18	0.05	0.23	<0.01	-	-
34CrMo4	0.30	0.22	0.64	0.011	0.012	1.01	0.19	0.24	0.11	<0.01	-	-
36Cr6	0.36	0.25	0.49	0.021	0.020	1.54	0.16	0.03	0.21	<0.01	-	-
37MnSi5	0.38	1.05	1.14	0.035	0.019	0.23	-	-	-	0.02	-	-

Tab. 2: Experimental results of as-quenched and quenched and tempered properties of steels

Steel EN	Maximum hardness, HRC _{max}	Reference minimum hardness, HRC _{min}	Specific Jominy distance, <i>E_d</i>	Carbon equivalent, CE	As- quenched hardness, HRC _q	Hardness after quenching and tempering, HRC _t		
						600 °C	500 °C	400 °C
Ck45	57.15	3.49	4.72	0.58	51.62	24.18	33.30	37.66
					27.63	20.37	24.66	25.79
42MnV7	57.01	3.39	13.93	0.81	52.28	32.42	38.87	44.68
					36.52	27.06	30.48	34.27
41Cr4	56.51	3.05	21.13	0.82	51.59	27.68	37.63	46.77
					36.56	22.72	28.97	33.62
25CrMo4	46.99	0.15	0.15	0.6	44.20	24.19	34.49	39.25
					29.62	19.71	25.29	28.00
16MnCr5	41.52	0.10	12.77	0.56	39.71	20.00	27.49	35.34
					21.36	12.49	18.05	20.18
71Si7	65.01	13.07	8.53	0.89	63.49	35.02	45.47	54.97
					48.35	32.96	39.38	47.44
15CrNi6	41.14	0.10	38.61	0.63	38.81	22.84	32.15	35.77
					27.01	17.17	22.62	24.70
28NiCrMo74	51.00	0.74	5.06	0.6	49.22	20.91	26.57	33.22
					19.06	14.21	16.47	17.99
34Cr4	51.35	0.82	17.70	0.72	46.37	28.95	36.07	43.47
					36.28	25.45	29.61	34.75
34CrMo4	51.53	0.87	13.83	0.68	42.78	26.03	35.19	39.77
					33.51	23.45	29.76	31.69
36Cr6	52.52	1.16	23.00	0.78	48.41	33.10	39.46	47.23
					36.19	27.97	31.91	34.62
37MnSi5	56.88	3.30	7.35	0.62	53.41	24.69	35.68	46.71
					33.04	21.43	26.13	31.19

There is a multiple regression between the factor K on one side and the reference tempering temperature T_{tr} , the degree of hardening S , specific Jominy distance, E_d and the carbon equivalent CE on the other side [9,10]:

$$K = \exp \left[\left(\frac{T_{tr}}{a} \right)^{n_1} S^{n_2} E_d^{n_3} CE^{n_4} \right] \quad (5)$$

The value of the reference tempering temperature T_{tr} for one-hour duration of the tempering process is equal to the applied tempering temperature, while a , n_1 , n_2 , n_3 and n_4 are constants determined by regression analysis.

Hardenability properties of steel can be represented by the Jominy distance E_d , which corresponds to the distance with 50 % of martensite in the microstructure of quenched steel (Figure 1). In Figure 1 hardness HRC_q is achieved hardness at some specimen distance from quenched end of Jominy specimen. It is known that quenched and tempered hardness depends on the degree of hardening, S (Figure 1). Correlation between hardness of quenched steel with 50 % of martensite in the microstructure, $HRC_{50\%M}$, and maximum hardness, HRC_{max} exists [6]:

$$HRC_{50\%M} = 0.73HRC_{max} \quad (6)$$

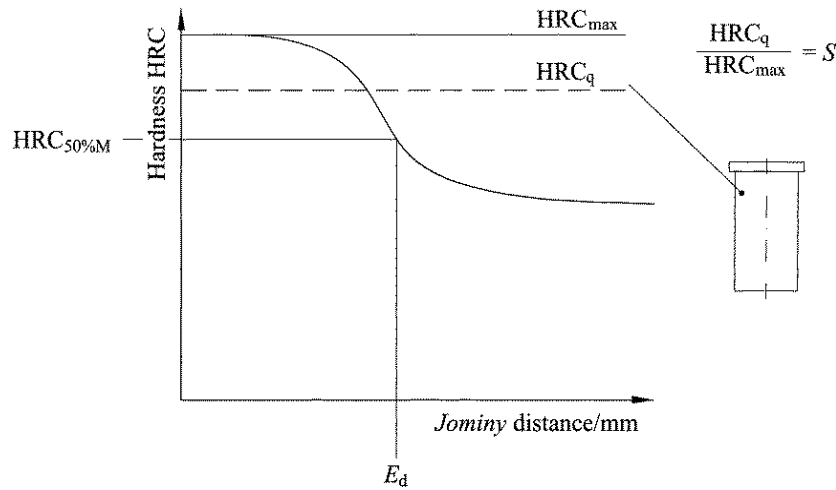


Fig. 1: Characteristic values of Jominy-curve

A formula suitable for predicting the hardenability properties of steels for quenching and tempering is the Dearden and O'Neill carbon equivalent formula, CE , adopted by the International Institute of Welding (IIW) in 1967:

$$CE = \%C + \frac{\%Mn}{6} + \frac{\%Cr + \%Mo + \%V}{5} + \frac{\%Cu + \%Ni}{15} \quad (7)$$

Using the established values for a , n_1 , n_2 , n_3 and n_4 , the factor K can be expressed as follows:

$$K = \exp \left[\left(\frac{T_{tr}}{811.63} \right)^{6.913} S^{1.294} E_d^{-0.3713} CE^{-0.4536} \right] \quad (8)$$

Since the hardness after quenching and tempering of steel can be expressed based on the as-quenched hardness, HRC_q , by [8, 11]:

$$HRC_t = \frac{HRC_q - HRC_{min}}{K} + HRC_{min} \quad (9)$$

the hardness after quenching and tempering of steel can be expressed by:

$$HRC_t = \frac{HRC_q - HRC_{min}}{\exp \left[\left(\frac{T_{tr}}{811.63} \right)^{6.913} S^{1.294} E_d^{-0.3713} CE^{-0.4536} \right]} + HRC_{min} \quad (10)$$

The comparison of hardness values after quenching and tempering of steel, given by the established relationship (equation (10)), with experimental results was carried out for numerous carbon and low-alloy steels (Figure 2). The R-square was equal to 0.9417.

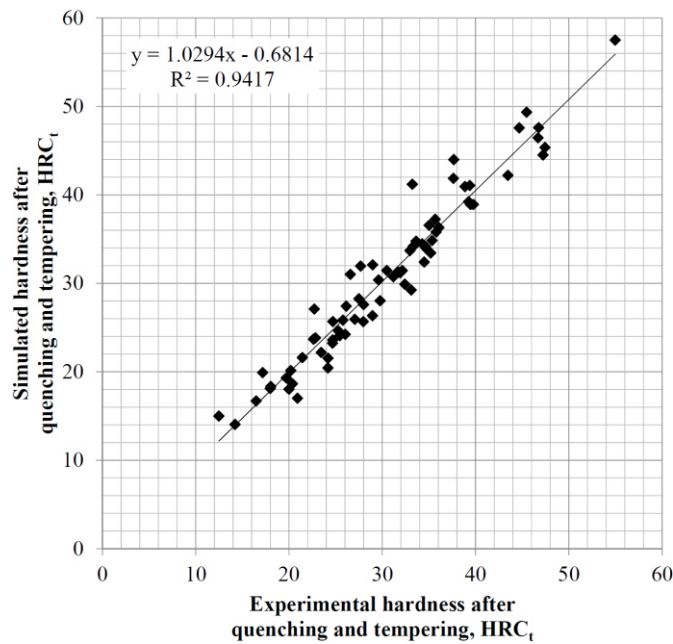


Fig. 2: The comparison of hardness values after quenching and tempering, given by the established algorithm (equation (10)), with experimental results

3. CONCLUSION

Some of the most useful mathematical expressions for hardness after quenching and tempering is the relation to as-quenched hardness according to the German standard DIN 17021 and the relation of E. Just. Both expressions assume one hour of tempering.

A new mathematical expression for prediction of hardness of quenched and tempered steel was presented. In addition to the tempering temperature and the degree of hardening, this expression includes the hardenability properties.

Since the steel hardenability is proportional to the diffusivity of the carbon and alloying elements in the steel, it was useful to establish expressions between the hardness of the steel after quenching and tempering on one side and the degree of hardening, the carbon equivalent and the tempering temperature on the other side. The influence of diffusivity on the kinetics of tempering processes is taken into account by using the carbon equivalent CE.

The established relationships were applied in mathematical modeling and computer simulation of quenching and tempering of low-alloy steel specimens. Comparison of the hardness after quenching and tempering predicted by a mathematical model with experimental results leads to the conclusion that the hardness of the steels considered could be successfully predicted by the proposed model.

Acknowledgement(s):

This research was funded in part by Croatian Science Foundation under the project IP-2020-02-5764 and by the University of Rijeka under the project number uniri-tehnic-18-116.

REFERENCES

- [1] ASM International Handbook Committee *ASM Handbook, Volume 4: Heat Treatment Process and Quality Control Considerations*. Material Park, OH: ASM International, 2006.
- [2] SMOLJAN, B. The calibration of the heat conductivity coefficient in mathematical model of steel quenching. In: *Proceedings of MicroCAD'99*. Miskolc: University of Miskolc, 1999, pp. 24-25.
- [3] SMOLJAN, B. Numerical simulation of as-quenched hardness in a steel specimen of complex form. *Communications in Numerical Methods in Engineering*. 1998, vol. 14, pp. 277-285.
- [4] PATANKAR, S. *Numerical Heat Transfer and Fluid Flow*, New York: McGraw Hill Book Company, 1980.
- [5] ROSE, A., WEVER, F. *Atlas zur Wärmebehandlung der Stähle I*, Düsseldorf: Verlag Stahleisen, 1954.
- [6] LIŠČIĆ, B. *Steel Heat Treatment, Steel Heat Treatment Handbook*. Boca Raton: CRC Press Taylor & Francis Group, 2007.
- [7] JUST, E. Vergüten-Werkstoffbeeinflussung durch Harten und Anlassen, *VDI-Ber.* 1976, vol. 256, pp. 125-140. (in German)

- [8] SMOLJAN, B., ILJKIĆ, D., SMOKVINA HANZA, S. Computer simulation of working stress of heat treated steel specimen, *Journal of Achievements in Materials and Manufacturing Engineering*. 2009, vol. 34/2, pp. 152-158.
- [9] ILJKIĆ, D. *A contribution to the development of the mechanical properties prediction of quenched and tempered steel and cast steel*. Rijeka, 2010. Dissertation, University of Rijeka.
- [10] SMOLJAN, B, ILJKIĆ, D., TOTTEN, G.E. Mathematical Modeling and Simulation of Hardness of Quenched and Tempered Steel, *Metallurgical and Materials Transactions B*, 2015, vol. 46/6, pp. 2666-2673. DOI: 10.1007/s11663-015-0451-6
- [11] RETI, T., FELDE, I., GUERRERO, M., SARMIENTO, S. Using Generalized Time-Temperature Parameters for Predicting the Hardness Change Occurring during Tempering. In: *International Conference on New Challenges in Heat Treatment and Surface Engineering (Conference in honour of Prof. Božidar Liščić)*. Dubrovnik-Cavtat: Croatian Society for Heat Treatment and Surface Engineering (CSHTSE), pp. 333-342.



VERIFICATION OF PAUT SYSTEM FOR AT RAIL WELD TESTING

Morana Mihaljević¹, Tomislav Kezele², Jure Burnać³

^{1,2} University of Zagreb, Faculty of Mechanical Engineering and Naval Architecture, Ivana Lučića 5, Zagreb, Croatia

³ PONDT d.o.o, 4. Barutanski ogranak 5/1, Zagreb, Croatia

Sažetak

Aluminotermijsko zavarivanje često je korišten postupak zavarivanja tračnica za vrijeme eksploatacije. S obzirom na složenu geometriju tračnica i same prirode aluminotermijskog postupka zavarivanja, moguće je nastajanje pukotina u zavarenom spoju. Međutim, europska norma i standardi ne propisuju zahtjeve za ultrazvučno ispitivanje i principe ocjenjivanja pri detekciji nepravilnosti primjenom višepretvorničkog ultrazvučnog ispitivanja (PAUT- *Phased Array Ultrasonic Testing*). PAUT pripada naprednoj ultrazvučnoj tehnici neraznog ispitivanja koja omogućuje ispitivanje volumena materijala. Najčešća primjena je ispitivanje zavarenih spojeva s ciljem detekcije pukotina, korozije i drugih vrsta nehomogenosti. Općenito, prije početka provođenja ultrazvučnog ispitivanja zahtjev je da se potvrdi ispravnost odabranog ultrazvučnog sustava.

U ovom se radu uspoređuju dobiveni rezultati ispitivanja aluminotermijski zavarenih spojeva tračnica primjenom PAUT i konvencionalne UT tehnike. Glavna svrha usporedbe je validacija PAUT tehnike za otkrivanje svih očekivanih nehomogenosti. Kako bi se osigurala sljedivost i valjanost dobivenih rezultata izrađen je radni etalon za validaciju PAUT tehnike ispitivanja.

Ključne riječi: PAUT, Višepretvorničko ultrazvučno ispitivanje, aluminotermijsko zavarivanje

Abstract

The aluminothermic welding method is usually used for welding the rails in service. Due to the complex geometry of the rails and the nature of aluminothermic welding, it is possible to occur flaws in welded joints. European standards and codes do not prescribe the requirements for ultrasonic inspection and evaluation principles to detect flaws when Phased Array Ultrasonic Testing (PAUT) is used. PAUT is an advanced non-destructive inspection ultrasonic technique that provides defect detection of the material's volume. One of the most common applications is weld inspection to detect cracks, corrosion, and other types of inhomogeneity. In general, before starting any ultrasonic inspection, the requirements are to verify the performance of the selected ultrasonic system.

This paper compares obtained testing results when aluminothermic weld inspection is made with the PAUT testing technique and conventional UT technique. The main purpose of method comparison is to validate of PAUT technique to detect all expected inhomogeneities. To ensure the traceability and validity of the obtained result the standard for PAUT validation was made.

Keywords: PAUT, Phased Array Ultrasonic Testing, aluminothermic welding



UČINAK NANOČESTICA Al I Ag NA ANTIKOROZIVNA I ANTIBAKTERIJSKA SVOJSTVA EPOKSIDNOG PREMAZA

EFFECT OF Al AND Ag NANOPARTICLES ON THE ANTICORROSION AND ANTIBACTERIAL PROPERTIES OF EPOXY COATING

Marina Samardžija¹, Vesna Alar², Vedrana Špada³, Suzana Jakovljević², Biserka Runje²

¹ Sveučilište u Zagrebu, Rudarsko-geološko-naftni fakultet, Pierottijeva 6, 10000 Zagreb, Hrvatska

¹ Faculty of Mining Geology and Petroleum Engineering, Department of Chemistry, Pierottijeva 6, 10000 Zagreb, Croatia

² Sveučilište u Zagrebu, Fakultet strojarstva i brodogradnje, Ul. Ivana Lučića 5, 10000 Zagreb, Hrvatska

² Faculty of Mechanical Engineering and Naval Architecture, Department of Welded Structures, St. Ivan Lučić 5, 10000 Zagreb, Croatia

³ Istarsko veleučilište, Riva 4 i 6, Zagrebačka 30, 52100 Pula, Hrvatska

³ Università Istriana di scienze applicate, Riva 4 i 6, Zagrebačka 30, 52100 Pula, Croatia

Sažetak

Metalne nanočestice imaju sposobnost produljenja životnog vijeka epoksidne prevlake na način da mogu fizički zaustaviti prodiranje korozivnog elektrolita unutar epoksidne matrice. Osim, barijerne i kemijske zaštite, mogu posjedovati i antibakterijska svojstva. U ovom radu ispitivano je djelovanje nanočestica aluminijske i srebra unutar epoksidne prevlake. Procijenjena su morfološka, antikorozivna, antibakterijska i migracijska svojstva nemodificiranih i modificiranih prevlaka. Prema SEM i EDS analizama nanokompozitna prevlaka nije sadržavala aglomerate, što potvrđuje kvalitetu disperzije anorganskih nanočestica. Ispitivanje pomoću elektrokemijske impedancijske spektroskopije (EIS) pokazuje da nanokompozitni uzorak sa srebrovim nanočesticama pokazuje najbolju korozivnu otpornost nakon 24 sata izloženosti u 3.5 % NaCl otopini. Impedancijske vrijednosti izjednačavaju se za oba nanokompozitna uzorka nakon 10 dana izloženosti u korozivnom mediju. Nanočestice aluminijske i srebra pokazuju izvrsna antibakterijska svojstva čime nanokompozitna epoksidna prevlaka dobiva dodatno svojstvo u odnosu na polazni nemodificirani materijal. Nanokompozit s aluminijskim nanočesticama pokazao se kao dobar izbor u zaštiti odvodnih cijevi od agresivnih okolišnih napadaja, te je na njemu provedeno praćenje površinske degradacije pomoću pretražne elektrokemijske mikroskopije (SECM).

Ključne riječi: *korozija, bakterije, epoksidna prevlaka, nanočestice.*

Abstract

Metal nanoparticles have the ability to produce epoxy coating life in such a way that they can physically stop the penetration of the corrosive electrolyte within the epoxy matrix. In addition to barrier and chemical protection, they can also have antibacterial properties. In this work, the effect of aluminium and silver nanoparticles inside the epoxy coating was examined. Morphological, anticorrosive, antibacterial and migration properties of unmodified and modified coatings were evaluated. According to SEM and EDS analyses, the nanocomposite coating did not contain agglomerate, which confirms the quality of dispersion of inorganic nanoparticles. Electrochemical impedance spectroscopy (EIS) testing shows that the nanocomposite sample with silver nanoparticles exhibits the best corrosion resistance after 24 hours of exposure in a 3.5% NaCl solution. Impedance values are equalized for both nanocomposite samples after 10 days of exposure in a corrosive medium. Nanoparticles of aluminium and silver show excellent antibacterial properties, which gives the nanocomposite epoxy coating an additional property compared to the original unmodified material. The nanocomposite with aluminium nanoparticles proved to be a good choice in protecting drainage pipes from aggressive environmental attacks, and surface degradation was monitored using scanning electrochemical microscopy (SECM).

Keywords: corrosion, bacteria, epoxy coating, nanoparticles.

This research was funded by “Development of anticorrosion protection system for multipurpose pipe use”, grant number KK.01.1.1.07.0045. This work was supported by the European Regional Development Fund under the Operational Program Competitiveness and Cohesion 2014–2020.



PROJEKT „PAMETNO POSTROJENJE ZA SUŠENJE TEKUĆIH PREMAZA“

PROJECT “SMART PLANT FOR DRYING LIQUID COATINGS”

Mirta Logar, Ivan Stojanović, Ivan Fatović, Ivan Juraga, Vinko Šimunović, Zdenka Keran, Daniela Rakela-Ristevski

Sveučilište u Zagrebu, Fakultet strojarstva i brodogradnje, Zagreb, Hrvatska
University of Zagreb, Faculty of Mechanical Engineering and Naval Architecture, Zagreb, Croatia

Sažetak

Na Fakultetu strojarstva i brodogradnje (FSB) u tijeku je projekt „Pametno postrojenje za sušenje tekućih premaza“ (referentna oznaka: KK.01.2.1.02.) koji je sufinanciran iz Europskog fonda za regionalni razvoj u sklopu Operativnog programa Konkurentnost i kohezija. Projekt se izvodi u suradnji s tvrtkama Končar – Metalne konstrukcije d.o.o. i Agenor automatika d.o.o. Voditelj projekta na FSB-u je izv. prof. dr. sc. Ivan Stojanović. Projekt je započeo 2020. godine i predviđa se završetak projekta krajem 2023. godine.

Ovim projektom nastoji se unaprijediti proces zaštite metalnih konstrukcija od korozije, prvenstveno u industriji transformatorskih kotlova. Pametno postrojenje koristit će tehnologiju infracrvenog (IC) zračenja za ubrzanje procesa sušenja tekućih organskih premaza. Nadalje, primjenom navedene tehnologije očekuju se jednako dobra ili bolja zaštitna svojstva, u odnosu na konvencionalno atmosfersko sušenje, odnosno sušenje dijelova pri mikroklimi prostora lakirnice.

Ključne riječi: *korozija, infracrveno zračenje, EU projekt, organski premazi*

Abstract

At the Faculty of Mechanical Engineering and Naval Architecture (FMENA), the project "Smart plant for drying liquid coatings", co-financed by the European Regional Development Fund within the Operational Programme Competitiveness and Cohesion. The project is a cooperation between FMENA and companies Končar – Steel structures d.o.o. and Agenor automation d.o.o. The project manager at FMENA is Assoc. Prof. Ivan Stojanović, Ph. D. The project has started in 2020 and is expected to be completed at the end of year 2023.

This project aims to improve the process of protecting metal structures from corrosion, primarily with application in the power transformers industry. The smart plant will use infrared (IR) radiation technology to accelerate the drying process of liquid organic coatings. Furthermore, by applying the mentioned technology, equally good or better protective properties are expected, compared to conventional atmospheric drying, i.e. drying of parts in the microclimate of the paint shop.

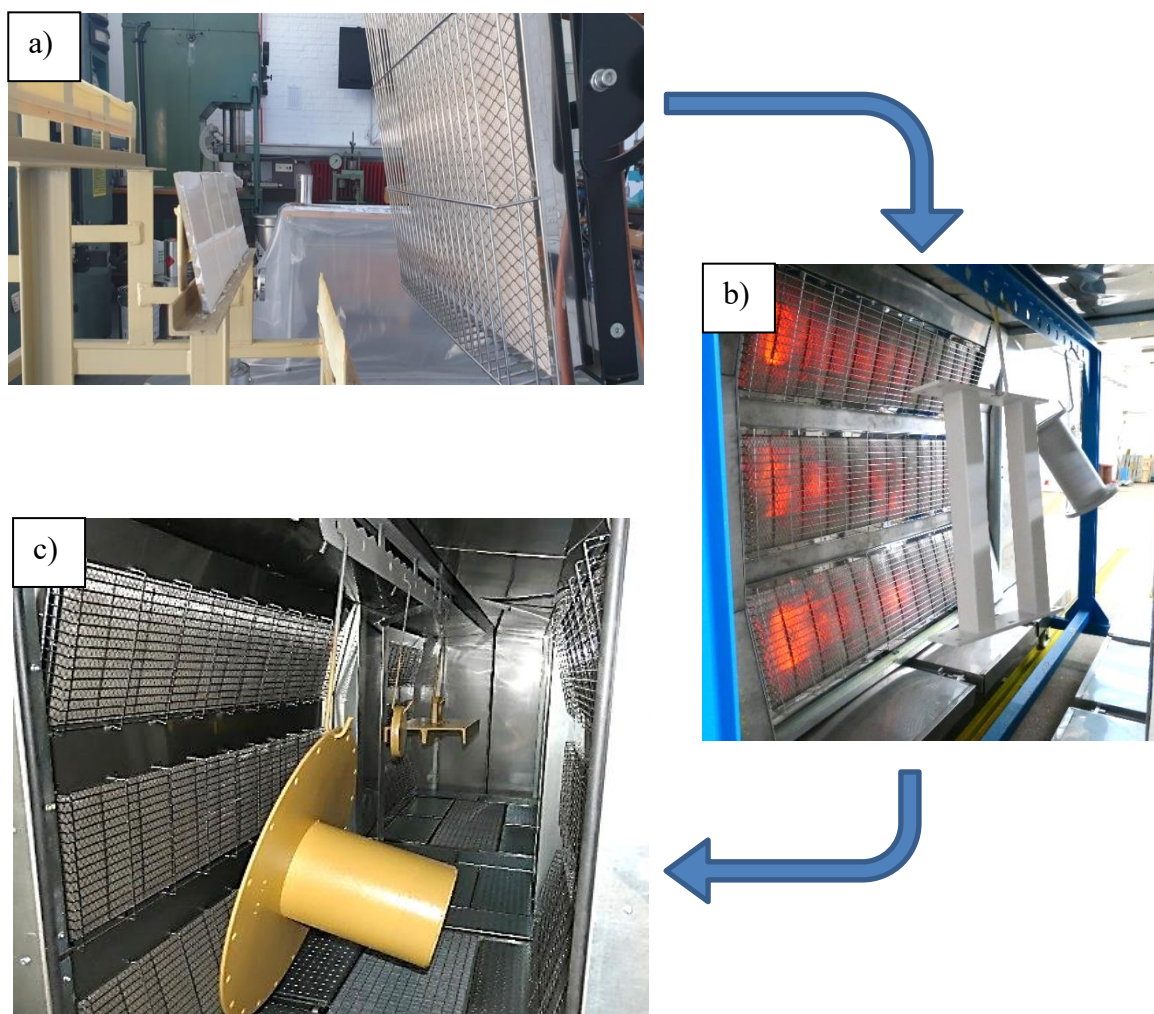
Keywords: *corrosion, infrared radiation, EU project, organic coatings*

1. UVOD

Cilj projekta PAMPOS je razviti pametno postrojenje za ubrzano sušenje organskih, tekućih premaza. Kabina za sušenje premaza sadrži plinske IC emitere koji rade na principu katalitičke infracrvene radijacije s valnim duljinama između 2 i 10 μm . Emiteri su postavljeni na pomične zidove koji se mogu približavati i udaljavati od predmeta koji se suše, a ostatak kabine prekriven je reflektirajućim površinama koje odbijaju IC zračenje kako bi ono došlo i do teže dostupnih dijelova predmeta komplicirane strukture. Svrha postrojenja je ubrzati proces sušenja, a da se pritom ne naruše zaštitna svojstva premaza i završni izgled proizvoda.

2. RASPRAVA

Tijek projekta podijeljen je na industrijsko istraživanje te eksperimentalni razvoj. Tijekom industrijskog istraživanja razmatrani su različiti koncepti i mogućnosti infracrvenog sušenja te je izrađen model kabine koji se u eksperimentalnoj fazi ispituje u praksi. U eksperimentalnoj fazi ispituju se mogućnosti i traže se optimalne postavke uređaja kako bi potrošnja plina bila što manja, a vrijeme sušenja što kraće. Končar – Metalne konstrukcije d.o.o. koristi u svom programu preko 50 različitih zaštitnih premaza na vodenoj i otapalnoj bazi te je potrebno za sve premaze definirati parametre sušenja.



Slika 1: Tijek razvoja pametne kabine za sušenje tekućih premaza

Slika 1. prikazuje tijek razvoja pametne kabine za sušenje tekućih premaza. Podslika a) prikazuje inicijalno sušenje premaza pomoću jednog IC emitera u prvoj fazi projekta. Na podslici b) prikazano je pilot postrojenje iz faze industrijskog istaživanja, dok je na podslici c) prikaz pogonskih ispitivanja u drugoj fazi projekta.

3. ZAKLJUČAK

Projekt PAMPOS primjer je uspješne i nužne suradnje industrije i istraživačkih organizacija. Korištenjem tehnologije infracrvenog zračenja značajno je skraćeno vrijeme potrebno za zaštitu elemenata iz programa Končar – Metalne konstrukcije od korozije, a da su pritom zaštitna svojstva premaza ostala jednaka ili postala bolja u odnosu na premaze sušene pri atmosferskim uvjetima.

Zahvala:

Istraživanje je provedeno u sklopu projekta „Pametno postrojenje za sušenje tekućih premaza” (Referentna oznaka: KK.01.2.1.02.) koji je sufinanciran u okviru Operativnog programa konkurentnost i kohezija, iz Europskog fonda za regionalni razvoj (<https://strukturnifondovi.hr/>). Sadržaj ove publikacije isključiva je odgovornost Fakulteta strojarstva i brodogradnje Sveučilišta u Zagrebu (<https://www.fsb.unizg.hr/index.php?pocetna&lang=hr>).

LITERATURA

- [1] Stojanović I., Cindrić I., Janković L., Šimunović V., Franjić H., Performance Assessment of Differently Dried Coating Systems for Potential Application in the Power Transformer Industry, *Coatings*, 12, 331, (2022).
- [2] Stojanović I., Cindrić I., Turkalj L., Kurtela M., Rakela-Ristevski D., Durability and Corrosion Properties of Waterborne Coating Systems on Mild Steel Dried under Atmospheric Conditions and by Infrared Radiation, *Materials*, 15, 8001, (2022).
- [3] Razumić A., Turkalj L., Horvatić Novak A., Stojanović I., Runje B., Influence of the mild steel coating application process, drying method and pigment on the surface topography, *Materials Testing*, 64(12) pp. 1773-1781, (2022).
- [4] Cindrić I., Janković L., Stojanović I., Juraga I., Mezdić D., Franjić H., Abrazijska i erozijska svojstva IC sušenih premaza, *Zavarivanje* 64, pp 173-179, (2021).
- [5] Stojanović I., Logar M., Fatović I., Alar V., Rakela-Ristevski D., Experimental Study of Atmospherically and Infrared-Dried Industrial Topcoats, *Coatings*, 13, 1343, (2023).

USPOREDBA RAZLIČITIH NAČINA UPRAVLJANJA KIDALICOM KOD STATIČKOG VLAČNOG ISPITIVANJA TIJEKOM HLADNE DEFORMACIJE

COMPARISON OF DIFFERENT TESTING MACHINE CONTROL IN STATIC TENSILE TESTING DURING COLD DEFORMATION

Tin Brlić¹, Stoja Rešković¹, Ivan Jandrlić¹, Željko Alar², Branko Grizelj³, Lorena Mrkobrada¹

¹ University of Zagreb, Faculty of Metallurgy, Aleja narodnih heroja 3, 44000 Sisak, Croatia

² University of Zagreb, Faculty of Mechanical Engineering and Naval Architecture, Ivana Lučića 5, 10002 Zagreb, Croatia

³ University of Slavonski Brod, Mechanical Engineering Faculty, Trg Ivane Brlić Mažuranić 2, 35000 Slavonski Brod, Croatia

Abstract

Static tensile tests were performed during the application of different types of loading rates during cold deformation on aluminum - magnesium alloy. The influence of different types of loading rates and different testing machine control on the distribution of temperature changes and deformations during cold deformation of aluminum - magnesium alloys were analyzed and compared. The analysis of the distribution of temperature changes and deformations of the performed tests was carried out using the methods of thermography and digital image correlation. The tests showed that different control of testing machine during static tensile testing affects the distribution of temperature changes and deformations during cold deformation of aluminum magnesium alloy.

Keywords: cold deformation, aluminum - magnesium alloy, static tensile testing, thermography, digital image correlation

1. INTRODUCTION

Aluminum alloys are one of the best choices for the automotive industry as a lightweight material for various automotive parts such as engine blocks, hoods, trunk lids, body panels, outer panels (doors) etc. The properties of aluminum alloys, such as low density, high strength and good corrosion resistance contribute significantly to their use in various industries such as transportation and structural applications [1,2]. Therefore the formability properties of aluminum alloys are very important. These characteristics can be improved by adjusting various parameters such as temperature and strain rate [3,4].

Plastic deformation of aluminum alloys, especially Al-Mg alloys, is of great importance in determining their formability properties. It is well known that inhomogeneous deformations appear in Al-Mg alloys during plastic deformation in the form of the Portevin – Le Chatelier effect (PLC effect), as well as Lüders bands [5]. The PLC effect shows up as serrations in the stress-strain diagrams during the plastic deformation of Al-Mg alloys. This effect is significant for the forming of Al-Mg alloys because it can leave undesirable traces on the surface of the products.

Thermography and digital image correlation (DIC) methods are very useful for detecting phenomena such as the PLC effect and Lüders bands. Therefore, these methods are highly desirable for the determination of temperature and strain distribution because they enable monitoring of temperature, which can be considered as stress changes, and strain changes during the entire deformation process [6,7]. These methods are widely used to monitor and determine the amounts and distribution of temperature and strain changes in Al-Mg alloys [8], as well as in other metallic materials such as different type of steel [9,10].

The study of stress and strain distribution is often carried out in the investigation of Al-Mg alloys. In [5,11,12] the distribution and amounts of strain and strain rate during the occurrence of PLC effect in Al-Mg alloy with DIC are studied. The research in [8] has shown the stress and strain distribution in an Al-Mg alloy at different strain rates. The stress and temperature distribution during a static tensile test was investigated on Al-Mg alloy 5754 using thermography [13,14]. The strain rate amounts and distribution during PLC evolution are studied in [15] using DIC at different strain rates. The effect of different strain rates on the mechanical properties, i.e. the stress-strain relationship, during a static tensile testing of Al–Mg–Si–Cu alloy is described in [16].

However, the literature review does not show the possible changes in temperature, i.e. stress, and strain distribution in Al-Mg alloys with different control of tensile testing machine during cold deformation. Therefore, the aim of this paper is to determine the influence of various control of tensile testing machine (with constant control of strain rate and stress rate) during cold deformation of Al-Mg alloy 5754. The distribution of temperature, i.e. stress, and strain amounts, during the different controls of tensile testing machine obtained by thermography and digital image correlation are compared in this paper.

2. EXPERIMENTAL PROCEDURE

In this research the tensile testing was conducted on a commercial Al-Mg (5754) alloy. The samples were taken in the form of flat test pieces with rectangular cross section cut from the cold rolled steel strip and prepared according to the standard ISO 6892-1:2019. The sample dimensions of measurement area were 55 mm of the original gauge length, 20 mm of the original width and 3 mm of the thickness.

The experiments were performed simultaneously using three methods: static tensile test, thermography and digital image correlation (DIC), Figure 1. The static tensile test was conducted to determine stress-strain relationship during using different testing machine control. The tensile testing machine Hegewald&Peschke Inspekt table 100 was used for the static tensile tests, Figure 1. The tests were performed using two different testing machine controls. Loading at a strain rate (C_D) of $0,003 \text{ s}^{-1}$ (corresponding to a crosshead separation rate of 10 mm/min) and a stress rate (C_R) of 10 MPa/s during the static tensile test was used in this research.

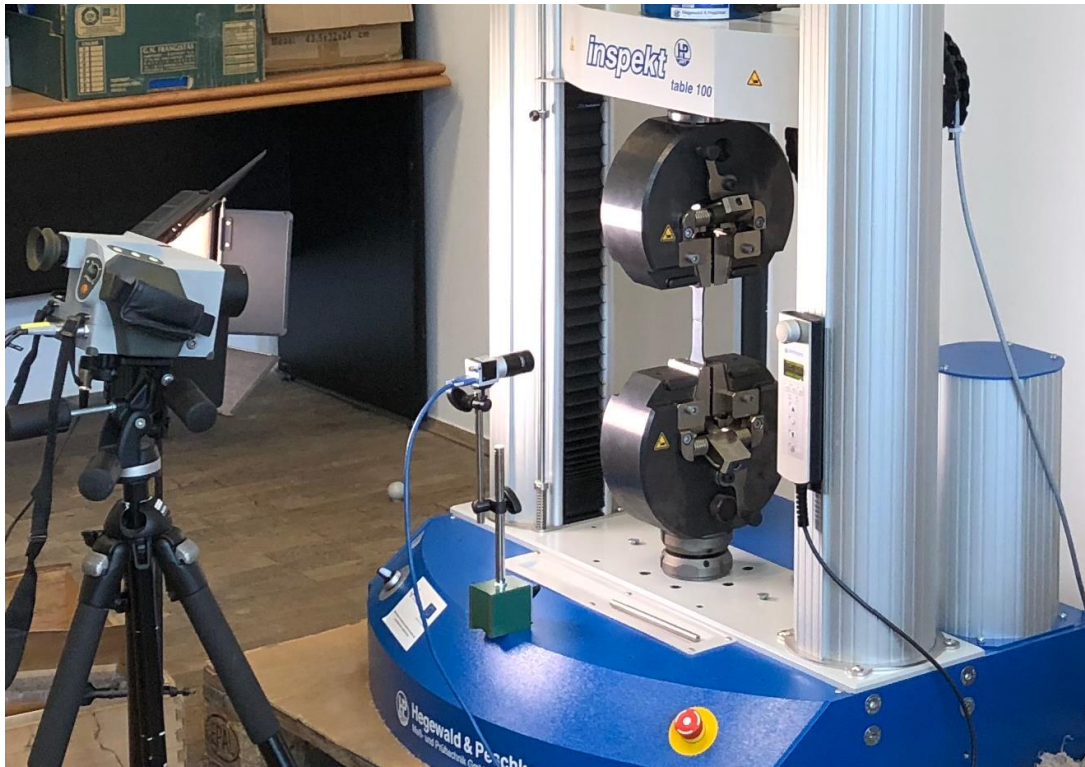


Fig. 1: Installed equipment: tensile testing machine, infrared camera and digital camera

Thermography and digital image correlation were used to determine the amounts and distribution of temperature and strain changes during cold deformation of an Al-Mg alloy. Black matte coating of ColorMatic RAL 9005, LECHSYS 29141 was applied on the samples for thermographic measurements. Thermographic camera JENOPTIK VarioCAM M82910 with temperature sensitivity of 80 mK was used to measure the temperature changes during cold deformation. The software package IRBIS3 professional was used for the analysis of temperature changes.

2D DIC was used to determine strain amounts and distribution. Samples for 2D DIC were prepared with the application of white markers on a black background, (Figure 2). Bianco Opaco RAL 9010 spray was used to apply the white markers on the black background. The camera used for 2D DIC was digital camera Basler acA2500 placed perpendicular to the test sample. The GOM Correlate software package was used for DIC analysis.



Fig. 2: Sample prepared for DIC experiment

3. RESULTS AND ANALYSIS

The stress-position diagram with comparison of different control of tensile machine during cold deformation of commercial 5754 Al-Mg alloy is shown in Figure 3.

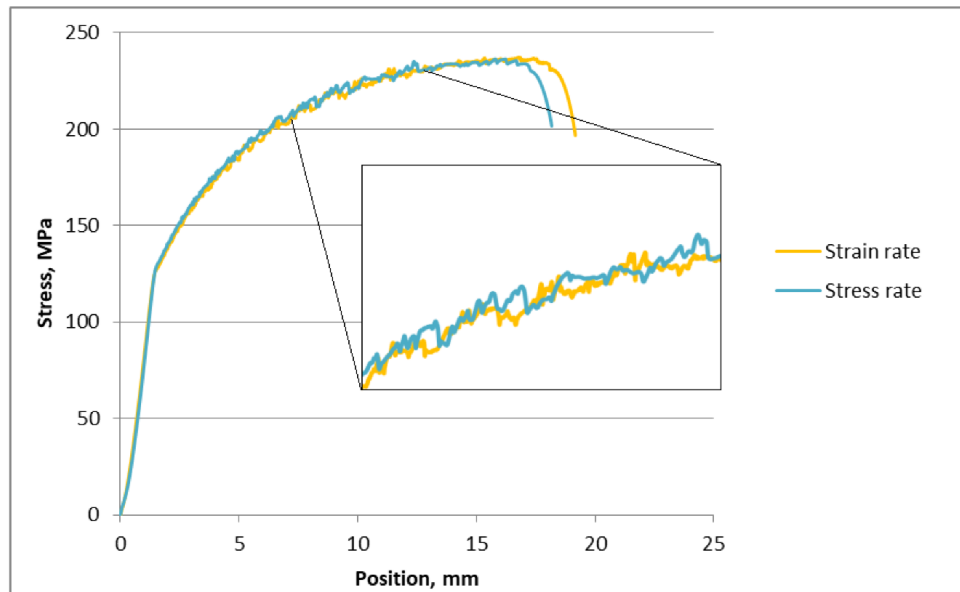


Fig. 3: Static tensile testing diagram during control with: a) strain rate (C_D) and b) stress rate (C_R)

The analysis of the stress-position diagram obtained by static tensile tests has shown some differences between the results given by different controls of the tensile testing machine with strain rate (C_D) of $0,003 \text{ s}^{-1}$ and stress rate (C_R) of 10 MPa/s , Figure 3.

Qualitative and quantitative analysis of the distribution of temperature and strain changes were conducted in four selected points: at the start of the tensile test (start),

halfway between yield strength and tensile strength (point 2), at tensile strength (R_m) and at the moment of test sample fracture (fracture).

A comparison of qualitative results, between different testing machine control of strain rate (C_D) and stress rate (C_R), is carried out. The distribution of temperature and strain changes, shown in the form of differently colored measurement areas on the tested samples using deformation maps during the different testing machine controls, have shown in Figure 4.

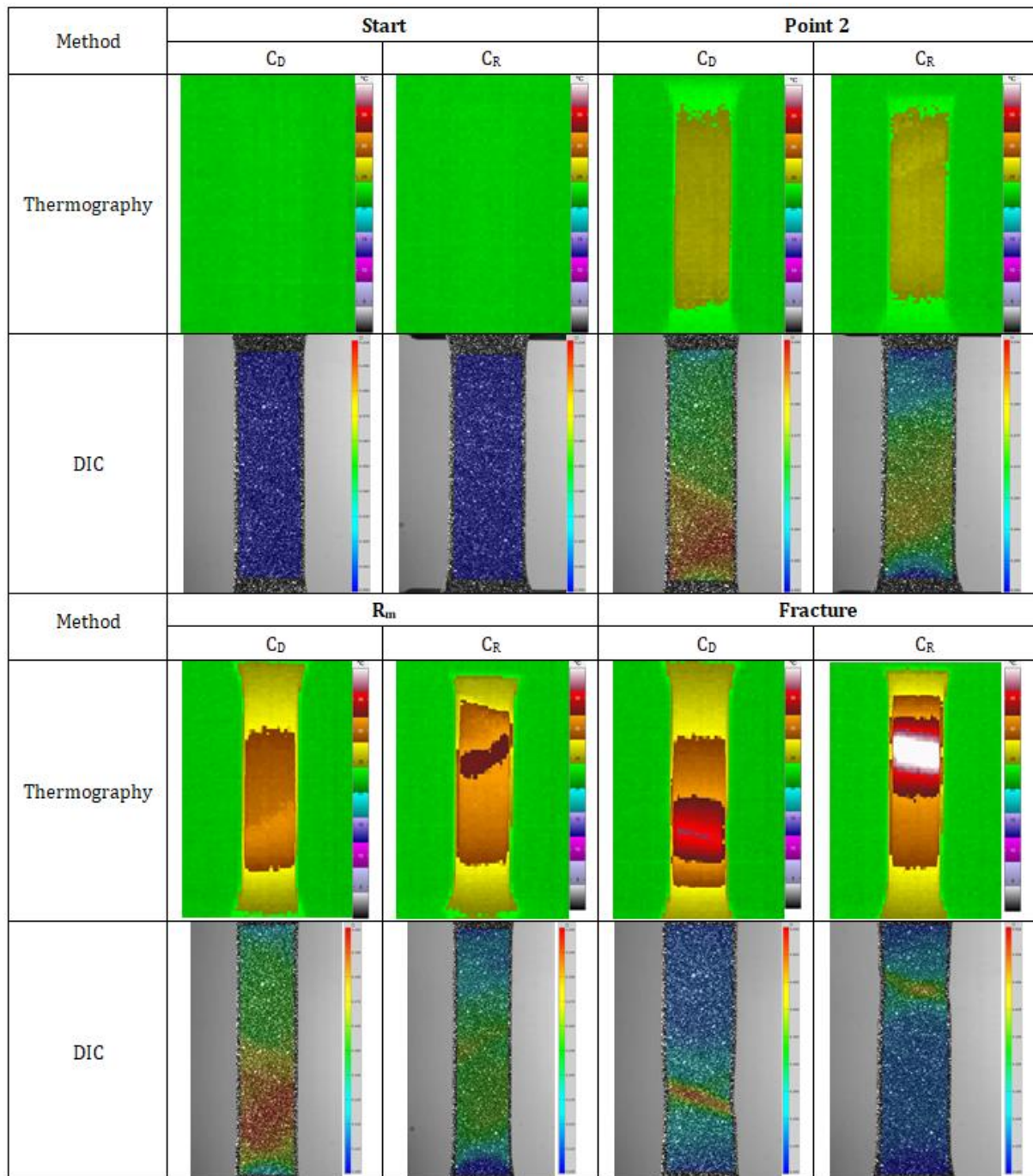


Fig. 4: Qualitative results of temperature and strain changes during different testing machine control

Qualitative analysis has shown that during the deformation process exists different distribution of temperature and strain changes during control of tensile testing machine with control of strain rate (C_D) and stress rate (C_R). It is obvious that there are no differences between results of the different testing machine controls at the start of deformation process. However, it is clear that in other points (point 2, R_m and fracture) are visible significant differences in distribution of temperature and strain changes, Figure 4. It can be concluded that in all points (except the starting point) are higher temperature changes during control of tensile testing machine with stress rate (C_R). On the other hand, the strain amounts are higher in the control with strain rate (C_D) than in the control of tensile testing machine with stress rate (C_R).

A more detailed investigation of these changes is given in the rest of the research. Therefore, it was carried out a quantitative analysis of the amounts of maximum temperature changes and strains. The results of the quantitative analysis of maximum temperature and strain changes amounts are shown in Figures 5 and 6.

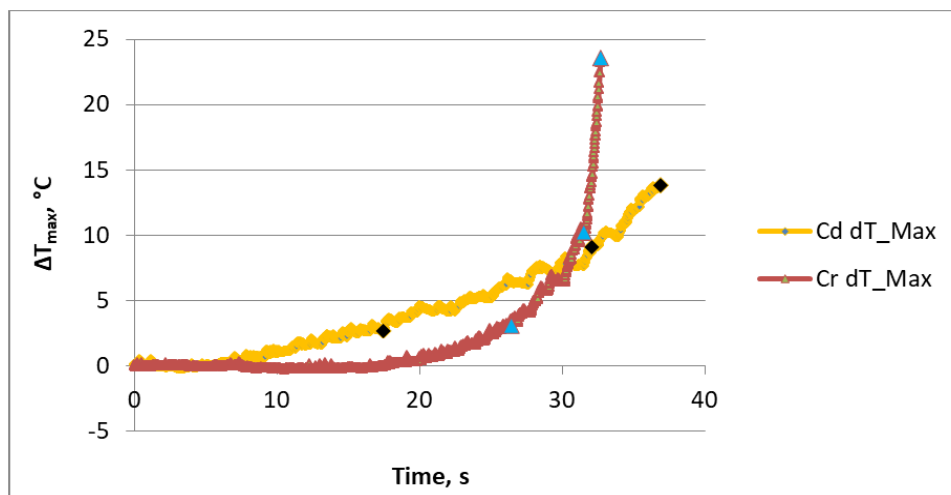


Fig. 5: Quantitative results of temperature changes with different testing machine control during deformation

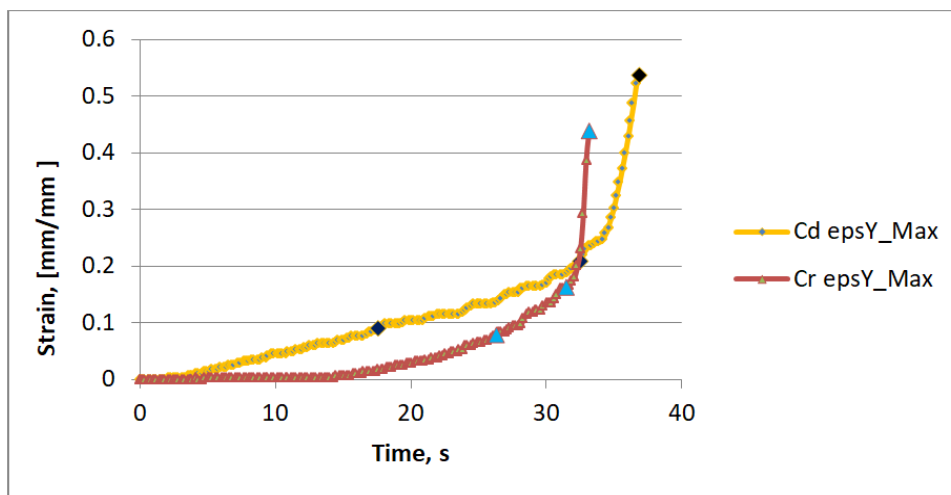


Fig. 6: Quantitative results of strain changes with different testing machine control during deformation

The quantitative results confirm the qualitative results of the deformation maps. It is clear that in interested points (point 2, R_m and fracture) are higher temperature changes, i.e. stress changes, and lower strain amounts during control with stress rate (C_R) regard to control with strain rate (C_D). The difference in the amounts of temperature and strain changes, between the different controls of the testing machine (red triangles in Figures 5 and 6), is lower in point 2 than at points R_m and fracture, Figures 5 and 6. Therefore, it can be concluded that the difference in the amounts of temperature and strain changes during the different controls of the testing machine increases with the deformation degree.

The quantitative results confirm that the distribution of temperature and strain changes is different during the testing machine control with strain rate (C_D) and stress rate (C_R) because of different serrations in diagrams, Figures 3, 5 and 6. Different serrations in stress, temperature and strain changes are determined during both controls of testing machine. These serrations characterize the appearance of the PLC effect in 5754 Al-Mg alloys as the temperature and strain amounts changes randomly in measuring area of the tested samples.

For a clear determination of the occurrence of the PLC effect during both controls of the tensile testing machine the results of the measured and analysed strain rates, with DIC, in interested points (point 2, R_m and fracture) are shown in Figure 7.

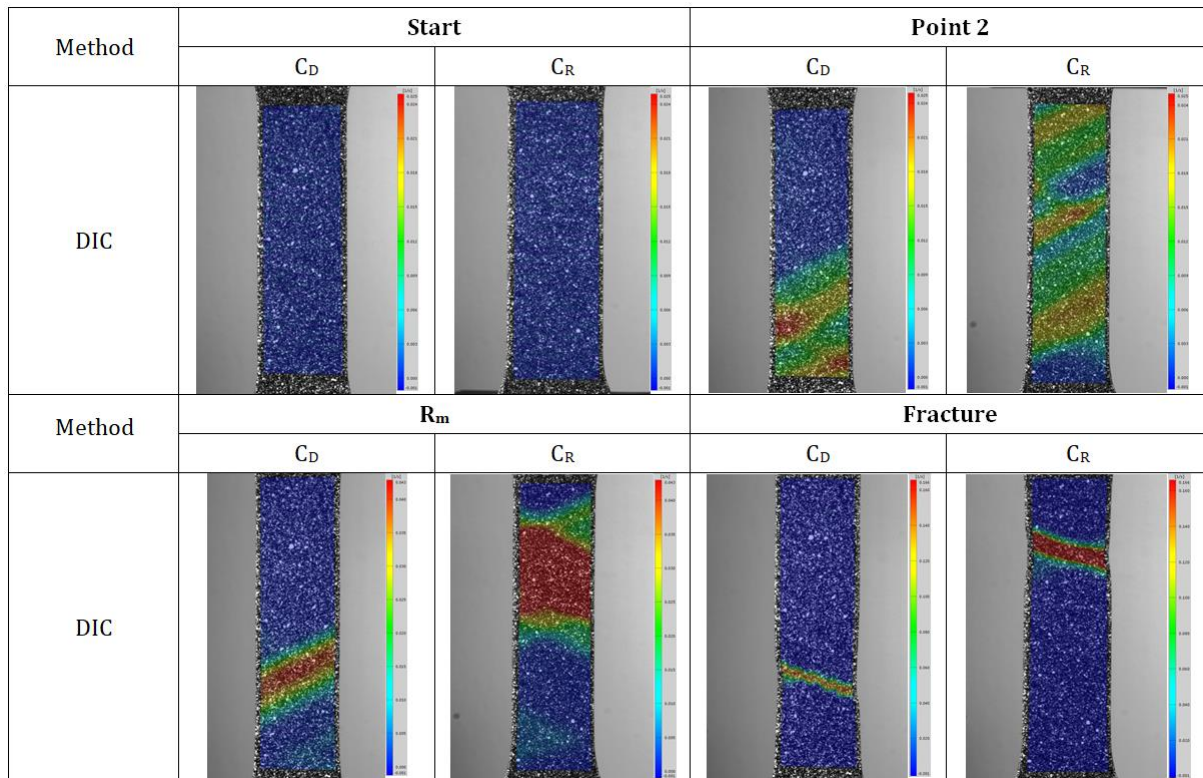


Fig. 7: Qualitative results of strain rate changes with different testing machine control during deformation

The monitoring of strain rate changes clearly shows that for both controls of the testing machine, the PLC effect occurs in the tested 5754 Al-Mg alloy during cold deformation. It can be clearly seen how the strain rate amounts randomly move around the measuring

area of the tested samples. It is found that there are differences in strain rate distribution, during the PLC effect, for different controls of the tensile testing machine.

The serrations of both curves in the stress-position diagram confirmed that the PLC effect occur during control of testing machine with strain rate (C_D) and stress rate (C_R), Figure 3.

4. CONCLUSION

Research has shown that the different control of the testing machine between the strain rate (C_D) and the stress rate (C_R) has influence on the distribution and amounts of temperature and strain changes during the cold deformation of the commercial 5754 Al-Mg alloy. A different distribution of temperature and strain changes during control of tensile testing machine between strain rate (C_D) and stress rate (C_R) control is determined.

Controlling the test machine with the stress rate (C_R) have shown higher temperature changes, i.e. stress changes, and lower strain amounts compared to controlling with the strain rate (C_D). The difference in the amounts of temperature and strain changes for the different testing machine controls increases with the deformation degree.

The phenomenon of PLC effect is established during both testing machine control of strain rate (C_D) and stress rate (C_R) during cold deformation of 5754 Al-Mg alloy. It is found that there are differences in the distribution of strain rate during PLC effect with different control of tensile testing machine.

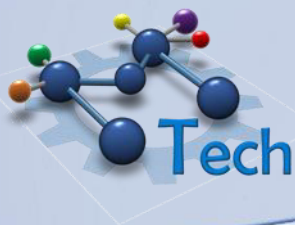
ACKNOWLEDGEMENT

This paper has been performed within infrastructural scientific project VIRTULAB-Integrated Laboratory for Primary and Secondary Raw Materials, Code: KK.01.1.1.02.0022.

REFERENCES

- [1] Xua H., Liua X., Zhang D., Zhanga X., Minimizing serrated flow in Al-Mg alloys by electroplasticity, *Journal of Materials Science & Technology*, 35, pp. 1108-1112, (2019).
- [2] Sakurai T., The latest trends in aluminum alloy sheets for automotive body panels. *Kobelco Technol Review* 28, pp. 22-28, (2008).
- [3] Ozturk F., Toros S., Pekel H., Evaluation of tensile behaviour of 5754 aluminium-magnesium alloy at cold and warm temperatures, *Materials Science and Technology*, 25, 919-924, (2009).
- [4] Li D., Ghosh A., Tensile deformation behavior of aluminum alloys at warm forming temperatures, *Materials Science and Engineering A*, 352, 279-286, (2003).
- [5] Tretyakova T.V., Wildemann V.E., Study of spatial-time inhomogeneity of serrated plastic flow Al-Mg alloy: using DIC technique, *Frattura ed Integrità Strutturale*, 27, pp. 83-97, (2014).
- [6] Brlić T., Lazić L., Franz M., Jandrić I., Rešković S., Stress distribution at different deformation degrees in low carbon steel during cold deformation, *Engineering Review*, 42, pp. 103-108 (2022).
- [7] Brlić T., Rešković S., Jurković Z., Janeš G., Mathematical modeling of influence parameters during formation and propagation of the Lüders bands, *Facta Universitatis, Series: Mechanical Engineering*, 18, 595-610, (2020).
- [8] Ait-Amokhtar H., Fressengeas C., Crossover from continuous to discontinuous propagation in the Portevin-Le Chatelier effect, *Acta Materialia*, 58, pp. 1342-1349, (2010).

- [9] Ren S., Morgeneyer T., Mazière M., Rousselier G., Forest S., Effect of Lüders and Portevin-Le Chatelier localization bands on plasticity and fracture of notched steel specimens studied by DIC and FE simulations, *International Journal of Plasticity*, 136, pp. 102880, (2021).
- [10] Brlić T., Appearance of Lüders bands in niobium microalloyed steel [Doctoral dissertation], Sisak: University of Zagreb Faculty of Metallurgy, (2020).
- [11] Szalai Sz., Harangozó D., Czinege I., Characterisation of Inhomogeneous Plastic Deformation of AlMg Sheet Metals During Tensile Tests, *IOP Conference Series: Materials Science and Engineering*, 903, pp. 012023, (2020).
- [12] Yuzbekova D., Mogucheva A., Borisova Yu., Kaibyshev R., On the mechanisms of nucleation and subsequent development of the PLC bands in an AlMg alloy, *Journal of Alloys and Compounds*, 868, pp. 159135, (2021).
- [13] Dahdouh S., Mehenni M., Ait-Amokhtar H., Kinetics of formation and propagation of type A Portevin-Le Chatelier bands in the presence of a small circular hole, *Journal of Alloys and Compounds*, 885, pp. 160982, (2021).
- [14] Ait-Amokhtar H., Fressengeas C., Boudrahem S., The dynamics of Portevin-Le Chatelier bands in an Al-Mg alloy from infrared thermography, *Materials Science and Engineering A*, 488, pp. 540–546, (2008).
- [15] Yuzbekova D., Mogucheva A., Zhemchuzhnikova D., Lebedkina T., Lebyodkin M., Kaibyshev R., Effect of microstructure on continuous propagation of the Portevin-Le Chatelier deformation bands, *International Journal of Plasticity*, 96, pp. 210-226, (2017).
- [16] Wang X., Shi T., Wang H., Zhou S., Xie C., Wang Y., Mechanical behavior and microstructure evolution of Al-Mg-Si-Cu alloy under tensile loading at different strain rates, *Materials Research Express*, 6, pp. 066548, (2019).



Tribocorrosion Aspects of Biomedical Implants: Current status and new directions

Mathew T. Mathew

*Regenerative Medicine and Disability Research Lab, Department of Biomedical Sciences, UIC College of Medicine at Rockford,
Department of Restorative Dentistry, College of Dentistry, University of Illinois at Chicago
Department of Biomedical Engineering, University of Illinois at Chicago.
Department of Orthopedic Surgery, Rush University Medical Center, Chicago.*

Abstract

Metal-based implant devices have become increasingly prevalent due to their ability to restore the physical function of patients with disability. However, this growth has proportionally resulted in an increase in implant failures due to wear and corrosion (tribocorrosion), with recent data reporting infection as its primary cause. The clinical reports on the peri-implantitis (dentistry) and peri-prosthetic infections (orthopedics) are very common. Despite recent studies on implant failure, there is a lack of research regarding the cellular response to an inflammatory/infectious environment when exposed to metal ions/particles released due to tribocorrosion from implants. Additionally, our recent study demonstrated that the body's immune response to infection, specifically the release of macrophages, might accelerate implant corrosion, called cell-accelerated corrosion (CAC). Therefore, this lecture will address, basics of tribocorrosion aspects of implants (focusing on hip implant) and the effect of infectious and inflammatory conditions on the cellular viability of osteoblast cells (MG-63), and corrosion aspects of the implants under macrophages challenged by these conditions. The talk will also include some future research directions to minimize the risk associated with implant failures.

COMPARISON OF VARIOUS MINERAL AND VEGETABLE OILS AS QUENCHING MEDIA IN THE HARDENING PROCESS

USPOREDBA RAZLIČITIH MINERALNIH I BILJNIH ULJA KAO MEDIJA ZA GAŠENJE U PROCESU KALJENJA

Izabela Martinez¹, Božidar Matijević¹, Tonća Čaleta Prolić²

¹ University of Zagreb, Faculty of Mechanical Engineering and Naval Architecture, Zagreb, Croatia

² INA MAZIVA Ltd., Zagreb, Croatia

Sažetak

Postizanje martenzitne mikrostrukture kod čeličnih obradaka nakon kaljenja nužno je za dobivanje odgovarajućih željenih mehaničkih svojstava. Općenito, svojstva postignuta gašenjem s temperature austenitizacije ne ovise samo o svojstvima materijala koji se toplinski obrađuje, već i o svojstvima medija za ohlađivanje. Poznavanjem fizikalnih i kemijskih svojstava te karakteristika ohlađivanja korištenog sredstva za gašenje možemo preciznije kontrolirati proces gašenja. Danas se od sredstava za gašenje najčešće koriste mineralna ulja, međutim, zbog ekološke prihvatljivosti i obnovljivosti sve se više istražuje primjena biljnih ulja. Ovaj rad istražuje razlike između fizikalnih i kemijskih svojstava različitih konvencionalnih mineralnih ulja i biljnih ulja, ali i razlike u tehničkim performansama ovih ulja dobivenih na temelju karakteristika ohlađivanja izmjerenih prema standardu ISO 9950.

Ključne riječi: gašenje, medij za ohlađivanje, mineralna ulja, biljna ulja.

Abstract

Achieving a martensitic microstructure in steel components after hardening process is necessary to obtain the appropriate desired mechanical properties. In general, the properties achieved by quenching from the austenitization temperature depend not only on the properties of the heat-treated material, but also on the properties of the cooling medium. By knowing the physical and chemical properties and the cooling characteristics of the quenching media used we can more precisely control the quenching process. Today, mineral oils are the most used quenching fluids, however, due to their ecological acceptability and renewable nature, the use of vegetable oils is increasingly being researched. This paper investigates the differences between the physical and chemical properties of various conventional mineral and vegetable oils, but also the differences in the technical performance of these oils based on the cooling characteristics measured according to the ISO 9950 standard.

Keywords: Quenching, Quenching Media, Mineral Oils, Vegetable Oils.

1. INTRODUCTION

Different heat treatment processes are widely applied in the industry to enhance mechanical properties of components made of steel [1]. Hardening is one of the most common processes to improve final product in steel manufacturing by increasing hardness which consists of heating an object to an austenitising temperature (ϑ_a), holding it at that temperature for a set period followed by fast cooling to a room temperature (quenching) in order to achieve a transformation into a martensitic microstructure [2], [3]. Phases obtained after a heat treatment can be controlled by adjusting the process parameters [1]. Therefore, immersion in the quenching medium is the most critical part of the process of hardening [4]. Too slow cooling rates can lead to formation of an undesirable microstructure constituents such as ferrite and pearlite, while too fast cooling rates can distort some materials due to thermal shock [5], [6]. Thus, it is very important to choose the appropriate quenchant for a specific purpose. Different types of oils, water and polymer solutions are just some of quenching media designed for rapid and controlled cooling of steel [6]. Mineral or petroleum based oils are the most widely used quenchants as they provide appropriate cooling rates and therefore minimize risks of residual stresses and distortion in the material [2], [7]. However, despite many advantages and applications there are some disadvantages and limitations such as the creation of vapour blanket that surrounds the object at the start of quenching and lowers the cooling rate (one of three phases of Leidenfrost phenomena), but more importantly, they are hazardous for environment and health, non-biodegradable and non-renewable [2], [4], [8]. For the past decade, an increased environmental awareness and a need for recognizing the importance of environmental issues regarding global warming encourage innovations and sustainable development across the manufacturing industry [9]. Lower impact evaluations in terms of global warming, water intact, pollution and human toxicity, and a need to reduce the reliance on imported petroleum crude oils had led to the search for possible environment-friendly alternatives to mineral, petroleum-derived quenching oils [10]. Due to their biodegradability, renewability and non-toxic nature, vegetable oils are being investigated as innovative alternative to such oils [11], [12]. Some studies show that vegetable oils have displayed excellent lubrication properties and desirable characteristics in laboratory investigations, making them very attractive lubricants for many practical applications [10], [12]. In this paper, a comparative study between a mineral, petroleum-derived and vegetable oils is performed. To obtain the overview of the vegetable oil quenching performance in comparison to mineral oil quenching performance, physical and chemical properties, cooling curves, and cooling characteristics obtained according to ISO 9950 were determined. The oils that were studied included two commercial mineral oils as well as two vegetable oils, olive oil and canola oil.

2. EXPERIMENTAL

In this paper, different oils are compared based on their physical and chemical properties, but also cooling curves and quenching characteristics obtained by conducting tests according to ISO 9950. A total of 4 different oil samples were examined and compared, of which 2 are commercial mineral-based oils, and the remaining 2 are vegetable oils (olive oil and canola oil). Of the two commercial mineral-based oils, named Mineral oil 1 and Mineral oil 2, respectively one is less additive (0.5 % by mass) while the other is more strongly additive (3 % by mass). Useful characteristics for identifying a particular quenching oil are its physical and chemical properties. Using standardized laboratory

methods for determining physical and chemical properties, tests of the characteristic properties of selected oil samples were conducted. Oils are described by appearance and colour, density, kinematic viscosity at 40 °C, kinematic viscosity at 100 °C, viscosity index, base number, acid number, flash point, pour point, copper corrosion and volatility. The measurement unit and description of each property are shown in Table 1.

Tab. 1: Description of the physical and chemical properties of oils

Property	Unit	Description
Appearance and colour	-	Visual description of an oil sample
Density	g/cm ³	Mass of the unit of volume
Kinematic viscosity	mm ² /s	The ratio of dynamic viscosity to density
Viscosity index	-	Evaluates the dependence of viscosity on temperature
Base number	mgKOH/g	Amount of KOH in mg required for free organic acids contained in 1 g of the examined oil to be neutralised
Acid number	mgKOH/g	Shows whether acid formation has occurred in the oil as a result of oxidation combustion products
Flash point	°C	Temperature at which the oil educes such an amount of gasses that when are set to fire stay on fire for at least 5 s
Pour point	°C	Temperature at which the oil changes from a liquid to a solid state
Copper corrosion (Cu, 100 °C, 3 h)	-	Indicates the behavior of the oil in the presence of oxygen
Volatility (Naoack)	%	The amount of fluid that evaporates in a prescribed time at a prescribed place temperature

Appearance and color are physical properties of quenching oils that are determined visually. Oil density was measured according to ASTM D4052. Kinematic viscosity was tested at temperatures of 40 °C and 100 °C according to ISO 3104 using a capillary viscometer. The capillary is filled with a certain amount of liquid, a then heated to a certain temperature. When the capillary heats up, the valves open, and a liquid begins to flow through the capillary. The time it took for the liquid to pass through capillary was measured. By measuring the required time for the oil to leak through the capillary and multiplying by a capillary constant, kinematic viscosity is obtained. Viscosity index was determined from the kinematic viscosities at 40 °C and 100 °C according to ISO 2909. The flash point was determined according to ISO 2592. The pour point was measured according to ISO 3016. The procedure for determining copper corrosion was done according to ISO 2160 by putting both a sample of examined oil and a copper plate into a glass test tube. The test tube with oil and a plate is then placed into a device that imitates the conditions of exploitation. The device heats a test tube at a temperature of 120 °C. After 3 hours, the test tube is taken out and the changes on the copper plate are observed. The copper plate changes color and is compared with the spectrum color on the ASTM scale, thus determining the class of resistance to oxidation. The volatility of the oil was tested using the Noack test, which is a standardized laboratory method for evaluation of

oil volatility at high temperatures. The oil sample is poured into the automatic device to determine evaporation. In the device, the tested oil sample is heated up to a temperature of 250 °C for a period of 1 hour, while the amount of volatile components of the oil is measured. The amount of volatile components is expressed as mass loss in percentage, and the smaller the mass loss is, the greater is the oil's resistance to evaporation at high temperatures. To predict the behavior of quenchants, an accelerated oxidation test (Baader ageing test) was also performed according to DIN 51554. The following characteristics of quenchants are presented: kinematic viscosity at 40 °C after the test, increase of viscosity at 40 °C, acid number after the test, increase of acid number, IR spectrum before the test and IR spectrum after the test. To monitor the cooling process for the purpose of testing the cooling characteristics of the quenching oils, a measuring probe with dimensions $\Phi 12,5 \times 60$ mm made of Inconel 600 alloy was used with an insulated K-type thermocouple (diameter 1,5 mm) installed in the centre of the probe with polished or finely ground surface. The measuring probe is an integral part of the IVF Smart Quench measuring and analytical system. The IVF Smart Quench measuring system consists of a measuring probe, a furnace, a measuring vessel, an electronic data acquisition system and the IVF SQ Integra computer program. The performance of the cooling curves test consisted of the phase of heating the measuring probe to a temperature of 855 °C and the phase of cooling the probe in examined stationary quenching oils. During cooling, the electronic measuring system recorded and stored the temperature values in the centre of the test probe with the selected sampling frequency. The temperature of the measuring probe at the beginning of cooling was 855 °C. Start temperature was set to 850 °C and the reason for selecting a heating temperature of 855 °C is that the probe must be moved from the furnace to the quenching media to be tested. The time of heating the measuring probe was 5 minutes. The temperature of the tested quenching oils at the beginning of the recording of the cooling curves was 80 °C and the oil sample volume was two litres. The time of collecting records on the cooling of the centre of the sample was 60 s. The sampling frequency was 100 records/second. Using the IVF SQ Integra computer program and the recorded cooling data of the centre of the probe, the appearance and values of the temperature and cooling rate curves and the following calculated data shown in Table 2 were determined.

Tab. 2: Characteristic data calculated automatically for each quenchant

Quenching characteristic	Unit	Description
CR_{\max}	°C/s	Maximum cooling rate
$T(CR_{\max})$	°C	Temperature at maximum cooling rate
$t(CR_{\max})$	s	Time to reach the maximum cooling rate
CR_{300}	°C/s	Cooling rate at 300 °C
CR_{550}	°C/s	Cooling rate at 550 °C
<i>Time to 600 °C</i>	s	Time to reach 600 °C
<i>Time to 400 °C</i>	s	Time to reach 400 °C
<i>Time to 200 °C</i>	s	Time to reach 200 °C
T_{vp}	°C	Temperature for transition from vapour phase to boiling phase
T_{cp}	°C	Temperature for transition from boiling phase to convection phase

3. RESULTS AND DISCUSSION

Physical and chemical properties of Mineral oil 1, Mineral Oil 2, Olive oil and Canola oil obtained by standardized laboratory methods are shown in Table 3.

Tab. 3: Physico-chemical properties of examined oils

Property	Unit	Quenchant sample			
		Mineral oil 1	Mineral oil 2	Olive oil	Canola oil
Appearance and color	-	Clear, brown	Clear, brown	Clear, yellow	Clear, yellow
Density	g/cm ³	0,8540	0,8579	0,9151	0,9204
Kinematic viscosity at 40 °C	mm ² /s	22,10	24,05	39,88	35,46
Kinematic viscosity at 100 °C	mm ² /s	4,38	4,69	8,70	8,16
Viscosity index	-	107	113	204	215
Base number	mgKOH/g	0,35	1,89	0,03	0,02
Acid number	mgKOH/g	0,02	0	0,23	0,06
Flash point	°C	195	205	288	320
Pour point	°C	-18	-15	-18	-30
Copper corrosion	-	1b	1a	1a	1a
Volatility (Noack)	%	23,0	23,8	0,5	0,5
Baader ageing test, 110 °C / 72 h					
Kinematic viscosity at 40 °C, after the test	mm ² /s	22,39	24,20	48,85	51,87
Increase of kinematic viscosity at 40 °C	%	1,31	0,21	22,49	46,28
Acid number after the test	mgKOH/g	0,04	0,00	0,70	0,28
Increase of acid number	%	100,00	0,00	204,35	366,68
IR spectrum before the test	-	typical	typical	typical	typical
IR spectrum after the test	-	No oxidation peak	No oxidation peak	Oxidation peak 1555 cm ⁻¹	Strong oxidation peak 1559 cm ⁻¹

The experiment showed that the viscosity values for vegetable oils are considerable higher than those of commercial mineral-based oils, which would reduce the cooling rate during quenching process. Also, the viscosity index values of vegetable oils are higher than those of mineral-based oils, which means that their viscosity is more dependant on temperature. Flash point temperature values are higher for vegetable oils, which results in lower risk of ignition at elevated temperatures. Pour point temperature values for all quenchant samples meet the needs for tempering process. Base and acidic number of mineral-based oils showed more favourable results than those of vegetable oil, which may result in a lower risk of corrosion. Noack test showed that for both olive and canola oil the values obtained are less than 1 %, while those obtained for mineral oils are much higher. Furthermore, after carrying out the Baader test, a large oxidation of canola and olive oil is visible due to the increase in acid number and kinematic viscosity. Mineral oil 1 has less additives (0.5 % by mass), so the acid number has changed, while Mineral oil 2 has more additives (3.0% by mass) and no oxidation of the oil occurs at all.

Cooling characteristics of Mineral oil 1, Mineral oil 2, Olive oil and Canola oil measured according to the ISO 9950 standard are shown in Table 4.

Tab. 4: Quenching characteristics of each examined oil

Quenching characteristic	Unit	Quenchant sample			
		Mineral oil 1	Mineral oil 2	Olive oil	Canola oil
CR_{max}	°C/s	77,98	105,07	98,96	109,49
$T(CR_{max})$, °C	°C	543,43	603,28	626,73	652,05
$t(CR_{max})$	s	10,78	7,06	5,08	3,09
CR_{300}	°C/s	5,77	4,89	11,27	11,45
CR_{550}	°C/s	77,90	90,15	71,72	70,15
Time to 600 °C	s	9,97	7,09	5,35	3,59
Time to 400 °C	s	14,09	11,08	9,58	7,68
Time to 200 °C	s	53,02	53,80	36,96	35,58
T_{vp}	°C	632,17	716,98	761,95	849,57
T_{cp}	°C	370,21	378,07	329,16	268,10

Temperature vs. time and cooling rate vs. temperature curves of Mineral oil 1 examined at the temperature of 80 °C are shown in Figure 1.

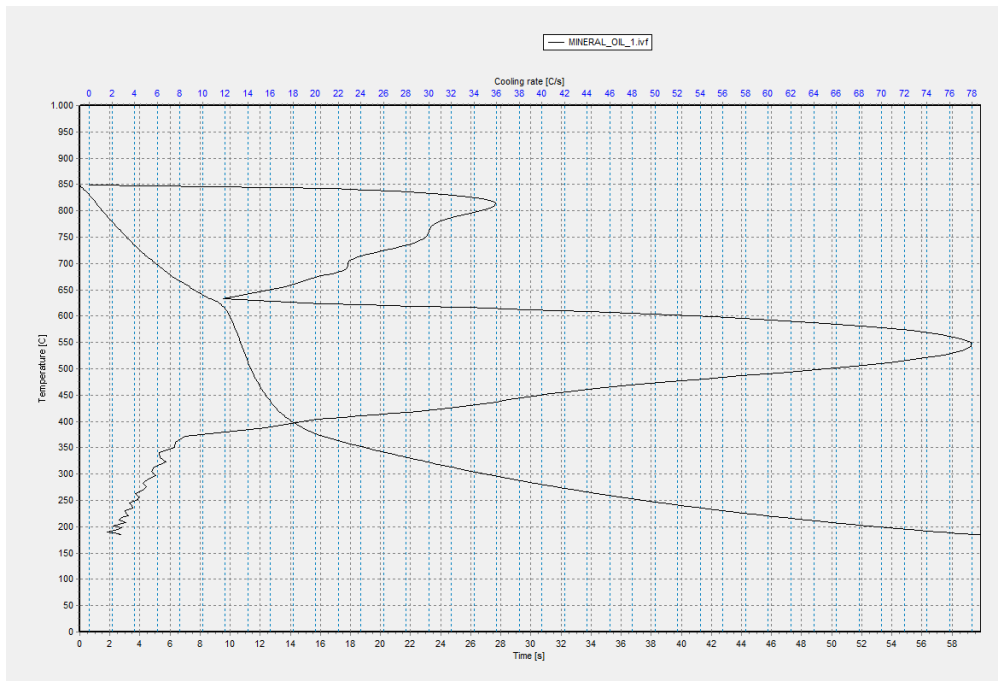


Fig. 1: Temperature vs. time and cooling rate vs. temperature curves of Mineral oil 1 at 80 °C

Temperature vs. time and cooling rate vs. temperature curves of Mineral oil 2 examined at the temperature of 80 °C are shown in Figure 2.

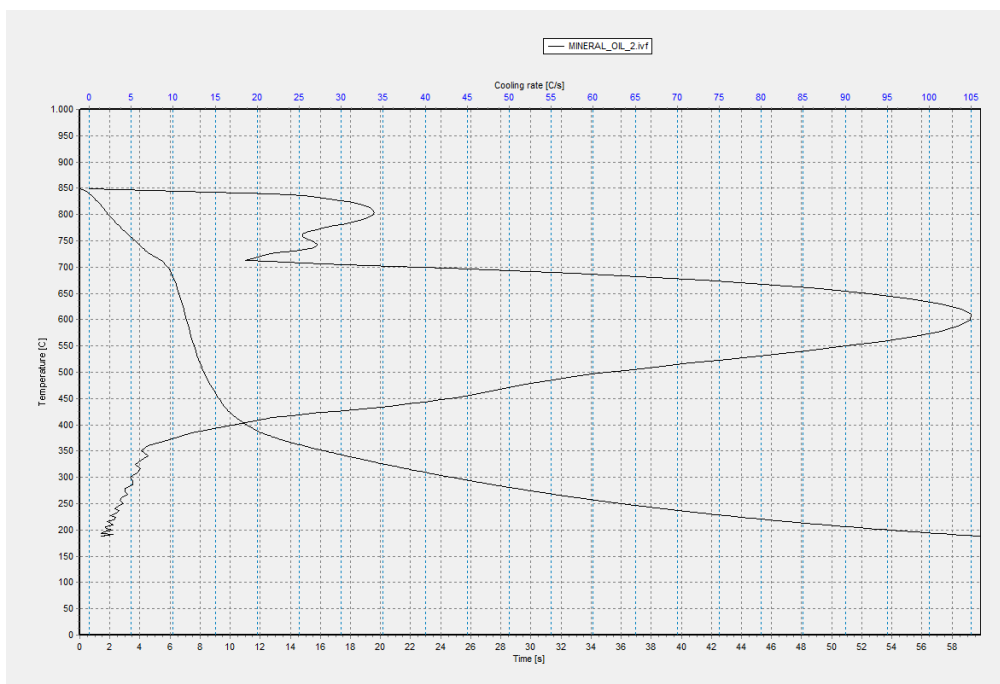


Fig. 2: Temperature vs. time and cooling rate vs. temperature curves of Mineral oil 2 at 80 °C

Temperature vs. time and cooling rate vs. temperature curves of Olive oil examined at the temperature of 80 °C are shown in Figure 3.

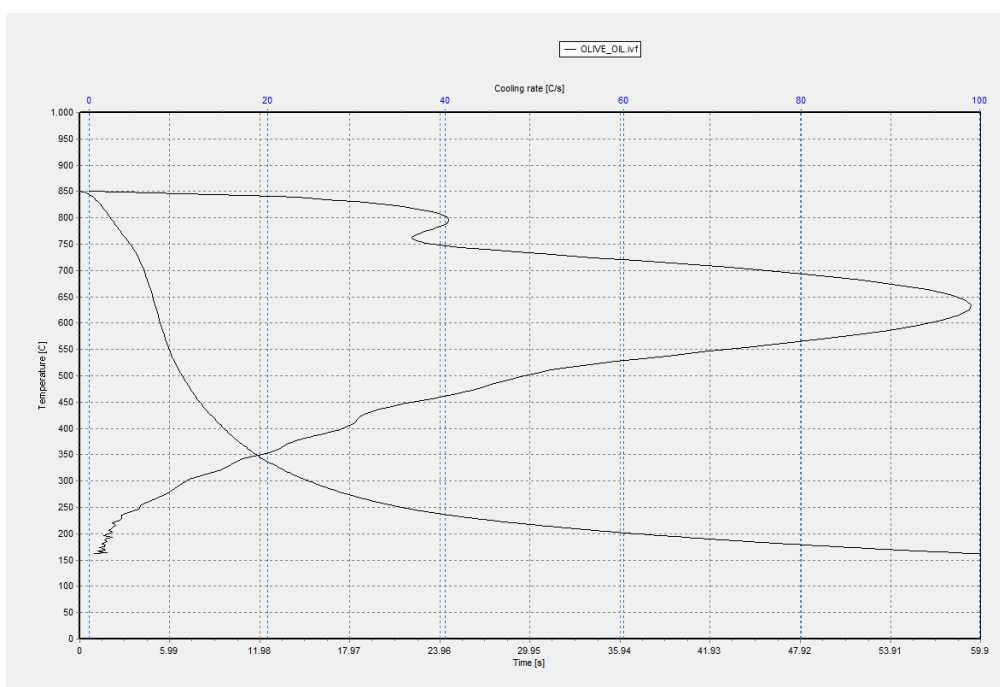


Fig. 3: Temperature vs. time and cooling rate vs. temperature curves of Olive oil at 80 °C

Temperature vs. time and cooling rate vs. temperature curves of Canola oil examined at the temperature of 80 °C are shown in Figure 4.

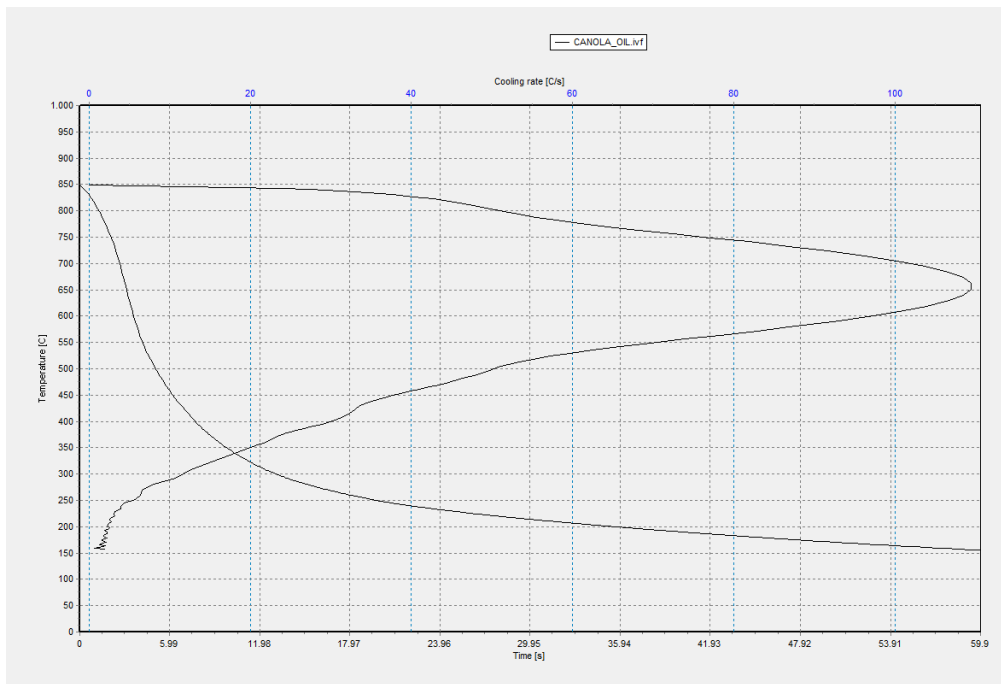


Fig. 4: Temperature vs. time and cooling rate vs. temperature curves of Canola oil at 80 °C

The cooling curves of all 4 examined oils are shown in Figure 5.

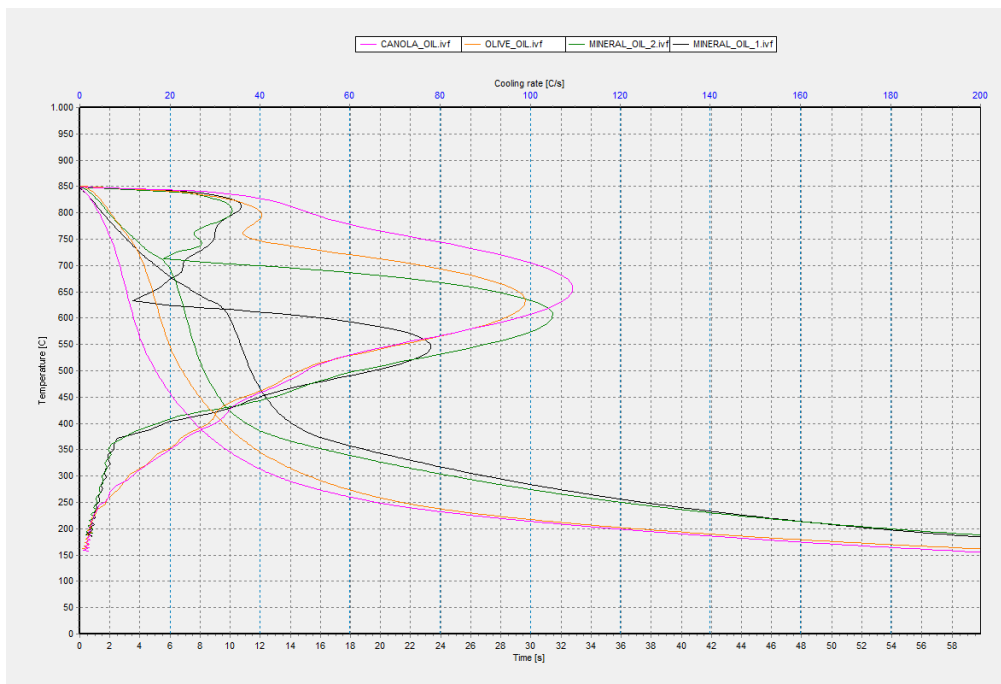


Fig. 5: Cooling curves of all examined oils

4. CONCLUSION

The cooling characteristics of the quenching oil that affect the quality and cooling rate of the workpiece during the quenching process are the result of the physical and chemical properties of these oils. Investigation of physical and chemical properties and cooling characteristics of two commercial mineral-based oils and two vegetable oils was obtained, and it can be concluded that, considering the similarity of the results, vegetable oils could be suitable for quenching processes. However, by performing the Baader test in order to evaluate the long-term behaviour of quenchants, a large oxidation of canola and olive oil is evident from the increase in acid number and kinematic viscosity.

Regarding the importance of sustainable development, vegetable oils are an interesting substitute for existing industrial oils used in the quenching process. However, when choosing a suitable quenchant, longevity is one important aspect. Therefore, the oxidative and ageing stability of vegetable oils must be further investigated.

REFERENCES

- [1] B. Laxmi, S. Sharma, J. Pk, and A. Hegde, 'Quenchant oil viscosity and tempering temperature effect on mechanical properties of 42CrMo4 steel', *J. Mater. Res. Technol.*, vol. 16, pp. 581–587, Jan. 2022, doi: 10.1016/j.jmrt.2021.11.152.
- [2] M. P. Prathviraj, A. Samuel, and K. Narayan Prabhu, 'Reprocessed waste sunflower cooking oil as quenchant for heat treatment', *J. Clean. Prod.*, vol. 269, p. 122276, Oct. 2020, doi: 10.1016/j.jclepro.2020.122276.
- [3] B. Matijevic and L. Pedisic, 'Influence of Additive Chemistry on the Physical, Chemical and Cooling Properties of Quenching Oils', *Mater. Perform. Charact.*, vol. 3, pp. 283–292, Dec. 2014, doi: 10.1520/MPC20130105.
- [4] G. Kerekes, M. Baan, and I. Felde, 'Possibility of Use Bio Oils as Quenchant', Jan. 2016. doi: 10.26649/musci.2016.082.
- [5] P. Brito, P. A. Ramos, L. P. Resende, D. A. de Faria, and O. K. Ribas, 'Experimental investigation of cooling behavior and residual stresses for quenching with vegetable oils at different bath temperatures', *J. Clean. Prod.*, vol. 216, pp. 230–238, Apr. 2019, doi: 10.1016/j.jclepro.2019.01.194.
- [6] S. G. Lee, M. Kaviani, and J. Lee, 'Role of quenching method on cooling rate and microstructure of steels: Variations in coolant and its flow arrangement', *Int. J. Heat Mass Transf.*, vol. 189, p. 122702, Jun. 2022, doi: 10.1016/j.ijheatmasstransfer.2022.122702.
- [7] D. Scott MacKenzie, 'Selection of oil quenchants for heat treating processes', *Int. Heat Treat. Surf. Eng.*, vol. 8, no. 1, pp. 8–14, Mar. 2014, doi: 10.1179/1749514813Z.00000000089.
- [8] V. Venkitesh and S. Dash, 'Role of extended surfaces on the enhancement of quenching performance', *Int. J. Therm. Sci.*, vol. 171, p. 107235, Jan. 2022, doi: 10.1016/j.ijthermalsci.2021.107235.
- [9] H. I. Akbar, E. Surojo, D. Ariawan, and A. R. Prabowo, 'Experimental study of quenching agents on Al6061–Al203 composite: Effects of quenching treatment to microstructure and hardness characteristics', *Results Eng.*, vol. 6, p. 100105, Jun. 2020, doi: 10.1016/j.rineng.2020.100105.
- [10] F. Lenzi, G. Campana, A. Lopatriello, M. Mele, and A. Zanotti, 'About the Use of mineral and vegetable Oils to improve the Sustainability of Steel Quenching', *Procedia Manuf.*, vol. 33, pp. 701–708, Jan. 2019, doi: 10.1016/j.promfg.2019.04.088.
- [11] Bhagyalaxmi, S. Sharma, P. K. Jayashree, and A. Hegde, 'Vegetable oil quench effect on impact toughness and hardness of 42CrMo4 steel', *Mater. Today Proc.*, vol. 63, pp. 113–116, Jan. 2022, doi: 10.1016/j.matpr.2022.02.349.

- [12] N. J. Fox and G. W. Stachowiak, 'Vegetable oil-based lubricants—A review of oxidation', *Tribol. Int.*, vol. 40, no. 7, pp. 1035–1046, Jul. 2007, doi: 10.1016/j.triboint.2006.10.001.



UTJECAJ TOPLINSKE OBRADE NA MEHANIČKA I KOROZIJSKA SVOJSTVA ALUMINIJSKE LEGURE ALSI1MGMN

EFFECT OF HEAT TREATMENT ON MECHANICAL AND CORROSION PROPERTIES OF ALSI1MGMN ALUMINUM ALLOY

Darko Landek¹, Marin Kurtela¹, Domagoj Fekonja¹, Jurica Jačan¹

¹ University of Zagreb, Faculty of Mechanical Engineering and Naval Architecture, Zagreb, Croatia

Sažetak

Aluminijske legure iz skupina EN-AW 20XX, EN-AW 60XX i EN-AW 70XX svoja uporabna svojstva postižu nakon precipitacijskog očvršćivanja. Parametri toplinske obrade značajno utječu na mikrostrukturu, mehanička i korozijska svojstva obrađene legure. U radu je provedno precipitacijsko očvršnuće legure AlSi1MgMn homogenizacijskim žarenjem na 560 °C/6h i umjetnim starenjem na temperaturi 150 °C i 175 °C u trajanju 5 h i 10 h. Na ispitnim uzorcima provedeno je ispitivanje tvrdoće metodom Vickers i određena je otpornost na elektrokemijsku koroziju u vodenoj otopini 3,5 % NaCl metodom Tafel. Prema kriteriju najveće tvrdoće i najmanje brzine korozije optimalna temperatura i trajanje umjetnog starenja iznose 175 °C/5h.

Ključne riječi: *precipitacijsko očvršnuće, umjetno starenje, elektrokemijska korozija, AlSi1MgMn*

Abstract

Aluminum alloys from the groups EN-AW 20XX, EN-AW 60XX and EN-AW 70XX achieve their useful properties after precipitation hardening. Heat treatment parameters significantly affect the microstructure, mechanical and corrosion properties of the treated alloy. In this paper, precipitation hardening of AlSi1MgMn alloy was carried out by homogenization annealing at 560 °C/6h with artificial aging at temperature of 150 °C and 175 °C for 5 h and 10 h. The test samples were tested for hardness using the Vickers method. Resistance to electrochemical corrosion in a 3.5% NaCl aqueous solution was determined by the Tafel method. According to the criterion of the highest hardness and the lowest corrosion rate, the optimal temperature and duration of artificial aging are 175 °C/5h.

Keywords: *precipitation hardening, artificial aging, electrochemical corrosion, AlSi1MgMn*

1. INTRODUCTION

Aluminum alloys are the most commonly used materials for the fabrication of metal structures after iron and steel. They find wide applications and continual development in the fields of shipbuilding, aerospace, electrical engineering, automotive industry, and weapon manufacturing due to their favorable properties such as low density, high specific strength, ease of processing, good corrosion resistance, and excellent electrical and thermal conductivity. Based on composition, microstructure, and processing properties, aluminum alloys can be divided into cast and wrought alloys. Generally, the alloying element content in cast alloys ranges from 10-12%, while in wrought alloys, it is around 1-2%, although in some cases, it can be up to 6-8%. Based on their capability for precipitation hardening, aluminum alloys can further be categorized into heat-treatable and non-heat-treatable [1, 2]. The thermal treatment of aluminum alloys consists of three stages: (1) solution annealing at a temperature below the eutectic temperature where substitutional alloying elements dissolve in aluminum, (2) quenching at a critical rate to room temperature, where the alloying elements remain dissolved in the unstable solid solution of aluminum crystal lattice, and (3) artificial aging by heating at a temperature below 200 °C for a specified time. During aging, the alloying elements precipitate from the unstable solution of aluminum crystal lattice in the form of nanometer-sized intermetallic compounds, thereby strengthening the aluminum alloy. Aging of solution-annealed aluminum alloys can also be performed at room temperature over a considerably longer period than artificial aging. The mechanical and corrosion properties of precipitation-hardened aluminum alloys are significantly influenced by the heat treatment parameters: solution annealing temperature and time, quenching rate, and aging temperature and time.

Depending on the type of aluminum alloy, the solution annealing temperature typically ranges from 441 °C to 527 °C. If the temperature is too low, the maximum strength of the alloy will not be achieved. If the temperature is too high, there is a risk of melting the low-solubility constituents (eutectic melting), significantly deteriorating properties in certain alloys. To achieve optimal properties, it is recommended to maintain the solution annealing temperature within a very narrow allowable deviation range (± 10 °C) [1, 3]. The objective of the solution annealing process for the AlSi1MgMn alloy (EN-AW 6082) is to achieve the maximum concentration of dissolved alloying elements within the solid solution, including copper, zinc, magnesium, and/or silicon. The concentration and dissolution rate of these elements increase with the temperature. The holding time depends on the alloy type and the thickness of the object, ranging from 10 minutes for thin sheets to 12 hours for heavy forged materials. For heavy parts, the recommended holding time at the solution annealing temperature is approximately 1 hour for every 2.5 cm thickness of the cross-section. It is advisable to select the minimum required holding time to achieve optimal properties. If the holding time is too short, the constituents will not completely dissolve in the solid solution; on the other hand, excessively long holding time increases the risk of high-temperature surface oxidation [3, 4].

Quenching of solution-annealed aluminum alloy is typically carried out in water with a quenching intensity sufficient to retain the dissolved alloying elements in the forced solution of the aluminum crystal lattice. The highest quenching rate will provide the best combination of strength, toughness, general corrosion resistance, and stress corrosion resistance. However, it should be noted that increasing the quenching rate leads to higher residual stresses and distortion, so the optimal quenching rate that achieves the

desired properties needs to be determined. The influence of quenching rate on the occurrence of precipitation reaction is described by continuous Time Temperature Precipitation (TTP) cooling diagrams. The shape of the continuous TTP diagram and the incubation time until the start of precipitation of unwanted coarse precipitates depend on the chemical composition of the aluminum alloy, solution annealing temperature, and cooling curve shape [1, 6, 7, 8]. Despite their importance in understanding precipitation reactions, TTP diagrams for aluminum alloys are rarely constructed due to the complexity of dilatometric, mechanical, and microstructural tests. Figure 1 shows a schematic phase diagram and TTP diagram with curves for the onset of primary precipitate precipitation in aluminum alloy EN-AW 6082. It is observed that each solution annealing temperature results in a characteristic curve of the onset of precipitation of coarse beta phase precipitates that need to be avoided by sufficiently fast cooling [7, 9, 10].

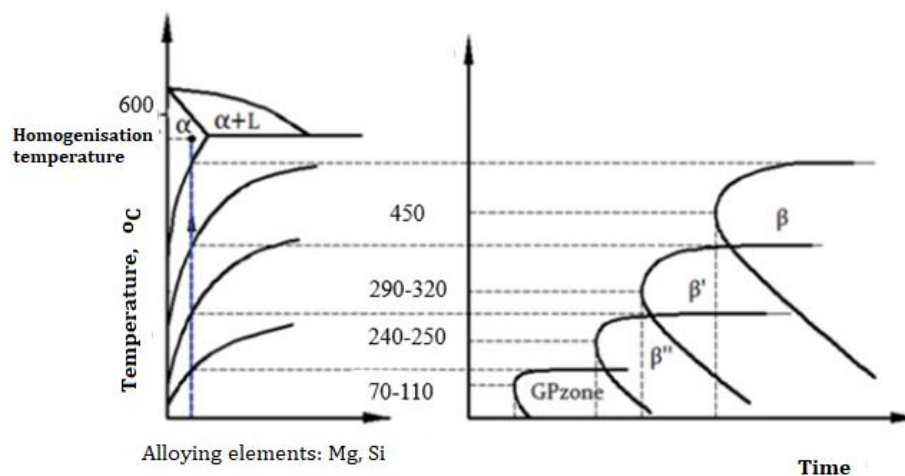


Fig. 1: Schematic representation of the phase diagram and TTP precipitation curves for aluminum alloy EN-AW 6082 [9]

The solution-annealed and quenched alloy is easily workable by particle separation and deformation in the cold state. Some manufacturers retain the structure in such a state by storing alloys at temperatures below zero until further shaping. However, most solution-annealed alloys are not stable after quenching at room or elevated temperatures, and precipitation of intermetallic compounds from supersaturated solution begins, known as natural aging [1, 5].

The temperatures of precipitation hardening for aluminum alloys depend on the chemical composition of the alloy and the desired properties, and typically range from 107 °C to 191 °C. The artificial aging temperature must be precisely and reliably maintained within a few degrees of the specified temperature (± 3 °C) to achieve optimal mechanical and corrosion properties. The holding time of aluminum alloys at a specific aging temperature ranges from 4 to 24 hours [1, 4, 6, 10]. With the increase in precipitation hardening temperature, excessive aging reduces tensile strength, yield strength, elongation, and corrosion resistance of overaged alloys.

Aluminum alloys from the EN-AW 6xxx group contain silicon and magnesium in proportions sufficient to form magnesium silicide (Mg_2Si), making them heat-treatable. Although they do not have high strength like most aluminum alloys from the EN-AW 2xxx and EN-AW 7xxx groups, they have excellent formability, weldability, machinability, and moderate strength with excellent corrosion resistance. In alloys from the EN-AW 6xxx group, Mg_2Si precipitates occur in three basic forms: (a) coherent β''

precipitates, emitted in the form of very fine rods densely dispersed in the microstructure, (b) partially coherent β' precipitates, of slightly larger rod-like shape, and (c) incoherent β precipitates, precipitated in the form of large, cube-like particles. The improvement in the mechanical properties of aluminum alloys EN-AW 6xxx is significantly contributed by only coherent β'' precipitates, while the contribution of other precipitates is negligible. During artificial aging between 150 °C to 200 °C, the alloying elements start forming ordered arrays of atoms in the aluminum matrix, called Guinier-Preston (GP) zones, which significantly strengthen the alloy while maintaining good corrosion resistance [4].

Due to the influence of the chemical composition of a specific aluminum alloy and the action of heat treatment parameters on mechanical and corrosion properties, the boundary values within which the parameters of the artificial aging process can be selected to achieve the best combination of mechanical hardening and resistance to electrochemical corrosion are not sufficiently researched. For future optimizations of heat treatment parameters, this study investigates the influence of temperature and time of artificial aging of the AlSi1MgMn alloy (EN-AW 6082) on the increase in hardness and resistance to electrochemical corrosion in a 3.5% NaCl aqueous solution.

2. MATERIALS AND METHODS

From a hot extruded rod of aluminum alloy AlSi1MgMn (EN-AW 6082), 12 samples with a diameter of 30 mm and a thickness of 9 mm were cut. The chemical composition of the samples was analyzed using a portable Olympus XRF spectrometer and is listed in Table 1. The measured proportions of metallic elements comply with the chemical composition of this alloy as stipulated by DIN EN 573-3:2019 standard.

Tab. 1: Chemical composition of aluminum alloy EN-AW 6082

% wt of metal element							
Si	Fe	Cu	Mn	Mg	Cr	Zn	Al
1.20	0.27	0.05	0.45	2.08	0.05	0.34	95.87

The flat surfaces of the samples were planar ground using a belt grinder with abrasive papers of grit #80 and #240, followed by a final polish using waterproof abrasive paper with a grit size of #800. Sample designations and the planned heat treatment are provided in Table 2. The heat treatment consists of solution annealing at 560°C for 6 hours in a small laboratory electric furnace, followed by quenching in still water at room temperature.

Tab. 2: Designations of aluminum alloy EN-AW 6082 samples and their heat treatment

No.	Designation	Heat Treatment Parameters
1.	A11	560 °C/6 h/water _{20 °C} + 150 °C/5 h/air
2.	A12	560 °C/6 h/water _{20 °C} + 150 °C/10 h/air
3.	A21	560 °C/6 h/water _{20 °C} + 175 °C/5 h/air
4.	A22	560 °C/6 h/water _{20 °C} + 175 °C/10 h/air

The water quenching curve was recorded according to ISO 9950:1995 using the IVF Smart Quench System in the Heat Treatment Laboratory (FMENA). This system records the water quenching curve of a temperature probe with a diameter of 12.5 mm and a

length of 60 mm made of Inconel 600 alloy, utilizing a type K thermocouple embedded in the center of the probe. The water cooling curve and cooling rate curve are shown in Figure 2. Artificial aging was performed in the same laboratory electric furnace at temperatures of 150°C and 175°C for durations of 5 hours and 10 hours, respectively.

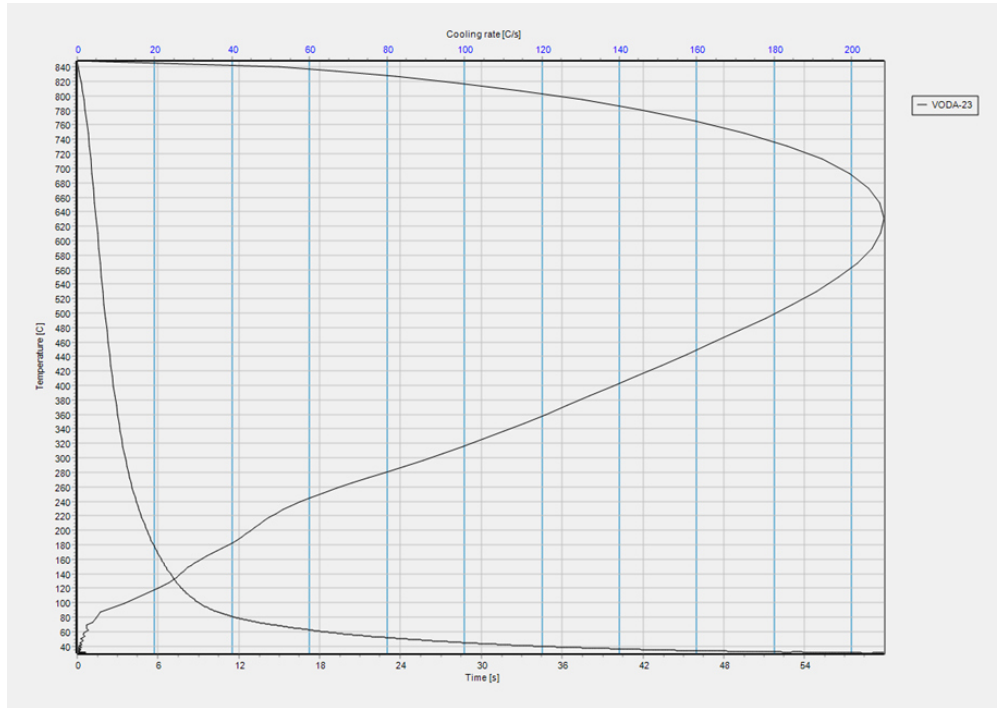


Fig. 2: Cooling curve and cooling rate curve in 23°C water

Hardness measurements on the surface of the heat-treated samples were conducted using the Vickers HV1 method at the Surface Engineering Laboratory (FMENA) on an INSTRON Wilson-Wolpert Tukon 2100B hardness tester. Hardness testing was repeated 5 times for each heat-treated condition of the test samples.

The evaluation of resistance to electrochemical corrosion was carried out in a 3.5% NaCl aqueous solution by measuring the polarization resistance and cyclic polarization of the test sample surfaces. The results of cyclic polarization were analyzed using Tafel extrapolation. The Potentiostat/Galvanostat Model 273A EG&E device, electrochemical cell, and computer program 352 SoftCorr III in the Materials Protection Laboratory (FMENA) were utilized for electrochemical testing. The electrochemical cell, as shown in Figure 3, consisted of a working electrode (test sample with a surface area of 0.785 cm²), auxiliary graphite electrodes, and a saturated calomel reference electrode. A detailed description of the testing can be found in [11, 12]. Using Tafel extrapolation, the corrosion rate v_{kor} was determined, while cyclic polarization established the tendency of the aluminum alloy to pitting corrosion characterized by the pitting potential (E_{pit}) and the protective (E_{zpit}) potential [11, 12, 13].

The appearance of the corroded surface of the test samples was analyzed using a Leica MZ6 stereomicroscope. For microstructure analysis, the test samples were metallographically ground and polished. Etching of the polished surface was performed in Keller's reagent for 30 s. Keller's reagent is a solution comprising 95 mL of distilled water, 2.5 mL of nitric acid, 1.5 mL of hydrochloric acid, and 1 mL of hydrofluoric acid.

The microstructure of the test samples was analyzed after metallographic preparation using optical microscopy on an Olympus GX 51 microscope in the Materialography Laboratory (FMENA).

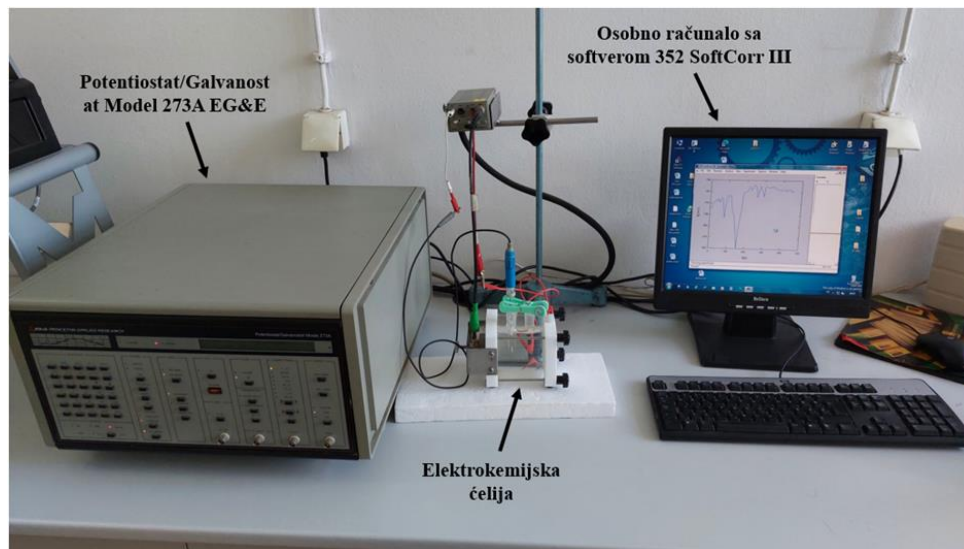


Fig. 3: Test apparatus for determining resistance to electrochemical corrosion

3. RESULTS AND DISCUSSION

3.1. Hardness

The hardness of the test samples after solution annealing at 560°C / 6 h followed by water quenching was 65 ± 5 HV1. The hardness of the samples after artificial aging is shown in Figure 4. The histogram in Figure 4 reveals that the maximum and minimum hardness values differ by 36 HV1, depending on the chosen parameters of artificial aging. The highest hardness of 126 HV1 was achieved after artificial aging at a temperature of 150°C / 10 h (sample A12), followed by sample A21, artificially aged at 175°C / 5 h. The lowest hardness of 90 HV1 was obtained for sample A22, which was artificially aged at 175°C / 10 h.

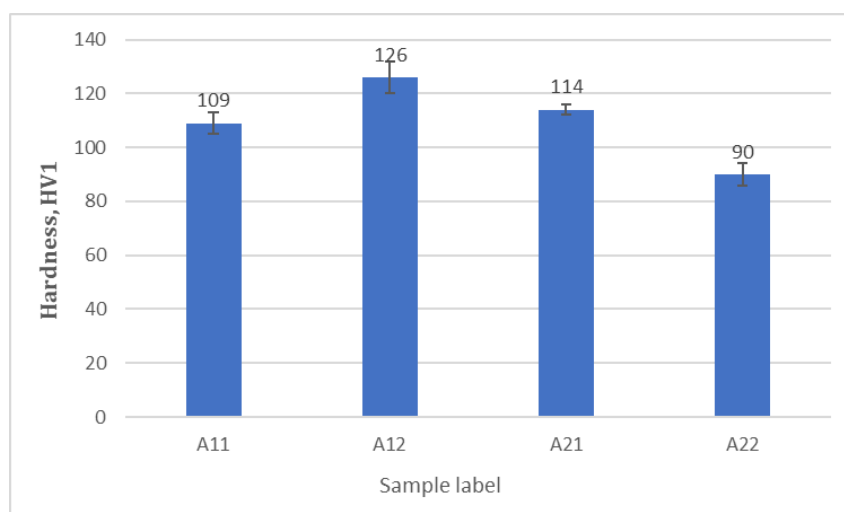


Fig. 4: Hardness of EN-AW 6082 alloy samples after artificial aging

3.2. Electrochemical corrosion resistance

The corrosion rate and corrosion potential of each test sample were determined by extrapolating the anodic and cathodic Tafel slopes. By extending these slopes to their intersection, the corrosion potential E_{kor} and the corrosion current density j_{kor} were determined, from which the corrosion rate v_{kor} was calculated. The corrosion potential values for all test samples were negative and ranged from -727 ± 10 mV. Negative values indicate that exposure to the corrosive medium (in this case, 3.5% NaCl) would result in corrosive damage to the tested surfaces. Corrosion current density and corrosion rate are directly proportional, so the extrapolation of the anodic and cathodic slopes determined the lowest current density (and thus the calculated corrosion rate) for sample A11, while the highest corrosion rate was determined for sample A22. Table 3 shows the values of E_{kor} , j_{kor} and v_{kor} obtained by extrapolating the anodic and cathodic directions.

Tab. 3: Corrosion potential, current density, and corrosion rate values determined by tafel extrapolation on heat-treated EN-AW 6082 alloy samples

Sample	Parameters of Electrochemical Testing		
	E_{kor} [mV]	j_{kor} [$\mu\text{A}/\text{cm}^2$]	v_{kor} [mm/year]
A11	-724	0,65	$7,12 \times 10^{-3}$
A12	-731	1,39	$1,52 \times 10^{-2}$
A21	-726	0,85	$9,32 \times 10^{-3}$
A22	-730	1,10	$1,21 \times 10^{-2}$

The susceptibility of the test samples to pitting corrosion in a 3.5% NaCl solution was determined using cyclic polarization, which provided the pitting potential E_{pit} and the protective potential E_{zpit} . The results of cyclic polarization testing are presented in Table 4. Similar to Tafel extrapolation, the cyclic polarization curves for all samples almost overlap, with minimal deviations, and the obtained potential values do not significantly differ from one another. Pitting corrosion was observed in all samples, with the most negative potential determined for sample A12 at -767 mV. Comparing the corrosion potential results from Table 3 and the pitting potential results from Table 4, it can be seen that the values at which pitting corrosion occurs (E_{pit}) are slightly higher than the corrosion potential values (E_{kor}), indicating the rapid onset of pitting shortly after contact with the corrosive medium. The results indicate that the EN-AW 6082 aluminum alloy is susceptible to localized pitting corrosion in a 3.5% NaCl aqueous solution.

Tab. 4: Pitting Potential and Protective Potential Values for Pitting Corrosion Determined on Heat-Treated EN-AW 6082 Alloy Samples

Sample	Parameters of Electrochemical Testing	
	E_{pit} [mV]	E_{zpit} [mV]
A11	-654	/
A12	-767	/
A21	-657	/
A22	-699	/

3.3. Corroded surface analysis

After the electrochemical tests, the surfaces of the samples were observed using a Leica MZ6 stereomicroscope. The images of the corroded surfaces are shown in Figure 5. The photographs of the corroded surface were taken at a magnification of 12.5:1, with a scale of 1 mm in the lower right corner for all samples. Localized pitting corrosion damage was observed on all samples after the tests. It is evident that many samples exhibited intense corrosion due to the aggressive nature of the 3.5% NaCl solution. Different densities and sizes of pits are noticeable on all samples. After cyclic polarization, it is clear that all samples suffered significant corrosion damage across the entire test surface, which is much larger and deeper than after the Tafel method of electrochemical corrosion testing.

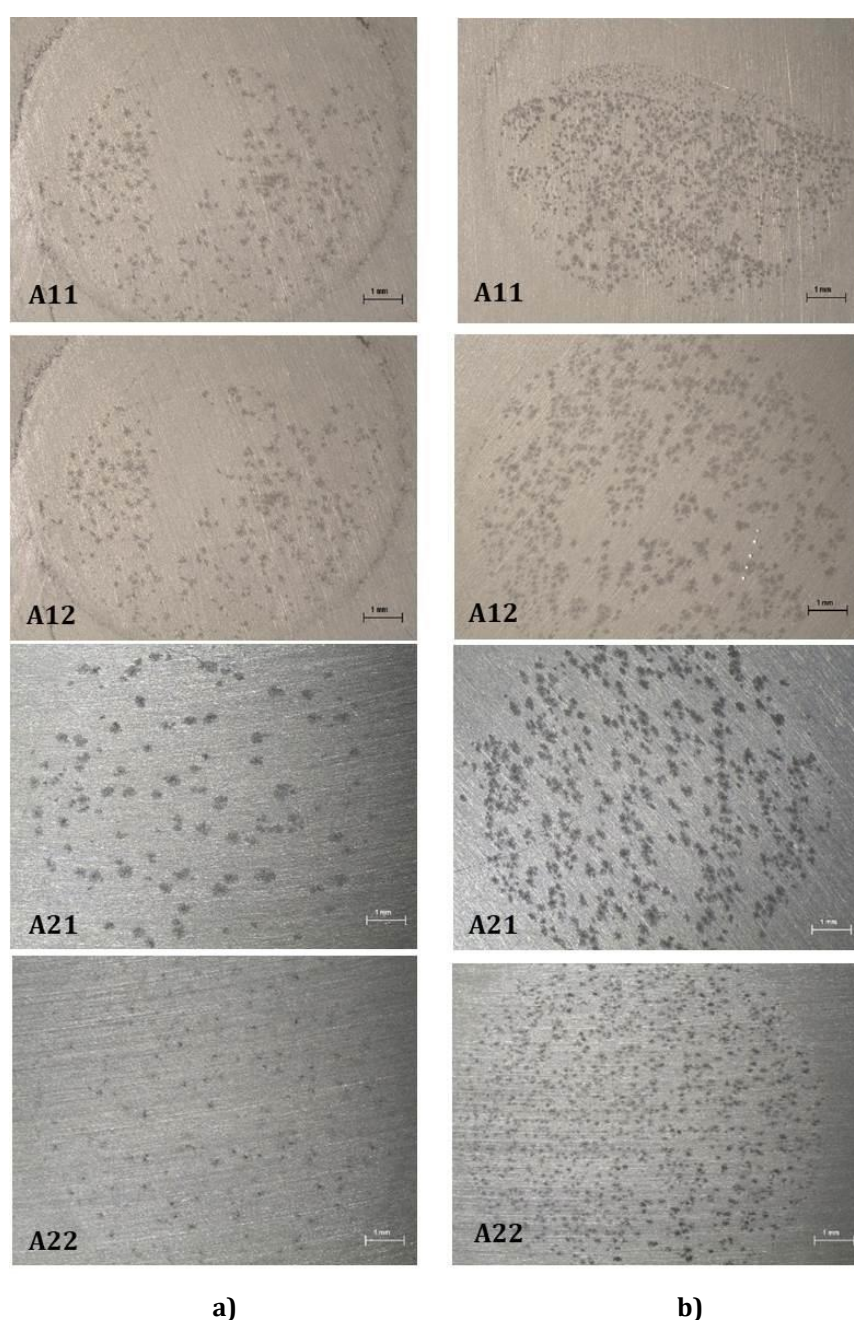


Fig. 5: Surface of test samples after: a) Tafel method testing, b) cyclic polarization

3.4. Microstructure analysis

The microstructure of test samples A12 and A22 is shown in Figure 6. The microstructure of both samples appears similar, with finely distributed precipitates of Mg_2Si evenly dispersed within the aluminum matrix. Pores and microcracks are also clearly visible, randomly distributed across the entire test surface. These structural imperfections result from plastic deformation during the manufacture of the aluminum alloy using hot extrusion pressing.

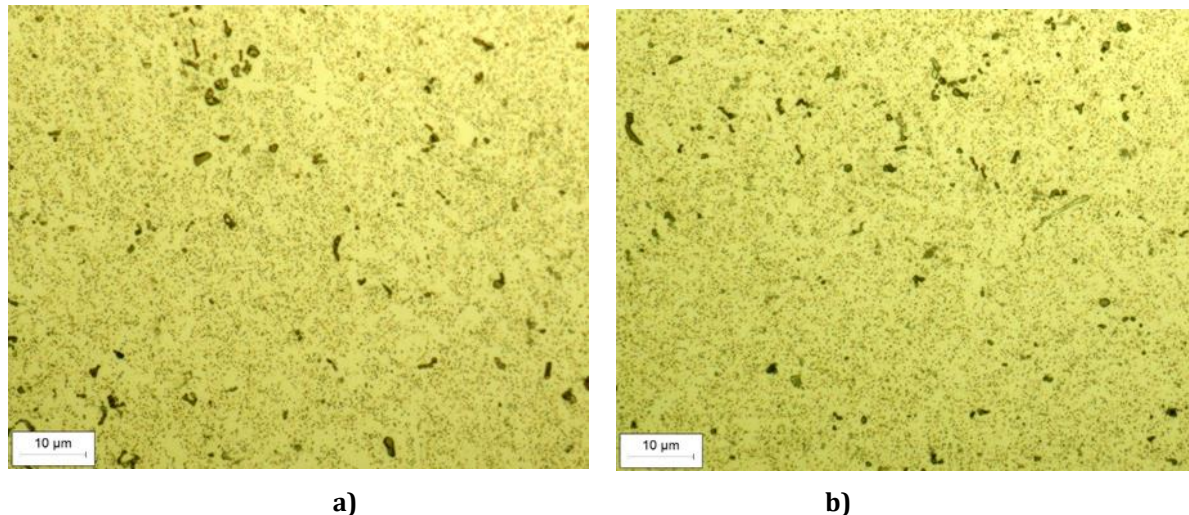


Fig. 6: Microstructure of Samples after Artificial Aging of EN-AW 6082 Alloy: a) A12, b) A22

4. CONCLUSION

Significant improvements in the mechanical properties of the $AlSi1MgMn$ aluminum alloy can be achieved through heat treatment. After solution annealing, water quenching, and artificial aging, hardness values of up to 126 HV1 can be obtained with artificial aging at $150^{\circ}C$ / 10 h, and 114 HV1 after aging at $175^{\circ}C$ / 5 h.

The tested aluminum alloy is not resistant to general electrochemical corrosion in a 3.5% NaCl aqueous solution, as evaluated by the Tafel method. Negative corrosion potential values were obtained for all tested samples, accompanied by visible corrosion damage on the tested surfaces. However, among the tested conditions, the highest corrosion resistance, indicating the lowest corrosion rate (and current density), was demonstrated by the sample artificially aged at $150^{\circ}C$ / 5 h.

Cyclic polarization tests revealed a high susceptibility of the $AlSi1MgMn$ alloy to localized pitting corrosion in a 3.5% NaCl aqueous solution for all test samples. The damage observed on the tested surfaces after cyclic polarization was significantly larger and deeper than after the Tafel method of electrochemical corrosion testing.

Microstructure analysis confirmed the achievement of a desirable microstructure with the selected heat treatment parameters, characterized by evenly dispersed fine precipitates of Mg_2Si in the aluminum matrix.

In future research, it is recommended to conduct additional mechanical tests to determine the dependence of tensile strength, yield strength, elongation, and toughness on heat treatment parameters.

Acknowledgement:

The authors wish to acknowledge the projects KK.01.1.1.07.0045 "Development of an anti-corrosion protection system for the multi-purpose use of pipes", funded from the Ministry of Science and Education of Republic Croatia and The Central Agency for Financing and Contracting Programs and Projects of the European Union (SAFU) for their financial support.

REFERENCES

- [1] Liščić, B., Tensi H. M., Canale, L. C.F., Totten, G. E.: Quenching Theory and Technology, 2nd Edition, CRC Press, 2010
- [2] Zhang J, Song B, Wei Q, Bourell D, Shi Y. A review of selective laser melting of aluminum alloys: Processing, microstructure, property and developing trends. *J Mater Sci Technol.* 2019;35(2):270–84
- [3] Vončina M, Kresnik K, Volšak D, Medved J. Effects of homogenization conditions on the microstructure evolution of aluminium alloy EN AW 8006. *Metals (Basel).* 2020;10(3)
- [4] Krishna Pal Singh Chauhan. Influence of Heat Treatment on the Mechanical Properties of Aluminium Alloys (6xxx Series): A Literature Review. *Int J Eng Res.* 2017;V6(03):386–9
- [5] Mac Kenzie D. S. Heat treating aluminum for aerospace applications. *Heat Treat Prog.* 2005;5(4):36–43.
- [6] Milkereit B, Wanderka N, Schick C, Kessler O. Continuous cooling precipitation diagrams of Al-Mg-Si alloys. *Mater Sci Eng A.* 2012;550:87–96
- [7] Milkereit B, Starink MJ, Rometsch PA, Schick C, Kessler O. Review of the quench sensitivity of aluminium alloys: Analysis of the kinetics and nature of quench-induced precipitation. *Materials (Basel).* 2019;12(24)
- [8] Milkereit B, Kessler O, Schick C. Determination of Critical Cooling Rate for Hardening Aluminum Alloys using HyperDSC. *Perkin Elmer.* 2010;375:1–6.
- [9] Li N, Zheng J, Zhang C, Zheng K, Lin J, Dean TA. Investigation on fast and energy-efficient heat treatments of AA6082 in HFQ processes for automotive applications. *MATEC Web Conf.* 2015;21:0–6
- [10] Staley J.T., Tiryakioglu M. The use of TTP curves and quench factor analysis for property prediction in aluminum alloys. *Adv Metall Alum Alloy.* 2001;(December):6–15
- [11] Popov, B. N.: Corrosion Engineering: Principles and Solved Problems, Elsevier, 2015
- [12] Lisac, E.S., Korozića i zaštita konstrukcijskih materijala, Sveučilište u Zagrebu, Fakultet kemijskog inženjerstva i tehnologije, Zagreb, 2007
- [13] Juraga I, Alar V., Stojanović I.: Korozića i zaštita premazima, Fakultet strojarstva i brodogradnje, Zagreb, 2014



COMMENTS ON ULTRASONIC THICKNESS MEASUREMENT DEVIATIONS

Damir Markučić

University of Zagreb, Faculty of Mechanical Engineering and Naval Architecture, Ivana
Lučića 5, Zagreb, Croatia

Abstract

Basic requirement for accreditation of inspection bodies or testing laboratories that perform ultrasonic wall thickness measurement is to provide the evidence that the measurements are performed in compliance with approved and valid procedure. Unfortunately, inspection bodies in Croatia do not refer to ISO 16809 standard for that purpose. ISO 16809 standard provides systematic and comprehensive representation of all relevant aspects that shall be considered to achieve results that can be reliably used for decision regarding the minimum acceptable wall thickness. Nevertheless, experience from practice shows that ultrasonic wall thickness measurements are in many cases performed not following the ISO 16809 technical requirements so there is no evidence or information about the accuracy or uncertainty of the measurement results. Hence this paper is going to provide the overview and case analysis of the most influencing factors contributing to the deviations of the ultrasonic thickness measurement results.

Keywords: *ISO 16809, ultrasonic wall thickness measurement, uncertainty, accuracy, ISO/IEC 17020, ISO/IEC 17025*

1. INTRODUCTION

One of the critical inspection activities for the integrity assessment of the structures, especially pressure equipment, is wall thickness measurement. For this purpose ultrasonic method is commonly used. Taking into account only pressure equipment, companies performing ultrasonic wall thickness measurement shall be accredited as inspection bodies or as testing laboratories according to ISO/IEC 17020 [1]) or ISO/IEC 17025 [2] respectively. In that case the reference standard providing technical requirements for ultrasonic wall thickness measurements is ISO 16809 [3].

Standard ISO 16809 [3] provides very comprehensive representation of all relevant aspects that shall be considered. Beside general requirements and provisions for selection of the probes and instruments for certain application conditions, the most useful parts of the standard are clauses 8 and 9 discussing influences on accuracy and influences of measured component and material.

Since, one could rarely find that inspection bodies use and/or rely on the ISO 16809 technical requirements and specifications in the practice in Croatia, this paper is going to present several case analyses of the most influencing factors contributing to the deviations of the ultrasonic thickness measurement results.

2. DISCUSSION OF INFLUENCING FACTORS

There are quite a number of influencing factors explained in clauses 8 and 9 in ISO 16809 standard, like: surface condition and temperature, metallic and non-metallic coatings, geometry of the component, equipment resolution. Furthermore, acoustical parameters are also relevant: ultrasonic probe features, inhomogeneity and anisotropy of the material, acoustical attenuation, condition of reflecting surface and as well conditions of contact surface. This paper will discuss **only** the most influencing factors as they were revealed as the most significant from the observed measurement performances and round robin tests organised by our NDT laboratory at the Faculty, such as:

- a) measurement mode used
- b) surface coatings
- c) contact surface conditions
- d) ultrasound velocity
- e) calibration procedure / ultrasonic probe type

2.1 Measurement mode used

Standard ISO 16809 [3] introduces 4 measurement modes that can be used although 3 measurement modes can be commonly found in the practice. These are presented on Figure 1.

Measurement **mode 1** is inherent for the older types of ultrasonic thickness gages. Dual or single-element probes can be used. Since the Time Of Flight (TOF) in this mode is measured from an initial excitation pulse to a first returning ultrasonic pulse, which is “*single-echo mode*”, it provides the worst accuracy in comparison to other two measurement modes because all relevant conditions on the contact and reflecting surface will contribute to the deviations, and consequently errors of the measurement results. Setting the “zero correction” is essential to reduce the measurement error.

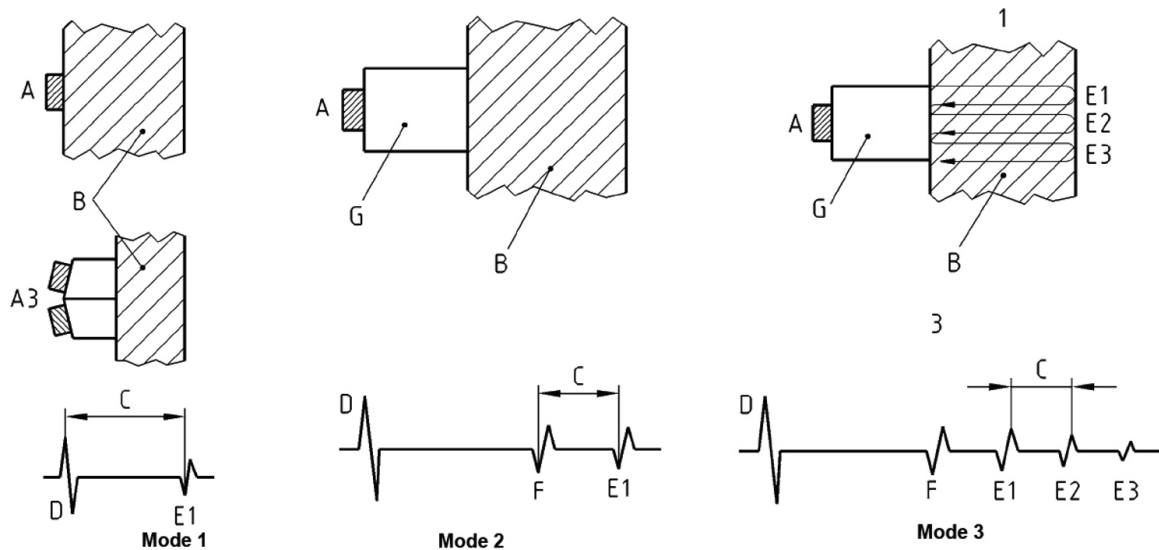


Fig. 1: Ultrasonic thickness measurement modes [3]

Measurement **mode 2** measures the TOF from the end of a delay line to the first back wall echo. Dual or single-element probes can be used. It is also known as “*single-echo delay line mode*”.

Measurement **mode 3**, also known as “*multiple-echo mode*”, measures the TOF between back wall echoes. The accuracy of this measurement mode can be further improved using the averaging algorithm for TOF between E1 and E2, E2 and E3, E1 and E3 divided by 2, etc. Accordingly, this mode can be assumed to provide the best accuracy, since the TOF between multiple echoes is not affected by surface (interface F) conditions.

2.2 Surface coatings

Ultrasonic wall thickness measurement is commonly applied within in-service inspection of the pressure equipment vessels. This application assumes measurement through the coatings, usually non-metallic coatings, as it is shown on Figure 2.



Fig. 2: Ultrasonic wall thickness measurement through the coating

This kind of the setup implies specific arrangement of the echoes as it is presented on the Figure 3.

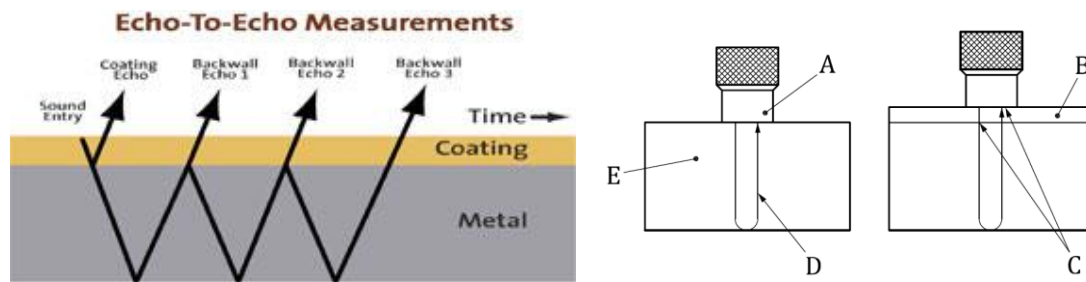


Fig. 3: A series of multiple ultrasonic echoes travelling through the coating

It is obvious that the TOF through the coating has to be subtracted to obtain the accurate result. For example: the true thickness of the parent material is 3,1 mm ("D" on the Figure 3) and the coating thickness is 100 μm ("B" on the Figure 3). The velocity of the ultrasonic longitudinal wave is 5920 m/s, while the ultrasound velocity through the non-metallic coating is approximately 2100 m/s. As the ultrasonic gage is calibrated to 5920 m/s, the calculated result will be 3,282 mm (e.g. 3,3 mm displayed depending on the resolution of the gage) instead of 3,1 mm, giving the measurement error of 0,2 mm (TOF for the ultrasonic path "C" on the Figure 3). It is especially tricky that this kind of error overestimates the true wall thickness which can mislead the acceptance decision and integrity assessment of the measured component. So, for the ultrasonic measurements through the coatings the usage of measurement mode 3 is preferable to avoid such measurement errors. If mode 2 or mode 1 is used than the ultrasound velocity need to be known and correction of the result is required.

2.3 Contact surface condition

Probably it is irrelevant to mention that the contact area should be clean of corrosion products, especially during the in-service inspection of tanks and pipelines where very often quite corroded surfaces can be found. Given that inspectors mostly take care about adequate preparation of corroded surfaces we found that surface profile, roughness and temperature are often neglected.

Figure 4 clearly indicates the problems of placing the ultrasonic probe contact surface to the object surface. Obviously, such situations can significantly contribute to deviations and/or errors of measurement results.

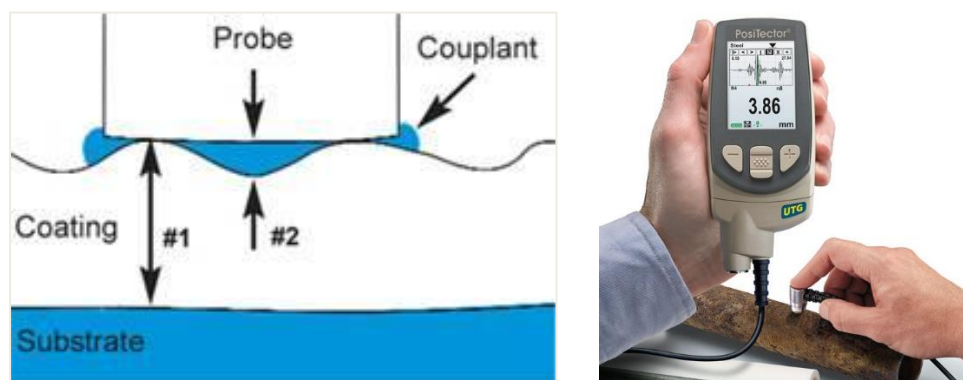


Fig. 4: A series of multiple ultrasonic echoes travelling through the coating

ISO 16809 standard does not refer to other standards for ultrasonic testing, however the requirements set by general principles for ultrasonic testing [4] provide the following provisions:

- The gap between the probe and the surface should not exceed 0,5 mm [5].
- Surface finish of $R_a = 6,3 \mu\text{m}$ for machined surfaces and $12,5 \mu\text{m}$ for shotblasted surfaces are recommended [5].

One can undoubtedly understand the order of magnitude of the measurement errors that can occur from these values. Consequently, the measurement results shall not be considered more accurate than the surface conditions allow.

Minor changes in the surface temperature, or minor difference between the temperature of the calibration block and object surface will not result in significant deviations of the measurement results. If this values for temperature changes and/or differences are of greater amount, special care and procedure is required.

2.4 Ultrasound velocity

While the most probes are designed for use between -20°C and $+60^\circ\text{C}$, the care about influence of the material temperature on ultrasound velocity over this temperature range is often neglected.

While the longitudinal wave velocity in most steels changes only by approximately $0,8 \text{ ms}^{-1}\text{C}^{-1}$, the influence of temperature on velocity in acrylic is $2,5 \text{ ms}^{-1}\text{C}^{-1}$. Since the acrylic is normally used for probe delays in specific situations the compensation or special calibration procedure shall be applied. It means that temperature difference between calibrating the probe on the calibration block and on the surface that is measured shall be minimal.

If the temperature difference between the calibration block and contact surface is for example 10°C , what is commonly assumed as not important, the temperature in the acrylic (which is probe delay material) will adjust to the surface temperature during the measurements since the probe is in contact with the surface. Temperature difference of 10°C will result in ultrasound velocity change of 25 ms^{-1} in acrylic, which is already 1 % of the nominal velocity in the acrylic. It is not necessary to mention that the probe delay setting on the gage will not be valid anymore in such situation contributing to the error of the measurement results.

Considering the ultrasound velocity influence on accuracy of measurement results obtained on steel structures primarily assume the difference between ultrasound velocities in calibration block steel and steel that is measured. In order to promptly analyse this kind of influence, let's take as a possibility that the difference in ultrasound velocities between calibration block and measured material is only 60 ms^{-1} , since the ISO standards for calibration blocks [6, 7] allow the tolerance for the longitudinal wave velocity in "calibration steel" $\pm 30 \text{ ms}^{-1}$. The difference of 60 ms^{-1} is approximately 1 % of the velocity that is set on the ultrasonic gage, consequently resulting with the same measurement result error. Therefore, for the nominal wall thickness of 10 mm the error resulting from this type of "influence" will be 0,1 mm.

2.5 Calibration procedure

Not having on mind (subjective) human factor contributing to the calibration procedure only (objective) setting factors will be discussed.

Today, ultrasonic gages have option for automatic calibration, available also with only one calibration thickness. Assuming the linearity of the ultrasonic gages (algorithm based on the TOF is linear), calibrating the linear function with only one reference point mathematically is not achievable for unknown ultrasound velocity. Although such option is possible on ultrasonic gages, two reference points are minimally required to define accurately linear response. Thus, automatic calibration using only one reference point can result in higher magnitude of measurement errors. Therefore, the calibration using two calibration thicknesses is must when higher accuracies are required.

Another aspect regarding reference (calibration) thickness(es) is value of the calibration thickness(es) in relation to the nominal thickness to be measured. Standard practice commends to use calibration thickness which is as close as possible to the measured thickness. The best measuring results will be achieved when two thicknesses are used, a little bit thicker calibration thickness and thinner calibration thickness in comparison with the measured thickness. Despite these provisions are taught on training courses in the practical applications different routines could be observed.

The significant influencing factor that sometimes is not taken into account is setting the V-path correction. This is valid only for dual-element probes, coming from the design of the probe, actually because of the ultrasound path for which the TOF is measured. In that case the ultrasound path is not the double wall thickness but the longer path in shape of the “V” letter as it is shown on the Figure 5.



Fig. 5: Dual-element probes and ultrasound V-path

Unfortunately, technicians are not aware of magnitude of measurement error that can result if V-path is not set properly. What is more important the common perception is that the V-path is not so important when measuring thin wall thicknesses that is quite opposite to the mathematical calculations presented in the Table 1.

Older ultrasonic gages and even new “simple” and cheap ultrasonic gages, do not have option for V-path correction setting. In that case, it is mandatory to correct the obtained results with the value inherent for the obtained value of the result. Table 1 presents the orientational values of errors, that are corrections.

Tab. 1: Errors if the V-path correction is not set

Wall thickness t , mm	Distance along the ultrasound path s , mm	Measurement error e , mm
9	9,22	0,22
8	8,25	0,25
7	7,28	0,28
6	6,32	0,32
5	5,39	0,39
4	4,47	0,47
3	3,61	0,61
2	2,83	0,83
1	2,24	1,24

3. FINAL REMARKS

Actually, all the aspects presented in this paper are fairly known and they are mandatory content for the training courses leading to the certification of personnel performing ultrasonic thickness measurements. Nevertheless, experience from the practice seems very different. NDT laboratories and inspectors very often do not take care about performance capabilities of the equipment used or about achieved accuracy and/or uncertainty of the measurement results. Results of the round robin measurements presented on Figures 6 and 7, nicely indicate that the more serious attention is missing for different influencing factors discussed above.

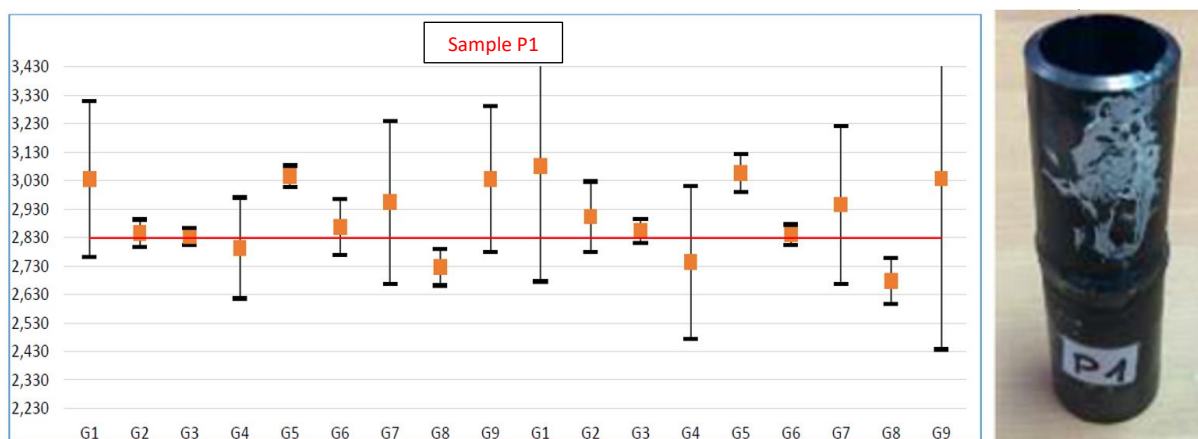


Fig. 6: Round robin results for measuring the pipe wall thickness

The round robin measurements were run by different “groups” (G) consisting of different technicians, probes, gages and working instruction how to calibrate the gage.

The interval of the measurement deviations on Figure 6 (pipe) is from -0,4 mm to +0,5 mm and even more for some groups.

The interval of the measurement deviations on Figure 7 (steel plate) is from -0,6 mm to +0,6 mm.

Some of the groups achieved very good precision, meaning small deviations of the results, but this could give wrong self-perception for the group as being good and accurate, since the systematic errors are obvious despite good precision, particularly on Figure 7.

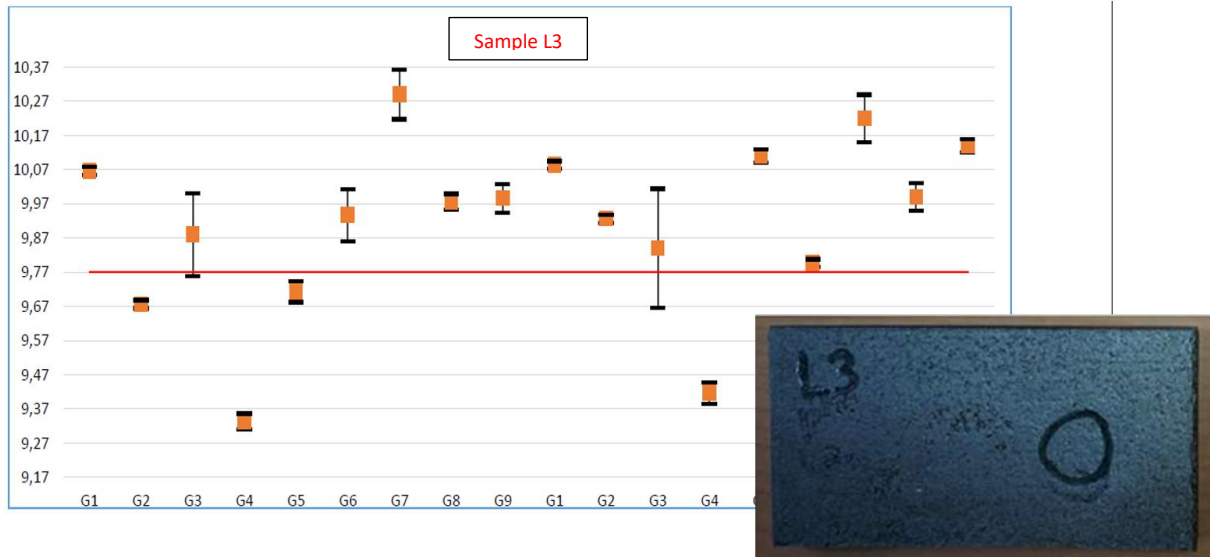


Fig. 7: Round robin results for measuring the steel plate thickness

Especially, results of the groups G2, G4 and G5 on Figure 7 are critical, showing high precision but underestimating the wall thickness that could mislead to the wrong nonacceptance of the structure that is inspected.

Hence, the intention of this paper is to remind for the importance of the presented aspects giving the quantified examples of resulting deviations. Presentation of the round robin results indicates that the overall contribution of the mentioned influencing factors can be very severe, regardless of whether it is about magnitude of the precision or systematic errors.

REFERENCES

- [1] ISO/IEC 17020:2012 — Conformity assessment — Requirements for the operation of various types of bodies performing inspection
- [2] ISO/IEC 17025:2017 — General requirements for the competence of testing and calibration laboratories
- [3] ISO 16809:2017 — Non-destructive testing — Ultrasonic thickness measurement
- [4] ISO 16810:2012 — Non-destructive testing — Ultrasonic testing — General principles
- [5] ISO 16827:2012 — Non-destructive testing — Ultrasonic testing — Characterization and sizing of discontinuities
- [6] ISO 2400:2012 — Non-destructive testing — Ultrasonic testing — Specification for calibration block No. 1
- [7] ISO 7963:2022 — Non-destructive testing — Ultrasonic testing — Specification for calibration block No. 2

PA ULTRAZVUČNO ISPITIVANJE TRAČNICA ZAVARENIH AT POSTUPKOM

PA ULTRASONIC TESTING OF AT WELD JOINTS IN RAILS

Aleksandar Dragojević¹, Ivica Garašić², Tomislav Kezele²

¹ IDEF d.o.o., Kranjčevićeva 30, Zagreb, Hrvatska

² Sveučilište u Zagrebu, Fakultet strojarstva i brodogradnje, Ivana lučića 1, Zagreb, Hrvatska

Sažetak

U ovom radu provedeno je usporedno ispitivanje s dva različita ultrazvučna sustava na aluminotermijskim zavarenim spojevima tračnice. Ispitivanje je provedeno konvencionalnim sustavom i višepretvorničkim sustavom. Podešavanje osjetljivosti provedeno je na umjetno napravljenim reflektorima na uzorku tračnica, dok je usporedbeno ispitivanje provedeno na tračnici sa stvarnim pogreškama. Zbog složene geometrije tračnice i vrste pogrešaka koje mogu nastati samo ispitivanje može biti izazov u odabiru sustava i tehnike ispitivanja. Cilj rada je prikazati s obzirom na ograničenja ultrazvučnih sustava rezultate ispitivanja koji ukazuju na prednost višepretvorničkog ultrazvučnog sustava u odnosu na konvencionalni sustav.

Ključne riječi: *ultrazvučno ispitivanje, aluminotermijski zavareni spoj, ispitivanje tračnica.*

Abstract

In this paper, a comparative test with two different ultrasonic systems was performed on the aluminothermic welded joints of the rail. The test was carried out with a conventional system and a phased array system. Sensitivity adjustment was carried out on artificially made reflectors on rail and a comparative test on the rail with real imperfections. Due to the complex geometry of the rail and the type of errors that can occur, the test itself can be a challenge in selecting the test system and technique. The aim of the paper is to show, considering the limitations of ultrasound systems, test results that indicate the advantage of a phased array ultrasound system compared to a conventional system.

Keywords: *ultrasonic testing, aluminothermic welded joint, rail inspection.*

1. UVOD

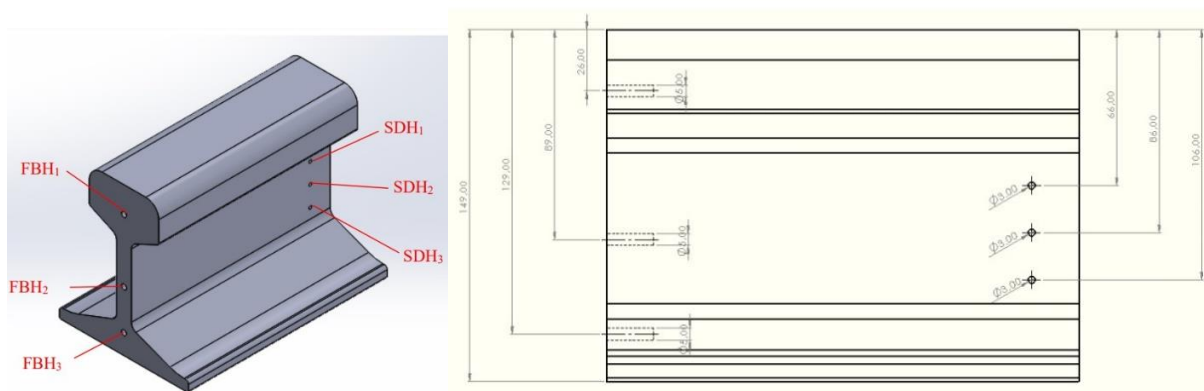
Aluminotermijsko zavarivanje je postupak zavarivanja tračnica termitnom smjesom pri čemu se uslijed egzotermne reakcije oduzima kisik željeznom oksidu te nastaje rastaljeno željezo koje služi kao dodatni materijal. Osnovni materijal i kalup se predgrijavaju plinskim plamenom (acetilen-kisik ili propan butan-kisik) na temperaturu oko 900-1000 °C. Egzotermnom reakcijom se postiže temperatura od približno 2450 °C te se nakon ciklusa predgrijavanja i formiranja taline otvara ispust pa uz gravitacijsko djelovanje dolazi do popunjavanja kalupa. Kvalitetna priprema kalupa i pregrijavanje nužni su za miješanje taline i osnovnog materijala tračnice te formiranje zavarenog spoja. Nakon završene aluminotermijske reakcije kalup se razbija i višak materijala se mehanički uklanja. Kao posljedica neodgovarajuće metode i tehnologije zavarivanja ovisno o postupku, pripremi i kvaliteti materijala mogu nastati nepravilnosti u zavarenom spoju koje se mogu detektirati nerazornim metodama ispitivanja.

U ovom radu razmatrana je problematika detekcije jedne vrste pogrešaka u aluminotermijskom zavaru tračnice konvencionalnim ultrazvučnim (UT-Ultrasonic Testing) ispitivanjem i višepretvorničkim ultrazvučnim (PA-UT – Phased array ultrasonic testing) ispitivanjem. Ispitivanje su se provodila po gaznoj površini tračnice simulirajući situacije ispitivanja zavarenih spojeva kada nije moguće provoditi ispitivanje na vratu ili stopi tračnice zbog nedostupnosti ili neodgovarajuće površine potrebne za provedbu ultrazvučnog ispitivanja.

Provjera oba sustava provedena su na referentnom uzorku poznatih umjetno napravljenih reflektora. Nadalje, usporedba rezultata ispitivanja provedena je na aluminotermijskom zavarenom spoju s realnom pogreškom u vratu tračnice.

1.1. Referentni uzorak za provjeru osjetljivosti sustava

Prije početka provođenja ispitivanja odabrani ultrazvučni ispitni sustav potrebno je odgovarajuće podesiti. S ciljem provjere podešavanja osjetljivosti ultrazvučnog sustava izrađen je referentni etalon s bočnim provrtima oznaka SDH₁, SDH₂ i SDH₃ promjera 3 mm prema slici 1 [2].



Slika 1. Referentni uzorak i nacrt umjetno napravljenih reflektora

Podešavanje osjetljivosti ultrazvučnog sustava

Odabrani ultrazvučni sustav u okviru ovog istraživanja sastoji se od dva ultrazvučna uređaja Krautkramer GE USM36 i GE Mentor UT 32:128, te svaki od uređaja ima pripadajuće ultrazvučne sonde odgovarajućih karakteristika kako bi se osiguralo prozvučavanje ispitivanog volumena tračnica [2]. Odabrani ultrazvučni sustav s pripadajućim etalonima za podešavanje i odabranom vrstom kontaktnog sredstva prikazan je u Tablici 1.

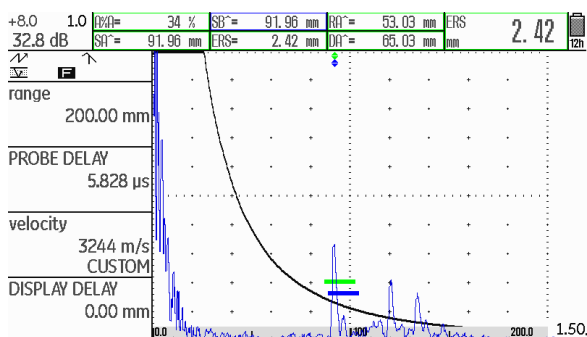
Tablica. 1: Korištena oprema i sredstva UT i PA-UT sustava

Sustav	Naziv uređaja	Sonda	Etalon	Kontaktno sredstvo
UT	Krautkramer GE USM36,	MWB 45 -2 SWB 45 - 2	V2 V1	GE – ZG-F
PA-UT	GE Mentor UT 32:128,	PA-2M8E1P,	PAUT IIW block	

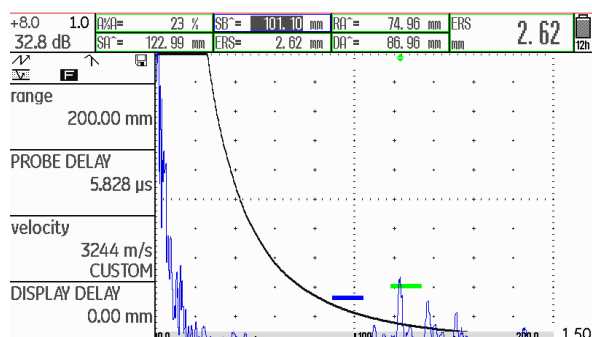
Za svaki odabrani ultrazvučni sustav provedena je provjera podešavanja osjetljivosti na izrađenom referentnom etalonu (slika 1). U tom smislu za svaku kombinaciju odabira ultrazvučnog uređaja i pripadajuće ultrazvučne sonde provjera osjetljivosti je provedena na ukupno tri bočna provrta oznaka SDH₁, SDH₂ i SDH₃. Rezultati podešavanja osjetljivosti nalaze se u Tablici 2.

Tablica. 2: Prikaz provjere osjetljivosti na radnom etalonu ovisno o sustavu i referentnom mjestu

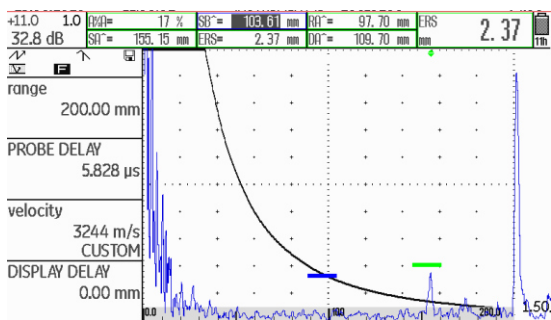
Sustav	Reflektor	Prikaz reflektora na radnom etalonu		Procjena veličine Ø mm (ERS)/dubina mm (DA)	
		MWB 45 -2	SWB 45 - 2	MWB 45 -2	SWB 45 - 2
UT	SDH ₁	Slika 2	Slika 5	2.42/65	3.29/66
	SDH ₂	Slika 3	Slika 6	2.62/86	2.81/85
	SDH ₃	Slika 4	Slika 7	2.37/109	2.70/106
PA-UT		PA-2M8E1P		Dubina indikacije mm (DA)	
	SDH ₁	Slika 8		66,6	
	SDH ₂	Slika 9		85,8	
	SDH ₃	Slika 10		106,7	



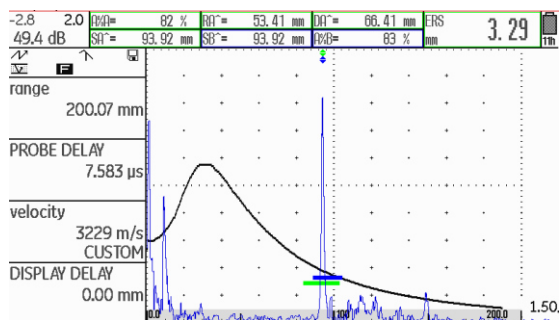
Slika 2. Prikaz odjeka od referentnog reflektora SDH₁ (MWB 45-2)



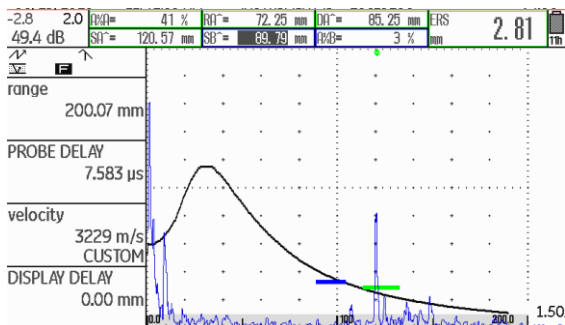
Slika 3. Prikaz odjeka od referentnog reflektora SDH₂ (MWB 45-2)



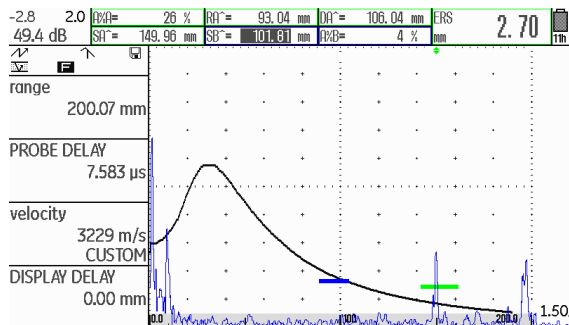
Slika 4. Prikaz odjeka od referentnog reflektora SDH₃ (MWB 45-2)



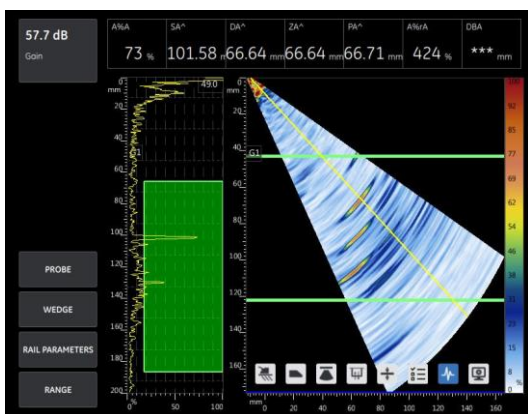
Slika 5. Prikaz odjeka od referentnog reflektora SDH₁ (SWB 45-2)



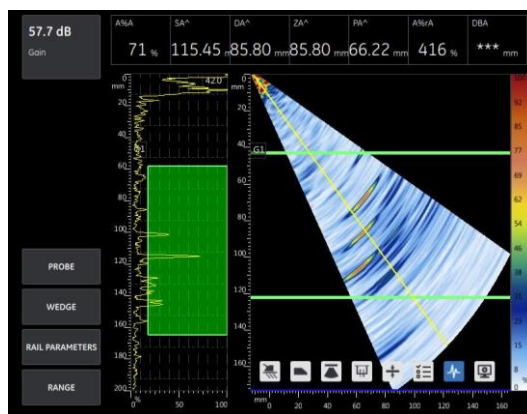
Slika 6. Prikaz odjeka od referentnog reflektora SDH₂ (SWB 45-2)



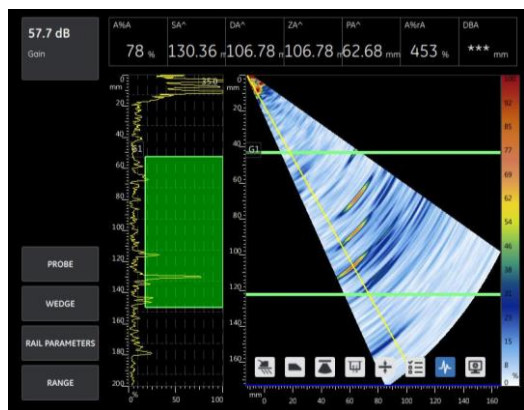
Slika 7. Prikaz odjeka od referentnog reflektora SDH₃ (SWB 45-2)



Slika 8. Prikaz odjeka od referentnog reflektora SDH₁ (PA-2M8E1P)



Slika 9. Prikaz odjeka od referentnog reflektora SDH₂ (PA-2M8E1P)



Slika 10. Prikaz odjeka od referentnog reflektora SDH₃ (PA-2M8E1P)

1.2. Zaključak provjere podešavanja osjetljivosti na referentnom etalonu

Podešavanje osjetljivosti primjenom konvencionalnog ultrazvučnog sustava (dvije ultrazvučne sonde) provedeno je prema beskonačnom reflektoru na etalonu V2 – R50 i V1- R100 te je konstruirana DGS krivulja na promjeru \varnothing 1,5 mm. S ciljem provjere podešenosti osjetljivosti konstruirana je krivulja prema bočnom provrtu SDH2. Usporedbom amplitudnih odziva nisu uočene značajne razlike u procjeni veličine reflektora (ERS).

Prema dobivenim rezultatima i odjecima na A prikazu uređaja može se zaključiti da su rezultati ostvareni sa sondom SWB 45-2 za ovu vrstu tračnice i referentnih reflektora bolji u odnosu na rezultate ostvarenih sa sondom MWB 45-2 kako je prikazano u Tablici 2 [2].

Podešavanje osjetljivosti PA-UT sustava provedeno je prema bočnim provrtima na referentnom uzorku SDH1, SDH2 i SDH3. U svrhu boljeg podešavanja osjetljivosti korištena je funkcija TCG-a (Time Corrected Gain), te je dobivena ujednačena osjetljivost uzimajući u obzir poziciju reflektora u vratu tračnice (Slika 8, Slika 9 i Slika 10) [1].

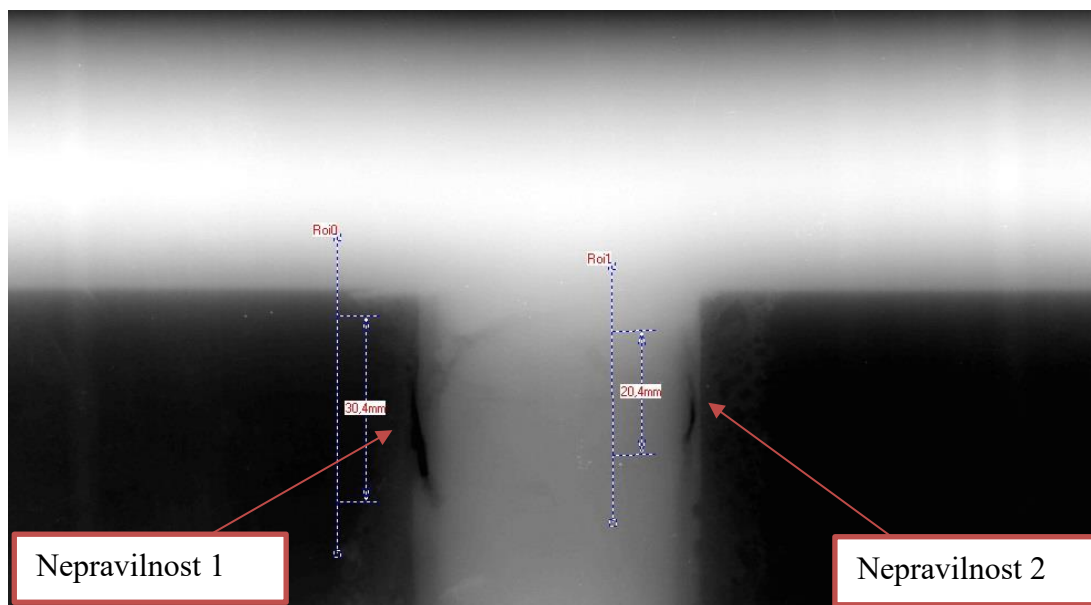
2. Referentni uzorak s nepravilnostima u vratu tračnice

Referenti uzorak aluminotermijski zavarenih tračnica (Slika 11) ima više vrsti nepravilnosti u vratu tračnica, te je prethodno ultrazvučnom ispitivanju provedeno računalno radiografsko ispitivanje – cRT s ciljem točnijeg određivanja vrste nepravilnosti.

Dobiveni odzivi od nepravilnosti primjenom UT i PAUT ultrazvučnog ispitivanja usporedit će se s onima dobivenim primjenom računalne radiografije.



Slika 11. Referentni uzorak tračnice



Slika 12. Radiogram referentong uzorka tračnice s prikazanim vrijednostima parametara nepravilnosti

Tablica. 3: Korištena oprema i ispitni parametri cRT sustava

Metoda	Oprema	Ispitni parametri
cRT	rendgenski uređaj – Balteau 300d	veličina fokusa: 2x2,5 mm FF: 700 mm, napon: 175 kV struja: 4 mA vrijeme ekspozicije: 2,5 min
	skener – VMI 5100	napon lasera: 15 V napon fotomultiplikatora: 5,25 V rezolucija skeniranja: 50 µm
	slikovna ploča	kodak industrex flex Blue 10 x 12"

2.1 Pogreške u aluminotermijskim zavarenim spojevima tračnica

Od nepravilnosti se pri aluminotermijskom zavarivanju najčešće pojavljuju:

- Pukotine; pukotine nastaju kao posljedica vlačnih naprezanja prilikom hlađenja. To je posebno naglašeno u području metala zavara pri solidifikaciji i situaciji niskih okolišnih temperatura.
- Porozitet i plinski uključci; najčešće nastaju kao posljedica vlage u području spoja koja može doći iz nečistoća i masnoće te kondenzata u kalupu. Također, ako je dodatni materijal (porcija) kontaminiran u metalu zavara je česta pojava pora.
- Šupljine; nastaju kod skrućivanja rastaljenog materijala u kalupu posebno kada nema dovoljno dodatnog materijala (neodgovarajuća porcija ili istjecanje kroz neodgovarajuće postavljene, zabrtvljene ili puknute kalupe). Prilikom solidifikacije dolazi do smanjenja volumena (fenomen skupljanja zavara) pa ako prilikom

zavarivanja nije postignuto dovoljno miješanje veća je i vjerojatnost pojave šupljina.

- Naljepljivanje; nastaje kao posljedica nedovoljnog predgrijavanja osnovnog materijala ili neprilagođavanja tehnologiji niskim temperaturama okoliša. Iz tog razloga se striktno traži ovisno o gradaciji čelika postizanje i držanje temperature predgrijavanja kako bi se postiglo dobro miješanje sa stranicama žlijeba tj. osnovnim materijalom tračnice.
- Uključci; u metalu zavora mogu se pojaviti i nemetalni uključci nastali iz kontaminiranog praška u porciji ili npr. oksidni uključci nastali kao rezultat loše pripreme spojne površine te neodgovarajuće kvalitete rezanja plinskim plamenom. Također, mogu ostati i uključci od pijeska za brtvljenje.
- Nepravilna geometrija zavora na stopi, vratu i kruni tračnice; nastaju zbog lošeg postavljanja ili krive geometrije kalupa. Pri ovome je svakako važna uvježbanost i vještina operatera koji postavljaju kalup.



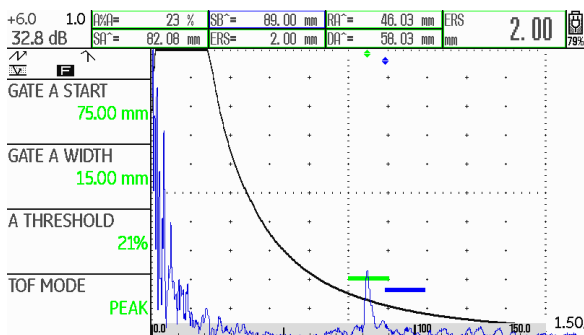
Slika 13. Prikaz makrostrukture u vratu tračnice bez nepravilnosti

Na slici 12. vidljiva je šupljina uz područje intenzivnog nepovezivanja rastaljenog metala i stijenke tračnice. Uzrok predmetnoj nepravilnosti može se tražiti u neodgovarajućem toku rastaljenog metala u kalup pri čemu je došlo do turbulencije taline i neravnomjernog skrućivanja. Dodatno, ako stijenka tračnice nije dovoljno predgrijana ne dolazi do dovoljnog miješanja. Iz ove situacije dodatno se naglašava važnost adekvatne pripreme i predgrijavanja stijenke te savjesnosti i uvježbanosti operatera.

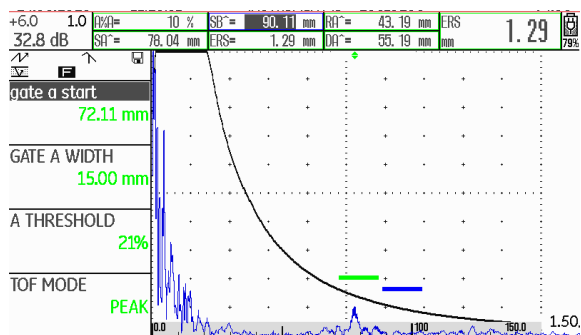
3. REZULTAT ISPITIVANJA REFERENTNOG UZORKA TRAČNICE I ZAKLJUČAK

Tablica. 4: Rezultati ispitivanja referentnog uzorka tračnice

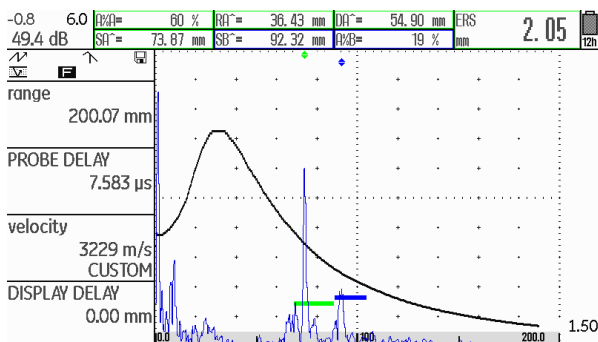
Sustav	Reflektor	Prikaz reflektora na radnom etalonu		Procjena veličine (ERS)		Procjena duljine
		MWB 45 - 2	SWB 45 - 2	MWB 45 - 2	SWB 45 - 2	
UT	Nepravilnost 1	Slika 14	Slika 16	2.00	2,05	3-5 mm
	Nepravilnost 2	Slika 15	Slika 17	1.29	1.50	2-4 mm
		PA-2M8E1P				
PA-UT	Nepravilnost 1	Slika 17				21 mm
	Nepravilnost 2	Slika 18				12,6 mm



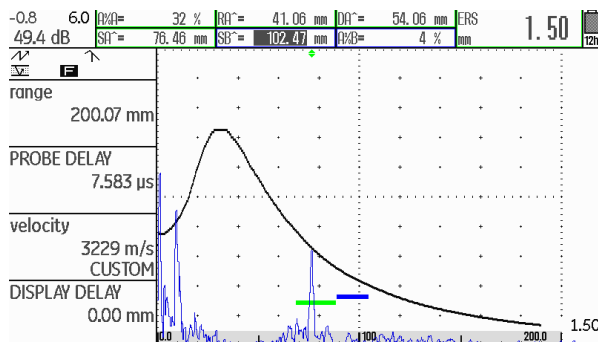
Slika 14. Prikaz odjeka od nepravilnosti 1 (MWB 45-2)



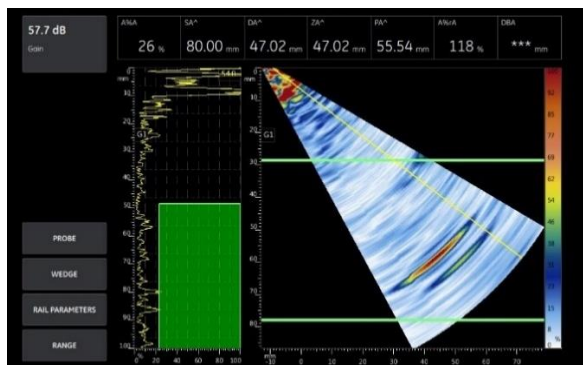
Slika 15. Prikaz odjeka od nepravilnosti 2 (MWB 45-2)



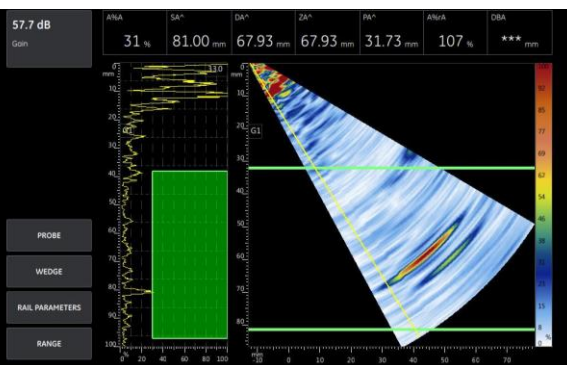
Slika 16. Prikaz odjeka od nepravilnosti 1 (SWB 45-2)



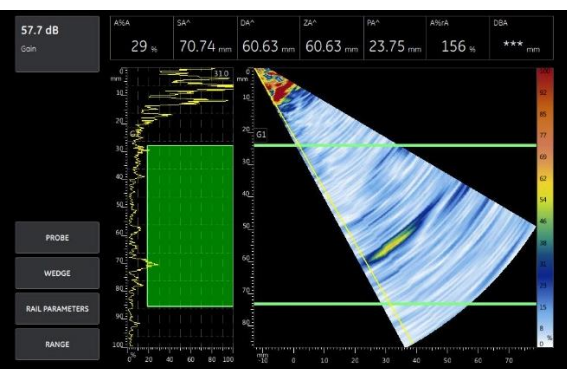
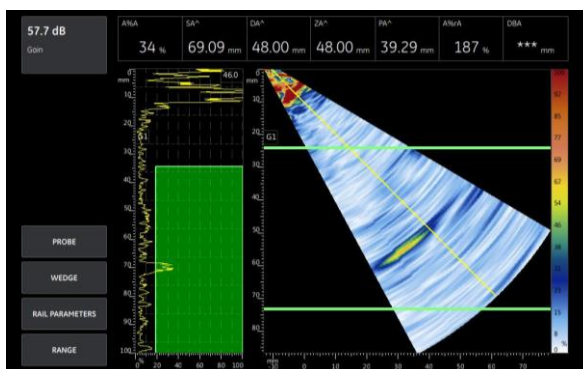
Slika 17. Prikaz odjeka od nepravilnosti 2 (SWB 45-2)



Slika 18. Prikaz odjeka od nepravilnosti 1 (PA-2M8E1P)



Slika 19. Prikaz odjeka od nepravilnosti 2 (PA-2M8E1P)



ZAKLJUČAK

Uslijed eksploatacije može doći do razvoja pukotina unutar zavara tračnice te je odabir odgovarajuće metode i tehnike provedbe nerazornog ispitivanja od velikog značaja.

S obzirom na ograničenja ultrazvučnih sustava prikazanih u ovom radu, rezultati ispitivanja ukazuju na prednost višepretvorničkog ultrazvučnog sustava (PA-UT) u odnosu na konvencionalni sustav. Prednost spomenutog sustava posebno je vidljiv prilikom pronalaska nepovoljno orijentiranih indikacija u uskim dijelovima vrata tračnice. Prema ostvarenim rezultatima procjene veličine nepravilnosti kao i njezine uvjetne duljine primjenom konvencionalnog ultrazvučnog sustava može se zaključiti da se ne radi o značajnim nepravilnostima. Prema spomenutom, zavareni spoj sukladno kriteriju prihvatljivosti može se ocijeniti kao prihvatljiv za daljnju uporabu u uvjetima eksploatacije. Međutim, rezultati ostvareni primjenom višepretvorničkog sustava jasno ukazuju suprotno.

REFERENCES

- [1] HRN EN 14730-1:2010 Željeznički sustav — Željeznički gornji ustroj — Aluminotermijsko zavarivanje tračnica — 1. dio: Odobravanje postupaka zavarivanja (EN 14730-1:2010)
- [2] Jagodić N., Ispitivanje ultrazvukom aluminotermijskih zavarenih tračnica. Diplomski rad Zagreb: Sveučilište u Zagrebu, Fakultet strojarstva i brodogradnje, 2022. urn:nbn:hr:235:536312



ULTRASONIC CHARACTERIZATION OF ADDITIVELY MANUFACTURED SAMPLE

Maria Grozdanić¹, Morana Mihaljević¹

¹ University of Zagreb, Faculty of Mechanical Engineering and Naval Architecture, Ivana Lučića 5, Zagreb, Croatia

Abstract

Mechanical, physical, and acoustic properties are directional dependent in additively manufactured parts due to the process of building parts, usually layer by layer. Generally, destructive methods are used to characterize and inspect additively manufactured parts, but also using non-destructive testing is becoming more common. Since the propagation of ultrasonic waves through the material enables the determination of the properties of the material, ultrasonic testing (UT) has found its application in the characterization of additively manufactured parts. This paper investigated whether the manufacturing process affects selected properties in two perpendicular directions: in the direction of the layer and the build-up direction. Directional dependence was researched by determining the velocity of longitudinal waves and Young's modulus. The Pulse overlap technique was used for ultrasonic velocity measurement on the additively manufactured sample. The statistical method and comparison with the reference value determined whether selected properties differ in different directions.

Keywords: *additive manufacturing, ultrasonic characterization, pulse overlap, direction-dependent properties*

1. INTRODUCTION

Additive manufacturing (AM) is an advanced fabrication method that enables the production of customizable components with higher complexity by adding materials layer by layer according to the 3D model [1]. Generally, destructive methods are used to characterize and inspect additively manufactured parts, but also non-destructive testing (NDT) is becoming more and more common on AM parts. They replace destructive methods to determine different mechanical and physical properties of materials. Since the propagation of ultrasonic waves through the material enables the determination of the mechanical properties of the material, ultrasonic testing (UT) has found its application in the characterization of additively manufactured parts [2]. Usually, UT is used to detect defects and determine mechanical properties [3]. By measuring the time-of-flight between two back wall echoes in the time domain the ultrasonic velocity can be calculated. The ultrasonic velocity is one of the relevant factors for material characterization [4]. One of the possible applications is that by measuring the ultrasonic wave velocities within the specimen the material elastic constants can be determined, for instance, Young's modulus, E (by knowing longitudinal wave velocity, v_L), and shear modulus G (by knowing transverse wave velocity, v_T).

In addition to many advantages of AM, such as higher product quality, flexibility in the development and production of parts with complex internal geometries, along with lower costs and shorter development and production times, AM also has negative effects on AM parts, such as anisotropy and heterogeneity. Microstructures and mechanical properties of AM parts are drastically different from their wrought counterparts [5], therefore, numerous research is conducted on additively manufactured samples. Research carried out so far shows that mechanical properties in AM parts have a strong directional dependence since thermal gradients during solidification can cause variations in pore geometry and anisotropic texture in AM parts [5]. Kok et al. [6] made a detailed review of the anisotropy and heterogeneity of microstructure and mechanical properties for various AM parts. They concluded that the main influencing factors to the anisotropy and heterogeneity of additively manufactured parts were microstructure and manufacturing processes, with an emphasis on AM process parameters. As a result of anisotropy in the microstructure, anisotropic mechanical properties occur, therefore, the ultrasonic velocity and elasticity constants can differ in different directions. Honarvar et al. [7] made an overview of the previous research on the material characterization of AM samples. The main reasons for the effectiveness of the UT method in the characterization of AM parts are additive manufacturing processes and used ultrasonic techniques. The mechanical properties of AM parts depend on the material and process parameters, therefore the AM device must be correctly adjusted before the manufacturing process.

Almost all additive technologies, due to the nature of building parts layer by layer, have direction-dependent properties, which means different properties in the build-up direction than in the direction of the layers. Since the ultrasonic velocity depends on the microstructure and metallurgical state of the material, as well as external influences such as temperature and stress, its change can also occur within the same material, if the material is not of homogeneous structure [8].

Javidrad et al. [9] investigated the effects of changes in the parameters of AM part manufacturing on the elasticity constants of materials in different directions. The elastic constants of the material were determined by determining the ultrasonic velocities in the

samples. Lin et al. [10] carried out the measurement of the time-of-flight of ultrasonic waves and the calculation of the L-wave velocity in different directions in the samples (in the build-up direction and the direction of the layer) on samples of 316L stainless steel made by Selective laser melting process and different power laser. They determined that the L-wave velocity in the direction of the layer is higher than the L-wave velocity in the build-up direction and that with an increase in the density of the material, L-wave velocities increase.

In this work, the influence of the build-up direction of the additively manufactured sample on the characterization of the material was investigated. Directional dependence was researched by determining the velocity of longitudinal waves (L-waves), v_L , and Young's modulus, E , in two perpendicular directions (in the direction of the layer and the build-up direction). At different directions, L-wave velocities were compared with each other, and Young's moduli were compared with a reference value.

2. MATERIALS AND METHODS

2.1 Additively manufactured sample

The sample was made of maraging steel X3NiCoMoTi 18-9-5 on the EOSINT M280 3D printer from EOS GmbH with Direct Metal Laser Sintering (DMLS) manufacturing process. Nominal dimensions of the sample are (140×15×15) mm. The sample is shown in Figure 1.



Fig. 1: Additively manufactured sample

2.2 Experimental setup and ultrasonic velocity measurement procedure

The ultrasonic velocity measurement in different directions in the sample was conducted on an oscilloscope LeCroy 9310AM by the pulse overlap technique and normal probe K5N that has a nominal frequency of 5 MHz, frequency bandwidth of 70 %, and crystal size of 10 mm. The experimental setup is shown in Figure 2.

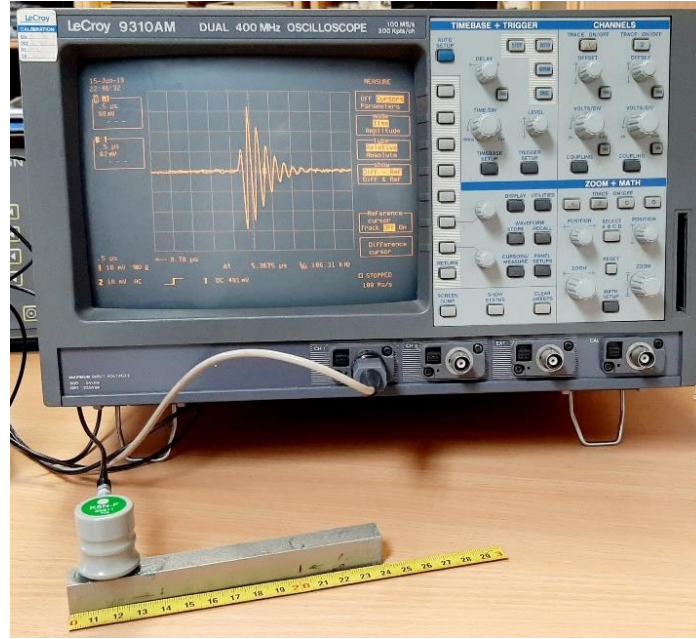


Fig. 2: Experimental setup

The ultrasonic velocity is determined by measuring the time-of-flight (t_{TOF}), which is required for the ultrasonic pulse to travel through the thickness of the measured component (d), provided that the path of the ultrasound (s) is known. The ultrasonic velocity of longitudinal waves (v_L) is calculated according to the equation:

$$v_L = \frac{s}{t_{TOF}} \quad (1)$$

Where s is the double thickness of the measured component, i.e. the path that the ultrasonic pulse travels from the ultrasonic probe to the back wall of the measured component and returns to the probe.

Directional dependence was investigated by determining the ultrasonic velocities at two perpendicular measuring places – one at each side of the sample: MP1 in the direction of the layer (x-axis) and MP2 in the build-up direction (z-axis). Measuring places are shown in Figure 3.

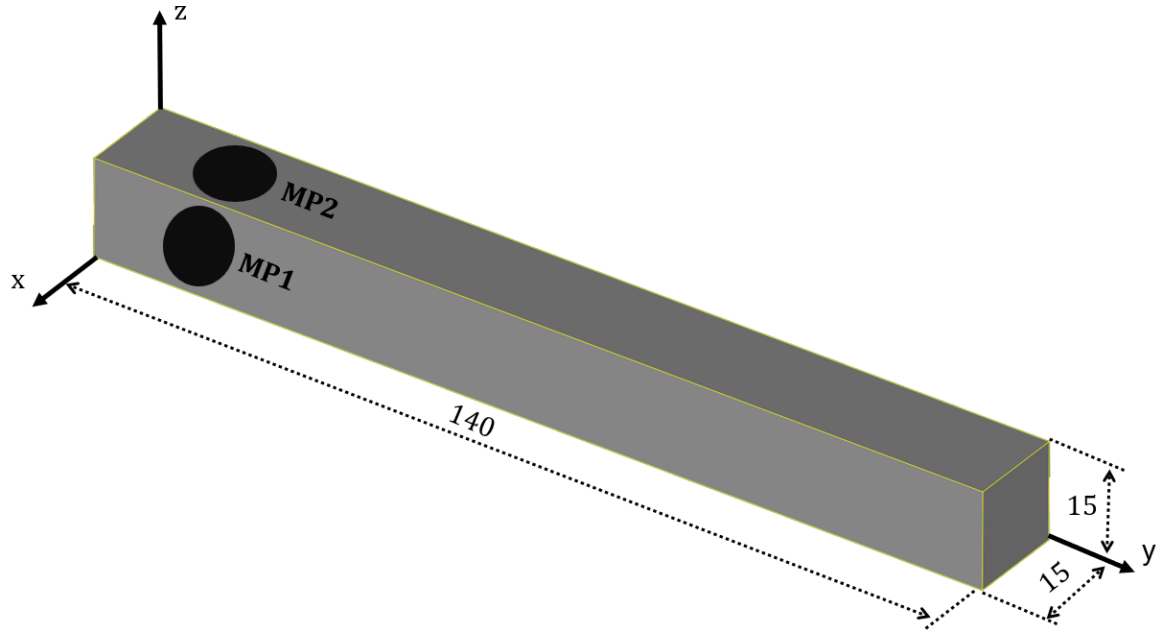


Fig. 3: Measuring places

2.3 Thickness measurement

The thicknesses of the measuring places were measured with Mitutoyo LH-600 digital altimeters. The thicknesses value of measuring places are given in Table 1.

Tab. 1: Thickness of the measuring places

Measuring places	Sample thickness, d mm
MP1	15.09
MP2	14.91

3. RESULTS AND DISCUSSION

3.1 Time-of-flight measurement and ultrasonic velocity calculation

The pulse overlap technique was used to perform TOF measurements. In this technique, TOF is measured by overlapping ultrasonic pulses. Two signals on the oscilloscope display are fitted to fit as visually as possible. The time difference between the first and second back wall echoes was measured. On the pulse overlap it was selected five points (T1 – T5) where the results of the time-of-flight were measured as shown in Figure 4. The measurements were repeated five times at the same measuring place.



Fig. 4: Display of measurement points on two overlapped signals reflected from the back wall of the sample

Calculated L-wave velocities (using equation 1) at the measuring places are shown in Table 2. The ultrasonic velocity is expressed with an expanded measurement uncertainty of 3.6 m/s (with a coverage factor of $k = 2$).

Tab. 2: L-wave velocities at the measuring places

Measuring place	Repeated measurement	L-wave velocity, v_L m/s
MP1	1	5601
	2	5614
	3	5601
	4	5606
	5	5617
	average	5608 ± 3.6
MP2	1	5582
	2	5583
	3	5592
	4	5583
	5	5595
	average	5587 ± 3.6

A visual presentation of the distribution of ultrasonic velocity measurement results is made by using Box plots, shown in Figure 5.

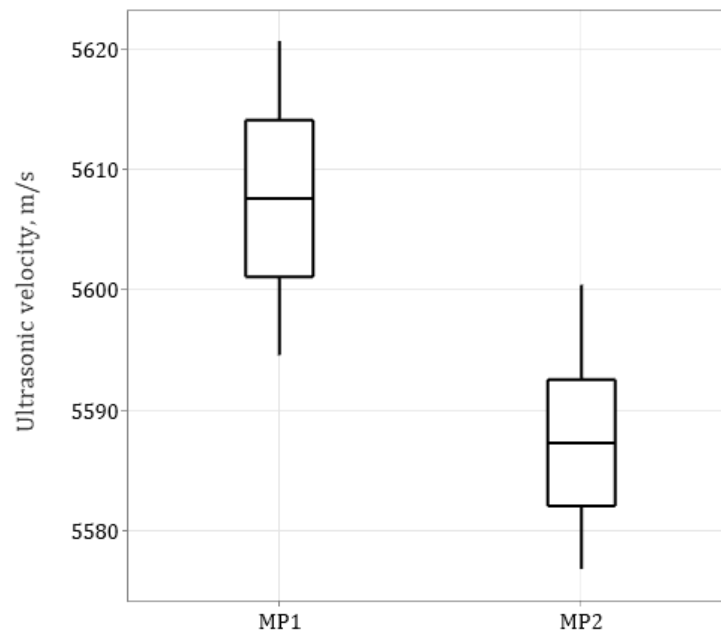


Fig. 5: Box plots for the ultrasonic velocities

Comparing the arithmetic means of the L-wave velocities on MP1 and MP2, that is L-wave velocities in perpendicular directions, the difference is 21 m/s.

It was tested whether the ultrasonic velocities follow a normal distribution so that statistical processing could be performed on them. A probability plot was made, since the probability plot is a graphical technique for assessing if sample data is approximately normally distributed. The probability plot is shown in Figure 6.

Hypothesis are established:

- Null hypothesis: The sample data follows the normal distribution.
- Alternative hypothesis: The sample data do not follow the normal distribution.

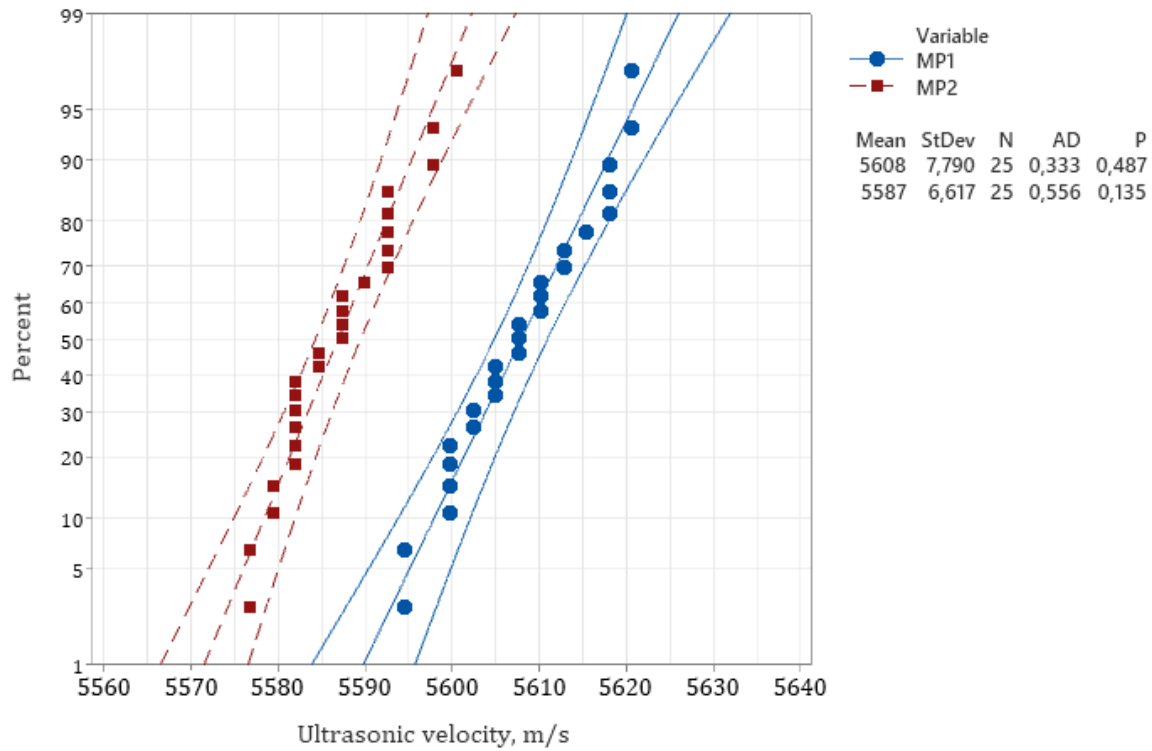


Fig. 6: Probability Plot

Because the P -value is 0.487 on MP1, and 0.135 on MP2, which is greater than the significance level of 0.05 ($P\text{-value} > \alpha$), the decision is to fail to reject the null hypothesis.

To determine whether there is a statistically significant difference between the L-wave velocities means paired t-test was performed. The results are presented in Table 3. For t-test results, first, a confidence interval for the population mean difference was determined. The estimate for the population mean difference is 20.99, with 95 % confidence that the population mean difference is between 17.43 and 24.56. Second, to determine whether a build-up direction affects the ultrasonic velocities, and to determine whether there is a statistically significant difference between the means of the L-wave velocities in two perpendicular directions, P -value is compared to the significance level ($\alpha = 0.05$).

Hypothesis are established:

- Null hypothesis: The mean difference of the ultrasonic velocities is 0.
- Alternative hypothesis: The mean difference of the ultrasonic velocities is not equal to 0.

Tab. 3: Paired t-test

	Mean	Standard deviation	Standard error of the mean	t -value	$t_{crit.}$	P -value
MP1 and MP2	20.99	8.64	1.73	12.15	2.06	< 0.01

Comparing the obtained P -value, which is < 0.01 (the exact P -value is $9.5956 \cdot 10^{-12}$), to the significance level $\alpha = 0.05$, it is evident that the difference between the means is statistically significant ($P\text{-value} \leq \alpha$). The decision is to reject the null hypothesis and conclude that there is a difference in ultrasonic velocities in different directions in additively manufactured sample.

3.2 Young's modulus calculation

Young's modulus is a mechanical property that measures the tensile or compressive stiffness of a solid material when force is applied [11]. Usually, Young's modulus is obtained from the linear elastic region of a uniaxial tensile stress-strain curve and is defined as the ratio of stress to strain during elastic loading. Furthermore, Young's modulus can be estimated by knowing ultrasonic velocities in the material.

L-wave velocity and Young's modulus relate by the following equation:

$$v_L = \sqrt{\frac{E(1-\nu)}{\rho(1+\nu)(1-2\nu)}} \quad (2)$$

where ρ is the material density, and ν is Poisson's ratio.

Material density for maraging steel is 8030 kg/m^3 , and Poisson's ratio is 0.3 [12].

Young's modulus, from equation (2), is:

$$E = \frac{v_L^2 \rho (1+\nu)(1-2\nu)}{1-\nu} \quad (3)$$

The results of Young's moduli are shown in Table 4.

Tab. 4: Young's moduli at the measuring places

Measuring place	Young's modulus, E GPa
MP1	188
MP2	186

The obtained experimental result of Young's modulus, shows that Young's moduli in both directions correspond well with a reference value of $160 \text{ GPa} - 200 \text{ GPa}$ given in MatWeb [13].

4. CONCLUSION

In this paper, the directional dependence of mechanical and acoustic properties of the additively manufactured sample was investigated. The additively manufactured sample

was made of X3NiCoMoTi 18-9-5 maraging steel and produced by Direct metal laser sintering manufacturing process. The time-of-flight in two perpendicular directions, i.e., in the direction of the layer, and the build-up direction, was measured. In both directions, L-wave velocities and Young's modulus were determined. The experimental results showed that the L-wave velocity depends on the direction in which the measurement was performed on the AM sample. The L-wave velocity in the direction of the layer is 5608 ± 3.6 m/s and is higher than the L-wave velocity in the build-up direction which is 5587 ± 3.6 m/s. According to the conducted statistical test, the difference of 21 m/s between ultrasonic velocities in different directions is significant ($P\text{-value} \leq \alpha$). Young's modulus is for 2 GPa different in two perpendicular directions, 188 GPa on MP1 and 186 GPa on MP2, but both values are within the regular values for AM sample material. More uniform material properties, because of a more homogeneous microstructure, can be achieved by subjecting AM sample to appropriate heat treatment. Therefore, further research will be devoted to subjecting the sample to heat treatment and re-taking measurements to determine how much the ultrasonic velocity difference in different directions reduces.

REFERENCES

- [1] G. Ian, D. Rosen, and B. Stucker, *Additive Manufacturing Technologies: 3D Printing, Rapid Prototyping, and Direct Digital Manufacturing*, 2 ed. (no. XXI). Springer New York, NY, 2015, p. 498.
- [2] S. H. Park, K. Y. Jhang, H. S. Yoon, and H. Sohn, "Porosity Evaluation of Additive Manufactured Parts: Ultrasonic Testing and Eddy Current Testing," *Journal of the Korean Society for Nondestructive Testing*, vol. 41, no. 1, pp. 1-10, Feb 2021, doi: 10.7779/jksnt.2021.41.1.1.
- [3] D. Pandey and S. Pandey D. Dissanayak, Ed. *Ultrasonics: A Technique of Material Characterization, Acoustic Waves*. InTech, 2010.
- [4] Z. Keran, M. Mihaljevic, B. Runje, and D. Markucic, "Ultrasonic testing of grain distortion direction in cold formed aluminium profile," *Archives of Civil and Mechanical Engineering*, vol. 17, no. 2, pp. 375-381, Feb 2017, doi: 10.1016/j.acme.2016.11.003.
- [5] C. Kim, H. S. Yin, A. Shmatok, B. C. Prorok, X. Y. Lou, and K. H. Matlack, "Ultrasonic nondestructive evaluation of laser powder bed fusion 316L stainless steel," *Additive Manufacturing*, vol. 38, Feb 2021, Art no. 101800, doi: 10.1016/j.addma.2020.101800.
- [6] Y. Kok *et al.*, "Anisotropy and heterogeneity of microstructure and mechanical properties in metal additive manufacturing: A critical review," *Materials & Design*, vol. 139, pp. 565-586, Feb 2018, doi: 10.1016/j.matdes.2017.11.021.
- [7] F. Honarvar and A. Varvani-Farahani, "A review of ultrasonic testing applications in additive manufacturing: Defect evaluation, material characterization, and process control," *Ultrasonics*, vol. 108, Dec 2020, Art no. 106227, doi: 10.1016/j.ultras.2020.106227.
- [8] V. Krstelj, *Ultrazvučna kontrola*. Zagreb: Sveučilište u Zagrebu, Fakultet strojarstva i brodogradnje, 2003.
- [9] H. R. Javidrad and S. Salemi, "Determination of elastic constants of additive manufactured Inconel 625 specimens using an ultrasonic technique," *International Journal of Advanced Manufacturing Technology*, vol. 107, no. 11-12, pp. 4597-4607, Apr 2020, doi: 10.1007/s00170-020-05321-x.

- [10] Y. Lin, D. Zou, G. Ye, and J. Liang, "Density Analysis of Additive Manufactured Metal Parts Using Laser Ultrasonics," ed. *2021 3rd International Academic Exchange Conference on Science and Technology Innovation (IAECST)*, Guangzhou, China, 2021, pp. 953-956.
- [11] "Britannica." britannica.com. <https://www.britannica.com/science/Youngs-modulus> (accessed March 15, 2023).
- [12] "MatWeb." matweb.com. <https://www.matweb.com/search/DataSheet.aspx?MatGUID=adaadfebf20417db13ce8d3683dbccc> (accessed March 15, 2023).
- [13] "Matweb." matweb.com. <https://www.matweb.com/search/DataSheet.aspx?MatGUID=e9f7cb19eb81450d8f67966151bd1802> (accessed March 16, 2023).



RISK ASSESSMENT OF PRESSURE VESSELS BY USING FRACTURE MECHANICS AND ADVANCED ULTRASONIC TESTING

Mirjana OPAČIĆ, Aleksanda SEDMAK, Gordana BAKIĆ, Nenad MILOŠEVIĆ, Nikola MILOVANOVIĆ

Abstract

Risk assessment of cracked cylindrical pressure vessels for compressed air by using basic fracture mechanics and advanced methods of non-destructive testing (NDT), such as Phased Array Ultrasound (PAUT) and Time-of-Flight Diffraction (TOFD), is presented. Basic fracture mechanics equations are used to calculate the stress intensity factor, K_I , in the case of unacceptable defects found in the pressure vessel 970 in the Reversible Hydro Power Plant "Bajina Basta", and get the ratio K_I/K_{Ic} , according to the minimum measured values for fracture toughness for welded joints, as the typical zones where crack-like defects are found. The ratio S_{net}/S_c , where S_{net} is the net stress in cross-section with a crack, and S_c is the critical stress, is then evaluated to define the operating point in the Failure Assessment Diagramme (FAD), and thus, to estimate the likelihood of failure of the pressure vessel 970. In combination with estimated high consequence for the pressure vessel 970, the risk matrix was used, as a simple tool to assess the risk. In this paper the focus is on one aspect of this procedure, being the NDT role, since it is of utmost importance to use as precise as possible method for detected defects in welded joints. In this paper advanced ultrasound methods, PAUT and TOFD, are used to get precise image of defects in pressure vessel 970 welded joints, which were previously detected by conventional NDT methods. It is shown that use of PAUT and TOFD is of utmost importance for decision making process in this case.

Keywords: *Structural Integrity; Risk Assessment; PAUT, TOFD*

ANALIZA ELEKTRIČNOG OTPORA ELASTOMERNIH ELEMENATA SUSTAVA PRIČVRŠĆENJA NA KOLOSIJEČNIM KONSTRUKCIJAMA U URBANIM SREDINAMA

ANALYSIS OF ELECTRICAL RESISTANCE OF ELASTOMER COMPONENTS OF THE FASTENING SYSTEMS IN URBAN RAILWAY TRACKS

Katarina Vranešić¹, Stjepan Lakušić¹, Marijana Serdar¹, Vesna Alar²

¹ Sveučilište u Zagrebu, Građevinski fakultet, Kačićeva 26, Zagreb, Hrvatska

² Sveučilište u Zagrebu, Fakultet strojarstva i brodogradnje, Ul. Ivana Lučića 5, Zagreb, Hrvatska

Sažetak

Kod kolosijeka u urbanim sredinama gdje se tračnice koriste kao povratni vodič struje važno je osigurati visoku vrijednost električnog otpora između tračnice i tla i na taj način spriječiti lutajuće struje. Jedna od načina smanjivanja lutajućih struja kod kolosijeka s diskretno oslonjenim i pričvršćenim tračnicama jest korištenje indirektnih sustava pričvršćenja kod kojih je upotrebom izolacijskih materijala spriječen tok struje kroz elemente pričvršćenja. Međutim, glavne karakteristike koje elastomerni elementi moraju zadovoljiti uglavnom su samo krutost i tvrdoća kako bi se utjecalo na smanjivanje visokih razina buke i vibracija uslijed prolaska tračničkog vozila, a električne karakteristike su posljedica primarnih svojstava. U ovome je radu analiziran električni otpor elastomernih podloški različitih sustava pričvršćenja pri čemu je pokazana velika razlika u dobivenim rezultatima. Dodatnom je analizom ustanovljeno da je dobivena razlika posljedica različitog sastava elastomernog materijala, odnosno ovisi o punilima koja se dodaju kaučuku prilikom procesa vulkanizacije.

Ključne riječi: kolosijek, sustav pričvršćenja, lutajuće struje, električni otpor, podtračničke podloške

Abstract

For tracks in urban areas where the rails are used as current return conductors, it is important to ensure a high value of rail-to-earth resistance to prevent stray currents. For tracks with discretely supported and fastened rails, stray current can be reduced by using an indirect fastening system in which current flow through the fasteners is prevented by the use of insulating material. However, the most important properties that elastomeric elements must meet are stiffness and hardness to reduce high noise and vibration levels, and the electrical properties are a consequence of the primary properties. In this work, the electrical resistance of elastomeric pads of different fastening systems was analysed, and a large difference in the result was found. Additional analysis showed that this difference is due to the different composition of the elastomer material, i.e. it depends on the fillers added to the rubber during the vulcanization process.

Keywords: track, fastening system, stray current, electrical resistance, elastic rail pad

1. INTRODUCTION

Due to its large capacity and velocity, rail transport has become the main type of public transportation in many cities around the world. Urban railways must be able to withstand high traffic load, which is ensured by modernising the track structure, using different types of the tracks, different fastening systems, etc. Track structures can be divided based on their location, construction, type of rail fastening system, etc. In the city of Zagreb, tracks with discretely supported and fastened rails are used, where the rail is supported every 1 m on a levelling layer and fastened using different types of the fastening system - on the steel plate, which is laid on on the rail pad 2 and levelling layer made from concrete reinforced with microsyntetic fibers (Fig. 1b). Fastening is ensured by using the clips and T-bolts or anchor bolts, depending on the type of the fastening system.

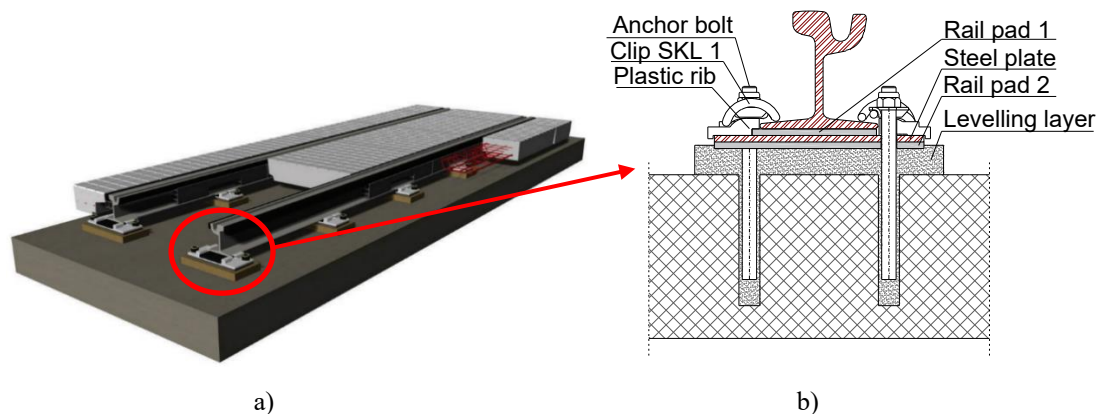


Fig. 1: a) track with discretely fastened rail, b) cross section of fastening system [1]

The primary role of the rail fastening system is to position and fasten the rail and to transfer the vehicle load from the rails to the track substructure. However, during the construction of the track structure, care must also be taken to ensure that the rail and fasteners are isolated from the other track elements to successfully reduce the high values of stray currents. Since today the rails are mostly used as the return current path from the vehicle to the traction power station (TPS), if rails and fastening systems are not completely insulated (i.e., if sufficient rail-to-ground resistance is not achieved), the return current can leak from the rail [2,3]. This current is called stray current. The current leaves the rail because it finds a path of lower electrical resistance to return to the source, which is usually buried metal pipelines located near the track [4].

Stray currents cause devastating localized corrosion (stray current-induced corrosion) at the points where the current leaks from the metal structure into the electrolyte (concrete, ground, water) [5]. Stray current corrosion causes great material losses, resulting in high maintenance costs mostly on buried metal pipelines and reinforced concrete structures. This type of corrosion is also noticed on the metal elements of the track structure, especially the rail foot and the metal components of the fastening system [2,6-9]. Because of these negative consequences, it is important to prevent stray currents at the source, i.e., at the track, which is usually obtained by increasing rail-to-ground resistance [10]. In tracks with discretely fastened rails, fastening points are “discharge” points for the current, since only at these points rail is connected to the ground [11]. Therefore, stray current can be prevented by using fastening systems with higher electrical resistance, or to simplify a bit: by using a fastening system whose elastic components prevent current from flowing from the rail through the fastening system into the track substructure [11].

However, electrical resistance of the fastening system in most cases is not one of defined characteristic, which is also shown in paper [12], where the electrical resistance of various types of fastening systems used on tracks with discretely fastened rails was analysed. The electrical resistance depends on the type of fastening system and the electrical resistance of its elastomer components. However, even though elastomer components (rail pads, pads under the steel base plate, pads for anchor bolts) are used, it is not necessary that fastening system has high electrical resistance. Elastomer elements are manufactured from a rubber in vulcanization process [13]. During vulcanization, various additives are added to the rubber – fillers, pigments, softeners, additives to improve workability, etc. What additive is added depends on the characteristic of the final product. The electrical properties of elastomers depend not only on the type of rubber used, but also on the type and quantity of additives, primarily softeners and fillers [13,14]. The electrical conductivity of the elastomer is increased by the addition of carbon black, which is the most used filler in the vulcanization process. Today, the rubber industry uses more than 90% of the total carbon black consumption. The electrical resistivity of carbon black can vary from 0.44 to 150 Ωcm [13]. Based on the above, it is understandable that the distribution of carbon black in the rubber influences the electrical resistance values of the mixture [13]. The change in the structure of the rubber-filler system during the vulcanization process is also reflected in the change in electrical resistance.

However, if it is required electrical insulation properties above $2.54 \times 10^7 \Omega\text{m}$ fastener stiffness would be compromised. The upper electrical resistance limit of compounds containing carbon black is $2.54 \times 10^6 \Omega\text{m}$. Compounds containing carbon black must be avoided if very high resistance is required, and, in this case, silicone elastomers would have the required electrical insulation performance but poor stiffness properties [15].

The aim of this paper is to detect the electrical resistivity of elastomer components in different types of the fastening systems that are used in tracks with discretely fastened rails and to analyse how the material composition effect on electrical resistivity. Testing method is explained in section 2 and results are presented in section 3.

2. TESTING AND METHODS

Laboratory testing was conducted on elastic components taken from five different types of the fastening system. Four of these fastening systems are used on the tram track in the city of Zagreb, and one is a newly developed fastening system where electrical resistance is one of its defined characteristics. Since in each analysed fastening system all elastic components are made using the same material, the electrical resistivity was measured only on rail pad.

During the test, rail pad was placed directly on a steel base plate and a rail was placed on the pad. Due to the high weight of the rail placed on the pad, good contact was achieved between the steel plate and the elastomeric pad and between the elastomeric pad and the rail. The rail was connected to the laboratory power supply, which generated a 26 V DC current. The circuit was closed through a steel base plate (Fig. 2a). It was assumed that the current flows from the rail to the steel base plate through the entire contact area of the observed elements (area marked in yellow in Fig. 2b).

The current intensity and voltage were measured continuously using the multimeter on each sample over a period of 1 hour and data were recorded on the computer.

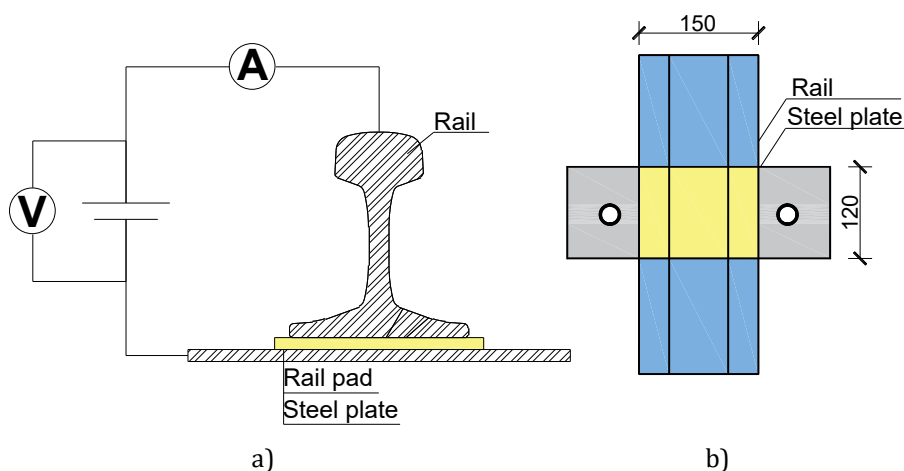


Fig. 2: a) Measurement of electrical resistance of rail pad placed between the steel plate and rail, b) rail pad-rail and rail pad-steel plate contact area

After the measurement, the electrical resistivity of all testing samples was calculated. To determine whether the different values of electrical resistivity are a consequence of the different material composition of the tested samples, the samples with the lowest and the highest measured value were selected for further analysis using Fourier transform infrared spectroscopy (FTIR) (Fig. 3).



Fig. 3: FT-IR Spectrometer, IRTracer-100: SHIMADZU (Shimadzu Corporation)

Infrared spectroscopy is based on the fact that most molecules absorb light in the infrared region of the electromagnetic spectrum and convert it into molecular vibrations [16]. This absorption corresponds to the bonds in the molecule. With a spectrometer, absorption of infrared radiation by the sample material is measured in relation to the wavelength [16,17]. Infrared spectroscopy was used to detect differences in the recorded vibration bands of the observed test samples, indicating the different composition of the sample materials.

In addition, elemental analysis on carbon, hydrogen and nitrogen (CHN analysis) was carried out a CHN analyzer, and the proportion of each element was determined according to the ASTM D5291 standard [18].

3. RESULTS

Based on the collected data, the value of the electrical resistivity of the elastic pad was calculated based on the expression:

$$\rho = R \cdot \frac{S}{l} \quad (1)$$

Where:

- ρ [Ωm] – electrical resistivity,
- R [Ω] – electrical resistance calculated using the Ohm's Law and measured value,
- S [m^2] – area of cross section of conductor in current circuit,
- l [m] – length of the conductor in current circuit.

Since the electrical resistance of rail and steel plate in comparison with the elastic pad is very low, it was neglected so in this current circuit it was assumed that measured electrical resistance is the resistance of the elastic pad. Because of this reason, in equation 1 the characteristics of the elastic pad were only taken. In all observed cases, the analyzed area of cross section is the contact area of the pad and rail foot, and it is 0.018 m^2 ($0.15 \times 0.12 \text{ m}$). The height of all analysed rail pads is 0.01 m . The results of calculated electrical resistivity are shown in Fig. 4.

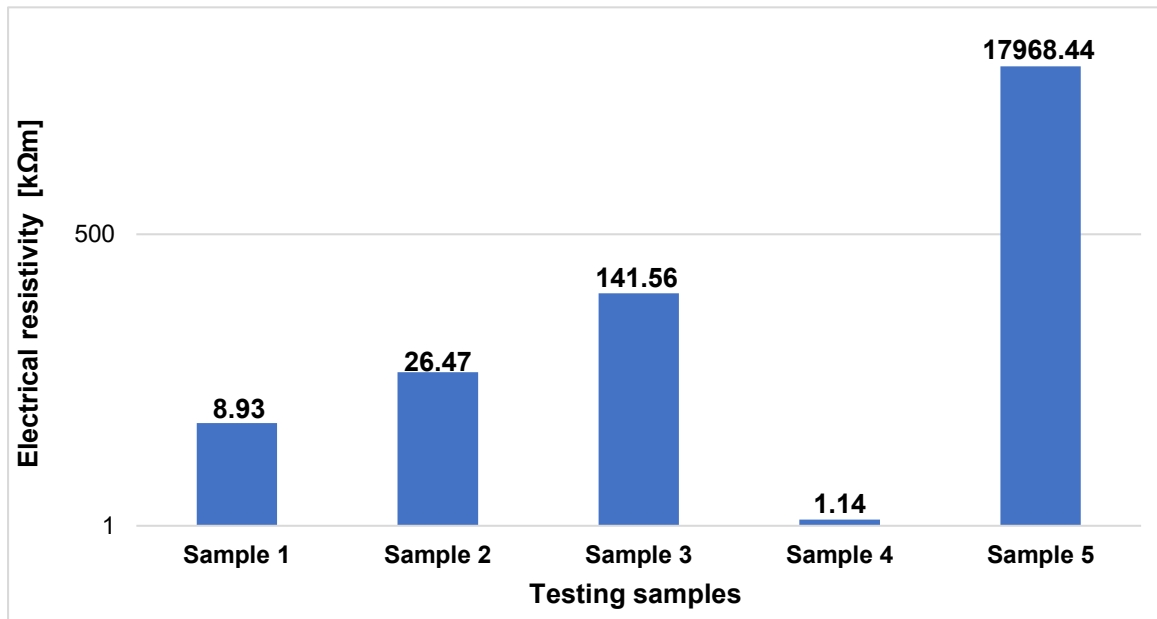


Fig. 4: Calculated electrical resistivity from the tested elastic pads

As it can be seen from the Fig. 4, electrical resistivity values of the analysed pads are very different, indicating that electrical resistance is not one of their defined properties. Only in the case of the sample 5 very high electrical resistance value of the pad was obtained. To confirm that the reason for the differences in electrical resistivity was due to the different material composition, samples 4 and 5 were subjected to further analysis using Fourier transform infrared spectroscopy (FTIR). The spectrums of the two test samples recorded with a Fourier transform infrared spectrometer (FTIR) are shown in Fig. 5. The vertical axis is the transmittance, which indicates how strongly light was absorbed at each frequency. The solid line shows the transmittance values for each wavelength that passed

through the sample. The peaks visible in the wavenumber and transmittance diagrams are called absorption bands. A molecule has a large number of covalent bonds, and each bond has different vibrational modes, so the IR spectrum of a compound usually has multiple absorption bands. The horizontal axis indicates the position of an absorption band, but instead of using frequency to represent absorbed radiation, wavenumbers are commonly used in IR spectra. Since values of transmittance and wavenumber for absorption bands are different in obtained diagram, it can be concluded that material composition of these testing samples is different. Characteristic bands with the wavenumber and transmittance are shown in Tab. 1.

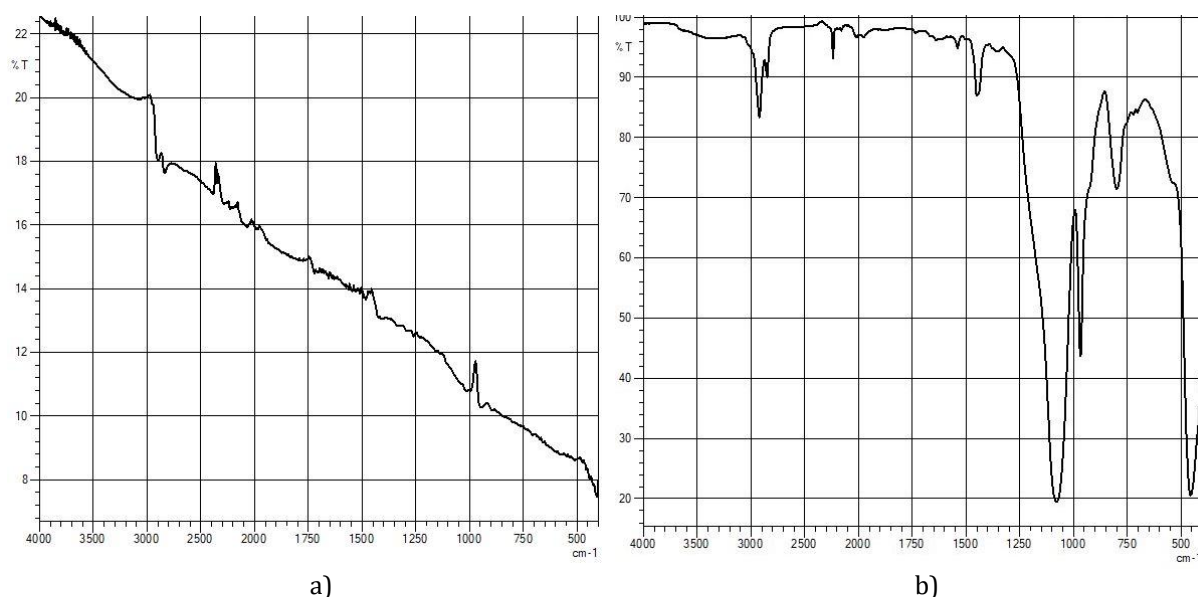


Fig. 5: Spectrum of testing sample 4 (a) and 5 (b)

Tab. 1: Wavenumber and transmittance for characteristic absorption bands of samples 4 and 5

Sample 4		Sample 5	
Wavenumber [cm ⁻¹]	Transmittance [%]	Wavenumber [cm ⁻¹]	Transmittance [%]
2840	17.6	2920	83.5
2450	18.0	2210	93.0
1452	14.0	1450	86.5
970	11.7	1075	19.5
		960	43.5
		800	71.5
		450	20.5

Elemental analysis on carbon, hydrogen and nitrogen (CHN analysis) was carried out and the results of the sample analysis using the elemental analysis technique of CHN are shown in Tab. 2. Through this analysis, it was found that carbon, hydrogen and nitrogen make up 91.64% of the composition of the material in sample 4 and 64.23% in sample 5.

Therefore, it is concluded that the low value of electrical resistivity in sample 4 is a consequence of the high percentage of carbon, while the reduction of carbon and the use of other fillers amounting to 35.77% in sample 5 achieves a very high value of electrical resistivity.

Tab. 2: The proportion of carbon, hydrogen, and nitrogen in rail pads of the samples 4 and 5

	Percentage of material [%]	
	Sample 4	Sample 5
Carbon	82.56	52.13
Hydrogen	6.14	6.57
Nitrogen	2.94	5.53
Total:	91.64	64.23

From the above results, it can be concluded that the composition of the material used in the vulcanization process to produce elastomeric elements plays an important role in the properties of the final product. Therefore, to successfully prevent stray currents, it is necessary to determine in advance the electrical resistivity value that the elastomeric elements must meet.

4. CONSLUSION

To reduce stray current on tracks with discretely fastened rails, it is important to ensure high electrical resistance of the fastening system. This can be achieved by isolating the components of the fastening system, i.e., preventing direct contact of the fasteners or contact of the fasteners with the rail, using the elastomeric elements with high electrical resistance.

However, as can be seen from the tests carried out, the value of electrical resistance is not usually one of the parameters defined during the manufacture of the elastomeric elements of the fastening system, but is a consequence of their primary function, which is to achieve a certain level of hardness and stiffness to effectively reduce the high noise and vibration levels caused by rail traffic.

It can be concluded that the prevention of stray currents is still a secondary characteristic that is not given much attention during track construction and reconstruction. However, considering the increasing demands on track structures and the increasing traffic loads to which tracks are subjected, the reduction of stray currents must become one of the characteristics of tracks to reduce the maintenance costs of the surrounding structures, which are threatened by harmful corrosion processes due to stray currents.

REFERENCES

- [1] Vranešić K., Lakušić S., Serdar M., Influence of Stray Current on Fastening System Components in Urban Railway Tracks, *Applied Science*, 2023, 13 (9)
- [2] Peng P., Zeng X., Leng Y., Yu K., Ni Y., A New On-line Monitoring Method for Stray Current of DC Metro System, *IEEJ Trans Electr Electron Eng*, 2020, 15 (10), pp. 1482–1492
- [3] Ogunsola A., Sandrolini L., Mariscotti A., Evaluation of stray current from a DC-electrified railway with integrated electric-electromechanical modeling and traffic simulation, *IEEE Trans Ind Appl*, 2015, 51 (6), pp. 5431–5441
- [4] Tzeng, Y.S., Lee, C.H., Analysis of rail potential and stray currents in a direct-current transit system, *IEEE Trans Power Deliv*, 2010, 25 (3), pp. 1516–1525
- [5] Chen, Z., Koleva, D., Van Breuge, K., A review on stray current-induced steel corrosion in infrastructure, *Corrosion Reviews*, 2017, 35 (6), pp. 397–423
- [6] Juybari, E.Z., Gholami, A., Evaluation of Ground Systems Performance on Rail Potential and Stray Current in Tehran Railway System, *Journal of Modeling & Simulation in Electrical & Electronics Engineering (MSEEE)*, 2022, 4 (1), pp. 43-49
- [7] Xu, W., Zhang, B., Deng, Y., Wang, Z., Jiang, Q., Yang, L., et al., Corrosion of rail tracks and their protection, *Corrosion Reviews*, 2021, 39 pp. 1–13
- [8] Kurth, J.C., Krauss, P.D., McGormley, J. C., Harper, J., Accelerated Corrosion Study of Direct-Fixation Fasteners, *Corrosion Conference and Expo 2015*. Dallas, Texas, USA: NACE International, pp. 1–16 (2015)
- [9] Ye, J., Cao, X., Long, Y., Li, Y., Liu, L., Liang, Y., Application of spectrum detection technology in rail-ground transition resistance of urban rail transit, *IEEE Int Conf High Volt Eng Appl ICHVE* (2022)
- [10] Lin, S., Zhang, J., Liu, X., Zhang, X., Cai, Z., Chen, X., Study on Distribution Characteristics of Metro Stray Current and Evaluation of Cumulative Corrosion Effect, *Adv Civ Eng*, 2022.
- [11] Charalambous, C.A., Comprehensive Modeling to Allow Informed Calculation of DC Traction Systems' Stray Current Levels, *IEEE Trans Veh Technol*, 2017, 66 (11), pp. 9667–9677
- [12] Vranešić, K., Haladin, I., Lakušić, S., Burnać, K., Convenient Procedure for Measuring the Electrical Resistance of Fastening Systems in Urban Railway Tracks, *Energies*, 2023, 16 (4)
- [13] Vranešić, K., Bhagat, S., Mariscotti, A., Vail, R., Measures and Prescriptions to Reduce Stray Current in the Design of New Track Corridors, *Energies*, 2023, 16 (6252)
- [14] Burcar, D., Ispitivanje svojstava gumenih tvorevina. Sveučilište u Zagrebu, 2010.
- [15] Daniels, L.E., *Track-Related Research: Direct-Fixation Track Design Specifications, Research, and Related Material*; The National Academies Press: Washington, DC, USA, 2005.
- [16] Infracrvena spektroskopija, Aparatura - Analitička oprema i sustavi, <https://aparatura.hr/prodajni-program/infracrvena-spektroskopija>, accessed: 1 September 2023
- [17] Subramanian, A., Prabhakar, V., Rodriguez-Saona, L., Analytical Methods: Infrared Spectroscopy in Dairy Analysis, *Reference Module in Food Science*, 2016, pp. 1–13
- [18] ASTM International - ASTM D5291-10(2015) Standard Test Methods for Instrumental Determination of Carbon, Hydrogen, and Nitrogen in Petroleum Products and Lubricants, ASTM International 2008.

ISPITIVANJE GALVANSKE KOROZIJE U SLANOJ ATMOSFERI

TESTING OF GALVANIC CORROSION IN A SALT ATMOSPHERE

Ivan Stojanović, Vesna Alar, Marin Kurtela

Sveučilište u Zagrebu, Fakultet strojarstva i brodogradnje, Ivana Lučića 5, 10002 Zagreb, Hrvatska

Sažetak

Korozija je nepoželjan rezultat kemijske ili elektrokemijske reakcije između metala ili metalne legure i njegove okoline. Intenzitet korozijskog oštećivanja ovisi o svojstvima okoline u kojoj se nalazi, kao i o značajkama određenog materijala, kao što su: kemijski sastav, stanje površine, oblik i veličina kristalnog zrna, prisustvo zaostalog naprezanja, oblikovanje konstrukcijskog elementa itd. Galvanska ili bimetalna korozija vrsta je korozije koja se odvija pri spajanju najmanje dva materijala različitog potencijala uz prisutnost elektrolita pri čemu dolazi do formiranja galvanskog članka kod kojeg je manje plemeniti, odnosno elektronegativniji metal anoda, a plemenitiji i elektropozitivniji metal katoda. Rezultat razlike potencijala predstavlja napon članka odnosno uzrokuje nastajanje elektromotorne sile koja je tim veća što je razlika potencijala veća, što u konačnici uzrokuje trošenje anode. U eksperimentalnom dijelu rada prikazani su rezultati ispitivanja različitih spojeva metala u slanoj komori.

Ključne riječi: *galvanska korozija, slana atmosfera, odabir materijala*

Abstract

Corrosion is an undesirable result of a chemical or electrochemical reaction between a metal or metal alloy and its environment. The intensity of corrosion damage depends on the properties of the environment in which it is located, as well as on the characteristics of a certain material, such as: chemical composition, surface condition, shape and size of crystal grain, presence of residual stress, design of structural element, etc. Galvanic or bimetallic corrosion is a type of corrosion that takes place when at least two materials of different potential are joined in the presence of an electrolyte, resulting in the formation of a galvanic cell in which the less noble or more electronegative metal is the anode, and the more noble and more electropositive metal is the cathode. The result of the potential difference represents the voltage of the cell, that causes the generation of an electromotive force which is greater when the potential difference is greater, which ultimately causes the wear of the anode. In the experimental part of the paper, the testing results of different metal compounds in the salt chamber are presented.

Keywords: *galvanic corrosion, salt atmosphere, material selection*

1. INTRODUCTION

The successful consideration of corrosion prevention and control during the materials selection phase of the design process is key to developing systems which should have good quality, reliability and durability during the expected operating conditions. The process of properly selecting an individual material is very important, because it will not be used only for the manufacture of some individual component or the entire structure, but can be used in combination with other different materials that possess the necessary mechanical, thermal, electrical and physical properties necessary to fulfill the exploitation requirements, and at the same time providing the necessary resistance to the aggressive influence of the environment, i.e. corrosion. In addition to the correct selection of materials, it is of utmost importance that the designer takes care of corrosion prevention and control (CP&C) in the early stages of the project in order to minimize the probability of the appearance of various corrosion phenomena during the working life of the structure. Due to the extremely large number of materials, including the variety of different manufacturing processes and heat treatment, as well as environmental conditions, it is too expensive and almost impossible to test all combinations of materials and environments. For this reason, accelerated laboratory tests, using salt spray or controlled humidity and temperature chambers, are often used to investigate the possibility and time period of a material corrosion or the proper functioning of CP&C technology. [1]

Galvanic corrosion occurs when two metals having different electrical potentials (dissimilar metals) are electrically connected, either through physically touching each other or through an electrically conducting medium, such as an electrolyte. The potential difference established between electrically connected materials in a conducting medium produces electron flow and causes the metal (alloy) with more negative potential to preferentially corrode. The electrochemical corrosion process consists of two partial electrochemical reactions: the anodic partial reaction, consisting of oxidation/dissolution of the metal, and the cathodic partial reaction, consisting of the reduction of water, hydrogen, or oxygen gas (Fig. 1). Each site constitutes a half electrode reaction system, making up two half-cells, like that of a galvanic cell. [1-3]

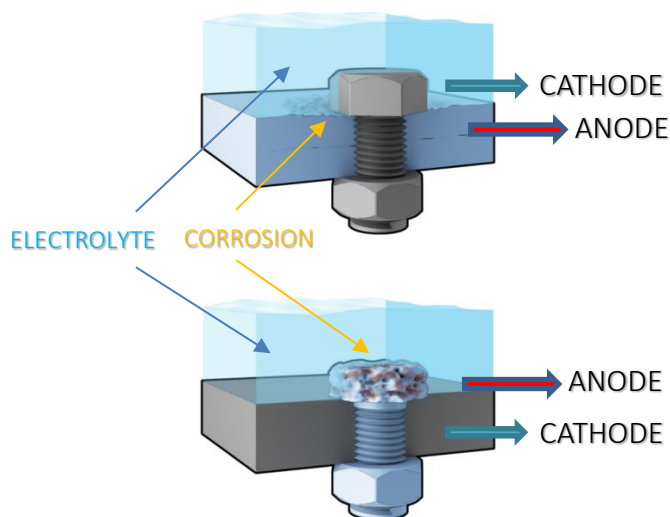


Fig. 1: Galvanic corrosion of different materials in a clamping joint

The metal with a more negative potential preferentially corrodes. The more positive metal acts as a cathode and is cathodically protected by the more negative metal, which becomes the anode (Fig. 2). The corrosion reaction/corrosion current (flow of electrical current) is driven by an electrical potential gradient. The potential difference of two metals is qualitatively determined by their relative placement on the galvanic series where typical electrical potentials for some metallic elements are shown in Fig. 2. A difference of 0.05V between the potentials of two metals/alloys is said to be the critical potential difference for galvanic corrosion to occur [9]; however, the exact value is not only related to the thermodynamic factors, but also depends on the reaction kinetics and the area ratio between the electrodes. Experience shows that galvanic corrosion only occurs when the two metals in contact have a difference in potential of at least 100 mV. [1-6]

Oxidizing Agent		Reducing Agent	Reduction Potential (V)
F_2	$+ 2e^- \rightarrow$	$2F^-$	2.87
H_2O_2	$+ 2H^+ + 2e^- \rightarrow$	$2H_2O$	1.78
MnO_4^-	$+ 8H^+ + 5e^- \rightarrow$	$Mn^{2+} + 4H_2O$	1.51
Au^{3+}	$+ 3e^- \rightarrow$	Au	1.50
Cl_2	$+ 2e^- \rightarrow$	$2Cl^-$	1.36
O_2	$+ 4H^+ + 4e^- \rightarrow$	$2H_2O$	1.23
$Cr_2O_7^{2-}$	$+ 14H^+ + 6e^- \rightarrow$	$2Cr^{3+} + 7H_2O$	1.23
Br_2	$+ 2e^- \rightarrow$	$2Br^-$	1.07
NO_3^-	$+ 4H^+ + 3e^- \rightarrow$	$NO + 2H_2O$	0.96
Ag^+	$+ e^- \rightarrow$	Ag	0.80
I_2	$+ 2e^- \rightarrow$	$2I^-$	0.54
Cu^+	$+ e^- \rightarrow$	Cu	0.52
O_2	$+ 2H_2O + 4e^- \rightarrow$	$4OH^-$	0.40
Cu^{2+}	$+ 2e^- \rightarrow$	Cu	0.34
$2H_2O^+$	$+ 2e^- \rightarrow$	$H_2 + 2H_2O$	0.00
Pb^{2+}	$+ 2e^- \rightarrow$	Pb	-0.13
Sn^{2+}	$+ 2e^- \rightarrow$	Sn	-0.14
Ni^{2+}	$+ 2e^- \rightarrow$	Ni	-0.26
Fe^{2+}	$+ 2e^- \rightarrow$	Fe	-0.45
Cr^{3+}	$+ 3e^- \rightarrow$	Cr	-0.74
Zn^{2+}	$+ 2e^- \rightarrow$	Zn	-0.76
$2H_2O$	$+ 2e^- \rightarrow$	$H_2 + 2OH^-$	-0.83
Mn^{2+}	$+ 2e^- \rightarrow$	Mn	-1.19
Al^{3+}	$+ 3e^- \rightarrow$	Al	-1.66
Mg^{2+}	$+ 2e^- \rightarrow$	Mg	-2.37
Na^+	$+ e^- \rightarrow$	Na	-2.71
Ca^{2+}	$+ 2e^- \rightarrow$	Ca	-2.87
Ba^{2+}	$+ 2e^- \rightarrow$	Ba	-2.91
K^+	$+ e^- \rightarrow$	K	-2.93
Li^+	$+ e^- \rightarrow$	Li	-3.04

Fig. 2: a) Standard reduction potentials v.s. SHE in aqueous solutions at 25 °C [4]

The energy change of the partial corrosion reactions provides a driving force (potential difference) for the process and controls its direction. Electrochemical corrosion reactions have different thermodynamic and kinetic properties than chemical reactions. The energy change of the partial corrosion reactions provides a driving force for the process and controls its direction. There are a number of driving forces that influence the occurrence of galvanic corrosion and the rate at which it occurs. Among these influencing factors are the difference in the electrical potentials of the coupled metals, the relative area, and the system geometry. Other driving forces influencing the promotion or prevention of galvanic corrosion include the polarization (the shift in electrode potential during electrolysis) of the metals, the electrical resistance and electrical current of the system, the type, pH, concentration of the electrolyte and degree of aeration or motion of the electrolyte. The rate of galvanic corrosion in specific environments, however, should not be determined based on the standard electrode potentials of metals. These standard potentials are determined as the potential of a metal in equilibrium with a specific concentration of the electrolyte. The size of the metal components in the galvanic system also influences the rate and degree of corrosion. For example, a system with a relatively large cathode (less stable metal) and a relatively small anode (more stable metal) will corrode via galvanic corrosion to a greater extent than will a system with electrodes of equal size. Furthermore, a system with a relatively large anode compared to a small cathode will not typically exhibit galvanic corrosion on the anode to a significant extent. In general, corrosion of the anode is proportional to the relative area of the cathode. That is, the induced electrical current increases proportionally with an increase in cathodic

area relative to the area of the anode. The opposite is generally true as well: current decreases proportionally with a decrease in relative cathodic area. Component geometry is another factor affecting the flow of current, which consequently influences the rate of galvanic corrosion. Current does not easily travel around corners, for instance. The rate of galvanic corrosion is partially dependent on the concentration, oxygen content and motion of the electrolyte, as well as the temperature of the environment. For instance, higher temperatures typically cause an increase in the rate of galvanic corrosion, while higher concentrations of the electrolyte will result in a decrease in the corrosion rate. The pH of the electrolyte solution may also affect the occurrence of galvanic corrosion in a dissimilar metal system. For example, a metal that is the cathode in a neutral or basic electrolyte may become the anode if the electrolyte becomes acidic. A higher oxygen content in the electrolyte also typically results in an increase in the rate of galvanic corrosion. Electrolyte motion can also increase the rate of corrosion, since it may remove some of the oxidized metal from the anode surface, allowing for further oxidation of the metal. [6-10]. Galvanic corrosion compatibilities of metals and alloys in seawater are shown in Tab. 1.

Tab. 1: Galvanic corrosion compatibilities of metals and alloys in seawater [1]

		S - Small Metal A to Metal B Area Ratio		E - Equal Area Ratio		L - Large Metal A to Metal B Area Ratio		• Unfavorable - Galvanic Acceleration Expected		x Uncertain - Variable Direction and/or Magnitude of Galvanic Effect		o Compatible - No Galvanic Acceleration Expected										
Metal A	Metal B	Magnesium Alloys	Zinc	Aluminum Alloys	Cadmium	Mild Steel, Wrought Iron	Cast Iron	Low Alloy High Strength Steel	Brasses, Mn Bronze	Copper, Si Bronze	Lead-Tin Solder	Tin Bronze (G & M)	90/10 Copper-Nickel	70/30 Copper-Nickel	Nickel-Aluminum Bronze	Silver Brazed Alloys	Types 302, 304, 321 & 347 Stainless Steel	Alloys 400, K-500	Types 316 & 317 Stainless Steel	Alloy 20, Alloy 825	Titanium, Alloys C, C-276, 625	Graphite, Graphitized Cast Iron
Magnesium Alloys	S	•	•	•	•	•	•	•	•	•	•	•	•	•	•	•	•	•	•	•	•	•
	E	•	•	•	•	•	•	•	•	•	•	•	•	•	•	•	•	•	•	•	•	•
	L	•	•	•	•	•	•	•	•	•	•	•	•	•	•	•	•	•	•	•	•	•
Zinc	S	•	•	•	•	•	•	•	•	•	•	•	•	•	•	•	•	•	•	•	•	•
	E	•	•	•	•	•	•	•	•	•	•	•	•	•	•	•	•	•	•	•	•	•
	L	•	•	•	•	•	•	•	•	•	•	•	•	•	•	•	•	•	•	•	•	•
Aluminum Alloys	S	•	•	•	•	•	•	•	•	•	•	•	•	•	•	•	•	•	•	•	•	•
	E	•	•	•	•	•	•	•	•	•	•	•	•	•	•	•	•	•	•	•	•	•
	L	•	•	•	•	•	•	•	•	•	•	•	•	•	•	•	•	•	•	•	•	•
Cadmium	S	•	•	•	•	•	•	•	•	•	•	•	•	•	•	•	•	•	•	•	•	•
	E	•	•	•	•	•	•	•	•	•	•	•	•	•	•	•	•	•	•	•	•	•
	L	•	•	•	•	•	•	•	•	•	•	•	•	•	•	•	•	•	•	•	•	•
Mild Steel, Wrought Iron	S	•	•	•	•	•	•	•	•	•	•	•	•	•	•	•	•	•	•	•	•	•
	E	•	•	•	•	•	•	•	•	•	•	•	•	•	•	•	•	•	•	•	•	•
	L	•	•	•	•	•	•	•	•	•	•	•	•	•	•	•	•	•	•	•	•	•
Cast Iron	S	•	•	•	•	•	•	•	•	•	•	•	•	•	•	•	•	•	•	•	•	•
	E	•	•	•	•	•	•	•	•	•	•	•	•	•	•	•	•	•	•	•	•	•
	L	•	•	•	•	•	•	•	•	•	•	•	•	•	•	•	•	•	•	•	•	•
Low Alloy High Strength Steel	S	•	•	•	•	•	•	•	•	•	•	•	•	•	•	•	•	•	•	•	•	•
	E	•	•	•	•	•	•	•	•	•	•	•	•	•	•	•	•	•	•	•	•	•
	L	•	•	•	•	•	•	•	•	•	•	•	•	•	•	•	•	•	•	•	•	•
Brasses, Mn Bronze	S	•	•	•	•	•	•	•	•	•	•	•	•	•	•	•	•	•	•	•	•	•
	E	•	•	•	•	•	•	•	•	•	•	•	•	•	•	•	•	•	•	•	•	•
	L	•	•	•	•	•	•	•	•	•	•	•	•	•	•	•	•	•	•	•	•	•
Copper, Si Bronze	S	•	•	•	•	•	•	•	•	•	•	•	•	•	•	•	•	•	•	•	•	•
	E	•	•	•	•	•	•	•	•	•	•	•	•	•	•	•	•	•	•	•	•	•
	L	•	•	•	•	•	•	•	•	•	•	•	•	•	•	•	•	•	•	•	•	•
Lead-Tin Solder	S	•	•	•	•	•	•	•	•	•	•	•	•	•	•	•	•	•	•	•	•	•
	E	•	•	•	•	•	•	•	•	•	•	•	•	•	•	•	•	•	•	•	•	•
	L	•	•	•	•	•	•	•	•	•	•	•	•	•	•	•	•	•	•	•	•	•
Tin Bronze (G & M)	S	•	•	•	•	•	•	•	•	•	•	•	•	•	•	•	•	•	•	•	•	•
	E	•	•	•	•	•	•	•	•	•	•	•	•	•	•	•	•	•	•	•	•	•
	L	•	•	•	•	•	•	•	•	•	•	•	•	•	•	•	•	•	•	•	•	•
90/10 Copper-Nickel	S	•	•	•	•	•	•	•	•	•	•	•	•	•	•	•	•	•	•	•	•	•
	E	•	•	•	•	•	•	•	•	•	•	•	•	•	•	•	•	•	•	•	•	•
	L	•	•	•	•	•	•	•	•	•	•	•	•	•	•	•	•	•	•	•	•	•
70/30 Copper-Nickel	S	•	•	•	•	•	•	•	•	•	•	•	•	•	•	•	•	•	•	•	•	•
	E	•	•	•	•	•	•	•	•	•	•	•	•	•	•	•	•	•	•	•	•	•
	L	•	•	•	•	•	•	•	•	•	•	•	•	•	•	•	•	•	•	•	•	•
Nickel-Aluminum Bronze	S	•	•	•	•	•	•	•	•	•	•	•	•	•	•	•	•	•	•	•	•	•
	E	•	•	•	•	•	•	•	•	•	•	•	•	•	•	•	•	•	•	•	•	•
	L	•	•	•	•	•	•	•	•	•	•	•	•	•	•	•	•	•	•	•	•	•
Silver Brazed Alloys	S	•	•	•	•	•	•	•	•	•	•	•	•	•	•	•	•	•	•	•	•	•
	E	•	•	•	•	•	•	•	•	•	•	•	•	•	•	•	•	•	•	•	•	•
	L	•	•	•	•	•	•	•	•	•	•	•	•	•	•	•	•	•	•	•	•	•
Types 302, 304, 321 & 347 Stainless Steel	S	•	•	•	•	•	•	•	•	•	•	•	•	•	•	•	•	•	•	•	•	•
	E	•	•	•	•	•	•	•	•	•	•	•	•	•	•	•	•	•	•	•	•	•
	L	•	•	•	•	•	•	•	•	•	•	•	•	•	•	•	•	•	•	•	•	•
Alloys 400, K-500	S	•	•	•	•	•	•	•	•	•	•	•	•	•	•	•	•	•	•	•	•	•
	E	•	•	•	•	•	•	•	•	•	•	•	•	•	•	•	•	•	•	•	•	•
	L	•	•	•	•	•	•	•	•	•	•	•	•	•	•	•	•	•	•	•	•	•
Types 316 & 317 Stainless Steel	S	•	•	•	•	•	•	•	•	•	•	•	•	•	•	•	•	•	•	•	•	•
	E	•	•	•	•	•	•	•	•	•	•	•	•	•	•	•	•	•	•	•	•	•
	L	•	•	•	•	•	•	•	•	•	•	•	•	•	•	•	•	•	•	•	•	•
Alloy 20, Alloy 825	S	•	•	•	•	•	•	•	•	•	•	•	•	•	•	•	•	•	•	•	•	•
	E	•	•	•	•	•	•	•	•	•	•	•	•	•	•	•	•	•	•	•	•	•
	L	•	•	•	•	•	•	•	•	•	•	•	•	•	•	•	•	•	•	•	•	•
Titanium, Alloys C, C-276, 625	S	•	•	•	•	•	•	•	•	•	•	•	•	•	•	•	•	•	•	•	•	•
	E	•	•	•	•	•	•	•	•	•	•	•	•	•	•	•	•	•	•	•	•	•
	L	•	•	•	•	•	•	•	•	•	•	•	•	•	•	•	•	•	•	•	•	•
Graphite, Graphitized Cast Iron	S	•	•	•	•	•	•	•	•	•	•	•	•	•	•	•	•	•	•	•	•	•
	E	•	•	•	•	•	•	•	•	•	•	•	•	•	•	•	•	•	•	•	•	•
	L	•	•	•	•	•	•	•	•	•	•	•	•	•	•	•	•	•	•	•	•	•

The aim of this paper is to detect the effects of galvanic corrosion on connecting elements and contact points of various metal surfaces that are protected by the most common metal coatings. Testing method is explained in section 2 and results are presented in section 3.

2. TESTING AND METHODS

The examination included corrosion resistance testing on various bolted joints (24 pieces) after exposure in a salt chamber for a period of 96 hours, in accordance with HRN ISO 9227, with periodic inspection every 24 hours. Evaluation of material degradation in the form of rusting was conducted. Components made of different materials and metal coatings in the clamping joint are shown in Fig. 3.

Materials of the components in the clamping joint								
	Sample	Bolt	Spring washer	Plain washer	Material/ Coating	Plain washer	Nut	
	1	ISO 14583	DIN 6796	DIN 125 A	Ni	DIN 125 A	DIN 934	
	2	ISO 14583	DIN 6796	DIN 125 A	Ni	DIN 125 A	DIN 934	
	3	ISO 14583	DIN 6796	DIN 125 A	Ag	DIN 125 A	DIN 934	
	4	ISO 14583	DIN 6796	DIN 125 A	Cu bare	DIN 125 A	DIN 934	
	5	ISO 14583	JIS B/Tupe 2 Heavy Load	/	Cu bare	/	DIN 934/HNT2-STN	
	6	ISO 14583	DIN 6796	DIN 125 A	Sn	DIN 125 A	DIN 934	
	7	ISO 14583	JIS B/Tupe 2 Heavy Load	/	Sn	/	DIN 934/HNT2-STN	
	8	ISO 14583	DIN 6796	DIN 125 A	Ni	DIN 125 A	DIN 934	
	9	ISO 14583	DIN 6796	DIN 125 A	Ni	DIN 125 A	DIN 934	
	10	ISO 14583	JIS B/Tupe 2 Heavy Load	/	Ag	/	DIN 934/HNT2-STN	
	11	DIN 912	DIN 6796	DIN 125 A	Cu bare	DIN 125 A	DIN 934	
	12	DIN 912	DIN 6796	DIN 125 A	Ni	DIN 125 A	DIN 934	
	13	DIN 912	DIN 6796	DIN 125 A	Ag	DIN 125 A	DIN 934	
	14	DIN 912	DIN 6796	DIN 125 A	Sn	DIN 125 A	DIN 934	
	15	ISO 14583	DIN 6796	DIN 125 A	Sn	DIN 125 A	DIN 934	
	16	ISO 14583	JIS B/Tupe 2 Heavy Load	/	Sn	/	DIN 934/HNT2-STN	
	17	DIN 912	DIN 6796	DIN 125 A	Zn	DIN 125 A	DIN 934	
	18	ISO 14583	DIN 6796	DIN 125 A	Al bare	DIN 125 A	DIN 934	
	19	DIN 912	DIN 6796	DIN 125 A	Al bare	DIN 125 A	DIN 934	
	20	ISO 14583	JIS B/Tupe 2 Heavy Load	/	Al bare	/	DIN 934/HNT2-STN	
Legend								
	Stainless steel	Zinc plated	Nickel plated	Aluminium	Silver	Copper	Tin	Zinc

ASSEMBLY ORDER

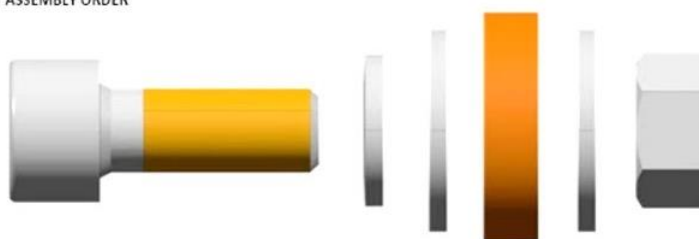


Fig. 3: Types of materials and metal coatings of components in the clamping joint

The actual appearance of the clamping joint components before testing in the salt chamber for a period of 96 hours is shown in Fig. 4.



Fig. 4: Appearance of the clamp components prior to salt chamber testing

During the test, samples were placed directly in Ascott salt spray chamber, model S450 according to the standard HRN ISO 9227 for a period of 96 hours. Testing parameters are given in Tab. 2.

Tab. 2: Testing parameters in neutral salt spray chamber

Parameters	HRN ISO 9227	Testing conditions
Testing duration, <i>h</i>	According to request	24/96
Temperature inside chamber during testing, °C	35±2	35±0.1
Temperature of the compr. air. humidifier, °C	45 - 50	50
Pressure of the air, <i>bar</i>	0.7 – 1.4	1,4
Used solution	NaCl	NaCl
Concentration of solution, %	5	5
Collected solution, <i>ml/80cm²/h</i>	1.5±0.5	2.0
pH of the collected solution at 25±2°C	6.5 – 7.2	6.63
El. conductivity of distilled water, <i>µS/cm at 25±2°C</i>	max. 20	< 10

The examination included corrosion resistance testing of samples (24 pieces) with periodic inspection every 24 hours. After each inspection period, each sample was revised in detail and photographed in order to determine potential corrosion products or surface degradation of the anode material in the clamping joint. The appearance of the samples in the salt chamber before the test is shown in Fig. 5.

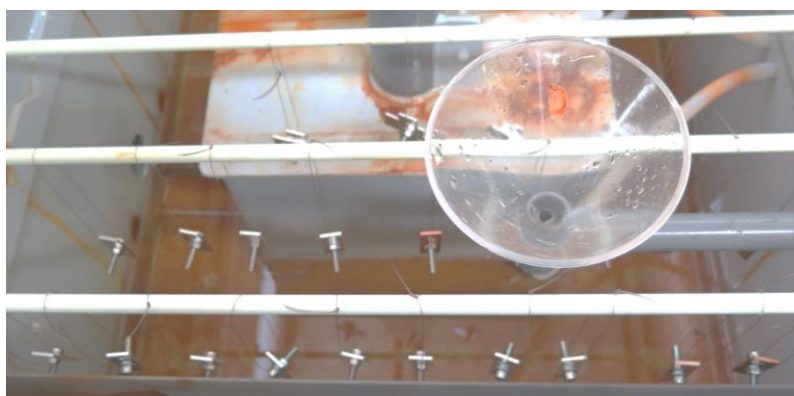


Fig. 5: The appearance of samples in a salt chamber before testing

3. RESULTS

The appearance of the samples after testing in the salt chamber after 24 hours is shown in Fig. 6 and Fig. 7.

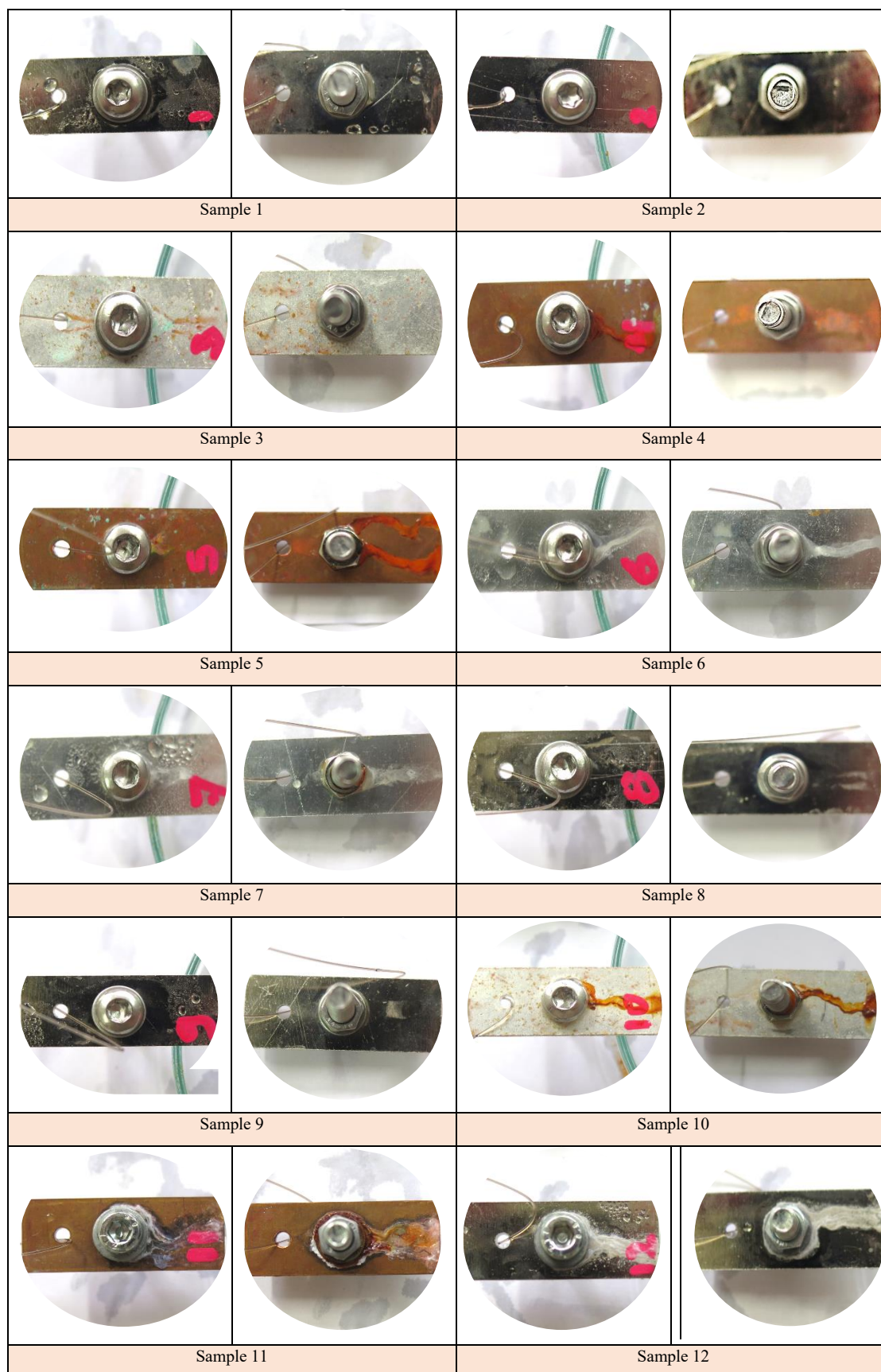


Fig. 6: The appearance of samples 1-12 after 24-hour test in the salt chamber

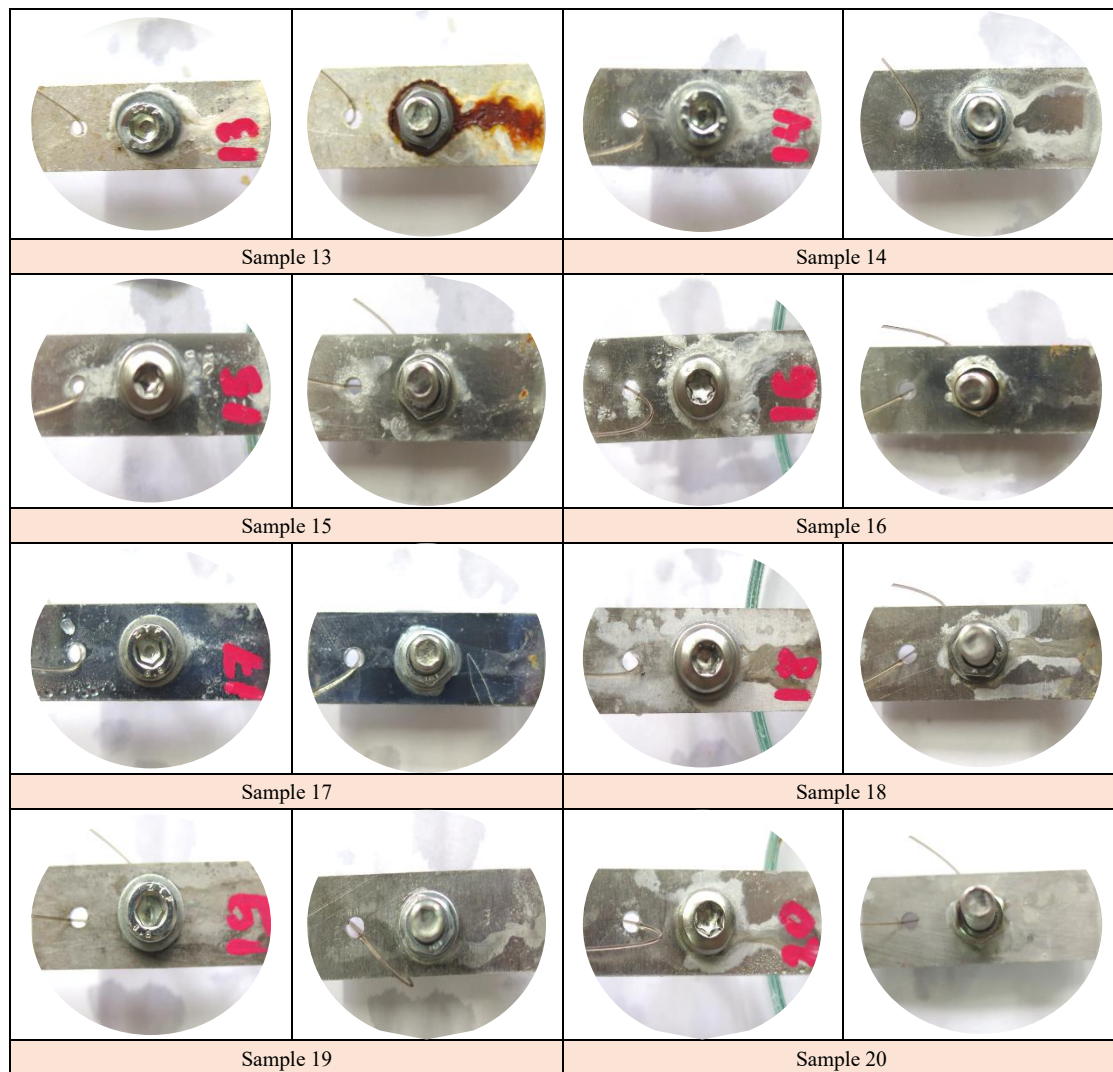


Fig. 7: The appearance of samples 13-20 after 24-hour test in the salt chamber

As a result of contact corrosion between various connecting elements and the metal surfaces, after testing for 24 hours corrosion products were found on all parts except for samples 1, 2, 3, 8 and 9 (Fig. 6 and Fig. 7). After testing for 24 hours, according to ISO 4628, peeling was detected on samples 15 and 16. The numerical test values are presented in table 3 and refer to the total test surface of each assembly element.

Tab. 3: Test results of samples 1-20 in the salt chamber after 24 hours according ISO 4628

Sample	ISO 4628-3	ISO 4628-5
	Corrosion	Peeling
1	Ri 0	0
2	Ri 0	0
3	Ri 0	0
4	Ri 2	0
5	Ri 3	0
6	Ri 2	0
7	Ri 2	0
8	Ri 0	0
9	Ri 0	0
10	Ri 4	0
11	Ri 5	0
12	Ri 5	0
13	Ri 5	0
14	Ri 4	0
15	Ri 2	1
16	Ri 3	1
17	Ri 1	0
18	Ri 3	0
19	Ri 1	0
20	Ri 3	0

The appearance of the samples after testing in the salt chamber after 24 hours is shown in Fig. 8 and Fig. 9.

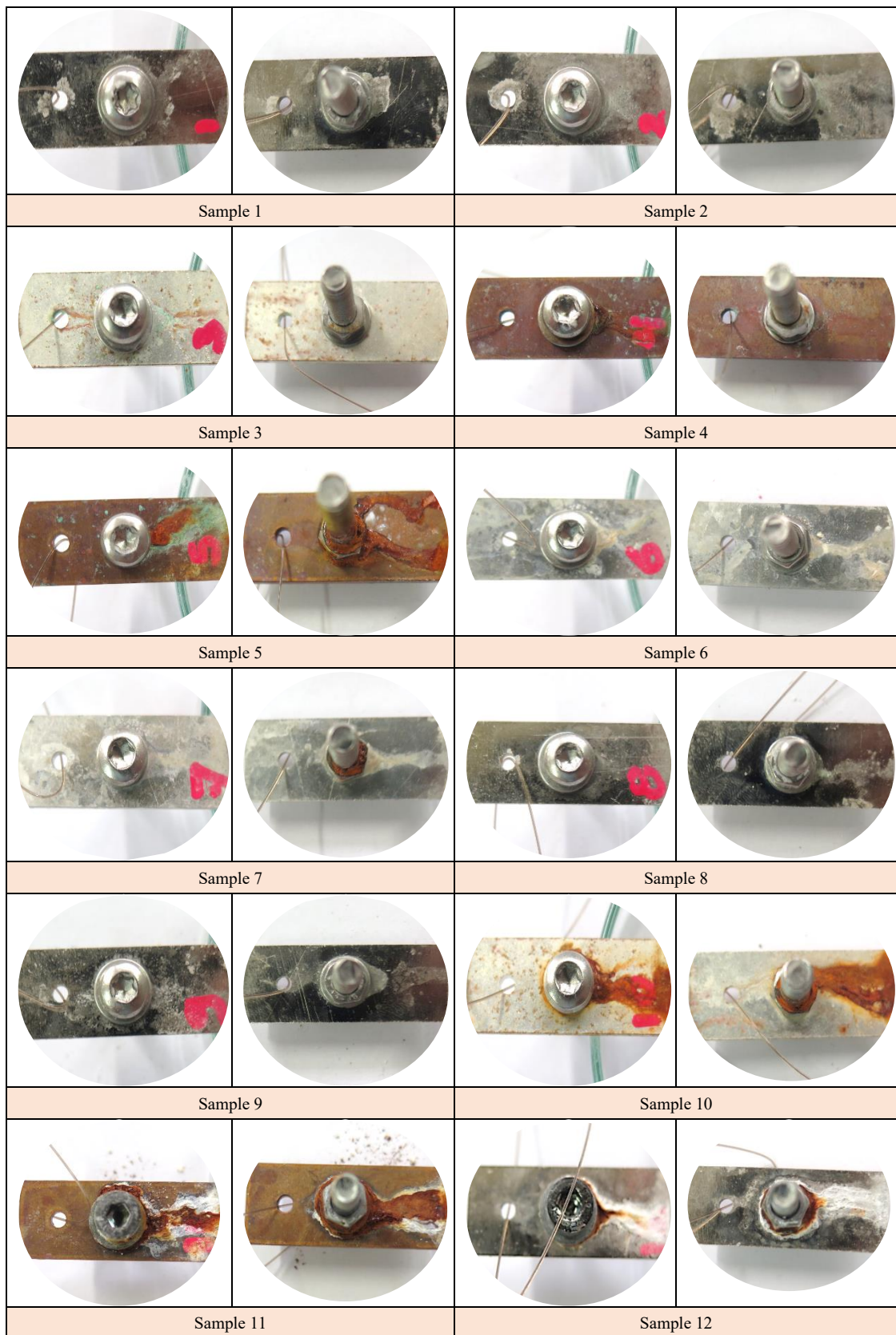


Fig. 8: The appearance of samples 1-12 after 96-hour test in the salt chamber

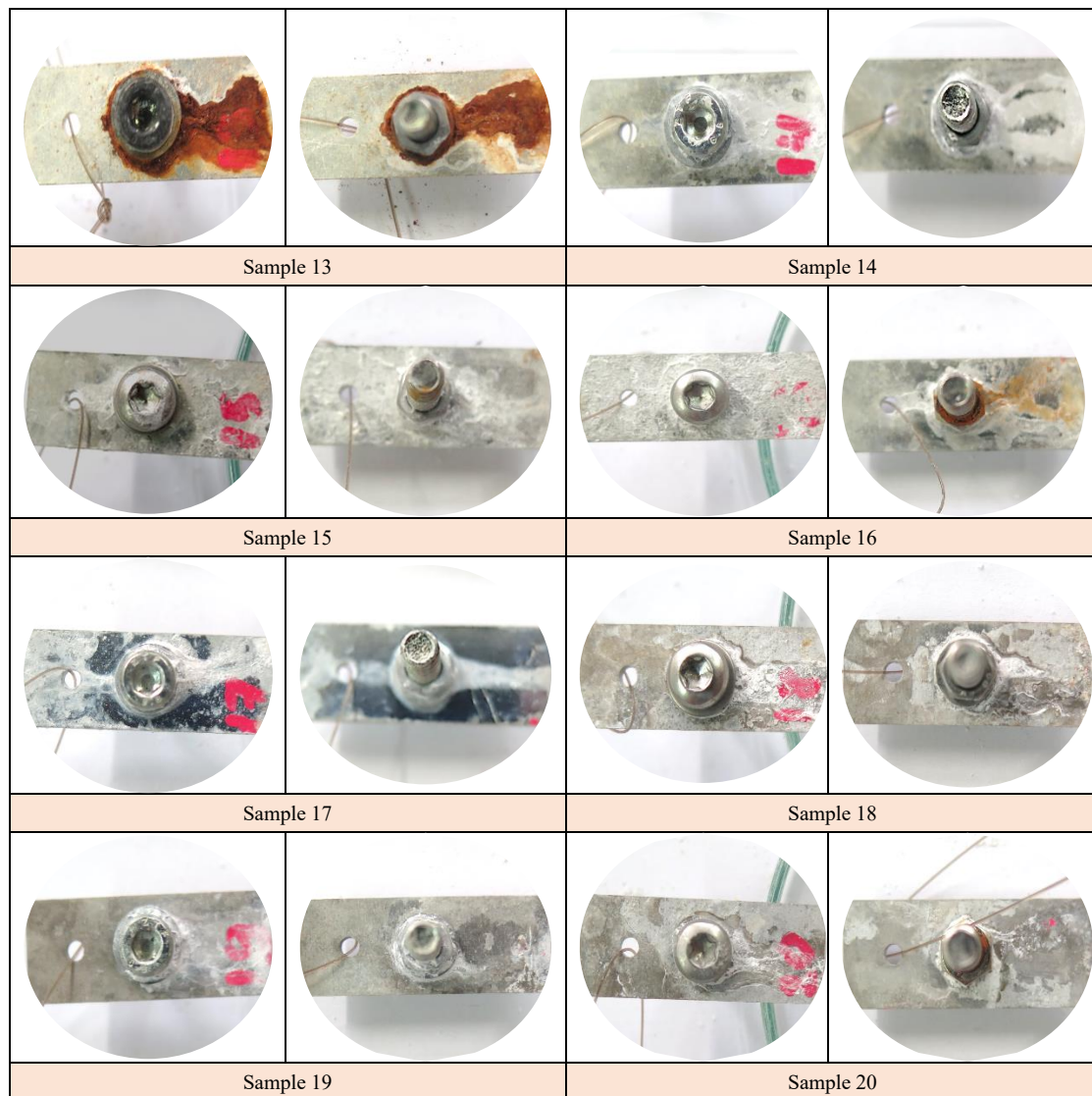


Fig. 9: The appearance of samples 13-20 after 96-hour test in the salt chamber

The appearance of unscrewed samples after **96-hour** test in the salt chamber is shown in Fig. 10.



Fig. 10: The appearance of unscrewed samples 1-20 after 96-hour test in the salt chamber

As a result of contact corrosion between various connecting elements and the metal surfaces, after testing for 96 hours corrosion products were found on all parts except for samples 1, 2, 3, 8 and 9 (Fig. 8, Fig. 9 and Fig. 10). After testing for 96 hours, according to ISO 4628, peeling was detected on samples 15 and 16. The numerical test values are presented in table 4 and refer to the total test surface of each assembly element.

Tab. 4: Test results of samples 1-20 in the salt chamber after 96 hours according ISO 4628

Sample	ISO 4628-3	ISO 4628-5
	Corrosion	Peeling
1	Ri 0	0
2	Ri 0	0
3	Ri 0	0
4	Ri 3	0
5	Ri 5	0
6	Ri 3	0
7	Ri 4	0
8	Ri 0	0
9	Ri 0	0
10	Ri 5	0
11	Ri 5	0
12	Ri 5	0
13	Ri 5	0
14	Ri 4	0
15	Ri 4	5
16	Ri 5	5
17	Ri 3	0
18	Ri 5	0
19	Ri 3	0
20	Ri 4	0

4. CONSLUSION

If proper design, material selection, implementation and maintenance steps are followed, there is a high probability that the contact form of corrosion in the designed system will be avoided. It is necessary to avoid the unfavorable area effect of a small anode and large cathode. Small parts or critical components such as fasteners should be the more noble metal compared to the materials being joined. Another way to avoid galvanic corrosion is to insulate dissimilar metals wherever practical, for example, by using a gasket, coatings, polymeric materials.

Based on the conducted laboratory tests, in accordance with the standard HRN ISO 9227 for 96 hours, it can be concluded that according to degree of rusting (contact corrosion) and rusted area, the highest corrosion resistance in salt chamber were determined on the samples 1, 2, 3, 8 and 9. After testing for 96 hours, according to ISO 4628, peeling was detected on the samples 15 and 16.

Generally, combination of stainless steel connecting elements in contact with the nickel and silver coating or copper plate, due to optimal potential difference represents the best choice or corrosion stability of the assembly when it comes to clamping joints of metal materials. It was also found that coating blocks the diffusion of the ions and corrosion products, thus preventing the establishment of galvanic coupling between the local anodes and cathodes. [4].

REFERENCES

- [1] Popov N. B., "Corrosion Engineering: Principles and Solved Problems", 2015, Elsevier.
- [2] Craig B. D., Lane R. A., Rose D. H. "Corrosion Prevention and Control", 2006, Ammtiac.
- [3] Lazzari L., "Engineering Tool for Corrosion", 2012, Woodhead Publishing.
- [4] Lei Y., "Corrosion and protection of marine engineering materials", 2023, CRC Press.
- [5] Zafara F., Ghosal A., Sharmin E., "Corrosion Fundamentals and Protection Mechanisms", 2022, digital
- [6] Francis R., "Galvanic Corrosion: A Practical Guide for Engineers", 2nd Edition, 2017, NACE.
- [7] Ambat R., Piotrowska R., "Humidity and Electronics: Corrosion Reliability Issue and Preventive Measures, 2022, Woodhead Publishing.
- [8] Collier E., "The Boatowner's Guide to Corrosion", 2006, International Marine / McGraw-Hill.
- [9] Bardal E., "Corrosion and Protection", 2003, Springer
- [10] Satodeh K., "Case Studies of Material Corrosion Prevention for Oil and Gas Valves", 2022, CRC Press.

ALUMINIJSKA NANOKOMPOZITNA EPOKSIDNA PREVLAKA ZA ANTI-KOROZIJSKU I ANTIBAKTERIJSKU ZAŠTITU

ALUMINIUM NANOCOMPOSITES EPOXY COATING FOR ANTICORROSION AND ANTIBACTERIAL PROTECTION

Marina Samardžija¹, Vesna Alar², Ivan Stojanović², Vedrana Špada³, Marin Kurtela²,

¹ Sveučilište u Zagrebu, Rudarsko-geološko-naftni fakultet, Zavod za kemiju, Pierottijeva 6, 10000 Zagreb, Hrvatska

¹ Faculty of Mining Geology and Petroleum Engineering, Department of Chemistry, Pierottijeva 6, 10000 Zagreb, Croatia

² Sveučilište u Zagrebu, Fakultet strojarstva i brodogradnje, Zavod za zavarene konstrukcije, Ul. Ivana Lučića 5, 10000 Zagreb, Hrvatska

² Faculty of Mechanical Engineering and Naval Architecture, Department of Welded Structures, St. Ivan Lučić 5, 10000 Zagreb, Croatia

³ Istarsko veleučilište, Riva 4 i 6, Zagrebačka 30, 52100 Pula, Hrvatska

³ Università Istriana di scienze applicate, Riva 4 i 6, Zagrebačka 30, 52100 Pula, Croatia

Sažetak

U ovom radu epoksidna prevlaka modificirana je nanočesticama aluminijske (Al NP) u svrhu zaštite površine cijevi od sivog lijeva. U današnje vrijeme postoji potreba za razvojem nove generacije prevlaka za zaštitu unutarnje površine cijevi od korozije i utjecaja mikroorganizama. Uzorci su promatrani pomoću SEM i EDX analize kako bi se procijenila i karakterizirala jednolika distribucija Al NP u nanokompozitima. Učinak zaštite od korozije nanokompozita analiziran je pomoću pretražne elektrokemijske mikroskopije (SECM) i elektrokemijske impedancijske spektroskopije (EIS). Ova analiza potvrđuje poboljšanje korozijske otpornosti nanokompozita u usporedbi s epoksidnom matricom bez nanočestica. Uvođenjem Al NP u epoksidnu matricu mehanička svojstva su se neznatno povećala. Nadalje, antimikrobni test pokazao je da nanokompoziti imaju baktericidno djelovanje protiv bakterija *Pseudomonas aeruginosa* i *Bacillus subtilis*. Mala veličina aluminijskih čestica i njihova brza oksidacija omogućuju ovom nanokompozitu dvojaka svojstva. Nanokompoziti poboljšavaju mehanička, antikorozivna i antimikrobna svojstva što znači da pružaju bolju otpornost na vanjske mehaničke utjecaje te učinkovito sprječavaju koroziju i rast bakterija.

Ključne riječi: korozija, bakterije, nanočestice, epoksidna prevlaka.

Abstract

*In this work, aluminium nanoparticles (Al NPs) as fillers were homogenized with epoxy coating in order to protect the surface of pipes made of gray cast iron. Nowadays, there is a need to develop a new generation of coatings to protect the inner surface of pipes from corrosion and microorganisms' influences. The samples were analyzed with SEM observation and EDX to evaluate and characterize the uniform distribution of Al NP in the nanocomposites. The effect of corrosion protection performance of nanocomposite was analyzed using scanning electrochemical microscopy (SECM) and electrochemical impedance spectroscopy (EIS). This analysis confirms improvement of the corrosion resistance of nanocomposite in comparison with epoxy matrix without nanoparticles. The introduction of Al NP into epoxy matrix the mechanical properties has been slightly increase. Furthermore, the antimicrobial test indicated that the nanocomposites had bactericidal activity against *Pseudomonas aeruginosa* and *Bacillus subtilis* bacteria. The small size of the aluminium particles and their rapid oxidation enable this nanocomposite to possess dual properties. Nanocomposites improve mechanical, anticorrosive and antimicrobial properties which means that they provide the better resistance to external mechanical influences and effectively prevent corrosion and bacterial growth.*

Keywords: corrosion, bacterial, nanoparticles, epoxy coating.

1. INTRODUCTION

Cast iron is a material that is commonly used for drainage pipe systems as it is resistant to varying and moderately high internal pressures [1]. This material poses good thermal conductivity, relatively low melting temperature, high damping capacity, and excellent castability [1] [2]. Unfortunately, these properties deteriorate when metals interact with certain elements that recur within their environments, a process technically called corrosion [3]. The most effective way of dealing with this issue is to apply a coating system. For this purpose, epoxy coatings are used as they have good protective barrier properties, high adhesion to the metal substrate, are easy to apply, and are not expensive [4]. In recent years, scientists and researchers have been motivated to develop coatings with new features, and nanoparticles are used for this purpose. Nanoparticles have been widely used as resin fillers to block micropores and improve the corrosion resistance and the mechanical properties of the resins due to their great surface-to-volume proportion with respect to conventional macroscopic materials [5]. Nanocomposite material is obtained by incorporating nanoparticles into the epoxy coating [6].

The aim of this paper is to compare the anticorrosive and antibacterial properties of two types of coatings. The first coating is an unmodified epoxy coating, while the second one contains 1% Al NP. Our interest is the development of a new anticorrosive and antibacterial nanocomposite coating for the protection of grey cast iron. The morphological properties of the coating were examined using SEM and EDS analysis. Thickness, hardness, adhesion, and color change show the mechanical properties. The anticorrosive properties of the samples were investigated using electrochemical techniques (EIS and SECM). Antibacterial tests were made for the bacteria *Pseudomonas aeruginosa* and *Bacillus subtilis*. Using all these analyses, the aluminum epoxy nanocomposite shows an improvement in properties.

1. MATERIALS AND METHODS

2.1. Materials

The metallic substrate used during this study was gray cast iron with chemical composition 2.5 C, 1.5 Si, 1.05 Mn, 0.5 P, 0.07 S, and Fe in balance (wt.%). The epoxy coatings and hardener (polyamine) that we used in this work were obtained from Hempel (Umag, Croatia). Aluminum nanoparticles with an average particle size of about 100 nm were provided by Guangzhou Hongwu Material Technology Co., Ltd., Guangzhou, China.

2.2. Preparation of the aluminium nanocomposite epoxy coating

The coating and hardener were mixed in a ratio of 4 to 1. At ambient temperature, 1% of Al NPs were incorporated into the epoxy coating under sonicate agitation for 20 min with a delay in the process due to the cooling of the nanocomposite. Hardener was added to the nanocomposite and mechanically stirred using a glass stirrer.

Before applying the coating, the panels of 9.5 cm × 0.9 cm × 15 cm gray cast iron were abrasively blasted and cleaned with ethanol (70 wt.%). The nanocomposite mixture was applied using a film applicator with a wet film thickness of 150 μm. The samples were

kept at room temperature for 24 h, and then another layer of nanocomposites was applied in the opposite direction. The samples were left at room temperature for 7 days.

2.3. Characterisation of the aluminium nanocomposite epoxy coating

The morphology of the Al NPs, unmodified epoxy coating, and aluminium epoxy nanocomposite were investigated by scanning electron microscope (SEM) (TESCAN Brno, Brno, Czech Republic). The size distribution and dispersion of nanoparticles, the homogeneity of the layer, and the occurrence of agglomeration were observed using energy-dispersive (EDS) detector.

The mechanical properties of the epoxy coating and aluminium epoxy nanocomposite that were observed are: thickness (Elcometer Limited, Edge Lane, Manchester, UK), hardness (DeFlesko Corporation, Ogdensburg, NY, USA), adhesion Elcometer 510, model T, Manchester, UK), and colour (RAL gGmbH, Siegburger, Germany).

The corrosion protection performance of the epoxy coating and aluminium epoxy nanocomposite were studied in 3.5 wt.% NaCl solution by EIS (VersaSTAT 3, AMETEK Scientific 131 Instruments, Princeton applied research, Berwyn, PA, USA) and in tap water using Intermittent Contact-Scanning Electrochemical Microscopy (ic-ac-SECM) (M470, BioLogic, France). The EIS electrochemical cell consisted of a graphite rod as the auxiliary electrode, a saturated calomel electrode as the reference, and the epoxy coating and/or aluminium epoxy nanocomposite specimen as the working electrode. The frequency range of 0.1 to 10^5 Hz with an amplitude of 10 mV was used. The impedance data were fitted using the ZSimpWin software. The ic-ac-SECM test of unmodified epoxy coating and aluminium epoxy nanocomposite was used to observe real impedance distribution over a certain area. The 3DIsoPlot program was used to obtain the topography of the samples in 3D view. A three-electrode system, immersed in tap water, was above the surface of the nanocomposite. This three-electrode system consisted of the Ag/AgCl/KCl reference electrode, the platinum sheet as the counter electrode, and of the UltraMicroElectrode (UME) probe for measuring the local electrochemical activity.

Pseudomonas aeruginosa and *Bacillus subtilis* were used as test bacteria. Bacterial culture was inoculated from fresh colonies on agar plates into 20 mL of Muller Hinton culture medium. Nanoparticle samples dissolved in distilled water (100 g/mL) were added from stock to each well. The zone of inhibition was measured using a ruler. After 24 hours, the appearance of the zone of inhibition was observed. The surface of the epoxy coating and 1% Al epoxy nanocomposite was cut to a size of 50 mm by 50 mm and inoculated with 0.4 mL of 10^5 CFU bacterial suspension and placed in a Petri dish and incubated at 35°C and 90% relative humidity (RH) for 24 h. The number of live bacterial cells was determined by plating different dilutions on plate counting agar, incubating the plates for 24 hours at 37°C, and then visually counting the colonies [7].

2. RESULTS AND DISCUSSION

3.1. SEM and EDS analysis

Fig. 1 shows the SEM and EDS analysis result.

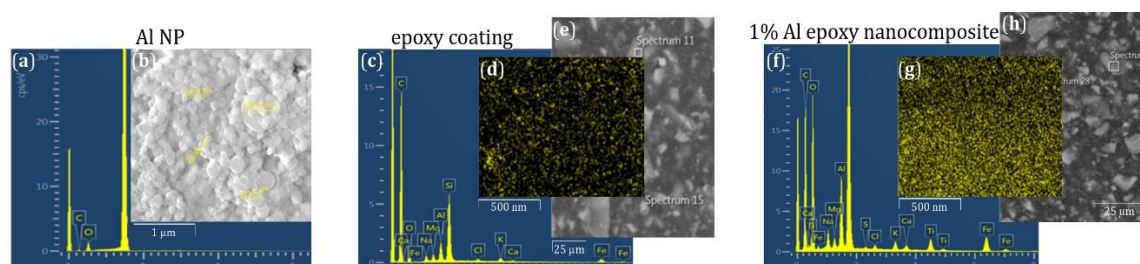


Fig. 1: SEM and EDS analysis of the (a, b) Al NP, (c, e) epoxy coating, (f, h) 1% Al NP nanocomposite. The EDS mapping of distribution of microparticles of (d) Al in epoxy coating and nanoparticles of (g) Al in the nanocomposite.

The EDS analysis of the elemental composition of the nanoparticle powder showed a high proportion of Al NPs (Fig. 1a). From Fig. 1 b we can see that the Al NPs have spherical particles. The EDS analyses of epoxy coating (Fig. 1c) showed that epoxy coating contains microparticles of Al. It was assumed that these microparticles of aluminium were used as a pigment in the epoxy coatings [1]. The SEM analysis of the epoxy coating showed irregularities and alien particles, and the surface was not homogeneous (Fig. 1e). The presence of Al microparticles in the initial epoxy coating showed small irregularities and the appearance of agglomerates (Fig. 1d). The EDS analysis determined that nanocomposite sample contained a certain percentage of nanoparticles that deviated very slightly from the added 1% nanoparticles (Fig. 1f). With the addition of nanoparticles, the rough surface morphology of nanocomposites remained the same (Fig. 1h). The action of the sonication process improved the distribution of the added aluminium particles (Fig. 1g).

3.2. Physical test

The results of the effect of Al NP on the mechanical properties of epoxy coating are shown in Table 1.

Tab. 1. Results of mechanical resistance tests for epoxy coating 1% Al NP epoxy nanocomposite.

sample	thickness, µm	hardness, Shore D	adhesion, MPa	RAL colors
epoxy coating	249.90	83.40	8.34	3013
1% Al NP nanocomposite	255.50	84.10	14.18	8017

It is evident that the addition of 1% Al NP did not change the thickness and hardness of the coating. Adhesion of the coating to the metal substrate showed a small increase with the addition of Al NPs to the epoxy coating. A significant change is visible in the color change of the coating.

3.3. Electrochemical measurement

Fig. 2a shows the Nyquist plot for unmodified epoxy coating and 1% Al NP nanocomposite during 0 days of exposure in 3.5% NaCl solution. In Fig. 2 b and c, we can see the distribution of impedance values on the surface of these samples.

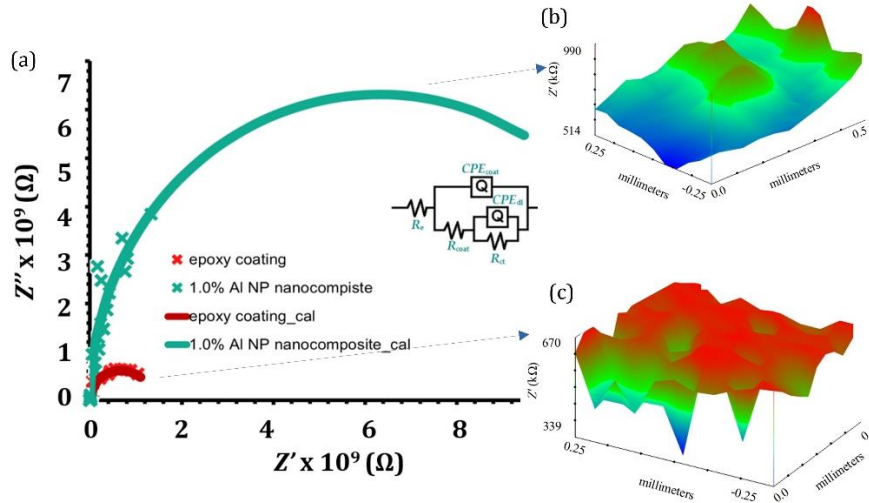


Fig. 2. Nyquist plots of (a) epoxy coat and 1% Al NP nanocomposite immersed in 3.5 wt.% NaCl solution. ic-ac-SECM distribution of real impedance per surface for samples: (c) epoxy coating, and (b) 1% Al NP nanocomposite.

According to Fig. 2a, the unmodified epoxy coating showed a lower resistance value than the nanocomposite. The increase in resistance was significantly more pronounced in the sample containing 1.0% Al NPs. The reason for the increase in impedance values with nanocomposites can be explained by the labyrinth effect where nanoparticles block the flow of electrolyte and thus further protect the degradation of the epoxy coating and the corrosion of gray cast iron. The distribution of impedance values on the surface was obtained using the ic-ac SECM method (Fig. 2b and c). Nanocomposite shows higher impedance values than epoxy coating.

3.4. Antibacterial test

Fig. 3 shows the mass concentration of Al NPs in simulated wastewater.

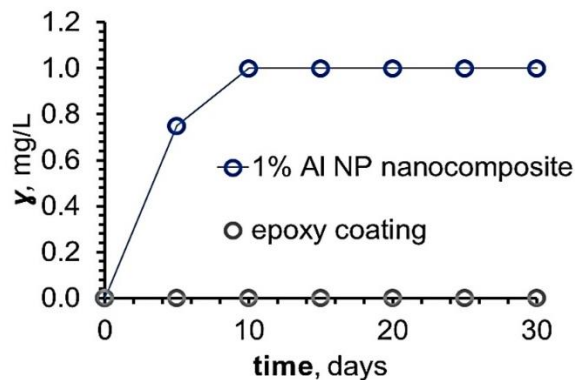


Fig. 3. The mass concentration of the migration of Al^{3+} ions from epoxy coating, 1% Al NP nanocomposite to simulated wastewater for 30 days.

The increase in Al NP concentration in wastewater occurs due to the presence of the nanocomposite system. During the first 10 days, the concentration increases linearly, after which it becomes constant. The cessation of the concentration change could be explained by the possibility of Al NP oxidation. The resulting oxidation layer will have a larger volume than the Al NP, which prevents further electrolyte flow.

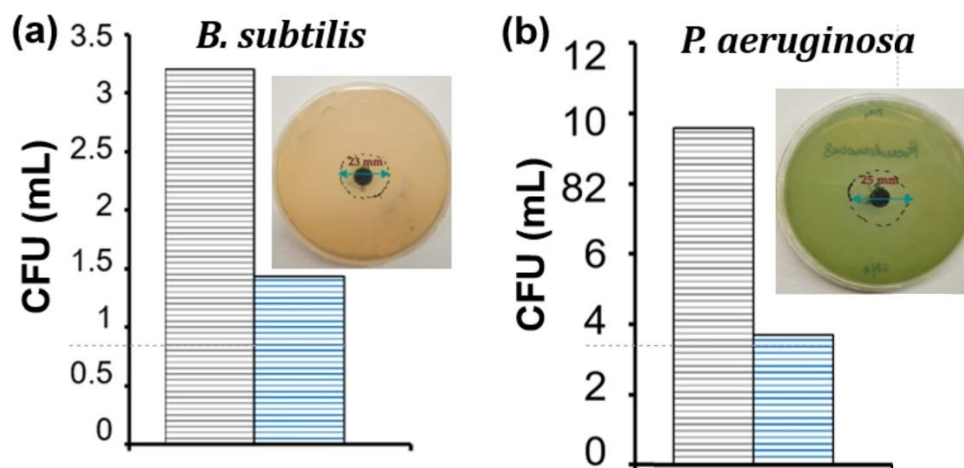


Fig. 4. Antibacterial activity of all samples according to the ISO 22196 standard. Zone of inhibition of Al NP against (a) *B. subtilis*, (b) *P. aeruginosa*.

Fig. 4a and b show a reduced concentration of viable bacteria within the bacterial suspension together with the epoxy coating and the nanocomposite. The nanocomposite with 1% Al NP in epoxy coating has the highest antibacterial effect, with a reduction of about 54% for *B. subtilis* and 60.5% for *P. aeruginosa*. Likewise, Fig. 4 shows the antibacterial effect of the nanoparticles themselves where it is seen that Al NPs show an inhibition zone in the presence of *P. aeruginosa* and *B. subtilis*.

CONCLUSION

The Al NP nanocomposite was successfully dispersed in the epoxy coating, without agglomerates and the appearance of air bubbles. It can be concluded that the addition of Al NPs in the epoxy coating improves the resistance to the electrolyte, but at the same time enables the migration of Al^{3+} ions up to a certain concentration.

The tests of antimicrobial properties against two typical bacteria of *P. aeruginosa* and *B. subtilis* indicate that the surface antibacterial layer of Al NPs possesses excellent antimicrobial properties.

Acknowledgement:

This work was supported by the European Regional Development Fund under the Operational Program Competitiveness and Cohesion 2014–2020. This research was funded by “Development of anticorrosion protection system for multipurpose pipe use”, grant number KK.01.1.1.07.0045.

REFERENCES

- [1] Melchers R. E., Post-perforation external corrosion of cast iron pressurised water mains. Corrosion Engineering Science and Technology, 52, pp. 541–546 (2017).

- [2] Seikh A. H., Sarkar A., Singh J. K., Mohammed S. M: A: K., Alharthi N., Ghosh M., Corrosion characteristics of copper-added austempered gray cast iron (AGCI), *Materials*, 12, pp. 1–17 (2019).
- [3] Umoren S. A., Solomon M. M., Recent developments on the use of polymers as corrosion inhibitors-a review, *Open Materials Science Journal*, 8, pp. 39–54 (2014).
- [4] Khodaei P., Shabani-Nooshabadi M., Behpour M., Epoxy-Based nanocomposite coating reinforced by a zeolite complex: Its anticorrosion properties on mild steel in 3.5 wt% NaCl media, *Progres in Organic Coatings*, 136, pp. 105254 (2019).
- [5] Jain P., Patidar B., Bhawsar J., Potential of Nanoparticles as a Corrosion Inhibitor: A Review, *Journal of Bio- Tribo-Corrosion*, 6, pp. 1–12 (2020).
- [6] Nguyen-Tri P., Nguyen T. A., Carriere P., Xuan C. N., Nanocomposite Coatings: Preparation, Characterization, Properties, and Applications, 4749501 (2018).
- [7] ISO 4833–1; Microbiology of the Food Chain—Horizontal Method for the Enumeration of Microorganisms—Part 1: Colony Count at 30 °C by the Pour Plate Technique. International Organization for Standardization: Geneva, Switzerland (2018).

PARAMETRI SUŠENJA VODORAZRJEDIVIH PREMAZA

DRYING PARAMETERS OF WATER-BORNE COATINGS

Ivan Fatović, Mirta Logar, Ivan Stojanović, Vesna Alar, Marin Kurtela

Sveučilište u Zagrebu, Fakultet strojarstva i brodogradnje, Ivana Lučića 5, Zagreb, Hrvatska
University of Zagreb, Faculty of Mechanical Engineering and Naval Architecture, Zagreb, Croatia

Sažetak

Vodorazrjedivi sustavi premaza sve su popularnija metoda zaštite od korozije. Njihova velika prednost u odnosu na otapalne premaze je niža emisija hlapljivih organskih spojeva (HOS), što ih čini manje otrovnima i manje zapaljivima. Jedan od izazova primjene vodorazrjedivih premaza je njihova velika osjetljivost na niske temperature i visoku vlažnost. Ako je vlažnost zraka visoka, hlapljenje vodene pare iz premaza je otežano i premaz neće otvrdnuti. Rješenje ovog problema je kontinuirani dotok svježeg zraka koji ima veću sposobnost apsorbaranja vlage. Dobra cirkulacija zraka, kao i povišena temperatura skratit će vrijeme sušenja vodorazrjedivih premaza. Prije izlaganja premaza povišenoj temperaturi, važno je vrijeme predušenja, tzv. „flash off“ period, kako bi se spriječilo bubrenje premaza. Cilj ovog rada je odrediti parametre sušenja vodorazrjedivih premaza koristeći postrojenje za sušenje koje radi na principu infracrvenog (IC) zračenja. Provedena su ispitivanja tvrdoće prema Shore D metodi i prionjivosti vlačnom metodom. Na temelju dobivenih rezultata definirani su sigurni parametri sušenja kod kojih neće doći do pojave defekata na površini premaza.

Ključne riječi: *Vodorazrjedivi organski premazi, IC sušenje, antikorozijska zaštita.*

Abstract

Waterborne coating systems are an increasingly popular method of corrosion protection. Their advantage compared to solvent coatings is the lower emission of volatile organic compounds (VOC), which makes them less toxic and less flammable. One of the challenges of applying waterborne coatings is their high sensitivity to low temperatures and high humidity. If the humidity is too high, it is more difficult for air to absorb water vapor released during drying and the film will not cure. The solution to this problem is a continuous flow of fresh air, which has a greater ability to absorb moisture. Good air circulation, as well as elevated temperature, will shorten the drying time of water-borne coatings. Before exposing the coating to elevated temperature, the "flash off" period is important to prevent swelling of the coating. The aim of this work is to determine the drying parameters of water-borne coatings using an infrared (IR) drying plant. Hardness of tested coatings was determined using Shore D method. Adhesion tests were performed using pull-off method. Based on the obtained results, safe drying parameters were defined that would not cause defects on the surface of the coating.

Keywords: *Water-borne organic coatings, IR drying, anticorrosion protection.*

1. UVOD

Korozija i metode usporavanja korozijskih procesa na metalnim konstrukcijama predstavljaju zahtjevno inženjersko područje. Cilj borbe protiv korozije je usporavanje korozijskih procesa što jeftinijim metodama, a da se pritom zadovolje eksploatacijski uvjeti konstrukcije. Jedna od takvih metoda je zaštita organskim premazima. Dugo vremena upotrebljavali su se zaštitni premazi na bazi otapala, no u današnje vrijeme sve više se zahtijeva upotreba premaza na vodenoj bazi. Vodorazrjedivi premazi kao otapalo koriste vodu te se na taj način smanjuje ispuštanje emisija hlapljivih organskih spojeva u okoliš što je sve češći zahtjev naručitelja [1]. Dodatna prednost upotrebe vodorazrjedivih premaza je upotreba antikorozivnih pigmenata koji ne sadrže teške metale poput olova i kroma koji su otrovni. Jedan od nedostataka prilikom aplikacije premaza je nešto dulje vrijeme sušenja. Da bi se ubrzalo sušenje mogu se koristiti razne tehnologije prisilnog sušenja kao što su upotreba termokomora i IC komora [2]. U svrhu ovog istraživanja, korištena je IC tehnologija za sušenje tekućih premaza. Upotreba IC tehnologije omogućuje znatno brže sušenje, brže umrežavanje te bolju adheziju premaza na površinu [2]. Testiranje se provelo na pametnom postrojenju za sušenje tekućih premaza (**Slika 1**) sa 6 plinskih InfraCat panela snage 9-15 kW.



Slika 1: Infracrvena (IC) komora za sušenje tekućih premaza, Pilot postrojenje tvrtke Končar – Metalne konstrukcije

2. MATERIJALI I METODE

Za ispitivanje parametara sušenja koristili su se vodorazrjedivi dvokomponentni (2K) epoksi i poliuretanski premazi njemačkog proizvođača premaza (**Tablica 1**), koji se koriste u tvrtki Končar – Metalne konstrukcije. Jedan od premaza upotrebljava se kao međusloj, a drugi premaz kao završni premaz. Premazi su naneseni na testne pločice debljine 8 mm ručnim aplikatorom (**Slika 2**) u zadanoj debljini mokrog filma (DMF) od 150 μm za epoksi premaz, te 100 μm za poliuretanski premaz te su takve ostavljene da se predsuše prisilnim propuhivanjem uz pomoć sušila 10-50 min prije ulaska u IC komoru (**Slika 3**). Predsušenje (flash-off) se pokazalo kao nužna aktivnost kako bi glavina vode ishlapila iz premaza prije izlaganja IC zračenju. Ako bi se preskočila ova aktivnost dolazi do mjehuranja premaza na površini što je estetski i tehnološki neprihvatljivo. Kontaktnom metodom upotrebom olovke utvrđivalo se kada je premaz suh. Laganim prislanjanjem i potezanjem olovke po površini premaza provjeravalo se stanje premaza. Ukoliko nije ostajao trag olovke po površini premaza, premaz se smatrao suhim i spreman za vađenje iz komore za sušenje. Također nastojalo se da premaz ne prelazi temperaturu od 80 °C kako ne bi degradirao. Sušenje se provodilo na udaljenosti od 80 cm od IC panela do površine premaza.

Tablica 1 Ispitni premazi

Međuslojni premaz	Dvokomponentni epoksidni premaz na bazi vode	EPw	DMF 100 µm
Završni premaz	Dvokomponentni poliuretanski premaz na bazi vode	PUw	DMF 150 µm



Slika 2: Nanošenje premaza ručnim aplikatorom na ispitne pločice



Slika 3: Predsušenje premaza prisilnim propuhivanjem (ventilacijom)

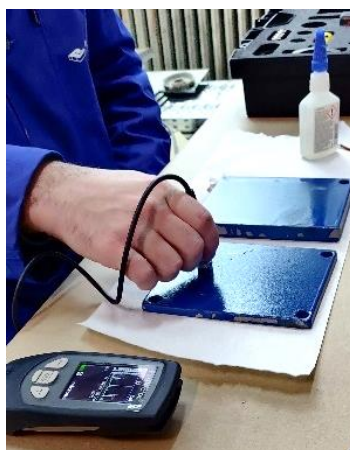
Za mjerenje debljine suhog filma (DSF), prema HRN EN ISO 2808 [3], korišten je instrument Elcometer 456 koji radi na principu ne-destruktivne magnetske indukcije. Mjerenja su provedena na deset različitih lokacija po uzorku s točnošću $\pm 2,5 \mu\text{m}$. Postupak mjerenja sastojao se od prislanjanja mjerne sonde na suhu površinu premaza te očitavanja vrijednosti sa uređaja. Izbjegavali su se rubovi testnih pločica jer se na tim mjestima pojavljuje zadebljanje premaza koje bi moglo utjecati na prosjek od deset mjernih lokacija.

Prionjivost premaza određena je pomoću Elcometer 510 uređaja s točnošću mjerenja $\pm 0,4 \text{ MPa}$, prema HRN EN ISO 4624 [4]. Mjerenje se radi na minimalno dvije lokacije na testnoj pločici uz prethodnu pripremu pločice. Priprema se sastoji od laganog ohrapljivanja površine brusnim papirom zbog ravnomjernije prionjivosti ljepila. Zatim se na takvu površinu kontaktnim ljepilom učvrste čunjići propisanog promjera koji su izolirani od okolnog premaza te se povežu sa uređajem Elcometer 510. Uređaj tada ravnomjernom silom čupa mjerne čunjiće te se očitava sila pri kojoj dolazi do odvajanja čunjića od premaza (**Slika 4**). Očitana sila je vrijednost adhezije premaza.



Slika 4: Ispitivanje adhezijskih svojstva uređajem Elcometer 510

Tvrdoća premaza određena je Shore D metodom, uređajem Positector SHD po normi ASTM D2240-15 [5]. Metodom Shore D ispituje se tvrdoća duromera utiskivanjem po normi definirane penetrirajuće stope (**Slika 5**). Vrijednost prodiranja penetrirajuće stope izravno se očitava sa uređaja i predstavlja bezdimenzijsku vrijednost na skali od 0-100 pri čemu veća vrijednost predstavlja tvrđu prevlaku. Za potrebe ispitivanja mjerenje se provelo na deset različitih lokacija po ispitnoj pločici te je uzet prosjek mjerenja za vrijednost tvrdoće uzorka.



Slika 5: Ispitivanje tvrdoće po Shore D metodi uređajem Positector SHD

3. REZULTATI I DISKUSIJA

Vodorazrjedivi premazi zahtijevaju vrijeme predsušenja (flash-off) kako ne bi došlo do mjehuranja na površini premaza. Do mjehuranja dolazi jer se zaostala voda u premazu zbog ubrzanog sušenja pretvara u vodenu paru kojoj je onemogućen spor izlazak iz premaza. Uslijed nagle promjene volumena vode površina premaza počinje mjehurati (Slika 6).



Slika 6: Mjehuranje premaza

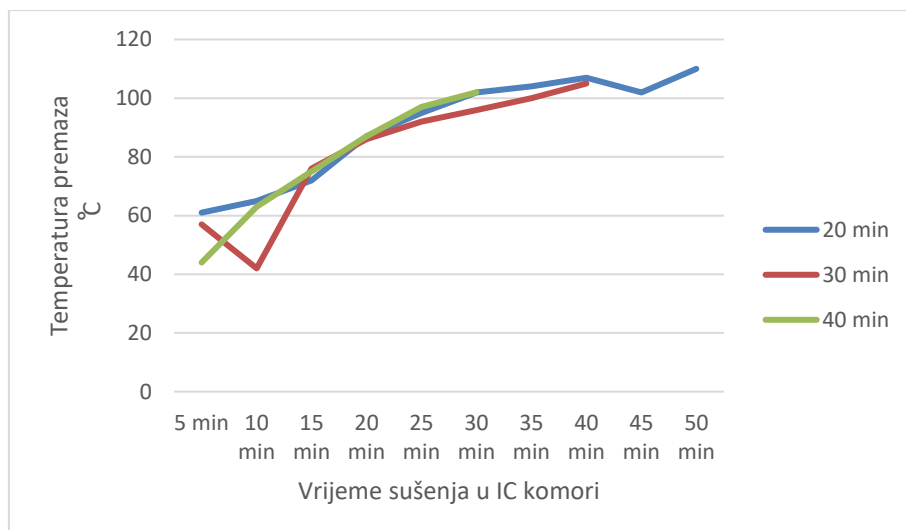
Rješenje ovog problema ima više pristupa, a može biti produljenje vremena predsušenja, sporije zagrijavanje premaza te prisilno propuhivanje (ventilacija). Za industrijsku primjenu potrebno je optimizirati sustav da se dobije što kraće vrijeme predsušenja. Rezultati ispitivanja pokazali su da se vodorazrjeđivi epoksidni sustavi mogu kraće predsušiti (**Tablica 2, Dijagram 1**) odnosno potrebno im je oko 20 min za predsušenje da bi za 20 min u IC komori na udaljenosti od 80 cm postigli zadovoljavajuću temperaturu potrebnu za umrežavanje, a da pritom ne dođe do mjehuranja.

Završni vodorazrjeđivi poliuretanski premaz potrebno je predsušiti 40 min da bi se sigurno mogao sušiti u IC komori na udaljenosti od 80 cm do potrebne temperature za umrežavanje premaza (**Tablica 3, Dijagram 2**). Prilikom ispitivanja primijećeno je da kod kraćeg vremena predsušenja dolazi do mjehuranja premaza na zadebljanjima na rubovima.

Fizikalna svojstva pokazala su se zadovoljavajuća prilikom sušenja u IC kabini na udaljenosti od 80 cm za EPw i PUw premaz, odnosno produljenjem vremena predsušenja neznatno se povećava tvrdoća premaza te adhezijska svojstva (**Tablica 4**).

Tablica 2: Postignute temperature EPw premaza na 80 cm udaljenosti IC panela

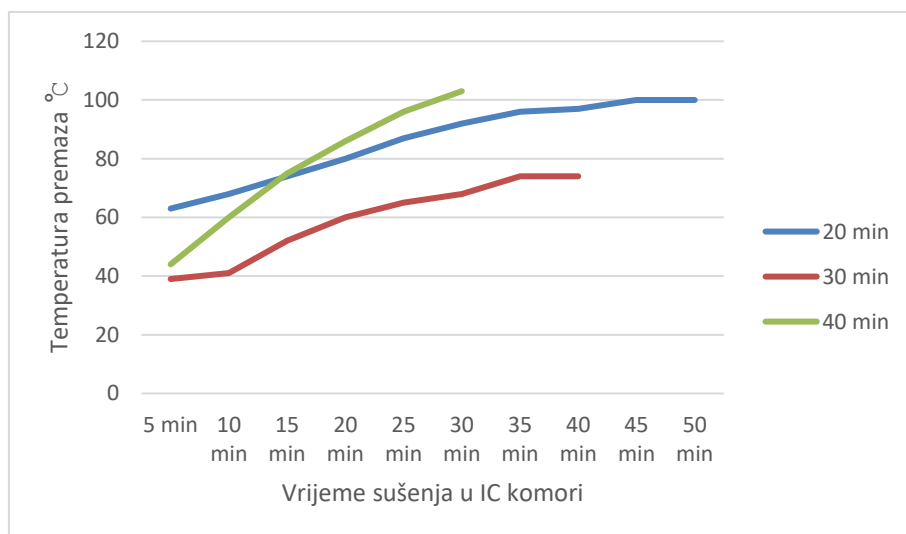
EPw		Temp, °C									
		5 min	10 min	15 min	20 min	25 min	30 min	35 min	40 min	45 min	50 min
Predsušenje	20 min	61	65	72	87	95	102	104	107	102	110
	30 min	57	42	76	86	92	96	100	105		
	40 min	44	63	75	87	97	102				



Dijagram 1: Postignute temperature EPw premaza za tri vremena predušenja

Tablica 3: Postignute temperature PUw premaza na 80 cm udaljenosti IC panela

PUw		Temp, °C									
		5 min	10 min	15 min	20 min	25 min	30 min	35 min	40 min	45 min	50 min
Predsušenje	20 min	63	68	74	80	87	92	96	97	100	100
	30 min	39	41	52	60	65	68	74	74		
	40 min	44	60	75	86	96	103				



Dijagram 2: Postignute temperature PUw premaza za tri vremena predušenja

Tablica 4: Fizikalna svojstva EPw i PUw premaza sušenih na 80 cm od IC panela

EPw	Vrijeme predsušenja			PUw	Vrijeme predsušenja		
	20 min	30 min	40 min		20 min	30 min	40 min
DSF	57,19	61,14	53,52	DSF	58,87	71,21	63,17
Shore D	92,4	92,2	92,6	Shore D	92,2	92	92,6
Pull-off	14,74	16,57	17,5	Pull-off	11,66	14,29	12,3

Slika 7 prikazuje Pull-off vrijednosti prionjivosti EPw i PUw premaza sušenih na 80 cm od IC panela. Niti kod jednog ispitivanja nije došlo do odvajanja premaza od podloge.



Slika 7: Pull-off vrijednosti prionjivosti EPw i PUw premaza sušenih na 80 cm od IC panela

4. ZAKLJUČAK

Cilj ovog rada bio je utvrditi parametre sušenja vodorazrjeditivih epoksi i poliuretanskih zaštitnih premaza. Kao glavni problem kod sušenja premaza na bazi vode utvrđeno je mjehuranje premaza. Navedeni se problem može popraviti uvođenjem odgovarajućeg vremena predušenja. Na temelju provedenih ispitivanja, može se zaključiti da je EPw premaz zahvalniji za rad, budući da ne zahtijeva toliko dugo vrijeme predušenja, kao što to zahtijeva PUw premaz.

Primijećeno je podjednako vrijeme zagrijavanja površine EPw i PUw premaza. Od fizikalnih svojstava, tvrdoća po Shore D metodi pokazala se podjednaka u svim situacijama. Adhezijska svojstva pokazala su tendenciju poboljšanja vrijednosti s povećanjem vremena predušenja, prilikom sušenja na udaljenosti 80 cm od IC panela. Sušenje premaza IC tehnologijom znatno ubrzava proces sušenja, a samim time ubrzava i proizvodnju. Za razliku od otapalnih, vodorazrjeditivi premazi zahtijevaju nešto duži proces sušenja, koji nužno uključuje predušenje, nanošenje premaza u nešto tanjem sloju te sušenje slabijim intenzitetom infracrvenog zračenja, što se postiže udaljavanjem premaza koji se suši od IC panela. Na taj način dozvolit će se zaostaloj vodi unutar premaza izlazak bez prethodnog mjehuranja površine premaza.

Zahvala:

Istraživanje je provedeno u sklopu projekta „Pametno postrojenje za sušenje tekućih premaza“ (Referentna oznaka: KK.01.2.1.02.) koji je sufinanciran u okviru Operativnog programa konkurentnost i kohezija, iz Europskog fonda za regionalni razvoj (<https://strukturnifondovi.hr/>). Sadržaj ove publikacije isključiva je odgovornost Fakulteta strojarstva i brodogradnje Sveučilišta u Zagrebu (<https://www.fsb.unizg.hr/index.php?pocetna&lang=hr>).

LITERATURA

- [1] S. Li, Z. Liu, L. Hou, Y. Chen and T. Xu, "Effect of polyether/polyester polyol ratio on properties of waterborne two-component polyurethane coatings," *Progress in Organic Coatings*, vol. 141, 2020.
- [2] R. S. Davidson i R. J. Holman, »Developments and trends in radiation curing,« *Review of Progress in Coloration and Related Topics*, svez. 33, br. 1, pp. 46-58, 2003.
- [3] I. Stojanović, M. Logar, I. Fatović, V. Alar i D. Rakela-Ristevski, »Experimental Study of Atmospherically and Infrared-Dried,« *Coatings*, 2023.
- [4] »HRN EN ISO 2808 Boje i lakovi - Određivanje debljine filma,« International Organization for Standardization, Ženeva, Švicarska, 2019.
- [5] HRN EN ISO 4624; Boje i lakovi - Ispitivanje prionljivosti vlačnom metodom, Ženeva, Švicarska: International Organization for Standardization , 2016.
- [6] »ASTM D2240-15 (2021) Standard Test Method for Rubber Property—Durometer Hardness,« 2021.

CORROSION PROPERTIES OF AA5083 IN MARINE ENVIRONMENT UNDER STAGNANT AND FLOW CONDITIONS

KOROZIJSKA SVOJSTVA AA5083 LEGURE U MORSKOM OKOLIŠU U STACIONARNIM I PROTOČNIM UVIJETIMA

Lea Lokas¹, Vesna Alar²

¹ Razvojno inovacijski centar AluTech, Velimira Škorpika 6, Šibenik, Hrvatska

² Sveučilište u Zagrebu, Fakultet strojarstva i brodogradnje, Ivana Lučića 5, Zagreb, Hrvatska

Sažetak

AA5083 alloys are widely used in marine environments due to their favorable corrosion properties. These alloys are commonly used in the construction of ship hulls and deck panels because of their high strength-to-weight ratios. To accurately understand and predict the behavior of AA5083 alloys in real marine environments, it is crucial to simulate conditions as closely as possible. In this study, the corrosion properties of AA5083 in marine environments under stagnant and flow conditions were investigated. The study aimed to assess the corrosion behavior of AA5083 in freshly sampled seawater and determine the effect of temperature elevation from 10°C to 30°C using AC and DC electrochemical measurement.

Ključne riječi: *aluminium alloy, seawater, corrosion, AA5083*

Abstract

Aluminijske legure AA5083 imaju široku primjenu kao konstrukcijski material u morskom okolišu i brodograđevnoj industriji, posebice u konstrukciji brodskih trupova i brodske palube zbog svog visokog omjera čvrstoće i mase te povoljnih korozijskih svojstava. Kako bi se u potpunosti razumjeli korozijski fenomeni povezani s korozijom aluminijskih legura u morskom okolišu te predvidjelo ponašanje AA5083, potrebno je što je više moguće simulirati realne uvjete. Cilj ovog rada je proučavanje korozijskih svojstava AA5083 u stacionarnim i protočnim uvjetima svježe uzorkovane morske vode te istraživanje utjecaja povišenja temperature od 10°C do 30°C korištenjem AC i DC elektrokemijskih mjerenja.

Keywords: *aluminijske legure, morska voda, korozija, AA5083*

1. INTRODUCTION

The corrosion of aluminium alloys when exposed to seawater is a well-known phenomenon and the corrosion occurrence as well as corrosion rate can be influenced by various factors. Seawater environment poses unique challenges due to its corrosive nature and presence of aggressive Cl^- ions. Studies have shown that beyond salinity (1, 2) and temperature (2, 3) greatest effect have fluid dynamics (4, 5) AA5083 alloys have widespread use in marine applications and its mainly used in the construction of ship hulls and deck panels since have desirable combination of good mechanical properties, weldability, good corrosion resistance compared to other aluminium alloys and excellent formability. (6, 7)

The corrosion properties of AA5083 during exploitation in seawater can vary depending on the environmental conditions, such as whether the alloy is exposed to stagnant or flowing seawater. (8, 9) Seawater flow enhances the mass-transfer of corrosive agents like chloride ions to the surface of AA5083, potentially leading to higher localized concentrations and an accelerated corrosion rate. However, this process also introduces complexities stemming from fluid dynamics. Varying flow velocities and turbulence can create regions of stagnation that foster localized corrosion, such as pitting or crevice corrosion. (8, 10) At higher seawater velocities due to turbulent flow only erosion-corrosion was recorded. (5, 11) Contrariwise, seawater flow and enhanced mass-transfer of oxygen diffusion toward the metal surface can be favourable to the formation of an oxide film on the Al-surface. (12)

In addition, it is well known that corrosion resistance of AA5083 in seawater is closely linked with alloy microstructure and presence of intermetallic particles (IMPs). The sensitivity to localized corrosion is typically heightened by the presence of intermetallic particles, which establish micro-galvanic cells with the surrounding matrix, resulting in accelerated metal dissolution on a localized level. (13) Numerous studies in the literature extensively discuss the impact of secondary phase particles on the localized corrosion tendencies of aluminum alloys. For instance, Al_3Mg_2 has been reported to be more anodic compared to the Al-matrix of AA5083 alloy in marine environment across a wide pH range (pH 2–10). (13-16) Anodic character and active dissolution in NaCl environment has been reported for Mg_2Si second phase particle. (1, 8, 17, 18) On the other hand, there are second phase particles such as $\text{Al}_x(\text{Fe},\text{Mn})_y\text{Si}$ particles which are more noble with regards to the Al matrix and cause peripheral trenches of the surrounding matrix. (19, 20)

The main aim of the study was to understand the corrosion phenomena of AA5083 alloy and how it behaves under different conditions being specifically focused on the effect of temperature elevation from 10°C to 30°C on the corrosion properties of AA5083 alloy in marine environments under both stagnant and flow conditions.

2. MATERIALS AND METHODS

Testing samples used in this research were taken from the AA5083 sheet with diameter of 1.45 cm. The chemical composition of alloy was obtained using X-ray fluorescence spectrometry (XRF) and spectrometer Olympus Innov-X. and is shown in wt.% in Table 1. All samples were soldered to insulated copper wire in order to ensure electrical contact and moulded in epoxy resin where exposed surface for measurement was 1.65cm^2 . After moulding the sample surface was mechanically with SiC emery paper from 320 up to 2500 grit using Metkon Digiprep Acura automatic grinding and polishing machine on 400-rpm ($41,89\text{ rad/s}$) disc speed. Prior electrochemical measurements the

surface was ultrasonically degreased in ethanol, rinsed with distilled water and dried in cold air stream.

Tab. 1: Chemical analysis of AA5083

Composition, wt.%										
Elements	Mg	Si	Cr	Ni	Fe	Mn	Zn	Cu	Pb	Al
AA5083	4,22	0,26	0,05	0,026	0,37	0,57	0,081	0,038	0,014	Balance

In order to collect various electrochemical parameters environments under stagnant and flow conditions and to assess corrosion behaviour of AA5083 seawater electrochemical tests were performed in accordance with ASTM G5 and HRN EN ISO 17475 standards. The experiments conducted under flow condition were performed in flow corrosion cell and flow system created for the purpose of this research while experiments conducted under stagnant condition were performed in a three-electrode standard corrosion cell with double jacket glass. Both setups were shown on figure 1. The corrosion cell in stagnant set up was connected to water bath Huber 212B to maintain stable electrolyte temperature. The flow system was composed of: two tanks, one for cooling and the other for heating purpose of the electrolyte, flowmeter, pump, thermostat and a flow cell connected with a tank filled with seawater.

Fresh sampled seawater with averagely salinity of 38‰ were used as an electrolyte. In order to monitor influence of temperature change on corrosion behaviour of AA5083 under stagnant and the flow conditions each test was carried at temperature 10 °C and 30 °C. All tests were performed using Bio-Logic SP-200 potentiostat/galvanostat and EC-lab software to collect the data. The reference electrode was saturated calomel electrode (SCE) while two graphite electrodes were used as counter electrode. All experiments were performed under the laminar flow condition with flow rate of 190 L/h and $Re=949$.



a)



b)

Fig. 1. Measurement equipment set up for measurement in a) stagnant condition and b) flow condition

Experiments were started with open circuit potential (OCP) monitoring for 60 minutes with data collecting every 20 seconds. Afterward, electrochemical impedance spectroscopy (EIS) was conducted in the frequency range from 50 kHz to 30 mHz and with perturbation of ± 10 mV at the corrosion potential. Linear polarization was carried out in the potential region of ± 10 mV around corrosion potential with the scanning rate of 0.167 mV/s. Potentiodynamic polarization was performed in the potential region of ± 0.250 V around E_{cor} using scanning rate of 0.167 mV/s while cyclic potentiodynamic polarizations measurements were conducted using same scan rate starting from E_{cor}

towards more anodic potentials and, when a current of 5 mA/cm² was reached, reverse back to E_{cor} .

3. RESULTS AND DISCUSSION

Figure 1. illustrate open circuit potential monitoring (OCP) that was performed trough 60 minutes with data gathering every 20 seconds prior to each test. From presented it is visible that potential becomes more negative in flowing seawater with temperature elevation while in still water it is oposite. Oscillatory behaviour that can be related with cycles of localised formation/dissolution of the oxide layer in potential can be noticed in flowing and still conditions at both temperatures but it is more pronounced in flowing seawater. In flowing seawater at 10°C during the OCP monitoring potential moves towards more noble values while at 30°C have same more steeper trend for the first 7 minutes, afterwards remains similar for the next 20 minutes, when sharp dececrease towards negative values can be seen indicating activity of present oxygen on alloy surface. In still seawater values during OCP monitoring are pretty constant during 60 minutes measurement window at 30°C. At 10°C for the first 7 minutes potential shift towards more negative values has been recorded afterwards remains mostly constant.

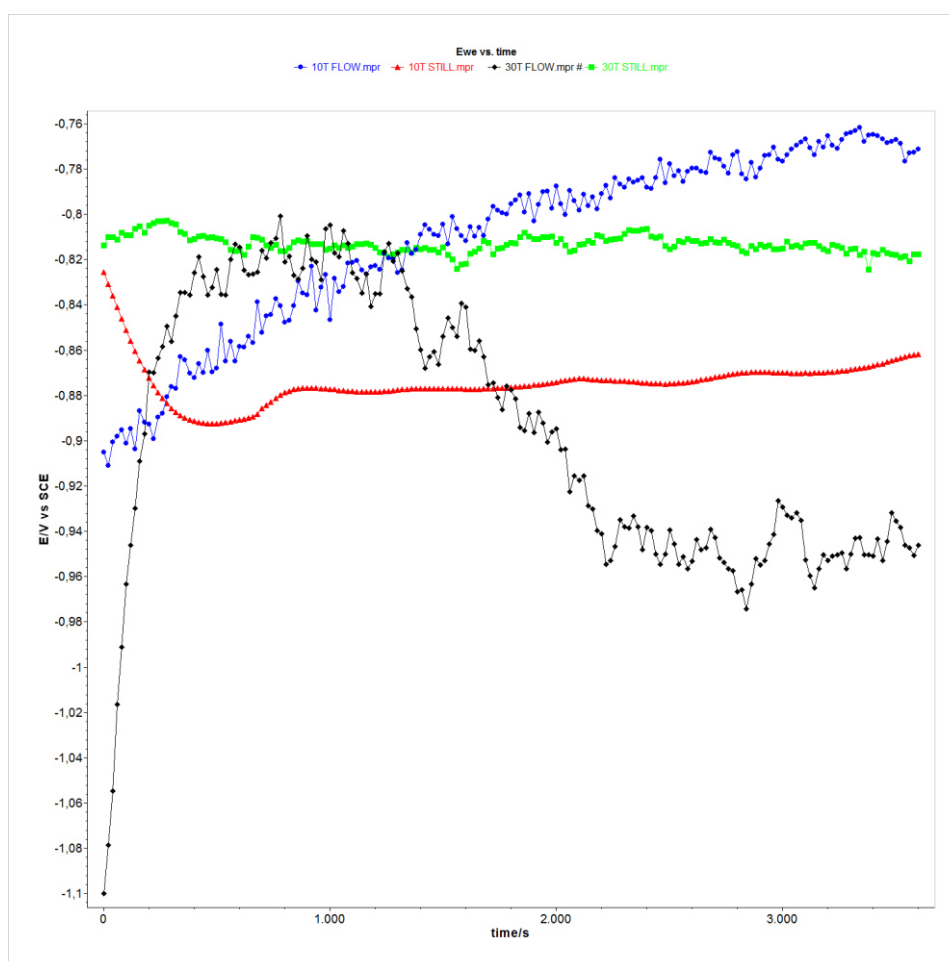


Fig. 1. Open circuit potential measurements (OCP) of AA5083 in flowing and still seawater at 10°C and 30°C

Electrochemical impedance spectroscopy (EIS) was performed right after OCP monitoring in still and flowing seawater at 10°C and 30°C. Collected spectra was show as a Niquist and Bode plot in Fig 2., while equivalent electrical circuit proposed to fit the experimental data can be seen in Fig 3. Used equivalent electrical circuit contain the following elements: R_s that represent the solution resistance, due to dielectric behaviour of oxide film R_{ox} represent resistance of oxide layer while Q_{ox} is capacitance of the oxide layer with constant phase element (CPE) behaviour, R_{ct} is charge transfer resistance and C_{dl} is double layer capacitance. Impedance of CPE, i.e. Q_{ox} , can be calculated using following equation:

$$Z(Q_{ox}) = Y^{-1}(j\omega)^{-n} \quad (1)$$

where Z is impedance of Q_{ox} , j is imaginary component, ω is the angular frequency, Y is the frequency independent admittance and n is the power of Q_{ox} . Data collected from EIS measurement in shown in Table 2.

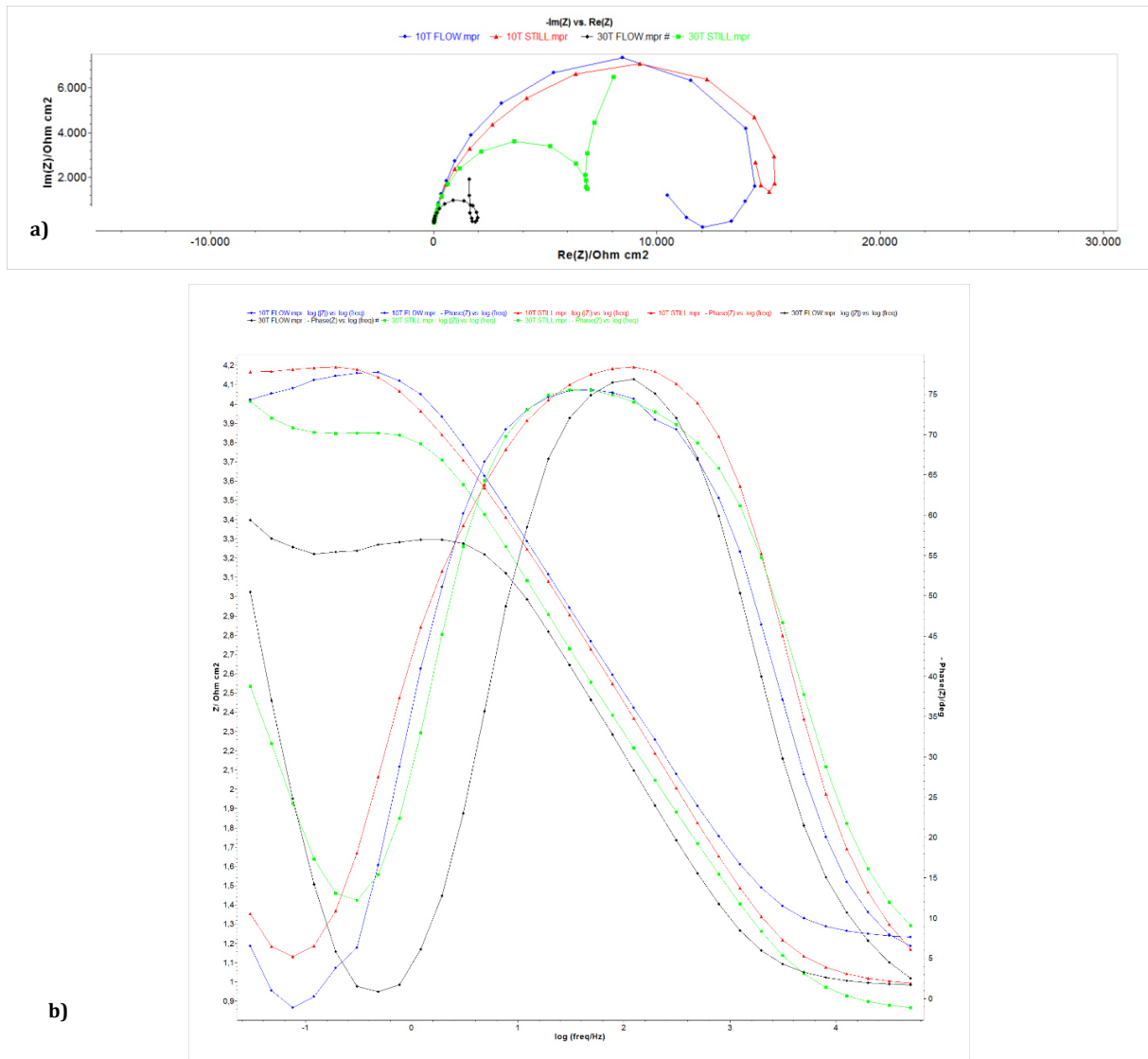


Fig. 2. Niquist (a) and Bode (b) plots of AA5083 in still and flowing seawater at 10°C and 30°C

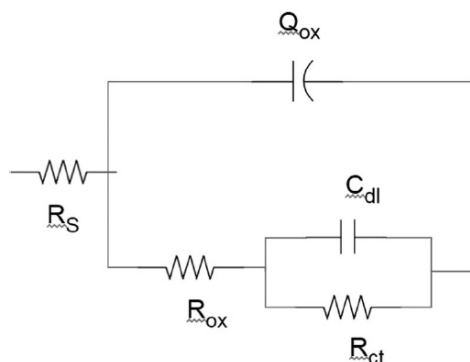


Fig 3. Equivalent circuit used for fitting of the experimental data

From presented spectra, three characteristic regions and existence of two time constants can be seen as. First characteristic region belongs to high frequency range and represent seawater resistance. Second characteristic region represent capacitive behaviour of system and can be seen in medium frequency range. Third characteristic region in low frequency range contributes to alloy resistance and charge transfer resistance. First time constant is revealed in high frequency range and can be related with oxide layer on the alloy surface, while other is associated with localized dissolution at lower frequencies. Furthermore, on Fig. 2 on each spectra there is visible capacitive depressed semicircle at high frequencies and a pseudo-inductive loop at lower frequencies. Such a behaviour can be related with creation and absorption of Cl⁻ complexes on AA5083 surface which can accelerate alloy dissolution.(21)

Tab. 2: Electrochemical impedance parameters of AA5083 in still and flowing seawater at 10°C and 30°C fitted using proposed equivalent electrical circuit

	Temperature, °C	R_s ($\Omega \text{ cm}^2$)	$Q_{ox} \times 10^{-6}$ ($\text{F cm}^{-2} \text{ s}^{n-1}$)	n_1	R_{ox} ($\Omega \text{ cm}^2$)	$C_{dl} \times 10^{-6}$ (F cm^{-2})	R_{ct} ($\Omega \text{ cm}^2$)
Still water	10	5.859	19.66	0.891	9487	39.36	10355
	30	4.458	27.56	0.882	4695	1348.1	8024
Flowing water	10	10.240	18.29	0.879	10659	-145.5	-3525
	30	6.057	22.88	0.954	1128	4693.1	-5535

From presented results can be seen that with temperature increase in stagnant as well as in flowing condition values of R_{ox} , R_{ct} , Q_{ox} and C_{dl} decrease. Shift in phase angle toward more negative values can be associated with re-passivation of oxide film and formed pits.

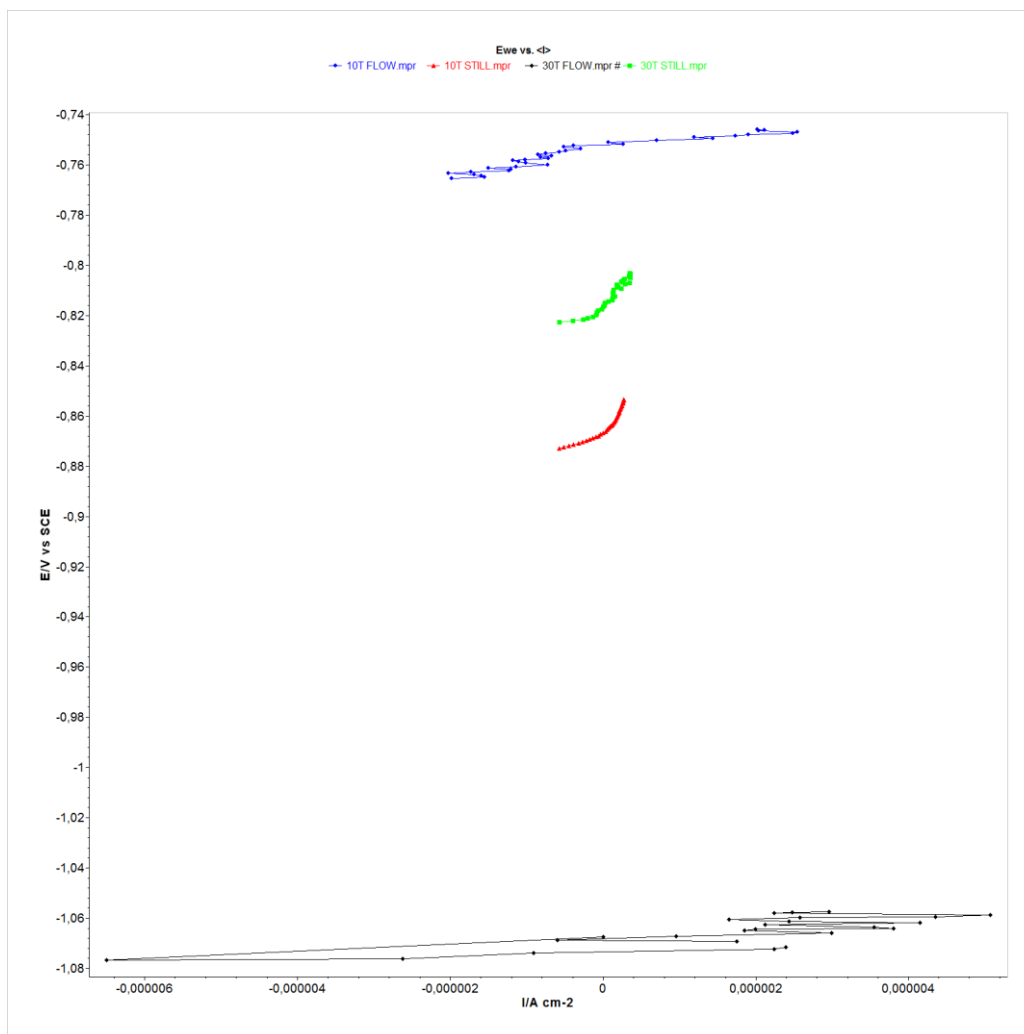


Fig 4. Linear polarization curves of AA5083 in still and flowing seawater at 10°C and 30°C

E-i plot shown in Fig. 4. represent linear polarisation measurements for AA5083 in still and flowing seawater at 10°C and 30°C taken after electrochemical impedance spectroscopy. The slope of linear part of the curves correspond to polarization resistance (R_p) and collected values can be found in table 3. From presented results, it is visible that with temperature elevation in stagnant water slope of the curves as well as R_p tends to decrease. Under laminar flow regime during linear polarisation measurements AA5083 have quite similar resistance to corrosion with only slight decrease in curve slope as well as in recorded R_p value at 30°C.

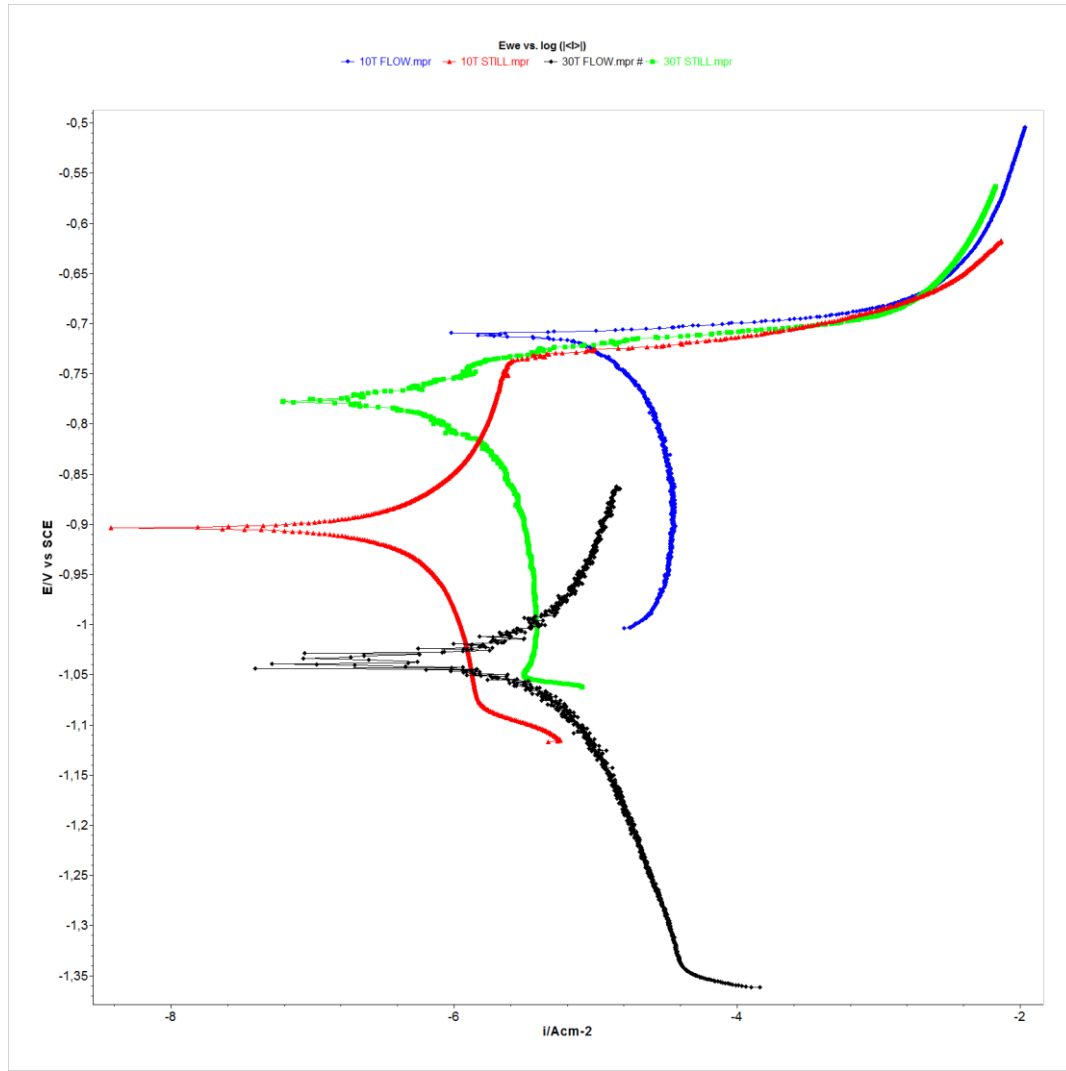


Fig 5. Potentiodynamic polarization curves of AA5083 in still and flowing seawater at 10°C and 30°C

After potentiodynamic polarization measurements, in order to get values of corrosion current density (i_{cor}) and corrosion rate ($C.R.$) of AA5083 under stagnant and flowing seawater at 10°C and 30°C, Tafel extrapolation was performed. Obtained i_{cor} values were shown in table 3. as well as corrosion rate values which are calculated using following equation:

$$C.R. = \frac{K \cdot i_{cor} \cdot (E.W.)}{d \cdot A} \quad (2)$$

where i_{cor} is corrosion current density, $E.W.$ is the equivalent weight of metal, d is the density of AA5083, A is sample area and K is constant that defines the units of the corrosion rate in millimetre per year (mmpy); $K = 3272 \text{ mm}/(\text{A cm year})$.

In stagnant seawater collected corrosion rate values for AA5083 demonstrate that increase in temperature from 10°C to 30°C enhance corrosion rate for 9.52 μmpy . Contrary to expectations and previous EIS measurements, corrosion rate values obtained under the laminar flow regime indicate that decreasing temperature from 30°C to 10°C

increase corrosion rate values for 232.21 $\mu\text{m/yr}$. In fact, at 10°C under the flowing condition AA5083 exhibit highest corrosion values. Difference between corrosion rate under stagnant and flowing condition seawater at 10°C was 279.70 $\mu\text{m/yr}$, while at 30°C was 37.94 $\mu\text{m/yr}$.

Such a behaviour can be explained with E -log i plots obtained using potentiodynamic polarisation. Obtained curves can be divided in two parts; cathodic - where oxygen reduction take place, and anodic part that represent alloy dissolution. Under flowing conditions at 10° C cathodic part of the curve exhibit higher current density values compared to other measurement indicating increased cathodic kinetic. Increased cathodic kinetic arises due to higher oxygen solubility at lower temperatures, constant motion and transport of dissolved oxygen and aggressive Cl^- ions as well as accelerated diffusion of the oxygen to AA5083 surface under laminar flow regime.(3, 22, 23) Anodic part of the curve is also affected; since corrosion potential is shifted in positive direction, and close to pitting potential of AA5083, there is no active nor passive region. Alloy dissolution starts immediately after E_{cor} values are reached, afterwards alloy shows some kind of transpassive behaviour. Similar behaviour in anodic region can be seen at 30°C under stagnant condition. At 10°C under stagnant condition the passive, active and transpassive regions are visible and under this condition AA5083 exhibit lowest corrosion rate. Under laminar flow regime at 30°C E_{cor} values are shifted towards more negative values resulting in expanding the AA5083 passive region and increasing alloy passivity, so break down potential in potentiodynamic measurements has not been recorded. (24, 25)

Tab. 3: Electrochemical parameters of AA5083 in still and flowing seawater at 10°C and 30°C obtained from potentiodynamic and cyclic polarization measurements

	Temperature, °C	E_{cor} vs SCE, V	i_{cor} , $\mu\text{A cm}^{-2}$	R_p , Ohm cm^2	E_p vs SCE, V	E_{rev} vs SCE, V	E_{RP} vs SCE, V	Corrosion rate, $\mu\text{m/yr}$
Still seawater	10	-0.818	1.058	13665	-0.726	-0.613	-0.811	7.29
	30	-0.862	2.438	11678	-0.716	-0.688	-0.735	16.82
Flowing seawater	10	-0.771	41.603	2614	-0.709	-0.660	-	287.10
	30	-0.946	7.941	2145	-0.734	-0.650	-0.809	54.79

Since is for AA5083 in seawater environment most dominating corrosion is pitting corrosion cyclic polarization was conducted to get insight on temperature influence on pitting tendency and values of pitting potential (E_p), the reverse potential (E_{rev}) and re-passivation potential (E_{RP}). All collected values under stagnant and flow condition are shown in table 3. while obtained curves are presented in Fig. 6. From presented it can be seen that in each measurement there is visible passive region where current density are almost negligible increased until E_p was reached and dissolution of oxide layer and formation of pits started. Larger passive window can be noticed at 30°C under laminar flow

regime since corrosion potential of AA5083 is shifted in negative direction and E_p values are quite similar in each measurmet, within potential range of $\pm 25\text{mV}$. Propagation of formed pits take place until re-passivation potential (E_{RP}) was reached and after that, no new pits can initiate or propagate. (26) Re-passivation potential was not observed only at 10°C under the flow condition. Reason for such a behaviour might be in a fact that lower seawater temperature moves pitting potential towards more positive values, close to potential region where pitting corrosion occurs on AA5083 in seawater.

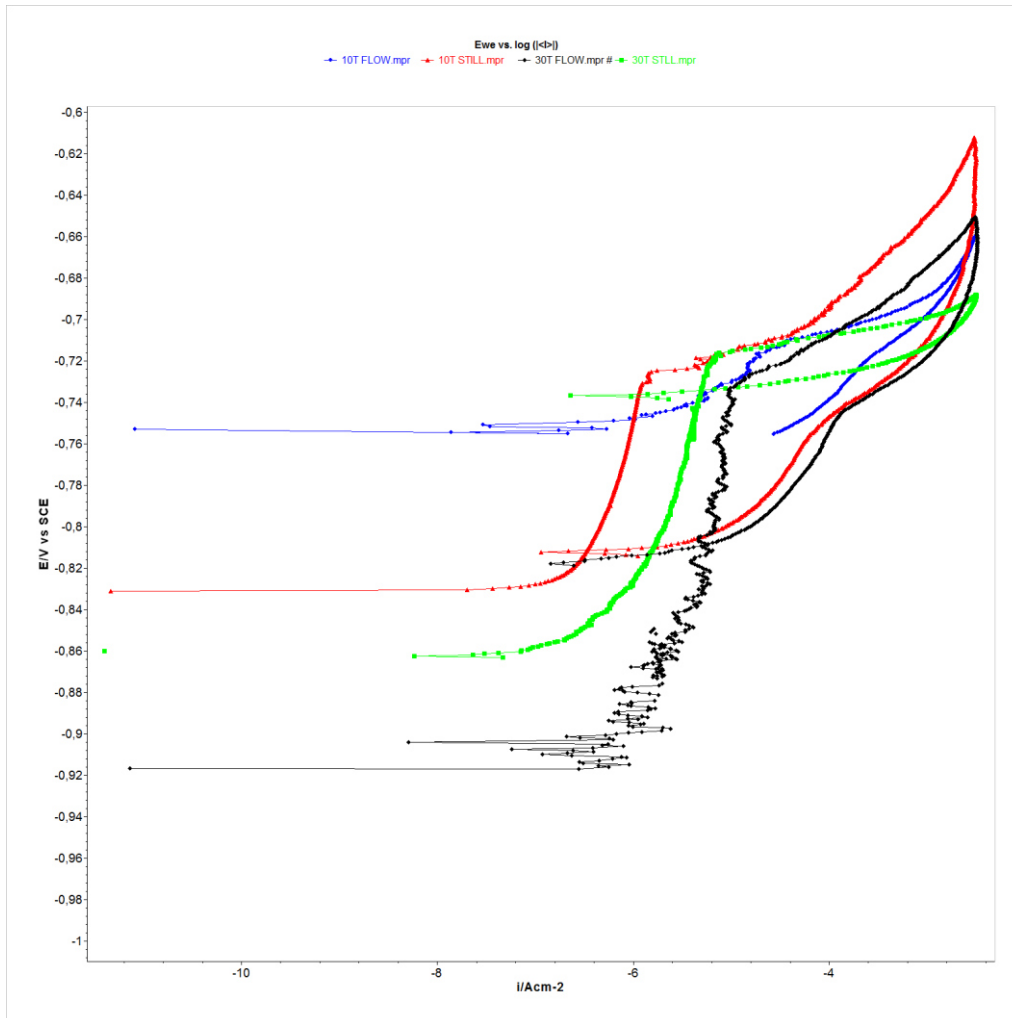


Fig 6. Cyclic polarization curves of AA5083 in still and flowing seawater at 10°C and 30°C

4. CONCLUSION

This research work aimed to assess the corrosion behavior of AA5083 in freshly sampled seawater and determine the effect of temperature elevation from 10°C to 30°C using AC and DC electrochemical measurement. The main conclusions can be summarized as follows:

- Corrosion potential is moved toward negative values in flowing seawater with temperature elevation while in still water it is opposite.
- With temperature increase in stagnant as well as in flowing condition values of R_{ox} , R_{ct} , Q_{ox} and C_{dl} decrease. Shift in phase angle toward more negative values can be associated with re-passivation of oxide film and formed pits.

- With temperature elevation in stagnant water slope of the curves as well as R_p tends to decrease. Under laminar flow regime during linear polarisation measurements AA5083 have quite similar resistance to corrosion with only slight decrease in curve slope as well as in recorded R_p value at 30°C.
- In stagnant seawater collected corrosion rate values for AA5083 indicate that increase in temperature from 10°C to 30°C enhance corrosion rate for 9.52 $\mu\text{m/yr}$. Contrary to expectations corrosion rate values obtained under the laminar flow regime indicate that decreasing temperature from 30°C to 10°C increase corrosion rate values for 232.21 $\mu\text{m/yr}$. Difference between corrosion rate under stagnant and flowing condition seawater at 10°C was 279.70 $\mu\text{m/yr}$, while at 30°C was 37.94 $\mu\text{m/yr}$.
- At 10°C under the flowing condition AA5083 exhibit highest corrosion values.
- The cyclic polarization curves reveal that re-passivation potential was not observed only at 10°C under the flow condition. At 30°C under laminar flow regime larger passive window can be noticed. E_p values are quite similar in each measurement, within the potential range of $\pm 25\text{mV}$.

REFERENCES

1. Deng C-M, Xia D-H, Zhang R, Behnamian Y, Hu W, Birbilis N. On the localized corrosion of AA5083 in a simulated dynamic seawater/air interface-Part 2: effects of wetting time. *Corrosion Science*. 2023;221.
2. Lokas L, Alar V. The effect of temperature on corrosion behavior of AA5083 in brackish water and seawater. *Materials and Corrosion-Werkstoffe Und Korrosion*. 2019;70(10):1817-25.
3. Ezuber H, El-Houd A, El-Shawesh F. A study on the corrosion behavior of aluminum alloys in seawater. *Materials & Design*. 2008;29(4):801-5.
4. Kim YB, Kim SJ. Effect of Flow Rate on Erosion Corrosion Damage and Damage Mechanism of Al5083-H321 Aluminum Alloy in Seawater Environment. *Corrosion Science and Technology-Korea*. 2020;19(3):115-21.
5. Xu YZ, Tan MY. Probing the initiation and propagation processes of flow accelerated corrosion and erosion corrosion under simulated turbulent flow conditions. *Corrosion Science*. 2019;151:163-74.
6. Kaibyshev R, Musin F, Lesuer DR, Nieh TG. Superplastic behavior of an Al-Mg alloy at elevated temperatures. *Materials Science and Engineering a-Structural Materials Properties Microstructure and Processing*. 2003;342(1-2):169-77.
7. Toros S, Ozturk F, Kacar I. Review of warm forming of aluminum-magnesium alloys. *Journal of Materials Processing Technology*. 2008;207(1-3):1-12.
8. DENG Chengman LZ, XIA Da-Hai, HU Wenbin. Localized Corrosion Mechanism of 5083-H111 Al Alloy in Simulated Dynamic Seawater Zone. *Journal of Chinese Society for Corrosion and protection*. 2023;43(4):683-92.
9. Jafarzadeh K, Shahrabi T, Ajdarzadeh Oskouei A. Novel approach using EIS to study flow accelerated pitting corrosion of AA5083-H321 aluminum-magnesium alloy in NaCl solution. *Journal of Applied Electrochemistry*. 2009;39(10):1725-31.
10. Jafarzadeh K, Shahrabi T, Hadavi SMM, Hosseini MG. Morphological characterization of AA5083-H321 aluminum alloy corrosion in NaCl solution under hydrodynamic conditions. *Anti-Corrosion Methods and Materials*. 2009;56(1):35-42.

11. Yabuki A, Yasunaga DT, Shibutani T, Shinkai K. Corrosion of an aluminum alloy chilled in flowing seawater and the effect of cathodic prevention. *Materials and Corrosion-Werkstoffe Und Korrosion*. 2007;58(5):340-4.
12. Queuedo MC, Galicia G, Mayen-Mondragon R, Genesca Llongueras J. Role of turbulent flow seawater in the corrosion enhancement of an Al-Zn-Mg alloy: an electrochemical impedance spectroscopy (EIS) analysis of oxygen reduction reaction (ORR). *Journal of Materials Research and Technology-Jmr&T*. 2018;7(2):149-57.
13. Liew Y, Ornek C, Pan JS, Thierry D, Wijesinghe S, Blackwood DJ. In-Situ Time-Lapse SKPFM Investigation of Sensitized AA5083 Aluminum Alloy to Understand Localized Corrosion. *Journal of the Electrochemical Society*. 2020;167(14).
14. Li Y, Cai JM, Guan L, Wang G. pH-dependent electrochemical behaviour of Al₃Mg₂ in NaCl solution. *Applied Surface Science*. 2019;467:619-33.
15. Lyndon JA, Gupta RK, Gibson MA, Birbilis N. Electrochemical behaviour of the beta-phase intermetallic (Mg₂Al₃) as a function of pH as relevant to corrosion of aluminium-magnesium alloys. *Corrosion Science*. 2013;70:290-3.
16. Zhang R, Knight SP, Holtz RL, Goswami R, Davies CHJ, Birbilis N. A Survey of Sensitization in 5xxx Series Aluminum Alloys. *Corrosion*. 2016;72(2):144-59.
17. Xia DH, Ji YY, Zhang RF, Mao YC, Behnamian Y, Hu WB, et al. On the localized corrosion of AA5083 in a simulated dynamic seawater/air interface-Part 1: Corrosion initiation mechanism. *Corrosion Science*. 2023;213.
18. Wloka J, Burklin G, Virtanen S. Influence of second phase particles on initial electrochemical properties of AA7010-T76. *Electrochimica Acta*. 2007;53(4):2055-9.
19. Klumpp RE, Donatus U, Araujo JVS, Redígolo MM, de Sc Machado C, Costa I. - The Effect of Acid Pickling on the Corrosion Behavior of a Cerium Conversion-Coated AA2198-T851 Al-Cu-Li Alloy. *Journal of Materials Engineering and Performance*. 2020;29(1):167 – 74.
20. Donatus U, Thompson GE, Omotoyinbo JA, Alaneme KK, Aribo S, Agbabiaka OG. Corrosion pathways in aluminium alloys. *Transactions of Nonferrous Metals Society of China*. 2017;27(1):55-62.
21. Bastidas JM, Forn A, Baile MT, Polo JL, Torres CL. Pitting corrosion of A357 aluminium alloy obtained by semisolid processing. *Materials and Corrosion-Werkstoffe Und Korrosion*. 2001;52(9):691-6.
22. Queuedo MC, Galicia G, Mayen-Mondragon R, Llongueras JG. Role of turbulent flow seawater in the corrosion enhancement of an Al-Zn-Mg alloy: an electrochemical impedance spectroscopy (EIS) analysis of oxygen reduction reaction (ORR). *Journal of Materials Research and Technology-Jmr&T*. 2018;7(2):149-57.
23. Aromaa J, Forsen O. Factors Affecting Corrosion in Gulf of Finland Brackish Water. *International Journal of Electrochemistry*. 2016;2016.
24. Harshmeet S. THE CORROSION BEHAVIOUR OF ALUMINIUM ALLOY B206 IN SEAWATER: THE UNIVERSITY OF BRITISH COLUMBIA; 2016.
25. Al-Moubaraki AH, Al-Rushud HH. The Red Sea as a Corrosive Environment: Corrosion Rates and Corrosion Mechanism of Aluminum Alloys 7075, 2024, and 6061. *International Journal of Corrosion*. 2018;2018.
26. Reboul MC, Baroux B. Metallurgical aspects of corrosion resistance of aluminium alloys. *Materials and Corrosion-Werkstoffe Und Korrosion*. 2011;62(3):215-33.

JEDNOLIKOST POVRŠINSKE TVRDOĆE REFERENTNIH PLOČICA PROIZVEDENIH SLM TEHNOLOGIJOM I TOPLINSKOM OBRADOM

SURFACE HARDNESS UNIFORMITY OF THE HARDNESS REFERENCE BLOCKS PRODUCED BY SLM TECHNOLOGY AND HEAT TREATMENT

Daniel Pustički¹, Željko Alar¹

¹ University of Zagreb, Faculty of Mechanical Engineering and Naval Architecture, Ivana Lučića 5,
10000 Zagreb, Croatia

Sažetak

Kvaliteta proizvodnje referentnih etalonskih pločica tvrdoće ima izravan utjecaj na mjeru nesigurnosti pri kalibraciji ispitnih strojeva za tvrdoću i predstavlja nezaobilazan element u mjernom lancu slijedivosti mjerenja. Tehnološki napredak u proizvodnji referentnih pločica značajno se promijenio s dolaskom aditivnih postupaka izrade koji omogućuju stvaranje materijala pogodnijih svojstava u usporedbi s konvencionalnim metodama proizvodnje. Tehnologija aditivne proizvodnje kao što je selektivno lasersko taljenje (SLM), ističe se zbog dobivanja iznimno povoljnih mehaničkih svojstava koja su rezultat brzog stvrdnjavanja materijala i postizanja homogene mikrostrukture polaznih metalnih materijala. Maraging 300, često korištena legura u SLM-u, prolazi kroz složene procese toplinske obrade, uključujući starenje nakon kaljenja, što rezultira formiranjem martenzitne matrice s disperzijom precipitata. Ovaj postupak omogućava dobivanje specifične i definirane vrijednosti tvrdoće, čineći ga iznimno prikladnim materijalom za referentne etalonske pločice u umjeravanju ispitnih tvrdomjera.

Ključne riječi: Referentne etalonske pločice tvrdoće, SLM, Vickers

Abstract

The manufacturing quality of the reference standard blocks directly affects the measurement uncertainty when calibrating the hardness testing machines, and they are an indispensable part of the measurement traceability chain. The technologies for producing reference blocks did not change significantly until the advent of additive processes that enable the production of materials with a greater range of changes in properties compared to conventional processes, which allow the precise production of blocks with a specific hardness. Maraging steel, produced through additive manufacturing techniques like selective laser melting (SLM) which promote rapid solidification and uniform microstructure, offers superior mechanical properties compared to conventional methods. Maraging 300, a commonly used steel in SLM, undergoes heat treatments like aging after annealing which form a martensitic matrix with dispersed precipitates, yielding specific and narrow hardness values.

Keywords: Reference hardness blocks, SLM, Vickers.

1. INTRODUCTION

Hardness, as commonly defined, refers to a material's resistance to penetration by a harder foreign object into its surface. Vickers hardness testing is a straightforward and reliable method essential for assessing fundamental mechanical properties and, consequently, material quality control [1,2]. To ensure measurement reliability, traceability to national standards is crucial, allowing for the best possible realization of the hardness scale definition. Reference hardness blocks play a key role in this by simultaneously verifying influential factors in hardness testing, such as indenter geometry, applied load, reading device, and loading cycle [3]. Reference hardness blocks must possess three fundamental properties: hardness uniformity, long-term stability and reliability of reference values [3-5]. Achieving a homogeneous microstructure is crucial for hardness uniformity, ensuring that indentations made with different loads yield consistent hardness values on the material's surface.

Traditionally, Vickers hardness reference blocks were made from carbon or low-alloy tool steels, but they have shortcomings, including corrosion issues and structural inhomogeneity [6]. To address these problems, reference hardness blocks for mid-range hardness values have been shifting toward using steels with higher alloying percentages or those obtained through additive manufacturing techniques.

Selective Laser Melting (SLM) is increasingly used to produce machine parts and products, yielding steels with superior mechanical properties compared to conventional methods [7]. The nature of SLM technology involve melting of a small amount of metal powder and rapid solidification, results in a more uniform microstructure across the cross-section. Parameters like powder layer thickness, laser power, and scanning speed optimization can achieve similar or superior properties compared to conventional methods [8,9].

MARAGING steel exhibits excellent strength and ductility and is commonly used for the production of machine parts. Heat treatment processes that includes aging leads to a microstructure consisting of uniformly distributed high-hardness precipitates within a martensitic matrix, resulting in specific hardness values with a narrow scattering interval [9-11]. The difference between MARAGING 300 steel obtained through SLM and conventional methods lies in the martensitic matrix's formation through melting and rapid cooling during production, avoiding the need for solution annealing. Residual stresses, mainly due to large thermal gradients, can be reduced through post-processing steps like annealing [12]. Studies show that the hardness uniformity in MARAGING steel samples produced without heat treatment have consistent hardness values under different loads and at different positions, offering a path for further sample modification using heat treatment processes and microstructure analysis to achieve optimal reference hardness blocks [13].

Given the knowledge gained about the production of samples using the SLM process, there is an opportunity to obtain microstructure and material properties suitable for the production of reference hardness blocks with equal or better-defined characteristics than the ones produced with conventional methods, and the first step is to determine the uniformity of the surface hardness.

2. MATERIALS AND METHODS

Test specimens were fabricated from MARAGING 300 steel powder through the application of Selective Laser Melting (SLM) technology on the EOS M 290 3D printing machine (Figure 1). A sample after the production is shown in Figure 2. The manufacturing process followed the recommended parameter settings provided by the metal powder manufacturer, which are known to be ideal for creating machine parts with excellent mechanical properties. However, it's important to note that these parameters were not considered when defining the subsequent heat treatment process.



Figure 1. EOS M 290



Figure 2. MARAGING steel sample

To investigate the impact of aging heat treatment, various parameters were adjusted, and the specimens were exposed to different holding times at precise temperatures, thus yielding a spectrum of hardness levels. The number of test samples was determined using a central composite experimental design, which belongs to the class of higher-order non-factorial experimental designs. Utilizing the experimental design framework, incorporating two independent entry variables (holding time and temperature), a comprehensive set of 12 distinct experimental states was generated and is presented in Table 1.

Table 1. Sample definition

	Factor 1	Factor 2
Sample number	Temperature °C	Holding time h
1	405	4,5
2	430	1
3	430	8
4	490	0,5
5	490	4,5
6	490	4,5
7	490	4,5
8	490	4,5
9	490	9,5
10	490	9,5
11	550	8
12	575	4,5

The samples were treated in a heating chamber at the Laboratory for Testing Mechanical Properties at the Faculty of Mechanical Engineering and Naval Architecture as depicted in Figure 3, following the parameters obtained from the experimental design plan from Table 1.

Subsequent to the fabrication process, mechanical processing in accordance with the HRN EN ISO 6507-3:2018 standard (particle separation using cutting tools, grinding, and fine polishing) was performed on the specimens to ensure precise hardness measurement.

Following the preparation phase, an extensive series of hardness tests was conducted across different regions of the specimen's surface, utilizing a range of distinct loads using Vickers hardness testing method. This examination was aimed at precisely assessing the uniformity of hardness distribution throughout the specimen's surface for all of the 12 samples with different obtained hardness values. The testing was performed on the Zwick ZHV μ hardness testing machine at the Laboratory for Testing Mechanical Properties (Figure 4) using two different loading forces: 2 kgf and 5 kgf.



Figure 3. heat treatment chamber



Figure 4. Zwick ZHV μ hardness testing machine

3. RESULTS AND DISCUSSION

15 hardness measurements were conducted in total on each sample at three distinct lines, gradually moving from the outer edges of the samples surface towards the center as shown on Figure 5. The values of hardness along each line from the sample's edge to its center are depicted in Figure 6. The main goal was to assess the difference of hardness values across the whole surface geometry to ensure deviations resulted in heat treatment or machining of the samples.

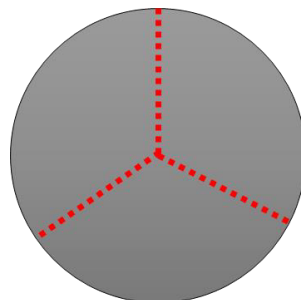


Figure 5. Surface measurement lines

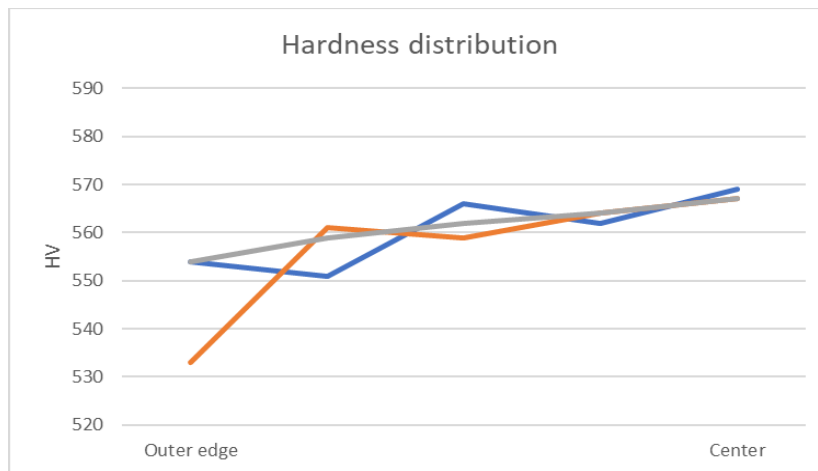


Figure 6. Hardness distribution for sample 490°C- 4h

A similar pattern is observed across all 12 samples. The assessment of surface hardness uniformity reveals a discernible trend, with hardness values progressively rising towards the sample's center. This phenomenon is attributable to the elevated temperatures that occur during automated polishing processes, resulting in notable microstructural modifications.

The main hardness results for all samples using HV2 and HV5 method indicate a slight uniformity of main surface hardness that varies within 5 percent, regardless of the applied load, as shown on Figure 7. Uniform hardness through the whole surface area, irrespective of the applied load, indicates an exceptionally homogeneous structure of the blocks. Distinct hardness values obtained through heat treatment align with literature findings, affirming the correct execution of the aging process. Variations in input factors influence the overall hardness differently, verifying the initial experimental design model.

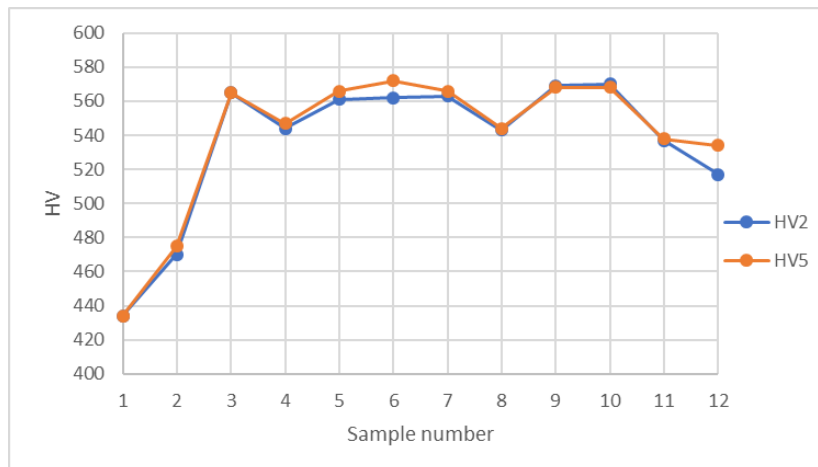


Figure 7. Mean hardness values at different loads.

Hardness uniformity/non-uniformity (r_{rel}) represents the ratio of the difference between the maximum and minimum hardness to the mean of the measured hardness values, expressed as a percentage. It serves as a crucial indicator in assessing the consistency of material hardness across a sample and depends on the number of measurements on a single block. Hardness uniformity is particularly valuable in quality control and engineering applications, providing insight into the reliability of material properties and ensuring compliance with the standards. It is defined as:

$$r_{\text{rel}} = 100 \times \frac{H_n - H_1}{\bar{H}}$$

Where is:

H_n – Highest measured value for n measurements

H_1 – Lowest measured value

\bar{H} - Average hardness

Depending on the number of measurements per sample, applied load and resultant hardness, the hardness uniformity, as per HRN EN ISO 6507-3:2018, must remain below a specified threshold. For HV2 and HV5 methods the uniformity percentage must be below 6 %. Figure 8 illustrates the hardness uniformity values for all samples measured using the HV2 method, while Figure 9 depicts the hardness uniformity values for all samples measured with the HV5 method.

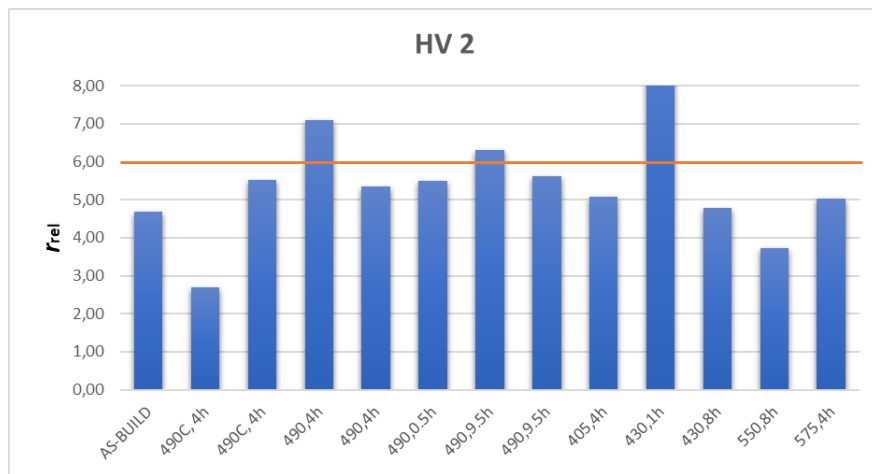


Figure 8. Hardness uniformity for HV2

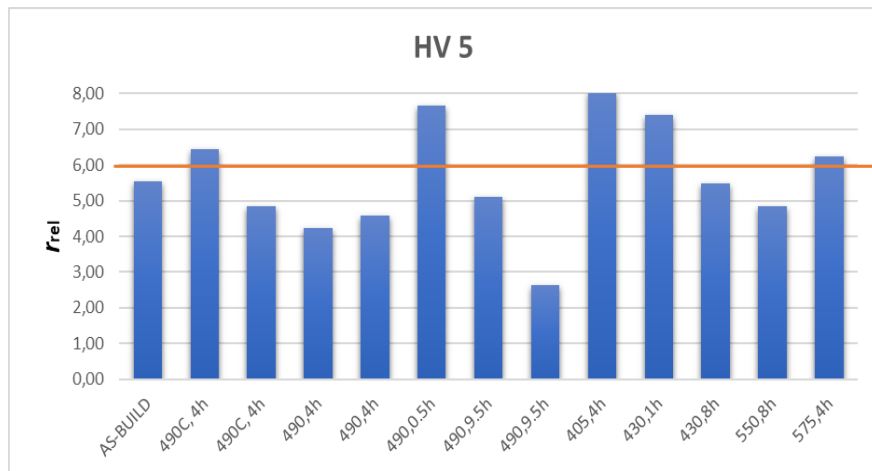


Figure 8. Hardness uniformity for HV5

It is evident that nearly all hardness uniformity values for the HV2 method fall below the permissible limit as per the standard. For the HV5 method, deviation values are slightly higher, although most remain within the allowed range. Applying a lower load increases the likelihood of larger deviations because the indentation covers a smaller local area where it is possible to encompass different microstructural phases, which is not the case here. The results in general reveal minimal fluctuation in hardness levels across the samples surface, highlighting the consistent and reliable hardness characteristics of the tested material.

4. CONCLUSION

This research explored the impacts of aging heat treatment parameters on the resultant hardness characteristics of MARAGING 300 steel, fabricated using SLM technology. Leveraging the advantages of SLM technology, the fabrication of samples boasting a highly homogeneous microstructure is achievable.

The thorough optimization of heat treatment parameters further expanded the spectrum of attainable hardness values while upholding the critical uniformity of surface hardness within the predefined range of 360 HV to 570 HV. Measurement outcomes adhered to the standards delineated in the HRN EN ISO 6507-3:2018 guideline, thereby fortifying the credibility and precision of the acquired results.

The inherent uniformity of microstructure translates to consistent surface hardness in the as-built state, as in the heat-treated samples aligning precisely with the prescribed process parameters. In the experimental phase of the study, it was observed that the hardness uniformity values, obtained under various applied loads, remained within the predefined limits by the standard ($r_{\text{rel}} \leq 6\%$).

In essence, the fusion of SLM technology and MARAGING steel offers a potent avenue for fabricating materials that excel in both homogeneity and hardness versatility, fully adhering to international standards. The findings underscore the potential for manufacturing reference hardness blocks with uniformly distributed surface hardness, an indispensable aspect of additive technology. These findings indicate the potential to manufacture reference hardness blocks with uniform surface hardness, a critical element in the reference blocks production. Further exploration of microstructural and physical properties can fine-tune production parameters for the future production of usable reference hardness blocks.

REFERENCES

- [1] Alar, Ž. (2008). 'Analysis of Influential Factors on the Measurement Uncertainty of a Reference Hardness Tester', Dissertation, University of Zagreb, Faculty of Mechanical Engineering and Naval Architecture
- [2] Aleksandrov Fabijanić, T. (2014). 'Development of Vickers Hardness Reference Blocks Using Powder Metallurgy', Dissertation, University of Zagreb, Faculty of Mechanical Engineering and Naval Architecture.
- [3] Yamamoto, T. (2009) 'Role and Use of Standard Hardness Blocks', Journal of Material Testing Research Assoc., 54, 2p.131
- [4] Metallic materials -- Vickers hardness test -- Part 3: Calibration of reference blocks (ISO 6507-3:2018; EN ISO 6507-3:2018)
- [5] Yamamoto, T. (2006). The Present and Future of Hardness Standard Blocks. Solid State Phenomena, 118, 457–462. <https://doi.org/10.4028/www.scientific.net/ssp.118.457>
- [6] Elizabeth, I., Kumar, R., Garg, N. (2019). *et al.* Measurement Uncertainty Evaluation in Vickers Hardness Scale Using Law of Propagation of Uncertainty and Monte Carlo Simulation. MAPAN 34, 317–323. <https://doi.org/10.1007/s12647-019-00341-9>
- [7] Suzki, Asuka & Nishida, Ryoya & Takata, Naoki & Kobashi, Makoto & Kato, Masaki. (2019). Design of laser parameters for selectively laser melted maraging steel based on deposited energy density. Additive Manufacturing, 28. 10.1016/j.addma.2019.04.018.
- [8] Yan, Jujie, Yinghao Zhou, Ruinan Gu, Xingmin Zhang, Wai-Meng Quach, and Ming Yan. (2019). "A Comprehensive Study of Steel Powders (316L, H13, P20 and 18Ni300) for Their Selective Laser Melting Additive Manufacturing" *Metals* 9, no. 1: 86. <https://doi.org/10.3390/met9010086>
- [9] T. Silva, F. Silva, J. Xavier, A. Gregório, A. Reis, P. Rosa, P. Konopík, M. Rund, A. Jesus (2021), Mechanical Behaviour of Maraging Steel Produced by SLM, Procedia Structural Integrity, Volume 34, 2021, Pages 45-50, ISSN 2452-3216, <https://doi.org/10.1016/j.prostr.2021.12.007>.
- [10] Bae, K.C., Kim, D.H., Kim, Y., Oak, J.J., Lee, H., Lee, W.J., & Park, Y.H. (2021). Effect of heat treatment, building direction, and sliding velocity on wear behavior of selectively laser-melted maraging 18Ni-300 steel against bearing steel. *Wear*, 203962.
- [11] Becker, T., Dimitrov, D. (2017) The achievable mechanical properties of SLM produced Maraging Steel 300 components. *Rapid Prototyping Journal*. Vol. 22, str. 487-494.
- [12] Bai, Y., Wang, D., Yang, Y., Wang, H. (2019) Effect of heat treatment on the microstructure and mechanical properties of maraging steel by selective laser melting. *Materials Science and Engineering: A*. vol. 760, str. 105-117.
- [13] Bouzakis, E., Arvanitidis, A., Kazelis, F., Maliaris, G., & Michailidis, N. (2020). Comparison of Additively Manufactured vs. Conventional Maraging Steel in Corrosion-Fatigue Performance after various surface treatments. *Procedia CIRP*, 87(Complete), 469–473. <https://doi.org/10.1016/j.procir.2020.03.003>
- [14] Takata, N., Nishida, R., Suzki, A., Kobashi, M., Kato, M. (2018). Crystallographic Features of Microstructure in Maraging Steel Fabricated by Selective Laser Melting. 10.20944/preprints201805.0373.v1.



ŽARENJE DEBELOSTIJIENIH ZAVARENIH LIMOVA ZA SMANJENJE ZAOSTALIH NAPREZANJA

ANNEALING OF THICK-SOLID WELDED SHEETS TO REDUCE RESIDUAL STRESSES

Darko Landek¹, Ivica Garašić¹, Mislav Štefok¹, Jurica Jačan¹

¹ University of Zagreb, Faculty of Mechanical Engineering and Naval Architecture, Zagreb, Croatia

Sažetak

Nakon zavarivanja u zavaru i zoni utjecaja topline nastaju zaostala naprezanja koja treba ukloniti naknadnom toplinskom obradom kako bi se postigla dobra mehanička svojstva zavarenog spoja. U radu je opisan utjecaj žarenja u vakuumskoj peći s Hollomon-Jaffeovim parametrom $P = 17.161$ na smanjenje tvrdoće i zaostalih naprezanja u zavarima limova debljine 120 mm od čelika S235JR. Nakon žarenja zavora u vakuumskoj peći postignuto je prosječno smanjenje tvrdoće u zavaru za 8 - 12 HV. Zaostala naprezanja na presjeku zavora su nakon žarenja promijenila iznos između -287 MPa do 224 MPa u odnosu na naprezanja prije žarenja te postala tlačna po cijelom presjeku zavora.

Ključne riječi: zavarivanje pod praškom, zaostala naprezanja, rendgenska difrakcija, S235JR

Abstract

After welding, in the weld and in the heat-affected zone, residual stresses occur, which should be removed by subsequent heat treatment in order to achieve good mechanical properties of the welded joint. stresses in welds of 120 mm thick S235JR steel sheets. After annealing the weld in a vacuum furnace, an average reduction in hardness in the weld by 8 - 12 HV was achieved. After annealing, the residual stresses on the weld cross-section changed from -287 MPa to 224 MPa compared to the stresses before annealing and became compressive throughout the weld cross-section.

Keywords: powder welding, residual stresses, X-ray diffraction, S235JR

1. INTRODUCTION

Submerged Arc Welding (SAW) is one of the high-productivity processes used for joining thick sheets exceeding 10 mm in a horizontal position. During the joining process, the weld is covered by a layer of powder and slag through which an electrically conductive electrode passes. The powder protects the weld from oxidation, regulates heat dissipation to the surroundings, and shapes the weld. Common preparations for welding in this process are I-joint and Y-joint. The shape of the weld depends on welding parameters, the inclination of the weld to the horizontal plane, the type of powder, the location of the grounding connection on the workpiece, and the chemical composition of the welded steel. The weld properties are most influenced by current density, voltage, and welding speed [1, 2].

After welding thick sheets, due to the high amount of heat input and slow cooling, coarser grains are formed in the weld, which can result in lower weld toughness [1]. For welded sheets thicker than 10 mm after the SAW process, significant residual stresses are formed, which need to be removed by subsequent heat or mechanical treatment. Mechanical treatment by vibration or impacts does not introduce enough energy to break down the residual stresses in thicker welded sheets, so thermal treatment, stress relief annealing, remains the method of choice. Holding the weld at annealing temperature reduces the yield strength of the metal material and initiates plastic deformation through which elevated residual stresses are broken down. The reduction of residual stresses is carried out without microstructural changes in the weld [3]. The implementation of this annealing is prescribed by the ISO/NP 14745:2007 standard for sheets and plates up to 90 mm in thickness, while for sheets thicker than 100 mm, there are only recommendations regarding the choice of annealing parameters. For non-alloy and low-alloy structural steels, annealing is prescribed at a temperature between 550 °C to 600 °C. The holding time at annealing temperature is specified depending on the sheet thickness (between 2 h to 6 h), aiming to achieve the highest value of the Hollomon-Jaffe parameter $P_{crit} = 17,5$. The value of this parameter is determined according to the expression [4]:

$$P = T \cdot (20 + \log t) \cdot 10^{-3} \quad (1)$$

where T [K] is the annealing temperature, and t [h] is the holding time. The heating and cooling rate of welded constructions thicker than 90 mm must be less than 55 K/h, in the range between 300 °C and the annealing temperature. This requirement can be achieved by using a programmable furnace with controlled heating and cooling. During the heating and holding cycle, the protective atmosphere in the furnace must be reducing or neutral to avoid oxidation of the weld surface.

Residual stress measurement on the weld surface can be performed using non-destructive methods, among which the most commonly used are The magnetic Barkhausen noise (MBN) method, X-ray diffraction, neutron diffraction, and ultrasonic method [5, 6]. Destructive methods such as stress measurement on the weld cross-section and hole-drilling method are commonly used for research purposes [7].

This work explores the relationship of the Hollomon-Jaffe model to determine annealing parameters and achieved reduction of residual stresses in SAW welds of thick sheets made of non-alloy steel S235JR. The mathematical model is validated by measuring residual stresses through X-ray diffraction and hardness testing on the weld cross-section.

2. MATERIALS AND METHODS

For model testing, two plates of dimensions 150 mm x 120 mm x 150 mm made of structural steel S235JR were prepared. X-joint for welding under powder flux was milled on the plates. The plates were welded using the SAW process in two passes with direct current strength of 600 A, voltage of 28 V, welding speed of 45 cm/min, and wire diameter of 4 mm. Protective powder SA FB 1 55 AC H5 was used for welding, complying with the properties prescribed by the standard EN ISO 14174:2012. In the first pass, the upper part of the X-joint was welded in a horizontal position. In the second pass, the sheets were turned to weld the other segment of the X-joint. Between the first and second pass, the weld was cooled to room temperature. Three test samples of dimensions 290 mm x 120 mm x 18 mm were cut from the welded plate using a band saw for metal, with abundant cooling by emulsion. The cross-sectional surface of all samples was machined by planing and grinding. Figure 1 shows a test sample with a grid marked for hardness and residual stress testing. Hardness testing was carried out at 48 nodes of the grid, and residual stress testing was carried out at 6 nodes before and after annealing. The spacing between the nodes of the rectangular grid was 20 mm. The weld boundary to the base metal was marked in the grid.

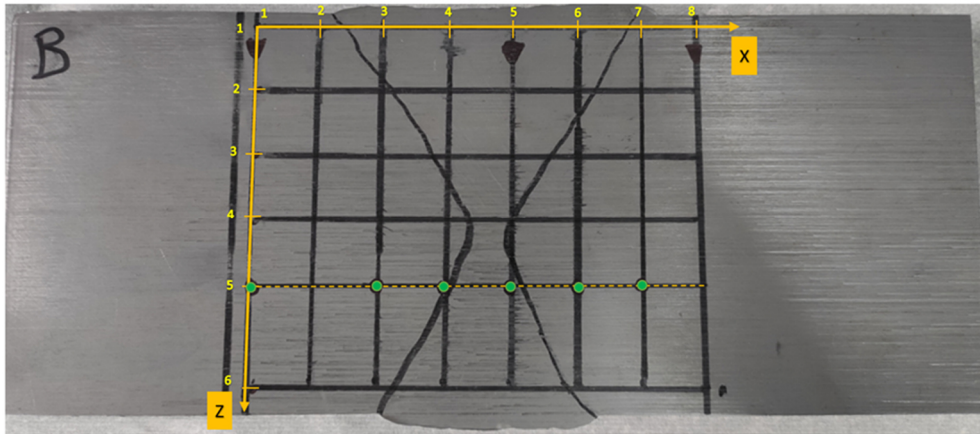


Fig. 1: Weld sample with a grid of measurement points for hardness and residual stress testing [8]

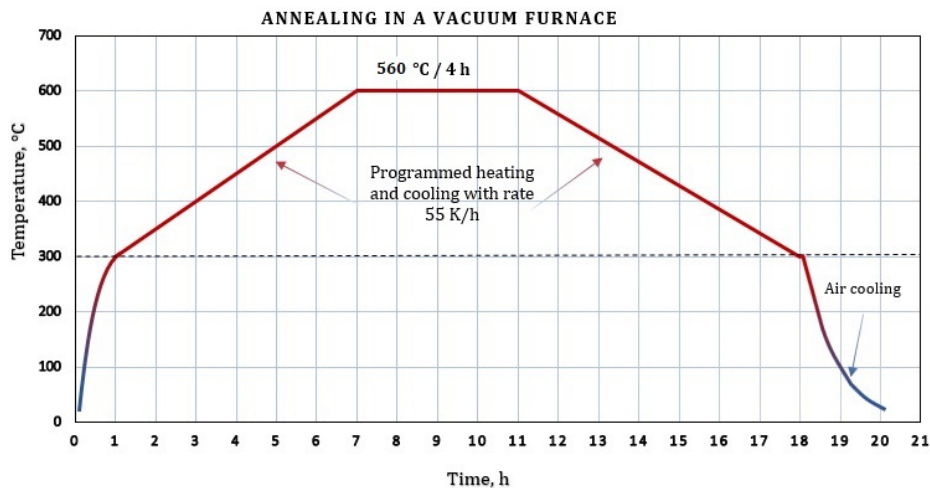
The heat treatment of the sample was performed twice. The first annealing for the reduction of residual stresses was performed for each sample separately in an electric chamber furnace without a protective atmosphere with internal chamber dimensions of 190 mm x 190 mm x 300 mm. The annealing parameters were as follows: (A1) 550 °C/2 h, (B1) 600 °C/3 h, (C1) 650 °C/4 h. Heating of the samples to the annealing temperature and cooling from the annealing temperature to 300 °C was automatically regulated to achieve a constant temperature change rate of 55 K/s. Despite the automatic regulation of heating and cooling rates, the samples cooled with a significant temperature difference of 80 °C to 120 °C between the sample surface near the furnace door and the sample surface near the furnace bottom. Such large temperature differences introduced additional residual thermal stresses into the welds instead of eliminating them. The hardness and residual stress values after the first annealing are listed in table 1. Therefore, a repeated second annealing for the reduction of residual stresses was performed in the Rübigen PC 70/90 furnace in a vacuum chamber with a diameter of 700 mm and a height of 900 mm, using the following parameters: chamber pressure $p = 2$ mbar, gas flow rates $N_2 = 5$ l/h, $H_2 = 5$ l/h, annealing temperature / time = 560 °C / 4 h,

Hollomon-Jaffe parameter $P = 17.161$. Figure 2 shows the diagram of the annealing process in the vacuum furnace.

Hardness testing at the nodes of the grid shown in Figure 1 was performed using the portable United Precision Instruments AHT200 Leeb device with a type D measuring probe. Hardness was tested three times at each node, before and after annealing. The measurement error of the hardness testing by the Leeb method and the conversion of the results to the Vickers scale was ± 6 HV.



a)



b)

Fig. 2: Device and heat treatment process: a) vacuum furnace Rübige PC 70/90, b) diagram of the annealing process of welded samples in the vacuum furnace Rübige PC 70/90

Residual stresses were measured in the x and z-axis directions at 6 measuring points marked in green in Figure 1 using the portable X-ray diffractometer Sentenso Pulstec μ -X360s, which was mounted on a robot arm. The residual stresses were measured at 6 points in the longitudinal (x) and transverse (z) directions on the welded X-joint. The

measurement principle of the Pulstec μ -X360s diffractometer is described in references [8, 9]. The measurement cell for residual stress testing installed in the Welding Laboratory (FMENA) is shown in Figure 3. The measurement part of the device consists of a low-intensity X-ray source obtained by ionizing a chromium electrode, a filter for passing X-rays of a specific wavelength, and a plate with sensors for detecting the reflected X-ray beam from the sample surface. In the conducted tests, the samples were irradiated using a beam current of 1.5 mA and a voltage of 30 kV. The X-ray beam was directed to be incident on each sample at an angle of 35.0 degrees. The distance from the specimen and detector to capture the D-S ring image was set to $D = 50$ mm. The X-ray Cr K-alpha wavelength (λ) used for X-ray diffraction was 2.29\AA .

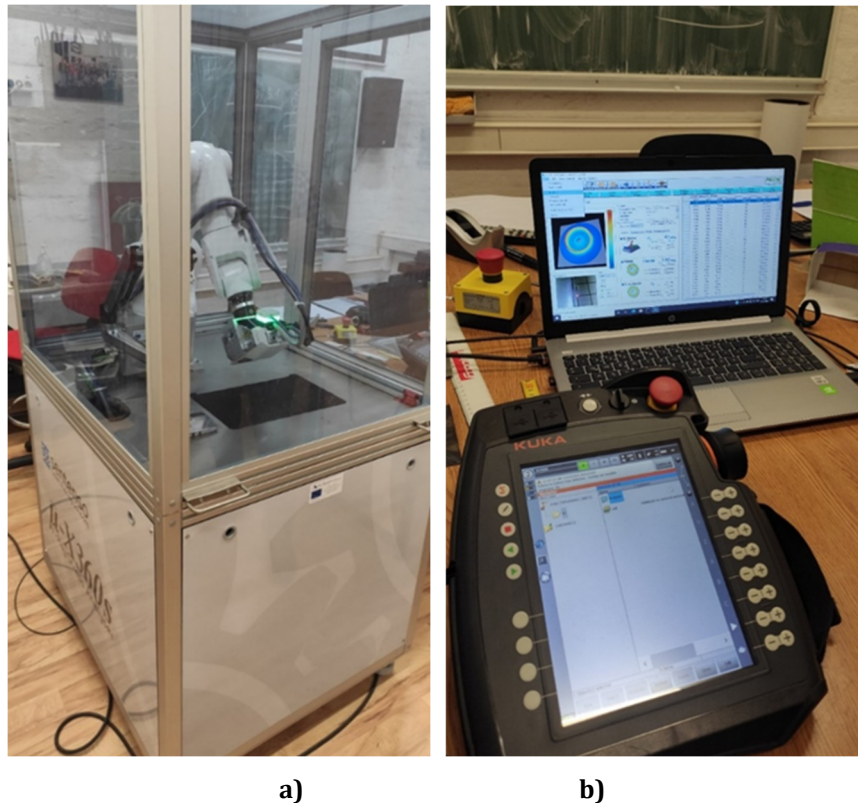
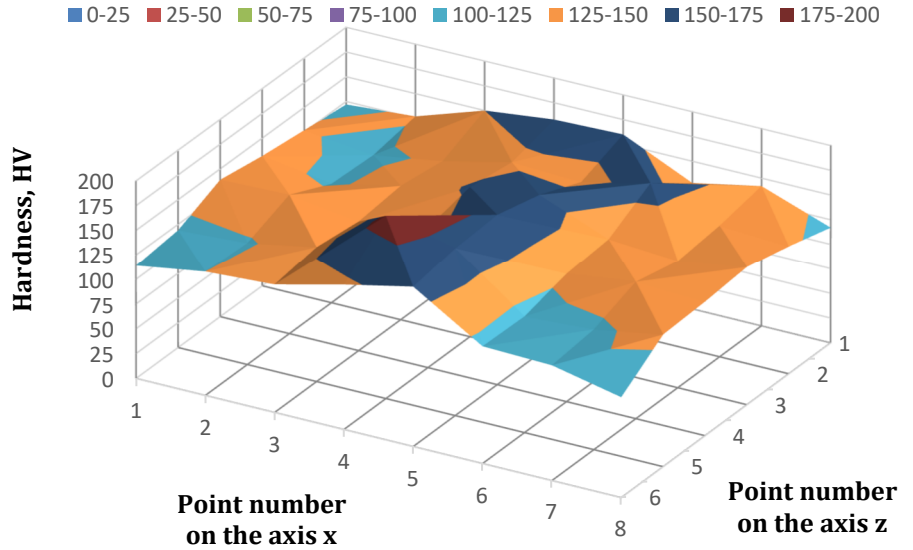


Fig. 3: Residual stress measurement cell: a) Sentenso μ -X360s diffractometer mounted on a robot arm, b) control unit and measurement computer

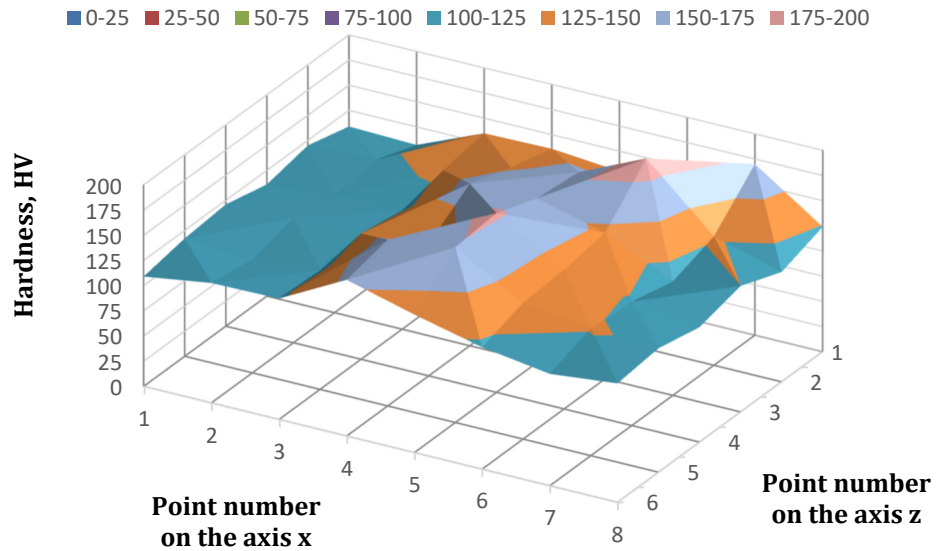
3. RESULTS AND DISCUSSION

3.1. Hardness on the weld crosssection

Figure 4 shows the hardness values after the first and second annealing of welded sample A1 measured at 48 nodes of the grid indicated in Figure 1. By comparing the spatial distribution of hardness across the weld cross-section, a reduction in hardness after annealing in the vacuum furnace can be observed (Figure 4b), although a uniform hardness across the entire cross-section has not yet been achieved. The average reduction in hardness after annealing in the vacuum furnace for sample A is 12 ± 8 HV. A similar average reduction in hardness after annealing in the vacuum furnace was achieved for samples B1 (12 ± 10 HV) and C1 (8 ± 6 HV).



a)



b)

Fig. 4: Hardness distribution across the weld cross-section for sample A after annealing: a) in a small laboratory furnace (sample A1), b) in the vacuum furnace Rübigen PC 70/90 (sample A2)

3.2. Residual stresses on the weld cross-section

The values of residual stresses in the x and z-axis directions at the 6 measurement points marked in green in Figure 1 are shown in Table 1. Negative values indicate compressive, and positive values indicate tensile stresses. After the first annealing in the small laboratory furnace, the values of residual stresses increased compared to the initial state after welding. From the presented results of residual stress measurements, it can be observed that only after annealing in the vacuum furnace, a state of residual compressive stresses was achieved on all examined welds in both x and z-axis directions ($\sigma_x, \sigma_z < 0$). For sample A1, after the second annealing in the vacuum furnace, the largest change in residual stress was achieved in the z-axis direction, $\Delta\sigma_z = -287$ MPa. For sample B1, the largest change in stress was in the x-axis direction, $\Delta\sigma_x = 166$ MPa. For sample C1, the largest change in stress was also in the x-axis direction, $\Delta\sigma_x = 224$ MPa.

The points of the greatest changes in residual stresses are located at the center of the weld in measurement points 4 and 5. The average stress values on the weld samples in the x and z-axis directions after the second annealing in the vacuum furnace are shown in Figure 5. The highest stress values in both axes are on sample C2, which before annealing in the vacuum furnace was also in the state of the highest residual stresses.

Tab. 1: Residual stresses on the weld cross-section before and after annealing

Residual stresses in the x-axis direction σ_x , MPa								
Sample mark		Ordinal number of the measuring point on the x-axis						
		1	2	3	4	5	6	7
A	Before annealing (A0)	8	-	-10	-31	-58	-12	44
	After 1 st annealing (A1)	-16	-	12	64	7	-84	-14
	After 2 nd annealing (A2)	-43		-41	-44	-32	-32	-31
B	Before annealing (B0)	not measured						
	After 1 st annealing (B1)	119	-	130	118	-33	88	124
	After 2 nd annealing (B2)	-8		-32	-18	-26	-1	-42
C	Before annealing (C0)	not measured						
	After 1 st annealing (C1)	63	-	89	92	182	144	108
	After 2 nd annealing (C2)	-135		-97	-48	-42	-15	-83
Residual stresses in the z-axis direction σ_z , MPa								
Sample mark		Ordinal number of the measuring point on the x-axis						
		1	2	3	4	5	6	7
A	Before annealing (A0)	61		52	71	-72	-31	30
	After 1 st annealing (A1)	-185		-237	-308	-190	-225	-263
	After 2 nd annealing (A2)	-35		-27	-21	-95	-36	-27
B	Before annealing (B0)	not measured						
	After 1 st annealing (B1)	-143		-84	-141	-174	-108	-190
	After 2 nd annealing (B2)	-82		-47	-42	-31	-19	-48
C	Before annealing (C0)	not measured						
	After 1 st annealing (C1)	-138		-130	-153	-119	-141	-141
	After 2 nd annealing (C2)	-94		-30	-40	-42	-47	-149

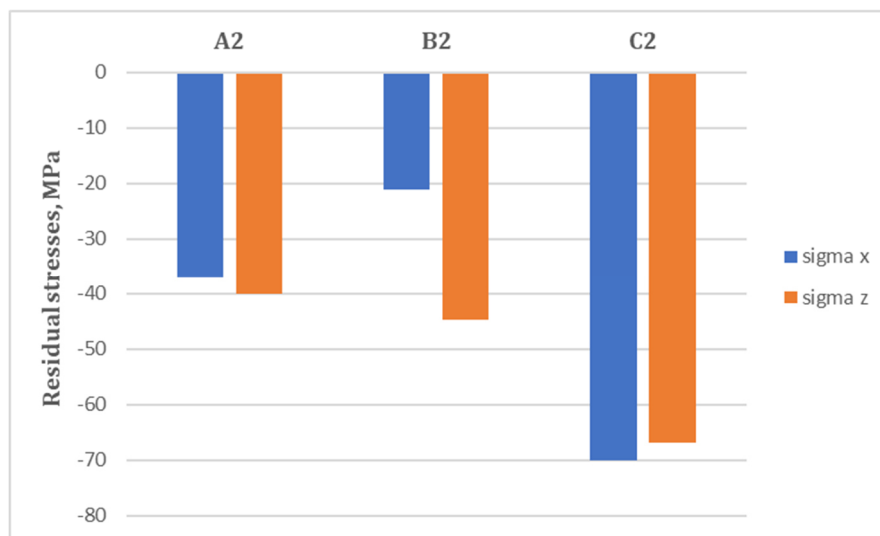


Fig. 5: Average stress values on the weld cross-section after annealing in the vacuum furnace.

4. CONCLUSION

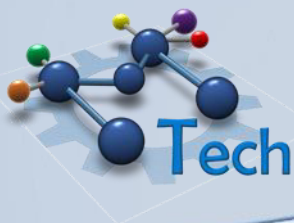
In this study, two annealings of SAW welds on thick sheets were performed to reduce residual stresses. In the first annealing conducted in a small laboratory furnace, regardless of the selected combination of temperature and annealing time, a reduction of residual stresses was not achieved, but rather their increase compared to the initial welded state. In the second annealing carried out in a vacuum furnace of significantly larger volume compared to the volume of test samples, a reduction in hardness of 12 HV compared to the hardness after the unsuccessful first annealing was achieved, along with a significant reduction in residual stresses. Residual stresses on the entire cross-section of welded samples were changed from tensile to compressive in both the longitudinal and transverse directions of the weld. A programmed cooling from annealing temperature to 300 °C and then cooling in air achieved a uniform distribution of residual stresses across the weld cross-section, and these parameters can be recommended for subsequent heat treatment of SAW welds on thick sheets.

Acknowledgement:

The authors wish to acknowledge the project **KK.0.1.1.07.0076** "ImproWE - Improvement of high efficiency welding technology" funded from the Ministry of Science and Education of Republic Croatian and The Central Agency for Financing and Contracting Programs and Projects of the European Union (SAFU) for their financial support".

REFERENCES

- [1] S. Kralj, Z. Kožuh, Š. Andrić: Priručnik Zavarivački i srodni postupci, HDTZ; 2015, Zagreb
- [2] Lee E. Allgood: Submerged Arc Welding, ASM Handbook, Vol 6A, metals park, USA, 2011
- [3] G. Totten, M. Howes, T. Inoue : Handbook of Residual Stress and Deformation of Steel, ASM International, Metals park, 2002
- [4] Canale, L.C.F., Yao, Y., Gu, J., Totten, G.E., A historical overview of steel tempering parameters, International Journal Microstructure and Materials Properties, Vol. 3, No. 4/5, 474-525 (2008)
- [5] H.H. Lai, W. Wu: Practical examination of the welding residual stress in view of low-carbon steel welds. Journal of Materials Research and Technology. 2020;9(3):2717–2726
- [6] N.S. Rossini , M. Dassisti , K.Y. Benyounis , A.G. Olabi: Methods of measuring residual stresses in components, Materials & Design, 35, 2012, 572-588
- [7] J. Frankel, A. Abbate and W. Scholz: The Effect of Residual Stresses on Hardness Measurements Experimental Mechanics, 33, 164–168 (1993)
- [8] K. Zorić: Žarenje za smanjenje zaostalih naprezanja u zavarima čelika S235JR, diplomski rad, FSB, Sveučilište u Zagrebu, 2022
- [9] K. Tanaka: The cos α method for X-ray residual stress measurement using two-dimensional detector, Mechanical Engineering Reviews, Vol.6, No.1, 2019, 1-15



THE INFLUENCE OF DIFFERENT FOAMING AGENTS ON ALUMINIUM FOAM PORE SIZE

Tomislav Rodinger¹, Danko Ćorić¹

¹ University of Zagreb, Faculty of Mechanical Engineering and Naval Architecture, Ivana Lučića 5,
10000 Zagreb, Croatia

Abstract

The choice of foaming agent and its mass fraction significantly affect the size and number of pores of the metal foam. The powder metallurgy process was used for the production of aluminium foams with the addition of various foaming agents: titanium hydride (TiH_2) and calcium carbonate (CaCO_3). TiH_2 was added in an amount of 0.4 wt. %, while the quantity of CaCO_3 varied between 3 and 5 wt. %. The produced foams, with approximately the same degree of porosity, were scanned using a non-destructive computed tomography method. The number and size of pores were analysed on the obtained three-dimensional models. The results showed that foams foamed with TiH_2 have much larger pores, i.e., their number per cm^3 is much lower compared to foaming with CaCO_3 . By considering the influence of CaCO_3 fraction on the morphology of aluminium foam, it can be concluded that a smaller quantity of CaCO_3 (3 wt. %) provides a macrostructure with smaller cells compared to foams produced with 5 wt. % CaCO_3 . They contain a slightly larger cells, but still much smaller than foams with TiH_2 foaming agent at the same degree of porosity.

Keywords: *aluminium foam, calcium carbonate, titanium hydride, computed tomography, pore size*

1. INTRODUCTION

The most used agent for foaming aluminium is titanium hydride (TiH_2), which dissolves into titanium (Ti) and hydrogen (H_2) when heated to temperatures above $465\text{ }^\circ\text{C}$. At that temperatures H_2 is released from solid material and creates pores in aluminium. However, TiH_2 has disadvantages, and one of them is that its density (3.75 g/cm^3) is significantly higher than the density of aluminium (2.7 g/cm^3). During its application, under the influence of gravity, TiH_2 particles accumulate in the lower part of the mold which results in a non-uniform distribution of cell sizes and shapes. The disadvantage of TiH_2 is also the relatively low dissolution temperature, well below the solidus temperature of commercial Al alloys [1].

Alternatives to TiH_2 are carbonate-based foaming agents, such as calcium carbonate (CaCO_3), magnesium carbonate (MgCO_3), dolomite ($\text{CaMg}(\text{CO}_3)_2$) and similar carbonates [2]. Unlike TiH_2 , which dissolves into Ti and gaseous H_2 and does not increase the stability of the aluminium foam, dissolving carbonates in the presence of aluminium creates solid particles (such as calcium oxide (CaO) and aluminium oxide (Al_2O_3)) that increase the stability of the foam [3]. By differential thermal (DTA) and thermogravimetric (TGA) analysis of CaCO_3 powder, it can be confirmed that its decomposition begins at a temperature of $650\text{ }^\circ\text{C}$ and ends at around $900\text{ }^\circ\text{C}$ [4]. By heating CaCO_3 to a temperature above $650\text{ }^\circ\text{C}$, it dissolves into CaO and carbon dioxide (CO_2) [5]. This forms an oxide layer on the cell walls, which results in a finer morphological structure of the foam [6]. Since TiH_2 , in relation to CaCO_3 , at the same temperature and pressure releases approximately twice the amount of gas [7], for the same foam porosity, a larger amount of CaCO_3 should be added. In addition to the quantity of foaming agent, attention should also be paid to the size of these particles [3,8]. Larger CaCO_3 powder particles contribute to higher porosity, but the density, relative density and compressive strength decrease [5,9]. The advantage of CaCO_3 foaming agent compared to TiH_2 is also much lower price, which significantly reduces the production costs of aluminium foams [1,10,11].

To get an insight into the structure of the foam, i.e., the size, arrangement and number of pores, the sample needs to be cut, which eliminates the possibility of conducting subsequent examinations. For non-destructive testing of the foam macrostructure, it is possible to use computed tomography (CT) [12–14]. On the obtained three-dimensional models, any cross-section of the sample can be analysed, thus allowing the size and distribution of pores to be determined, as well as whether there are irregularities in any part of the foam. Subsequently, those samples can be subjected to mechanical testing or exploitation since they were not destroyed during the pore analysis.

2. MATERIALS AND METHODS

For the production of aluminium foams, the precursors produced by the powder metallurgy method were used. Aluminium powder (99.8 wt. %), grain size up to $37\text{ }\mu\text{m}$, and CaCO_3 powder as a foaming agent in quantities of 3 and 5 wt. % were used to make the foamable precursors. Two different mixtures, with different quantities of CaCO_3 powder, were mixed in a turbular mixer for 60 min to achieve a homogeneous mixture. After mixing, the powders were compacted by the cold isostatic pressing (CIP) at 150 MPa at room temperature and were subsequently hot extruded at a temperature $400\text{ }^\circ\text{C}$ with the ram speed of 0.4 mm/s to achieve as high density as possible. The extruded

precursors had a rectangular cross-section with dimensions 5 x 20 mm. An identical mass of precursor materials was placed in the molds to obtain foams of approximately the same density. To compare the size and number of pores in samples foamed with different foaming agents, equal quantity of commercially available AlMgSi0.6 alloy precursor with 0.4 wt. % TiH₂ foaming agent was also used. The closed molds were placed in an electric furnace preheated to 750 °C for approximately 10 min, until the end of the foaming process. After the molds were taken out of the furnace, they were cooled with compressed air. Produced samples are shown in Figure 1. The mass and volume of the foamed samples were measured to determine the degree of porosity, density, and relative density (ρ_{rel}) in a relation to monolithic aluminium.



Fig. 1: Aluminium foam samples foamed with different foaming agents

The prepared samples were then scanned by a non-destructive computed tomography (CT) method on a Nikon XT H 225 device with a voxel resolution of 62 μm with the aim of obtaining three-dimensional models for further processing and analysis. Figure 2 shows resulted sample models foamed with CaCO₃ and TiH₂. The obtained models were processed in the VG Studio Max software for the analysis of number and size of internal pores.

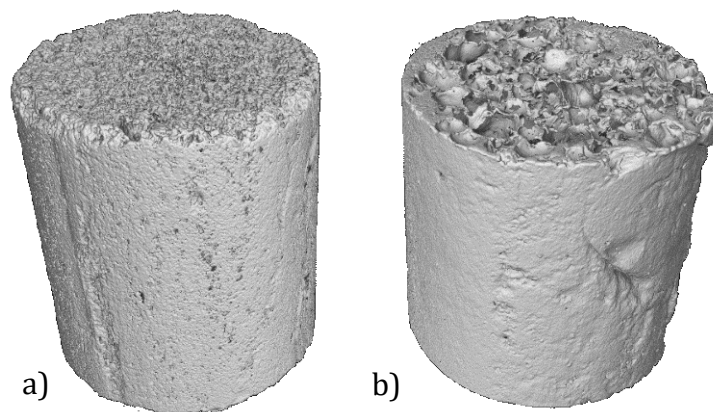


Fig. 2: Three-dimensional models of scanned samples foamed with CaCO₃ (a) and TiH₂ (b)

3. RESULTS AND DISCUSSION

The foamed samples mass (m_f), weighted on a precision balance, and volume (V_f), calculated using the sample dimensions, were measured with the aim of determining their density, relative density and porosity, Table 1. The foam density (ρ_f) was calculated using the equation:

$$\rho_f = \frac{m_f}{V_f} \quad (1)$$

Relative density (ρ_{rel}) of samples was determined by the equation:

$$\rho_{rel} = \frac{\rho_f}{\rho_{Al}} \quad (2)$$

where ρ_{Al} is the density of aluminium (2.7 g/cm³). Porosity of the samples, expressed as a percentage, was calculated using the following equation:

$$porosity = (1 - \rho_{rel}) \times 100\% \quad (3)$$

Tab. 1: Mass, volume, density, relative density and porosity of Al foam samples

Sample	Chemical composition	Mass, g	Volume, cm ³	Density, g/cm ³	Rel. density	Porosity, %
3-1	Al + 3 wt. % CaCO ₃	21.37	39.58	0.53992	0.20	80.00
3-2	Al + 3 wt. % CaCO ₃	23.46	42.10	0.55724	0.2064	79.36
5-1	Al + 5 wt. % CaCO ₃	25.34	41.05	0.61730	0.2286	77.14
5-2	Al + 5 wt. % CaCO ₃	19.58	39.42	0.49670	0.1840	81.60
T-1	AlMgSi0.6 (0.4 wt. % TiH ₂)	16.16	37.61	0.42967	0.1591	84.09
T-2	AlMgSi0.6 (0.4 wt. % TiH ₂)	14.94	37.05	0.40324	0.1493	85.07

Table 1 shows that samples with CaCO₃ foaming agent have approximately the same degree of porosity, cca. 80%, while samples foamed with TiH₂ have slightly higher porosity, cca. 85%.

By analyzing the scanned models shown in Fig. 3, an insight into the pore sizes and its number was obtained, Table 2. The largest pore in foams with 3 wt. % CaCO₃ has a volume of 34.49 mm³, in foams with 5 wt. % CaCO₃ the largest volume is 38.50 mm³, while in foams with 0.4 wt. % TiH₂ the maximum volume exceeds 420 mm³. The standard deviation of the pore volume is less than 1 mm³ and 14 mm³ in foams with CaCO₃ and TiH₂ respectively. Figure 3 shows cross-sections of two scanned samples with the pores of different volumes marked with different colours, the smallest ones are blue, while the largest are red.

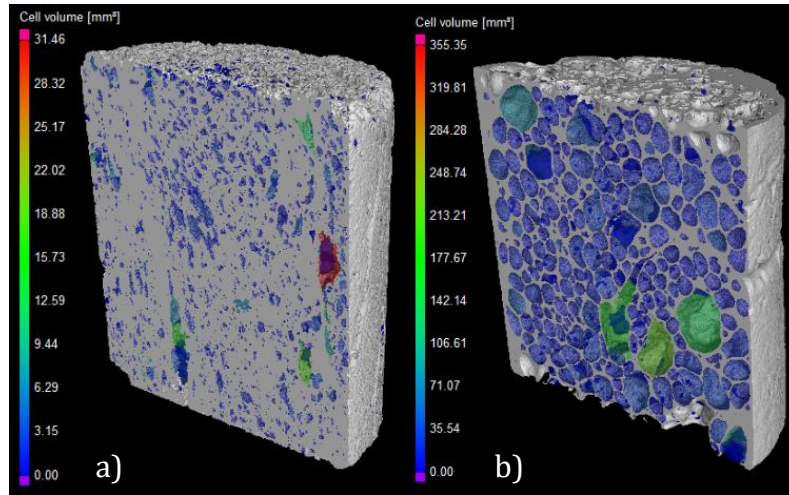


Fig. 3: Pore volume analysis of samples with CaCO_3 (a) and TiH_2 (b)

Tab. 2: Number and volume of pores

Sample	Number of pores	Pores per cm^3	Min. pore volume, mm^3	Max. pore volume, mm^3	Average pore volume, mm^3	St. deviation, mm^3
3-1	35 508	897.1	0.01	34.49	0.34	0.80
3-2	35 867	851.9	0.01	31.46	0.20	0.55
5-1	26 472	644.9	0.01	24.55	0.15	0.46
5-2	27 667	701.8	0.01	38.50	0.23	0.68
T-1	4 942	131.4	0.01	355.35	4.55	11.93
T-2	4 861	131.2	0.01	420.33	4.36	13.85

Table 2 shows that samples made with CaCO_3 have a much higher overall number of pores compared to samples T-1 and T-2. Due to different number of pores and a certain deviation in the samples volume, reducing the pore number per unit of volume gives a clearer insight into their distribution, Figure 4. The samples with 3 wt. % CaCO_3 have the largest number of pores, in the samples with 5 wt. % CaCO_3 there is a slightly smaller number, while in samples foamed with TiH_2 the number of pores is significantly lower.

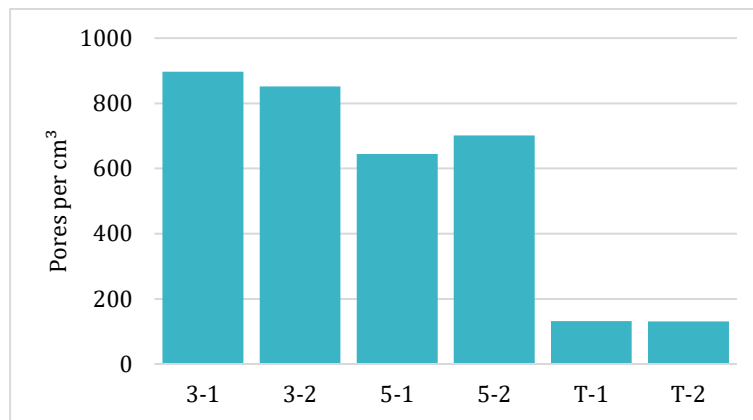


Fig. 4: Number of pores per cm^3 for different samples

Figures 5 – 7 show the pore volume distributions for samples with 3 wt. % CaCO_3 , 5 wt. % CaCO_3 and 0.4 wt. % TiH_2 respectively.

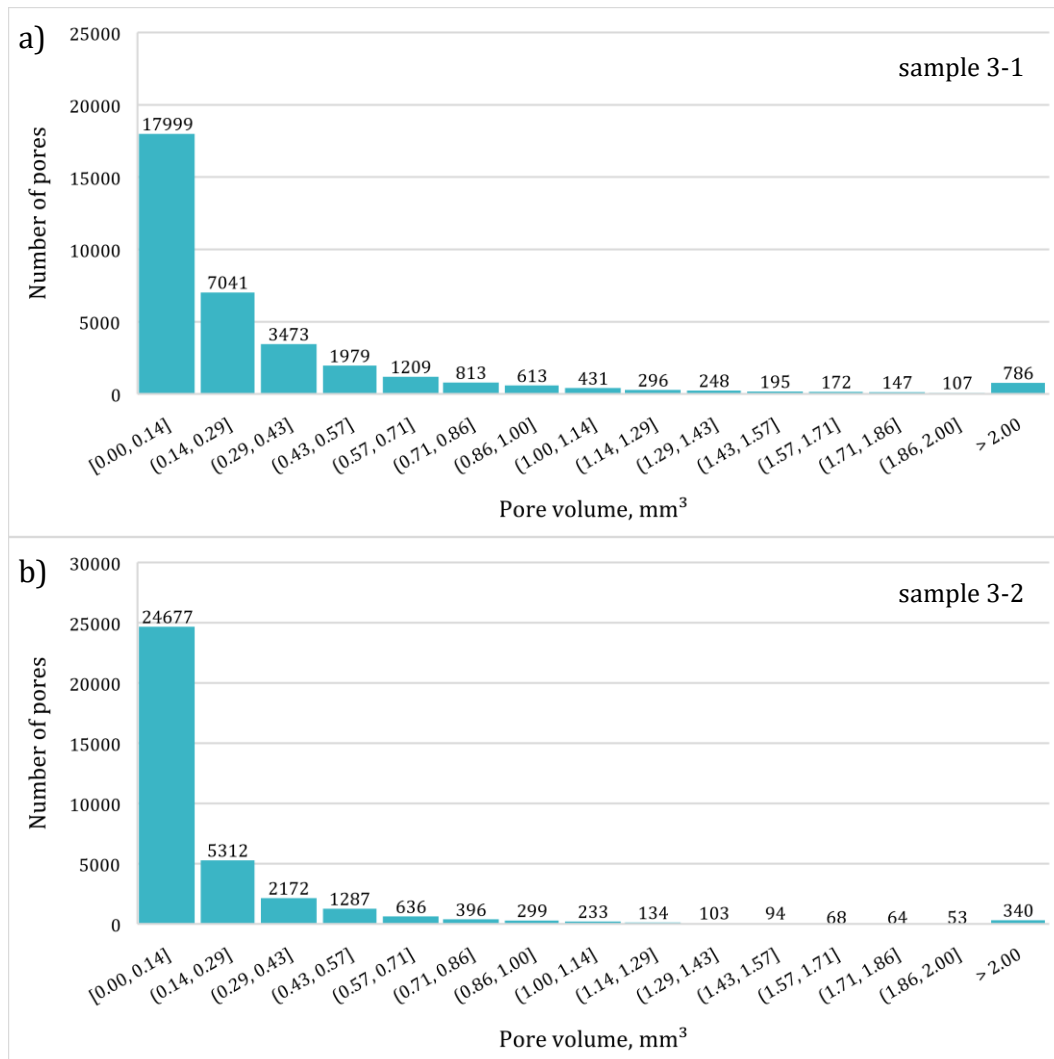


Fig. 5: Pore volume distribution of samples 3-1 (a) and 3-2 (b)

Figure 5 shows that in sample 3-1, approximately 50% of all pores have a volume of up to 0.14 mm^3 , while in sample 3-2 this percentage is slightly higher (68.8%). The small number of pores have volume larger than 2.00 mm^3 (2.2% for sample 3-1), and only 0.9% in the sample 3-2.

In samples with 5 wt. % CaCO_3 (Figure 6), the total number of pores is slightly lower, but their percentage with a volume of up to 0.14 mm^3 is larger; 77.7%, and 68.9% for samples 5-1 and 5-2 respectively. In these samples there are also several pores formed with a volume that exceeds 2.00 mm^3 , in sample 5-1 this percentage is only 0.9%, and in sample 5-2 it is 1.4%.

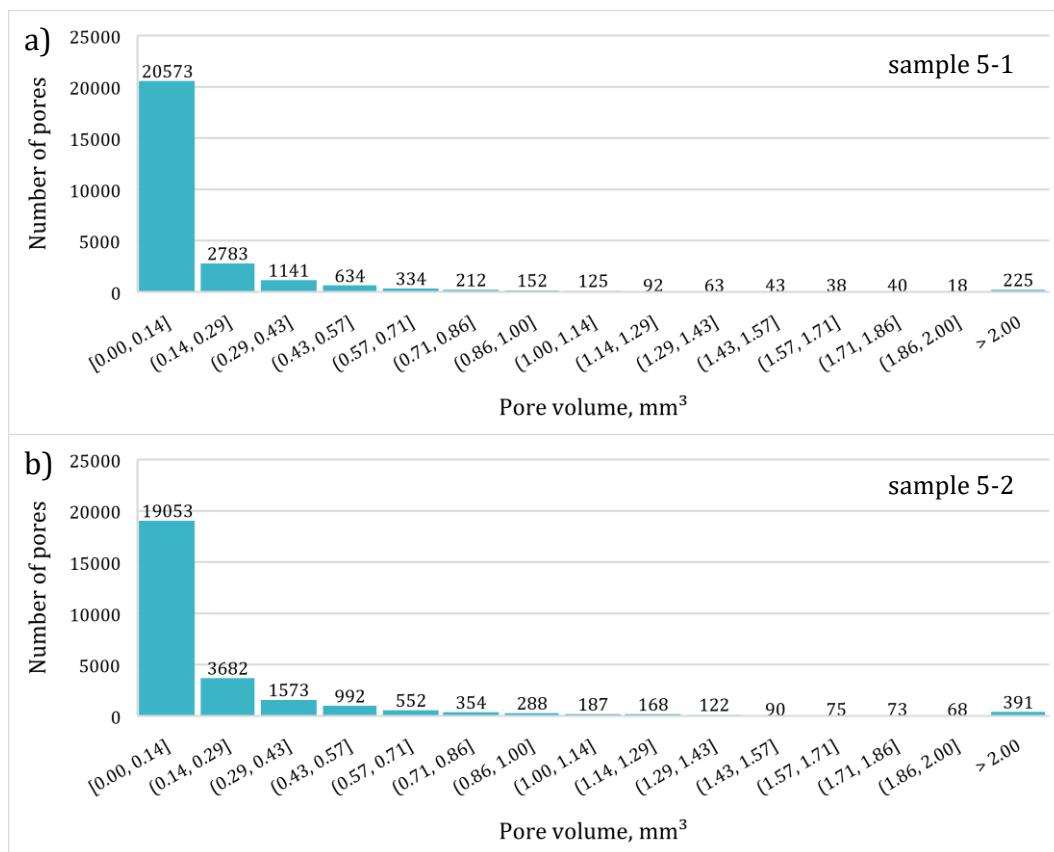


Fig. 6: Pore volume distribution of samples 5-1 (a) and 5-2 (b)

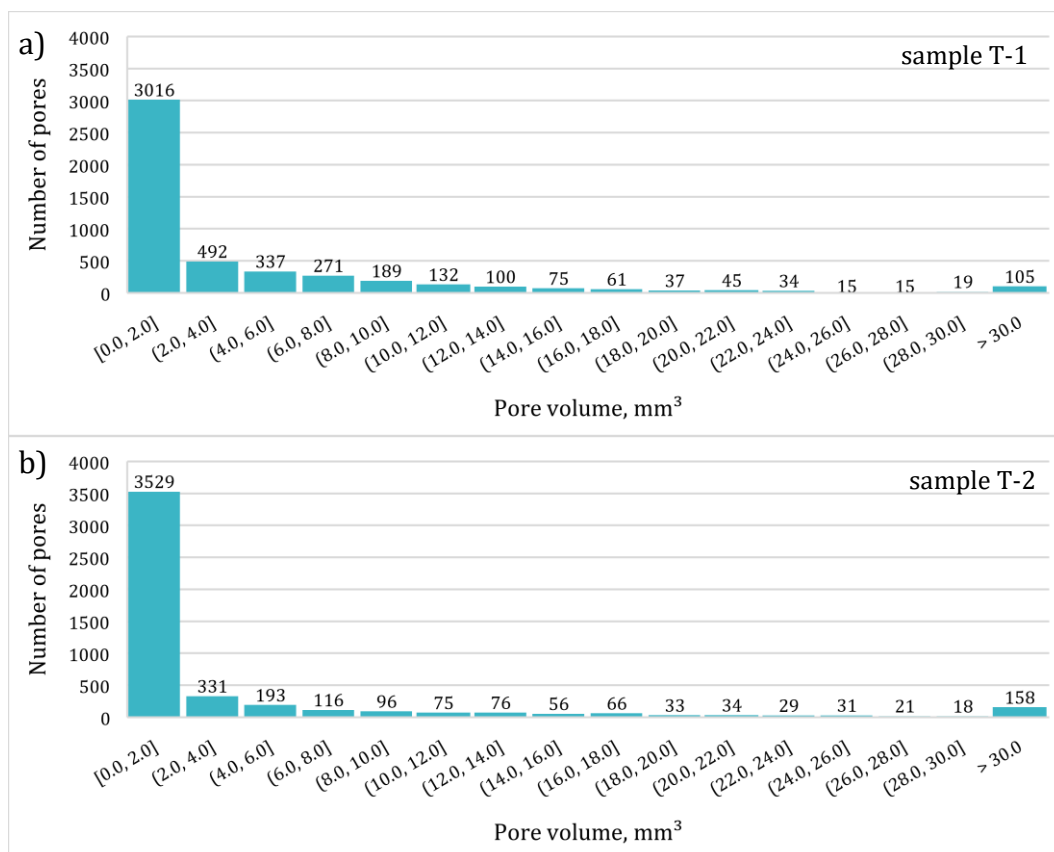


Fig. 7: Pore volume distribution of samples T-1 (a) and T-2 (b)

Unlike the previous samples, those that are foamed with TiH_2 have much larger pores, which is evident from the pore volume distribution shown in Figure 7. While in the foams with CaCO_3 , more than 97% of the pores have a volume smaller than 2.00 mm^3 , in foams T-1 and T-2 this percentage is 61.0% and 72.6% respectively.

The average pore volume in foams with CaCO_3 is very small ($0.15 - 0.34 \text{ mm}^3$), and its value in foams with TiH_2 is several times higher (cca. 4.45 mm^3), Figure 8.

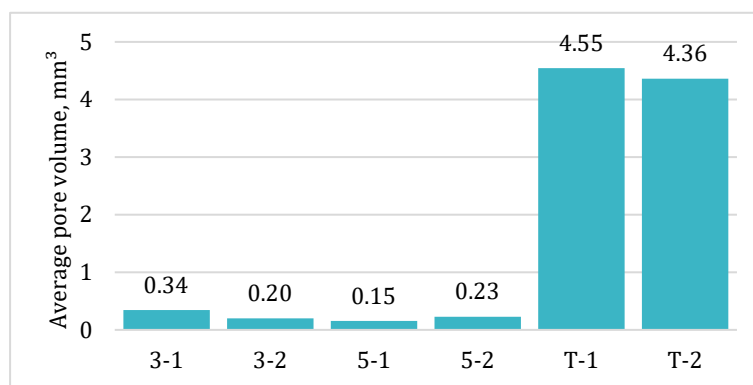


Fig. 8: Average pore volume for different samples

4. CONCLUSION

In this article, the computed tomography method was used to gain insight into the morphology of aluminium foams. The method is non-destructive and consists of three-dimensional scanning of the samples and subsequent analysis of the obtained models in the software. Since the samples in this process are not destroyed, it is possible to use them for further mechanical examinations or for industrial applications.

Aluminium precursors were produced by the powder metallurgy process and foamed with CaCO_3 (3 and 5 wt. %) and TiH_2 (0.4 wt. %). Based on the analysis of the influence of these foaming agents on the number and size of pores, the following can be concluded:

- Foams with 3 wt. % CaCO_3 have the smallest pores, and their number is more than 850 per cm^3 . Samples with 5 wt. % CaCO_3 have somewhat larger pores, and a slightly smaller number per cm^3 . Foams made with TiH_2 characterize much larger pores.
- In CaCO_3 samples, the largest pore has a volume of 38.50 mm^3 , while in TiH_2 samples, this volume even exceeds 420 mm^3 . The average pore volume of TiH_2 foams is also more than ten times higher than that of CaCO_3 foams.
- Foams made with CaCO_3 have more than 97% of pores with a volume smaller than 2.00 mm^3 , while foams with TiH_2 have only 66.8% of such pores.

REFERENCES

- [1] Paulin, I. Synthesis and Characterization of Al Foams Produced by Powder Metallurgy Route Using Dolomite and Titanium Hydride as a Foaming Agents. *Materiali in tehnologije* **2014**, 48, 943–947.

- [2] Soloki, A.; Esmailian, M. Carbonate-Foaming Agents in Aluminum Foams: Advantages and Perspectives. *Metallurgical and Materials Transactions B* **2015**, *46*, 1052–1057, doi:10.1007/s11663-014-0262-1.
- [3] Jaafar, A.H.; Al-Ethari, H.; Farhan, K. Modelling and Optimization of Manufacturing Calcium Carbonate-Based Aluminum Foam. *Mater Res Express* **2019**, *6*, 0865g1, doi:10.1088/2053-1591/ab2602.
- [4] Singh, R.; Arora, R.; Sharma, J.D. Effect of Viscosity Enhancing Agents on Quasi-Static Compression Behavior of Aluminum Foams. *Mater Today Proc* **2021**, *39*, 1661–1666, doi:10.1016/j.matpr.2020.06.056.
- [5] Bisht, A.; Gangil, B.; Patel, V.K. Selection of Blowing Agent for Metal Foam Production: A Review. *Journal of Metals, Materials and Minerals* **2020**, *30*, 1–10, doi:10.14456/jmmm.2020.1.
- [6] Byakova, A.; Gnyloskurenko, S.; Vlasov, A.; Yevych, Y.; Semenov, N. The Mechanical Performance of Aluminum Foam Fabricated by Melt Processing with Different Foaming Agents: A Comparative Analysis. *Metals* **2022**, *12*, 1384, doi:10.3390/met12081384.
- [7] Paulin, I. Stability of Close-Cell Al Foams Depending on the Usage of Different Foaming Agents. *Materiali in tehnologije* **2015**, *49*, 983–988, doi:10.17222/mit.2015.322.
- [8] Mirzaei-Solhi, A.; Khalil-Allafi, J.; Yusefi, M.; Yazdani, M.; Mohammadzadeh, A. Fabrication of Aluminum Foams by Using CaCO₃ Foaming Agent. *Mater Res Express* **2018**, *5*, 096526, doi:10.1088/2053-1591/aad88a.
- [9] Heidari Ghaleh, M.; Ehsani, N.; Baharvandi, H.R. Compressive Properties of A356 Closed-Cell Aluminum Foamed with a CaCO₃ Foaming Agent Without Stabilizer Particles. *Metals and Materials International* **2021**, *27*, 3856–3861, doi:10.1007/s12540-020-00807-5.
- [10] Koizumi, T.; Kido, K.; Kita, K.; Mikado, K.; Gnyloskurenko, S.; Nakamura, T. Method of Preventing Shrinkage of Aluminum Foam Using Carbonates. *Metals* **2011**, *2*, 1–9, doi:10.3390/met2010001.
- [11] Geramipour, T.; Oveisi, H. Effects of Foaming Parameters on Microstructure and Compressive Properties of Aluminum Foams Produced by Powder Metallurgy Method. *Transactions of Nonferrous Metals Society of China* **2017**, *27*, 1569–1579, doi:10.1016/S1003-6326(17)60178-X.
- [12] Duarte, I.; Fiedler, T.; Krstulović-Opara, L.; Vesenjaj, M. Brief Review on Experimental and Computational Techniques for Characterization of Cellular Metals. *Metals* **2020**, *10*, 726, doi:10.3390/met10060726.
- [13] Wang, N.; Maire, E.; Cheng, Y.; Amani, Y.; Li, Y.; Adrien, J.; Chen, X. Comparison of Aluminium Foams Prepared by Different Methods Using X-Ray Tomography. *Mater Charact* **2018**, *138*, 296–307, doi:10.1016/j.matchar.2018.02.015.
- [14] Varga, T.A.; Mankovits, T. Metal Foam Analysis Based on CT Layers. *Acta Materialia Transilvanica* **2018**, *1*, 57–60, doi:10.2478/amt-2018-0020.



ANALIZA TROŠENJA NAVARA NA OBLOGAMA SANJKI HELIKOPTERA

ANALYSIS OF WELDED LAYER WEAR ON HELICOPTER SLIDE LINER

Darko Landek¹, Anita Peran², Mirko Jakopčić³

¹ University of Zagreb, Faculty of Mechanical Engineering and Naval Architecture, Zagreb, Croatia

² Ministry of Defence of the Republic of Croatia, Zagreb, Croatia

³ Croatian Defence Academy "Dr. Franjo Tuđman", Zagreb, Croatia

Sažetak

Tijekom slijetanja helikoptera najveće opterećenje i trošenje se javljaju na njegovom podvozju koje se uobičajeno očvršćava toplinskom obradom i dodatnim nanošenjem navara metalnih kompozita povišene tvrdoće. U radu se predlaže postupak karakterizacije materijala i analize trošenja navara na oblogama sanjki helikoptera primjenom normama propisanih postupaka ispitivanja mikostrukture, tvrdoće i izgleda navara te određivanjem brzine abrazijskog trošenja metodom „suhi pijesak/gumeni kotač“ prema normi ASTM G65:2016. Na temelju rezultata laboratorijskog ispitivanja abrazijskog trošenja komercijalno nabavljene obloge sanjki s tvrdim navarima i Archard-ove jednadžbe trošenja, predložen je matematički model za predviđanje brzine abrazijskog trošenja u uvjetima slijetanja helikoptera na pješčano tlo.

Ključne riječi: obloga sanjki helikoptera, navar, otpornost na abraziju

Abstract

During the landing of the helicopter, the greatest load and wear occurs on its undercarriage, which is usually hardened by heat treatment and additional application of coatings made of metal composites of increased hardness. The paper proposes a procedure for material characterization and wear analysis of the wear of helicopter skid shoe by applying the procedures prescribed by standards for testing the microstructure, hardness and appearance of the wear and determining the rate of abrasive wear using the "dry sand/rubber wheel" method according to the ASTM G65:2016 standard. Based on the results of a laboratory test of abrasive wear of a commercially available sled liner with hard welded tracks and Archard's wear equation, a mathematical model was proposed for predicting the rate of abrasive wear under conditions of helicopter landing on sandy soil.

Keywords: lining of helicopter skids, welded strip, abrasion resistance

1. INTRODUCTION

Transportation of people and goods over short distance utilising multipurpose light helicopters is constantly increasing. Their tasks encompass pilot training, medical flights, conducting search and rescue operations, demining, fire monitoring, VIP transport, etc. According to AC 27-1B:2008 of the USA agencies The Federal Aviation Administration (FAA), helicopters used for the application of legal regulations and certification, are classified into normal and transport helicopters. Light helicopters belong to the group of so-called normal helicopters with the maximum takeoff weight with external load up to 3500 kg. Moreover, it transports a total of up to 7 people and one or two pilots. Empty light helicopters are usually weighing less than 1000 kg. The horizontal flight speeds of such helicopters reach about 220 km/h. Depending on the flight regime, their range is up to 700 km with fuel tank capacity of 350 l. [1]. For helicopter ground manouvering, takeoff, landing and shock absorption during landing, the construction and choice of undercarriage material is essential. Depending on its purpose, the helicopter undercarriage can be tricycle gear, tail-wheel gear, pontoons, tandem landing gear, skid type or their combinations [2]. The construction of the skid type landing gear consists of three or four console brackets that move outwards while landing on the ground as shown in Fig. 1. Ski deflection conducts the role of shock absorber during landing. The calculation of ski dimensions is subject to stress and deformation equations when bending console brackets and beams under static and dynamically variable load conditions and analysis of material fatigue [3, 4].

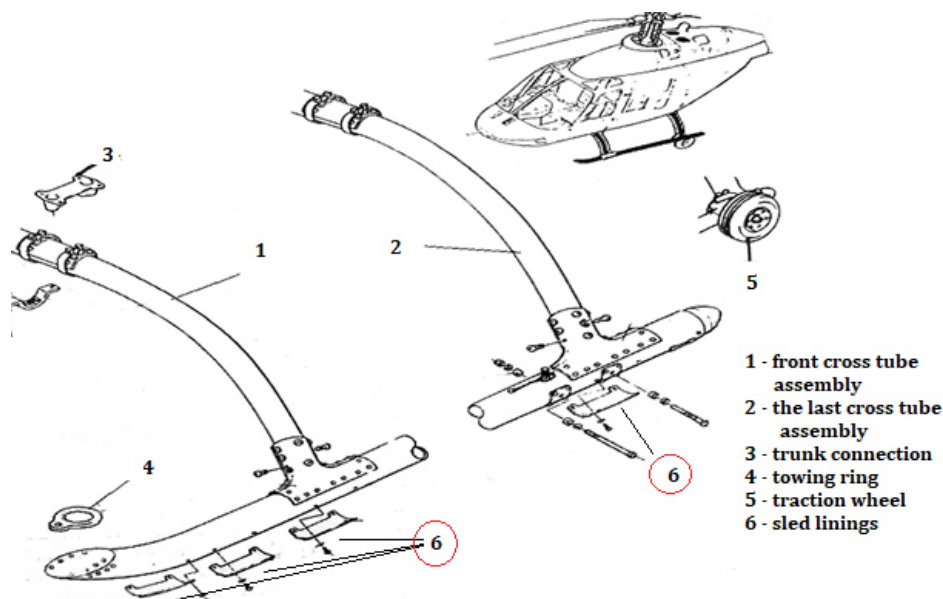


Fig 1: The position of the lining (horseshoe) on the helicopter skid [2]

During take-off, ground travel and helicopter landing operations, the lower surface of the skis is exposed to high contact pressures, inertial forces, impacts and wear and is usually protected by replaceable skid shoes (so-called horseshoes). Damage and dilapidation of the skid shoes directly affects the vibrations and stability of the helicopter during take-off and landing and the possibility of deformation and breakage of the undercarriage. The skid shoes are additionally strengthened by hard welded layers to protect against

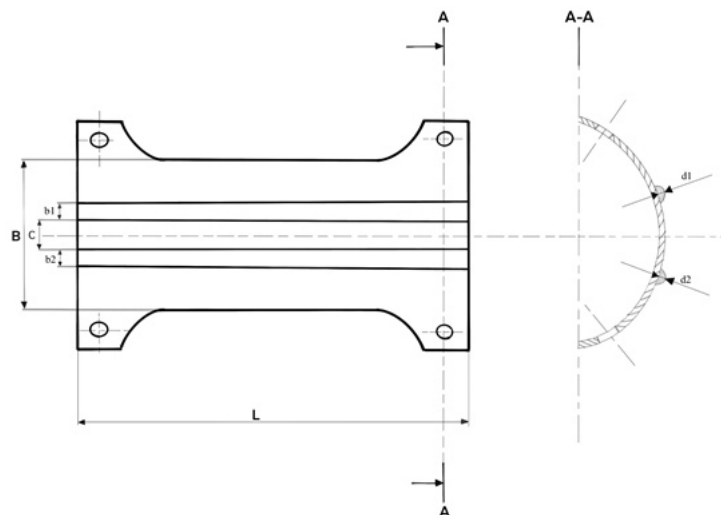
abrasion and erosion wear. While landing on a certain dirty surface, road or on a helipad, abrasion wear of skid shoes is dominant. In condition of landing on sand or on a surface with hard particles, abrasion-erosion wear is present. The basic processes and the appearance of worn surfaces in these wears are described in detail in the literature [5,6].

Inspection of the condition of the skid shoes and wear of the welded layer is performed by qualitative visual control during periodic maintenance and in pre-flight and post-flight checks [1]. Skid shoes are available on the market as a commercial product, with prescribed dimensions and mechanical properties. However, the criteria for choosing between skid shoes from different manufacturers, matching the type of skid shoes with the usual purpose of the helicopter and determining the rate of wear are not fully defined.

This paper proposes a procedure for characterizing the microstructure and properties of commercially available helicopter skid shoes and investigates the possibility of predicting the rate of abrasive wear of welded layers under laboratory condition with "dry sand/rubber wheel" method".

2. MATERIALS AND METHODS

Mechanical, microstructural and tribological tests were carried out on two partially worn samples of the skid shoes marked W1 and W2, shown schematically in Fig. 2. The worn part of the skid shoe was separated by cutting for microstructural analysis, and two samples were prepared from the unworn part of the skid shoe for tribological testing. Both samples belong to the same type of skid shoe, purchased from the same manufacturer, which guarantees the reproducibility of the properties of the skid shoe in deliveries. The coatings were installed over a period of one month on the same helicopter that took off and landed on different surfaces. The outer dimensions of the skid shoe body are 100 mm x 45 mm. The width of the welded layer before wear was 6.5 ± 0.5 mm, and the height was 1.6 ± 0.4 mm.



Legend

L – plate length, B – plate width, b_1 – width of 1st strip (W1), b_2 – width of 2nd strip (W2), c – distance between strips, d_1 – thickness of first strip, d_2 – thickness of second strip

Fig 2: Dimensions and shape of welded layers on the helicopter skid shoe

The characterization of the properties of the welded layers consisted of the following stages: (1) examination of the chemical composition by a non-destructive spectroscopy method, (2) visual analysis of the worn surfaces of the original welded layers by stereomicroscopy, (3) analysis of the microstructure on the metallographic sample, (4) hardness tests on the section of the welded layers, (5) resistance assessment of welded layers to abrasive wear.

The presence and proportion of metal elements in the welded layer and skid shoe body was determined by the method of X-ray fluorescence spectroscopy (eng. X-ray fluorescence technology) using a portable spectrometer XRF Olympus, manufactured by Innov-X Systems, Inc, model DS 2000-C at the Chair of Materials Protection (FMENA). The portable XRF spectrometer requires minimal sample preparation and it is one of the fastest ways to test the chemical composition on the surface of metal samples of various shapes and sizes.

The analysis of the microstructure on the section of the welded layer and the body was performed after metallographic preparation, which consisted of cutting the welded layer's sample from the skid shoe on a Mecatome T260 device with a diamond cutting plate with intensive emulsion cooling. The cut sample was poured into a polymer mass that was permanently hardened in a Pneumet Press. The metallographic sample was then grinded and polished on a MECATECH 250 SPC device, utilising a rotating grinding disc for hard metals, with a rotation speed of 300 rpm. Polishing is performed on the same device as grinding, but instead of water for cooling, a suspension of alcohol and water is used as a lubricant. Polishing was carried out in two phases with a speed of rotation of the polishing disk of 150 rpm for 10 min. In the first stage, a Struers SP3 ss diamond suspension with an average grain size of 3 μm was used. In the second phase, a diamond paste with a diameter of abrasive particles of 0.03 μm was utilised. The metallographic sample was analyzed using light microscopy on an Olympus GX 51 microscope in the Materialography Laboratory (FMENA).

The hardness test on the metallographic sample of the welded layer and body was carried out using the Vickers HV1 method on the INSTRON Wilson-Wolpert Tukon 2100B hardness tester in the Surface Engineering Laboratory (FMENA). The hardness of the welded layer, the heat affected zone and the body were tested.

Testing the resistance to abrasive wear using the "dry sand/rubber wheel" method according to the ASTM G65:2016 standard was carried out in the Tribology Laboratory (FMENA). The test method and device are described in ref. [5] and showed in Fig. 3. In the conducted tests, a wheel with a diameter of 200 mm was used with a rubber coating of hardness 60 Shore-. On the wheel rotating at a speed of 200 \pm 10 rpm, a test sample of welded layers is pressed with a force of 200 N. Two samples of welded layers were tested. The test was carried out five times on each sample for 60 s. After each test, the sample was cleaned of dust and abrasive grains in an ultrasonic bath by immersion in a 70% aqueous solution of ethyl alcohol for 60 s. After cleaning, the mass of the worn samples were measured on an analytical balance Mettler Zurich M 56 1000 with a measurement error of ± 0.001 g. From the measurement results, the cumulative mass loss of the sample was determined after every 60 s of wear. According to Archard's wear equation, the mass loss of the worn material (m) is proportional to the wear path (S) and the normal force (N) that presses the sample on the rubber wheel [7]:

$$m = \kappa \cdot (S \cdot N) \quad (1)$$

in which κ is the wear coefficient. The cumulative wear path (S) is determined according to the expression:

$$S = 2 \cdot R \cdot \pi \cdot \frac{n}{60} \cdot t \quad (2)$$

where n is the wheel rotation speed (rpm), t is the cumulative wear time (s).



Fig 3: Device for testing resistance to abrasive wear using the "dry sand-rubber wheel" method

The measurement of wear was carried out with a Vernier caliper gauge and a micrometer at the Depo Overhaul Center of the Ministry of Defense. Visual analysis of the worn parts was performed on a Leica MZ6 stereomicroscope in the Leica Application computer program.

3. RESULTS AND DISCUSSION

3.1. Chemical composition

The proportion of metal elements in the welded layer is shown in table 1. From the presented proportion of metal elements, it is evident that the welded layer is composed of carbides, characteristic of hard welded alloys. The presence of Cd in the test sample was registered due to the protective coating that was galvanically applied to the helicopter skid shoe after welding. The presence of Fe was registered due to the welded layer and skid shoe on which it was deposited. From the stated chemical composition, it is not possible to define exactly what kind of hard alloy the welded layer is made of, but the search for electrodes for hard welding can be restricted to those electrodes in which are present the following metal elements: Ti, Cr, W, Co, Zr and Fe. A more accurate

chemical analysis of the welded layer can be performed on a metallographically prepared sample using a scanning electron microscope and energy-dispersive spectroscopy (EDS).

Tab. 1: The chemical composition of the welded layer as was determined using the X-ray fluorescence method and using a portable spectrometer

Sample label	Contents of chemical elements, wt.%						
	Cr	Ti	W	Co	Zr	Cd	Fe
W1	21.97	12.59	13.84	1.60	1.74	20.51	27.33
W2	23.76	13.22	13.79	1.53	1.74	24.09	21.38

3.2. Analysis of worn surface on the welded layer

Fig. 4 shows the partially worn helicopter skid shoe. Due to the visual inspection, several examples of worn helicopter skid shoes emphasize four ways of wear:

- Abrasive wear in conditions of landing on a slope, i.e. side landing, during which one welded layer in its entire length wears faster than the other.
- Abrasive wear in conditions of landing under angle, where only the front part of the welded layer wears the most, as shown in Fig. 4a.
- Abrasive wear in landing conditions with an evenly loaded front side of the skid shoe where welded layers are worn evenly along its entire length
- Impact wear, in which a brittle fracture of welded layers is observed, as a result of the skis hitting the chute or solid objects during landing

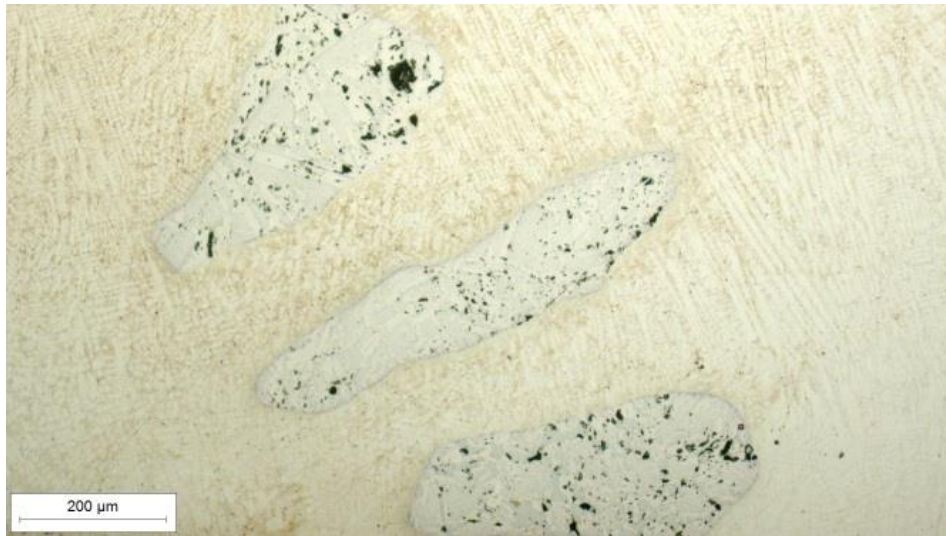
Uniform abrasive wear of the surface (case c) is the least intense and represents the usual way of wear under ideal conditions of helicopter take-off and landing.



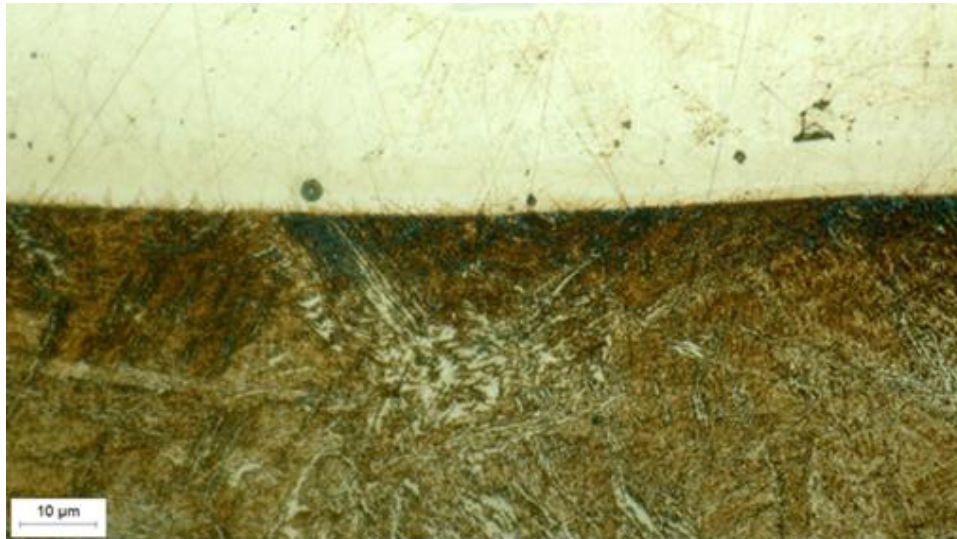
Fig. 4: Partially worn helicopter skid shoe: a) the entire shid shoe, b) the surface of the welded layer

3.3. Microstructure

The microstructure of the welded layer and the heat affected zone below it, is shown in Fig. 5. In Fig. 5a, the dendritic microstructure of the welded layer's matrix formed by rapid solidification of the melt and the carbides embedded in the matrix, can be seen. Fig. 5b presents a narrow heat-affected zone under the welded layer and the microstructure of the softened martensite in the material of the helicopter skid shoe.



a)



b)

Fig. 5: The microstructure of welded layer and heat affected zone of helicopter skid shoe: a) microstructure of welds with carbides, b) welds and heat-affected zone; etched by 3 % NITAL

3.4. Hardness

Fig. 6 compares the hardness on the cross-section of the skid shoe, in the heat-affected zone and in the welded layer. The hardness of matrix and carbides of the welded layer was also examined. During the hardness test, the microcracks appeared on the carbide grains at the edges of the impression. After all, the welded layer is 1.8 times harder than the plectet (skid shoe body). The hardness of the carbide in the matrix of welded layer is in the range of 1000-2000 HV1.

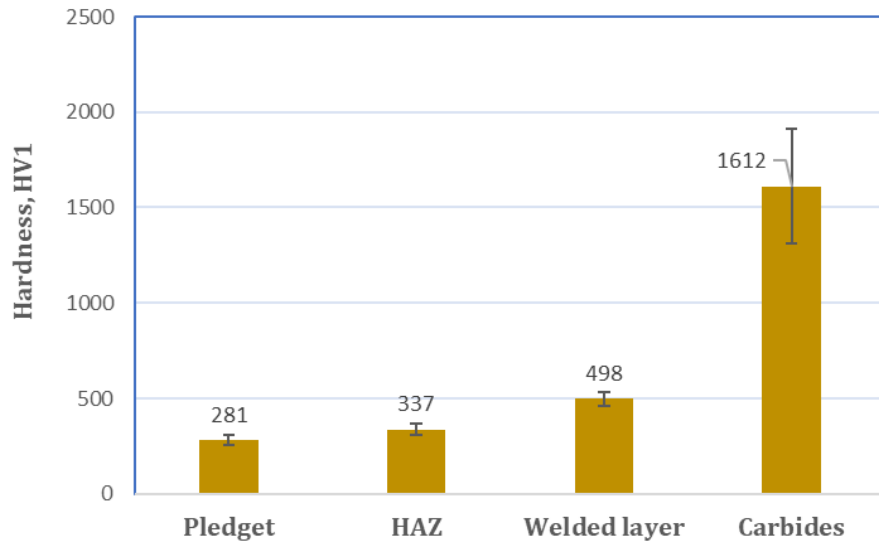


Fig. 6: Hardness of helicopter skid lining and lining welds

3.5. Wear resistance

The appearance of the worn surface of the welded layer after 5 minutes of wearing is shown in Fig 7. In the experiment, uniform wear on the top side of the welded layer was achieved, without the carbide being pulled out of the matrix. On the surface of the sample, only furrows and scratches are visible, typical of abrasive wear by sharp hard particles of quartz sand.



Fig. 7: Weld surface W1 after 5 min wear according to the "dry sand-rubber wheel" method

The mass loss after wear of the weld test samples is shown in Fig. 8. From the course of the cumulative mass loss curves, in Fig 8a, the initial equal wear of both welded layers can be observed. After 240 s of wearing, welded layer 1 (W1) begins to wear more than welded layer 2 (W2). Fig. 8b shows the change in the abrasive wear coefficient κ depending on the wear path determined according to the equation (3):

$$\kappa = \frac{m}{S \cdot N} \quad (3)$$

where S is the wear path and N is the normal force which presses the sample against the rubber wheel. The wear coefficient represents the rate of wear, for a certain combination of the wear path and the normal force acting on the worn surface. Figure 6a presents that welded layer W2 with lower values of the wear coefficient is more resistant to abrasive wear than welded layer 1 (W1) by about 16%. It is assumed that the cause of this welded layer behavior is a repercussion of a slightly higher proportion of Cr and Ti in welded layer W2 than in welded layer W1, which create a slightly higher proportion of carbides

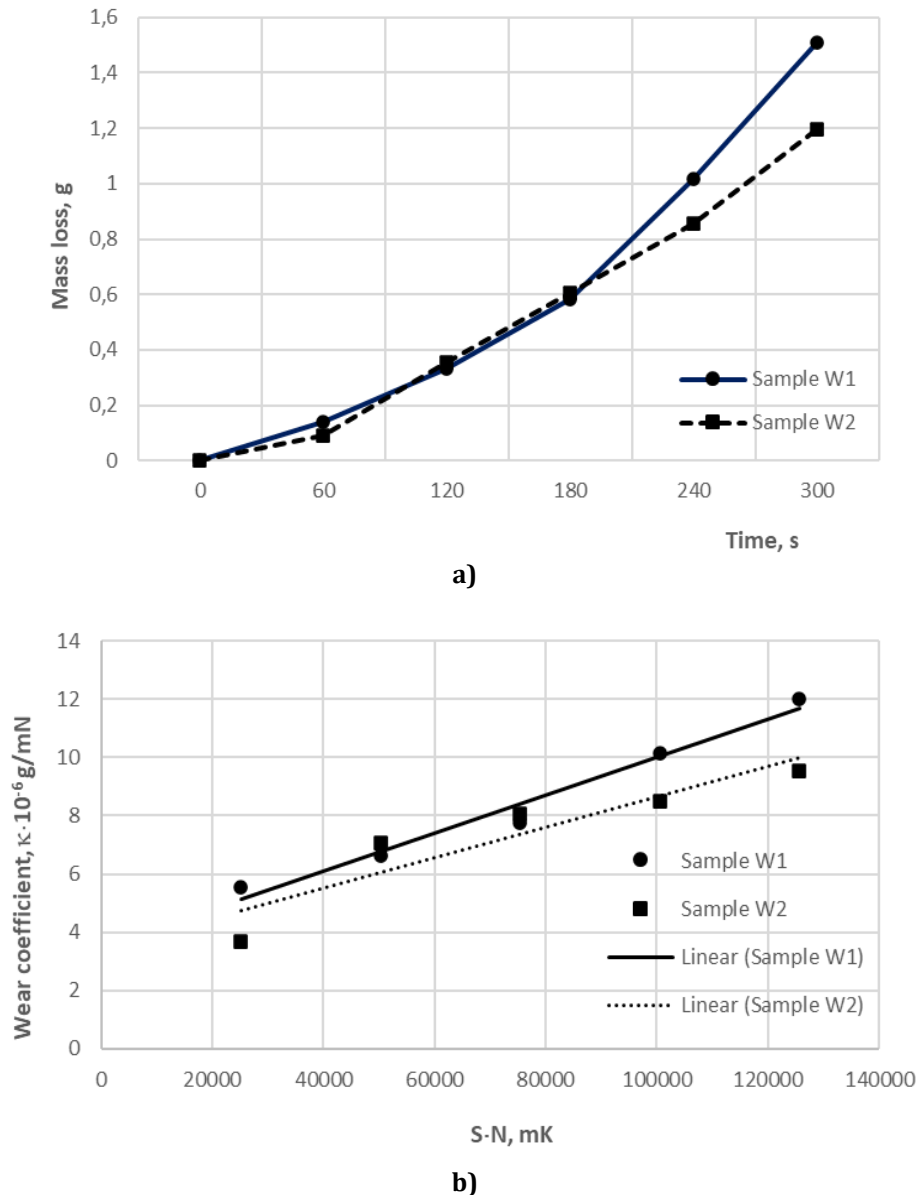


Fig. 8: Abrasive wear of welds using the "dry sand - rubber wheel" method: a) cumulative mass loss, b) coefficient of abrasive wear

4. CONCLUSION

The helicopter skid shoes represent a structural part exposed to high contact pressures, impacts and wear during take-off and landing of the helicopter, as well as during its maneuvering on the ground. The paper proposed a laboratory testing procedure for

comparing the quality of helicopter skid shoes consisting of five phases: (1) testing of the chemical composition using the non-destructive method of X-ray fluorescence spectroscopy, (2) visual analysis of the welded surfaces using stereomicroscopy, (3) microstructure analysis on a metallographic sample, (4) tests of hardness on the welded layer's cross-section and (5) resistance assessment of welded layers to abrasive wear. According to the Archard wear equation, abrasive wear coefficient was determined on two layers from the same type of skid shoe. After 5 minutes of wearing, using the "dry sand-rubber wheel" method, the difference in the wear coefficient between them was determined to be about 16%. The stated procedure for testing the chemical composition and properties of helicopter skid shoes can be recommended for the selection of skid shoe suppliers and quality control of commercially procured skid shoes.

Acknowledgement(s):

The authors would like to thank the Aviation Technical Center d.d. Velika Gorica, Croatia on handing over the helicopter skid shoe for testing.

REFERENCES

- [1] Padfield, R.R.: Learning to Fly Helicopters, Mc graw Hill Education, 2nd ed., New York, Chicago, (2014)
- [2] Vrkić, M., Konstrukcija zrakoplova, Priručnik, GS OS RH, Zagreb, (2008)
- [3] Božić, Ž.: Osnove konstrukcije helikoptera, Skripta, Fakultet strojarstva i brodogradnje, Sveučilište u Zagrebu, (2010)
- [4] Sadraey, M.H.: Aircraft design : a systems engineering approach, John Wiley & Sons, Ltd, Chichester, UK (2013)
- [5] K. Grilec, K., Jakovljević, S., Marić, G., Tribologija u strojarstvu, Fakultet strojarstva i brodogradnje, Zagreb, (2017)
- [6] Blau, P.J. (Ed): ASM Handbook, Volume 18, Friction, Lubrication, and Wear Technology, ASM International, Metals park, USA (1997)
- [7]. Hutchings, I.M.: Tribology: Friction and Wear of Engineering Materials, Arnold, London, UK (1992)



MATERIAL CHARACTERIZATION OF THE FREE-FORGED MACHETE

Andrija Cestar¹, Vera Rede¹, Helena Lukšić¹

¹ University of Zagreb, Faculty of Mechanical Engineering and Naval Architecture, Ivana Lučića 5, 10002 Zagreb, Croatia

Abstract

In the paper, the material characterization of a free-forged machete made of steel of unknown chemical composition was carried out. Material characterization included chemical composition analysis, microstructure analysis, and microhardness measurement before and after free-forging. It was found that the machete was made of low-alloy spring steel 55Cr3 which has a martensitic-bainitic microstructure. The mean microhardness value in the cross-section before forging was 468 HV0.2. After free-forging microstructure in the cross-section of the machete consists of martensite, bainite, and carbides precipitated at the crystal grain boundaries. Due to differences in cooling and intensity of forging volume fractions of martensite and bainite are not the same in certain parts of the cross-section of the machete, which also was reflected in the microhardness values. The highest mean microhardness value was measured on the blade of the machete and was 481 HV0.2, while the lowest microhardness was measured on the middle of the machete and was 417 HV0.2. Along the spine of the machete, the hardness was 453 HV.02.

Keywords: *material characterization, microstructure, microhardness, free-forging*

1. INTRODUCTION

Metal forging is a process by which the starting material is plastically deformed, in one or more steps, into a useful part without changing the mass and chemical composition of the material [1]. Forging aims to achieve dimensional accuracy of the forging, as well as good mechanical properties and microstructure [2]. During forging, the material being processed goes through a series of microstructural changes – recovery of the material due to static or dynamic loading, recrystallization of crystal grains, and growth of crystal grains. The mentioned microstructural changes are influenced by forging parameters such as forging force, temperature, strain, and strain rate [2,3]. According to the temperature, forging can be divided into hot forging, cold forging, and warm forging. Regarding the shape of the pressure surfaces, forging can be free-forging or die-forging [1]. During hot forging, the microstructure changes by heating and cooling the forging, and thus the mechanical properties can be adjusted. Processing parameters during hot forging must ensure the required shape and dimensions in addition to the required mechanical properties such as strength, hardness, toughness, creep resistance, etc [3]. In history, various products such as machetes and knives for everyday use were often forged. Some of the famous machetes obtained by forging are the Damascus sword and Japanese swords (katanas). The Damascus sword was produced in medieval Damascus and was made of "wootz" steel. The blade of the Damascus sword had high hardness and strength, and it had a characteristic appearance - light gray wavy stripes on a dark gray background. This characteristic appearance was obtained by specially determined forging, quenching, and annealing parameters [4]. Fig. 1 shows the microstructure of a Damascus sword.

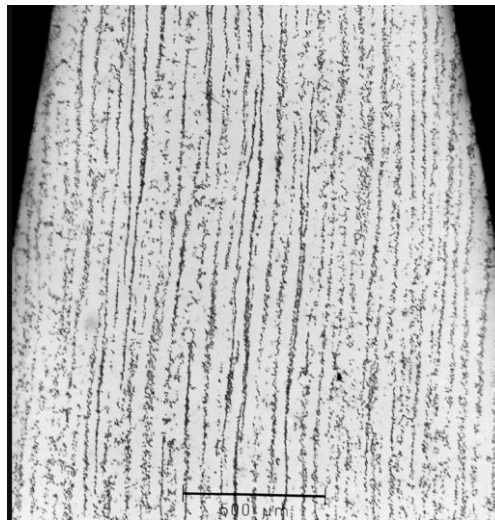


Fig. 1: Microstructure of Damascus sword [5]

Japanese swords were made of "tamahagana" steel. The blades of Japanese swords had very good mechanical properties, such as hardness and strength, obtained by a special traditional forging process called "tatara" [6].

This work aims to carry out the material characterization of a free-forged machete made of steel of unknown chemical composition. As part of the material characterization, the following tests were carried out:

- chemical composition analysis
- microstructure analysis
- microhardness measurement HV0.2.

2. MATERIAL AND METHODS

As a starting material for making a machete, a used leaf spring of an unknown manufacturer, about 50 years old, was taken. The dimensions of the spring leaf were $890 \times 60 \times 7$ mm. From the initial shape, a sample was cut with a hand grinder, from which the machete was made by forging. The shape and dimensions of the sample are shown in Fig. 2.

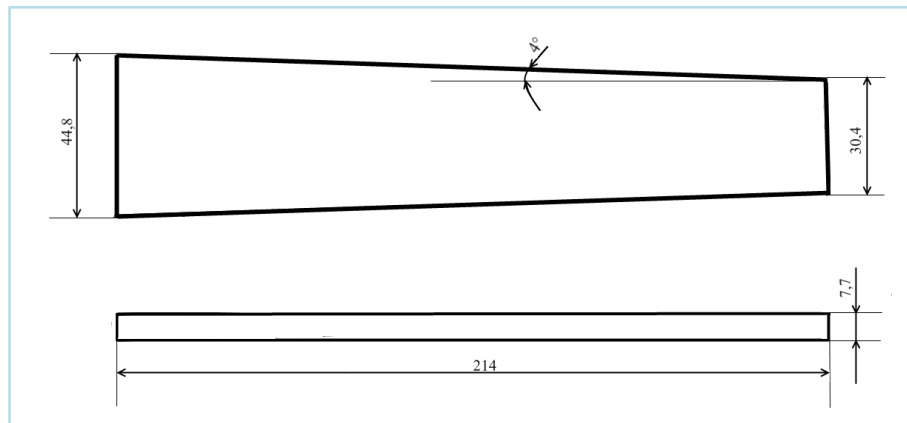


Fig. 2: The shape and dimensions of the cut sample

Free forging was carried out in an amateur forge at temperatures between 533 and 1032 °C. Forging was carried out in 8 cycles. One forging cycle involves heating the forging in the forge fire, removing it from the fire, and forging. The temperature of the forging was measured with a laser thermometer immediately after removing it from the fire (before the start of forging) and after the forging process. In the first 5 cycles, rough forging was carried out, during which a 3 kg forging hammer was used. In the remaining 3 cycles, fine forging was carried out, i.e., a 1 kg forging hammer was used. After the last forging cycle, the machete was left to cool in the air to room temperature. The cooling lasted about 20 minutes.

Fig. 3 shows the forged machete before grinding to the final shape.

Tab. 1 shows the initial and final forging temperatures and the heating time of the forging for all 8 cycles.



Fig. 3: Forged machete

Tab. 1: Initial and final forging temperatures and the heating time of the forging

Cycle	Starting temperature of forging, °C	Finishing temperature of forging, °C	Heating time, s
1	1032	752	175
2	985	758	96
3	968	670	60
4	940	660	120
5	952	655	57
6	1030	755	55
7	948	552	180
8	935	533	53

After forging, a part of the reinforcing steel rod is welded to the narrow side of the machete, which is later wedged into the wooden handle.

In order to remove the oxides formed during heating from the surface of the machete, reduce the roughness of the surface, and finally shape the blade of the machete, the forging was ground. Grinding of the forging was carried out in several steps. The final grinding of the machete blade was carried out with fine (P100) and very fine (P240) sandpaper.

Fig. 4 shows the finished machete.

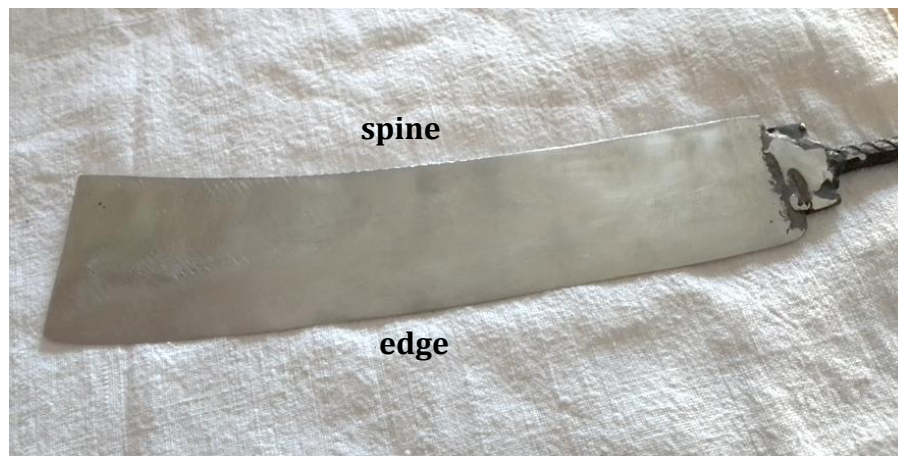


Fig. 4: Finished machete

2.1. Chemical composition analysis

The sample for the analysis of the chemical composition in the initial state was cut from the initial material (the spring leaf), and its dimensions were 15 × 15 × 7 mm. The chemical composition of the material was determined by optical emission spectrometry on a LECO GDS 850A spectrometer.

2.2. Microstructure analysis

The microstructure analysis was performed on the Olympus GX51 light microscope, in the polished and etched state, at magnifications between 50× and 1000×. The microstructure of the cross-section spring leaf before forging and the microstructure of the cross-section of the machete were analyzed. Before analyzing the microstructure, the samples were properly prepared. The samples were filled in polymer mass, ground, and polished. Grinding and polishing were carried out on the Mecatech 250 device. During grinding, the plate rotated at a speed of 300 rpm, and water was used for cooling and lubrication. Grinding started with P320 quality sandpaper, continued with P600, P1000, and P2400, and finished with P4000 quality sandpaper. The abrasive particles of all sandpapers were made of silicon carbide (SiC). After the grinding process, a 2-step polishing process followed. During polishing, the plate rotated at a speed of 150 rpm. In the first polishing step, a diamond paste with a mean particle diameter of 3 μm was used and spread over the polishing cloth. The lubricant was used for cooling and lubrication. In the second polishing step, a polishing liquid with abrasive particles of 0.03 μm was used. After the second polishing step, the surface of the samples is ready for microstructure analysis in the polished state. After analyzing the microstructure in the polished state, surface etching of the samples was carried out. The surface of the sample was etched in a 3 % solution of nitric acid in ethyl alcohol (Nital). The sample was immersed in the specified solution for a few seconds and then washed in distilled water.

Fig. 5 shows specimens filled in polymer mass. Specimen 1 was taken as the initial material and cut directly from the spring leaf before forging, while specimens 2a and 2b were cut from a finished forged machete. Specimen 2a is part of the cross-section near the spine of the machete and specimen 2b is part near the edge of the machete.

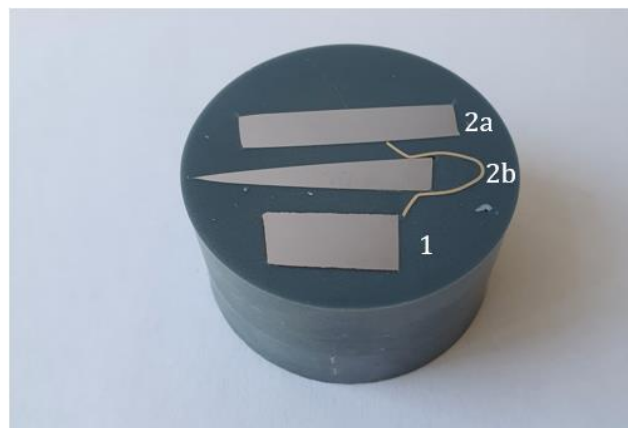


Fig. 5: Sample for microstructure analysis

2.3. Microhardness measurement

The microhardness measurement HV0.2 was carried out on specimens 1, 2a and 2b, using the Vickers method, with an indenter in the form of a diamond four-sided pyramid with an apex angle of 136°. The force with which the indenter was pressed into the material was 1.962 N. A total of 30 microhardness measurements were performed, and the mean value of the hardness at a particular location of the sample was calculated.

3. RESULTS AND DISCUSSION

3.1. Results of chemical composition analysis

The results of the chemical analysis of the material are shown in Tab. 2.

Tab. 2: Chemical composition of the starting material

wt. %										
C	Si	Mn	P	S	Cr	Mo	Ni	Cu	V	Fe
0.53-0.68	0.32	0.81-0.83	<0.02	<0.02	0.75-0.76	0.007-0.014	0.06-0.07	0.064-0.080	0.006	bal.

According to the proportion of C, Si and Mn, S and P, and other elements, it can be concluded that it is low-alloyed steel 55Cr3, which is used to produce springs. The proportion of impurities in steel (S and P) is very low, and this steel belongs to the group of high purity steels.

3.2. Results of microstructural analysis

55Cr3 steel has a mixed, grain-oriented microstructure with martensite and bainite on the cross-section of the spring leaf before forging (specimen 1), as shown in Fig. 6. At lower magnification, gray deposits of manganese sulfide (MnS) can be observed in the microstructure.

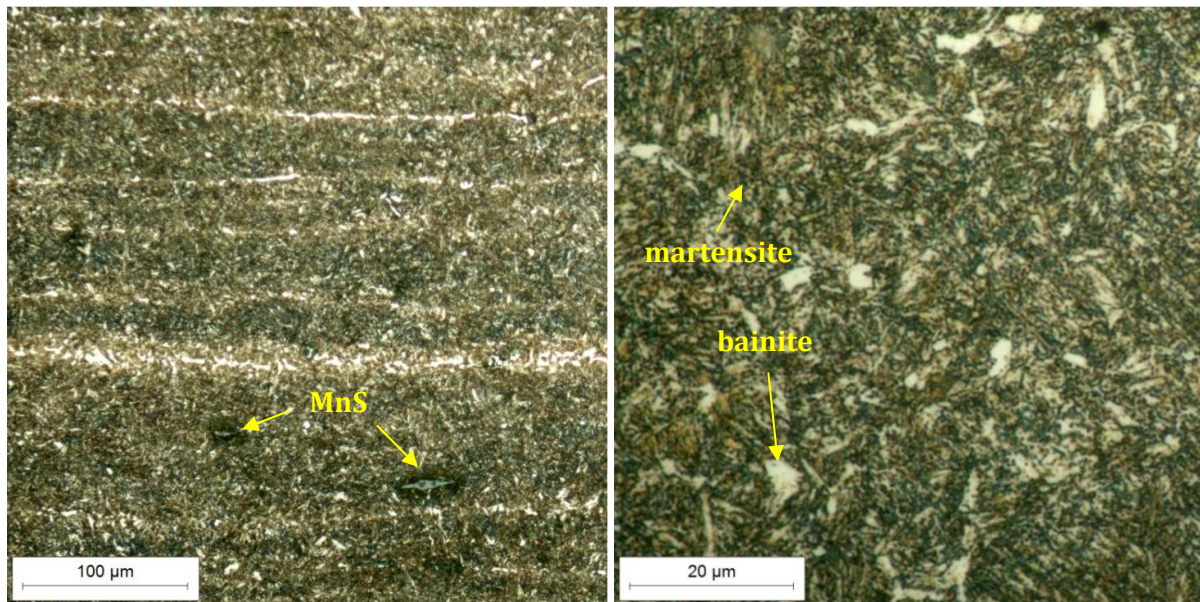


Fig. 6: Martensitic and bainitic microstructure on cross-section of spring leaf before forging (specimen 1) at lower (left) and higher magnification (right)

The microstructure of the cross-section of the forged machete, after 8 cycles of free forging at temperatures between 1032 and 533 °C and air cooling to room temperature, consisted of martensite, bainite and carbides. The volume fractions of martensite and

bainite are not equal in different parts of the cross section. The carbides are distributed along the boundaries of crystal grains, and they are most noticeable in the edge of the machete (specimen 2b). Given that the forging intensity was not equal in all parts of the machete, there is an evident difference in the degree of deformation of the microstructure.

Fig. 7 shows the microstructure of the cross-section near the spine of the machete (specimen 2a), and Fig. 8 shows the microstructure near the edge of the machete (specimen 2b).

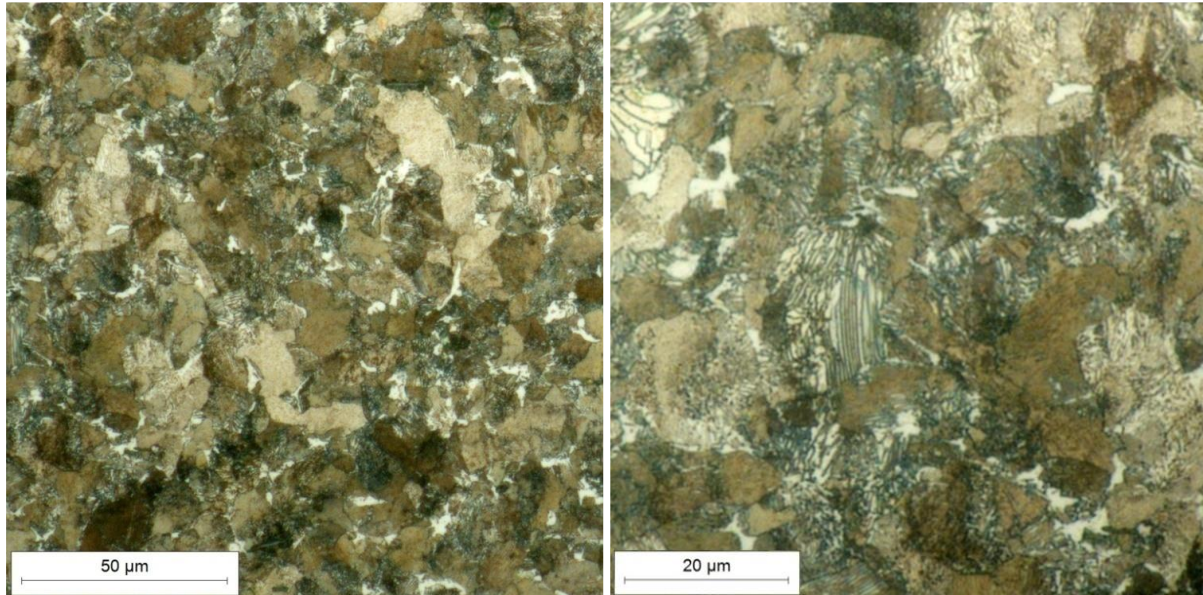


Fig. 7: The microstructure of the cross-section near the spine of the machete (specimen 2a) at lower (left) and higher magnification (right)

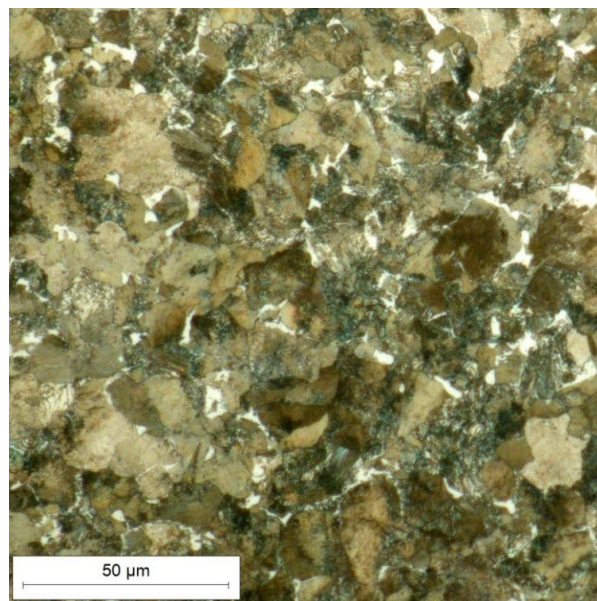


Fig. 8: The microstructure near the edge of the machete (specimen 2b)

Considering that during forging, the machete was cooled continuously in the air at a cooling rate of about 5 °C/s, it can be seen from the TTT diagram for this steel that the achieved microstructure will be composed of bainite and martensite, which coincides with the results of the microstructural analysis. Fig. 9 shows the TTT diagram of steel 55Cr3. It can be seen from the TTT diagram that faster cooling would result in a completely martensitic microstructure, and slower cooling would result in a completely pearlite microstructure [7].

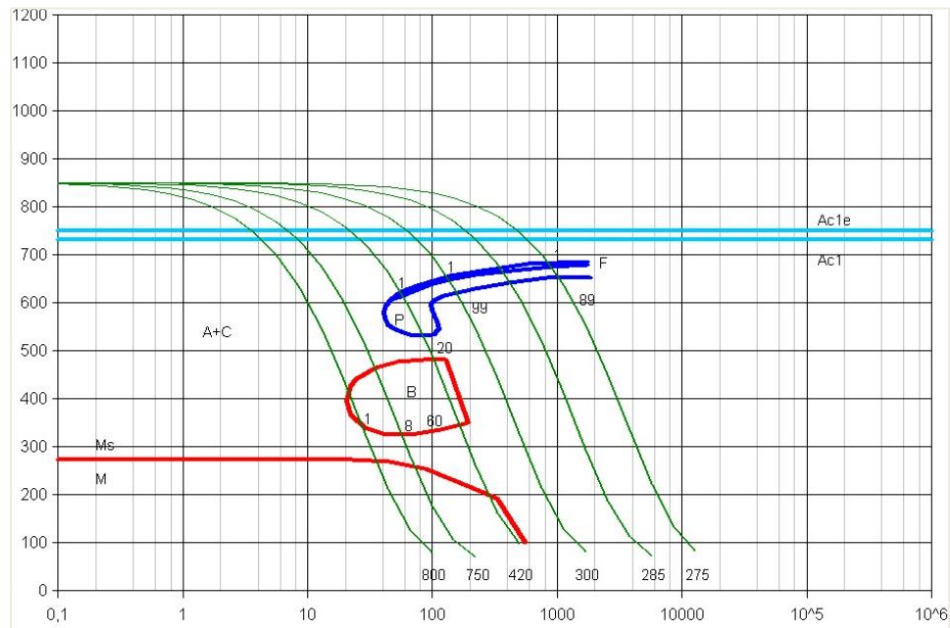


Fig. 9: TTT diagram of steel 55Cr3

3.3. Results of microhardness measurement HV0.2

The microhardness HV0.2 of the initial material measured on the cross-section of the spring leaf (specimen 1) corresponds to the microhardness of steel 55Cr3, with a martensitic-bainite microstructure. The microhardness in the middle of the section is the highest and is 515 HV0.2, and on the edges, it is between 417 and 473 HV0.2.

The microhardness measured on the machete after forging and cooling differed in individual parts of the cross-section. On the blunt part of the machete, next to the spine (specimen 2a), microhardness values between 407 HV0.2 and 480 HV0.2 were measured. This part of the machete, compared to other parts of the section, is the least subject to forging. In the middle of the cross-section of the machete, the lowest mean microhardness values were obtained, between 374 HV0.2 and 432 HV0.2.

The highest microhardness values on the cross-section were measured along the edge of the machete, from 460 HV0.2 to 524 HV0.2 (specimen 2b). This area was intensively forged, and the proportion of carbide is the highest in it.

Fig. 10 shows the results of microhardness measurements of the cross-section spring leaf before forging (specimen 1) and the microhardness values of the forged machete (specimen 2).

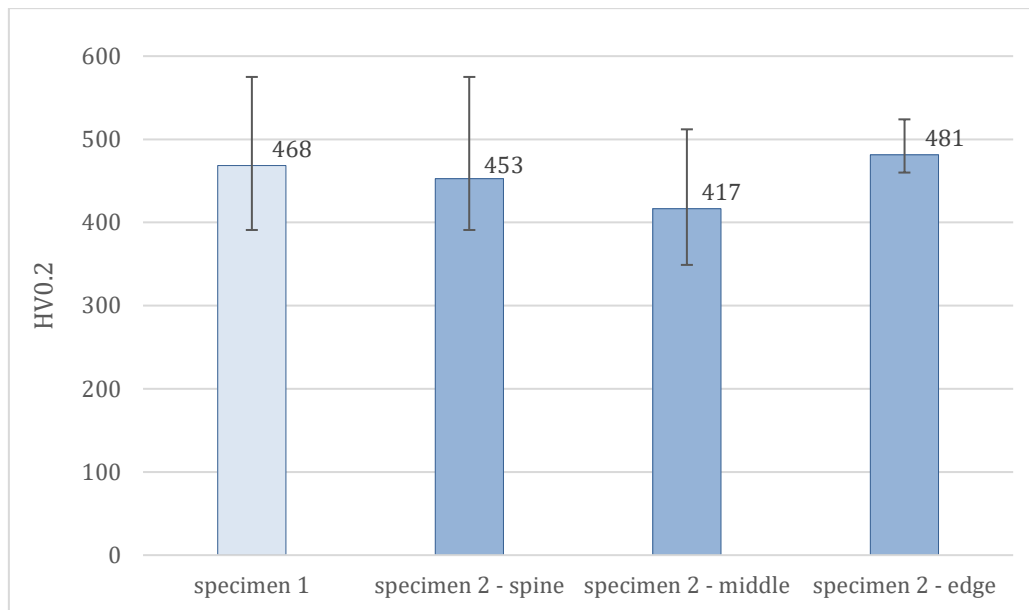


Fig. 10: Microhardness HV0.2

4. CONCLUSION

Based on the conducted tests and analysis of the results obtained, the following can be concluded:

- Analysis of the chemical composition revealed that the machete is made of low-alloy spring steel 55Cr3.
- The microstructure of the material before forging consists of martensite and bainite. The mean microhardness value in the cross-section was 468 HV0.2.
- The microstructure of the forged machete, in cross-section, consists of martensite, bainite and carbides precipitated at the crystal grain boundaries. Volume fractions of martensite and bainite are different in certain parts of the cross-section of the machete.
- There is a noticeable difference in the degree of deformation of the microstructure in different parts of the machete, which occurs due to the different intensities of forging.
- The differences in the microstructure and the degree of deformation were reflected in the microhardness in different parts of the machete. The highest mean microhardness value was at the edge of the machete (481 HV0.2), while the lowest mean microhardness value was in the middle of the machete (417 HV0.2).

REFERENCES

- [1] Rathi MG, Jakhade NA. An Overview of Forging Processes with Their Defects. International Journal of Scientific and Research Publications 2014;4.
- [2] Gao Z, Grandhi R V. Microstructure optimization in design of forging processes. vol. 40. 2000.

- [3] Rasouli D, Khameneh Asl S, Akbarzadeh A, Daneshi GH. Effect of cooling rate on the microstructure and mechanical properties of microalloyed forging steel. *J Mater Process Technol* 2008;206:92–8.
- [4] Levin AA, Meyer DC, Reibold M, Kochmann W, Pätzke N, Paufler P. Microstructure of a genuine Damascus sabre. *Crystal Research and Technology* 2005;40:905–16.
- [5] Wadsworth J. Damascus steels: history, processing, properties and carbon dating. *Indian Journal of History of Science*; v 42(4); p 533-558 n.d.
- [6] Matsumoto C, Das AK, Ohba T, Morito S, Hayashi T, Takami G. Characteristics of Japanese sword produced from tatara steel. *J Alloys Compd* 2013;577.
- [7] Matjeke VJ, van der Merwe JW, Vithi NL. Determination of critical transformation temperatures for the optimisation of spring steel heat treatment processes. *Metals (Basel)* 2021;11.



ELECTRON-BEAM PROCESSING OF METALS AND ALLOYS – TECHNIQUES AND TRENDS

Stefan Valkov^{1,2}, Dimitar Dichev¹, Maria Ormanova², Iliya Zhelezarov¹

¹ Technical University of Gabrovo, 4 H. Dimitar Str., 5300 Gabrovo, Bulgaria

² Institute of Electronics, Bulgarian Academy of Sciences, 72 Tzarigradsko Chausse Blvd, 1784 Sofia, Bulgaria

Abstract

The electron-beam technologies have been widely used for the processing of metals and alloys. These methods are known as accurate and efficient and are characterized by many advantages in comparison with the conventional ones, such as uniform distribution of the energy of the electron beam, very short process time, precise control of the beam parameters, etc. Currently, modern trends in the processing of metals and alloys are based on the combination of electron-beam technologies with other methods, such as thin film deposition, etc. These techniques result in a significant improvement in the functional properties of the materials which can be involved in new fields of modern industry. This paper aims to summarize the topics related to welding, surface treatment and modification of metals and alloys, and physical vapor deposition of thin films and coatings by electron-beam technologies. In this work, the development and growth of electron-beam processing techniques for surface treatment, and alloying are considered in detail. The benefits of these technologies, as well as their combination with other methods, are extensively discussed.

Keywords: *Electron-beam processing, metals and alloys, electron-beam surface treatment, electron-beam welding, electron-beam physical vapor deposition.*

1. Introduction

Currently, the fabrication of new materials with enhanced functional properties is of major importance for the modern industry. The implementation of new technologies for their development, as well as for the modification of the structure and functional properties of modern materials is expected to open new applications in a number of industrial branches, such as aerospace, aircraft, automotive, railway, and other industries [1-4]. The electron-beam methods and techniques for developing new materials, as well as for the modification of their structure and properties are currently considered very promising due to their low cost in comparison to the conventional technologies, very short process time, very high reproducibility of the applied technological conditions, uniform distribution of the energy of the electron beam, etc. [5]. At these technologies, a thermal distribution from the surface to the bulk is formed due to the transformation of the kinetic energy of the electrons into heat. It is very important to note that the heating

and cooling rates are quite high (10^4 - 10^5 K/s for continuous and 10^7 - 10^8 K for pulsed mode), leading to transformations of the structure and improvement of the functional properties of the materials. Currently, the techniques for electron-beam treatment can be used for different types of modification of the surface of metallic materials, namely electron-beam surface hardening, combined technique for hardening of the surface, electron-beam surface alloying, and others [6]. These types of modification strongly depend on the requirements that the properties of a certain metal and alloy to be improved in a specific way, for example, hardening, corrosion properties enhancement, etc. Figure 1 presents a machine for electron-beam surface treatment (Evobeam cube 400) available on the territory of the Technical University of Gabrovo.



Fig. 1: An image of electron-beam treatment equipment at the Technical University of Gabrovo

In this paper, the topics related to surface modification by an electron-beam treatment are summarized and a discussion about the techniques and trends for the enhancement of the functional properties of metals and alloys is presented. Special attention is paid to surface modification in continuous mode.

2. Heat processes

At these technologies, of major importance are the energy parameters, namely the accelerating voltage (U) [V], the current of the electron beam (I) [mA], the diameter of the electron beam (d), and the input energy density (E), which can be expressed by (1)

$$E = \frac{U \cdot I \cdot t}{S}$$

In (1) E is the input energy density [J/mm^2]; t is the irradiation time [s]; S is the irradiated area [mm^2]. The electron beam scanning frequency (f [Hz]) and the speed of the motion of the specimen (v [mm/s]) are also of major importance for the resultant structure and properties of the processed material [6, 7]. A typical scheme of electron-beam equipment for surface modification is presented in Figure 2. The electron beam is generated by an electron gun. The emitted electrons from the electron source are accelerated and stacked into a beam by the accelerating and focusing electric fields. Afterward, the beam is focused via the focusing lenses and deflecting coils, passes to the working chamber, and is guided to the surface of the processed sample.

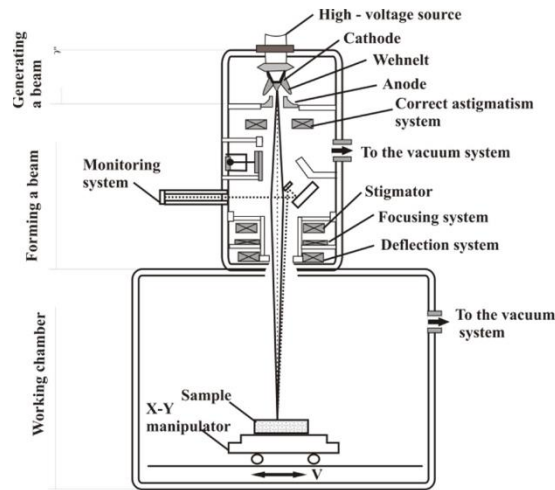


Fig. 2: A scheme of electron-beam treatment equipment [6]

Considering the continuous wave process, the treatment and modification of the structure and properties of different metals and alloys is realized by surface scanning. During the experimental procedure, the electrons can be deflected from the axis of normal distribution of the beam and different manners of scanning can be realized, namely linear, circular, elliptical, infinity, triangular, parabolical, and others. Figure 3 shows some examples of scanning geometries that can be realized during the electron-beam treatment experiments. The use of a linear manner of scanning (Figure 3a) leads to a significantly higher cooling rate in comparison with the circular or elliptical one. At the same time, the application of circular geometry (Figure 3b) leads to an increase in the lifetime of the molten material of the treated surface. This leads to a much more homogeneous distribution of alloying elements inside the molten material and is widely used for the formation and fabrication of surface alloys which are characterized by much better properties in comparison to the base substrate materials. The use of more complex figures leads to a redistribution of the kinetic energy of the electrons and the thermal field formed from the surface to the bulk will be more complex as well. Below are given some examples of different approaches for surface modification, such as hardening, formation of surface alloys, combined methods, etc. [6].

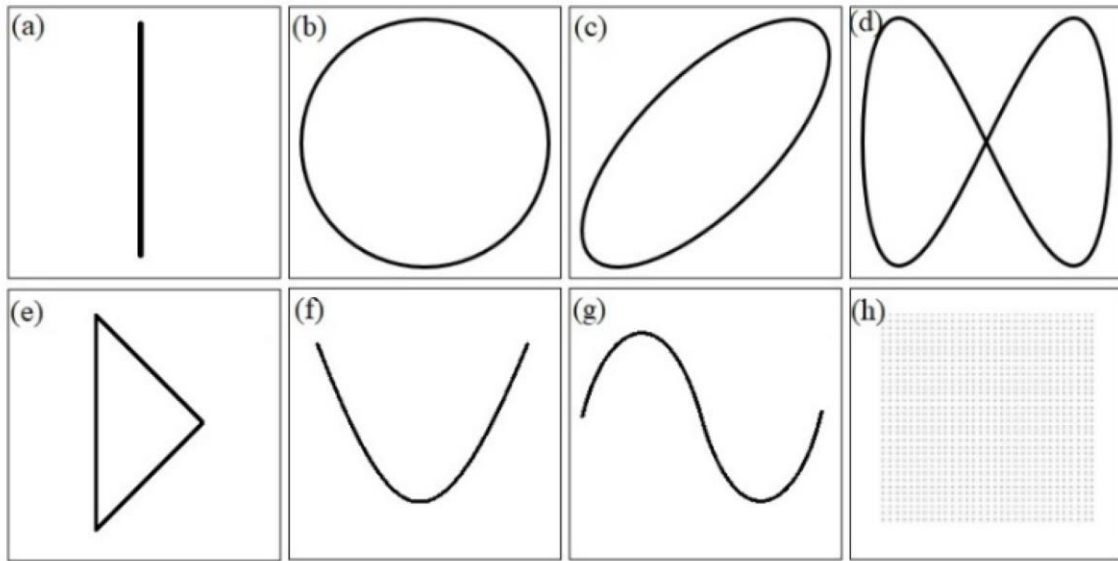


Fig. 3: Electron-beam scanning figures. (a) Line; (b) circle; (c) ellipse; (d) infinity; (e) triangle; (f) parable; (g) sine; (h) matrix. [6]

The authors of [8] have investigated the influence of different process parameters during the electron-beam surface modification technique on the formation of the thermal field, as well as the distribution of the heat from the surface to the bulk. The results showed that at a constant power of the electron beam and scanning frequency, the lower velocity of motion of the sample during the electron-beam treatment experiment leads to the formation increase in the surface temperature. However, the speed of the specimen motion during the modification process influences the thermal field very weakly. Also, the same authors [8] found that the increase in the beam power leads to the formation of a modified zone with higher thickness. The influence of the electron beam scanning frequency on the surface temperature and the depth of the modified zone was also studied. It was found that at higher values of electron beam scanning frequency, the temperature and depth of the treated zone are lower. These results are obtained on the basis of numerical modeling where the heat-transfer equation has been solved for various technological conditions and the solutions have been expressed by three-dimensional Green's function. Afterward, the numerical results were experimentally verified, and it was found that they are in good agreement with the experimental data [8].

3. Application of the electron-beam modification technology for a surface hardening

Electron beam surface hardening is widely used for the improvement of the surface properties of different metals and alloys. In this technology, the surface of the modified material is irradiated by the electron beam where of major importance is the very high cooling rate, leading to a significantly finer microstructure and improved functional properties.

In Ref. [9] the possibility of hardening 5CrMoMn steel by a scanning electron beam was studied where the current of the flux of the accelerated electrons was varied. It was found that at a beam current of 7 mA, the hardness rises about two times. By further

increase of the current of the electron beam, the hardness decreases due to the reduced amount of carbon and martensite. The authors of [9] concluded that the optimal functional properties and surface roughness were achieved at the electron-beam treatment with a beam current of 7 mA.

The authors of [10] have studied the possibility of a surface hardening of 30CrMnSiA as a function of the input energy density. The microstructure of the modified zones was studied in detail, and it was found that it is mostly in the form of martensite. The results showed that the highest values were achieved at an input energy density of 1.875 kJ/mm².

It should be noted that titanium and Ti-based alloys are also important for modern industry and are widely used in the aircraft and automotive industries, etc. due to their lightweight and attractive mechanical and corrosion properties. However, these materials are characterized by low hardness, and therefore, the hardening of the surface will open new potential practical applications for these alloys. The authors of [11] have investigated the possibilities of electron beam hardening of TA2 titanium-based alloy. The results showed that the surface roughness decreases after the application of the treatment procedure. Also, the nanohardness increases due to the grain refinement and a rise in the dislocation density.

In Ref. [12] the electron-beam surface treatment of TA15 titanium alloys was performed. It was found that the treatment procedure leads to the formation of a significantly finer microstructure and the hardness increases gradually. The thickness of the modified area was established to be 25 μm where a gradient in the hardness was observed.

4. Combined methods

The combined methods for surface hardening and modification are currently a subject of investigation by many researchers. These methods combine two or more methods, such as electron-beam treatment, plasma nitriding, thin film deposition, etc. The main idea is to combine the advantages of all methods used. The authors of [13] investigated the improvement of the surface properties of 40X steel by plasma nitriding and subsequent electron-beam treatment. It was found that the hardness of the modified specimen is three times higher than that of the base material. Also, the combination of both techniques, namely plasma nitriding and electron-beam treatment has led to an increase in the wear resistance of more than two times than the case of modification only by plasma nitriding.

Similarly, the combination of plasma nitriding and electron-beam treatment, as well as electron-beam treatment followed by plasma nitriding of tool steel, has been presented by the authors of [14] and the results for the hardness were compared to those obtained for single-step modification of plasma nitriding. It was found that the plasma nitriding procedure leads to an increase in the microhardness of the tool steel. However, the application of subsequent electron-beam treatment leads to a further increase in the above-mentioned mechanical characteristic by about 20%. The combination of electron-beam treatment followed by plasma nitriding has led to the highest value of the microhardness of more than 1200 HV.

The authors of [15] have shown the combination of plasma nitriding, electron-beam treatment, and deposition of CrN film on the top of tool steel. The combination of the plasma nitriding and electron-beam surface modification has led to the formation of a

nitrogen-rich layer which is characterized by martensitic microstructure. The measured microhardness was higher than that of the specimen subjected to a single treatment of plasma nitriding. The application of the CrN layer led to a further increase in the microhardness on the surface of the tool steel.

It should be noted that the combination of two or more methods and techniques, based on electron-beam treatment, for surface modification is currently the last step for controlling and improving the surface structure and functional properties of metallic materials. The performed literature review shows that such combinations lead to a significant improvement in the functional properties of metallic materials, particularly in microhardness. For this reason, the combination of more than one technique for surface modification can be considered as a leading technology and the number of researchers that are working on this topic grows rapidly.

5. Electron-beam surface alloying

The process of alloying the surface by a scanning electron beam is based on the intensively melting of the surface and the introduction of alloying elements within the molten material. After the solidification of the molten material, a surface alloy with significantly improved surface properties is formed.

S. Valkov et al. [16-18] have studied the possibility of alloying Al substrate with Ti and Nb. For the purposes of this research, on commercially pure Al substrates Ti and Nb films with thicknesses of 2 μm for each layer have been deposited by DC magnetron sputtering. Afterwards, the specimens were subjected to electron-beam surface alloying where the influence of the speed of the specimen motion during the treatment procedure on the structure and properties of the obtained surface alloys was studied. Two experiments were realized where the velocity was 5 and 10 mm/s. The results showed that the measured microhardness of the formed surface alloys in the system of Al-Ti-Nb reached values of about 800 HV, which is more than 20 times higher than that of the base Al substrate. It was found that the microstructure is much more homogeneous in the case of the lower speed of the specimen motion than that of the specimen fabricated by the higher one. Figure 4 shows the obtained microstructure via both speeds of the sample's motion, namely 5 and 10 mm/s. The same authors of [16-18] performed a detailed discussion on the processes occurring during the experiments and concluded that the incorporation and homogeneously distribution of alloying elements within the molten material at electron beam welding is based on the convection flows caused by the high-temperature gradient within the molten material. It was established that these flows are much more intensive in the case of the lower velocity of movement of the samples. In this case, the surface temperature is higher, leading to a greater thermal gradient within the molten material.

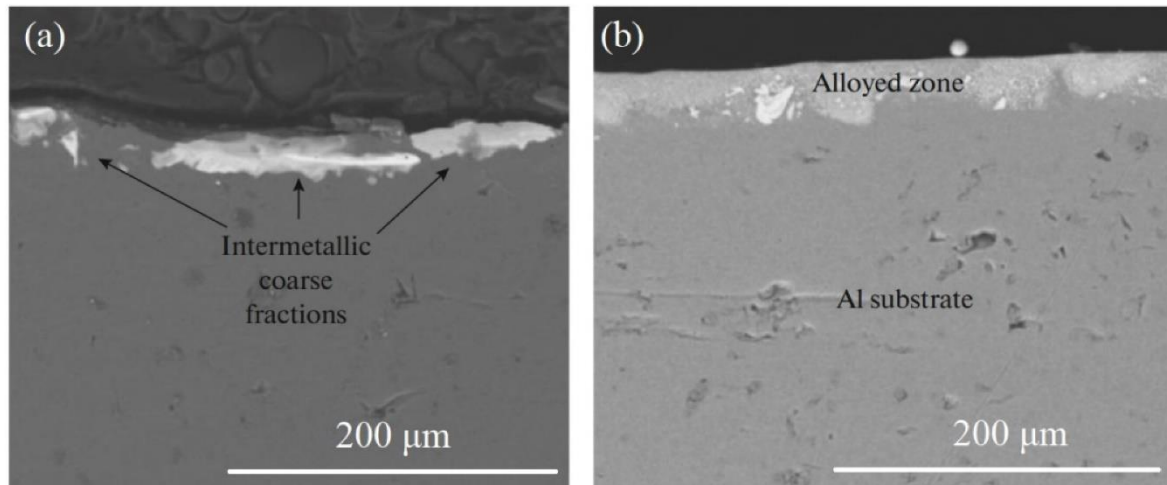


Fig. 4: Cross-sectional SEM images of Al-Ti-Nb surface alloys, formed by electron-beam surface alloying with (a) higher and (b) lower speed of specimen motion. [6, 17]

The authors of [19] have shown the formation of composite Ti/TiC layers by the electron-beam surface modification technique, including alloying (for incorporation of the C powder) and remelting (for the homogenization of the resultant microstructure) of C powder with Ti substrate. During the remelting procedure, two speeds of the movement of the specimens have been chosen, namely 5 and 15 mm/s. The investigated microstructure of the formed surface alloys shows that in both considered cases, it is in the form of a double-phase structure of fine TiC particles dispersed within the base Ti matrix. In the case of the lower speed of the specimen's motion, the particles are finer and much more homogeneously distributed than that of the formed surface layer by the higher speed of the specimen motion. Figure 5 shows the microstructure of the obtained composite surface alloys. Figures 5a and c show lower magnification of the formed surface alloys, while Figures 5 b and d show higher magnification of the structure. It was found that the lower speed motion of the specimens leads to higher values of the measured microhardness of about 2.5 times higher than that of the base Ti substrate. The application of the higher speed movement of the specimens leads to about 1.8 times increased microhardness in comparison to that of the base Ti material.

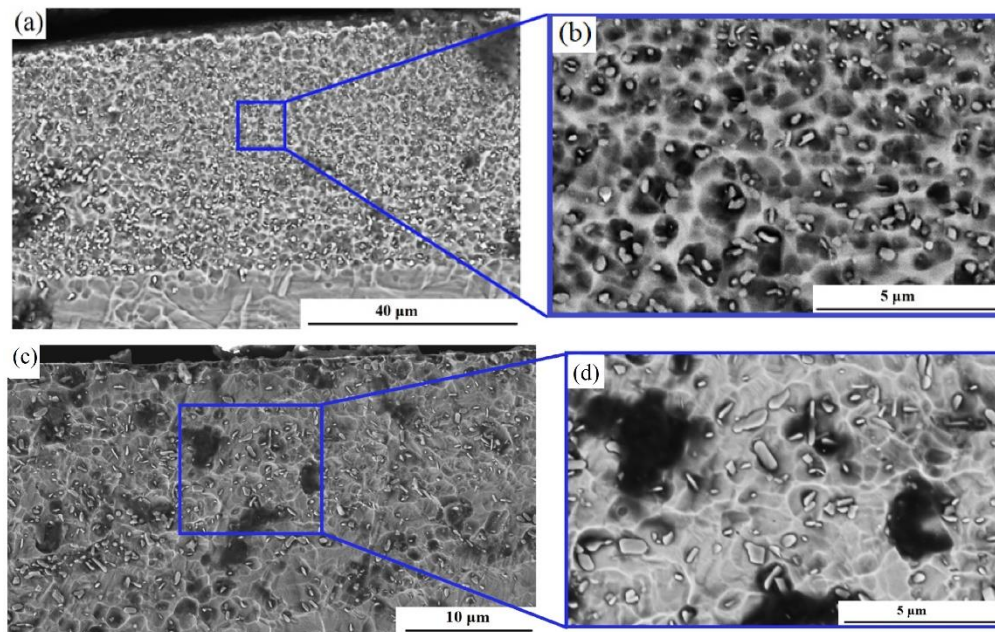


Fig. 5: A cross-sectional SEM image of the specimen alloyed by the speed motion of 5 mm/s: (a) lower magnification; (b) higher magnification and 15 mm/s (c) lower magnification; (d) higher magnification. [19]

It should be noted that the electron-beam surface alloying technique has a lot of applications for the improvement of the surface properties of metallic materials, particularly of Ti, Al, and their alloys. The comparison of the improvement in the surface properties of the metallic materials by electron-beam surface hardening vs alloying, the first approach leads to an improvement in the properties of the materials in the range from 20% to 40%, while the alloying approach leads to an enhancement of the mechanical properties of more than 20 times. It should be noted that the alloying approach is much more appropriate for metallic materials which are characterized by low density and weight, such as Ti and Al-based alloys.

(1)

6. CONCLUSION

This article summarizes the basics and current results of the electron-beam surface treatment and modification of metals and alloys. The basics, principles, and current results of electron-beam surface hardening, the combination of two or more methods based on the electron-beam treatment techniques, as well as the alloying approach were considered in detail. It was demonstrated that these techniques lead to a significant improvement in the functional properties of different metals and alloys and can find new practical applications in many industrial branches, such as aerospace, aircraft, automotive, railway, and other industries. The results obtained on these topics show that the functional characteristics of the metallic materials can be enhanced from about 20% to more than 20 times. This makes these techniques significantly more effective than the conventional methods. The current trends in electron-beam technologies for surface treatment and modification are based on the optimization of the technological conditions, corresponding structure, and properties of the processed materials. Moreover, their

implementation of new industrial branches is of major importance for the enhancement of human life. For this reason, some machines for electron-beam treatment are already installed in many industrial factories, and their number increases gradually every year.

Acknowledgement(s):

This research was funded by the Project of OP “Science and Education for Smart Growth”, “Creation and development of centres of competence”-**BG05M2OP001-1.002-0023-C01** “INTELLIGENT MECHATRONICS, ECO- AND ENERGY- SAVING SYSTEMS AND TECHNOLOGIES” (IMEEST).

REFERENCES

- [1] Yusuf S., Cutler S., Gao N., Review: The Impact of Metal Additive Manufacturing on the Aerospace Industry, *Metals*, 9, 1286, (2019).
- [2] Portoles L., Jorda O., Jorda L., Uriondo A., Esperson-Miguez, M.; Perinpanayagam, S. A qualification procedure to manufacture and repair aerospace parts with electron beam melting, *J. Manuf. Syst.*, 41, 65–75, (2016).
- [3] Juechter V., Franke M., Merend, T., Stich A., Korner C., Singer R., Additive manufacturing of Ti-45Al-4Nb-C by selective electron beam melting for automotive applications, *Addit. Manuf.*, 22, 118–126, (2018).
- [4] Murr L., Gaytan S., Ceytan A., Martinez E., Martinez J., Hernandez D., Machado B., Ramirez D., Medina F., Collins, S., et al. Characterization of titanium aluminide alloy components fabricated by additive manufacturing using electron beam melting, *Acta Mater.*, 58, 1887–1894, (2010).
- [5] Weglowski M., Blacha S., Philips A., Electron beam welding-Techniques and trends-Review, *Vacuum*, 130, 72–92, (2016).
- [6] Valkov S., Ormanova M., Petrov P., Electron-Beam Surface Treatment of Metals and Alloys: Techniques and Trends, *Metals*, 10, 1219, (2020).
- [7] Bocharov A., Murygin A., Laptinok V., Calculating the geometric parameters of the distribution of electron beam energy density on its section in EBW, *IOP Conf. Ser. Mater. Sci. Eng.*, 450, 032010, (2018).
- [8] Angelov V., Ormanova M., Kaisheva D., Lazarova R., Dimitrova R., Petrov, P., Selective electron beam surface alloying of aluminum with TiCN nanoparticles, *Nucl. Instrum. Methods Phys. Res. B*, 440, 88–94, (2019).
- [9] Wei D., Wang X., Wang R., Cui H., Surface modification of 5CrMnMo steel with continuous scanning electron beam process, *Vacuum*, 149, 118–123, (2018).
- [10] Fu Y., Hu J., Shen X., Wang Y., Zhao W., Surface hardening of 30CrMnSiA steel using continuous electron beam, *Nucl. Instrum. Methods Phys. Res. B* 2017, 410, 207–214.
- [11] Gao Y., Surface modification of TA2 pure titanium by low energy high current pulsed electron beam treatments, *Appl. Surf. Sci.*, 257, 7455–7460, (2011).
- [12] Gao Y., Influence of pulsed electron beam treatment on microstructure and properties of TA15 titanium alloy, *Appl. Surf. Sci.*, 264, 633–635, (2013).
- [13] Dimitrov D., Aprakova M., Valkanov S., Petrov P., Electron beam hardening of ion nitrided layers, *Vacuum*, 49, 239–246, (1998).
- [14] Zenker R., Electron meets nitrogen: Combination of electron beam hardening and nitriding, *Int. Heat Treat. Surf. Eng.*, 3, 141–146, (2009).
- [15] Grumbt G., Zenker R., Spies H., Franke R., Haase I., Improvement of the wear behaviour of highly-loaded components and tools by multi-combined surface treatment, *Mater. Eng.*, 21, 1–10, (2014).
- [16] Valkov S., Petrov P., Lazarova R., Bezdushnyi R., Dechev D., Formation and characterization of Al–Ti–Nb alloys by electron-beam surface alloying, *Appl. Surf. Sci.*, 389, 768–774, (2016).
- [17] Valkov S., Neov D., Bezdushnyi R., Beskrovnyi A., Kozlenko D., Petrov P., Study of the Microstructure, Crystallographic Structure and Thermal Stability of Al–Ti–Nb Alloys

Produced by Selective Electron Beam Alloying, J. Surf. Investig. X-ray Synchrotron Neutron Tech., 12, 436–441, (2018).

[18] Valkov S., Petrov P., Electron beam additive manufacturing of light metals, Journal of the Technical University of Gabrovo, 59, 17-19, (2019)

[19] Valkov S., Nedeva D., Dunchev V., Padikova F., Ormanova M., Stoyanov B., Nedyalkov N., Fabrication and Characterization of Ti/TiC Composite Layers by an Electron-Beam Surface Modification. Coatings, 13, 951, (2023).

PRIMJENA VISKOELASTIČNIH PREVLAKA NA BAZI POLIIZOBUTENA

APPLICATION OF VISCOELASTIC COATINGS BASED ON POLYISOBUTENE

Sven Radimiri

Feromihin d.o.o., Moslavačka 22, 10315 Novoselec, HR

Sažetak

Postojeće metode zaštite cjevovoda, iako štite tisuće kilometara cjevovoda, pokazuju određene nedostatke, što otvara prostor za inovativna rješenja na području zaštite od korozije. Konvencionalni sustavi bazirani su na materijalima s kemijski umreženim strukturama. Inovativni sustavi kreirani su na upravo suprotnome: neumreženoj amorfnoj viskoelastičnoj strukturi. Kao najadekvatiji polimer koji zadovoljava postavljene zahtjeve pokazao se poliizobuten. Strukturne jedinice poliizobutena povezane su kovalentnim vezama, a polimerni lanac se ne umrežuje što dovodi do tzv. „hladnog toka“, zbog čega će poliizobuten vremenom ispuniti i najsitnije pore na površini materijala. Materijali na bazi poliizobutena će kroz cijeli radni vijek ostati u polu-tekućem stanju s jakim adhezijskim silama na površinu. Istovremeno ostaje otporan na starenje i utjecaj kemikalija te nepropustan za vlagu, kisik i bakterije. Materijali na bazi poliizobutena osiguravaju dulji radni vijek, smanjenje troškova održavanja, najvišu razinu zaštite od korozije te bržu, jednostavniju i jeftiniju pripremu površine i aplikaciju sustava.

Ključne riječi: viskoelastični sustavi za zaštitu od korozije, poliizobuten

Abstract

Existing methods of pipeline protection, although they protect thousands of kilometers of pipelines, show certain shortcomings, which opens up space for innovative solutions in the field of corrosion protection. Conventional systems are based on materials with chemically cross-linked structures. Innovative systems are created on the exact opposite: a non-crosslinked amorphous viscoelastic structure. Polyisobutene proved to be the most adequate polymer that meets the set requirements. The structural units of polyisobutene are connected by covalent bonds, and the polymer chain does not cross-link, leading to "cold flow", which is why polyisobutene will eventually fill even the smallest pores on the surface. Polyisobutene-based materials will remain in a semi-liquid state throughout their entire working life with strong adhesion forces to the surface. At the same time, it remains resistant to aging and the chemicals and is impervious to moisture, oxygen and bacteria. Materials based on polyisobutene ensure a longer service life, lower maintenance costs, the highest level of corrosion protection, and faster, simpler and cheaper surface preparation and system application.

Keywords: viscoelastic corrosion protection system, polyisobutene

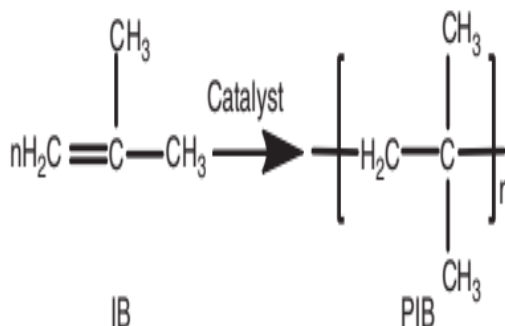
1. UVOD

Postojeći sustavi cjevovoda, kao i sustavi u izgradnji zahtijevaju moderne programe održavanja i zaštite od korozije u cilju produljenja intervala održavanja i osiguravanja pouzdanih i održivih operacija. Konvencionalne metode zaštite cjevovoda, iako štite tisuće kilometara cjevovoda, pokazuju određene nedostatke, što otvara prostor za inovativna rješenja na području zaštite od korozije. Takvi sustavi bazirani su na materijalima s kemijski umreženim strukturama. Inovativni sustavi kreirani su na upravo suprotnome: neumreženoj amorfnoj viskoelastičnoj strukturi. Kao najadekvantiji polimer koji zadovoljava postavljene zahtjeve pokazao se poliizobuten

2. POLIIZOBUTEN

2.1. Kemijska i fizikalna svojstva poliizobutena

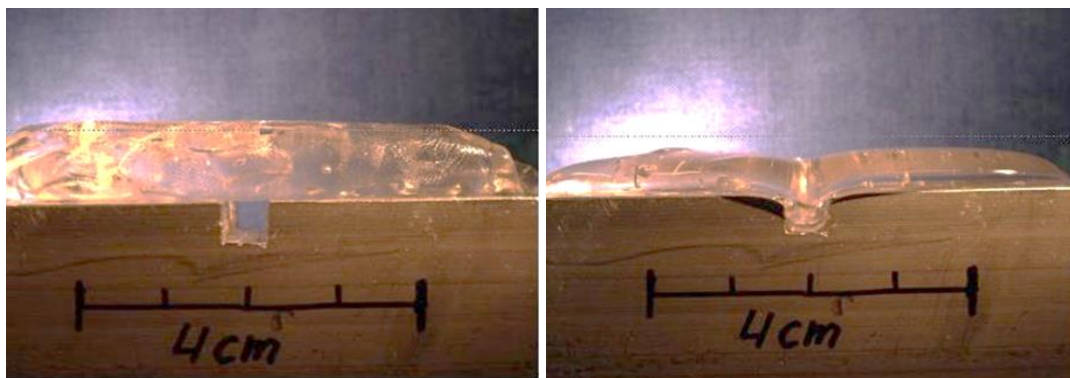
Polimerni lanac poliizobutena sastoji se od 180-650 jedinica izobutena koje su povezane samo kovalentnim vezama, a polimer se sastoji od samo dva elementa: vodika i ugljika. Polimerni lanac poliizobutena ostaje neumrežen i tijekom cijelog životnog vijeka ostati će kao jedinstvena struktura, što dovodi do tzv. „hladnog toka“, zbog čega će poliizobuten vremenom ispuniti i najsitnije pore na površini materijala.[1]



Slika. 1: Polimerizacija izobutena (IB) u poliizobuten (PIB) [2]

Poliizobuten ima određena svojstva kao što su otpornost na starenje, kemikalije i nepropusnost za vodu, zrak i bakterije. Ta svojstva prisutna su u rasponu temperature od -45°C do +120°C. [1] Osim navedenog, PIB pokazuje i oksidacijsku stabilnost i odlična adhezijska svojstva. PIB je bezbojan do blijedo žut, elastičan viskozni materijal. Nema mirisa ni okusa i ne-toksičan je. Zbog nepolarne i visoko parafinske strukture, topiv je u alifatskim i aromatskim ugljikovodičnim otapalima, a nije topiv u polarnim otapalima. Topivost mu značajno opada s povećanjem molekularne mase polimera. Zahvaljujući amorfnim svojstvima i niskoj temperaturi staklenog prijelaza ($T_g = -62^\circ\text{C}$) PIB je vrlo fleksibilan i prionjiv na površinu.[2]

PIB se koristi u proizvodnji adheziva, agrokulturalnih kemikalija, spojeva optičkih vlakana, brtvila, folija, električnih fluida, lubrikanata, papira, aditiva za gorivo, proizvoda za osobnu njegu i kao baza za žvakaće gume.[2]



Slika. 2: Poliizobuten (PIB) [3]

Adhezijska sile materijala proporcionalne su kohezijskim silama: ukoliko se sa cjevovoda pokuša ukloniti antikorozivna zaštita u obliku omotača, na površini će uvijek ostati dio materijala u obliku zaštitnog filma.



Slika. 3: Sloj materijala koji ostaje na površini u obliku zaštitnog filma [3]

Moderni viskoelastični materijalni za zaštitu od korozije na bazi poliizobutena pružaju krajnjim korisnicima unaprijeđena fizikalna svojstva imovine čime je ulaganje u zaštitu od korozije dugotrajnije, produljuju se intervali održavanja i smanjuju ukupni troškovi, smanjuje se stopa oštećenja prilikom održavanja zahvaljujući svojstvu samozacijeljivanja, te bržu, lakšu i jeftiniju aplikaciju pošto nema potrebe za specijalnom opremom i vještinama aplikatora.[2]

2.2. Primjena prevlaka na bazi poliizobutena na terenu

Zahvaljujući svojstvima viskoznosti i jake adhezije, priprema površine metalnih cjevovoda za aplikaciju prevlaka na bazi poliizobutena je vrlo jednostavna, bitno da je čista i suha. Priprema površine abrazivom nije potrebna, već je dovoljna priprema na -razinu St2/St3 prema ISO 8501-1 s time da okujina mora biti uklonjena. Za kvalitetnu adheziju nije potreban profil površine, štoviše, što je površina manje profilirana, to će jače materijal prionuti uz površinu. Temperatura aplikacije kreće se u rasponu od -45°C do $+90^{\circ}\text{C}$ i nije ograničena materijalom već radnim uvjetima za aplikatore. Jake adhezijske

sile osiguravaju da ne dođe do pojave katodnog odvajanja ili puzanja materijala.[1]
Adhezija je trajna i nastupa odmah, bez kemijske reakcije.



Slika. 4: Priprema površine za aplikaciju [3]

Nakon što je površina pripremljena, potrebno je napraviti test prionjivosti koji je relevantan pokazatelj da je površina spremna za aplikaciju. Test se izvodi na način da se komad zaštitne trake, okvirne duljine 150 mm aplicira na pripremljenu površinu. Nakon 5 minuta potrebno je pokušati ukloniti materijal s površine pod kutem od otprilike 135° brzinom od 100mm/min. Mora doći do kohezijskog odvajanja i preostali material trebao bi pokrivati $\geq 95\%$ površine. Ukoliko test nije zadovoljavajući, potrebno je površinu dodatno očistiti. Također, prije aplikacije potrebno je izmjeriti točku rosišta, kako bi se izbjegla mogućnost kondenzacije na površini cjevovoda. Aplikaciji se može pristupiti kada je temperatura površine minimalno 3°C iznad točke rosišta.

Nakon aplikacije sloja trake za zaštitu od korozije, pristupa se ispitivanju neprobojnosti ("Holiday test") na 15 kV. Ukoliko su rezultati zadovoljavajući odmah je moguće pristupiti aplikaciji drugog sloja trake koji služi kao mehanička zaštita. Po završetku aplikacije radi se vizualna kontrola, i u slučaju da su rezultati prihvatljivi, odmah je moguće pristupiti zatrpavanju, ukoliko se radi o ukopanom cjevovodu. Time se štedi vrijeme potrebno za aplikaciju.



Slika. 5: Aplikacija sustava za zaštitu od korozije [3]

Materijali za zaštitu od korozije na bazi poliizobutena najčešće su u obliku traka koje se namataju na cjevovode. Osim traka, takvi materijali mogu doći i u drugim oblicima, kao što su smjese koje je moguće oblikovati, tako da primjena takvih prevlaka nije ograničena samo na cjevovode, već je na gotovo isti način moguće od korozije zaštititi i razne nepravilne oblike kao što su slavine, t-komadi, prirubnice i dr.

2.3. Ekološki i sigurnosni aspekti

Materijali na bazi poliizobutena su netoksični i ne sadržavaju hlapive organske spojeve. Prilikom aplikacije ne dolazi do stvaranja buke, prašine, vibracija niti štetnih emisija. Materijal je pakiran u kartonskoj ambalaži s plastičnim filmom koji se odvaja prilikom aplikacije, što su oboje materijali koje je moguće reciklirati.

3. ZAKLJUČAK

Potreba za unaprijeđenjem sustava za zaštitu od korozije cjevovoda doprinjela je razvoju novih sustava zaštite, koji osim što imaju dulji radni vijek, omogućuju krajnjim korisnicima smanjenje troškova zbog duljih intervala održavanja te jednostavne i brze aplikacije (posljedično manje radnih sati opreme i djelatnika). Također, takvi materijali puno su ekološki prihvatljiviji, čemu se danas pridaje posebna pažnja, te nisu štetni niti za ljude koji njima manipuliraju, niti za okoliš, zbog čega su takva rješenja vrlo zanimljiva krajnjim korisnicima.

Sve češćom primjenom viskoelastičnih prevlaka javila se i potreba za standardizacijom istih, pa je u posljednjem izdanju standarda ISO 21809-3:2106 uvršteno poglavlje 13. "Non-crystalline low-viscosity polyolefin based coatings", što će sigurno doprinjeti razvoju inovativnih rješenja na području zaštite od korozije.

REFERENCE

- [1] Doddema JF, drs., "The use of visco-elastic self-healing pipeline coating", CORROSION 2010, San Antonio, Texas, March 2010., Paper Number NACE-10042
- [2] V. Lebedeva O., Willenbacher N., "Polyisobutene-Based Pressure-Sensitive Adhesives", University of Karlsruhe, 2008.
- [3] Huizing B., "STOPAQ Application Manual", 2nd Edition, Stopaq BV, Stadskanaal, NL, 2022.
- [4] <https://www.sealforlife.com/brands/stopaq/> consulted on 13 Jul 2023

OCJENA KVALITETE SUSTAVA ZAŠTITE OD KOROZIJE U EKSPLOATACIJSKIM UVJETIMA U INDUSTRIJI

QUALITY EVALUATION OF CORROSION PROTECTIVE SYSTEMS IN EXPLOITATION CONDITIONS IN INDUSTRY

Zoran Čeralinac, Tomislav Karažija, Dijana Vrsaljko

¹ KONČAR - Institut za elektrotehniku d.o.o., Fallerovo šetalište 22, 10 000 Zagreb, Hrvatska

¹ KONČAR - Electrical Engineering Institute Ltd., Fallerovo šetalište 22, 10 000 Zagreb, Croatia

Sažetak

Prilikom odabira odgovarajućeg sustava zaštite od korozije, kod industrijskih proizvoda, potrebno je uzeti u razmatranje klasu korozivnosti, vrstu materijala koji treba zaštititi te traženu trajnost sustava, kako bi se osiguralo najekonomičnije i tehnički najbolje rješenje za opterećenje u eksploataciji uslijed djelovanja korozivski agresivnog okoliša. Zbog navedenih zahtjeva od velike važnosti je laboratorijska provjera sustava zaštite od korozije, odnosno provedba ispitivanja simulacijom realnih uvjeta u eksploataciji. U radu će biti prikazana analiza rezultata ispitivanja provedenog za klasu korozivnosti okoliša C5 za dugi vijek trajnosti sustava zaštite od korozije (15-25 godina trajnosti) prema cikličkom programu ubrzanog starenja, odnosno ubrzanog utjecaja korozivskog okoliša, kombinacijom utjecaja suhe topline i UV zračenja, utjecaja slane magle te utjecaja snižene temperature u ukupnom trajanju od 1680 sati. Ispitivanja su provedena na različitim vrstama sustava zaštite od korozije apliciranim na različite supstrate: metalne prevlake cinka na podlozi od čelika, metalne prevlake srebra na podlozi od bakra, organski premazi na metalnoj prevlaci od cinka na podlozi od čelika i na podlozi od aluminijske, organski premazi na spojnim i kontaktnim mjestima komponenti izrađenih od aluminijske i nehrđajućeg čelika.

Ključne riječi: *sustav zaštite od korozije, organski premazi, metalne prevlake, cikličko ubrzano ispitivanje utjecaja okoliša.*

Abstract

When choosing an appropriate corrosion protection system for industrial products, it is necessary to take into consideration the corrosivity class, the type of material to be protected, the required durability of the system to ensure the most economical and technically best solution due to the load caused by the impact of a corrosively aggressive environment. Because of the mentioned requirements, it is of great importance to check the quality of the corrosion protection system, i.e., to carry out laboratory tests by simulating real conditions in exploitation. This paper will present an analysis of the results of the test conducted for environmental corrosivity class C5 for the long life of the corrosion protection system (15-25 years of durability) according to the cyclical program of accelerated aging, i.e. the accelerated impact of a corrosive environment, through a combination of the influence of dry heat and UV radiation, the influence of salt fog and the influence of reduced temperature for a total duration of 1680 hours. Tests were performed on different types of corrosion protection systems applied to different substrates: metallic zinc coatings on a steel substrate, metallic silver coatings on a copper substrate, organic coatings on a metallic zinc coating on a steel substrate and on an aluminum substrate, organic coatings on connection and contact spots on components made from aluminium and stainless steel.

Keywords: *corrosion protection system, organic coatings, metallic coatings, cyclic accelerated environmental impact testing*

1. INTRODUCTION

Depending on various climatic exploitation conditions, properties of corrosion protection systems and materials should be defined and validated to assure quality and resistance to harsh environmental influences. Industrial products and embedded component are exposed to negative influence from atmosphere like solar radiation, high and low temperature, humidity, high and low pressure, contaminated water, and corrosion.

When choosing an appropriate corrosion protection system for industrial products, it is necessary to take into consideration the corrosivity class, the type of material to be protected and the required durability of the system to ensure the most economical and technically best solution due to the load caused by the impact of a corrosively aggressive environment. Because of the mentioned requirements, it is of great importance to validate the quality of the corrosion protection system, i.e., to carry out laboratory tests by simulating real conditions in exploitation [1], [2].

During the long working life of industry products and constant negative impacts from atmosphere abnormal events could occur. Faults that may occur during operation could be consequence of accelerated ageing of the embedded materials. To prevent negative influence from environment components and products should be made of quality materials that improve their resistance and durability. To avoid costly breakdowns, damage, minimize downtimes and extend the lifespan of various industry products, an extensive knowledge of the embedded materials as well as a specific and precise analysis is fundamental.

This paper will present result analysis of tests conducted for environmental corrosivity classes C3, C4 and C5 (15-25 years of durability range) according to the cyclical program of accelerated aging. Accelerated impact of a corrosive environment through a combination of the influence of dry heat and UV radiation, the influence of salt fog and the influence of reduced temperature for a total duration of 480, 720 and 1680 hours will be presented [3].

2. EXPERIMENTAL PROCEDURE

Experimental procedure was defined according to requirements for corrosion resistance from standard HRN EN ISO 12944-6:2018, cyclic ageing test, ANNEX B [4].

The research was carried out for environmental corrosivity classes C3, C4 and C5 with high durability of the corrosion protection system (15-25 years of durability) according to the cyclical program of accelerated aging, i.e., the accelerated impact of a corrosively aggressive environment. One test cycle consisted of three phases [5]:

- The influence of dry heat and UV radiation for a total of 30 days,
- The influence of salt fog for a total of 30 days,
- The influence of reduced temperature for a total of 10 days.

Influence of dry heat and UV radiation was performed according to the requirements from standard HRN EN ISO 4892-2 [6], Method A, Cycle 1 with Black standard temperature of +65 °C, irradiance of 60 W/m² and with periodically water spray (condensation).

Influence of salt fog was performed according to the requirements from standard HRN EN ISO 9227 [7], Method NSS test, 5% solution of NaCl at temperature of +35 °C.

Influence of reduced temperature was performed according to the requirements from standard HRN EN 60068-2-1 [8] at temperature of -20 °C.

A total of 10 test cycles were carried out for a total duration of 1680 hours, with periodical control of samples of corrosion protection systems after 480 hours and 720 hours.

A schematic representation of one test cycle lasting 7 days is shown in Figure 1.

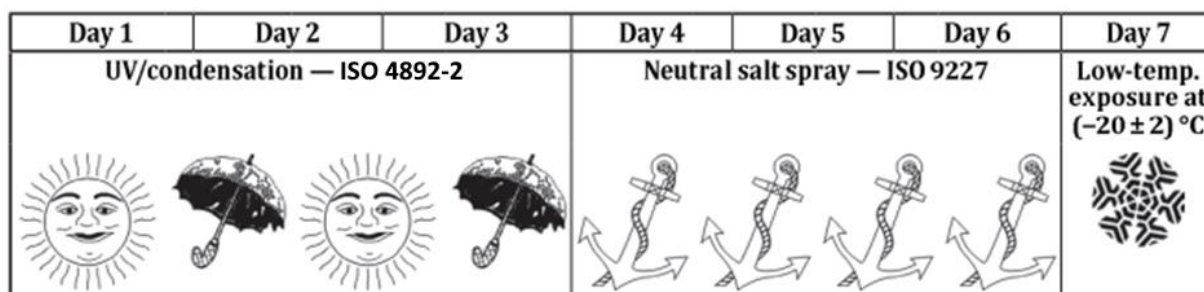


Fig. 1: One weekly test cycle according to the cyclical accelerated aging program [4].

After corrosion resistance testing all samples of corrosion protection systems were evaluated by following methods to determine their physical-chemical properties:

- Determination of the thickness of the corrosion protection system in the form of organic and metal coatings using the magnetic induction and eddy current method according to HRN EN ISO 2808 [9],
- Determination of the adhesion of organic coatings using the pull-off test method in the delivery state and after conditioning according to the instructions from standard HRN EN ISO 4624 [10],
- Determination of the adhesion of organic coatings using the cross-cut test method in the delivery state and after conditioning according to the instructions from standard HRN EN ISO 2409 [11],
- Determination of the adhesion of metal coatings using the thermal shock method according to the instructions in standards ASTM B 571 [12] and HRN EN ISO 2819 [13],
- Visual control of test samples with organic coatings to assess the degradation of the corrosion protection system in the form of blistering, rusting, cracking, and peeling according to the standards HRN EN ISO 4628-2 [14], HRN EN ISO 4628-3 [15], HRN EN ISO 4628-4 [16] and HRN EN ISO 4628-5 [17],
- Visual inspection of metal coatings after corrosion resistance testing according to the instructions from standards HRN EN ISO 10289 [18] and ASTM B 537 [19].

Corrosion resistance laboratory tests were performed on different types of corrosion protection systems applied to different substrates as follows:

- Metal zinc coatings on a steel substrate,
- Organic coatings on a zinc metal coating on a steel substrate,
- Organic coatings on a zinc metal coating on an aluminum substrate,
- Organic coatings on an aluminum substrate,
- Organic coatings on a steel substrate,

Specification of all tested corrosion protection systems are shown in Tables 1 to 5 below.

Tab. 1: Specification of corrosion protection system of metal zinc coating on steel substrate

Test system designation	Type of coating system	Total dry film thickness
Corrosion protection system 1	Hot dip metallic zinc coating	80 μm

Tab. 2: Specification of corrosion protection system of organic coating on a zinc metal coating on steel substrate

Test system designation	Type of coating system	Total dry film thickness
Corrosion protection system 2	Hot dip metallic zinc coating / Powder coating	240 μm

Tab. 3: Specification of corrosion protection systems of organic coatings on zinc metal coating on aluminium substrate

Test system designation	Type of coating system	Total dry film thickness
Corrosion protection system 3	Zinc flake coating / Epoxy coating	100 μm
Corrosion protection system 4	Zinc flake coating / Epoxy coating	60 μm

Tab. 4: Specification of corrosion protection systems of organic coatings on aluminium substrate

Test system designation	Type of coating system	Total dry film thickness
Corrosion protection system 5	<i>Without technological preparation of the aluminum substrate (washing of factory primer + application of 3 layers of coatings)</i> Epoxy primer coating / PUR coating / *AGV	60 - 90 μm
Corrosion protection system 6	<i>Sanding of the aluminum substrate (sanding of the factory primer, washing + application of 3 layers of coatings)</i> Epoxy primer coating / PUR coating / *AGV	60 - 90 μm
Corrosion protection system 7	<i>Sanding of the aluminum substrate (sanding of the factory primer, washing + application of 4 layers of coatings)</i> Wash primer / Epoxy primer coating / PUR coating / *AGV	80 - 120 μm

Note: *AGV - Anti-graphite varnish

Tab. 5: Specification of corrosion protection systems of organic coatings on steel substrate

Test system designation	Type of coating system	Total dry film thickness
Corrosion protection system 8	Zinc rich organic coating	<i>120 μm</i>
Corrosion protection system 9	Powder coating	<i>160 μm</i>
Corrosion protection system 10	Epoxy coating	<i>100 μm</i>
Corrosion protection system 11	Epoxy coating	<i>240 μm</i>

Corrosion initiation of coated structures often occurs in areas where the coating was not properly applied or suffered mechanical damage during transport and installation. This degradation provides conditions that allow corrosion initiation earlier than expected. The application process of the corrosion protection system is extremely important and should be suitable for the substrate and the environment and applied carefully [20].

The use of corrosion protection systems is essential to reach the expected service life for which a structure was designed. Different protection systems can be used to delay and mitigate corrosion initiation and its related consequences such as safety, structural integrity, and service life. A passive approach to corrosion protection involves depositing a barrier layer that prevents contact of a material with the corrosive environment. Active approaches reduce the corrosion rate when the protective barrier is already damaged and corrosive agents meet the metal substrate. Only the combination of both approaches can provide reliable protection against corrosion of metallic structures in harsh environments for the entire exploitation life [21].

3. RESULTS OF TESTING

3.1. Metal zinc coating on a steel substrate

The corrosion resistance of the corrosion protection system 1 (table 1) obtained by the hot-dip galvanizing process is 720 hours of exposure to accelerated aging by the method of cyclic corrosion testing in a chamber with salt fog, climatic chamber, and UV chamber. Adhesion of the zinc metal coating on the steel substrate after cyclic corrosion aging test determined by the thermal shock method is excellent, without cracking and peeling of the metal coating. By visual inspection of the sample surface after the corrosion resistance test, the appearance of white corrosion of zinc without the appearance of red corrosion of the steel substrate material was determined. The appearance of the samples of corrosion protection system 1 is shown in Figure 2.



Fig. 2: Metal zinc coating on a steel substrate after 720 hours of cyclic corrosion aging test on corrosion protection system 1

3.2. Organic coatings on a zinc metal coating on a steel substrate

The corrosion resistance of the corrosion protection system 2 on a steel substrate (table 2) is 1680 hours of exposure to accelerated aging by the method of cyclic corrosion testing in a salt fog chamber, climatic chamber, and UV chamber. Adhesion of the corrosion protection system 2 after cyclic corrosion aging test determined by the pull-off test method is poor with a mean value of adhesion 3,42 MPa. By visual inspection of the sample surface after the corrosion resistance test, no bubbling, cracking, or peeling of the coating was found, and no corrosion of the substrate material was observed. The appearance of the samples of corrosion protection system 2 is shown in Figure 3.



Fig. 3: Organic coatings (powder coating) on a zinc metal coating on a steel substrate after 1680 hours of cyclic corrosion aging test on corrosion protection system 2

3.3. Organic coatings on a zinc metal coating on an aluminium substrate

The corrosion resistance of the corrosion protection systems 3 and 4 (table 3) is 1680 hours of exposure to accelerated aging by the method of cyclic corrosion testing in a salt fog chamber, climatic chamber, and UV chamber. Adhesion of the corrosion protection systems 3 and 4 after cyclic corrosion aging determined by the pull-off test method is excellent. The mean value of the adhesion for corrosion protection system 3 is 17,30 MPa, and for the corrosion protection system 4 is 9,59 MPa. By visual inspection of the sample surface after the corrosion resistance test, no bubbling, cracking, or peeling of the coating was found, and no corrosion of the substrate material was observed on both

corrosion protection systems. The appearance of the samples of corrosion protection systems 3 and 4 is shown in Figure 5.



Fig. 4: Organic coatings on a zinc flake metal coating on an aluminium substrate after 1680 hours of cyclic corrosion aging test on corrosion protection system 3 (left picture) and corrosion protection system 4 (right picture)

3.4. Organic coatings on aluminum substrate

The corrosion resistance of the organic coatings on the aluminum substrate for samples of corrosion protection systems 5, 6 and 7 (table 4) is 1680 hours of exposure to accelerated aging by the cyclic corrosion test method in salt fog chamber, climatic chamber, and UV chamber. Adhesion of the organic coating on the aluminum substrate after cyclic corrosion aging, determined by the pull-off test method is good. The mean value of the adhesion for corrosion protection system 5 is 3,59 MPa, for corrosion protection system 6 is 2,42 MPa and for corrosion protection system 7 is 2,62 MPa. Adhesion of the organic coating to the aluminum substrate after cyclic corrosion aging determined by the cross-cut test method is excellent (Grade 0) for all three systems (table 4). By visual inspection of the sample surface after the corrosion resistance test, no bubbling, cracking, or peeling of the coating was found, and no corrosion of the substrate material was observed on corrosion protection systems 5, 6 and 7. The appearance of the samples of corrosion protection systems 5, 6 and 7 is shown in Figure 5.



Fig. 5: Organic coatings on aluminium substrate after 1680 hours of cyclic corrosion aging test on corrosion protection systems 5 (left picture), 6 (middle picture) and 7 (right picture)

3.5. Organic coatings on steel substrate

The corrosion resistance of corrosion protection system 8 (table 5) is 480 hours of exposure to accelerated aging by the method of cyclic corrosion testing in salt fog chamber, climatic chamber, and UV chamber. Adhesion of the zinc rich organic coating on the steel substrate after cyclic corrosion aging determined by the pull-off test method is

poor with a mean value of adhesion 3,57 MPa. By visual inspection of the sample surface no bubbling, cracking, or peeling of the coating was found, and no corrosion of the substrate material was observed. The appearance of the test samples of corrosion protection system 8 is shown in Figure 6.

*Note: * Slight corrosion is present only on edges of test samples and on edges of holes which are not taken under consideration for visual control of rusting because of sharp edge effect.*



Fig. 6: Zinc rich organic coatings on steel substrate after 480 hours of cyclic corrosion aging test on corrosion protection system 8

The corrosion resistance of the organic coating on the steel substrate for the sample of corrosion protection system 9 (table 5) is 720 hours of exposure to accelerated aging by the method of cyclic corrosion testing in salt fog chamber, climatic chamber, and UV chamber. Adhesion of the corrosion protection system 9 on the steel substrate after cyclic corrosion aging determined by the pull-off test method is poor with a mean value of adhesion 3,25 MPa. By visual inspection of the sample surface after the corrosion resistance test, no bubbling, cracking, or peeling of the coating was found, and no corrosion of the substrate material was observed. The appearance of the samples of corrosion protection system 9 is shown in Figure 7.

*Note: * Slight corrosion is present only on edges of test samples and on edges of holes which are not taken under consideration for visual control of rusting because of sharp edge effect.*

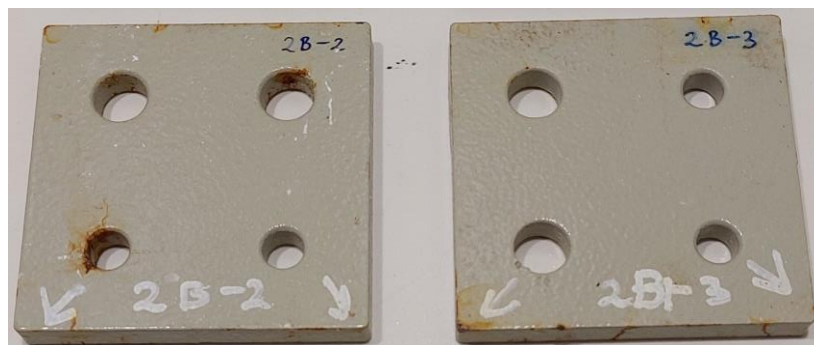


Fig. 7: Organic coatings (powder coating) on steel substrate after 720 hours of cyclic corrosion aging test on corrosion protection system 9

The corrosion resistance of the corrosion protection system 10 (table 5) is 1680 hours of exposure to accelerated aging by the method of cyclic corrosion testing in salt fog chamber, climatic chamber, and UV chamber. Adhesion of the organic coating on the steel substrate determined by the pull-off test method is excellent. The mean value of adhesion is 7,38 MPa. By visual inspection of the sample surface after the corrosion resistance test, no bubbling, cracking, or peeling of the coating was found, and no corrosion of the substrate material was observed.

The appearance of test sample of corrosion protection system 10 is shown in Figure 8.

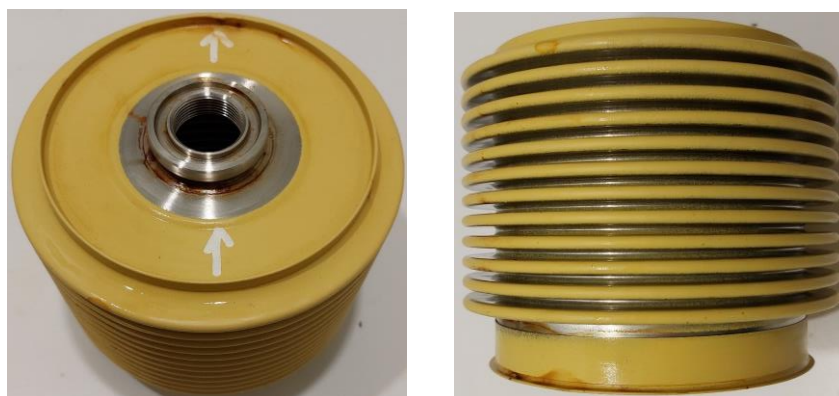


Fig. 8: Organic coatings on steel substrate after 1680 hours of cyclic corrosion aging test on corrosion protection system 10

The corrosion resistance of corrosion protection system 11 (table 5) is 1680 hours of exposure to accelerated aging by the method of cyclic corrosion testing in salt fog chamber, climatic chamber, and UV chamber. Adhesion of the organic coating on the steel substrate determined by the pull-off test method is excellent. The mean value of adhesion is 15,46 MPa. By visual inspection of the sample surface after the corrosion resistance test, no bubbling, cracking, or peeling of the coating was found, and no corrosion of the substrate material was observed. The appearance of test sample of corrosion protection system 11 is shown in Figure 9.

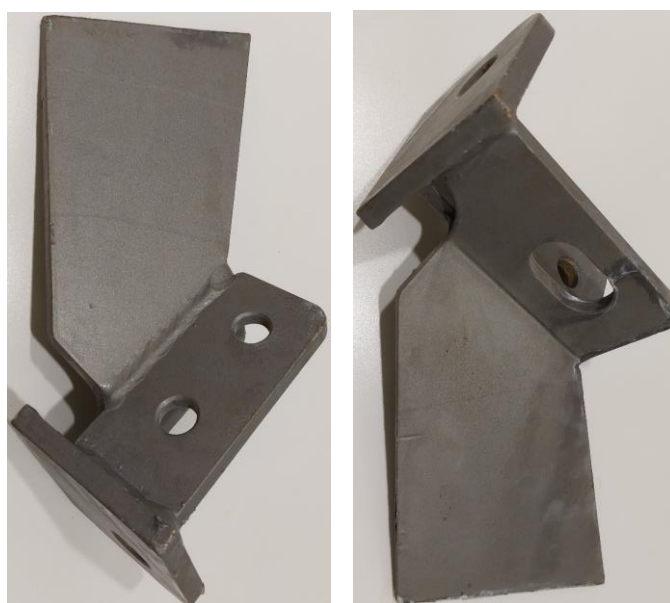


Fig. 9: Organic coatings on steel substrate after 1680 hours of cyclic corrosion aging test on corrosion protection system 11

4. CONCLUSIONS

By analyzing the obtained results of corrosion resistance testing on researched solutions of the corrosion protection systems, the following conclusions were made:

- Corrosion protection system 1 - Metallic zinc coating (hot-dip galvanizing) on a steel substrate in a thickness of 80 μm can be qualified for use in corrosion protection system for corrosivity class C4 with a long service life of 15 to 25 years,

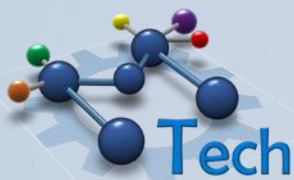
- Corrosion protection system 2 - Organic coating (powder coating) on a metallic zinc coating (hot-dip galvanizing) on a steel substrate with a total thickness of 240 μm can be qualified for use in corrosion protection system for corrosivity class C5 with a long service life of 15 to 25 years,
- Corrosion protection system 3 - Organic coating (Epoxy-primer) on a metallic Zinc flake coating on an aluminum substrate in a total thickness of 100 μm can be qualified for use in corrosion protection system for corrosivity class C5 with a long service life of 15 to 25 years,
- Corrosion protection system 4 - Organic coating (Epoxy primer) on a metallic Zinc flake coating on an aluminum substrate in a total thickness of 60 μm can be qualified for use in corrosion protection system for corrosivity class C5 with a long service life of 15 to 25 years,
- Corrosion protection system 5 - Three-layer organic coating system on an aluminum substrate in total thicknesses of 90 μm can be qualified for use in corrosion protection system for corrosivity class C5 with a long service life of 15 to 25 years,
- Corrosion protection system 6 - Three-layer organic coating system on an aluminum substrate in total thicknesses of 90 μm can be qualified for use in corrosion protection system for corrosivity class C5 with a long service life of 15 to 25 years,
- Corrosion protection system 7 - Four-layer organic coating system on an aluminum substrate in total thicknesses of 120 μm can be qualified for use in corrosion protection system for corrosivity class C5 with a long service life of 15 to 25 years,
- Corrosion protection system 8 - Zinc rich organic coating on a steel substrate with a total thickness of 120 μm can be qualified for use in corrosion protection system for corrosivity class C3 with a long service life of 15 to 25 years,
- Corrosion protection system 9 - Organic coating (powder coating) on a steel substrate with a total thickness of 160 μm can be qualified for use in corrosion protection system for corrosivity class C4 with a long service life of 15 to 25 years,
- Corrosion protection system 10 - Organic coating (Epoxy-primer, yellow color) on a stainless-steel substrate in a thickness of 100 μm can be qualified for use in corrosion protection system for corrosivity class C5 with a long service life of 15 to 25 years,
- Corrosion protection system 11 - Organic coating (Epoxy primer, gray color) on a steel substrate with a total thickness of 240 μm can be qualified for use in corrosion protection system for corrosivity class C5 with a long service life of 15 to 25 years.

Besides choosing an appropriate corrosion protection system, in accordance with the environmental conditions, and the verification of its class and durability by laboratory testing, an extremely important factor is the application process. Corrosion initiation often occurs in areas where the coating was not properly applied or suffered mechanical damage during transport and installation. Sharp and irregular edges also present corrosion initiation points. All mentioned factors provide conditions that allow corrosion initiation earlier than expected and as shown in this work, the use of proper corrosion protection system and its verification is essential to delay and mitigate corrosion initiation and to reach the expected service life of industrial products.

5. REFERENCES

- [1] T. Filetin, F. Kovačiček, J. Indof: Svojstva i primjena materijala, Sveučilišni udžbenik, Fakultet strojarstva i brodogradnje, Zagreb, (2002),
- [2] I. Juraga, V. Alar, I. Stojanović: Korozija i zaštita premazima, Sveučilišni udžbenik, Fakultet strojarstva i brodogradnje, Zagreb, (2014),

- [3] E. Stupnišek-Lisac: Korozija i zaštita konstrukcijskih materijala, Sveučilišni udžbenik, Fakultet kemijskog inženjerstva i tehnologije, Zagreb, (2007),
- [4] HRN EN ISO 12944-6, Paints and varnishes - Corrosion protection of steel structures by protective coating systems - Part 6: Laboratory performance test methods, (2018),
- [5] N. Lebozec, D. Thierry: Performance of marine and offshore paint systems: correlation of accelerated corrosion tests and field exposure on operating ships, Materials and corrosion, Volume 66, Issue 3, (2013),
- [6] HRN EN ISO 4892-2, Plastics -- Methods of exposure to laboratory light sources -- Part 2: Xenon-arc lamps, 2013,
- [7] HRN EN ISO 9227, Corrosion tests in artificial atmospheres - Salt spray tests, 2022,
- [8] HRN EN 60068-2-1, Environmental testing - Part 2-1: Tests - Test A: Cold, 2008,
- [9] HRN EN ISO 2808, Paints and varnishes - Determination of film thickness, (2019),
- [10] HRN EN ISO 4624, Paints and varnishes - Pull-off test for adhesion, (2016),
- [11] HRN EN ISO 2409, Paints and varnishes - Cross-cut test, (2020),
- [12] ASTM B571, Standard Practice for Qualitative Adhesion Testing of Metallic Coatings, (2018),
- [13] HRN EN ISO 2819, Metallic coatings on metallic substrates - Electrodeposited and chemically deposited coatings - Review of methods available for testing adhesion, (2018),
- [14] HRN EN ISO 4628-2, Paints and varnishes - Evaluation of degradation of coatings - Designation of quantity and size of defects, and of intensity of uniform changes in appearance - Part 2: Assessment of degree of blistering, (2016),
- [15] HRN EN ISO 4628-3, Paints and varnishes - Evaluation of degradation of coatings - Designation of quantity and size of defects, and of intensity of uniform changes in appearance - Part 3: Assessment of degree of rusting, (2016),
- [16] HRN EN ISO 4628-4, Paints and varnishes - Evaluation of degradation of coatings - Designation of quantity and size of defects, and of intensity of uniform changes in appearance - Part 4: Assessment of degree of cracking, (2016),
- [17] HRN EN ISO 4628-5, Paints and varnishes - Evaluation of degradation of coatings - Designation of quantity and size of defects, and of intensity of uniform changes in appearance - Part 5: Assessment of degree of flaking, (2022),
- [18] HRN EN ISO 10289, Methods for corrosion testing of metallic and other inorganic coatings on metallic substrates - Rating of test specimens and manufactured articles subjected to corrosion tests, (2001),
- [19] ASTM B537, Standard Practice for Rating of Electroplated Panels Subjected to Atmospheric Exposure, (2019),
- [20] S. J. Price, R. B. Figueira, Corrosion Protection Systems and Fatigue Corrosion in Offshore Wind Structures: Current Status and Future Perspectives, MDPI Coatings, 2017,
- [21] A. López-Ortega, Raquel Bayón J. L. Arana, Evaluation of Protective Coatings for High-Corrosivity Category Atmospheres in Offshore Applications, MDPI Materials, 2019.



PREGLED POSTUPAKA MODIFICIRANJA I PREVLAČENJA METALA

OVERVIEW OF METAL MODIFICATION AND COATING PROCESSES

Božidar Matijević¹, Mladen Stupnišek¹, Izabela Martinez¹

¹ University of Zagreb, Faculty of Mechanical Engineering and Naval Architecture, Zagreb, Croatia

Sažetak

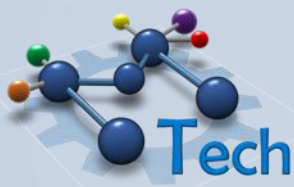
Primarni cilj inženjerstva površina je poboljšati površinska svojstva poput tvrdoće, otpornosti na trošenje i otpornosti na koroziju. Metode modificiranja i prevlačenja metalnih površina sistematizirane su na temelju fizikalnih i kemijskih principa ovih postupaka. U ovom radu opisane su temeljne zakonitosti postupaka kojima je u cilju prvenstveno povećanje otpornosti na trošenje te trenutno stanje takvih postupaka i njihova primjena. Znanstvena istraživanja i njihova praktična primjena izazov su zbog kojeg potiče dopunsko obrazovanje u području inženjerstva površina te usvajanje tehnika modifikacija i prevlačenja površina koje značajno produljuju životni vijek metalnih komponenti strojeva i alata. Nove vrste postupaka su u stalnom razvoju, čime se daje značajan doprinos podizanju kvalitete i funkcionalnosti proizvoda i povećanju ukupne učinkovitosti proizvodnje.

Ključne riječi: inženjerstvo površina, otpornost na trošenje, modificiranje, prevlačenje.

Abstract

The primary goal of surface engineering is to improve surface properties such as hardness, wear resistance, and corrosion resistance. Methods of modifying and coating metal surfaces are systematized based on the physical and chemical principles of these processes. This paper describes the basic principles of the processes whose goal is primarily to increase wear resistance, as well as the current state of such processes and their application. Scientific research and its practical application are a challenge that encourages supplementary education in the field of surface engineering and the learning of surface modification and coating techniques that significantly extend the life of metal components of machines and tools. Novel procedures are continually under development, making a significant contribution to raising the quality and functionality of products and increasing the overall efficiency of production.

Keywords: Surface Engineering, Wear Resistance, Modification, Coating.



ISTRAŽIVANJE ORGANIZACIJSKE KOMPETENTNOSTI U LABORATORIJSKOM OKRUŽENJU: HOLISTIČKI PRISTUP

EXPLORING ORGANIZATIONAL COMPETENCE IN LABORATORY ENVIRONMENT: A HOLISTIC APPROACH

Branimir Buntak, prof. dr.sc. Željko Alar

¹ Sveučilište u Zagrebu, Fakultet strojarstva i brodogradnje, I. Lučića 5, Zagreb, Hrvatska

Sažetak

Kompetentnost je temeljna komponenta koja doprinosi održivom uspjehu svake organizacije. U kontekstu laboratorijskih operacija, akreditacija od strane neovisne treće strane često potvrđuje kompetentnost laboratorija za provođenje određenih ispitivanja i zadataka. Tradicionalno, norme kao što su ISO 17025 i ISO 9000 naglašavaju kompetentnost ljudskog potencijala. Međutim, u posljednjem desetljeću, koncept organizacijske kompetentnosti stekao je na važnosti, nudeći integrativni i holistički okvir za ocjenjivanje i upravljanje kompetentnošću na razini cijele organizacije. Ovaj koncept razmatra četiri ključne domene kompetentnosti: kompetentnost ljudskog potencijala, tehničku kompetentnost, tehnološku kompetentnost i strukturnu kompetentnost. Ovaj poster ima za cilj predstaviti model organizacijske kompetentnosti, elaborirati svaku od njegovih komponenti, i istaknuti važnost holističke analize kompetentnosti u laboratorijskom okruženju u svjetlu relevantnih ISO grupe normi 9000 i 17000. Prikaz će omogućiti bolje razumijevanje kako norme i organizacijska kompetentnost zajedno doprinose postizanju izvrsnosti u laboratorijskim operacijam.

Ključne riječi: organizacijska kompetentnost, kompetentnost laboratorija

Abstract

Competence is a fundamental component contributing to the sustainable success of any organization. In the context of laboratory operations, accreditation by an independent third party often validates the competence of laboratories in conducting certain tests and tasks. Traditionally, standards such as ISO 17025 and ISO 9000 emphasize human potential competence. However, over the past decade, the concept of organizational competence has gained importance, offering an integrative and holistic framework for evaluating and managing competence at the organizational level. This concept considers four key domains of competence: human potential competence, technical competence, technological competence, and structural competence. This poster aims to present the model of organizational competence, elaborate on each of its components, and highlight the importance of holistic competence analysis in the laboratory environment in light of relevant ISO standards groups 9000 and 17000. The display will provide a better understanding of how standards and organizational competence together contribute to achieving excellence in laboratory operations.

Keywords: organisational competence, laboratory competence



INTERNATIONAL CONFERENCE ON MATERIALS heat treatment, corrosion, testing and tribology, 2023

We express our sincere gratitude to the conference sponsors for their generous support and invaluable contributions.



REPUBLIC OF CROATIA
Ministry of Science and
Education

